

Approved for public release;
distribution unlimited.

DTIC FILE COPY

AFOSR-TR-90 0743

②

PROCEEDINGS OF THE AD-A223 793 HIGH ENERGY DENSITY MATERIALS CONTRACTORS CONFERENCE

25-28 February 1990
Long Beach CA

Editors:
L. P. Davis
F. J. Wodarczyk



Air Force Office of Scientific Research
Astronautics Laboratory
Wright Research and Development Center
Air Force Systems Command

Approved for Public Release
Distribution is unlimited


DTIC
ELECTE
JUL 02 1990
S D
CO E

90 07 2 024

This report has been reviewed and is approved for publication.


FRANCIS J. WODARCZYK
Program Manager

FOR THE DIRECTOR


DONALD L. BALL
Director, Chemical and
Atmospheric Sciences

REPORT DOCUMENTATION PAGE

Form Approved
OMB No. 0704-0188

Public reporting burden for this collection of information is estimated to average 1 hour per response, including the time for reviewing instructions, searching existing data sources, gathering and maintaining the data needed, and completing and reviewing the collection of information. Send comments regarding this burden estimate or any other aspect of this collection of information, including suggestions for reducing this burden, to Washington Headquarters Services, Directorate for Information Operations and Reports, 1215 Jefferson Davis Highway, Suite 1204, Arlington, VA 22202-4302, and to the Office of Management and Budget, Paperwork Reduction Project (0704-0188), Washington, DC 20503.

1. AGENCY USE ONLY (Leave blank)		2. REPORT DATE May 1990		3. REPORT TYPE AND DATES COVERED	
4. TITLE AND SUBTITLE Proceedings of High Energy Density Materials Contractors Conference, 25-28 February 1990, Long Beach, CA				5. FUNDING NUMBERS 61102F 2303/B1	
6. AUTHOR(S) Larry P. Davis, Francis J. Wodarczyk, Editors					
7. PERFORMING ORGANIZATION NAME(S) AND ADDRESS(ES) Air Force Office of Scientific Research Building 410 Bolling AFB DC 20332-6448				8. PERFORMING ORGANIZATION REPORT NUMBER AFOSR-TR. 88 H-23	
9. SPONSORING/MONITORING AGENCY NAME(S) AND ADDRESS(ES) Air Force Office of Scientific Research Building 410 Bolling AFB DC 20332-6448 NC Dr. Wodarczyk				10. SPONSORING/MONITORING AGENCY REPORT NUMBER	
11. SUPPLEMENTARY NOTES Extended Abstracts from Fourth High Energy Density Materials Contractors Conference					
12a. DISTRIBUTION/AVAILABILITY STATEMENT Approved for Public Release: Distribution is Unlimited				12b. DISTRIBUTION CODE	
13. ABSTRACT (Maximum 200 words) This report documents presentations given by contractors and in-house researchers at the Fourth High Energy Density Materials Conference held in Long Beach, California on 25-28 February 1990. It consists of extended abstracts from both oral and poster presentations.					
14. SUBJECT TERMS metastable molecules, high energy density materials				15. NUMBER OF PAGES 410	
				16. PRICE CODE	
17. SECURITY CLASSIFICATION OF REPORT UNCLASSIFIED	18. SECURITY CLASSIFICATION OF THIS PAGE UNCLASSIFIED	19. SECURITY CLASSIFICATION OF ABSTRACT UNCLASSIFIED	20. LIMITATION OF ABSTRACT UL (UNLIMITED)		

TABLE OF CONTENTS

Foreword.....	ix
Technical Program Agenda.....	xi
Participants List.....	xvii

EXTENDED ABSTRACTS: ORAL PRESENTATIONS

This report includes those topics

→ "Limitations on Stored Energy Densities in Systems of Separated Ionic Species" Mario E. Fajardo, Astronautics Laboratory.....	3
→ "Matrix Isolation Spectroscopy of Metal Atoms Generated by Laser Ablation, the Li/RGS and Li/D ₂ Systems" Mario E. Fajardo, Astronautics Laboratory.....	5
→ "Photogeneration and Storage of Atomic Radicals in van der Waals Solids" V.A. Apkarian, University of California, Irvine.....	11
→ "High Energy Density Systems in Cryogenic Media: The Production and Reaction of Atoms and Radicals" Eric Weitz, Northwestern University.....	25
→ "A Percolation Theory of Solid State Chain Reactions" Charles A. Wight, University of Utah.....	35
"New Phases of Hydrogen at Megabar Pressures and Metallic Hydrogen" Isaac F. Silvera, Harvard University.....	41
"Triggered Energy Releases in Solid Hydrogen Hosts Containing Unpaired Atoms" G.W. Collins, Lawrence Livermore National Laboratory, J.R. Gaines, University of Hawaii, E.M. Fearon, J.L. Maienschein, E.R. Mapoles, R.T. Tsugawa, and P.C. Souers, Lawrence Livermore National Laboratory.....	47
→ "Energy Storage and Conversion in Solid Hydrogen, Theoretical Aspects" Chester Vause III, University of Hawaii.....	53
→ "Metal-Doped H ₂ ⁺ " (JES) → Daniel D. Konowalow, Astronautics Laboratory.....	55
"Infrared Emission Spectrum of H ₃ ⁺ in Jupiter Ionosphere and Absorption Spectrum of Ionized Solid Hydrogen" Takeshi Oka, University of Chicago.....	63
"Further Investigations of the Infrared Absorption Spectra of the Ionic Clusters of Hydrogen; Rotational Structure in the H ₅ ⁺ /D ₅ ⁺ System" M.W. Crofton, J.M. Price, G. Niedner-Schatteburg, and Y.T. Lee, University of California, Berkeley.....	71

"The Dynamics of Electronic Energy Quenching and Angular Momentum Reorientation: The Reaction of $H_2(B) + He$"	
C.B. Moore, C.D. Pibel, and K.L. Carleton, U. C. Berkeley.....	79
"Theoretical Study of Electronic Quenching and Rovibrational Energy Transfer in $He + H_2(B)$"	
Sheng-yu Huang and William A. Lester, Jr., U. C. Berkeley.....	95
"Multiresonant Spectroscopy and the Dynamics of Intramolecular Relaxation in Superexcited States of Molecules, Radicals and Complexes"	
F.X. Campos, K.S. Haber, Y. Jiang, Y.-F. Zhu, R. Shehadeh, and E.R. Grant, Purdue University.....	101
"Dynamic Constraints on Stochastic Behavior in the Chemistry of Highly Excited Molecules"	
Barry K. Carpenter and John R. Wiesenfeld, Cornell University.....	111
"Theoretical Studies of Highly Energetic CBES Materials"	
N.E. Brener, N.R. Kestner, J. Callaway, and H. Chen, Louisiana State U.....	115
"The Search for Tetrahedral N_4"	
Walter J. Lauderdale, Murray J. Myers, David E. Bernholdt, John F. Stanton, and Rodney J. Bartlett, University of Florida.....	121
"Computational Analyses of Some Nitrotetrahedranes, Nitrotriprismanes, and Their Aza Analogues"	
Peter Politzer, Jorge M. Seminario, Jane S. Murray, and Michael Grodzicki, University of New Orleans.....	135
"Theoretical and Experimental Investigations of Dications"	
W.C. Lineberger, S.R. Leone, and S.V. O'Neil, Joint Institute for Laboratory Astrophysics and University of Colorado.....	155
"Chemically Bound Excited Clusters III"	
C.A. Nicolaides, National Hellenic Research Foundation.....	161
"Potential New High Energy Density Materials: Cyclooctaoxygen O_8, Including Comparisons with the Well-Known Cyclo-S_8 Molecule"	
Henry F. Schaefer III, University of Georgia.....	169
"Decomposition of Energetic Molecules from Metastable Vibrational States"	
M.P. Casassa, B.R. Foy, J.C. Stephenson, and D.S. King, National Institute of Standards and Technology.....	181
"Potential Surface Control of the Dynamics of HN_3 Decomposition and Reaction"	
Millard H. Alexander, University of Maryland.....	187
"Dynamics on HN_3 Potential Energy Surfaces: The $H + N_3$ Reaction and the Photodissociation of HN_3"	
Paul J. Dagdigan, The Johns Hopkins University.....	193
"Theoretical Investigation of Energy Storage in Atomic and Molecular Systems"	
H.H. Michels and J.A. Montgomery, Jr., United Technologies Research Center..	199

"Properties of Small Energetic Clusters" Koop Lammertsma, University of Alabama at Birmingham.....	207
"Electronic Structure Calculations on AlLi" Marcy E. Rosenkrantz, Astronautics Laboratory.....	215
"Lewis Acid Behavior of Noble-Gas Cations and the Syntheses of Novel Ng-O and Xe-N Bonds (Ng = Kr, Xe)" Neil T. Arner, Alison Paprica, Jeremy C.P. Sanders, and Gary J. Schrobilgen, McMasterUniversity.....	223
"Experimental Studies on the Synthesis of New High Oxidation State Energetic Fluorine Compounds" W.W. Wilson and K.O. Christe, Rocketdyne Division of Rockwell International Corporation.....	229

EXTENDED ABSTRACTS: POSTER PRESENTATIONS

"Extremely Large Atom Densities in Tritiated Solid Hydrogen" G.W. Collins, P.C. Souers, E. R. Mapoles, F. Magnotta, J.R. Gaines, and P.A. Fedders, Lawrence Livermore National Laboratory.....	235
"Potential Energy Surfaces and Dynamics for Unusual Hydrides and Fluorides" Mark S. Gordon, Theresa L. Windus, and Nikita Matsunaga, North Dakota State University; Larry P. Davis and Larry W. Burggraf, AFOSR; and Donald L. Thompson, Oklahoma State University.....	241
"Synthesis of High Density BeH₂: A Potential High Hydrogen Fuel" J. Akella, G.S. Smith, N. Winter and Q. Johnson, Lawrence Livermore National Laboratory.....	245
"Synthesis of New High Energy Density Materials. Synthesis and Reactions of <i>meso</i>- and <i>d,l</i>-D₃-Trishomocubylidene-D₃-trishomocubane" Alan P. Marchand, University of North Texas.....	249
"Theoretical Study of Novel Bonding in Molecules" Roberta P. Saxon, SRI International.....	269
"Theoretical Studies of Spin-Forbidden and Electronically Nonadiabatic Processes: Avoided and Allowed Surface Crossings" David R. Yarkony, Johns Hopkins University.....	273
"Preliminary Studies of Energetic Room Temperature Carbon/Hydrogen Solids" Patrick Carrick, Astronautics Laboratory.....	279
"Stabilization of HEDM Materials" S.D. Thompson, R.A. van Opijnen, M.I. Kenney, and S.L. Rodgers, Astronautics Laboratory.....	283

"Theoretical Gas Phase Dissociation and Surface Adsorption Studies of Fluorine Azide"	
Neil R. Kestner, Nathan E. Brener, and Joseph Callaway, Louisiana State University.....	289
"Advanced Launch Vehicle Propulsion at the NASA-Lewis Research Center"	
Bryan Palaszewski, NASA-Lewis Research Center.....	295
"Spectroscopy and Dynamics of Energetic Halogen Amines"	
R.A. Conklin, J. Pestovich, R.F. Hanson, and J.V. Gilbert, U. of Denver.....	299
"Theoretical Studies of Metastable Molecular Systems"	
K. Kirby, Harvard-Smithsonian Center for Astrophysics.....	303
"Theoretical Studies of HEDM Molecules"	
Byron H. Lengsfeld III, Lawrence Livermore National Laboratory.....	309
"Metastable Metals in Matrix Materials"	
N. Presser, R. Poole, and A.T. Pritt, Jr., The Aerospace Corporation.....	315
"Synthesis and Properties of Novel Nitrocyclopropenes: Potential High Energy Density Materials"	
William P. Dailey, University of Pennsylvania.....	319
"Production and Properties of Cluster Ions"	
Y.K. Bae, SRI International.....	323
"Investigations of Metastable Molecules Containing Hydrogen"	
H. Helm, L.J. Lembo, D.L. Huestis, P.C. Cosby, and M.C. Bordas, SRI International	329
"New High Energy Oxidizer Systems for Propellant and Energy Storage Applications"	
Scott A. Kinkead, Jon B. Nielsen, and P. Gary Eller, Los Alamos National Laboratory.....	335
"Reactions of Size Selected Singly and Doubly Charged Transition Metal Ions and Cluster Ions"	
Michael T. Bowers, University of California.....	339
"Production of NCl(a) by Thermal Decomposition of ClN₃"	
M.A. Chowdhury, B.K. Winker, T.A. Seder and D.J. Benard, Rockwell International ScienceCenter.....	345
"Beryllium and Boron-Beryllium Hydrides: High Energy Fuels for the Future"	
Donald F. Gaines, Joseph R. Wermer, and Dovas A. Saulys, University of Wisconsin-Madison.....	349
"H₂/O₂ Three-Body Rates at High Temperatures"	
William J. Marinelli, William J. Kessler, Lawrence G. Piper, and W. Terry Rawlins, Physical Sciences Inc.....	359
"Laser and Fourier Transform Spectroscopy of Novel Propellant Molecules"	
Peter Bernath, The University of Arizona.....	365

"Energy Transfer Process in Rare Gas Solids"

L. Wiedeman, B. Weiller, and H. Helvajian, The Aerospace Corporation.....371

"Magneto Circular Dichroism (MCD) Spectroscopy of Cryogenic Metal-Containing Matrices Prepared by Laser Ablation"

John W. Kenney, III, Eastern New Mexico University.....377

"High Pressure Burn Rate Studies in a Diamond Anvil Cell"

Steven F. Rice and M. Frances Foltz, Lawrence Livermore National Lab.....383

Accession For	
NTIS GRA&I	<input checked="" type="checkbox"/>
DTIC TAB	<input type="checkbox"/>
Unannounced	<input type="checkbox"/>
Justification	
By _____	
Distribution/ _____	
Availability Codes	
Dist	Avail and/or Special
A-1	



FOREWORD

The High Energy Density Materials (HEDM) Program is administered jointly by the Astronautics Laboratory (AL), the Aeropropulsion Laboratory of the Wright Research and Development Center (WRDC/PO), and the Air Force Office of Scientific Research (AFOSR). The program is designed to search for new molecules and materials which have an energy content that could result in revolutionary improvements in rocket propulsion, yet have the stability required to be used as propellants. In scientific terms, it is a search for the "limits of metastability." The program plan includes periodic contractors conferences to share research results and evaluate the progress of the program.

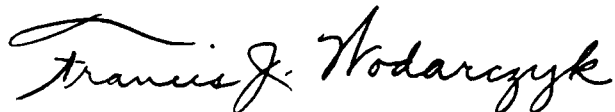
The fourth High Energy Density Materials Contractors Conference was held on 25-28 February 1990 on the Queen Mary in Long Beach, California. The meeting was attended by approximately 150 people. Overviews of the entire HEDM program were given by government program managers, and 28 presentations of research results were given by both in-house researchers from the Astronautics Laboratory and contractors of AL, WRDC/PO, and AFOSR. In addition, a poster session was held for the first time at a HEDM Contractors Meeting; 26 poster papers were presented.

This report represents the official documentation of the fourth conference. It includes extended abstracts of the material that was presented by the researchers at the conference, including both the oral presentations and the poster papers. The detail presented in these extended abstracts should be sufficient to allow an in-depth review of the type of research being conducted in the program. The responsibility of documenting each of these contractors conferences falls alternately on the Astronautics Lab and AFOSR. Thus reports on the first and third conferences were issued as Astronautics Lab Technical Reports (AFAL CP-87-002 and AL-CP-89-002) and the proceedings of the second conference were issued as an AFOSR Report (Report on Second High Energy Density Materials Contractors Conference, dated 27 May 1988).

The fifth High Energy Density Contractors Conference is scheduled for the late winter of 1991.



LARRY P. DAVIS, Lt Col, USAF
Editor



FRANCIS J. WODARCZYK
Editor

HIGH ENERGY DENSITY MATERIALS CONTRACTORS CONFERENCE

Technical Program

Sunday, 25 February 1990

5:00 - 7:00 PM: Reception, King's View Room, Hotel Queen Mary

Monday, 26 February 1990

7:00 AM - Registration and Continental Breakfast, R-Deck

Technical Session, Windsor Salon

Chairman - Patrick G. Carrick, Astronautics Laboratory

8:00 - Administrative Announcements

8:05 - Welcome, Richard R. Weiss, Director, Astronautics Laboratory

8:15 - "The Astronautics Laboratory HEDM Program," Stephen L. Rodgers, Astronautics Laboratory

8:30 - "The AFOSR High Energy Density Materials Program," Larry P. Davis and Frank J. Wodarczyk, AFOSR

9:00 - "Panel Perspectives on the Air Force HEDM Program," William C. Stwalley, Chairman, High Energy Density Materials Technical Review Panel

9:30 - "Rocket Performance Calculations," Ronn L. Carpenter, Thiokol

10:00 - BREAK

10:30 - "Limitations on Stored Energy Densities in Systems of Separated Ionic Species," and "Matrix Isolation Spectroscopy of Metal Atoms Generated by Laser Ablation: the Li/RGS and Li/D2 Systems," Mario E. Fajardo, Astronautics Laboratory

11:00 - "Photogeneration and Storage of Atomic Radicals in van der Waals Solids," V.A. Apkarian, University of California, Irvine

11:30 - "High Energy Density Systems in Cryogenic Media: The Production and Reaction of Atoms and Radicals." Eric Weitz, Northwestern University

12:00 - "Percolation and Runaway Chain Reactions in Disordered Media," Charles A. Wight, University of Utah

12:30 - LUNCH, Royal Salon

Technical Session, Windsor Salon

Chairman - Thomas E. Gist, Wright Research and Development Center

- 1:30 - "New Phases of Hydrogen at Megabar Pressures and Metallic Hydrogen," Isaac F. Silvera, Harvard University
- 2:00 - "Experimental Observations of Triggered Energy Releases in Solid Hydrogen Hosts Containing Unpaired Atoms," G.W. Collins, Ohio State University; James R. Gaines, University of Hawaii; E.M. Fearon, J.L. Maienschein, E.R. Mapoles, R.T. Tsugawa, and P.C. Souers, Lawrence Livermore National Laboratory
- 2:30 - "Theoretical Investigations of Atomic Hydrogen Stored in Solid Molecular Hydrogen," Chester A. Vause III, University of Hawaii
- 3:00 - "Metal-Doped Hydrogen," Daniel D. Konowalow, Astronautics Laboratory
- 3:30 - BREAK
- 4:00 - "Infrared Emission Spectrum of H_3^+ in Jupiter Ionosphere and Absorption Spectrum in Solid H_2 ," Takeshi Oka, University of Chicago
- 4:30 - "Observation of Rotational Structure in the Vibrational Predissociation Spectrum of H_5^+ ," M.W. Crofton, G. Niedner-Schatteburg, J.M. Price, and Y.T. Lee, University of California, Berkeley
- 5:00 - "Dynamics of Electronic Energy Quenching and Angular Momentum Reorientation: The Reaction of $H_2(B) + He$," Charles D. Pibel, Karen L. Carleton, and C. Bradley Moore, University of California, Berkeley
- 5:30 - "Theoretical Study of Electronic Quenching and Rovibrational Energy Transfer in $He + H_2(B)$," Sheng-yu Huang and William A. Lester, Jr., University of California, Berkeley
- 6:00 - ADJOURN
- 6:30 - MIXER WITH NO-HOST BAR, Britannia Salon
- 7:30- BANQUET, Britannia Salon
Guest Speaker: William Winberg, Historian, Hotel Queen Mary

Tuesday, 27 February 1990

7:00 AM - Continental Breakfast, R-Deck

Technical Session, Windsor Salon

Chairman, Frank J. Wodarczyk, AFOSR

8:00 - "Intramolecular Relaxation in Superexcited States," F.X. Campos, K.S. Haber, Y. Jiang, Y.-F. Zhu, R. Shehadeh, and E.R. Grant, Purdue University

8:30 - "Dynamic Constraints on Stochastic Behavior in the Chemistry of Highly Excited Molecules," Barry K. Carpenter and John R. Wiesenfeld, Cornell University

9:00 - "Theoretical Studies of Highly Energetic CBES Materials," N.E. Brener, N.R. Kestner, J. Callaway, and H. Chen, Louisiana State University

9:30 - "The Search for Tetrahedral N₄," Walter J. Lauderdale, John F. Stanton, David E. Bernholdt, Murray Myers, and Rodney J. Bartlett, University of Florida

10:00 - BREAK

10:30 - "Computational Analyses of Some Nitrotetrahedranes, Nitrotriprismanes, and Their Aza Analogues," Peter Politzer, Jorge M. Seminario, Jane S. Murray, and Michael Grodzicki, University of New Orleans

11:00 - "Theoretical/Experimental Investigations of the Structure and Dynamics of Highly Energetic Dication Species," W. Carl Lineberger, Stephen R. Leone, and Stephen V. O'Neil, JILA and the University of Colorado

11:30 - "Chemically Bound Excited Clusters III," Cleanthes A. Nicolaides, National Hellenic Research Foundation

12:00 - "Potential New High Energy Density Materials: Cyclooctaoxygen O₈, Including Comparisons with the Well-Known Cyclo-S₈ Molecule," Henry F. Schaefer III, University of Georgia

12:30 - LUNCH, Windsor Room

1:30 - 3:30 PM - POSTER SESSION, Windsor Room

Wednesday, 28 February 1990

7:00 AM - Continental Breakfast, R-Deck

Technical Session, Windsor Salon

Chairman - Peter J. Dolan, Astronautics Laboratory

8:00 - "Decomposition of Energetic Molecules from Metastable Vibrational States," M.P. Casassa, B.R. Foy, J.C. Stephenson, and D.S. King, National Institute of Standards and Technology

8:30 - "Potential Surface Control of the Dynamics of HN_3 Decomposition and Reaction," Millard H. Alexander, University of Maryland

9:00 - "Dynamics on HN_3 Potential Energy Surfaces: The $\text{H} + \text{N}_3$ Reaction and the Photodissociation of HN_3 ," Paul J. Dagdigian, Johns Hopkins University

9:30 - "Theoretical Investigation of Energy Storage in Atomic and Molecular Systems," H.H. Michels and J.A. Montgomery, Jr., United Technologies Research Center

10:00 - BREAK

10:30 - "Properties of Small Energetic Clusters," Koop Lammertsma, University of Alabama at Birmingham

11:00 - "Electronic Structure Calculations on AlLi ," Marcy E. Rosenkrantz, Astronautics Laboratory

11:30 - "Lewis Acid Behavior of Noble-Gas Cations and the Synthesis of Novel Ng-O and Xe-N Bonds ($\text{Ng} = \text{Kr}, \text{Xe}$)," Neil T. Arner, Alison Paprica, Jeremy C.P. Sanders, and Gary J. Schrobilgen, McMaster University

12:00 - "Experimental Studies on the Synthesis of New High Oxidation State Energetic Fluorine Compounds," W.W. Wilson and K.O. Christe, Rocketdyne Division of Rockwell International Corporation

12:30 ADJOURN

POSTERS

1. "Extremely Large Atom Densities in Tritiated Solid Hydrogen," Gilbert W. Collins, P.C. Souers, E. R. Mapoles, J.R. Gaines, and P.A. Fedders, Lawrence Livermore National Laboratory
2. "Potential Energy Surfaces and Dynamics for Unusual Silicon Hydrides," Mark S. Gordon and Theresa L. Windus, North Dakota State University; Donald L. Thompson, Oklahoma State University; Larry P. Davis and Larry W. Burggraf, AFOSR; and Rozeanne Steckler, San Diego Supercomputer Center
3. "Synthesis of High Density BeH_2 : A Potential High Hydrogen Fuel," J. Akella, G.S. Smith, N. Winter and Q. Johnson, Lawrence Livermore National Laboratory
4. "Synthesis of New High Energy Density Materials. Synthesis and Reactions of *meso*- and *d*,*l*- D_3 -Trishomocubylidene- D_3 -trishomocubane," Alan P. Marchand, University of North Texas
5. "Theoretical Study of Novel Bonding in Molecules," Roberta P. Saxon, SRI International
6. "Theoretical Studies of Spin-Forbidden and Electronically Nonadiabatic Processes: Avoided and Allowed Surface Crossings," David R. Yarkony, Johns Hopkins University
7. "Hydrogen Trapping in Room Temperature Carbon-Based Matrices," Patrick G. Carrick, Astronautics Laboratory
8. "Stabilization of HEDM Materials," Stephen L. Rodgers, Steven D. Thompson, and Roeland A. van Opijnen, Astronautics Laboratory
9. "Theoretical Gas Phase Dissociation and Surface Adsorption Studies of Fluorine Azide," Neil R. Kestner, Nathan E. Brener, and Joseph Callaway, Louisiana State University
10. "Advanced Launch Vehicle Propulsion at the NASA Lewis Research Center," Bryan Palaszewski, NASA Lewis Research Center
11. "Spectroscopy and Dynamics of Energetic Halogen Amines," R.A. Conklin, J. Pestovich, R.F. Hanson, and J.V. Gilbert, University of Denver
12. "Theoretical Studies of Metastable Molecular Systems," K. Kirby, Harvard-Smithsonian Center for Astrophysics
13. "Multireference CI Studies of High Energy Density Materials: The Stability of He_3^{++} , HeBe_2^{++} , $\alpha\text{-N}_2\text{O}_2$ and B_2H_2 ," Byron H. Lengsfeld III, Lawrence Livermore National Laboratory
14. "Metastable Metals in Matrix Materials," N. Presser, R. Poole, and A.T. Pritt, Jr., The Aerospace Corporation
15. "Synthesis and Properties of Novel Nitrocyclopropenes: Potential High Energy Density Materials," William P. Dailey, University of Pennsylvania

16. "Observation of High-Lying Vibrational Predissociation States of H_5^+ ," Y.K. Bae, SRI International
17. "Investigations of Metastable Molecules Containing Hydrogen," H. Helm, L.J. Lembo, D.L. Huestis, P.C. Cosby, and M.C. Bordas, SRI International
18. "Studies of Advanced Oxidizer Systems Containing the Fluoroperoxide Moiety," S.A. Kinkead, J.B. Nielsen, and P.G. Eller, Los Alamos National Laboratory
19. "Reactions of Size Selected Singly and Doubly Charged Transition Metal Ions and Cluster Ions," Michael T. Bowers, University of California
20. "Production of $NCI(a)$ by Thermal Decomposition of ClN_3 ," M.A. Chowdhury, B.K. Winker, T.A. Seder and D.J. Benard, Rockwell International Science Center
21. "Beryllium and Boron-Beryllium Hydrides: High Energy Fuels for the Future," Donald F. Gaines, University of Wisconsin-Madison
22. " H_2/O_2 Three-Body Rates at High Temperatures," William J. Marinelli, William J. Kessler, Lawrence G. Piper, and W. Terry Rawlins, Physical Sciences Inc
23. "Modulated Molecular Beam-Flowing Afterglow Instrument," Seksan Dheandhanoo, Edward L. McCall, and Wade L. Fite, Extrel Corporation
24. "Laser and Fourier Transform Spectroscopy of Novel Propellant Molecules," Peter Bernath, The University of Arizona

AL AFOSR WRDC/PO
HIGH ENERGY DENSITY MATERIALS CONTRACTORS CONFERENCE
FEBRUARY 25-28, 1990

Jagan Akella
Lawrence Livermore National Laboratory
University of California
L-201
Livermore, CA 94550

Peter F. Bernath
Department of Chemistry
University of Arizona
Tucson, AZ 85721

Millard Alexander
Department of Chemistry
University of Maryland
College Park, MD 20742

Mark A. Beyer
Air Force Systems Command
HQ AFSC/XTTS
Andrew AFB, DC 20334-5000

Earl L. Andersen
United Technologies Corporation
P. O. Box 49028
San Jose, CA 95161-9028

Peter Bletzing
Air Force Aeropropulsion Lab
WRDC/POOC-3
Wright-Patterson AFB, OH 45433

V. Ara Apkarian
Department of Chemistry
University of California
Irvine, CA 92717

Frank Bogardt
Lockheed Missiles & Space Company
P. O. Box 3504
Sunnyvale, CA 94088-3504

Young K. Bae
SRI International
333 Ravenswood Avenue
Menlo Park, CA 94025

Michael T. Bowers
Department of Chemistry
University of California
Santa Barbara, CA 93106

Rodney J. Bartlett
Department of Chemistry
University of Florida
362 Williamson Hall
Gainesville, FL 32611

Chris Brazier
Air Force Astronautics Lab
LSX
Edwards AFB, CA 93523

Jack L. Beauchamp
Department of Chemistry
California Institute of Technology
Pasadena, CA 91125

Nathan Brener
Louisiana State University
Department of Physics & Astronomy
Baton Rouge, LA 70803-4001

Charles F. Bender
Ohio Supercomputer Center
Ohio State University
1224 Kinnear Road
Columbus, OH 43212

Thomas B. Brill
Department of Chemistry
University of Delaware
Newark, DE 19716

Dennis J. Caldwell
Hercules Aerospace
P. O. Box 98
Bacchus Works, Magna, UT 84044

Karl O. Christe
Rocketdyne
6633 Canoga Avenue, BA26
Canoga Park, CA 91302

Daniel L. Calef
Lawrence Livermore National Laboratory
P. O. Box 808, L-282
Livermore, CA 94550

Daniel J. Collins
The Marquardt Company
16555 Saticoy
Van Nuys, CA 91409

Joseph Callaway
Department of Physics
Louisiana State University
Baton Rouge, LA 70803

Gilbert W. Collins
Lawrence Livermore National Laboratory
P. O. Box 808, L-358
Livermore, CA 94550

Yue Cao
University of Hawaii at Manoa
2505 Correa Road, Watanabe Hall 211
Honolulu, HI 96822

Robert C. Corley
Air Force Astronautics Laboratory
AL/LS
Edwards AFB, CA 93523

Ronn L. Carpenter
Thiokol Corporation
P. O. Box 707, M/S 244
Brigham City, UT 84302-0707

Paul J. Dagdigian
Department of Chemistry
The Johns Hopkins University
Charles and 34th Streets
Baltimore, MD 21218

Patrick Carrick
Air Force Astronautics Laboratory
AFAL/LSX
Edwards AFB, CA 93523

Dale E. Darling
Lawrence Livermore National Lab
L-389, P. O. Box 808
Livermore, CA 94550

Michael P. Casassa
National Institute of
Standards & Technology
B268/221, NIST
Gaithersburg, MD 20896

William P. Dailey
Department of Chemistry
University of Pennsylvania
Philadelphia, PA 19104-6323

May L. Chan
Naval Weapons Center
Code 3211
China Lake, CA 93555

Larry P. Davis
Air Force Office of Scientific Research
Building 410, Room B217
Bolling AFB, DC 20332-6448

Mark D. Chatfield
Science Applications International Corp.
10260 Campus Point Drive
Building C, M/S-31
San Diego, CA 92121

Vincent D. DiIoreto
The Marquardt Company
16555 Saticoy
Van Nuys, CA 91409

Peter J. Dolan
Air Force Astronautics Laboratory
AL/LSX
Edwards AFB, CA 93523-5000

Ernest A. Dorko
Air Force Weapons Laboratory
WL/ARDJ
Kirtland AFB, NM 87117-6008

Mario Fajardo
Air Force Astronautics Laboratory
AL/LSX
Edwards AFB, CA 93523-5000

Donald F. Gaines
Department of Chemistry
University of Wisconsin, at Madison
Madison, WI 53706

James R. Gaines
Department of Physics & Astronomy
University of Hawaii at Manoa
2505 Correa Road, Watanabe Hall 210
Honolulu, HI 96822

Bruce Garrett
Pacific Northwest Laboratory
Battelle Boulevard
Richland, WA 99352

Julanna V. Gilbert
Department of Chemistry
University of Denver
Denver, CO 80208

Jeffrey W. Gilman
Air Force Astronautics Laboratory
AL/LSX
Edwards AFB, CA 93523-5000

Thomas E. Gist
Adv. Plasma Research Group
Aero Propulsion & Power Lab
WRDC/PO
Wright-Patterson AFB, OH 45433-6563

Mark S. Gordon
Department of Chemistry
North Dakota State University
Fargo, ND 58105

Edward R. Grant
Department of Chemistry
Purdue University
West Lafayette, IN 47907

J. Paul Greene
Lockheed Missiles & Space Co., Inc.
1111 Lockheed Way
O/81-51, B/157 3W
Sunnyvale, CA 94089

Peter D. Haaland
Air Force Institute of Technology
AFIT/ENP
Wright-Patterson AFB, OH 45433

V. E. Haloulakos
McDonnell Douglas Space Systems Company
5301 Bolsa Avenue
Huntington Beach, CA 92647

Hanspeter Helm
SRI International
333 Ravenswood Avenue
Menlo Park, CA 94025

Henry Helvajian
The Aerospace Corporation
Los Angeles, CA 90009

Robert E. Hull
Lockheed Missiles & Space Co., Inc.
1111 Lockheed Way
O/81-51, B/157 3W
Sunnyvale, CA 94089

Winifred Huo
NASA Ames Research Center
MS 230-3
Moffett Field, CA 94035

Marilyn Jacox
Molecular Spectroscopy Section
MS B-268, Physics Building
National Institute of Standards
and Technology
Gaithersburg, MD 20899

Koop Lammertsma
Department of Chemistry
UAB Station
University of Alabama
Birmingham, AL 35294

Daniel H. Katayama
Air Force Geophysics Laboratory
GL(AFSC)/LIM
Hanscom AFB, MA 01731-5000

Merlin W. Larimer
Atlantic Research Corporation
5945 Wellington Road
Gainsville, VA 22065

John Kenney
Department of Physical Sciences
Eastern New Mexico University
Portales, NM 88130

Walter J. Lauderdale
Department of Chemistry
University of Florida
362 Williamson Hall
Gainesville, FL 32611-2085

Neil R. Kestner
Department of Chemistry
Louisiana State University
Baton Rouge, LA 70803

Yuan T. Lee
Department of Chemistry
University of California, Berkeley
Berkeley, CA 94720

Scott A. Kinkead
Los Alamos National Laboratory
P. O. Box 1663 - MS C346
Los Alamos, NM 87545

Byron Lengsfeld
Lawrence Livermore National Laboratory
Livermore, CA 94550

Kate P. Kirby
Harvard-Smithsonian Center
for Astrophysics
60 Garden Street
Cambridge, MA 02138

William A. Lester, Jr.
Department of Chemistry
University of California, Berkeley
Berkeley, CA 94720

J. Brooke Koffend
The Aerospace Corporation
P. O. Box 92957
M5-747
Los Angeles, CA 90009

W. Carl Lineberger
University of Colorado
JILA Campus Box 440
Boulder, CO 80309-0440

Daniel D. Konowalow
University of Dayton Research Institute
AL (AFSC)/LSX
Edwards AFB, CA 93523-5000

Richard L. Lou
GenCorp Aerojet
Building 05025, Dept. 8200
P. O. Box 15699
Sacramento, CA 95852

Jaroslava Kushnir
National Research Council
2101 Constitution Avenue, N. W.
Washington, D. C. 20418

Frank Magnotta
Lawrence Livermore National Laboratory
Livermore, CA 94550

Robert Mantz
Air Force Astronautics Laboratory
AL/LSX
Edwards AFB, CA 93523

Cleanthes A. Nicolaides
Hellenic Research Foundation
48 Vas Constoutiou Avenue
Athens, 11635 GREECE

Alan P. Marchand
Department of Chemistry
University of North Texas
NT Station, Box 5068
Denton, TX 76203-5068

Jon B. Nielsen
Los Alamos National Laboratory
P. O. Box 1663 - MS C346
Los Alamos, NM 87545

William J. Marinelli
Physical Sciences Inc.
20 New England Business Center
Andover, MA 01810

Takeshi Oka
Department of Chemistry
University of Chicago
5735 S. Ellis Avenue
Chicago, IL 60637

Thanhy Mather
Air Force Astronautics Laboratory
AL/LSX
Edwards AFB, CA 93523-5000

Susan T. Peters
Naval Ordnance Station
Code 6120C
Indian Head, MD 20640-5000

H. Harvey Michels
United Technologies Research Center
Silver Lane
East Hartford, CT 06108

Charles D. Pibel
Department of Chemistry
University of California
Berkeley, CA 94720

C. Bradley Moore
Department of Chemistry
University of California, Berkeley
211 Lewis Hall
Berkeley, CA 94720

Peter A. Politzer
Department of Chemistry
University of New Orleans
New Orleans, LA 70148

David S. Moore
Los Alamos National Laboratory
MS-J567
Los Alamos, NM 87545

Nathan Presser
The Aerospace Corporation
Los Angeles, CA 90009

Vincent McKoy
Department of Chemistry
California Institute of Technology
Mail Code 127-72
Pasadena, CA 91125

Alfred T. Pritt, Jr.
The Aerospace Corporation
P. O. Box 92957 - M/S: M2/251
Los Angeles, CA 90009-2957

Daniel M. Neumark
Department of Chemistry
University of California
Berkeley, CA 94720

Patrick K. Redington
Hercules Aerospace
P. O. Box 98, MS A2
Magna, UT 84044-0098

Michael Reeder
Rockwell International
MC AD59
12214 Lakewood
Downey, CA 90241

Hanna Reisler
Department of Chemistry
University of Southern California
Los Angeles, CA 90089

Steven F. Rice
Lawrence Livermore National Laboratory
P. O. Box 808, L-282
Livermore, CA 94550

Steven M. Robbins
Marketing Field Office
Morton Thiokol, Inc.
P. O. Box 1690
Lancaster, CA 93539

Stephen Rodgers
Air Force Astronautics Laboratory
AL/LSX
Edwards AFB, CA 93523

Marcy E. Rosenkrantz
Air Force Astronautics Laboratory
AL(AFSC)/LSX
Edwards AFB, CA 93523

Marvin Ross
Lawrence Livermore National Laboratory
P. O. Box/L-299
Livermore, CA 94550

Roberta P. Saxon
SRI International
333 Ravenswood Avenue
Menlo Park, CA 94025

Henry F. Schaefer, III
Department of Chemistry
University of Georgia
Athens, GA 30602

Robert Schmitt
SRI International
333 Ravenswood Avenue
Menlo Park, CA 94035

Gary J. Schrobilgen
Department of Chemistry
McMaster University
Hamilton, Ontario L8S 4M1
CANADA

Isaac F. Silvera
Department of Physics
Harvard University
Cambridge, MA 02138

Wayne C. Solomon
Department of Aeronautical
and Astronautical Engineering
University of Illinois, Urbana
101 Transportation Building
104 S. Mathews Avenue
Urbana, IL 61801

Alan Snelson
IIT Research Institute
10 West 35th Street
Chicago, IL 60616

William Spindel
National Research Council
2101 Constitution Avenue
Washington, DC 20418

William C. Stwalley
Department of Chemistry
University of Iowa
Iowa City, IA 52242

Carlyle B. Storm
Los Alamos National Laboratory
P. O. Box 1663
M-DO, MSP915
Los Alamos, NM 87545

Myron Tapper
Rockwell International

Donald L. Thompson
Department of Chemistry
Oklahoma State University
Stillwater, OK 74078

Steven Thompson
Air Force Astronautics Laboratory
AL/LSX
Edwards AFB, CA 93523-5000

Roeland van Opjinen
Air Force Astronautics Laboratory
AL/LSX
Edwards AFB, CA 93523-5000

Chester A. Vause III
Department of Physics & Astronomy
University of Hawaii, Manoa
2505 Correa Road, Watanabe Hall 434
Honolulu, HI 96822

Albert F. Wagner
Theoretical Chemistry Group
Argonne National Laboratory
9700 South Cass Avenue, 200 R-109
Argonne, IL 60439

Bruce Weiller
The Aerospace Corporation
Los Angeles, CA 90009

Richard Weiss
Air Force Astronautics Laboratory
AL/CC
Edwards AFB, CA 93523-5000

Eric Weitz
Department of chemistry
Northwestern University
2145 Sheridan Road
Evanston, IL 60201

Lawrence Wiedeman
Lawrence Livermore National Laboratory
Livermore, CA 94550

John R. Wiesenfeld
Department of Chemistry
Cornell University
Baker Chemistry Laboratory
Ithaca, NY 14853

Charles Wight
Department of Chemistry
University of Utah
Salt lake City, UT 84112

Tim Wiley
Air Force Astronautics Laboratory
AL/LSX
Edwards AFB, CA 93523

Curt Wittig
Department of Chemistry
University of Southern California
Los Angeles, CA 90089

Frank J. Wodarczyk
Air Force Office of Scientific Research
AFOSR/NC
Building 410, Room B210
Bolling AFB, DC 20332-6448

David R. Yarkony
Department of Chemistry
John Hopkins University
Remsen Hall
Baltimore, MD 21218

EXTENDED ABSTRACTS

ORAL PRESENTATIONS

HIGH ENERGY DENSITY MATTER CONTRACTORS CONFERENCE

25 February - 28 February 1990

Limitations on Stored Energy Densities in Systems of Separated Ionic Species

Mario E. Fajardo

ARIES Office

Astronautics Laboratory/LSX

Edwards AFB, CA 93523-5000

ABSTRACT

A classical electrostatic model of the energetics of systems of ionic species trapped in insulating solids is adapted from the standard theories of ionic crystals and continuum dielectrics. An analysis of the dependence of the stored energy density (energy/volume) of such systems on the separations between the ionic species is made which includes the effects of the Coulombic interactions amongst the ions, as well as the effects of the induced polarization of the insulating solid. Application of the analysis to systems composed of real chemical species at "reasonable" ionic concentrations reveals that the energy stored per ion pair is degraded by these effects to approximately one-half of the energy inherent to an infinitely separated gas phase ion pair. Nevertheless, the calculated stored energies are still sufficiently large that these systems may be potentially useful as rocket propellants, provided that several possible instabilities are not ultimately prohibitive.

NOTE: No long-form abstract was prepared for this presentation. A manuscript documenting this work was submitted for publication to the AIAA Journal of Power and Propulsion. Copies will be made available to interested parties by the author.

HIGH ENERGY DENSITY MATTER CONTRACTORS CONFERENCE

25 February - 28 February 1990

Matrix Isolation Spectroscopy of Metal Atoms Generated by Laser Ablation: the Li/RGS and Li/D₂ Systems

Mario E. Fajardo
ARIES Office
Astronautics Laboratory/LSX
Edwards AFB, CA 93523-5000

ABSTRACT

Results of experiments on lithium doped cryogenic solids (Ne, Ar, Kr, Xe, and D₂) prepared by laser ablation of solid lithium are presented.

The UV/VIS absorption spectra of Li/Ar and Li/Kr matrices generated by cocondensing the rare gas and laser ablated Li atoms at 12K are dominated by a "blue-shifted triplet" absorption not observed in previously published studies. Control experiments on Li/Ar and Li/Kr matrices generated using a Knudsen oven as the Li atom source showed exclusively an "unshifted triplet" absorption, in agreement with previous studies. The new absorption features are attributed to absorption by Li atoms trapped in novel sites in the Ar and Kr solids; sites not accessible to Li atoms generated by the conventional Knudsen effusion technique. Spectra of Li/Xe samples prepared by either method showed exclusively the "unshifted triplet" absorption pattern. All of these observations are explained by a simple model which compares the sizes of the various trapping sites in the rare gas solids to the collision diameters obtained from the Li atom-rare gas atom pair potentials.

Also presented are results of preliminary experiments on Li/Ne and Li/D₂ matrices prepared by laser ablation of solid Li, and subsequent cocondensation at 5K. These spectra constitute the first observations of the successful trapping of Li atoms in either solid, and suggest that the ultimate goal of this task: the isolation of Li atoms in solid H₂, may be possible with only a modest decrease in temperature.

EXPERIMENTAL

The experimental techniques are essentially the same as reported last year¹ and will be described here only briefly. Solids of the heavier rare gases (Ar, Kr, Xe) doped with lithium impurities were prepared in a closed cycle cryostat by co-condensing a slow flow (1 to 3 mmol/hr) of the rare gas, along with the products of a laser ablated lithium plume, onto a thin sapphire window cooled to 12 K. The ablated plume was generated by focussing the output of a XeCl excimer laser (308 nm) onto a rotating disk of lithium metal; typical pulse energies were ≈ 3 mJ, with resulting incident intensities of $\approx 10^8$ W/cm². Samples of lithium doped solid Ne and solid D₂ have been prepared by the same techniques at 5 K using a liquid helium transfer cryostat. For control experiments in the heavier rare gases, the ablation source was replaced by a Knudsen oven effusive lithium source; this source was constructed such that all exposed vacuum surfaces were made of stainless steel.

The rate of deposition of the matrix gas was monitored by back reflection interference using a HeNe laser. Transmission spectra of the matrices were obtained using a 600 W quartz-halogen lamp and an E.G.&G. optical multichannel analyzer equipped with an unintensified silicon photodiode array.

RESULTS

Figure 1 shows a comparison of the transmission spectra (arbitrarily normalized) of Li/Ar solids at 12 K prepared by laser ablation (solid curve) and by Knudsen effusion (dotted curve) of lithium. Figure 2 shows similar data for Li/Kr samples prepared by the two different methods. These spectra clearly indicate that Li/Ar and Li/Kr matrices prepared by laser ablation of lithium differ from matrices prepared using an effusive lithium source. In contrast, the transmission spectra of Li/Xe samples prepared by the laser ablation technique were practically identical with recently published^{2,3} spectra of Li/Xe matrices deposited using the effusive oven method; thus, effusive oven depositions of Li/Xe matrices were not pursued in this study.

Figure 3 shows the transmission spectrum of a Li/Ne sample at 5 K prepared by the laser ablation method. This spectrum represents the first proof of trapping of isolated Li atoms in solid Ne; in fact, two previous studies^{4,5} have reported failed attempts at isolating oven generated Li atoms in solid Ne at 2K. Figure 4 shows similar data for a Li/D₂ sample at 5 K; this represents the first example of matrix isolation of metal atoms of any kind in solid D₂. Unfortunately, this sample was only stable for ≈ 1 hour due to the high vapor pressure of D₂ at 5 K; for the same reason, attempts at depositing a solid Li/H₂ matrix at 5 K all failed.

DISCUSSION

Perhaps the most durable observation that was made during the early matrix isolation studies⁶⁻⁸ of the heavier alkali metal atoms was that their optical absorption spectra consisted of pairs of triplet absorption features; one triplet centered about the free atom $2P \leftarrow 2S$ absorption wavelengths, and the other shifted to the blue by ≈ 50 nm. Each of the triplets was shown to arise from atoms trapped in a single site; thus, two triplets imply two major trapping sites. The exact nature of the matrix perturbation, and the reasons for the appearance of the triplet structures are still being debated in the literature, but the consensus is that the blue shifted triplet represents atoms trapped in a "tighter" trapping site, hence the larger perturbation from the gas phase transition energy.

In contrast to the heavier alkali metals, experiments on lithium doped rare gas matrices^{2,5,9-12} showed only one unambiguous, reproducible, well-resolved triplet absorption, corresponding to the unshifted triplet mentioned above. Published spectra differed significantly, sometimes showing three^{2,5,9}, four^{2,5,9}, five^{2,9,10,12}, and even seven¹¹ peaks in the region around the free atomic lithium absorption, but no clear "doublet of triplets" feature was reported. In this light, the spectra in figures 1 and 2 can be seen as the "missing blue triplet" absorptions in Li/Ar and Li/Kr matrices, indicating that the laser ablated Li atoms do indeed access different, tighter, trapping sites than oven generated atoms.

In the present work, a model of the matrix deposition process is being developed¹ which seeks to explain both the differences between the laser ablation and Knudsen oven depositions, as well as the variation in behavior in the Ar and Kr matrices versus the Xe matrices. The most obvious difference between the two methods of producing the Li atoms is the much higher kinetic energy content of the laser ablated atoms. Laser ablation of metals, using incident intensities near the threshold for plasma production, primarily yields neutral metal atoms with kinetic energies in the 0 to 20 eV range, with typical energies of a few eV¹³⁻¹⁵. In contrast, the kinetic energy of Li atoms issuing from an effusive source at ≈ 750 K will be characterized by a Maxwell-Boltzmann distribution, with a typical kinetic energy of order 0.1 eV.

During the matrix deposition process, the major heat load on the sample is the accommodation of the room temperature kinetic energy of the matrix gas itself. Thus, it can be seen that a large thermal gradient will be established between this room temperature gas and the 12 K sapphire substrate, and, due to the poor thermal conductivity of the matrix, that the majority of this temperature drop will occur near the surface of the matrix. This local heating at the accreting surface of the matrix causes enhanced mobility of all species^{16,17} and allows for the formation of thermodynamically stable solid structures. So, during the subsequent cooling

and crystallization processes, slow Li atoms from an oven source will be stopped in this "accretion layer" and have the opportunity to jostle for elbow room--thus leading to the formation of locally equilibrated trapping sites. On the other hand, the faster laser ablated Li atoms may be able to penetrate through the accretion layer and into pre-existing crystalline rare gas structures, and thus trap in tighter sites. In this case the size of the trapping site would be constrained by the fixed density of the surrounding rare gas solid.

In order to estimate the energies of the various trapping sites and to test this idea of the mobility of Li atoms in closed-packed rare gas structures, a calculation was performed¹ of the potential energy surface experienced by a ground state Li atom trapped in solid Ar. The calculation was based on the assumption that the interactions of species in condensed phases can be approximated as a simple sum of gas phase pair potentials. By constraining all of the Ar atoms to remain rigidly at their undistorted fcc lattice positions, the energies for trapping of a Li atom in various unrelaxed sites were calculated. Because the Li-Ar ground state pair potential^{18,19} is repulsive at the separation corresponding to the Ar-Ar nearest neighbor distance²⁰ in fcc Ar, a Li atom will not easily fit into a single substitutional site in fcc Ar. The same holds true for the Li/Kr case, however the Li-Xe pair potential is actually attractive at the separation corresponding to the Xe-Xe separation in fcc solid Xe, therefore a Li atom should fit into a single substitutional site in fcc Xe. Additionally, the energetic barriers to mobility between the various sites were also calculated; specifically in the "impulsive" limit dictated by the constraint of no Ar atom recoil. The calculated barrier heights in fcc Ar were in the range of 1 to 3 eV, therefore, it is reasonable to expect that Li atoms with several eV of kinetic energy will be mobile in solid Ar, and, by inference, in other cryogenic molecular solids.

Finally, this model of the deposition process predicts an improved atomic isolation efficiency for the laser ablation deposition technique over the traditional effusive oven deposition method. The mobility of slow Li atoms that are stopped in the matrix accretion layer implies the possibility of their recombination to form molecules or clusters, thus lowering atomic isolation yields. The failures of the previous attempts at isolating Li atoms in solid Ne may have been due to such surface recombination. The success of the laser ablation technique in isolating Li atoms in the Li/Ne and Li/D₂ cases corroborates this prediction and lends credence to at least the qualitative features of the model presented herein.

CONCLUSIONS

Lithium atoms generated by laser ablation of solid lithium find different trapping sites in solid Ar and Kr than do Li atoms generated by Knudsen effusion. In solid Xe, both techniques yield atoms trapped in the same site. These results can be qualitatively explained by

a simple model of the deposition process which compares the sizes of the trapping sites to the scale of the Li-Rg potential to determine which trapping sites are accessible to Li atoms generated by the two techniques.

The laser ablation technique offers great improvements in atomic isolation yields over the Knudsen effusion technique. This improvement was demonstrated by the successful trapping of Li atoms in solid Ne and solid D₂ at 5 K. The same simple model explains this result as the penetration of the matrix accretion layer by the faster laser ablated atoms, resulting in their immobilization in the solid part of the matrix. The laser ablation technique should also yield trapped Li atoms in solid H₂, provided that the temperature of the sample substrate can be lowered to ≈ 3 K to allow for the vapor deposition of a solid H₂ matrix.

Plans for future work in this laboratory include further experiments on the Li/RGS systems. These experiments are much easier to perform than those requiring a liquid helium transfer cryostat, and are expected to provide important results on limiting atomic concentrations, optimum deposition conditions, and the dependence of the deposition process on the initial Li atom kinetic energies. These systems will also be studied in pulsed gas--pulsed metal depositions, in which the matrix gas will be introduced in ≈ 100 μ s pulses synchronized coincident or anti-coincident with the pulsed laser ablation of the metal. It is hoped that this experiment can be used to test the idea of the accretion layer by temporally localizing the heat load on the matrix. Finally, experiments in H₂ matrices will be pursued as quickly as possible.

REFERENCES

1. M.E. Fajardo, in Proceedings of the High Energy Density Matter (HEDM) Conference held 12-15 March 1989 in New Orleans LA, AL-CP-89-002.
2. P.A. Lund, D. Smith, S.M. Jacobs, P.N. Schatz, J. Phys. Chem., 88(1), 31-42 (1984).
3. J. Rose, D. Smith, B.E. Williamson, P.N. Schatz, M.C.M. O'Brien, J. Phys. Chem., 90(12), 2608-15 (1986).
4. A.A. Belyaeva, Y.B. Predtechenskii, L.D. Shcherba, Opt. Spektrosk., 34(1), 40-5 (1973).
5. J.J. Wright, L.C. Balling, J. Chem. Phys., 73(7), 3103-6 (1980).
6. M. McCarty, Jr., G.W. Robinson, Mol. Phys., 2(), 415-30 (1959).
7. W. Weyhmann, F.M. Pipkin, Phys. Rev., 137(2A), A490-6 (1965).
8. B. Meyer, J. Chem. Phys., 43(9), 2986-92 (1965).
9. L. Andrews, G.C. Pimentel, J. Chem. Phys., 47(8), 2905-10 (1967).

10. A.A. Belyaeva, Yu.B. Predtechenskii, L.D. Shcherba, *Opt. Spektrosk.*, 24(), 233-4 (1968).
11. R.B. Merrithew, G.V. Marusak, C.E. Blount, *J. Mol. Spec.*, 29(), 54-65 (1969).
12. T. Welker, T.P. Martin, *J. Chem. Phys.*, 70(12), 5683-91 (1979).
13. J.F. Ready, Effects of High-Power Laser Radiation, (Academic Press, 1971).
14. J.F. Friichtenicht, *Rev. Sci. Instrum.*, 45(1), 51-6 (1974).
15. H. Kang, J.L. Beauchamp, *J. Phys. Chem.*, 89(15), 3364-7 (1985).
16. H.E. Hallam, ed., Vibrational Spectroscopy of Trapped Species, (Wiley, 1973).
17. G.C. Pimentel, *Angew. Chem. internat. edit.*, 14(4), 199-206 (1975).
18. J. Pascale, J. Vandeplanque, *J. Chem. Phys.*, 60(6), 2278-89 (1974).
19. R. Scheps, C. Ottinger, G. York, A. Gallagher, *J. Chem. Phys.*, 63(6), 2581-90 (1975).
20. C. Kittel, Introduction to Solid State Physics, (Wiley, 1971).

Figure 1

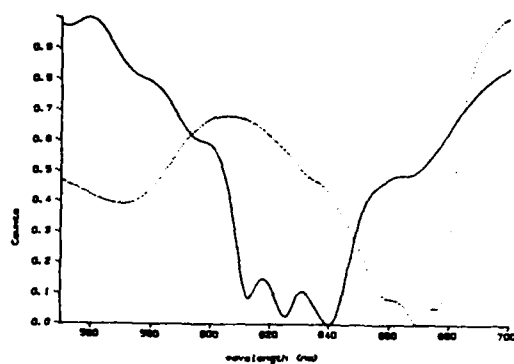


Figure 3

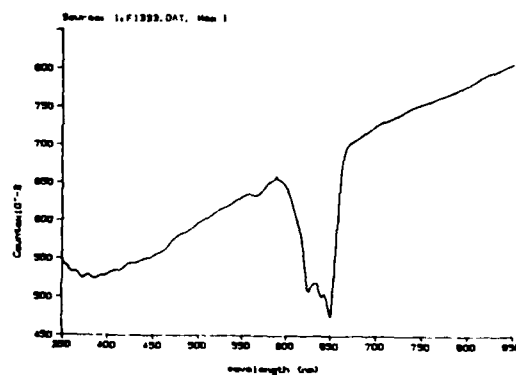


Figure 2

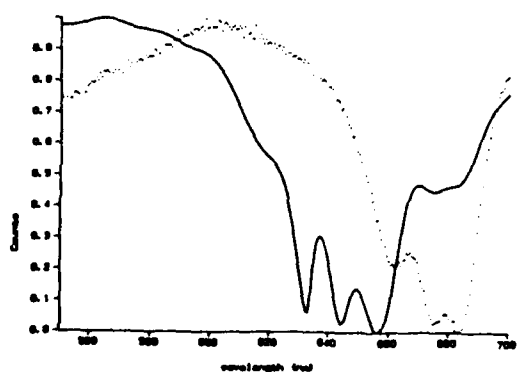
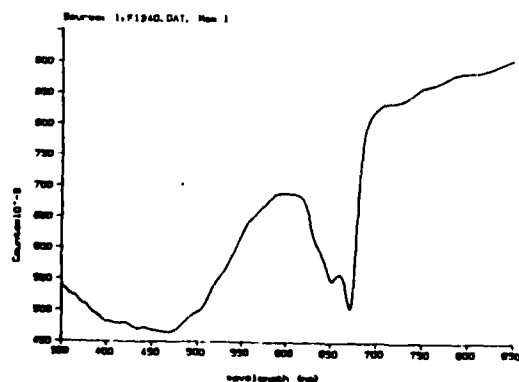


Figure 4



Photogeneration and Storage of Atomic Radicals in van der Waals Solids

**Presented at the Third Annual Contractors Meeting on
High Energy Density Materials
(Long Beach, 1990)**

**V.A. Apkarian
Department of Chemistry
University of California
Irvine, California 92717**

The storage of radicals in solid fuels, as a means for increasing specific impulse, is a concept that dates at least as far back as the predecessor to the present HEDM program.¹ Even then, rare gas matrices were thought as ideal model systems for testing of the concept. Despite the fact that there has been nearly forty years of research in matrix isolated transient species,² the crucial inputs for a serious consideration of the concept remain very sketchy. Among the important, as yet not understood, questions are, a) What are the most efficient means for generating radicals in solids? b) What are the details of the controlling dynamics of such processes? c) What are the limits in attainable, and storable radical densities? d) What are the details of recombination mechanisms and how to control them?

In order to answer these questions in a quantitative fashion, we have initiated both theoretical and experimental studies on photodissociation of diatomics in rare gas solids and the subsequent recombination of the atomic fragments. For the first time, we can report data on systems in which experiment and theory can be compared. It will become obvious, below, that even now our understanding is rather poor and iteration between experiment and theory will be essential to pinpoint the crucial factors governing dynamics in compressible solids. To date, experiment and theory overlap in photodissociation studies of three systems: F_2 in crystalline argon and krypton, Cl_2 in crystalline xenon, and HI in crystalline xenon. Due to limitations in time, I limited my presentation to the first two systems, the same will be done here. To date, the theoretical simulations have been limited to simulations by classical Newtonian mechanics, and the experiments to time independent

measurements. Among the observables that can be compared between experiment and theory are: a) quantum yields of dissociation as a function of temperature, excitation energy, and pressure, b) initial sites and state dynamics (vibration, libration of trapped species), c) final sites of dissociation products, d) migration range of fragments, e) symmetry of cage exit (whether one or both dissociation fragments leave the initial cage). Details of such studies are already in print, here I will only highlight some of the more important findings, and discuss recombination dynamics which has not yet been rigorously treated theoretically.

Photodissociation of F₂ and mobility of F atoms in crystalline Ar and Kr

Early accounts on the photodissociation of F₂ in crystalline argon can be found in the first demonstrations of solid state XeF lasers.³ Two main findings discovered there are relevant to the present, namely: F₂ readily dissociates in solid Ar, and F atoms migrate long distances, both upon photodissociation and upon thermal activation. These findings are in sharp contrast with the earlier photodissociation studies in rare gas solids in which a nearly complete cage effect had been established.⁴ As an example, the quantum yield of Cl₂ dissociation in solid Ar, had been established to be less than 10⁻⁶. As such we initiated Molecular Dynamics (MD) simulations of F₂ in Ar.⁵

The MD simulations of F₂ in crystalline argon, showed that, a) dissociation occurs through well defined reaction cones in the trap site (see figure 1), b) dissociation was subject to a very minor cage barrier (~0.3 eV) and quantum yields reached unity at excess energies above 2.5 eV, c) most strikingly, it was discovered that upon dissociation, in some trajectories, F atoms migrated via a guided motion along crystal face diagonals, distances of order ~30 Å, d) an inverse temperature dependence for cage exit probabilities was discovered (at intermediate excess energies, the dissociation probabilities were nearly 50% higher at 4.5 K than at 12.5 K).

Experimental studies of F₂ in Ar,⁶ Kr,⁷ and in mixed Xe/Ar,⁸ Xe/Kr,⁹ have been used to verify all of these findings at least qualitatively. The photodissociation quantum yields of F₂ in solid Ar and Kr are shown in figure 2 and compared with theoretical predictions. The agreement is quite good in the asymptotic limit, however near the threshold, the experimental values are nearly an order of magnitude smaller than the theoretical predictions. We suspect that this deviation is due to the F-Rg potentials used in the simulations. The simulations have relied on the assumption of pairwise additive F-Rg (X²Σ_{1/2}) gas phase potentials, obtained from crossed molecular beam data.¹⁰ This potential forms the ground state in the C_{∞v} group of the isolated pair, and nearby are the covalent A(Π) states. In an fcc lattice, the cubic symmetry will clearly mix the Σ and Π

states leading to a degeneracy near cage center. Interactions on the repulsive wall of pairs may still be possible to represent by the gas phase potentials. A tested method for developing such potentials, or for running trajectories on multiple surfaces, does not yet exist. However, we already know that if the F-Rg (A) potential is used, smaller dissociation probabilities are obtained, moving the theoretical predictions closer to the experiment.

The inverse temperature dependence has been verified in solid Kr.⁷ This is shown in figure 3, in which one can clearly observe a factor of ~ 2 increase in dissociation yields between 12.5 and 4.5 K, for a dissociation excess energy of 1.9eV. The effect is even larger at longer photodissociation wavelengths. At a dissociation excess energy of 1.15eV, which corresponds to the Franck-Condon limit in excitation, dissociation quantum yields are a factor of three higher at 4.5 K than at 12.5 K.

The long range migration of F atoms upon photodissociation was verified by double doping experiments.⁹ In samples of F₂:Xe:Kr, it is first verified that F₂ and Xe isolate statistically. Subsequently, the direct formation of XeF pairs upon photodissociation of F₂ is monitored. It is found that at 12 K, at an excess energy of 1.9eV, photodissociation product F atoms remain in the Kr bulk, while at an excess energy of 2.4eV, the F atoms directly populate the Xe sites. The implication being, that at the higher energy, F atoms migrate by ~ 10 lattice sites upon dissociation.

The photomobility of F atoms has also been verified by a related study, namely the radiative dissociation of triatomic exciplexes.⁸ Upon radiation, triatomic exciplexes such as Rg₂X⁺, undergo a vertical transition to the repulsive wall of the Rg-X potential. This is illustrated in figure 4. The process is similar to photodissociation, and can lead to the migration of atoms. After complete dissociation of F₂ in solid Ar, the charge transfer states of F-Ar are pumped at 193nm. The exciplexic emission diminishes with time, due to the recombination of F atoms. The decay curve is hyperbolic in time, as would be expected for diffusion controlled recombination. From such studies, a migration length of $\sim 60\text{\AA}$ is obtained per photoexcited F atom. This can only be rationalized by the guided motion discovered in the MD simulations, and is taken as further verification of the MD results.⁵

Finally, thermally induced recombination of atoms in both solid Ar and Kr were measured. The data are shown in figure 5. The F atoms recombine on the timescale of several minutes at 27 and 17 K in solid Ar and Kr respectively. The process is activated, with a higher activation energy in Ar than in Kr. This is rationalized by the fact that while F-Ar and F-Kr potentials are very similar, due to the larger nearest neighbor distances in Kr, the activation volume is smaller there. Quantitative analysis of diffusion constants in these systems is presently underway. The detailed analysis is complicated by the fact that

the photogenerated F atoms are produced with an initial discrete F-F distribution that may not be homogeneous. Careful measurements of thermally induced recombination indicate that at large doping densities, recombination may be a cooperative process.

In conclusion, all of the qualitative aspects of the very peculiar photodynamics of F atoms in solid Ar and Kr are well understood and reproduced by our theoretical simulations. Given the simplicity of the system, a more exact simulation of the experiments is desirable. The observed deviations, mainly quantum yields of dissociation near threshold energies, seem to have their origin in the description of atom-atom pair potentials. Progress along these lines will be essential in order to treat more complicated systems and to make predications about possible fuel systems. Studies of recombination dynamics, should provide another source of information on the many-body potentials that govern dynamics in these media.

Cl₂ under high pressure:

In the previous section, we discussed the fact that although F₂ can be efficiently dissociated in rare gas solids, F atoms can only be maintained in the solid at cryogenic temperatures. Given that diffusion is an activated process, it is to be expected that in compressible solids pressure can have a dramatic effect on atomic mobilities. This was an important motivation for initiating photodissociation studies of Cl₂ in xenon under high pressures, in a diamond anvil cell (DAC).¹¹ A second motivation for these studies, was the existing background of information and the recent theoretical simulations of this system (at zero pressure) which we discuss below prior to presentation of our results.

The photodissociation of Cl₂ in rare gas solids has been known to be subject to a very large cage effect.⁴ However, the early experiments in this system were carried out under limited conditions (4 - 12 K matrices, and a dissociation excess energy of ~1.2eV). We had subsequently shown that in both Kr and Xe, Cl₂ can be dissociated via the Xe⁺Cl₂ charge transfer potentials, a process referred to as two-photon induced harpooning.¹² The absence of any dissociation via the covalent repulsive surface has been intriguing, and as such the subject of recent MD simulations.¹³ In their studies, Alimi and Gerber discovered that while indeed at cryogenic temperatures Cl₂ does not dissociate (at 1.2eV excess energy), when the solid is warmed up above 90 K, dissociation is observed. The threshold temperature for dissociation, also corresponds to the threshold in free rotation of the molecule in the lattice. Note the contrast between Cl₂ and F₂. In the case of Cl₂, the molecules are locked in an unfavorable geometry for dissociation, hence rotation opens up cage exit channels. In the case of F₂, at 4 K, the molecule traps in a librational well and points directly at one of the reactive cones; free rotations reduce the cage exit probability,

since the molecules sample the unreactive orientations. An even more dramatic prediction of the theoretical simulations was that cage exit quantum yields have a nonmonotonic temperature dependence. This effect, which has previously been observed in HI as well, has a very significant implication with respect to condensed phase dynamics, related to recrossings over the transition state barrier. The temperature range of relevance for these studies, 90 - 160 K, at which comparisons could be made with theory, is inaccessible to experiments. This is due to the fact that at temperatures near 120 K, self-diffusion of Xe sets in, and therefore isolated molecular dynamics is not practical to study. The DAC studies, clearly overcome this problem. Under a few kbar of pressure, Xe is a solid at room temperature.

The photodissociation of Cl_2 in solid xenon, in the DAC, was followed by the generation of Cl atoms.¹¹ The latter are monitored by the Xe_2Cl emission induced by charge transfer between Xe and Cl at 308 nm. The same wavelength was also used for the initial dissociation. Dissociation of a 1:500, Cl_2 :Xe sample could be completed at pressures above 50kbar. The product atoms, at pressures above 50kbar, were stable with respect to recombination for periods in excess of several weeks! This could be verified by monitoring the Xe_2Cl emission intensity over extended periods of time. The impurity fluorescence from the diamond windows served as a useful internal standard for such comparisons. In figure 6, spectra taken 20 days apart are shown, which indicate the absence of any recombination. From such measurements, it can be inferred that the diffusion constant of Cl in Xe at 50kbar is less than $10^{-20}\text{cm}^2/\text{s}$.

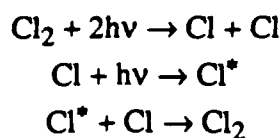
In order to investigate the photodissociation dynamics of Cl_2 , it was necessary to resort to lower pressures, to recombine the atoms. At 20kbar, the recombination time was several hours, yielding a diffusion constant of $\sim 10^{-17}\text{cm}^2/\text{s}$. Thus, nearly three orders of magnitude in diffusion constant reduction is attained by increasing the cell pressure by less than a factor of 3! This should be taken as the clearest demonstration of the dramatic effect of pressure on the stabilization, and therefore increased storage capabilities, of radicals in compressible solids.

Photomobility of Cl atoms, photodissociation of Cl_2 as a function of temperature, and as a function of photon fluence were studied in the 20kbar solids. The power dependence measurements indicate that in all cases, the observed dissociation is due to a two-photon process. As in the case of zero pressure solids, the mechanism is attributed to the harpoon process



This process is strongly temperature dependent. The two-photon dissociation cross section of Cl_2 in Xe at 20kbar increases by more than 3 orders of magnitude for the temperature range between 30 and 300 K.

As in the case of F doped solids, photomobility of Cl atoms is observed upon the radiative dissociation of Xe_2Cl . The latter process also shows a very strong temperature and pressure dependence. As a result, at room temperature, and in 20kbar solids, the dissociation cannot be carried out to completion. A photochemical steady state in Cl atom concentration is reached. The governing kinetics can be illustrated as:



Integration of the rate expressions associated with this mechanism yields a tanh behavior for the Cl atom concentration with irradiation time, and the data are well fit as such.

Given the known absorption coefficient of Cl_2 at the irradiated wavelength (308nm), for the measured two-photon dissociation cross section, an upper limit for the one-photon direct dissociation of Cl_2 via its $^1\Pi_u \leftarrow ^1\Sigma_g$ continuum absorption can be extracted. These results are summarized in figure 7. It can be seen there, that even at room temperature, the direct dissociation quantum yield of Cl_2 in Xe is less than 10^{-2} . The theoretical treatment for this process, for zero pressure solids, had predicted a quantum yield as high as 60% at 160 K. Whether this discrepancy of several orders of magnitude is due to pressure alone, is not known as yet. Simulations with pressure as a variable are planned. Comparisons between experiment and theory with the large temperature and pressure windows afforded by diamond anvil cell techniques should lead to a rigorous test of our understanding of molecular dynamics in these seemingly simple solids.

In conclusion, I hope to have illustrated with the above examples, that our understanding of dynamics in solids is at a preliminary stage. Rigorous comparisons between theory and experiment are only now becoming available. Many iterations will perhaps be necessary to establish a firm basis for the large variety of behaviors heretoforth encountered. The two examples I have discussed should also serve to point that both efficient generation and stable storage of radicals at relatively high densities are possible by optimization of controlling parameters.

References:

1. Formation and Trapping of Free Radicals, eds. A.M. Bass and H.P. Broida (New York, Academic Press, 1960).
2. A Bibliography of Matrix Isolation Spectroscopy, eds. D.W. Ball, Z.H. Kafafi, L. Fredin, R.H. Hauge, J.L. Margrave, (Rice University Press, Houston, 1988).
3. N. Schwentner and V.A. Apkarian, Chem. Phys Lett. 154, 413 (1989); A.I. Katz, J. Feld and V.A. Apkarian, Optics Lett.
4. L.E. Brus and V.E. Bondybey, J. Chem. Phys. 65, 71 (1976); V.E. Bondybey and C. Fletcher, J. Chem. Phys. 64, 3615 (1976); V.E. Bondybey and L.E. Brus, J. Chem. Phys. 62, 620 (1975); 64, 3724 (1976).
5. R. Alimi, R.B. Gerber and V.A. Apkarian, J. Chem. Phys. 92, 3551 (1990).
6. J. Feld, H. Kunttu and V.A. Apkarian, J. Chem. Phys. (in press).
7. H. Kunttu and V.A. Apkarian, J. Chem. Phys. (submitted).
8. H. Kunttu, J. Feld, R. Alimi, A. Becker and V.A. Apkarian, (J. Chem. Phys., in press).
9. H. Kunttu and V.A. Apkarian (manuscript in preparation).
10. C.H. Becker, P. Casavecchia, and Y.T. Lee, J. Chem. Phys. 70, 2986 (1979).
11. A.I. Katz and V.A. Apkarian, J. Phys. Chem. (in press).
12. M.E. Fajardo, R. Withnall, J. Feld, F. Okada, W. Lawrence, L. Wiedman, and V.A. Apkarian, Laser Chem. 2, 1 (1988).
13. R. Alimi, A. Brokman, and R.B. Gerber, J. Chem. Phys. 91, 1611 (1989).

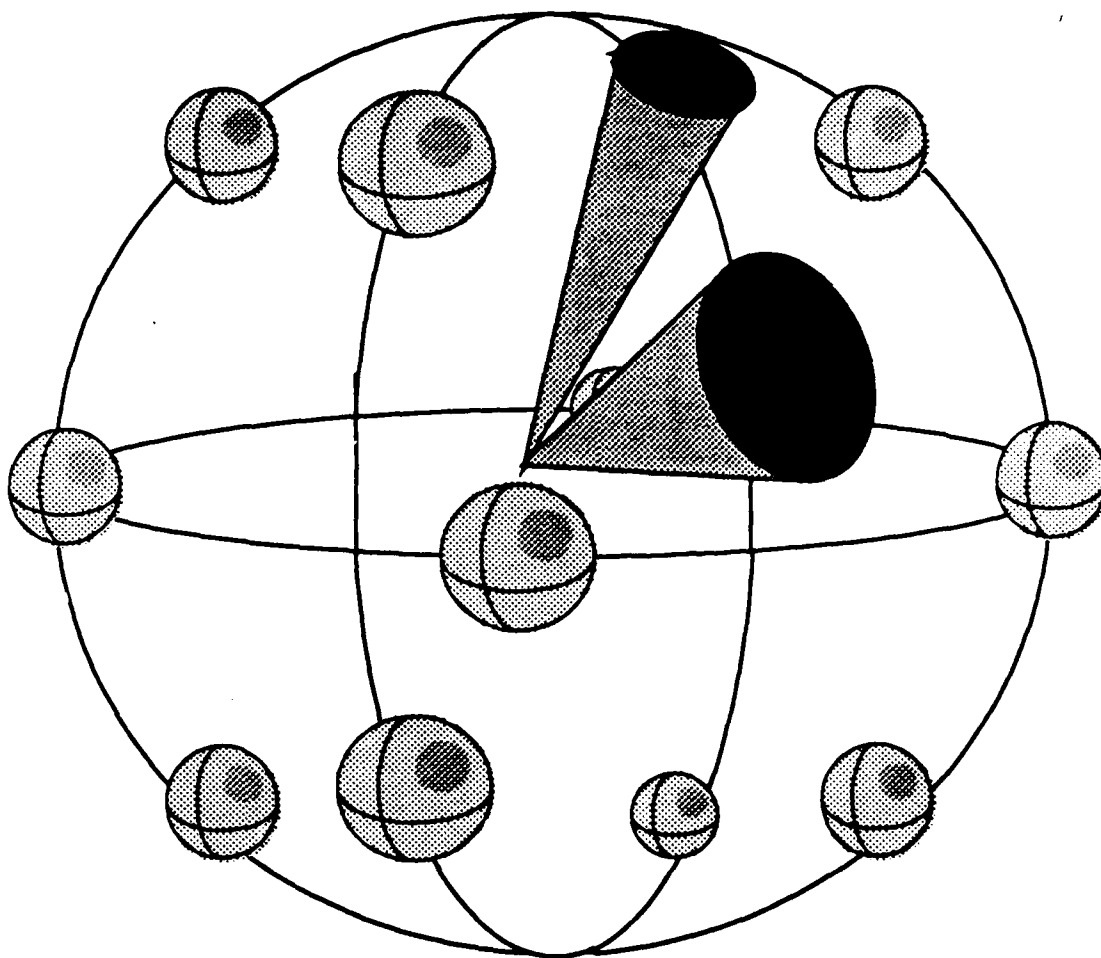


Figure 1. Reaction cones for F_2 dissociation in an fcc lattice of argon.

Figure 2. Photodissociation quantum yields of F_2 in a) solid Ar: (filled circles) = theory, (open circles) = experiment at 12 K; b) solid Kr: (diamonds) = experiment.

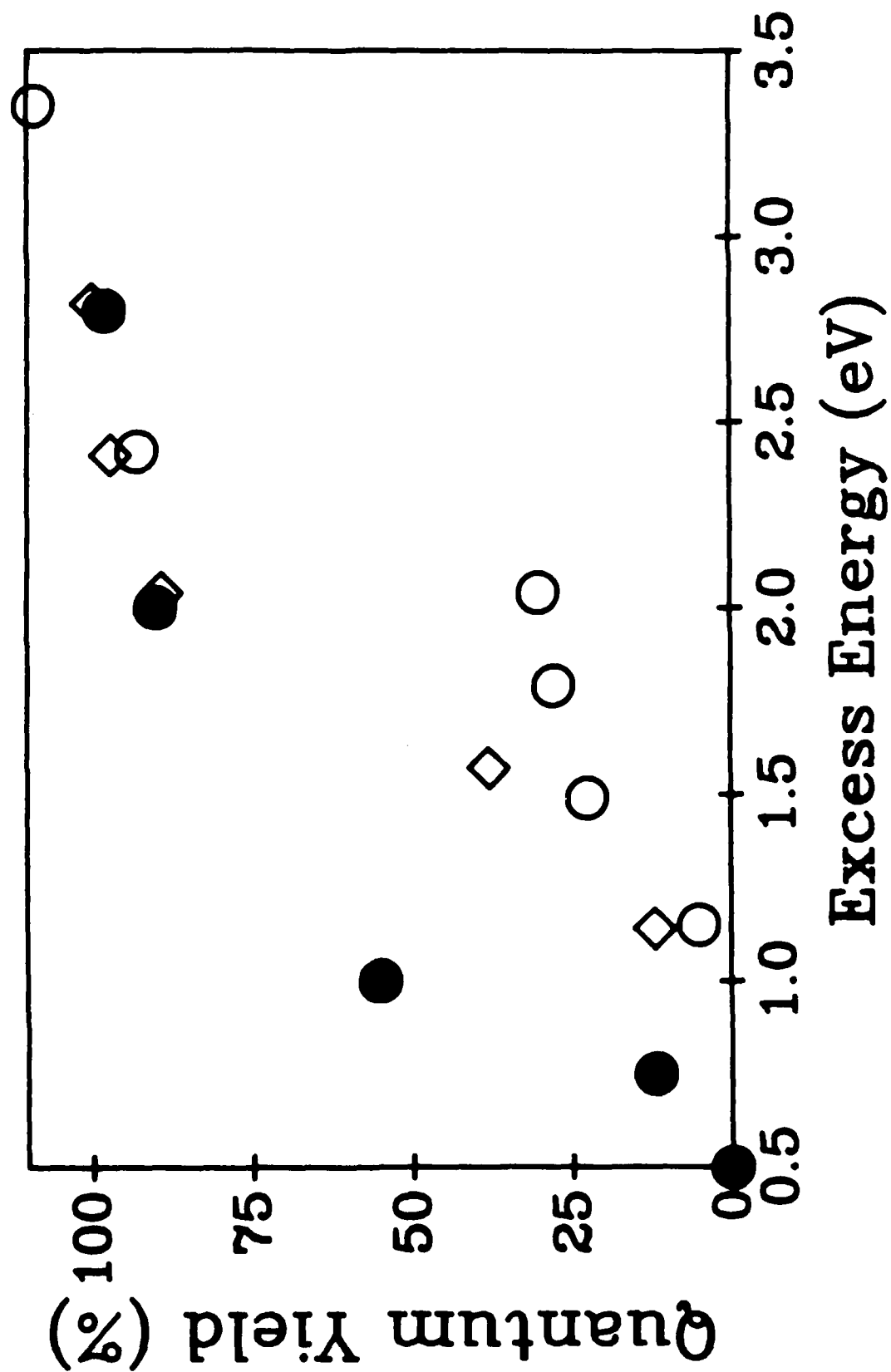
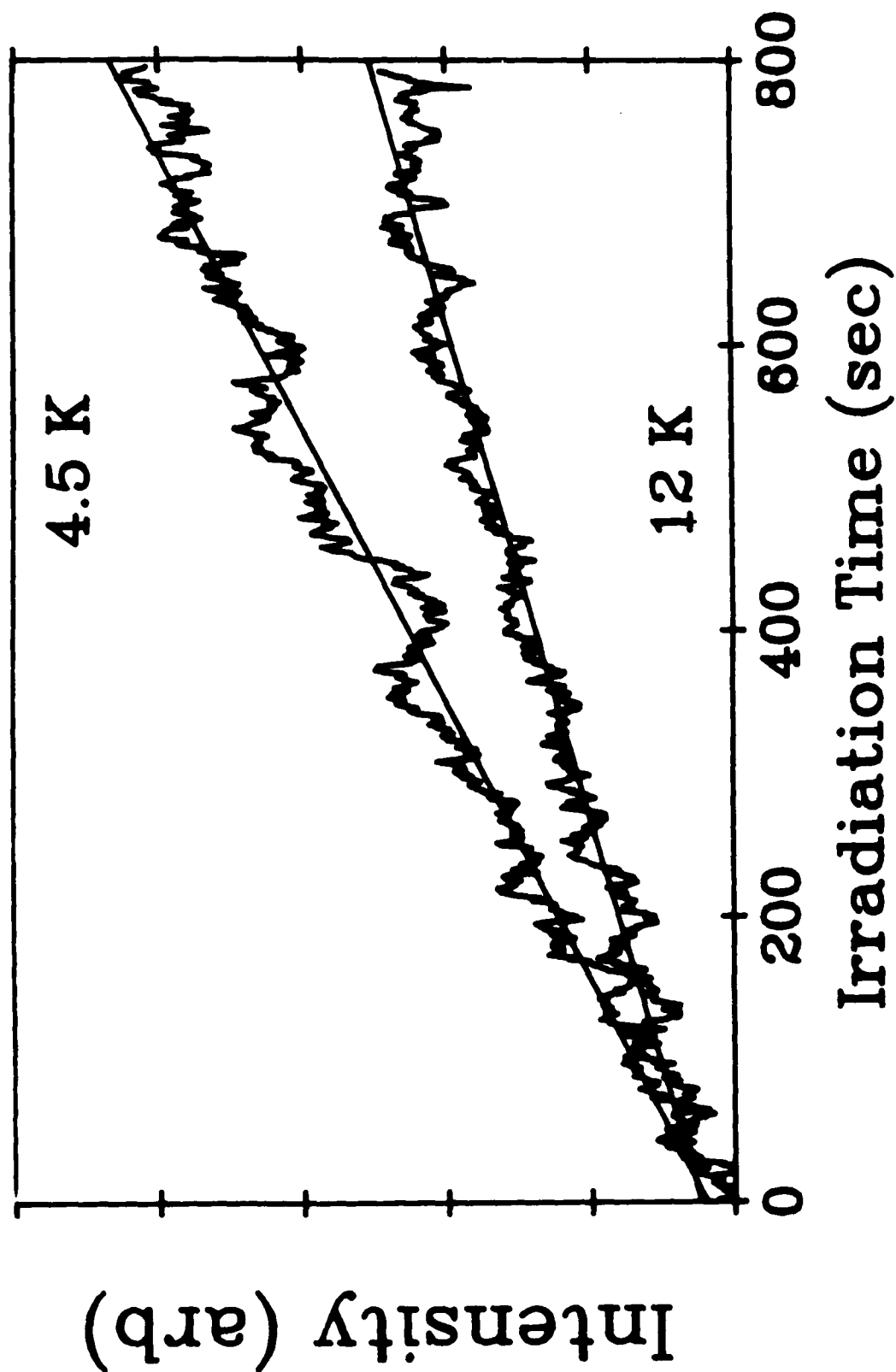


Figure 3. Photoproduction of F atoms in solid Kr irradiated at a) 12.5 K, b) 4.5 K. The production rate is a factor of 2 higher at the lower temperature.



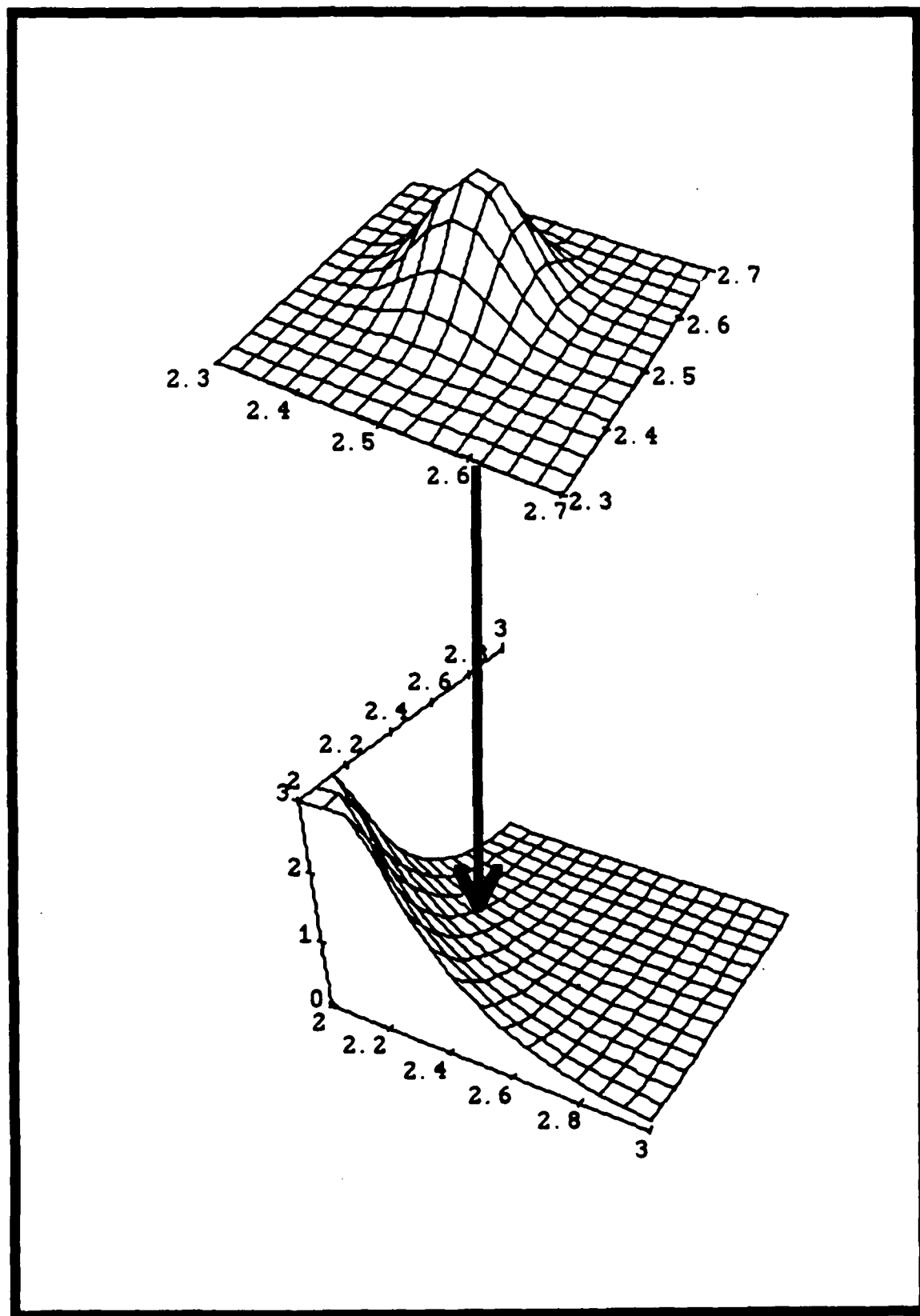


Figure 4. Radiative dissociation process for Rg_2^+X^- .

Figure 5. Thermally induced recombination of F atoms in solid Argon (open circles) and solid Kr (filled circles).

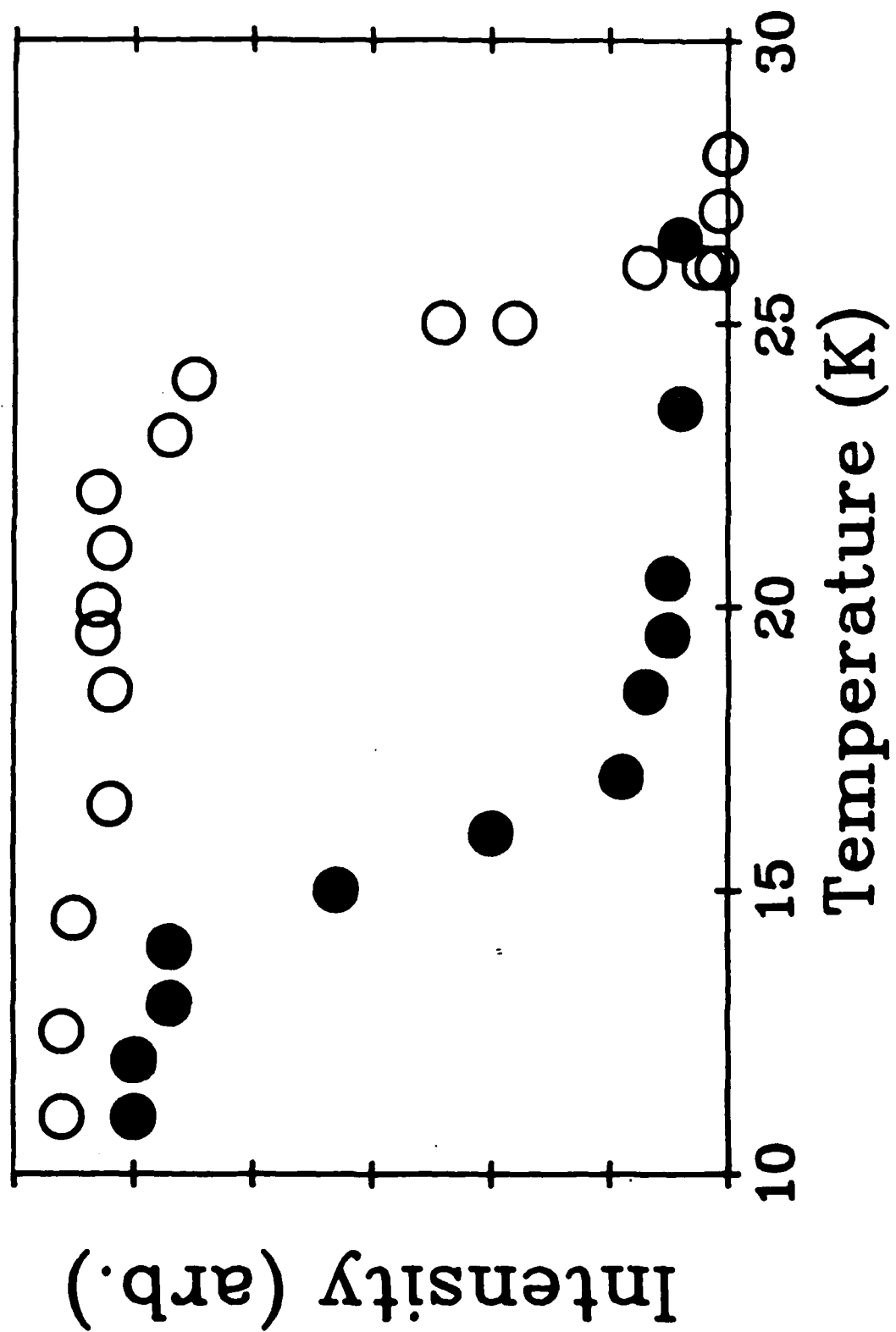
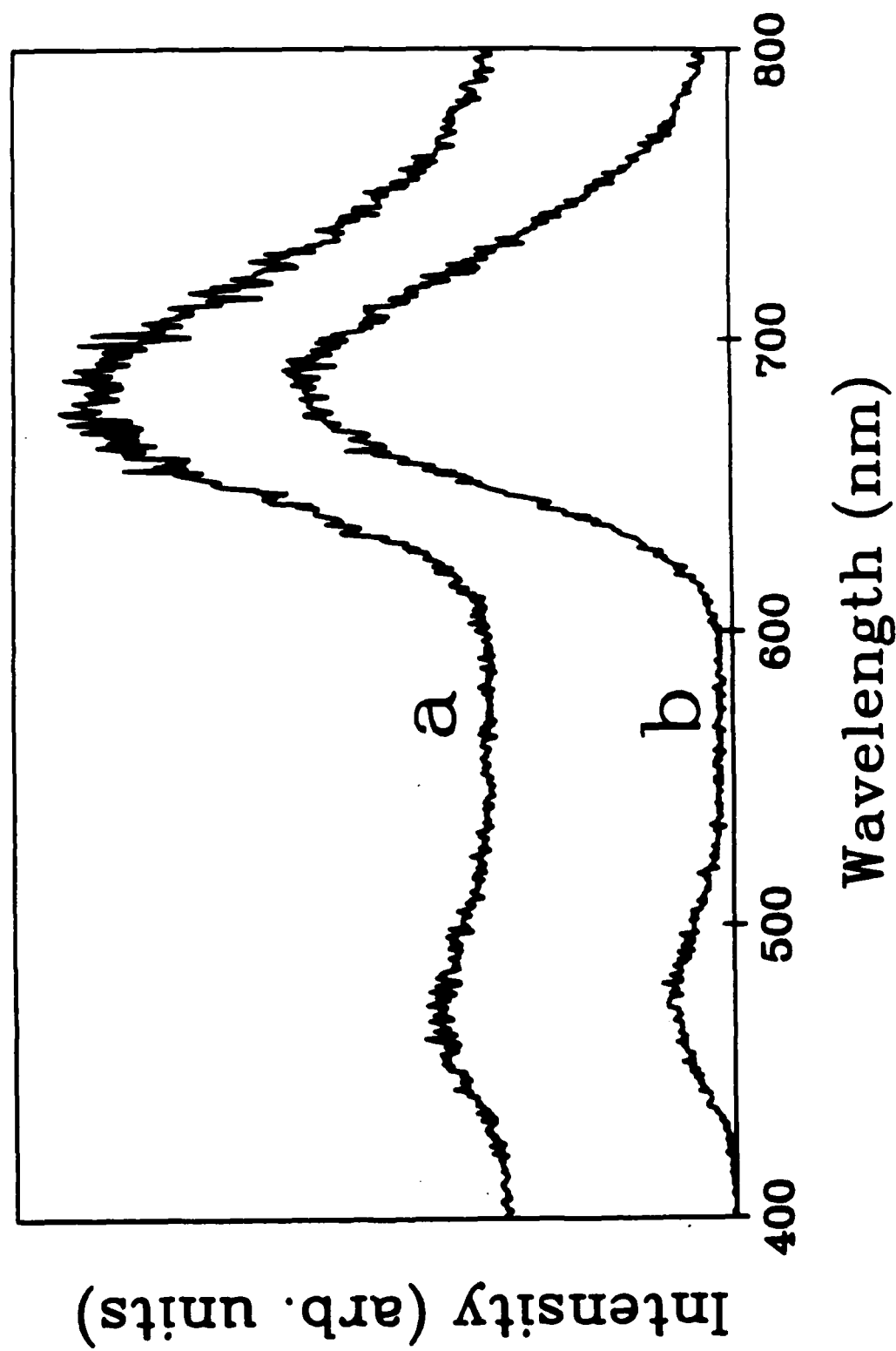


Figure 6. The absence of Cl atom recombination in a DAC at room temperature and 50kbar pressure. The two spectra were taken 20 days apart. The Xe_2Cl emission, at 690 nm, relative to the diamond impurity fluorescence, at 470 nm, indicates that no recombination has occurred over this time period.



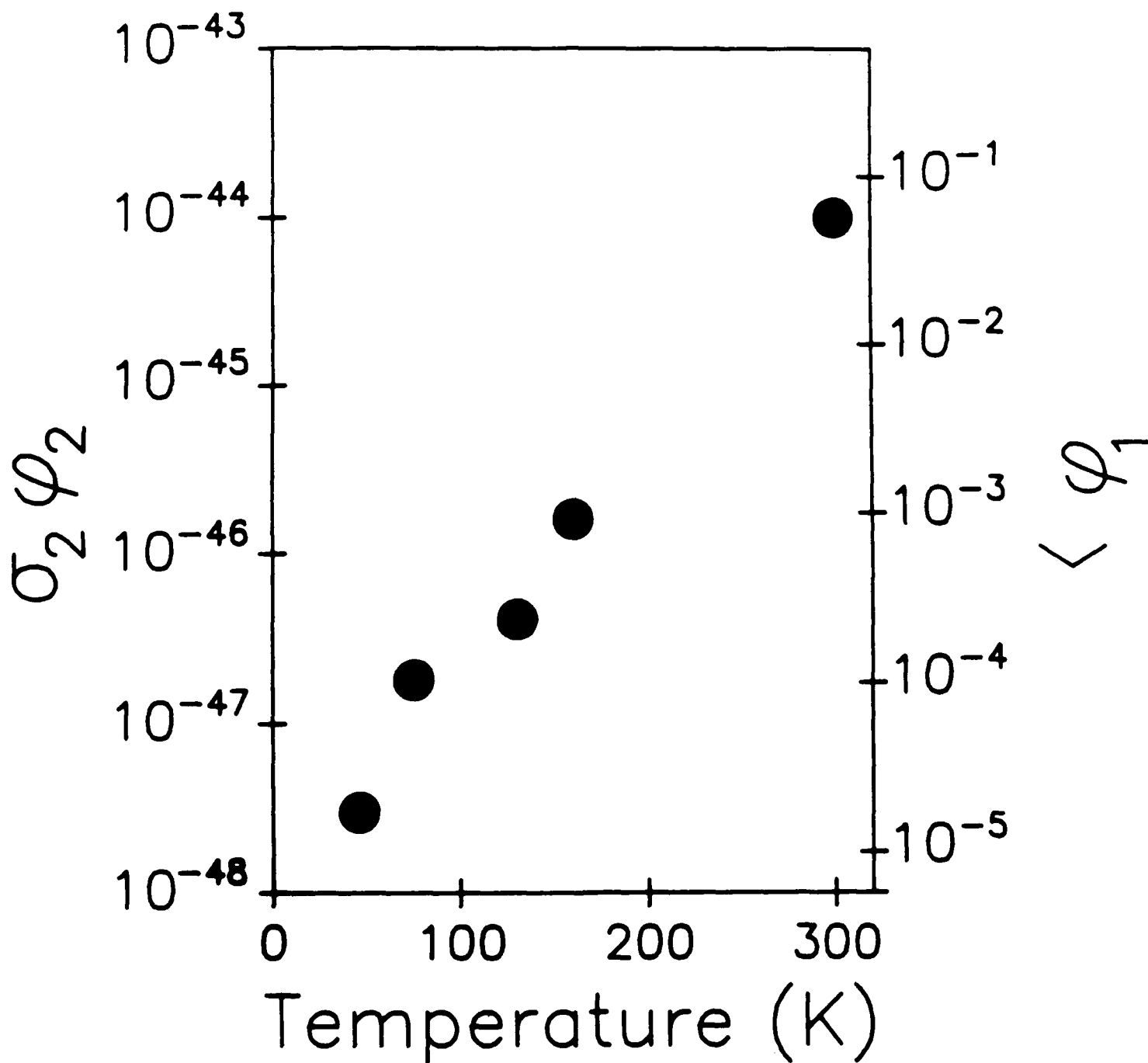


Figure 7. Two-photon induced Cl_2 photodissociation cross sections (left ordinate) are shown as a function of temperature ($P = 20$ kbar). The right ordinate is the upper limit for one-photon dissociation of Cl_2 , via its covalent Π_u surface.

**High Energy Density Systems in Cryogenic Media:
The Production and Reaction of Atoms and Radicals**

Eric Weitz

Department of Chemistry
Northwestern University
Evanston, IL 60208

The overall aim of our program is to investigate the effect of a condensed phase rare gas environment on the photochemistry, photophysics and subsequent chemistry of reactive species. Within the context of this overall goal the major areas of investigation in our AFOSR supported work have centered on:

- Measurements of the mobility of reactive species in low temperature condensed phase media with the objective of relating these measurements to the diffusion coefficients for these species and to the rates of diffusion limited reactions of these species as well as to the prospects for chemical energy storage involving reactive species.
- Investigations of the influence of low temperature condensed phase media on dynamical processes with an emphasis on energy transfer processes.

This report will summarize the results of our recent work in these areas.

Mobility of Reactive Species in Rare Gas Matrices

There is a large body of literature dealing with the production of stable products and/or reactive species via the reaction of an atom or radical with a molecule that is present as a dopant in rare gas matrices.¹ For example, the HO₂, HCO and HNO radicals can all be produced via the reaction of photolytically produced H atoms with O₂, CO and NO respectively.²⁻⁴ A variety of reactions of O atoms have been reported following the photolytic generation of these atoms.^{1,5} These observations have been widely interpreted to indicate that at least small atomic species are mobile in low temperature rare gas matrices on the time scale of seconds or minutes that is necessary to obtain a spectrum of the reaction products.⁵ However, surprisingly little has been done to quantify the mobility of such species in rare gas solids.

Since a variety of atom - atom and atom - diatom reactions have very low or zero activation energies, these reactions should be diffusion limited in low temperature rare gas solids.⁷ Thus, a measurement of the rate of reaction in these systems should be tantamount to the measurement of a diffusion coefficient in the context of the formalism of diffusion limited reaction kinetics.⁸

Two such systems that we have studied are the reactions of H + O₂ to give HO₂ and the reaction of O + CO to give CO₂. Previously we have reported on a method that uses transient

infrared spectroscopy to monitor the rate of reaction of these reactive species in doped rare gas matrices.⁶ The latter reaction was discussed at the 1989 AFOSR meeting on High Energy Density Materials while the former was reported on at the 1988 AFOSR Meeting on High Energy Density Materials. The O + CO system was particularly interesting. Via transient IR spectroscopy studies, we found that some CO₂ was produced on a time scale of less than 1 msec. However, the amount of CO₂ produced was typically less than 20% of the total expected based on the number of O atoms produced. These results seemed to imply that a relatively small sub-set of O atoms reacted relatively rapidly with CO to form CO₂ while the remaining O atoms were nonreactive on the timescale of observation. As a result of these observations, we set out to develop a method which would allow us to further quantify the lifetime for O atoms in rare gas matrices. We have now developed such a technique which has obvious extensions to other reactive species.

The apparatus for the technique is shown in figure 1. O atoms are conveniently produced via ArF laser photolysis of N₂O doped rare gas matrices. The O atom concentration can be

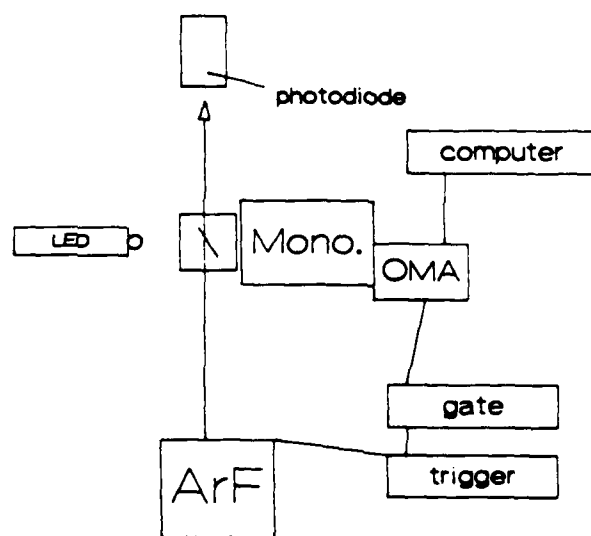


Fig. 1. Apparatus diagram for a typical experiment involving monitoring O atom concentration via XeO emission.

followed by the intensity of emission from XeO exciplex states where a subsequent laser pulse is used to excite XeO pairs (O atoms adjacent to Xe atoms) that are present in these xenon doped (or neat xenon) rare gas matrices. The XeO pairs, which are expected to be proportional to the concentration of O atoms are initially excited to charge transfer states which subsequently and rapidly decay to covalent exciplex states which then emit to the ground state.⁹ The intensity of this

emission as a function of time is a measure of the O atom concentration in these matrices. There is no evidence for reaction of O atoms with either N_2O or N_2 which is not surprising since O atom reactions with N_2O are significantly activated and the reaction of O with N_2 is spin forbidden for the ^3P ground state of O. Thus, the only reaction that is anticipated is O atom recombination to form O_2 .

Typically, a few hundred pulses are used to produce an initial O atom concentration and one or two pulses at each of a number of subsequent delay times are used to probe the current O atom concentration. Thus probe pulses do not significantly perturb the initial O atom concentration. A photodiode behind the matrix is used to monitor the UV transmittance of the matrix while a light emitting diode at approximately the XeO emission frequency is used to monitor and correct for time dependent changes in the transmission of the matrix at this frequency.

A typical time dependence for the XeO emission is shown in figure 2. Note that the data in figure 2 is the reciprocal of the intensity (number of counts) of the XeO emission signal at a

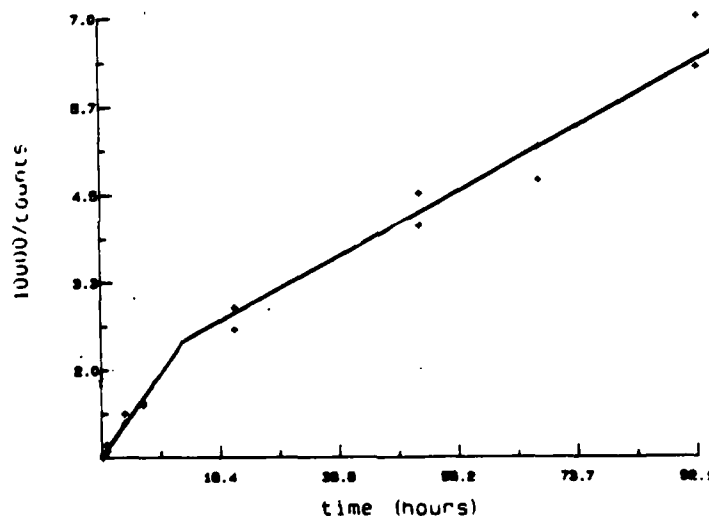


Fig. 2. A plot of $1/\text{conc}$ (1/counts) of O atoms vs. time (hours) in a 1:729, $\text{N}_2\text{O}:\text{Xe}$ matrix at 40 K. The initial ratio of O atoms to Xe is 1:6600.

given time following the initial production of O atoms. Since the only viable loss mechanism is $\text{O} + \text{O}$ atom recombination, a decrease in signal and thus O atom concentration with time probes the rate of this reaction when the signal intensity is corrected for changes in matrix transmission with time. Further evidence that O_2 is being produced as a result of $\text{O} + \text{O}$ recombination reactions can be obtained from studies in N_2O doped Kr matrices where O_2 emission can be directly observed following KrF or ArF laser excitation of O_2 formed as a result of the O atom recombination

reaction. However, these studies require a thicker or more concentrated matrix than is necessary for the studies involving XeO emission but they can be done without Xe doping of matrices and provide direct evidence for O₂ production.

Note that the timescale for loss of O atoms in figure 2 is hours. In particular, the first halflife for loss of O atoms is approximately 10 hours! Another interesting observation is the appearance of a faster loss process at short times. This is also seen in figure 3 where the rate of

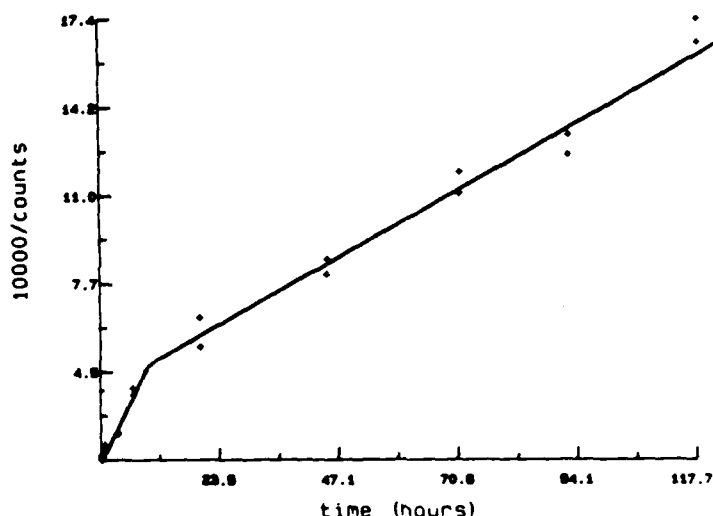


Fig. 3. A plot of 1/conc of O atoms vs. time in a 1:729 N₂O:Xe matrix at 32 K. The initial ratio of O atoms to Xe is 1:6600.

loss of O atoms seems to have two components. An initial fast component with a first halflife of a few hours and then a much longer timescale component with a first halflife of approximately 20 hours. Note that both components in the O atom loss data are slower at lower temperature as might have been anticipated. These changes in emission intensity with time should be corrected for changes in the matrix transmission at both the probe laser wavelength and at the emission wavelength. When these corrections are made the apparent rate of loss of O atoms is reduced (ie - some of the reduction in intensity of the XeO emission signal appears to result from a reduction in transmission of the matrix with time at the ArF and/or the XeO frequency). We are still working to make sure that the measurements we make of the change in transmission of the matrix are those that are representative of corrections that should be applied to the sample. However, it is clear that these corrections act to reduce the apparent rate of loss of O atoms. Thus, the uncorrected rate of loss can be viewed as an upper limit for the actual loss rate and the diffusion coefficient that can be derived from this data can be viewed as an upper limit for the diffusion

coefficient for O atoms in the relevant matrix. Using this data and the standard formulation for the apparent rate of a diffusion controlled reaction⁸ leads to a upper limit for the diffusion coefficient of O atoms in a Xe matrix at 40 K of approximately $2 \times 10^{-17} \text{ cm}^2 \text{ sec}^{-1}$.¹⁰ The only thing that could currently change this picture is if initial fast loss processes reduced the concentration of O atoms significantly from the concentration we determine based on IR measurements of N₂O photolysis. Via measurements of O₂ production in N₂O doped Kr matrices we have determined that no more than 20% of the O atoms that are initially generated rapidly (timescale of minutes or less) react to form O₂. From a variety of indirect measurements we believe that a similar percentage of O atoms rapidly react to form O₂ in Xe matrices. As long as the percentage of O atoms that react rapidly is not considerably higher, the aforementioned value for the upper limit of the diffusion coefficient in these systems will be valid. We are currently working to explicitly measure the magnitude of the immediate O atom loss processes in Xe matrices.

We have also performed similar experiments in Xe doped Kr matrices with similar results. The rate of loss of O atoms was measured at two temperatures. The long term loss process at 35 K had a first halflife of ~18 hours while at 25 K the first halflife was ~60 hours. Taking into account the respective concentrations of O atoms this yields an upper limit for the diffusion coefficient of 7×10^{-18} and $3 \times 10^{-18} \text{ cm}^2 \text{ sec}^{-1}$, respectively.¹⁰ As with Xe matrices, the lower temperature measurement also appears to have a faster initial O atom loss process. Since, at present we are reporting these diffusion coefficients as upper limits, care should certainly be exercised in interpreting the temperature dependence of these coefficients as attributable to an activation energy for diffusion. However, if the observed temperature dependence is attributed to an activation energy, this activation energy can be used to calculate a diffusion coefficient at lower temperature. Following this procedure, one calculates a first halflife for O atoms present at one part in 10,000 in Kr at 4.2 K of greater than 1 million years! Though this shouldn't be taken too seriously in a quantitative sense, it is an indication that O atoms are expected to be stable for long periods of time at low temperatures in rare gas matrices.

It is now interesting to consider how one can reconcile the observations of the two different types of experiments we have performed involving O atom diffusion. In the first, involving transient IR detection, a relatively small fraction of O atoms react rapidly and the rest do not react on a timescale of minutes. In the second, which uses XeO emission as a probe of O atom concentration, the majority of O atoms are seen to have a halflife of many hours with a more rapidly evolving component in the O atom concentration.

This situation suggests that we are looking at different "classes" of atoms. An appealing though not necessarily unique explanation is that the first "class" of atoms with the fastest reactive behavior involves those O atoms which are either formed in the same site as a reactant or are formed in a site that is linked to a nearest neighbor reactant site via a defect. The longest timescale process seems to be most reasonably assignable as involving motion of the O atoms through the bulk of the matrix. The middle timescale process, which is apparent in each of the Xe and at lower temperature in the Xe doped Kr experiments, and is suggestive of more rapid loss of O atoms at early times would then involve either O atoms that are not representative of the bulk distribution of O atoms (ie - possibly O atoms that are in nearest neighbor sites to other O atoms) or those that are linked to other O atom sites via longer range defects. Presumably this process is not as obvious in the higher temperature Xe doped Kr samples because its rate is now faster than we can now conveniently probe changes in O atom concentration, which is on the timescale of minutes, and which is now limited by our ability to achieve a stable signal for the XeO matrix following O atom production followed by a suitable time period that produces a measurable change in the XeO signal.

It is possible to prepare matrices with induced defects and it is also possible to perform similar experiments in rare gas crystals with fewer defects than is typically present in matrices. We plan to attempt both types of experiments to further clarify the process(es) that are responsible for the reaction of O atoms on timescale that are not consistent with bulk motion. It is also possible that a process taking place on a faster timescale than bulk motion involves terms in the diffusion equation of higher order than the long time scale solution.

We are also in the process of developing a "Monte Carlo" program which simulates diffusion in ordered lattices by introducing a fixed or random distribution of atoms and a fixed or random hop frequency. This will allow us to assess the role of nearest neighbor reactants and anomalous distributions which might result from attractive forces on the observed diffusion rates.

The fact that a significant fraction of O atoms in these rare gas matrices are stable with respect to reaction is an interesting and important result for "storage" of chemical energy in these systems. It implies that such systems are capable of long term storage of highly reactive species.

Energy Transfer

Isolated binary collision (IBC) models of vibrational energy transfer and relaxation processes in dense media have been developed in an effort to obtain a predictive ability for rates for these processes in dense media based on rates for the corresponding processes in a dilute gas phase environment. In its simplest form an IBC picture of vibrational relaxation in dense media assumes

that vibrational relaxation is due to binary interactions which are well separated in time (time between encounters that leads to energy transfer \gg vibrational period) and that the probability of relaxation per collision event, P , is independent of phase. Then

$$1/\tau = (1/\tau_c) \cdot P \quad (1)$$

where P can be determined from gas phase experiments. In this picture, the liquid phase problem boils down to a calculation of $1/\tau_c$, the collision rate in the dense media (condensed phase). A variety of approaches have been used to calculate $1/\tau_c$. The simplest is the cell model of Madigosky and Litovitz¹¹ where

$$1/\tau_c = \frac{\bar{v}}{(\rho^{-1/3} - \sigma)} = \left(\frac{8KT}{\pi\mu} \right)^{1/2} (\rho^{-1/3} - \sigma)^{-1} \quad (2)$$

Current treatments typically employ radial distribution functions and derive formulas of the type

$$1/\tau_\ell = \frac{1}{\tau_g} \frac{\rho_\ell}{\rho_g} \frac{g_\ell(R^*)}{g_g(R^*)} \quad (3)$$

where various methods are used to evaluate $g_\ell(R^*)$, the liquid phase radial distribution function at R^* , the effective distance for vibrational energy transfer.¹²

We have been interested in the applicability of IBC models to systems undergoing V-V energy transfer and those where complex formation may occur.¹³ Vibrational relaxation rates in condensed phase have been found to be well represented by an IBC treatment in virtually all systems studied to date.¹⁴ If this were uniformly true, then IBC treatments could be used to accurately estimate the rates for vibrational relaxation processes in condensed phase based on gas phase data. However, last year at the 1989 HEDM meeting we reported on the possible role of complexes in HF vibrational relaxation processes.¹⁵ The conclusion of this study was that in polar systems strong interactions may lead to complex formation in dense media which could lead to significant deviations from the predictions of IBC models. In addition, diffusion in high density media may limit the rate of interaction of two dilute species thus decreasing the apparent total relaxation rate of that species. To see whether HF is truly a uniquely anomalous system, we began an investigation of energy transfer processes in NO. Relaxation processes in NO are remarkable in that even though the NO first vibrational level is only a few hundred cm^{-1} lower than the corresponding level in CO, its collisional self relaxation rate is approximately 5 order of magnitude

faster than the corresponding rate in CO. Complexes have been implicated as a possible cause for this behavior.¹⁶

Though our studies of NO are not yet complete preliminary results indicate that the vibrational relaxation rate for NO in liquid rare gases may also be influenced by complex formation.¹⁷ To further aid in comparisons between gas phase and liquid phase data, we have developed a program based on the Metropolis method¹⁸ that will currently allow us to calculate a radial distribution function for a spherical Lennard-Jones molecule in a bath of other spherical Lennard-Jones molecules. As an example, a radial distribution function for NO in liquid Ar is shown in fig. 4. This program is currently being modified to allow us to treat non-spherical

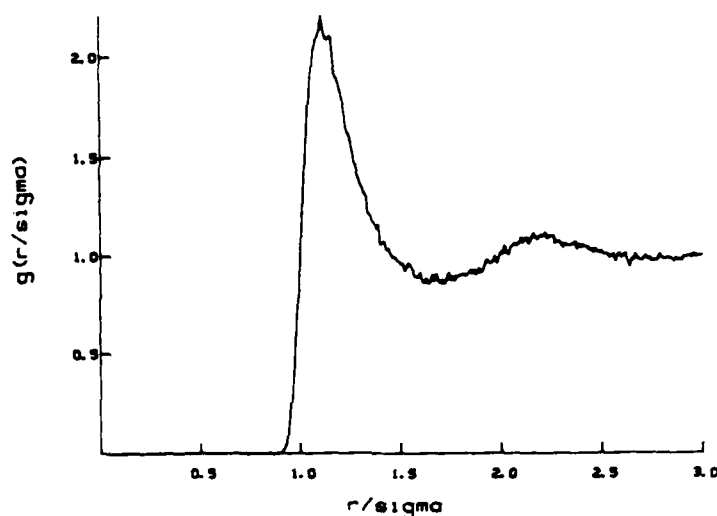


Fig. 4: A plot of the radial distribution function $g(r/\sigma)$ versus (r/σ) for NO in liquid Ar at 147 K.

molecules with arbitrary potentials.¹⁹ HF and NO may both be anomalies with respect to vibrational relaxation behavior and it is important to explore the nature of these anomalies and their causes. Nevertheless, in most cases vibrational relaxation rates will be predictable from gas phase rate constants and thus such energy transfer processes in condensed phase media can be modeled based on gas phase data.¹⁴

References

1. **Vibrational Spectroscopy of Trapped Species**, ed. by H. E. Hallan, Wiley-Interscience, Bristol, England, 1973.
2. D. E. Milligan and M. E. Jacox, *J. Chem. Phys.* **38**, 2627 (1963).
3. D. E. Milligan and M. E. Jacox, *J. Chem. Phys.* **41**, 3032 (1964).
4. M. E. Jacox and D. E. Milligan, *J. Mol. Spect.* **48**, 536 (1973).
5. See, for example, R. N. Perutz, *Chem. Revs.* **85**, 77 (1985) and *ibid.*, **85**, 97 (1985).
6. E. Weitz, 1988 and 1989 AFOSR HEDM Meeting and reports.
7. **Rate Constants of Gas Phase Reactions**, V. N. Kondratiev, Office of Standard Reference Data, NBS (1972).
8. See for example, **Diffusion in Solids, Liquids, Gases** by W. Jost, Academic (1960) NY.
9. W. F. Scott and W. C. Walker, *J. Chem. Phys.* **81**, 4903 (1984); J. Goodman, J. C. Tully, V. E. Bondybey and L. E. Brus, *J. Chem. Phys.* **66**, 4802 (1977).
10. H. Krueger and E. Weitz, manuscript in preparation.
11. W. M. Madigosky and T. A. Litovitz, *J. Chem. Phys.* **34**, 489 (1961); D. W. Oxtoby, *Adv. Chem. Phys.* **47**, 487 (1981).
12. J. Chesnoy and G. M. Gale, *An. Phys. Fr.* **9**, 893 (1984).
13. Y. P. Vlahoyannis, H. Krueger and E. Weitz, *J. Chem. Phys.* **86**, 3311 (1987); R. Granek, A. Nitzan and E. Weitz, *J. Chem. Phys.* **89**, 5589 (1988).
14. H. Krueger and E. Weitz, *Israeli J. Chem.*, in press.
15. A. K. Moustakas and E. Weitz, to be published.
16. E. Weitz and G. W. Flynn, *Ann. Rev. of Phys. Chem.* **25**, 275 (1974) and references therein.
17. A. K. Moustakas and E. Weitz, work in progress.
18. N. Metropolis, A. W. Rosenbluth, M. N. Rosenbluth, A. H. Teller and E. Teller, *J. Chem. Phys.* **21**, 1087 (1953).
19. H. Krueger and E. Weitz, work in progress.

A PERCOLATION THEORY OF SOLID STATE CHAIN REACTIONS^a

Charles A. Wight

Department of Chemistry
University of Utah
Salt Lake City, Utah 84112

Abstract

A simple theory is presented which describes the propagation of chain reactions in amorphous solids. It is developed within the framework of percolation on a Bethe lattice. Simple analytical formulae are obtained for the average chain lengths and chain length distributions. These are compared with computer simulations of bond percolation on three dimensional lattices and with recent experimental results. The theory is flexible enough to describe chain reactions in pure solids (e.g., polymerization of solid formaldehyde at 10 K) as well as chain reactions in binary solid solutions (e.g., reaction of Cl_2 with cyclopropane deposited as a van der Waals glass at 77 K). The predicted dependence of reaction chain length on the relative concentrations of the two reactants is in good accord with experimental results.

Introduction

The theory of percolation is a powerful methodology for describing the bulk behavior of a population based on interactions between its individual members.^{1,2} The theory finds application in a wide variety of problems such as modeling the flow of liquid through a porous medium (from which the theory derives its name), and prediction of epidemic diseases in a population of susceptible individuals. The theory has also found applications in describing the physical properties of amorphous materials³ such as electrical conductivity (Mott or Anderson transitions)⁴⁻⁷, magnetization^{8,9} (para/ferromagnetic transition), and melting (the glass transition)^{10,11}. Percolation theory has also been used to describe the chemistry of disordered systems. The most familiar application is to the sol-gel transition¹²⁻¹⁶ (i.e., condensation of aqueous $\text{Si}(\text{OH})_4$ to form silica gel). More recently, Grant *et al.* have used percolation statistics to model the volatilization of coal.¹⁷

We have recently reported the discovery of two classes of chain reactions which propagate in amorphous (glassy) solids at low temperatures. The first is polymerization of formaldehyde.^{18,19} The other class is photochlorination of simple hydrocarbons, typified by the reaction of Cl_2 with cyclopropane.^{20,21} All of the available evidence suggests that chain reactions in amorphous solids exhibit chain lengths which are very short in comparison with those in fluid media or in crystals. In this paper, we present a simple theory for describing the propagation of chain reactions in disordered solids. The theory provides a simple framework for understanding chain propagation in the absence of molecular diffusion. It describes chain reactions in pure solids as well as in binary solid solutions. It predicts average chain lengths and chain length distributions based on simple analytical formulae. It also identifies fundamental

^aSupported by AFAL Contract F04611-87-K-0023

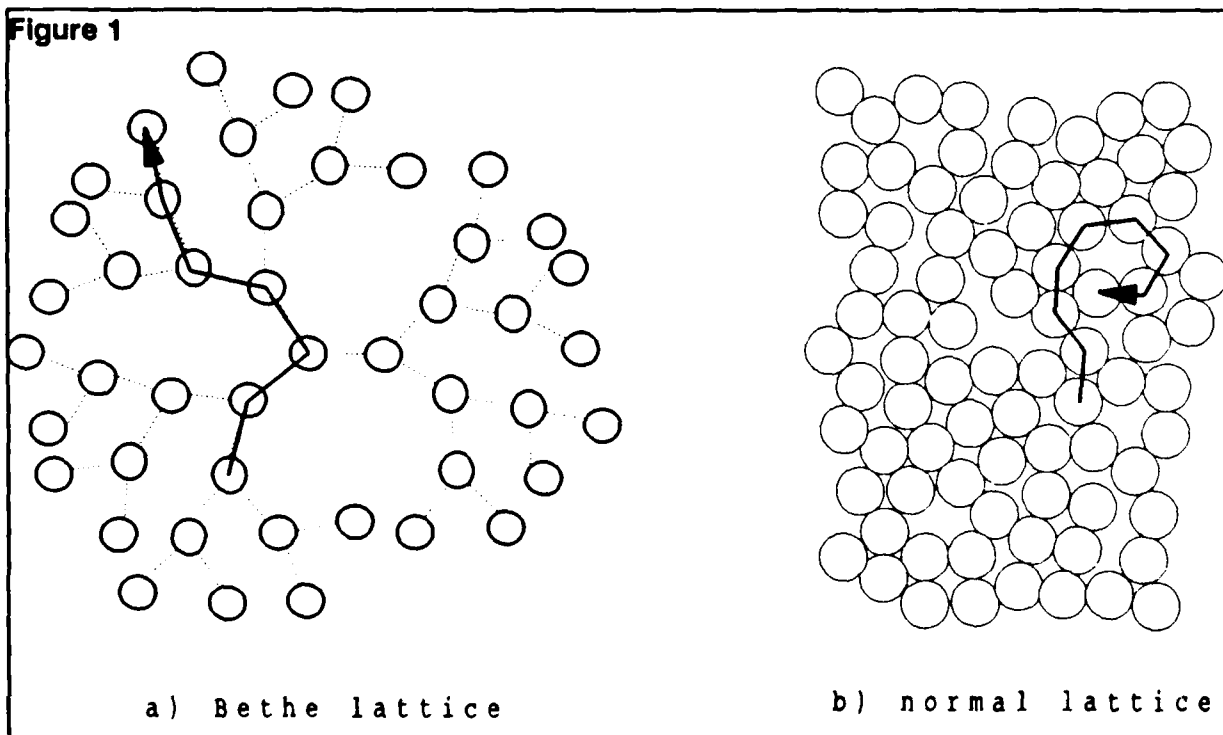
upper limits to the extent of chain reactions in the solid state. Possible extensions of the theory are described which include effects such as chemically induced phase transitions (melting or vaporization). Such an extended theory may be useful for identifying critical conditions for explosive reactions in amorphous high energy materials.

Polymerization on a Bethe Lattice

Bethe lattices were chosen as a model for solid state chain reactions because the simple form of the lattice connectivity permits analytical solutions to be found for average chain lengths and chain length distributions. One such lattice is depicted in **Figure 1(a)**. The reaction is initiated at any arbitrary site and propagates outward. The connectivity of the lattice is such that the reaction cannot "revisit" sites which were encountered earlier in the reaction. In the case of polymerization, the growing end of the polymer chain never encounters molecules which are already part of the polymer and instead is presented with "fresh" monomer molecules for each step in the reaction.

In three-dimensional simple cubic lattices, it is possible to form loops in which the reactive center revisits lattice sites. A two-dimensional representation of this is shown in **Figure 1(b)**. As reactive chains become longer, the number of possible ways for such revisitation to occur becomes extremely large. This makes analytic solutions for chain length distributions difficult or impossible to find and is the principal reason for choosing the Bethe lattice as the framework of our analytical model. Statistical evaluations of looping in self-avoiding random walks on real three-dimensional lattices is easily evaluated by computer simulations. We have chosen this approach for assessing the validity of the analytic solutions for percolation on Bethe lattices (*vide infra*).

We begin by considering the polymerization of non-spherical molecules which occupy sites on a Bethe lattice of connectivity M (the lattice depicted in **Figure 1(a)** has $M=3$). The



reaction is initiated at site 0. For simplicity, it is assumed that one of the M surrounding sites is blocked by the radical precursor molecule and that N=M-1 neighboring sites are occupied by potential reactant molecules (monomers). We define a reactivity factor ρ to be the probability that reaction can occur with any particular neighboring monomer molecule. The value of ρ necessarily lies in the range 0-1 with 0 representing a completely unreactive molecule and 1 representing a reactive molecule. The probability that no polymerization reaction occurs (all N neighboring monomers are unreactive in the first step) is

$$P(0) = y = (1-\rho)^N. \quad (1)$$

The probability that the reaction will proceed exactly one step is

$$P(1) = [1-P(0)](1-\rho)^N = y(1-y) \quad (2)$$

Continuation of this process leads to the general expression for the chain length distribution (probability of proceeding exactly k steps),

$$P(k) = y(1-y)^k. \quad (3)$$

This simple expression describes the normalized chain length distribution for a solid state polymerization reaction. By summing $k P(k)$ over all possible values of k, we calculate the average chain length,

$$\langle k \rangle = \sum_{k=0}^{\infty} k P(k) = y \sum_{k=0}^{\infty} k (1-y)^k = \frac{1-y}{y} = (1-\rho)^{-N} - 1. \quad (4)$$

Here, we have used the binomial series expansion to simplify the summation.

Chain Reactions in Binary Solids

The theory outlined in the previous section is easily extended to treat reactions in binary solid solutions (e.g., random mixtures of two components A and B). Chain reactions of chlorine with simple hydrocarbons are prototypical of this type of reaction, and often involve alternating propagation steps of the general type,



Proceeding exactly as before, the chain length distribution for completion of k complete cycles of the propagation steps (5) and (6) is

$$P(k) = (1-a)^k (1-b)^k (a+b-ab) \quad (7)$$

where

$$a = (1-x_A \rho_A)^N \text{ and } b = (1-x_B \rho_B)^N, \quad (8)$$

and x_A, x_B are the mole fractions of components A and B in the binary solid solution.

The average chain length is

$$\langle k \rangle = \sum_{k=0}^{\infty} k P(k) = \frac{(1-a)(1-b)}{a+b-ab} \quad (9)$$

The theory correctly predicts the effects of changing chemical composition of the solid on chain lengths. For example, it predicts that the average chain length will be longest in a 1:1 mixture of the two components, RH and Cl_2 . As the solid becomes rich in the hydrocarbon fraction, chains are terminated when alkyl radicals become trapped in sites where the local concentration of RH is high (no Cl_2 molecules are among the N nearest neighbors). Conversely, when the solids are made rich in the chlorine fraction, chains tend to be terminated when Cl atoms become trapped among Cl_2 neighbors.

Comparison of the Theory with Computer Simulations and Experiments

In order to evaluate the usefulness of the theory outlined in the previous sections, we have compared the results to computer simulations of polymerization kinetics on a three dimensional simple cubic lattice. In all of the simulations, the lattice consisted of 1000 sites which are interconnected with periodic boundaries so that edge effects of the finite lattice were eliminated. In such a lattice, each site has six nearest neighboring sites which contain potentially reactive molecules. The principal difference between the simulations and the theory (on a Bethe lattice) is that the simulations allow for revisitation of previously reactive sites (i.e., allow the growing polymer to become entangled in itself). Because the polymer is unreactive, this effect shortens the chain length.

Agreement between the chain length distributions obtained in the simulations and those predicted by the theory (Equation 3) is remarkably good in cases where the average chain length is short (less than about 10 steps). The probability for producing small chains is slightly underestimated by the theory, and the probability for forming long chains is slightly overestimated. This is more noticeable for the higher value of ρ . The interpretation of this effect is that the possibility of site revisitation on the simple cubic lattice shortens the average chain lengths somewhat. Clearly, molecules with large reactivity parameters (longer average chain lengths) will have more opportunities for revisitation and should have significantly shorter chain lengths than predicted by the analytical theory. This is borne out by the simulations.

The analytical theory is therefore most useful for analyzing experiments involving relatively short chain lengths in which the effects of site revisitation are small. Fortunately, these are also the conditions indicated by the experiments. For the particular case of formaldehyde polymerization, we find that the average chain length of the reaction is 6.5 steps per initiating event.

A simple physical interpretation of the reactivity parameter ρ is the fraction of molecular surface area for each monomer which is susceptible to attack by the growing polymer. Putting the experimentally determined chain length of 6.5 into the theory suggests that the reactivity parameter is about 0.2 (assuming $N \approx 9$). Considering that each step in the reaction involves attack at the oxygen end of the monomer and that formation of each C-O bond is only favorable if the angle of the incipient C-O-C bond is about 110 degrees, the predicted reactivity parameter of 0.2 seems quite reasonable.

We have also run comparisons between the analytical theory and computer simulations (on a simple cubic lattice) for the case of random binary solid solutions. As before, the theory somewhat overestimates the average chain lengths because site revisitation is not possible on the Bethe lattice. The effect is more severe in the case of binary solutions because two steps are required to complete each cycle of the propagation steps, whereas only one step is required for polymerization. The experimentally determined chain length for the reaction of Cl_2 with cyclopropane is 15 ± 3 (for an equimolar concentration of reagents). Comparison with theory suggests that the reactivity parameters for Cl_2 and cyclopropane are approximately 0.6 (again assuming $N \approx 9$). While this comparison cannot be construed to constitute agreement between experiment and theory, it does mean that the parameters (ρ) extracted from the comparison are reasonable in magnitude. The values of ρ for Cl_2 and cyclopropane are higher than the corresponding value found for formaldehyde. This is reasonable since both Cl_2 and cyclopropane have high molecular symmetry ($D_{\infty h}$ and D_{3h} , respectively) compared with formaldehyde (C_{2v}). Higher symmetry molecules have a relatively larger number of reactive geometries which corresponds naturally to higher reactivity parameters. We anticipate that as experimental studies of chain reactions are extended to reactants of even lower symmetry, shorter average chain lengths will be observed.

The Percolation Transition

We have thus far confined the discussion to the case where the chain lengths of the reactions are very short and have therefore not encountered anything resembling a percolation transition. In the context of this theory, a percolation transition corresponds to the point at which the chain lengths become infinite. In principle this could happen for polymerization of a spherical reactant (i.e., $\rho = 1$ in Eq. 5). However, if we include effects of site revisitation on a real lattice, the chain length once again becomes finite. In the case of binary chains, the average chain length is limited to about 2000 steps even for the extreme case ($x_A = x_B = 0.5$; $N = 12$; $\rho_A = \rho_B = 1$). Allowances for site revisitation on a real lattice will further decrease this limit. We therefore conclude that in the absence of cross-linking agents, it is not possible to achieve a percolation transition by means of solid state chain reactions.

Let us now consider a different kind of percolation limit for chain reactions in amorphous solids. Recall that the reactions under consideration are generally exothermic and that chain lengths in fluid media are several orders of magnitude larger than in the solid. If the heat released by the reaction is used to melt a local region of the solid, we may observe a thermal runaway. In the strictest sense, a thermal runaway does not correspond to a true percolation transition since all chain lengths are finite. However, consideration of this effect may be useful for predicting the onset of explosions, particularly in the case of amorphous energetic materials. This is of some practical significance since the consequences of such a "percolation transition" can be quite dramatic. Extension of our simple theory in this direction will necessarily include time-dependent effects such as reaction rates and thermal transport in amorphous materials. Detailed treatment of the problem will be reserved for a future publication.

Summary

We have introduced an approximate theory which describes the propagation of chain reactions in amorphous solids. The theory is formulated in the context of bond percolation on a Bethe lattice. It predicts average chain lengths and chain length distributions for reactions in pure solids (polymerization) and two-step chain reactions in binary solid solutions. The results

compare favorably with computer simulations of chain reactions in three dimensional simple cubic lattices when the chain lengths are short (≤ 10 steps). For longer chains, the failure of the analytical theory to account for site revisitation results in overestimation of the chain lengths. The results compare favorably with available experimental data, although sufficient data do not yet exist to completely determine all of the parameters of the theory. Future work will be directed towards including time-dependent processes such as reaction rates and thermal conductivity in the solid state.

References

1. Grimmett, G. Percolation Springer Verlag: New York, 1989.
2. Stauffer, Dietrich Introduction to Percolation Theory Taylor & Francis: London, 1985.
3. Zallen, R. The Physics of Amorphous Solids, Wiley: New York, 1983.
4. Anderson, P. W. Phys. Rev. **1958**, 109, 1492.
5. Mott, N. F.; Kaveh, M. Adv. Phys. **1985**, 34, 329.
6. Bauer, J. D.; Logovinsky, V.; Skinner, J. L. J. Chem. Phys. **1989**, 90, 2703.
7. Mott, N. F.; Davis, E. A. Electronic Processes in Non-Crystalline Materials Oxford: Oxford, 1979, 2nd ed.
8. Lee, P. A.; Ramakrishnan, T. B. Rev. Mod. Phys. **1985**, 57, 287.
9. Fisher, D. S.; Grinstein, G. M.; Khurana, A. Phys. Today **1988**, 41(12), 56.
10. Angell, C. A.; Rao, K. J. J. Chem. Phys. **1972**, 57, 470.
11. Abraham, F. F. J. Chem. Phys. **1980**, 72, 359.
12. Frisch, H. L.; Hammersley, J. M. J. Soc. Indust. Appl. Math. **1963**, 11, 894.
13. de Gennes, P. G. J. Phys. (Paris) **1976**, 37, L1.
14. de Gennes, P. G. Scaling Concepts in Polymer Physics Cornell University Press: Ithica, New York, 1979.
15. Flory, P. J. J. Am. Chem. Soc. **1941**, 63, 3083, 3091, 3096.
16. Stockmeyer, W. H. J. Chem. Phys. **1943**, 11, 45.
17. Grant, D. M.; Pugmire, R. J.; Fletcher, T. H.; Kerstein, A. R. Energy & Fuels **1989**, 3, 175.
18. Mansueto, E. S.; Ju, C.-Y.; Wight, C. A. J. Phys. Chem. **1989**, 93, 2143.
19. Mansueto, E. S.; Wight, C. A. J. Am. Chem. Soc. **1989**, 111, 1900.
20. Sedlacek, A. J.; Mansueto, E. S.; Wight, C. A. J. Am. Chem. Soc. **1987**, 109, 6223.
21. Sedlacek, A. J.; Wight, C. A. Laser Chem. **1988**, 8, 155.

New Phases of Hydrogen at Megabar Pressures and Metallic Hydrogen

Isaac F. Silvera

Lyman Laboratory of Physics
Harvard University, Cambridge MA 02138

Solid molecular hydrogen has been studied to pressures approaching 200 GPa. Three new phases have been observed, all involving some form of orientational order. One of these phases, called hydrogen-A, exists only for pressures in excess of 150 GPa. Measurements of the dielectric constant imply, by extrapolation, that the valence-conduction band gap goes to zero at the critical pressure for hydrogen-A. We draw the tentative conclusion that hydrogen-A is the metallic molecular phase of hydrogen.

We have studied solid molecular hydrogen in diamond anvil cells (DACs) to pressures of about 170 GPa and down to liquid helium temperatures. Using Raman scattering to study elementary excitations in the crystals, we have been able to identify three new phases of hydrogen in the megabar pressure range (1 megabar=100 GPa). These phases are 1) a phase which exists only for pressures above about 150 GPa, independent of ortho-para concentration.¹ We call this phase the hydrogen-A phase (H-A), 2) the broken symmetry phase (BSP) of pure para-hydrogen observed at 110 GPa at liquid helium temperatures,² and 3) a new phase transition of para-hydrogen which exists within the H-A phase, which we shall call para-H-A.² Furthermore, we have been able to show that both the H-A and para-H-A are associated with orientational order of the molecules.

In a different experimental approach we have measured the dielectric constant of hydrogen as a function of pressure up to 74 GPa, at room temperature in a DAC.³ Using an oscillator model, we were able to relate the real part of the dielectric constant to the optical electronic absorption edge, which in turn is related to the valence-conduction band gap. By extrapolating to higher pressure, we show that to within experimental error the bandgap goes to zero at the critical pressure for the H-A phase. This implies that the H-A phase is the metallic molecular phase of hydrogen.

At megabar pressures, hydrogen is predicted to become metallic, first having a transition from the insulating to the molecular metallic phase, due to band overlap. With increasing pressure a second transition occurs in which the molecules have a dissociative transition to become atomic metallic hydrogen. We believe that the H-A phase is the first of

these metallic phases. In the following, we shall first discuss the phases of the insulator and then present a picture of the very high pressure phenomena.

The solid hydrogens (hydrogen and its isotopes) have a very rich phase diagram at low pressures.⁴ Our recent experiments have shown that this becomes even richer than had been anticipated at megabar pressures. Hydrogen occurs in two species, ortho and para.⁵ At low temperatures and pressures the para species are in the $J=0$ rotational state which has the spherically symmetric spherical harmonic $Y_{Jm}=Y_{00}$ for the single molecule wavefunction; ortho is in the $J=1$ rotational state with anisotropic wavefunctions, Y_{1m} . As a result intermolecular interactions of para molecules are isotropic, whereas ortho molecules can have anisotropic interactions, dominated by the electric quadrupole-quadrupole (EQQ) interaction. At zero pressure and below 2.8K, crystals of ortho-hydrogen ($o\text{-H}_2$) go into an orientationally ordered state which minimizes the crystal energy; above 2.8K the molecules are orientationally disordered. Since the EQQ interaction increases as R^{-5} , where R is the intermolecular separation, the critical temperature increases strongly with increasing pressure. Mixed ortho-para crystals will also orientationally order, but with lower critical temperatures as the para molecules dilute the interactions between the ortho molecules, which thus, on the average, have larger separations than for a pure crystal.

By contrast $p\text{-H}_2$ crystals remain in the symmetric hexagonal close packed structure (hcp) down to 0K, as spherically symmetric molecules cannot order. As the pressure is increased the molecular overlap grows. At a critical pressure the anisotropic interactions become large enough that the description of the orientational distributions by spherical harmonics breaks down. Then, even the ground state orientational distribution of $p\text{-H}_2$ becomes anisotropic and the molecules can orientationally order. This happens abruptly as a phase transition, first at $T=0\text{K}$. This is the BSP transition, which was first observed in deuterium by Silvera and Wijngaarden⁶ at 28 GPa and $T=5\text{K}$. Searches in hydrogen up to 60 GPa failed to yield this transition, even though theoretical work predicted it to occur at a much lower pressure. More recently Ceperley and Alder have predicted a pressure of 100 GPa using quantum Monte Carlo calculational techniques. We have now experimentally detected the long sought BSP transition in hydrogen at 110 GPa by studying the rotational transitions and vibrational transitions. At this time, only one point on the phase line has been determined, at liquid helium temperatures, shown in fig.1.

The line defining the phase called H-A is shown in fig. 1 at a pressure of about 150 GPa. The critical temperature for this phase rises steeply with pressure and is independent of the ortho-para concentration to within experimental accuracy. A new phase in this region was first noted by

Hemley and Mao⁷ who observed a discontinuity in the vibron frequency at the phase line. They studied this over a broad temperature and pressure range but claimed that the critical temperature was independent of pressure. They identified this phase as an extension of the well-known low pressure phase of orientational order of ortho hydrogen. As we felt that the identification and the experimental data were in conflict, we reexamined the phase transition using Raman scattering of the vibron as a probe, and were able to establish the P,T line shown in fig.1, which we found to be independent of ortho-para concentration. Because of the pressure dependence of T_c and the insensitivity to ortho-para concentration, we can state that H-A is a new phase, unrelated to the low temperature phase of orientational order. The latter has a well defined dependence of T_c on density (or pressure): $T_c = T_c(\rho = \rho_0)(\rho/\rho_0)^{5/3}$ for EQQ interactions, where ρ is the molecular number density.

By lowering the temperature of the sample to 5 K it will eventually convert almost completely to the equilibrium para species. We carried out such a program at pressures and temperatures in the H-A phase, and then studied the rotational transitions. As the temperature was increased we observed an abrupt decrease in the rotational intensity, characteristic of a change in rotational order. The points defining this phase line are also shown in fig.1.

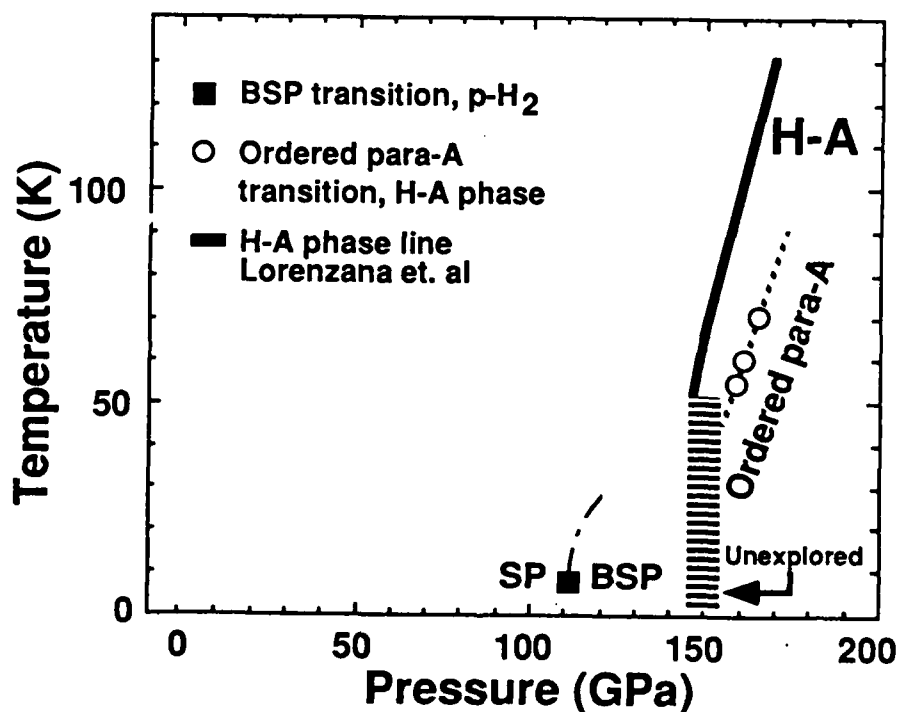


Figure 1. The new phase of hydrogen at megabar pressures.

Finally, when traversing the H-A phase line by increasing the temperature, the intensity for the rotational transitions falls abruptly to zero. This is characteristic of a transition to an orientationally disordered phase. However, the known and expected phases of orientational order have already been identified. H-A is a new, perhaps unexpected phase of hydrogen which also has orientational order-disorder as a property. The P,T phase line appears very much as one might expect for metallic molecular hydrogen and is also in the expected pressure region. In the following paragraphs we describe an experiment designed to confirm this possibility by measuring the dielectric constant as a function of pressure.

In general, the real part of the dielectric constant of a solid is a complex function of all of the high frequency optical absorption due to electronic transitions in the crystal. These transitions can be represented by oscillators. Using a single oscillator model, Wemple and DeDomenico⁸ relate

$$n^2 - 1 = \epsilon_1 - 1 = F_1 / (\omega_1^2 - \omega^2) \quad (1)$$

where n is the index of refraction, ϵ_1 is the real part to the dielectric constant, F_1 is an effective oscillator strength, ω_1 is the oscillator frequency and ω is the frequency of the electromagnetic radiation. Here a single oscillator represents all of the absorption due to optical electronic transitions, including the valence-conduction band gap transition. In spite of the simplicity, Wemple and DeDomenico applied it to over 100 substances and were able to get very nice agreement. The main problem is to relate the effective oscillator frequency to the bandgap frequency. In hydrogen we have used the zero pressure experimental values to relate these quantities. Hydrogen has another complication in that strong electronic excitons exist in the optical spectrum, below the gap energy. We have also been able to show that the effects of the excitons are unimportant and probably unobservable near the metal-insulator transition.

A few years ago, van Stratten and Silvera⁹ showed that a DAC could be used as a Fabry-Perot interferometer to measure the dispersion in the index of refraction and carried out measurements to 28 GPa in hydrogen. From these measurements they could use the model of Wemple and DeDomenico to extrapolate to find the critical pressure for band gap closure. Unfortunately the extrapolation was too long to give a useful value for the critical pressure. We have now carried out a similar experiment to 7.4 GPa,³ also at room temperature, which yields a much more accurate extrapolation. The resulting linear fit, based on the earlier and the current

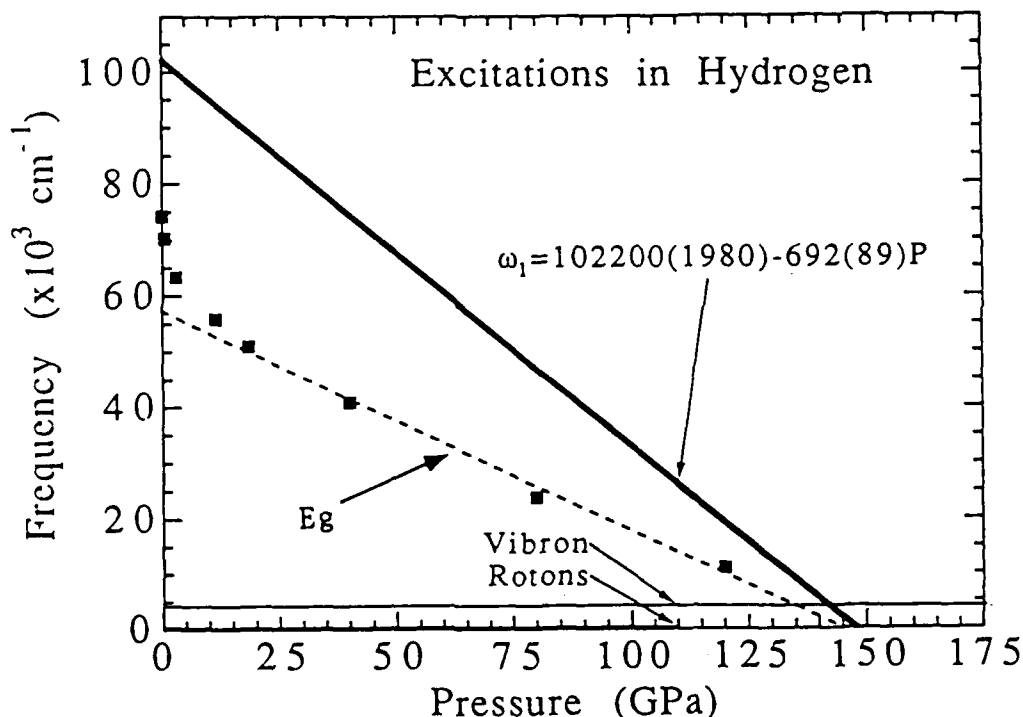


Figure 2. Crystal excitations in hydrogen as a function of pressure. The heavy solid line is a fit to the measured single oscillator frequency. The solid points are the calculated gap energies.

experimental results is shown by the solid line in fig.2. We also show a theoretical prediction for the gap, E_g , as a function of pressure based on a local density approximation calculation¹⁰ which supports the use of a linear extrapolation, and the pressure dependence of the vibron and roton excitations, which show that these are not useful in predicting the molecular metallization pressure. From the zero crossing of ω_1 we predict that E_g goes to zero at 173(22) GPa, in good agreement with the critical pressure of the H-A transition. On the basis of these observations we tentatively identify the H-A phase with the molecular metallic phase of hydrogen.¹¹ Experiments are currently underway to obtain measurements into the H-A phase at low temperature.

It is useful to show that this interpretation of metallization is consistent with all observations. First, we believe that the structure of H-A is probably hcp with the molecules ordered along the c axis. This is consistent with recent total crystal energy calculations.¹² We note that at the H-A transition the discontinuity in the vibron frequency is about a factor 5 larger than can be predicted from a model for orientational ordering. We believe that at the phase transition, charge is transferred from the molecular bond to the conduction band. This weakens the intramolecular binding and lowers the vibron frequency, as is experimentally observed. Next, we note that in the region we have studied

H-A it is transparent; on the basis of band structure calculations, molecular metallic hydrogen should be a semi-metal near the critical pressure, and would be transparent in the visible as the plasma frequency is in the infrared, similar to the case of metallic xenon.¹³ Ashcroft has predicted,¹⁴ using general band theoretical arguments, that orientational order favors metallization over a disordered phase at the same density; also larger zero-point motion favors metallization at the same density. We have observed that the H-A phase line is one of orientational order-disorder, in agreement with this prediction. Hemley and Mao¹⁵ have recently observed a transition in D₂ similar to H-A, but at a slightly higher pressure. This is also consistent with our interpretation, as hydrogen is lighter than deuterium and has larger zero-point motion. On the other hand, hydrogen and deuterium are expected to have the same density at a given pressure at high pressure. Thus the H-A critical pressure having a lower value than that of deuterium is consistent with the predictions of Ashcroft.

In summary, we have observed a number of new phenomena at megabar pressures in hydrogen. One of these, a transition to a new phase called hydrogen-A, has been tentatively identified as the metallic molecular phase. New experiments are under development to confirm these ideas.

Support of this research by the Air Force Avionics Laboratory Contract No. F04611-89K-003 is gratefully acknowledged.

1. H.E. Lorenzana, I.F. Silvera, and K.A. Goettel, Phys Rev.Lett. 63, 2080 (1989).
2. H.E. Lorenzana, I.F. Silvera, and K.A. Goettel, submitted for publication.
3. J.H. Eggert, K.A. Goettel, and I.F. Silvera, Europhysics Lett., accepted for publication.
4. I.F. Silvera, Proc. High Energy Density Materials Conference, 1988.
5. I.F. Silvera, Rev. Mod. Phys. 52, 393 (1980).
6. I.F. Silvera and R.J. Wijngaarden, Phys. Rev. Lett. 47, 39 (1981)
7. R.J. Hemley and H.K. Mao, Phys. Rev. Lett. 61, 857 (1988).
8. S.H. Wemple and M. DiDomenico, Jr., Phys. Rev. B 3, 1338 (1971).
9. J. van Straaten and I.F. Silvera, Phys. Rev. B, 37, 6478 (1988).
10. B.I. Min, H.J.F. Jansen, and A.J. Freeman, Phys. Rev. B 33, 6383 (1986)
11. It has been shown in ref. 3 that softening of the excitons to yield a transition to the excitonic insulator would be a difficult to observe effect, very close in pressure to the metal-insulator transition.
12. A. Garcia, T. Barbee, M.L. Cohen, and I.F. Silvera, to be published.
13. K. A. Goettel, J. Eggert, and I.F. Silvera, Phys. Rev.Lett. 62, 665 (1989).
14. N.W. Ashcroft, preprint.
15. R.J. Hemley and H.K. Mao, Phys. Rev. Lett 63, 1393 (1989).

Triggered Energy Releases in Solid Hydrogen Hosts Containing Unpaired Atoms

G. W. Collins

Department of Chemistry and Materials Science
Lawrence Livermore National Laboratory
Livermore, CA 94550 USA

J. R. Gaines

Department of Physics
University of Hawaii
Honolulu, HI 96822 USA

E. M. Fearon, J. L. Maienschein,

E. R. Mapoles, R. T. Tsugawa and P. C. Souers
Lawrence Livermore National Laboratory
Livermore, CA 94550 USA

I. Introduction

Solid molecular hydrogen is the lightest of the elements making it an attractive energy storage medium for applications where the ratio of energy stored to weight is important. One method of storing energy in solid molecular hydrogen is in the form of atoms that are metastable impurities in the molecular solid host. We have studied various molecular solid hydrogen hosts containing atoms that were produced in those hosts by the radioactive decay of tritium, either present naturally in T₂ or DT or intentionally added to H₂, D₂, or HD. At present, there is no theoretical limit to the amount of energy that can be stored in the molecular solids but we have found one practical limitation to the maximum density of atoms that can be maintained, namely the existence of energy releases which we have previously called "heat spikes".

We believe that the conditions under which heat spikes can be observed are fairly general and they may be observable in many other systems containing metastable impurities where the steady-state number of impurities increases with decreasing temperature. In the worst case, these energy releases provide a practical limit to the number of excitations that can be maintained in the host and could easily lead to very non-reproducible experimental results if not identified. On the positive side, the energy releases can be triggered so that the stored energy is released in a very short time interval making possible large values of the power.

We have observed the effects of these energy releases in four different experiments:

- (1) measurements of sample temperature resulting from a programmed temperature ramp;
- (2) ESR determinations of the atom density;
- (3) NMR signal heights; and
- (4) thermal conductivity measurements.

These experiments will be described briefly and measures to suppress the heat spikes given.

II. Experimental Observations of Heat Spikes

The most elementary way of observing heat spikes is by monitoring the sample thermometer. In Figure 1, we show the reading on a germanium resistance thermometer (a "heat spike") following a sudden increase in the sample temperature. The sample itself was 2.3 mmol of solid D-T (actually 25 mol% D₂-50% DT-25% T₂) in the shape of a cylinder of 2.0 mm radius and 3.5 mm height inside a sapphire cell used for NMR measurements. In Fig. 1, the sample controller was changed from 3.7 K to 4.9 K at 15 s. The unusual thermal response is seen for a D-T sample but not for a sample of HD under the same conditions. From observations of this kind, we find that heat spikes can be triggered by a sudden increase in sample temperature or they can occur without any apparent cause, i.e. spontaneously.

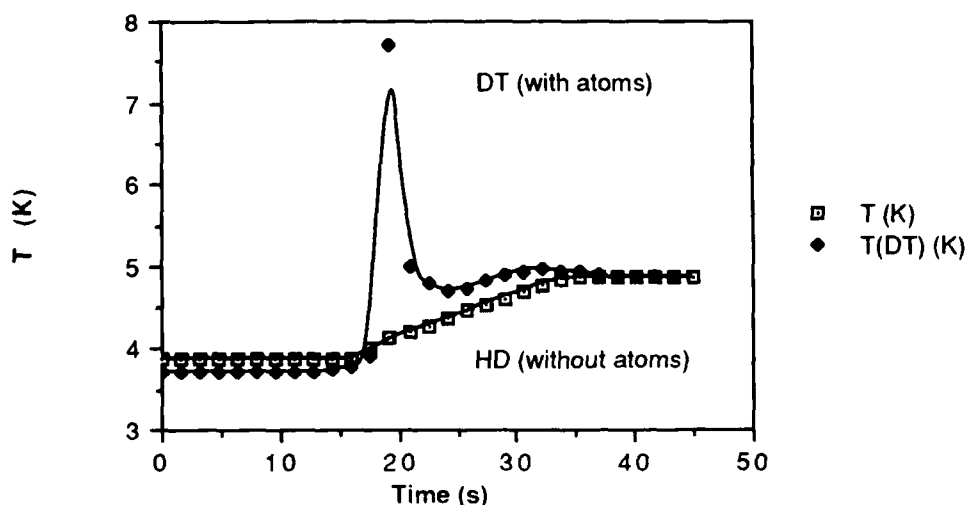


Figure 1

The most illuminating experimental observation of the heat spikes came from our X-band (9.4 GHz) electron spin resonance (ESR) experiments. The sample cell was made of sapphire in a geometry almost identical to that of the NMR cell. The average hydrogen sample size used was 2.2 mmol, so that 2 mW of radioactive decay heat was emitted from a pure tritium sample.

By monitoring the germanium resistance thermometer on a recorder, we could tell when a heat spike occurred. For our samples containing at least 2% of tritium, the steady-state atom density, as measured by ESR increases with decreasing temperature. During the course of the ESR measurements of the atom spin density, heat spikes could be triggered. Figure 2 shows the total atom concentration in parts per million (atoms to molecules) for solid D₂ containing 2 mol% tritium as measured by ESR with times where heat spikes occur indicated.

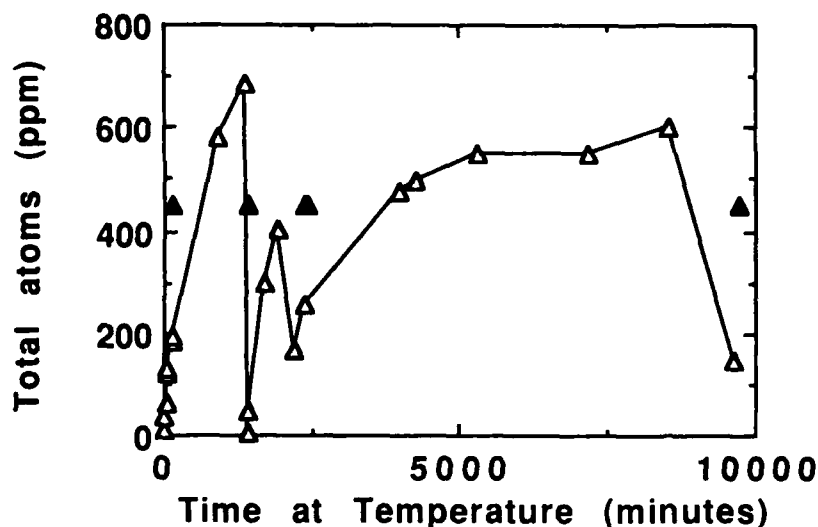


Figure 2

Note that as a result of a heat spike the atom density becomes very small. We have also seen spikes in solid D-T and T₂ below 2.2 K as well as in HD containing 2% T₂ between 1.2 K and 1.4 K. Only in H₂, to temperatures as low as 1.7 K were no spikes seen. *The correlation of the heat spikes with the decrease in ESR spin count indicates that the thermal spikes result from hydrogen atom recombination.*

Two other experiments where we have seen heat spikes are: NMR experiments and thermal conductivity experiments. The NMR signals from the molecules of the hydrogen hosts containing atoms provide a less direct, but still informative way of observing heat spikes. This is shown in Figure 3. In a pulsed NMR experiment, as long as Curie's Law is obeyed, the signal extrapolated to the end of the RF pulse (labeled FID in Figure 3) measures the ratio of the number of nuclear spins in the resonance to the spin temperature. This quantity as such gives a spin count or a temperature determination. From the figure, it is seen that the signal actually increases as the temperature increases following a heat spike. Because the sample temperature has increased, the most apparent explanation for this signal increase is that the number of spins "in the resonance" increased when the number of electron spins in the sample decreased. A "control experiment" was done on pure HD. No such anomalous results were seen there.

We interpret the NMR experiment in the following way: (i) At the lower temperature, when the number of atoms is at its dynamic equilibrium value, many nuclear spins are removed from the resonance line due to dipolar broadening from the electron spin. This number (for a static electron spin and the observed width of our NMR lines) is about 200 nuclear spins per electron spin. (ii) After a heat spike, the atoms have recombined and these 200 spins per atom are now "observable in the resonance line", offsetting the increase in temperature that would normally degrade the signal. The concept of nuclear spins in the "sphere of influence" of an electron spin is an old one but to our knowledge never demonstrated in the manner that we have.

Immediately after a heat spike, the nuclear spins near the former sites of electron spins have the same line broadening mechanisms as all other nuclear spins, but as atoms are formed, the nuclear spins near them are "lost" from the resonance line.

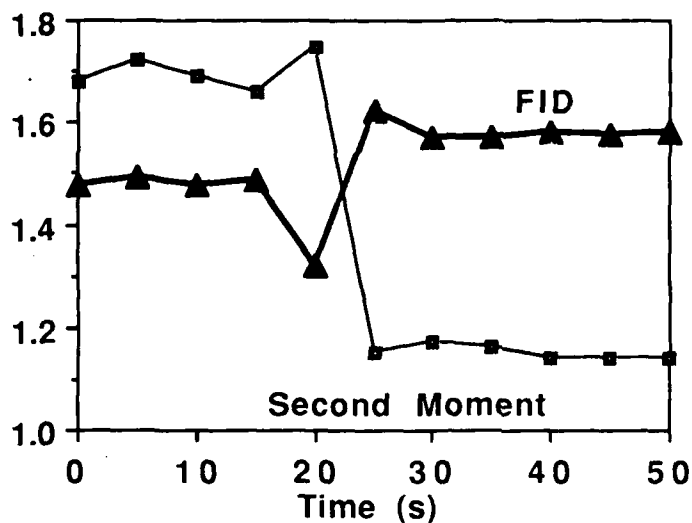


Figure 3

The last result to be used to describe the heat spikes was obtained in an experimental determination of the thermal conductivity.

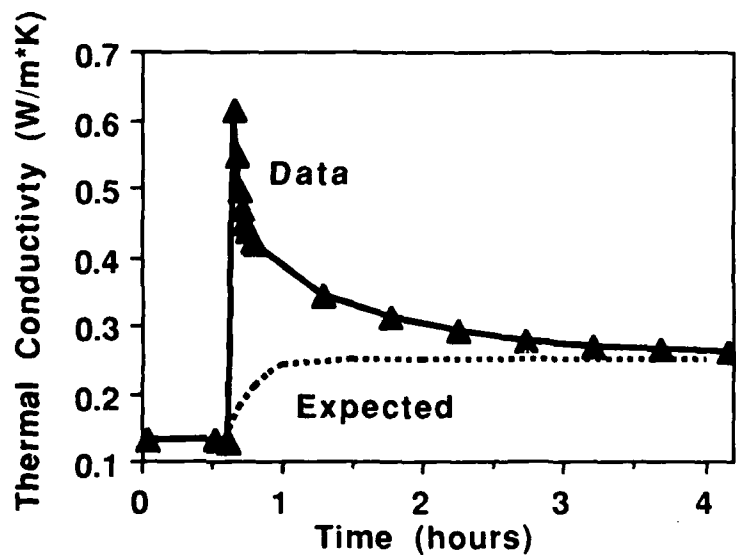


Figure 4

In Figure 4, we show the result of applying a temperature step (from 2.7 to 3.2 K) to the top (cold) plate with a solid D-T sample. Initially, the thermal conductivity is enhanced but it then diminishes with about a one hour time constant.

We interpret the short time transient response as the response to atom recombination. The long tail, we believe, is associated with renewed production of atoms (and defects) and rearrangement of the defects. This behavior of the thermal conductivity further supports the view that the heat spike clears away the hydrogen atoms and possibly other defects as well.

III. Suppression of the Heat Spikes

From the four experimental observations of the heat spikes, a relatively clear picture of the process emerges. After an incremental step in the sample temperature, the atom density is too high for the new temperature so rapid diffusion promotes recombination which reduces the number of atomic spins (decreased spin count). The heat derived from this recombination is so large that the host lattice temperature increases even more creating an avalanche. The atom density vanishes but then stabilizes at the new temperature. The coupling of the host lattice to an external heat bath must be included in the description of the phenomena.

These ideas formed the basis of the explanation of the heat spikes that were observed by Webeler⁽¹⁾ in H₂ (containing T₂). While both Rosen⁽²⁾ and Zeleznik⁽³⁾ assumed there were two types of atoms, "trapped" and "mobile" and used some rather complex equations to understand the heat spikes, they both saw the importance of the coupling of the sample to an external heat bath. The equations that we will use are (in Zeleznik's notation):

$$(1) \quad \frac{dT}{dt} = - \left[\frac{T - T_0}{t_c} \right] + \alpha km^2$$

where T is the instantaneous temperature, T₀ is the temperature the apparatus would cool to if there was no external heating, k is the atom recombination coefficient, α is the ratio of q, the heat liberated per recombination (4.5 eV), to the heat capacity of the solid hydrogen per molecule, (C_{Debye}/N), m is the atom concentration, and t_c is the relaxation time, given by the ratio (C_{Debye}/h), where h is the "heat transfer coefficient" of the thermal link between the sample and the apparatus heat sink assumed to be at temperature T₀. Our oversimplified picture considers all atoms to be equivalent.

In the presence of heating, either due to tritium beta decay, atom recombination heating, or power from a temperature controller, a steady-state temperature (T_{ss}) is reached, which is the solution of Eqn. 1 with (dT/dt) = 0. If the temperature is increased to a higher value, T_{ss} + ΔT, the temperature may "overshoot" producing a heat spike or a temperature spike. This condition can be realized if the first derivative of the temperature in Eqn. 1 is positive after the temperature step to value T_{ss} + ΔT.

In addition to the triggered heat spikes, we also observed "spontaneous" ones. Usually these were observed when at the minimum sample temperature with no reserve cooling power. In an attempt to eliminate these spontaneous heat spikes in our ESR experiments, we filled the remaining volume of the cavity with liquid ^4He . Under those conditions, the heat spikes were either unobservable or suppressed by several orders of magnitude. However, when the cavity contained only a small amount of ^4He , even with ^4He on top of the sample, we still observed heat spikes, both on the germanium resistance thermometer and on the vapor pressure of the liquid ^4He above the sample although the frequency of occurrence was reduced considerably.

As a practical note, we were able to suppress the heat spikes in the NMR cell since this cell was in good thermal contact through the NMR coil to the 3.5 K cold block. Breaking this link allowed heat to flow to the sapphire cell walls and the heat spikes occurred reproducibly.

In conclusion, the energy released by the continuous tritium beta decay can be temporarily stored in solid molecular hydrogen in the form of hydrogen (H, D, or T) atoms. The amount of energy that potentially can be stored increases with decreasing temperature. The energy stored in the free atoms is much larger than the lattice energy and the steady-state atom density decreases with increasing temperature so that the unusual thermal response (heat spike) is obtained following a positive temperature step. The stored energy can be recovered in a very short time by triggering a heat spike which sweeps out essentially all the atoms. The increase in power possible could prove useful for ceratin propulsion applications. Spontaneous heat spikes can be suppressed by improved thermal coupling with a heat reservoir.

IV. Acknowledgements

The experimental work performed at Lawrence Livermore National Laboratory was supported by the U.S. Department of Energy under contract No. W-7405-ENG-48. The project at the University of Hawaii is supported by AFOSR/AFAL through contract No. F04611-88K-0048.

References

1. R.W.H. Webeler, J. Chem. Phys. 64, 2253 (1976).
2. Gerald Rosen, J. Chem. Phys. 65, 1735 (1976), and 66, 5423 (1977).
3. Frank J. Zeleznik, J. Chem. Phys. 65, 4492 (1976).

Energy Storage and Conversion in Solid Hydrogen - Theoretical Aspects

Chester Vause III
Department of Physics and Astronomy
University of Hawaii at Manoa
Honolulu HI 96822

NO ABSTRACT RECEIVED

Metal-Doped H₂

**Daniel D. Konowalow
University of Dayton Research Institute
Astronautics Lab (AFSC)/LSX
Edwards AFB, CA 93523-5000**

It has long been known (Ref. 1) that a variety of finely divided metals or metal hydrides can enhance the specific impulse of a bipropellant such as H_2/O_2 . Technological difficulties (keeping the metal additive dispersed, improper combustion etc.) have prevented the use of such tripropellants in liquid rockets. The situation is different for solid rockets where, for example, a tripropellant of ammonium perchlorate and aluminum powder dispersed in an organic polymeric binder is in common use today.

It seemed worthwhile to reexamine the area of metal-doped propellants to see whether one could identify clusters of metal atoms or small molecules together with H_2 which would overcome some of the difficulties identified with metal additives and still afford enhanced performance as measured by specific impulse. Further, it is known (Ref. 1) that Li is second only to Be among the elements in improving the I_{sp} of H_2/O_2 or H_2/F_2 . It is obvious that the metal fuel should be as finely divided as possible to maximize the energy available from its combustion. The data in Table 1, provided by S.L. Rogers (Ref. 2), shows the increase in specific impulse (I_{sp}) with decreasing particle size of the Li metal additive to the H_2/O_2 system. It is curious that the optimum H_2/Li_2 molar ratio is about 8/1 while the optimum H_2/Li molar ratio is about 6/1. This suggests that one should seek to learn whether the "stoichiometric" clusters Li_2H_{16} and LiH_{12} can be made and whether they are any more stable than other Li_nH_{2m} van der Waals clusters.

TABLE 1. I_{sp} Calculations for Li - Containing Systems

Lithium/Hydrogen/Oxygen System	I_{sp} (sec)
$12.6 H_2 + 2.3 O_2 \rightarrow 4.6 H_2O + 7.9 H_2$	434
$1.0 Li_{(s)} + 5.0 H_2 + 0.5 O_2 \rightarrow 13.6 H_2 + 1.5 H_2O + 1.5 Li_2O_{(s)}$	447
$1.0 Li_{2(g)} + 8.5 H_2 + 0.5 O_2 \rightarrow 18.0 H_2 + 2.1 Li_2O_{(s)}$	480
$1.0 Li_{(g)} + 6.5 H_2 + 0.5 O_2 \rightarrow 14.7 H_2 + 1.4 Li_2O_{(s)} + 1.4 H_2O$	509

(molar ratio of reactants)

(moles/100 g of exhaust product)

vacuum, shifted, exhaust, epsilon 7.66

At the outset I chose to concentrate my attention on LiH_2 since it is the simplest interesting metal- H_2 system to investigate. A review of the literature shows that the Li- H_2 system is not well characterized. Krauss (Ref. 3) has shown that at large Li- H_2 separations the ground state interaction potential curve is repulsive, both in the linear ($C_{\infty v}$) and the T-shaped (C_{2v}) geometry. In 1979, Wu (Ref. 4) claimed an experimental proof of the existence of the stable molecule LiH_2 by mass spectrometric measurements over dilute solutions of hydrogen in liquid lithium. He found dissociation energy (D_0) of the H_2 -Li bond (in what is presumed to be the ground state) to be about 8300 cm^{-1} which was in fair agreement with an earlier estimate of 4700 cm^{-1} obtained by

Companion who used the Diatomics in Molecules method (Ref. 5). Those results are in distinct disagreement with the 1978 multiconfiguration self-consistent field (MCSCF) results of Wagner and coworkers (Ref. 6) whose exploratory calculations in the van der Waals region suggested that the depth of the van der Waals well is small ($< 0.5 \text{ kcal} = 175 \text{ cm}^{-1}$) with the Li atom at an equilibrium distance $R > 8 a_0$ from the center of ground state H_2 . The later report by Hobza and Schleyer (Ref. 7) of their MP2/6-31G(2d,2p) study of LiH_2 is confusing. In their abstract and in the text they call the Li-H_2 complex to be only a very weakly bound (ca $13 \text{ kcal} \approx 4500 \text{ cm}^{-1}$) van der Waals species in the linear arrangement but they found no binding in the T-shaped geometry. However, in their table of total and binding energies they indicate that linear Li-H_2 is bound by only 0.02 kcal (ca 7 cm^{-1}) where Li is $11.4 a_0$ distant from the center of H_2 . This weak binding result of reference 7 agrees within an order of magnitude with the qualitative prediction of Wagner and coworkers (Ref. 6), and of others (Ref. 8,9), and agrees likewise with my own intuition. In view of these uncertainties, a careful reexamination of the van der Waals region of Li-H_2 appears to be in order.

I carried out some second-order configuration interaction (SOCi) calculations for LiH_2 in $C_{\infty v}$ symmetry. The H basis I used is a reoptimized version of the H basis used by Meyer (Ref. 10) in his treatment of rare-gas- H_2 van der Waals interactions. Basically, Meyer augments the 9s Gaussian basis of Huzinaga (Ref. 11) with higher angular momentum functions suitable for a CI treatment and for describing the van der Waals interactions of H_2 with atoms or molecules. I have reoptimized the p and d functions on H to minimize the energy of H_2 at its equilibrium separation. For Li I used a 6-31G basis (Ref. 12) supplemented by a d and an f function to optimize the quadrupole- and octupole-polarizability of Li and hence to account for the leading terms in the long range interaction of Li with other atoms or molecules. The SOCi results suggest that $C_{\infty v}$ LiH_2 has $D_e \sim 13 \text{ cm}^{-1}$ at $R_e \sim 10 a_0$. Because of time and expense of these SOCi computations with 112 basis functions it was clear that I could not investigate substantially larger clusters using this approach. Thus, I turned to the interacting correlated fragments (ICF) approach of Liu and McLean (Ref. 13)

The basic idea of the ICF treatment of weak interactions is to carry out a limited CI comprised of all single excitations and the "split-singles" double excitations to the virtual space to describe the dispersion. "Split single" excitations are restricted to one excitation on each of the interacting fragments. A second feature is to carry out the excitations from a sequence of base configurations which incorporated a higher degree of correlation at each stage then to extrapolate these results to obtain the "final" answer. The ICF computations comprise two stages. For LiH_2 the first stage is a multiconfiguration self consistent field (MCSCF) step which comprises a "three-in-three" complete active space (CAS) calculation with the two core electrons on Li confined to the

Li core orbital. Thus, the three valence electrons are allowed to occupy any of the three orbitals which, in the limit of very large Li-H₂ separation, are essentially H₂(σ_g), H₂(σ_u), and Li(2s). This CAS comprises seven configurations which includes the dominant correlation term $\sigma_g^2 \rightarrow \sigma_u^2$ on H₂. The CI configuration list comprises these base configurations, plus the configurations resulting from all single excitations from the base into the virtual space and the "split-single" excitations described earlier. At each stage care is taken to avoid problems due to basis set deficiencies.

In order to characterize the weak Li-H₂ interactions essentially exactly, it is necessary to have a basis set that is fully optimized for the various polarizabilities of H₂. With T.R. Phillips, a National Research Council Resident Research Associate, I have carried out a series of optimizations of the H atom basis set to optimize the independent components of the H₂ molecule polarizabilities through the sixth rank. Table 2 lists the depth (D_e) and position (R_e) of the minimum in the potential energy curves for Li-H₂ interactions in the $C_{\infty v}$ and C_{2v} symmetry obtained with basis sets of increasing flexibility.

My initial ICF computations used a the Li basis set mentioned above. The H atom basis was a standard Huzinaga - Dunning (Ref. 14) triple-zeta-plus-polarization set with an additional p function ; one of the p functions was optimized crudely for the dipole polarizability of ground state H₂ along the bond axis. The combination comprises 43 basis functions of Set #1. The results of these preliminary ICF calculations listed in Table 2 suggest substantially greater binding than that which I obtained (ca 13 cm⁻¹) from my 112 basis-function SOCI calculations. However, I shall show that this prediction of relatively strong binding is most likely a basis set superposition error (BSSE).

I enhanced the basis set in a stepwise fashion. First, I discarded the H-atom TZP basis used in the basis set #1 calculations and substituted the van Duijneveldt (Ref. 15) 8s/5s basis to which I added the p and d functions I used in the SOCI calculations. I adjusted the most diffuse p function of H to obtain the maximum dipole polarizability of H₂ along the bond axis, and included a second d function on Li which brought the quadrupole polarizability of Li in essential agreement with that of Konowalow and Fish, (Ref. 16). This comprises basis set #2 which contains 26 functions on each H atom and 31 basis functions on Li. The ICF potential curves obtained with basis set #2 were substantially shallower than those obtained with basis set #1. I expect that the apparent deep binding obtained with basis set #1 is due to its inadequacy.

Basis set #3 with 95 basis functions, was formed from basis #2 by adding a d function on each H with the result that all three independent components of the quadrupole polarizability tensor for H_2 have near optimum values. Table 2 shows that the binding energy curves are deepened by over 10% compared with the basis set #2 results. Finally, I formed basis set #4, comprising 115 functions, by optimizing an f function to optimize, in a compromise fashion, the four independent components of the octupole polarizability of H_2 . Table 2 shows that this results in a slight deepening of the potential curves compared to the basis #3 results. It appears that little would be gained by further enhancements of the H atom basis.

Table 2 also shows that the binding obtained with basis #3 is deeper, by about 10%, when the H-H distance is increased from its equilibrium value to its average value $R=1.449 a_0$ in the ground vibrational level. A deepening is no surprise since H_2 is the more polarizable in its stretched condition.

It is easy to show that the repulsion of the bare nuclei in LiH_2 are such as to make the $C_{\infty v}$ approach the more repulsive at any given distance R between Li and the H_2 center. However, the dispersion interactions make the $C_{\infty v}$ approach the more attractive. This is largely due to the fact that the various polarizabilities of H_2 are anisotropic in such a way as to favor the approach parallel to the bond. For example, the dominant dipole-dipole polarizability of H_2 is about 50% larger in the bond direction than it is perpendicular to the bond.

It appears that calculations with an enhanced s and p basis on Li (to form basis #5) is in order. The final test of convergence will be to enlarge the size of the active space for the MCSCF computations. Only then will it be time to carry out the painstaking calculations needed (according to Ref. 13) to get an accurate estimate of BSSE and hence to obtain essentially definitive results.

Table 3 shows my results to date for Li_2H_2 . Here the CAS base for the ICF calculations comprises orbitals which can be described asymptotically as $1\sigma_g$ and $1\sigma_u$ on H_2 and $1\sigma_g$, $1\pi_x$, $1\pi_y$, $2\sigma_g$, $2\sigma_u$ on Li_2 . Thus, the CAS describes four electrons in seven orbitals. Since the Li_2H_2 calculations are substantially more costly than comparable ones for LiH_2 , I've tabulated the results for only two basis sets: The basis 1 calculations are relatively inexpensive to carry out, but the

Table 2. LiH_2^a ICF^b van der Waals

<u>Basis</u>	<u>NBF</u>	<u>Sym</u>	<u>De(cm⁻¹)</u>	<u>Re(a₀)</u>
1. H 3s 2p Li 3s 2p 1d 1f	43	C _{∞v} C _{2v}	114.2 106.1	8.85 8.92
[Tweak Li; optimize H ₂]				
2. H 5s 3p 2d Li 3s 2p 2d 1f	83	C _{∞v} C _{2v}	15.1 9.7	9.8 10.2
3. H 5s 3p 3d Li 3s 2p 2d 1f	95	C _{∞v} C _{2v}	17.1 11.1	9.54 9.98
3-s " R(H-H ₂) = <R> = 1.449	95	C _{∞v} C _{2v}	18.8 11.7	9.49 9.99
4. H 5s 3p 3d 1f Li 3s 2p 2d 1f	115	C _{∞v} C _{2v}	17.4 11.3 ^c	9.56 10.0 ^c

^a R(H-H) = 1.4 a₀

^b CAS MC + all singles + split doubles

^c Estimated

Table 3. Li₂ H₂ ICF Results

<u>Basis</u>	<u>NBF</u>	<u>Sym</u>	<u>De(cm⁻¹)</u>	<u>Re(a₀)</u>
1. H 3s 2p Li 3s 2p 1d 1f	68	C _{∞v} C _{2v}	114.0 ---	9.43 ---
3. H 5s 3p 3d Li 3s 2p 2d 1f	126	C _{∞v} C _{2v}	28.54 In progress	10.43

^a R(H-H) = 1.4 a₀, R(Li-Li) = 5.0 a₀

results are inaccurate. The basis 3 calculations are expensive and time-consuming, but the results should be relatively reliable (as judged by comparable LiH_2 results).

In summary, the van der Waals interaction of ground state Li or Li_2 with ground state H_2 has been investigated at various levels of quantum-mechanical theory and with basis sets of increasing complexity. At the present stage of the research it appears that Li atoms are insufficiently strongly bound to H_2 to make them a useful I_{sp} -boosting additive to liquid H_2 fuel; however, $\text{Li}_2(\text{H}_2)_m$ species are not yet ruled out by these calculations. The R_e values shown in Tables 2 and 3 suggest that neither Li atoms nor Li_2 molecules can occupy substitutional sites in crystalline H_2 . Either the atom or molecule could exist in lattice defects, whether they are preexisting or formed in the process of doping solid H_2 with Li_n .

REFERENCES

1. Siegel, B., and Schiele, L., Energetics of Propellant Chemistry, John Wiley and Sons Inc. New York, 1964.
2. Rodgers, S.L., private communication, June 1988.
3. Krauss, M., "Interaction Energy Surfaces for Li (2^2S) and Li (2^2P) with H_2 ", J. Research Nat. Bur. Stds. A Phys. and Chem., Vol. 72A, No. 6, pp. 553-557, Nov - Dec 1968.
4. Wu, C.H.J., "Binding Energies of LiH_2 and LiH_2^+ and the Ionization Potential of LiH_2 ", Chem. Phys., Vol. 71, No. 2, pp. 783-87, 15 July 1979.
5. Companion, A.L., "Applications of Diatomics-in-Molecules Theory. I. Prediction of Stable LiH_2 and Li_2H Molecules", J. Chem. Phys., Vol. 48, No. 3, pp. 1186-1191, 1 Feb 1968.
6. Wagner, A.F., Wahl, A.C., Karo, A.M., and Krejci, R., "Classical Inelastic Scattering in $\text{Li}+\text{H}_2$: A Comparison of Different Potential Energy Surfaces", J. Chem. Phys., Vol. 69, No. 8, pp. 3757-3774, 15 Oct 1978.
7. Hobza, P., and Schleyer, P. von R., "On the Nature of LiH_2 ", Chem. Phys. Lett.

Vol. 105, No. 6, pp. 630-34, 6 April 1984.

8. Garica-Prieto, J., Feng, W.L., and Novaro, O., "Theoretical Study of the $\text{Li}(2s^2S) + \text{H}_2 \rightarrow \text{LiH}_2$ Reaction", Chem. Phys. Lett., Vol. 119, Nos. 2, 3, pp. 128-134, 30 August 1985.
9. Matsumoto, S., Mizutani, K., Sekiguchi, A., Yano, T., and Toyama, M., Internat. J. Quantum Chem., Vol. XXXIX, No. 4, pp. 689-699, April 1986.
10. Meyer, W. "Dynamic Polarizabilities of H_2 and He and Long-Range Interaction Coefficients for $\text{H}_2\text{-H}_2$, $\text{H}_2\text{-He}$ and He-He ", Chem. Phys. Vol. 17, No. 1, pp. 27-33, January 1976.
11. Huzinaga, S., Approximate Atomic Functions I and II, Technical Report: Division of Theoretical Chemistry University of Alberta, (unpublished).
12. Poirier, R., Kari, R., and Csizmadia, I. G., Handbook of Gaussian Basis Sets, Elsevier, Amsterdam, 1985
13. Liu, B., McLean, A.D., "The Interacting Correlated Fragments Model for Weak Interactions, Basis set Superposition Error, and the Helium Dimer Potential", J. Chem. Phys. Vol. 91, No. 4, pp. 2348-2359, 15 August 1989.
14. Dunning, T. H. Jr., "Gaussian Basis Functions for use in Molecular Calculations. I. Contraction of (9d5p) Atomic Basis Sets for the First-Row Atoms", J. Chem. Phys., Vol. 53, No. 7, pp. 2823-34, 1 October 1970.
15. van Duijneveldt, F. B., Gaussian Basis Sets for the Atoms H-Ne for use in Molecular Calculations, IBM Research Report, RJ945, 10 December 1971.
16. Konowalow, D. D., and Fish, J. L., "Long-Range Interaction of $\text{Li}(2s^2S)$ with $\text{Li}(3s^2S)$," Chem. Phys., Vol. 77, pp. 435-448, 1983.

Infrared Emission Spectrum of H_3^+ in Jupiter Ionosphere and Absorption Spectrum of Ionized Solid Hydrogen

Takeshi Oka
Department of Chemistry and
Department of Astronomy and Astrophysics
The University of Chicago
Chicago, Illinois 60637

I. Spectroscopy of Ionized Solid Hydrogen.

A) The Idea.

A solid hydrogen crystal is bombarded with a beam of accelerated electrons with the energy of a few MeV. The sequence of events producing polyatomic hydrogenic ions occur as shown in Fig. 1.

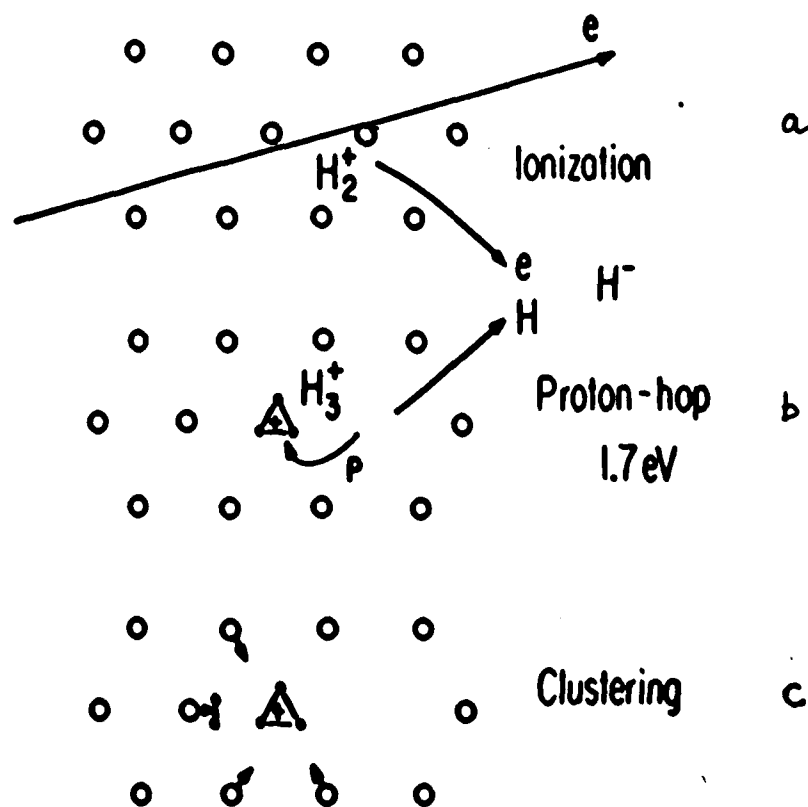


Fig. 1

First (Fig. 1a), many H_2 molecules are ionized by energetic electrons. Many of the ejected secondary electrons have sufficient energies to fly apart from the remaining H_2^+ and do not recombine quickly. Second (Fig. 1b), a proton hops from H_2^+ to a nearest neighbor H_2 to produce H_3^+ . The larger proton affinity of H_2 (4.4 eV) than that of H(2.7 eV) makes this reaction highly exothermic (1.7 eV) and the proximity of the nearest neighbor molecules (3.8 Å) makes the reaction instantaneous. The exothermicity is absorbed partly as the internal energy of the newly produced H_3^+ , partly by the remaining H and partly by the surrounding hydrogen molecules. The energy absorbed by H_3^+ will be eventually dissipate into surrounding molecules. The excess energy parted to H makes it fly apart from the site. The free electron and hydrogen atom ejected from the site by processes (a) and (b), respectively, wanders around in the crystal until they reach the wall or find each other to combine to form H^- and stabilize. The electron might recombine with other H_3^+ during this process.

Finally (Fig. 1c), the resultant H_3^+ will attract neighboring H_2 by the Langevin force to form ionic clusters such as H_5^+ , H_7^+ , H_9^+ , . . . H_{13}^+ , . . . etc.

B) Experiment

A schematic diagram of the experimental setup is shown in Fig. 2.

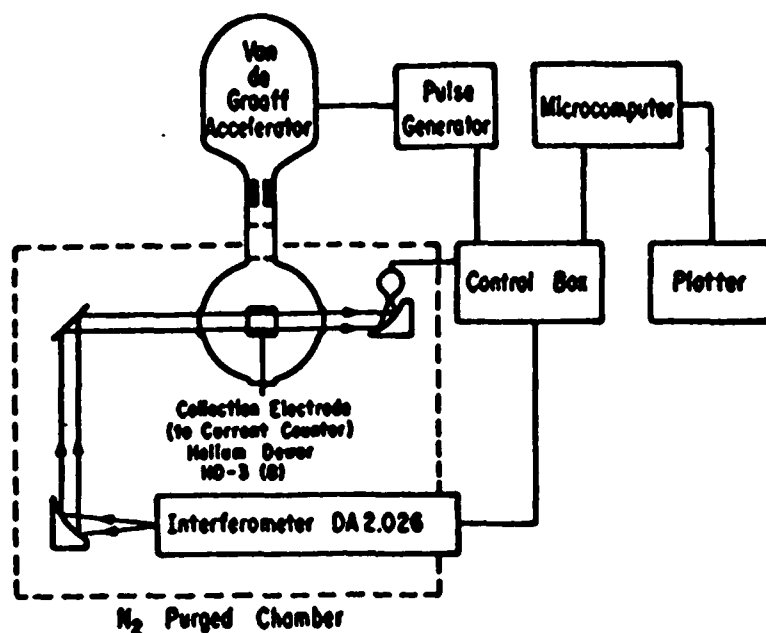


Fig. 2.

A transparent solid hydrogen crystal is grown in a cylindrical sample cell made of OFHC copper (~2 MeV) from a van de Graaff accelerator (we used the one in the Argonne National Laboratory). The beam enters the cell through a Ni foil (thickness 6 mil) which is sealed with an In O-ring.

Electrons are collected and the current measured. The infrared radiation for spectroscopy enters the cell and exits through two sapphire windows which are sealed with In O-rings. Bomem DA-2 FTIR

spectrometer is used for spectroscopy and data accumulation. The sampling of the infrared is synchronized with the pulsing of the van de Graaff acceleration to maximize the efficiency of data collection in case the lifetime of produced ions is short.

The experiments were conducted in the following nine days. July 26, 27, 1988, August 12, 15, 1988, September 29, 30, 1988, May 10, 11, 12, 1989.

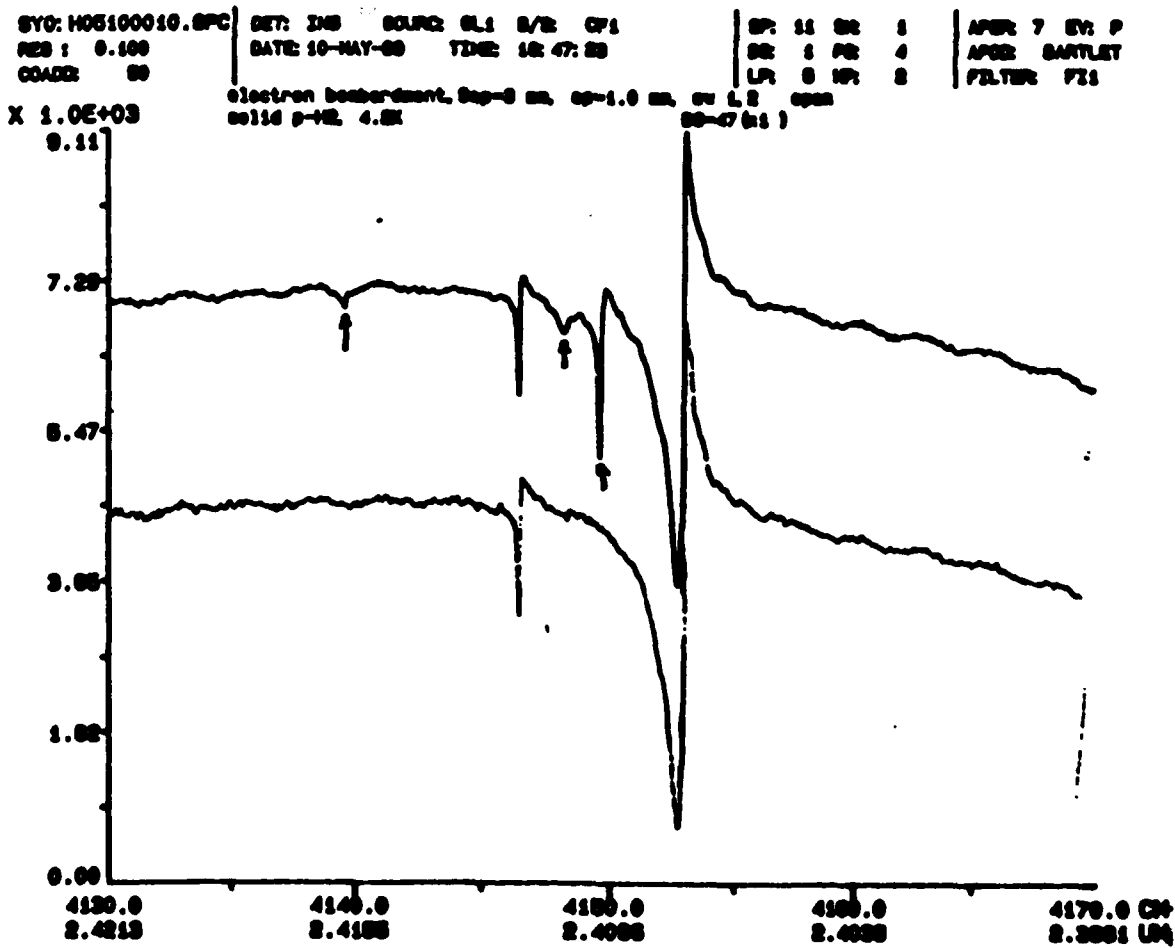
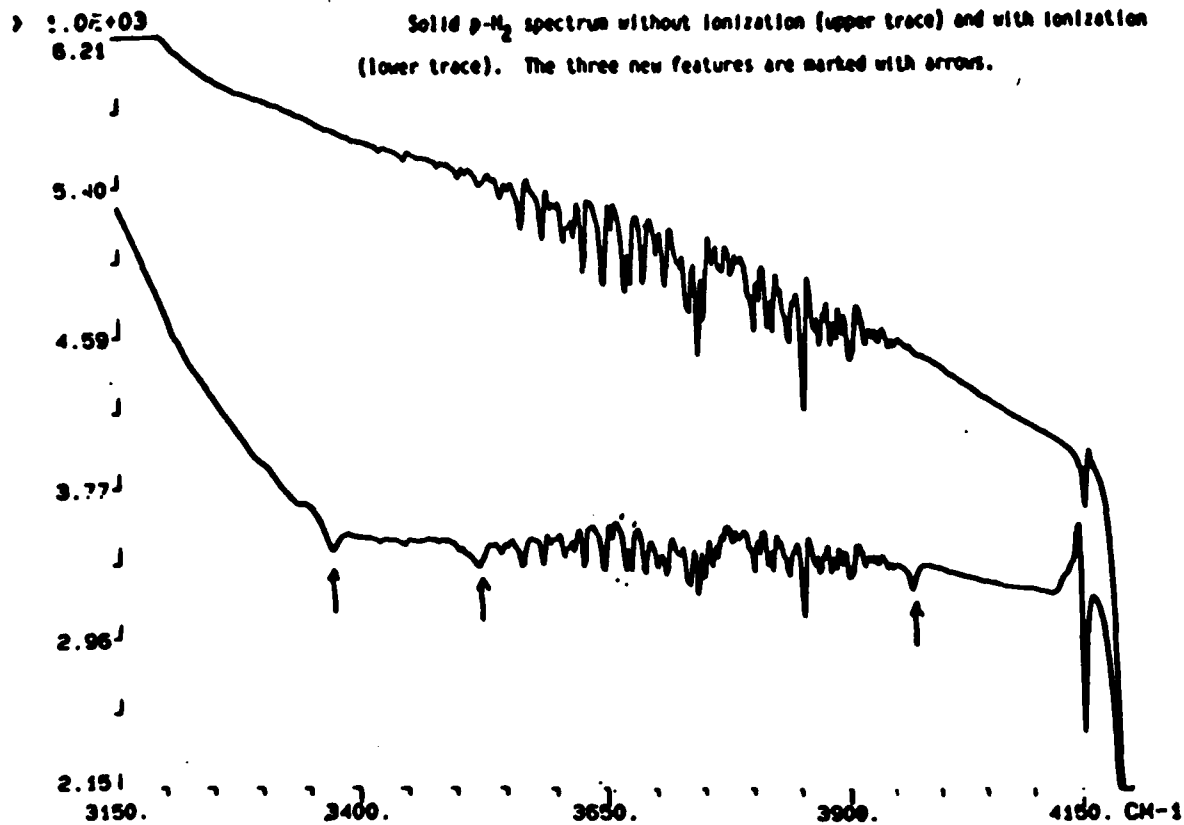
C) Observed Spectrum.

Examples of observed spectra are shown in Fig. 3 (next page). The new spectral lines induced by the electron beam bombardments are indicated with arrows. Observed frequencies and their tentative assignments are summarized in Table

Table . Frequencies of Spectral Lines Observed in Ionized Solid Hydrogen

Frequencies (in cm^{-1})	Assignments
4149.660 4148.24 4139.54	Shifted H_2 stretching
3970.7 3957.2 3764.6 3756.7	H_2 stretching in H_n^+
3569.6 3519.5 3426.9 3417.2 3317.2	ν_1 of H_3^+ in H_n^+
2230.2 2132.9 2109.7	ν_2 of H_3^+ in H_n^+

Figure 3



H₃⁺ Emission Spectrum in Jupiter

A) Serendipity

The H₃⁺ ion is one of the most fundamental hydrogen species, and its presence in space has been predicted by many theorists. I had been searching for this species for the last several years in molecular clouds in interstellar space, but I had never dreamt of searching for it in planetary atmospheres. While we were studying the highly excited states of H₃⁺ in the laboratory, the French astronomers Maillard and Drossart observed strong infrared emission lines in Jupiter. Using our laboratory data Jim Watson at the Herzberg Institute of Astrophysics was able to assign the spectrum to the H₃⁺ 2v₂→0 overtone emission band. This discovery was purely by chance; Maillard and Drossart were studying H₂ emission in Jupiter and accidentally hit upon the H₃⁺ spectrum. I was really stupid not to have thought about Jupiter!

B) Observation of the Fundamental Band

The news of the astronomical observation of H₃⁺ excited me to no measure. I decided to drop all my scheduled activity this summer and observe Jupiter myself. (I was scheduled to attend two international conferences in China.) Together with Tom Geballe I observed beautiful emission lines of the fundamental band of H₃⁺. Two examples are shown in Figs. 4 and 5.

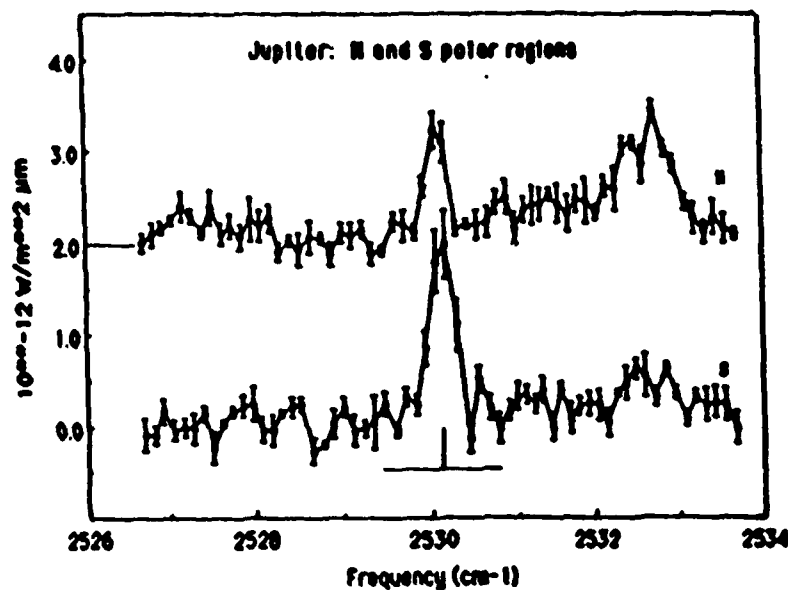


Figure 4: Spectra of the $1,0,-1 \rightarrow 1,0$ line of H_3^+ at 2530 cm^{-1} in the polar regions of Jupiter, observed at longitudes of 160° and 101° .

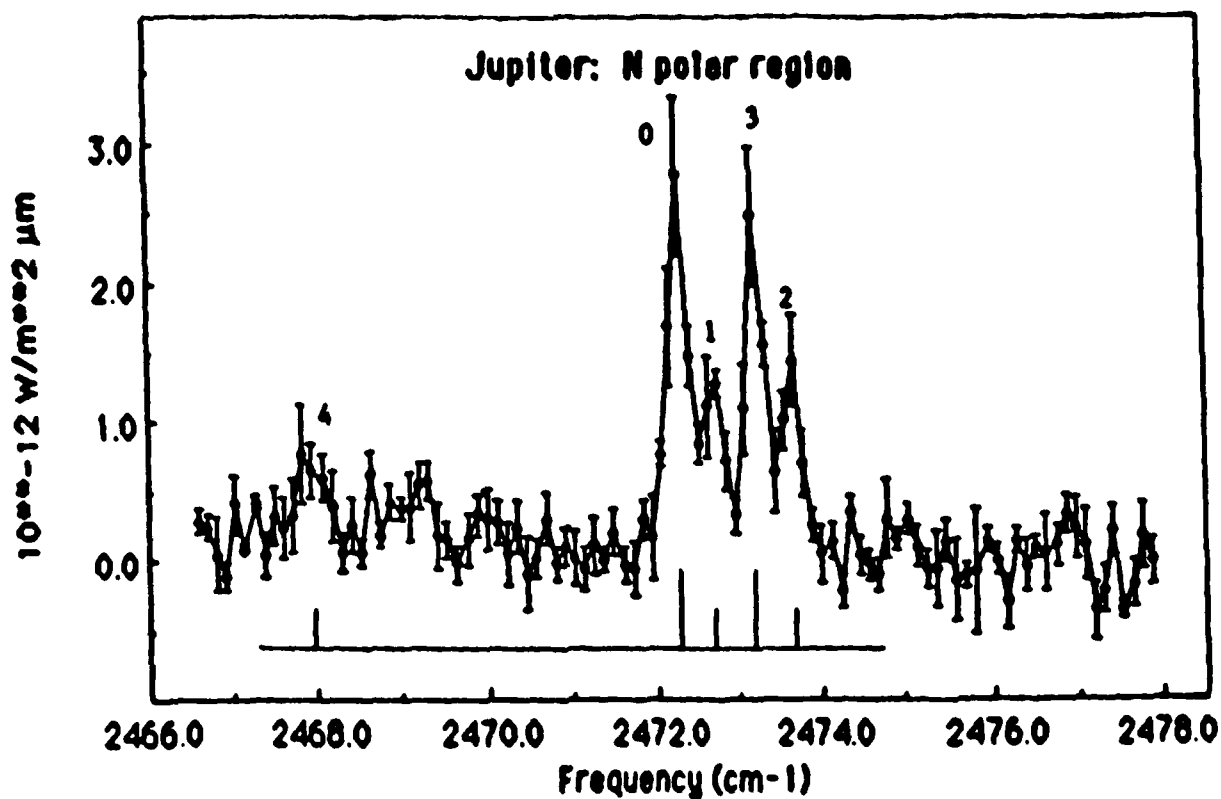


Figure 5 A quartet of lines in Jupiter connecting $J=5$ levels in the ν_2 band of H_3^+ . See Table 1 for identifications. The weak feature at 2468 cm^{-1} may be a blend of an H_3^+ line with $\text{H I Br } \alpha$.

The observed spectral lines indicate that there is an enormous amount of H_3^+ in the ionosphere of Jupiter ($\sim 2 \times 10^{13}/\text{cm}^2$) and that their states of excitation varies with time according to the dynamics of Io-Jupiter plasmas.

Further Investigations of the Infrared
Absorption Spectra of the Ionic Clusters of Hydrogen;
Rotational Structure in the H_5^+/D_5^+ System

M.W. Crofton, J.M. Price, G. Niedner-Schatteburg
and Y.T. Lee

Department Of Chemistry
University of California, Berkeley, California 94720

Previous studies in our laboratory of the vibrational predissociation spectra of mass selected ionic clusters of hydrogen, $H_3^+(H_2)_n$ (for $n=1-6$), have yielded only vibrational information about these systems.¹ Vibrational transitions were observed and assigned to motions of the clusters associated with both the H_3^+ ion core of these systems and the H_2 solvent molecules. This vibrational structure demonstrated convergence at high n to a value close to that known for the vibrational frequency of H_2 in a solid hydrogen matrix. Although no rotational structure in this early work was observed, the data were most consistent with *ab-initio* results for the structures consisting of an H_3^+ core solvated by H_2 molecules.

The fact that no rotational structure was observed was particularly surprising as theoretical predictions for the rotational constants of the smallest cluster, H_5^+ , have values of $A = 27 \text{ cm}^{-1}$, $B = 3.21$ and $C = 3.18 \text{ cm}^{-1}$ for the C_{2v} global minimum structure,² at the rather high level of theory 6s3p/CISD, considerably larger than the resolution of the laser system used. Possible explanations suggested for the unexpected result were homogeneous broadening of the transitions due to a particularly fast vibrational predissociation lifetime, or, spectral congestion due to high levels of internal excitation in the clusters being probed. This latter possibility was investigated by changing the means of generating the clusters from an electron impact ionization source to a high pressure corona discharge source,

known to produce vibrationally and rotationally colder clusters; rotational structure was not apparent for this source either.

In our studies, ions are produced in a high pressure (150-300 torr) discharge region and then undergo a supersonic expansion through a 70 μm nozzle for the formation of ionic clusters (see figure 1). It was necessary to keep the extraction field between nozzle and skimmer low (< 6 Volts/cm) in order to limit cluster dissociation and vibrational excitation in this region. The ionic cluster of interest is selected by means of a mass spectrometer and is held in a radio frequency ion trap while it interacts with a pulsed infrared laser (QuantaRay IR WEX). If the cluster ion absorbs sufficient energy from the laser, vibrational predissociation can take place, resulting in the loss of one or more solvent molecules. Spectra are obtained by using a second mass spectrometer to monitor the number of daughter ions produced as a function of laser wavelength.

Recent work on the H_5^+ system further reduced the internal excitation by means of an expansion of helium and hydrogen in a 3:1 ratio rather than pure H_2 as used previously. From the observed spectrum, we estimate the rotational temperature of the hydrogen cluster ions to be about 20 K. The source body itself was cooled to - 40° C. to limit the amount of vibrational excitation prior to expansion.

This work represents the first direct observation of rotational structure in the hydrogen cluster ion systems. In spite of the superior rotational cooling, one still expects a substantial amount of spectral congestion due to hotbands, tunneling splittings and a homogeneous linewidth determined by the rate of the predissociation process.

Figure 2 shows a spectrum of the $\text{H}_5^+ \nu_2$ band, obtained by averaging several scans with a laser limited resolution of 0.4 cm^{-1} and slightly smoothing the result to enhance the gross features. The maximum variation in the "fine structure" superimposed upon the band contour is only some 10% of the peak cross-section. Due to the inherently low product yield in this experiment, a low signal to noise ratio is inevitable even after days of signal

averaging. The contour of the $H_5^+ \nu_1$ band, which is centered at 3930 cm^{-1} , compares well with that of the ν_2 band (particularly on the high frequency side, where hotbands are less significant). This suggests that most of the "fine structure" features apparent in figure 2 are real.

There are obviously more features seen in figure 2 than are expected for jet-cooled rigid $C_{2v} H_5^+$ molecular ions. The width of some of these features seems to be quite narrow, probably laser-limited. If so, it seems likely that the multitude of features is associated with tunneling splittings resulting from internal motions.

There are two internal motions in H_5^+ which are expected to be associated with a low potential barrier, roughly 0.3 kcal/mole .² These are (1) internal rotation of the H_2 subunit about the A axis of the complex and (2) tunneling of the central proton through a D_{2d} transition state such that the " H_2 molecule" subunit becomes part of the " H_3^+ " subunit. A third internal motion is that of internal rotation of the " H_3^+ " about its 3-fold axis, with a predicted barrier of about 4 kcal/mole . The tunneling splitting associated with this last motion should be relatively small. For a given barrier height, we expect motion (2) to produce larger splittings than motion (1), because of the larger effective mass involved in the tunneling process in the latter case. In figure 2, each rotational transition appears to be split by $2\text{--}3\text{ cm}^{-1}$. In view of the above considerations and the suggestion by Yamaguchi et al.² that the barrier for motion (1) may be slightly higher than for (2), it seems most natural to attribute the splitting primarily to the tunneling motion of the central proton.

The tentative assignments given in figure 2 concern only P, Q or R branch and the total angular momentum quantum number, J, in the ground vibrational state. The center of a given transition, for example R(0), is at a local minimum of the intensity due to the $2\text{--}3\text{ cm}^{-1}$ splitting we have already mentioned.

We have investigated the D_5^+ spectrum also, since its spectrum can be expected to be simpler in appearance. This is so

because of the usual order of magnitude decrease in tunneling splittings for deuterated species, and because the ratio of vibrational energy to dissociation energy is not so large in D_5^+ as compared to H_5^+ . We have recorded the spectrum of the ν_1 band of D_5^+ , shown in figure 3, for the first time. The "fine structure" is simpler this time, and the centers of rotational transitions P(1) and R(0), at least, can be taken to coincide with local intensity maxima. The spectrum is still quite congested, however, and it is tempting to argue that the predissociation process is partly responsible for its appearance. From the separation of the prominent peaks P(1) and R(0), one deduces a value for $(B+C)/2$ of $1.73 \pm 0.1 \text{ cm}^{-1}$. This is in agreement with the same parameter suggested for H_5^+ by the spectrum seen in figure 2, of $3.4 \pm 0.2 \text{ cm}^{-1}$ (because of the D/H mass ratio, the rotational constants of D_5^+ are, of course, half those of H_5^+). These values are in reasonable agreement with those obtained from the *ab-initio* structure calculations.²

We anticipate a considerable improvement in the quality of these spectra in the next 6-12 months. We have already tried an optical parametric amplification scheme to increase the infrared laser power, but with limited success. However, we expect to have a 2-4 μm source with higher repetition rate as well as improved spectral brightness, resolution and beam quality within this time period. This should enable us to considerably reduce the uncertainty of the tentative analysis presented here. In addition, it is quite conceivable that we can eventually study the H_3^+ antisymmetric stretch in H_5^+ . This stretching state lies below the dissociation threshold.

References:

1. M. Okumura, L.I. Yeh and Y.T. Lee, *J. Chem. Phys.* **88**, 79 (1988); **83**, 3705 (1985).
2. Y. Yamaguchi, J.F. Gaw, R.B. Remington and H.F. Schaefer III, *J. Chem. Phys.* **86**, 5072 (1987).

Schematics of the Ion Spectroscopy Machine

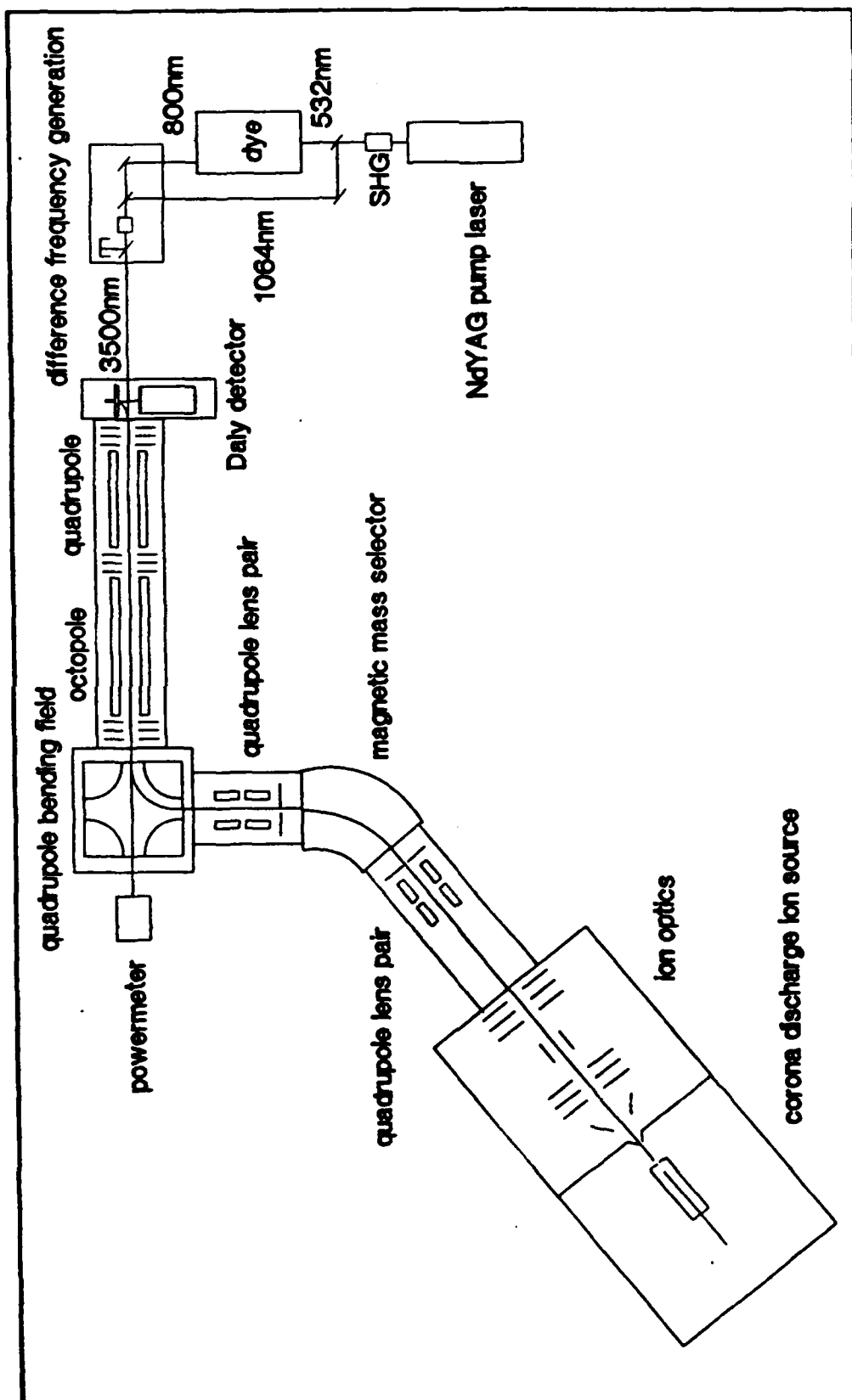


Figure 1

$\text{H}_5^+ \nu_2$ - band (H_3^+ -symm. stretch)

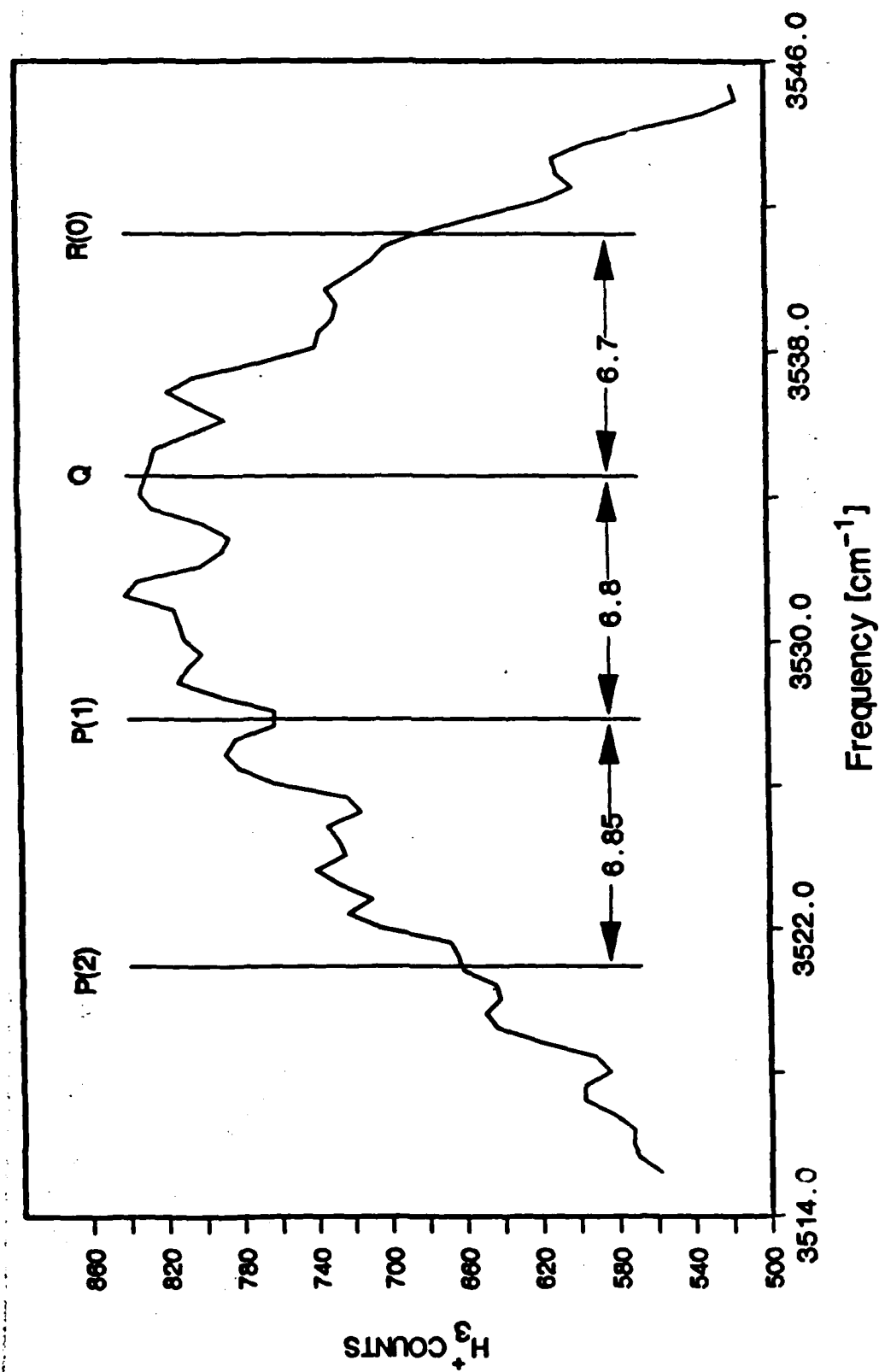


Figure 2

$D_5^+ \nu_1$ - band (D_2 -stretch)

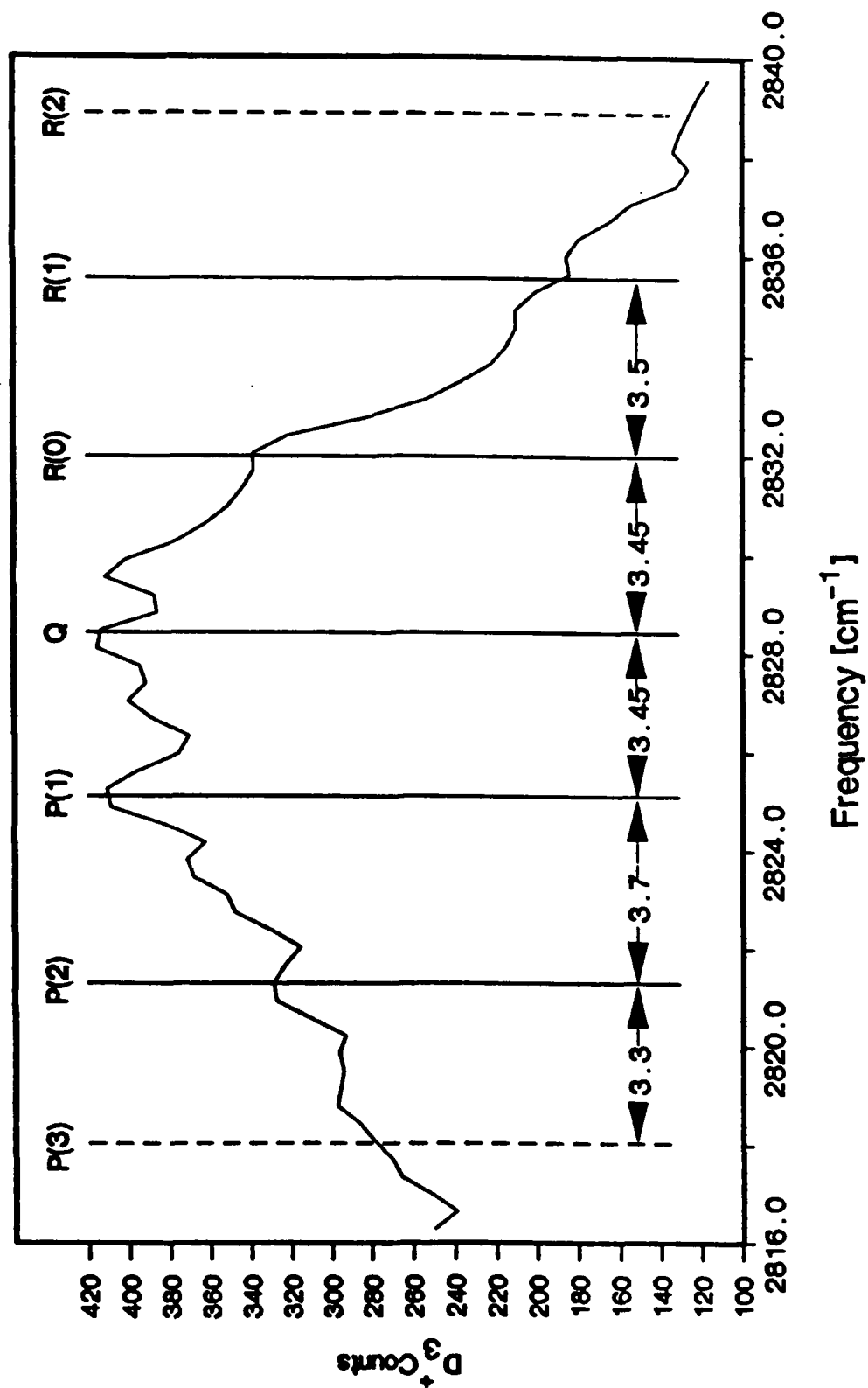


Figure 3

The Dynamics of Electronic Energy Quenching and Angular Momentum Reorientation: The Reaction of H_2 (B) + He

C. B. Moore, C. D. Pibel, and K. L. Carleton
Chemistry Department, U. C. Berkeley

The room temperature rate constants for quenching of the electronic energy of H_2 , HD, and D_2 (B) by He have been measured as a function of the initially excited rotational and vibrational level of the hydrogen molecule. The effective quenching cross sections increase with increasing vibrational energy from about 1 \AA^2 before leveling off at a value of about 5.5 \AA^2 . Quenching is thought to occur via formation of an electronically excited $(\text{H}_2\text{He})^*$ complex followed by crossing to the repulsive H_2 -He ground state potential energy surface (pes).¹⁻³ A schematic diagram of the ground and excited electronic pes's is shown in Fig. 1. The vibrational state dependence fits a vibrationally adiabatic model for complex formation. From this model, a barrier of $250 \pm 40 \text{ cm}^{-1}$ to complex formation is obtained. In addition, a difference in H-H stretching frequencies of $140 \pm 80 \text{ cm}^{-1}$ between H_2 (B) and the complex is also obtained. Both of these values are lower than their respective ab initio values of 800 and 300 cm^{-1} .² The lack of any rotational state dependence for the quenching of D_2 ($v'=0$) indicates that complex formation is most likely when H_2 is rotating in a plane perpendicular to the relative velocity vector. This is in qualitative agreement with the shape of the ab initio pes.^{1,3}

The cross sections for reorientation of the angular momentum vector for the three hydrogen isotopes ($v'=0, J'=1$) by He and Ne have been measured. The cross sections are quite large (40 \AA^2), indicating that the interaction potentials are highly rotationally anisotropic. The cross sections are the same, within experimental uncertainties, for each isotope and

each collision partner. Experiments done to measure the reorientation rate constant of hydrogen with Ar show that Ar has a much larger quenching cross section than either He or Ne.

Experimental:

The output from a Nd:YAG pumped dye laser is doubled in KDP "C" to give ultraviolet light near 330 or 318 nm. This light is focused into a Pyrex cell containing a pressure of Kr or Xe to generate light at 110 and 106 nm, respectively. The vacuum ultraviolet light then passes through a LiF window into a fluorescence cell. In the quenching experiments, the light then passed through a second LiF window into a second fluorescence cell. In the reorientation experiments, there was only a single fluorescence cell. Schematic diagrams of the two setups are shown in Figs. 2 and 3. The cell(s) are filled with a small pressure of hydrogen, the laser is scanned over a single $B \leftarrow X$ transition, and the laser excitation spectrum is recorded. In the quenching experiments, quenching gas is added to the first cell and the decrease in the fluorescence intensity, normalized to the intensity in the second cell, as the quenching gas pressure is increased is used to determine the quenching rate constant. In the reorientation experiments the fluorescence excitation spectrum is measured with two photomultiplier tubes, one detecting the fluorescence perpendicular and one detecting the fluorescence parallel to the electric vector of the excitation laser. The change in the ratio of these two signals is used to determine the rate constant for reorientation ($\Delta M_J = \pm 1$) of the angular momentum vector in space.

Discussion:

QUENCHING EXPERIMENTS

The dependence of the normalized fluorescence intensity on the pressure of the added quenching gas may be written as:

$$1/I = 1/I_0 (1 + k_Q' * M) \quad (1).$$

Here, I is the fluorescence intensity, I_0 is the intensity with no added quenching gas, k_Q' is the quenching rate constant divided by the fluorescence rate constant, and M is the pressure of the quenching gas. The quenching rate constant may be quite easily obtained from the slope of a plot of $1/I$ vs M . The quenching cross section is obtained by dividing the rate constant ($\text{cm}^3 \text{s}^{-1}$) by the average relative velocity (cm s^{-1}). The data for all of the levels of each isotope studied are given in Table I. The cross sections for quenching of $\text{D}_2(\text{B}, v'=0)$ with He are shown in Fig. 4. The lack of any rotational state dependence of the quenching cross section indicates that the most reactive collisions are the ones where the angular momentum vector of the hydrogen is aligned parallel to the relative velocity vector (parallel polarization).

The vibrational state dependence has been treated using a vibrationally adiabatic model. In this model, the vibrational motion of the hydrogen is uncoupled from the reaction coordinate. Not all of the vibrational energy may be used to overcome the barrier to complex formation. The cross section for quenching is written as:

$$\sigma = \sigma_0 \exp(-V_b/kT), \quad (2)$$

where

$$V_b = V_0(\rho) - 4\omega_e[\rho(v' + \frac{1}{2})] + \dots \quad (3)$$

Here, σ_0 is a limiting cross section, V_0 is the barrier to complex formation and includes the new bending vibration appearing at the transition state, $\Delta\omega_e$ is the difference in vibrational frequencies between the B-state hydrogen and the H-H stretching frequency of the transition state, and ρ is a reduced mass factor (1, 0.866, and 0.707 for H_2 , HD, and D_2 , respectively.) A fit of the data is shown in Fig. 5. From the fit, values for V_0 and $\Delta\omega_e$ of 250 ± 40 and $140 \pm 80 \text{ cm}^{-1}$, respectively, are obtained. These are both higher than the values of 800 and 300 cm^{-1} from the latest ab initio calculations from Perry and Yarkony.²

REORIENTATION EXPERIMENTS

The linear polarization of the excitation laser results in a selection rule of $\Delta M_J = 0$. When the hydrogen molecules are excited in an R(0) transition only the $M_J = 0$ levels are excited. The $M_J = \pm 1$ levels are unexcited. As a result, in the absence of collisions, the fluorescence is anisotropic in space relative to the electric vector of the laser. As collisions with other molecules destroy this initial alignment (change M_J) the fluorescence becomes more isotropic. The dependence of the fluorescence anisotropy on the pressure of the collision partner is given by:

$$A = I_{\perp}/I_{\parallel} = 1 + K * [(k_Q' * M + 1) / (k_Q' * M + 1.5k' * M + 1)] \quad (4)$$

I_{\perp} and I_{\parallel} refer to the fluorescence intensities observed perpendicular and parallel to the electric vector of the excitation laser; k_Q' is the quenching rate constant divided by the fluorescence rate constant; k' is the rate constant for collisions that change M_J , divided by the fluorescence rate, K

typical data are shown in Fig. 6. The results are listed in Table II. The cross sections are quite large. For comparison, Field and Norman have recently measured the cross sections for $M_J = \frac{1}{2}$ to $M_J = -\frac{1}{2}$ in CaF ($J = \frac{1}{2}$) to be 9 \AA^2 .⁴ The cross sections for $\text{He, Ne-H}_2(\text{B})$ are this large presumably because of the very anisotropic character of the interaction potentials. The data for the reorientation of D_2 (B) with Ar show that, unlike He and Ne, the quenching cross section for Ar is quite large, since the fluorescence anisotropy changes very little with Ar pressure. The increased quenching cross section may be due to the interaction of a low-lying Ar^*-H_2 pes with the $\text{Ar-H}_2(\text{B})$ pes.

References:

1. S. C. Farantos, G. Theodorakopoulos, and C. A. Nicolaides, Chem. Phys. Lett. 100, 263 (1983); S. C. Farantos, J. N. Murrell and S. Carter, Chem. Phys. Lett. 108, 367 (1984).
2. J. K. Perry and D. R. Yarkony, J. Chem. Phys. 89, 4945 (1988); and D. R. Yarkony (personal communication).
3. R. M. Grimes, Ph. D. thesis, U. C. Berkeley (1986); P. Pernot, R. M. Grimes, W. A. Lester, Jr., and C. Corjan, Chem. Phys. Lett. 163, 297 (1989).
4. J. B. Norman and R. W. Field, J. Chem. Phys. 92, 76 (1990).

Table I. Observed quenching rate constants and effective quenching cross sections.

$ v', J' \rangle$	Pumping Transition	k_Q^a ($\text{cm}^3/\text{molecule-s}$) $\times 10^{11}$	$\langle \sigma \rangle$ (\AA^2)
<hr/>			
		<u>D_2</u>	
$ 0,0\rangle$	P(1)	2.51 ± 0.09	1.42
$ 0,1\rangle$	P(2)	3.52 ± 0.39	1.99
$ 0,2\rangle$	P(3)	3.43	1.94
$ 0,3\rangle$	R(2), P(4)	3.70 ± 0.35	2.10
$ 0,4\rangle$	R(3), P(5)	3.53 ± 0.25	2.00
$ 0,5\rangle$	R(4)	3.43	1.94
$ 0,6\rangle$	R(5)	3.56	2.02
$ 0,7\rangle$	R(6)	3.09	1.75
$ 1,3\rangle$	P(4)	5.72	3.24
$ 1,4\rangle$	P(5)	5.83	3.30
$ 2,6\rangle$	P(7)	6.10	3.46
$ 4,3\rangle$	P(4)	9.79	5.56
<hr/>			
		<u>HD</u>	
$ 0,0\rangle$	P(1)	3.94	2.07
$ 0,3\rangle$	R(2)	4.85	2.55
$ 1,2\rangle$	P(3)	7.50	3.94
$ 2,5\rangle$	P(6)	8.21	4.31
$ 3,0\rangle$	P(1)	11.2	5.90
$ 4,3\rangle$	P(4)	9.47	4.98
$ 3,2\rangle$	R(1)		9.90 ^b

Table I. (continued)

$ v', J'\rangle$	Pumping Transition	k_Q^a ($\text{cm}^3/\text{molecule-s}$) $\times 10^{11}$	$\langle \sigma \rangle$ (\AA^2)
		H_2	
$ 0, 0\rangle$	P(1)	4.10	1.90
$ 0, 3\rangle$	R(2)	5.09	2.36
$ 1, 1\rangle$	P(2)	7.08	3.50
$ 2, 5\rangle$	P(6)	12.0	5.54
$ 3, 1\rangle$	P(2)	14.0	6.51
$ 4, 3\rangle$	P(4)	10.4	4.82

^a Uncertainties ($\pm 2\sigma$) are 15%, unless given.

^b Reference 1.

Table II. Observed reorientation rate constants and effective cross sections for $\Delta M_J = \pm 1$ processes.

System	Rate Constant ($\text{cm}^3 \text{ molecule}^{-1} \text{ s}^{-1}$) $\times 10^{11}$	Effective Cross Section (\AA^2) ^a
H ₂ - He	76.6	35.5 \pm 4.2
HD - He	77.0	40.5 \pm 4.8
D ₂ - He	73.5	42 \pm 14
H ₂ - Ne	72.8	39.5 \pm 6.5
HD - Ne	72.0	46.8 \pm 9.3
D ₂ - Ne	60.1	44 \pm 12

^a Uncertainties are ± 2 standard deviations from the least-squares fits to the data.

Figure Captions

Figure 1. Schematic diagram of the potential energy surfaces involved in the quenching of B-state hydrogen. The excited hydrogen and helium cross a barrier on the excited potential energy surface; they then enter a deep well where the H-H bond length grows to about 2 Å. At the bottom of this well, there is a seam of avoided crossings with the ground state surface. Quenching is thought to occur when a non-adiabatic transition takes the metastable $H_2(B)$ -He complex to the ground state surface, where the products are either $H_2(X)$ and He or two H atoms and He.

Figure 2. Experimental apparatus consisting of two fluorescence cells filled with the same pressure of hydrogen. Helium is added on top of the initial pressure of hydrogen in Cell #1, while Cell #2 is left unchanged. The vuv fluorescence is monitored with two solar-blind photomultiplier tubes (PM). The decrease in fluorescence in Cell #1 compared to Cell #2 is used to determine the quenching rates.

Figure 3. Experimental apparatus used in angular momentum reorientation experiments.

Figure 4. Rotational state dependence of the effective quenching cross sections for D_2 ($v'=0$). No significant change is seen for $J' = 1 - 7$.

Figure 5. The experimental data and the fit to the data assuming a vibrationally adiabatic description of the barrier to complex formation. The symbols are the same as in Fig. 6. The ($v'=0, J'=0$) data have been excluded, and the points for D_2 ($v'=0$) and D_2 ($v'=1$) represent averages of the data for non-zero J' . The solid line is the best fit to the data, and the dashed line is drawn where $V_b = 0$. The parameters from the best fit to the data give a barrier height of 250 cm^{-1} (the barrier on the electronic pes plus the zero-point energy in the bending vibration at the barrier) and a difference in the vibrational frequencies between $H_2(B)$ and the H-H stretch at the transition state of 140 cm^{-1} .

Figure 6. Experimental results for $HD(v'=0, J'=1)$ reoriented by He. The fluorescence anisotropy is the ratio of the fluorescence intensity measured perpendicular to the electric vector of the excitation laser divided by the fluorescence intensity measured coaxial with the electric vector of the excitation laser.

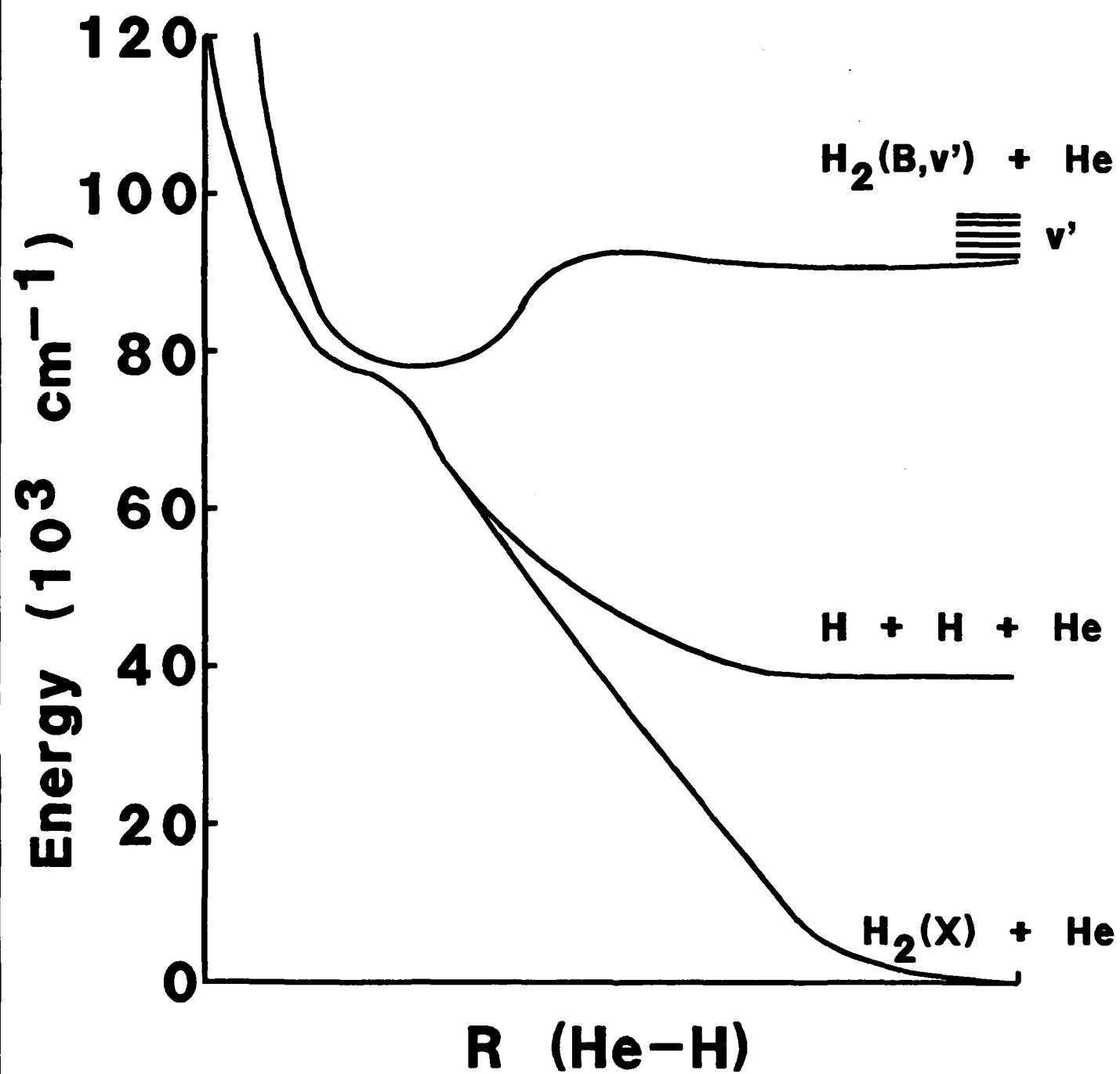


Fig. 1

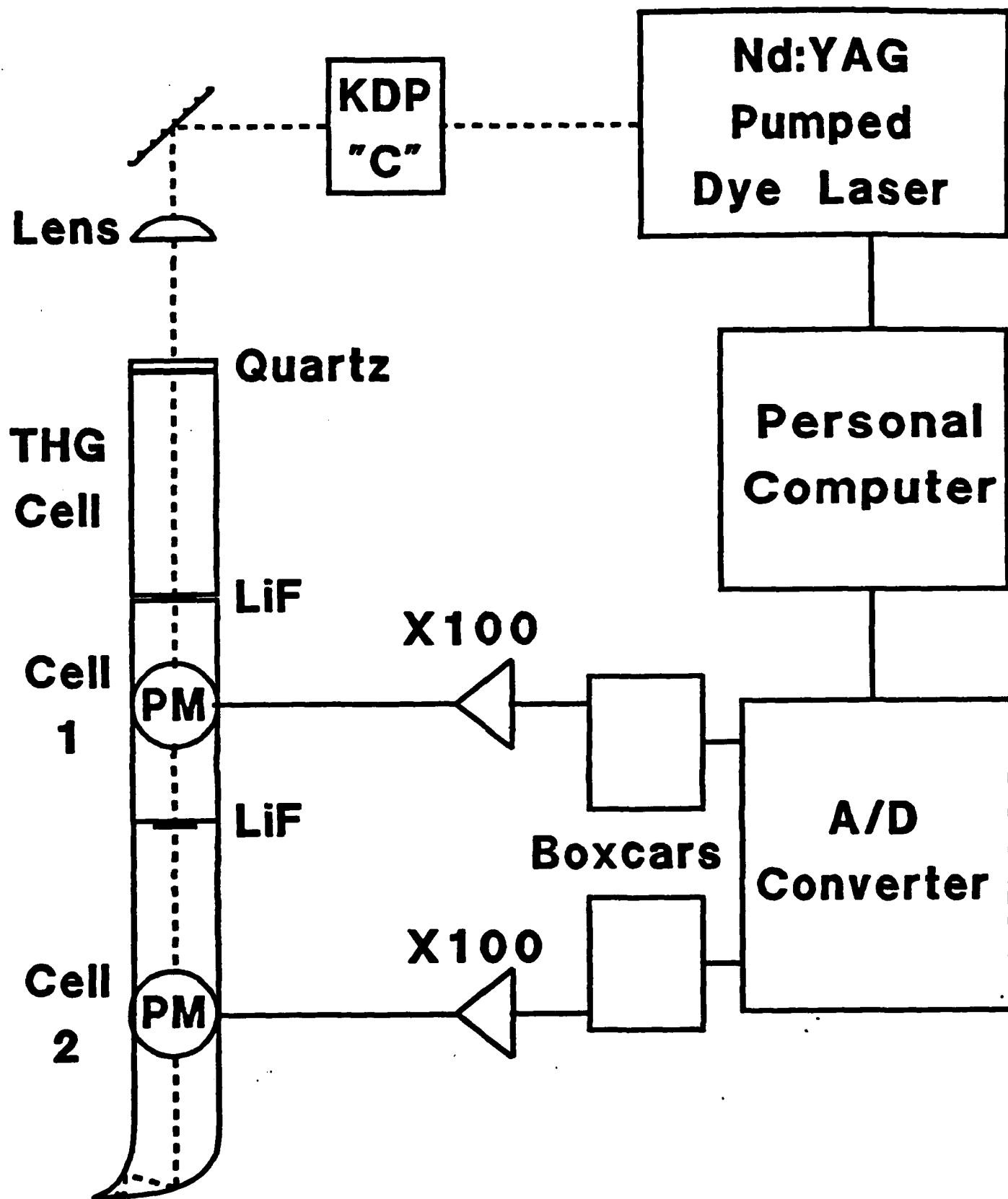


Fig. 2

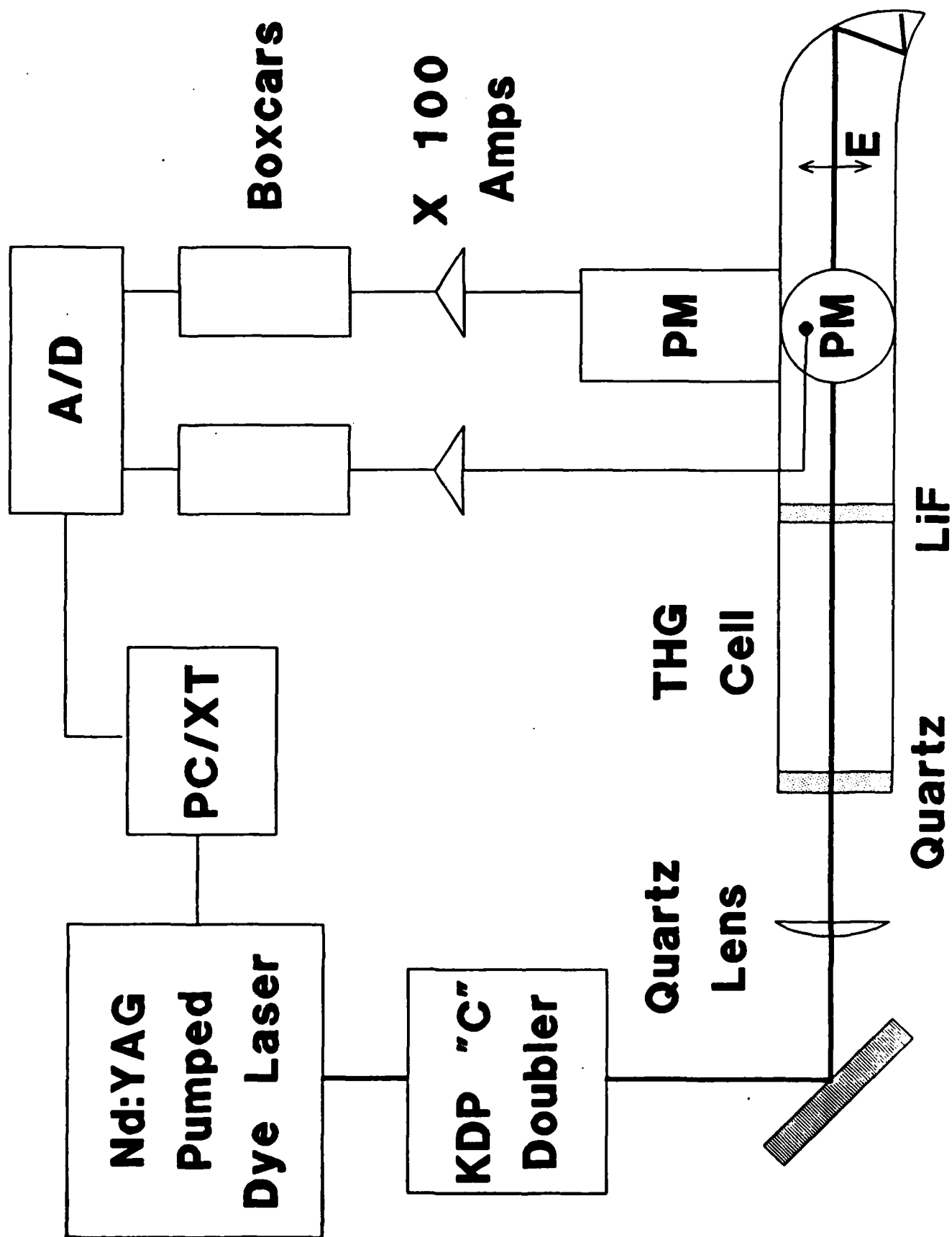


Fig. 3

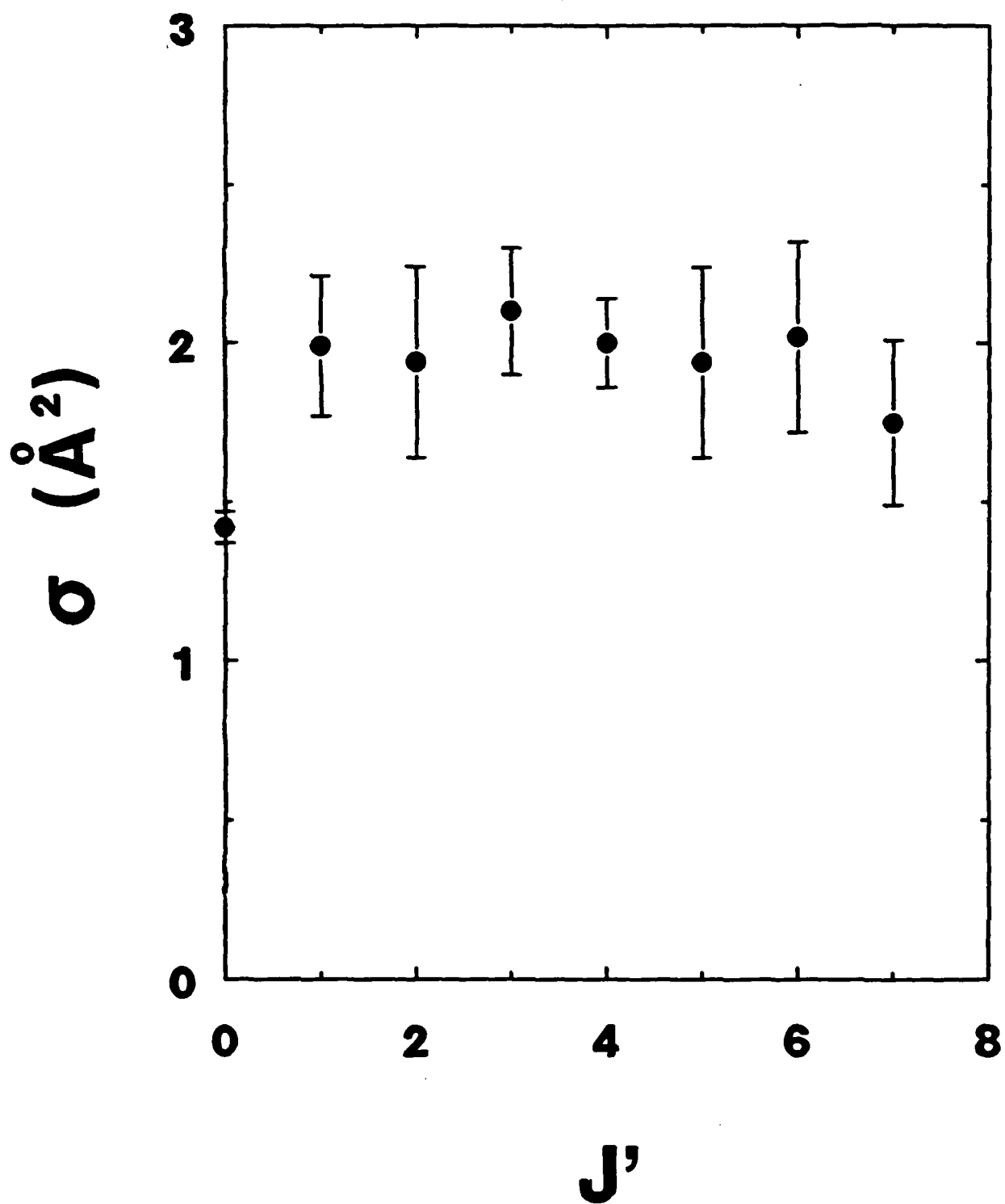


Fig. 4

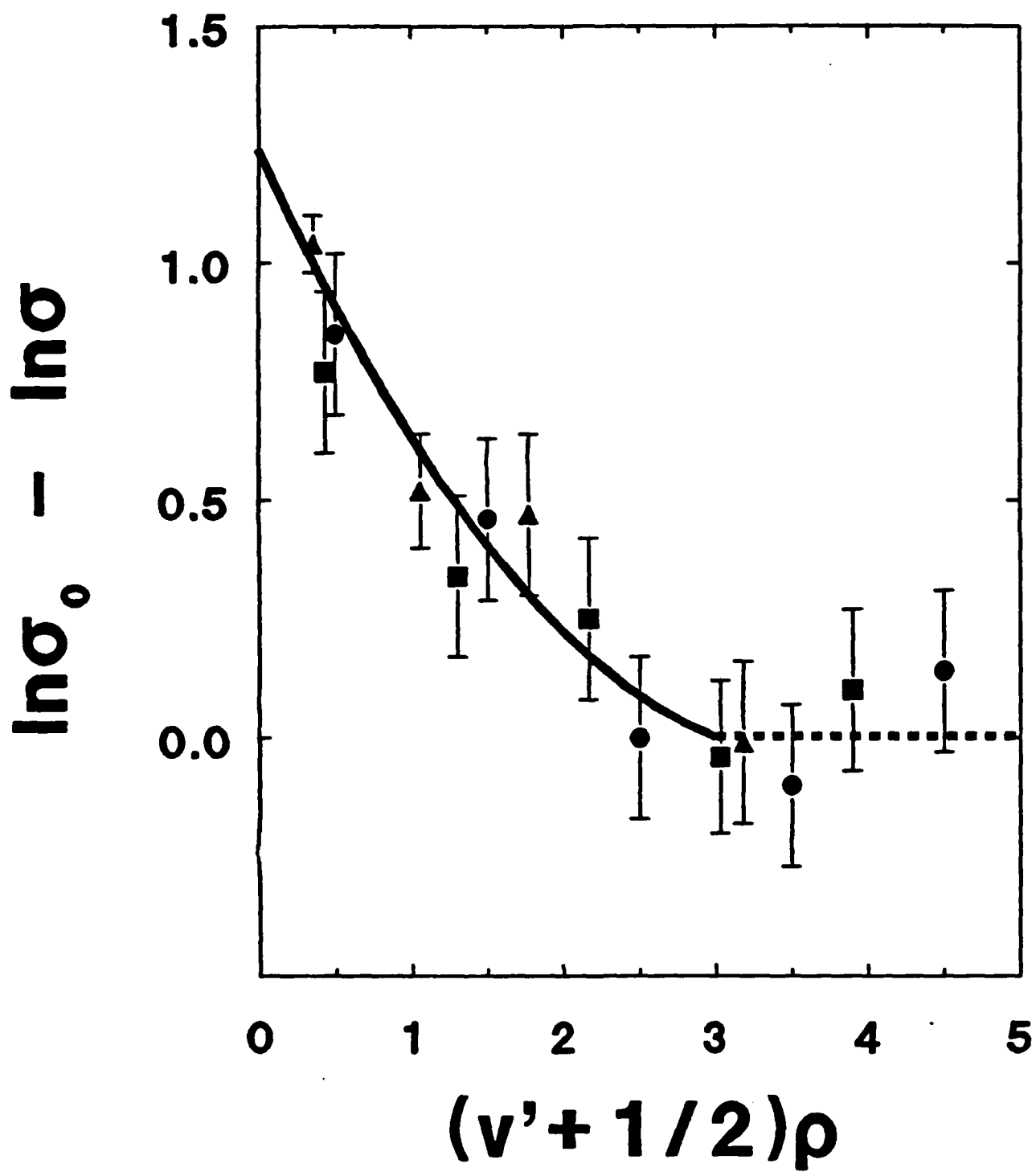


Fig. 5

HD - He

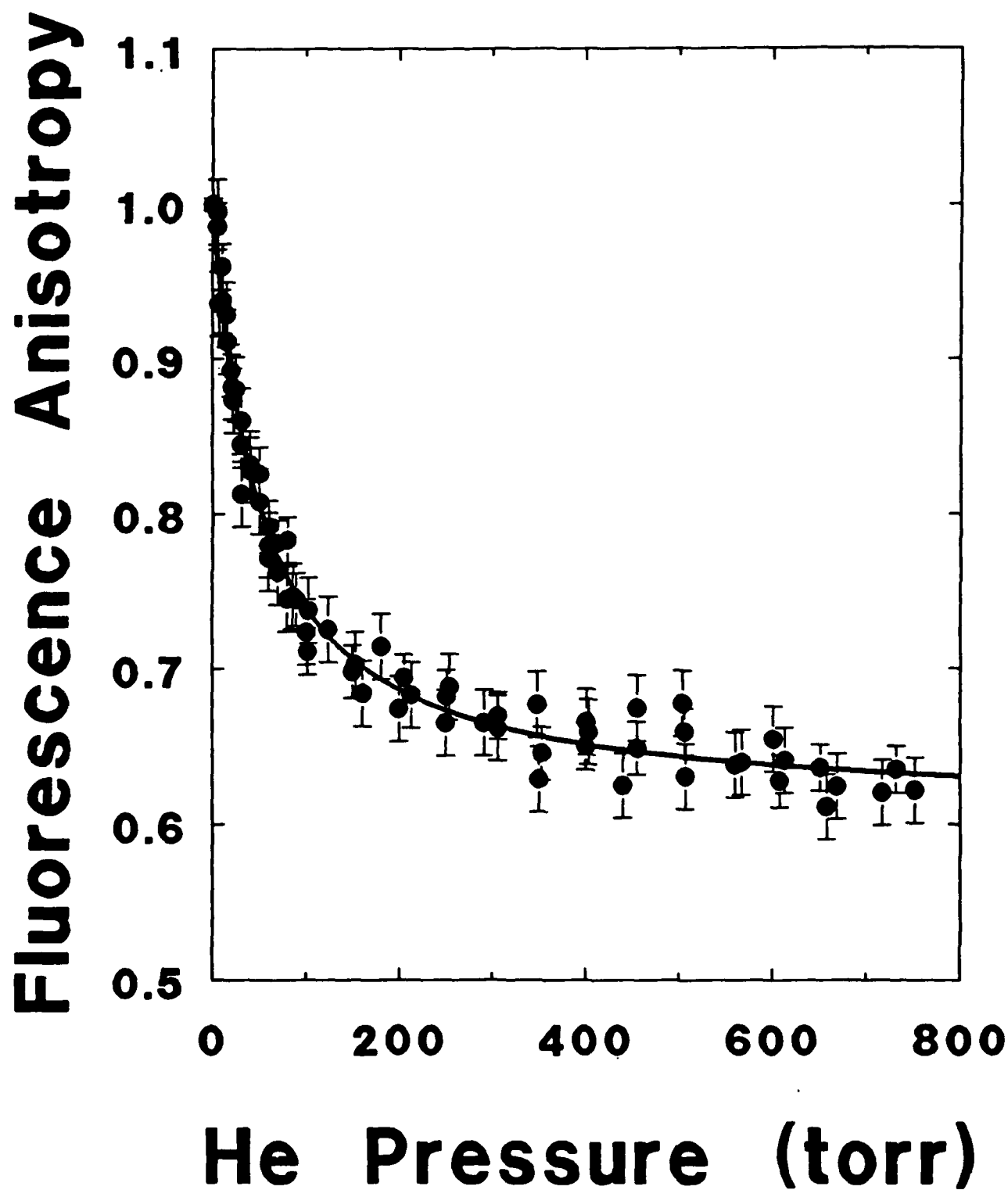


Fig. 6

Theoretical Study of Electronic Quenching and Rovibrational Energy Transfer in He + H₂(B)

Sheng-yu Huang and William A. Lester, Jr.
Department of Chemistry
University of California, Berkeley
Berkeley, CA 94720

The quenching of excited H₂(B ¹Σ_u⁺) molecule by rare gas atoms and ground state H₂(X ¹Σ_g⁺) has been found to be a very efficient process.¹ A number of experimental and theoretical studies involving H₂(B) with He or H₂(X) have been carried out in recent years.²⁻¹⁴ Our previous reports have focused on tetrahydrogen and provide insight on the very high efficiency of H₂(X) among all the quenchers of H₂(B) studied; the cross section is ~79 Å². The He quenching cross section is ~9 Å²; see ref. 1.

In an earlier potential energy surface (pes) study, an avoided curve crossing was found¹² at θ = 45° between the two lowest-lying states - one correlated asymptotically with H₂(B) + He and the other with H₂(X) + He. Here θ is the angle formed by the H₂ figure axis and the line drawn from He to the midpoint of H₂. At present, however, an accurate potential suitable for collision studies is not available. Comparison of a seam of avoided crossings between the ground (1A') and first-excited (2A') excited electronic states computed by Perry and Yarkony,¹⁴ using a second-order configuration interaction method, with that contained in the Farantos, Murrell, and Carter¹³ potential energy surfaces used recently in a model

collision study show significant differences. Yarkony's more reliable results give a small energy gap ($\Delta E < 0.5$ kcal/mole) between the 1A and $^1A'$ states. For the pes of the model dynamics study, the energy gap is 6-32 kcal/mole.

In order to carry out a study of quenching dynamics in $He + H_2(B)$ of high accuracy, the energy gaps, curve-crossing geometry, saddlepoint position, barrier height, and well depth all are important features that must be quantitatively determined. Insight on some of these features is provided in Fig. 1 which compares minimum energy paths slices at $\theta = 35^\circ, 45^\circ, 55^\circ$, and 65° for the ground and excited pes's used in the model study. From that excited-state pes, the lowest barrier is found at 65° , and the deepest well and the smallest energy gap (not discernible from the figure) are at 45° . Because of the previously-mentioned deficiencies of these surfaces, the insufficient range of points for scattering studies of ref. 14, and the quantitative accuracy needed for this system as inferred from recent experiments of C. B. Moore, we have chosen to revisit the $He + H_2(B)$ system.

Our goal is to construct accurate pes's using the quantum Monte Carlo method - the approach that provided highly accurate pes data for tetrahydrogen. Before carrying out QMC calculations, however, a pilot ab initio study over the full range of coordinates accessible in a collision study is essential to gain a qualitative description of the pes, test QMC trial functions, and to decide on which regions of the pes's should be the primary focus of QMC calculations. Table 1 shows our preliminary HF, MCHF, and SDCI results at nine geometries of interest. We obtain good agreement

with Yarkony's ground-state results, but only fair consistency with his excited-state results at the SDCI level, as expected. The latter arises because of the modest basis set and wavefunction employed by us in anticipation of the use of the wavefunction as a QMC trial function. A QMC calculation at the Perry-Yarkony saddlepoint geometry gives $E = -3.9430$ (35) a.u., a result that is lower than the SOCI energy by ~ 0.22 eV. Preliminary calculations have begun directed at the construction of pes's and couplings needed for the calculation of quenching and rovibrational cross sections.

References

1. E. H. Fink, D. L. Akins, and C. B. Moore, J. Chem. Phys. **56**, 900 (1972).
2. H. F. Schaefer, III, D. Wallach, and C. F. Bender, J. Chem. Phys. **56**, 1219 (1972).
3. a) W. Gerhartz, R. D. Poshusta, and J. Michl, J. Am. Chem. Soc. **98**, 6427 (1976); b) **93**, 4263 (1977).
4. a) J. D. Goddard and I. G. Csizmadia, Chem. Phys. Lett. **43**, 73 (1976); b) **64**, 219 (1979).
5. C. A. Nicolaides, G. Theodorakopoulos, and I. D. Petsalakis, J. Chem. Phys. **80**, 1705 (1984); **80**, 1900 (1984); **81**, 748 (1984).
6. E. Kassab, E. M. Evleth, G. Chambaud, and B. Levy, in Photochemistry and Photobiology, vol. II, edited by A. H. Zewail (Hardwood Academic, New York), 1983, pp. 1307.
7. S. Y. Huang and W. A. Lester, Jr., Theoretical Study of the Interaction of $H_2(B^1\Sigma^+)$ and $H_2(X^1\Sigma^+)$, to be published; also see R&D Status Reports of W. A. Lester, Jr. under this contract for the years, 1987-89.
8. E. M. Evleth and E. Kassab, J. Chem. Phys. **89**, 3928 (1988).
9. J. A. Montgomery, Jr. and H. H. Michels, J. Chem. Phys. **86**, 5882 (1987).
10. A. Metropoulos and C. A. Nicolaides, J. Phys. B: At. Mol. Opt. Phys. **21**, (1988) L77.

11. G. Theodorakopoulos, I. D. Petsalakis, and C. A. Nicolaides, J. Mol. Struc. (Theochem) **149**, 23 (1987).
12. S. C. Farantos, G. Theodorakopoulos, and C. A. Nicolaides, Chem. Phys. Lett. **100**, 263 (1983).
13. S. C. Farantos, J. N. Murrell, and S. Carter, Chem. Phys. Lett. **108**, 367 (1984).
14. J. K. Perry and D. R. Yarkony, J. Chem. Phys. **89**, 4945 (1988).
15. P. Pernot, R. M. Grimes, W. A. Lester, Jr., and Ch. Cerjan, Chem. Phys. Lett. **163**, 297 (1989).

Table 1. *Ab initio* calculations of the 11A and 12A states of HeH_2^+ .

Geometries			$E(^11A)$			$E(^12A)$	
R^a	r^b	θ^c	HF	MCSCF ^d	SDCI ^e	MCSCF ^d	SDCI ^e
2.690, 2.520, 64.178			-3.83874	-3.90447	-3.92804	-3.59824	-3.60920
1.625, 3.807, 45.882			-3.63172	-3.68911	-3.70579	-3.67442	-3.68686
2.129, 5.250, 25.491			-3.58582	-3.63970	-3.65578	-3.61244	-3.61982
1.929, 4.750, 30.766			-3.60840	-3.66114	-3.67861	-3.63654	-3.64440
1.843, 4.500, 33.678			-3.61678	-3.66911	-3.68724	-3.64502	-3.65310
1.750, 4.250, 36.837			-3.62341	-3.67531	-3.69421	-3.65212	-3.66040
1.660, 4.000, 40.315			-3.62788	-3.67943	-3.69915	-3.65747	-3.66595
1.625, 3.900, 41.767			-3.62887	-3.68030	-3.70036	-3.65877	-3.66729
1.594, 3.812, 43.100			-3.62850	-3.67987	-	-3.65781	

*Atomic units (a.u.) are used throughout.

^aDistance from He to the midpoint of H_2 .

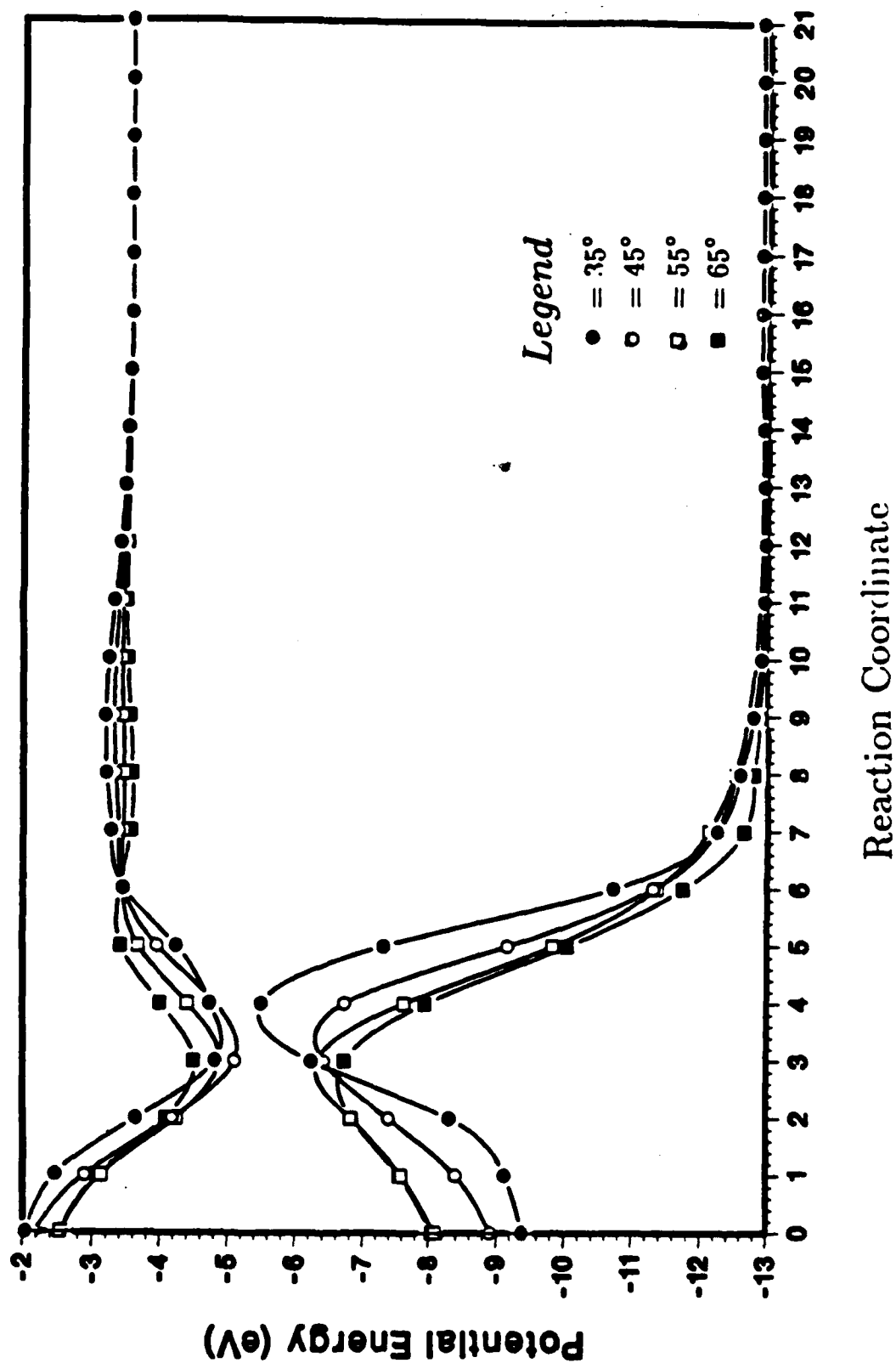
^b H_2 separation.

^cAngle formed by H-H axis and the line from He to the midpoint of H_2 .

^dState-averaged multiconfiguration self-consistent-field (SA-MCSCF) results.

^eSingle- and double-excitation CI from SA-MCSCF wavefunction.

HeH₂ at $\theta = 35^\circ, 45^\circ, 55^\circ, 65^\circ$ *



* From Ref. 13

Multiresonant Spectroscopy and the Dynamics of Intramolecular Relaxation in Superexcited States of Molecules, Radicals and Complexes

F. X. Campos, K. S. Haber, Y. Jiang, Y.-F. Zhu, R. Shehadeh and E. R. Grant

Department of Chemistry

Purdue University

West Lafayette, IN 47907

Thermodynamic gradients, kinetic barriers and dynamical factors that regulate the branching of competitive channels of decay all combine to determine the stability and detailed reaction paths of energetic molecules. Fundamental experimental research on tractable model systems can illustrate principles and provide important general guidance on these points, while also offering the potential to uncover practical routes to novel materials.

Presented below are results obtained over the past year by analysis of spectroscopic data on positions, lineshapes and intensities associated with ionization-detected absorption in jet-isolated molecules, radicals and dimers, that illuminate the behavior of highly energized systems. Our general approach is schematically pictured in Figure 1, which illustrates a typical transition terminating in a highly excited molecule, in this case a Rydberg state. To a first approximation, the process, as pictured, can be viewed as one that simply deposits the energy of the transition in the Coulomb separation between a cation core in a well-defined state, $|v>|J>$, and a hydrogenic electron. We might establish the occurrence of such a elementary excitation by observing subsequent vertical ionization with easily understood Franck-Condon factors and rotational selection rules.

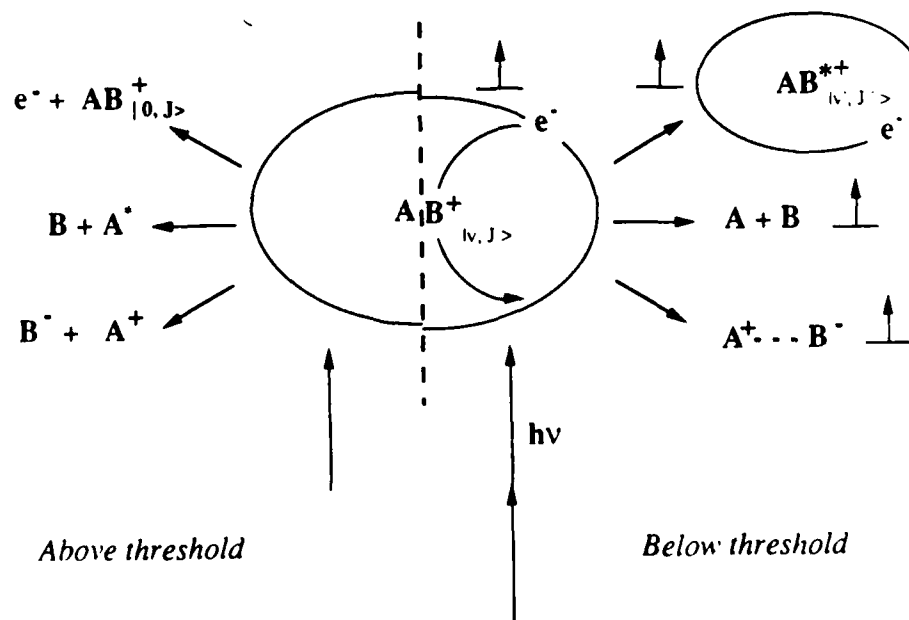


Figure 1. Excitation scheme diagramming paths for intramolecular relaxation / state mixing in highly excited molecules.

Alternatively, to complete the description of this excited state we might find it necessary to include processes that mix in (or scatter into) other accessible configurations. We look for evidence of the importance of these configurations in spectra. Thus, non-vertical ionization suggests Rydberg-Rydberg mixing. Neutral products, detected themselves or observed as a loss of ion signal, indicate fragmentation, and photolysis to ion pairs signifies the importance of charge-transfer configurations. In states above threshold, we look similarly for evidence of competition among available channels for dissociation to neutral and charged fragments.

In the past year we have applied the methodologies implied by this figure to investigate a range of problems related to the dynamics of intramolecular coupling in highly excited states of small molecules. By two-color double resonant photolysis, we have studied the dynamics of neutral fragmentation at $60,000\text{ cm}^{-1}$ from specified vibrational-rotational levels of Rydberg NO_2 . We have perfected instrumental methods for mass-resolving laser-generated anions following heterolytic photofragmentation of optically prepared charge-transfer states in isolated molecules. Using these methods, we have searched exhaustively for evidence of intramolecular proton transfer in $(\text{HCl})_2$ with negative results. We have completed work on the rotational-state-selected dynamics of spin-orbit autoionization in HCl . We have also begun to apply methods established for prototypical systems to important energetic radicals, including the boron and aluminum hydrides, which we generate by pulsed discharge, pyrolysis and evaporative filament supersonic expansion. Finally, we have established an unprecedented pattern of normal-mode selectivity in the 10 eV competition between vibrational autoionization and predissociation in triple-resonantly prepared NO_2 .

Neutral Fragmentation Dynamics of NO_2

Prominent in the absorption spectrum of NO_2 above $55,000\text{ cm}^{-1}$ are distinct vibrational progressions to linear Rydberg states. Many of these states, lying $40,000\text{ cm}^{-1}$ above the threshold for dissociation, exhibit subnanosecond lifetimes in pump-probe photoionization experiments. An interesting question arises whether dissociation proceeds along the internuclear axis of the photoprepared linear Rydberg state, or progresses through a bent repulsive state. Figure 2 shows part of the ionization-detected absorption spectrum of product NO following two-color double-resonant photodissociation of NO_2 via a selected low rotational level of the $3p\sigma^2\Sigma_u^+(200)$ vibronic state. It is clear from the strong lines in the NO product electronic spectrum originating from very high rotational states ($J = 60.5$ and above), together with the absence of transitions assignable to lower-lying rotational states, that fragmentation proceeds via a bent continuum.

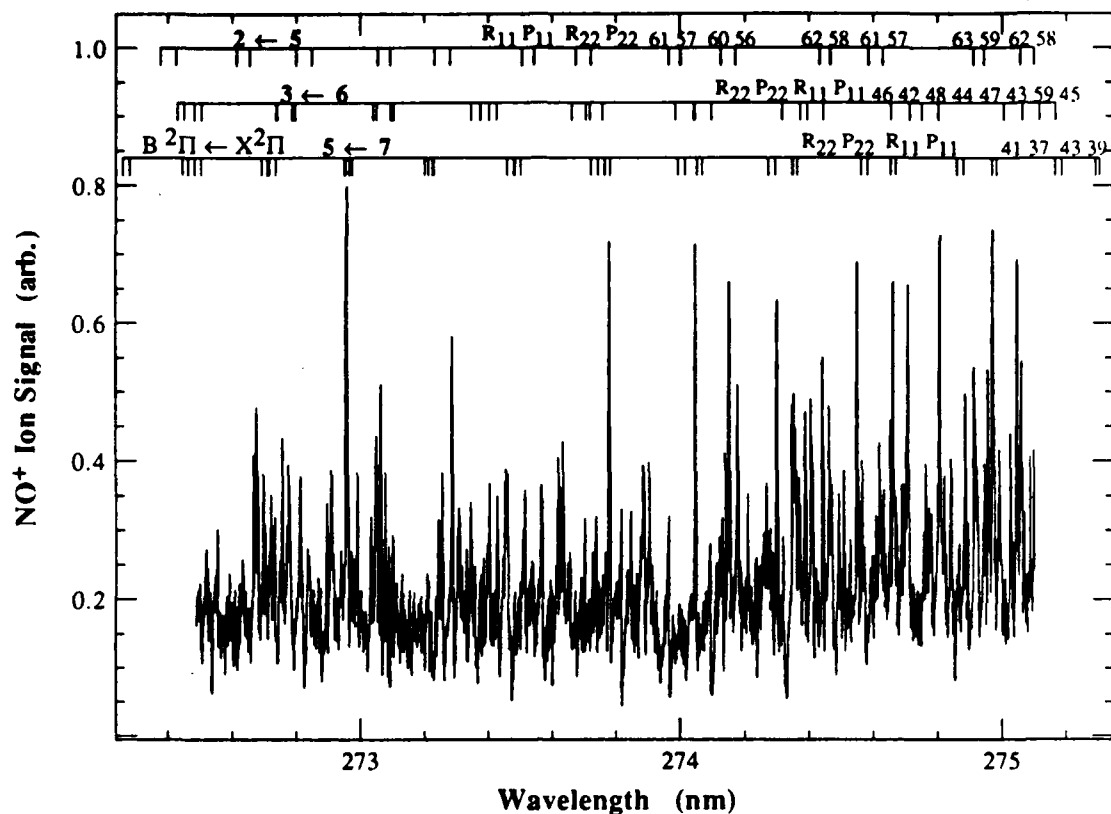


Figure 2. Resonant ionization spectrum of NO produced by double-resonant two-photon photodissociation of NO_2 via $3p\sigma \rightarrow 2\Sigma_u^+$ (200).

Charge-transfer states

It has been one of our experimental objectives to detect proton transfer in energized dimers. We have taken HCl as an ideal initial prototype. It readily forms dimers with itself, and the monomer alone exhibits substantial charge-transfer character in its energetic $V \ ^1\Sigma^+$ state. Figure 3 shows an anion mass spectrum of Cl^- from the photofragmentation of HCl to ion pairs. We now find it routine to collect such laser-generated anion signals, and we can signal average at the Cl^- mass while scanning the dye laser frequency to obtain rotationally resolved ion-pair detected two-photon absorption spectra, such as that of the $v=9$ band of the V state shown in Figure 4. In the dimer, the potential minimum of this state will be lowered by an amount approaching the proton affinity of HCl. It reaches its asymptotic limit, corresponding to H_2Cl^+ and Cl^- , at 8.5 eV. Under dimer-forming expansion conditions, we have searched the laser frequency region from the 293 nm two-photon threshold for ion-pair production to 240 nm. Thus far, we have found no evidence for Cl^- that we can associate with H_2Cl^+ . Apparently, despite strong thermodynamic driving forces, neutral fragmentation overrides proton transfer in the region Franck-Condon accessible from the dimer ground state.

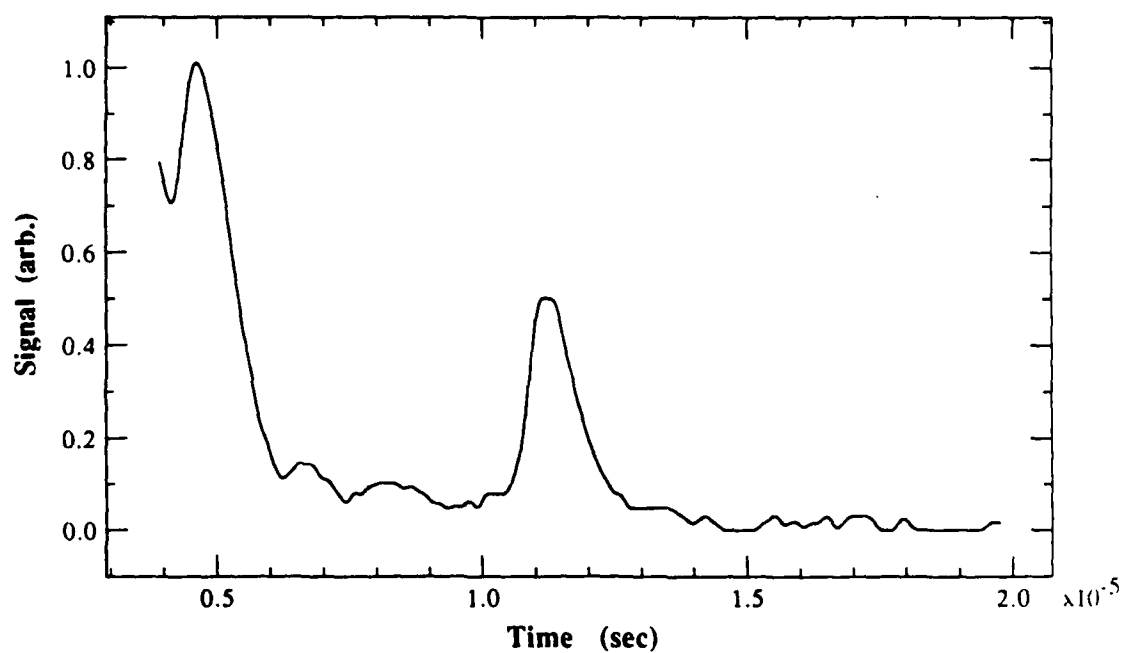


Figure 3. Anion mass spectrum showing Cl^- produced following multiphoton excitation of HCl via resonance with the $V\ ^1\Sigma^+ v=9\ Q(0)$ state.

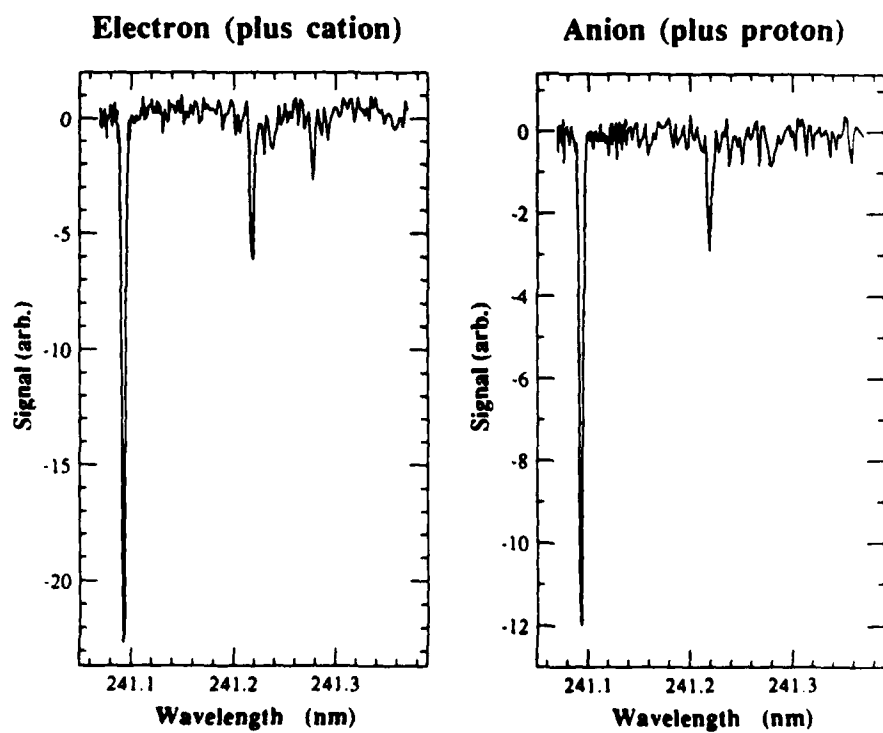


Figure 4. Spectra comparing electron-detected and anion-detected absorption spectra of the V state of HCl.

Rotational-state selected spin-orbit autoionization dynamics of HCl

Questions concerning the mechanism by which Cl^- is produced in one-color three-photon photoionization studies have motivated us to investigate the dynamics of charge separation after final photon absorption in this system by means of two-color, intermediate-state-selected double-resonance experiments. Our initial focus has been just above threshold, where Rydberg states converging to the upper $^2\Pi_{1/2}$ state of HCl^+ can decay by spin-orbit autoionization. Conventional methods fail to resolve the spectrum of this region to a meaningful level of detail because the spacing between adjacent electronic states is comparable to that between rotational states. By selecting a single rotational state ($4\pi\text{ F } ^1\Delta v=0, J=2$) using an intermediate two-photon transition, we isolate a subset of transitions which is assignable. Figure 5 shows the experimental double-resonant spectrum of autoionizing transitions accessible from $J=2$ of the F state, together with a simulation that assumes separable Hund's case c behavior, fitting constant quantum defects and monotonically varying widths and intensities to the complete set of electronic and rotational transitions allowed by angular-momentum selection rules. It can be seen that the ideal model does not correspond exactly to the data. We expect that no such simple parameterization can: Over the range of this scan, the system transforms to Hund's case e, and is subject to various levels of rotational-electronic perturbation. The simulation does, however, capture the correct density of transitions, and quite accurately describes serial structure over limited regions of the spectrum. Ultimately it is the deviations from ideal behavior that are most interesting, and the simple assignment we have made will be most useful as a starting point in identifying these. Their systematic characterization is the subject of collaborative efforts with theoreticians in the molecular spectroscopy group at Orsay.

Production and characterization of energetic radical hydrides of boron and aluminum

Also of interest to the Orsay group is an effort we are making to extend these methodologies to the related set of energetic boron and aluminum hydride radicals. We form compounds of interest, BH , AlH , together with their corresponding higher hydrides, in free-jet expansions by either of two methods. These are evaporative-filament pyrolysis and pulsed electric discharge, the nozzles for which are diagrammed in Figure 6. The discharge technique can be configured to produce electronically excited states which can be observed by emission spectroscopy, as illustrated for the aluminium- H_2 system by Figure 7. The filament nozzle, incorporating aluminum-coated tungsten, produces similar high-yields of ground-state radicals.

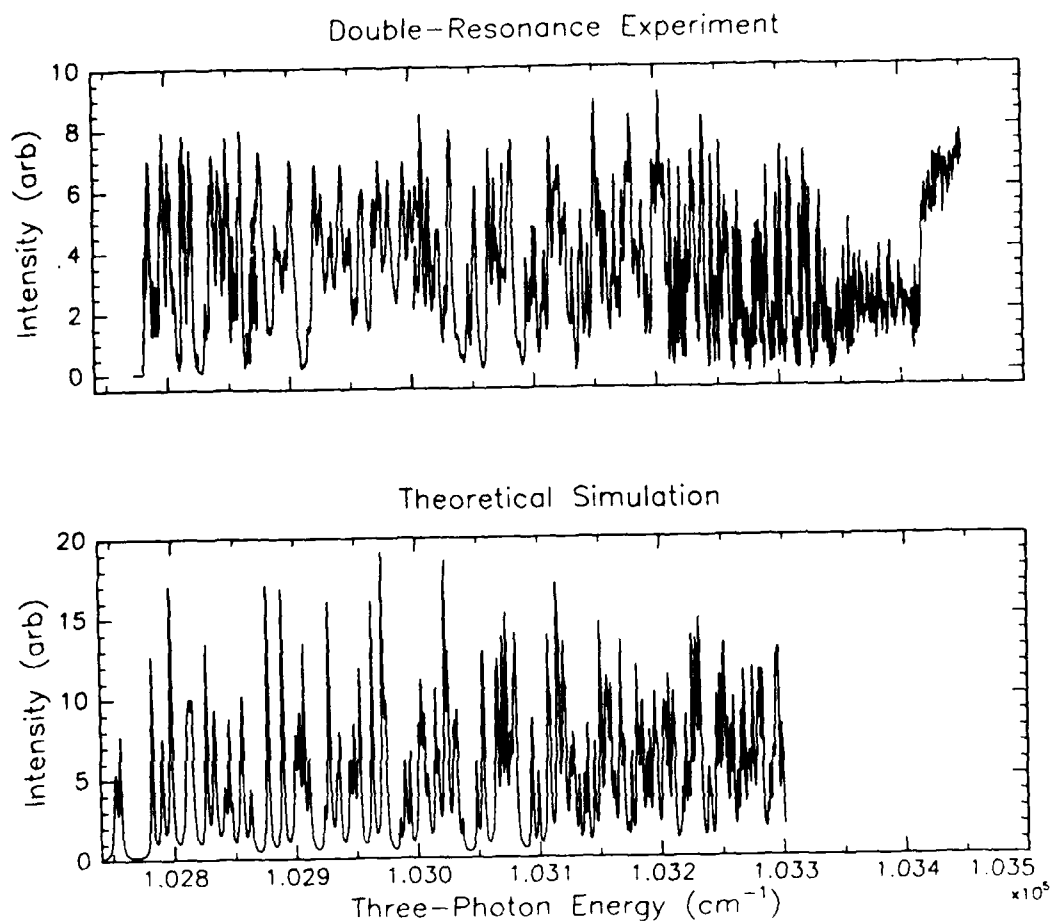


Figure 5. Experimental and computer simulated spectra of spin-orbit autoionizing transitions accessible in one-photon absorption from $J=2$ of the F state in HCl.

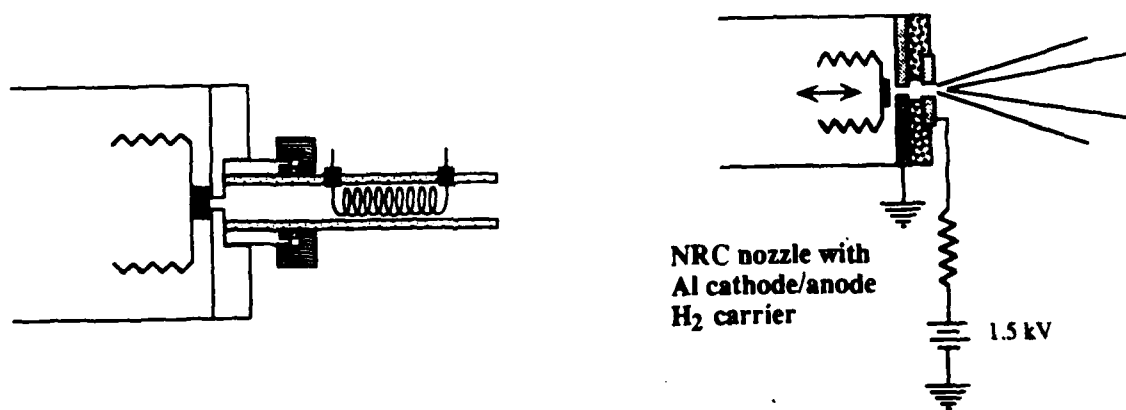


Figure 6. Evaporative filament (left) and discharge (right) pulsed nozzles.

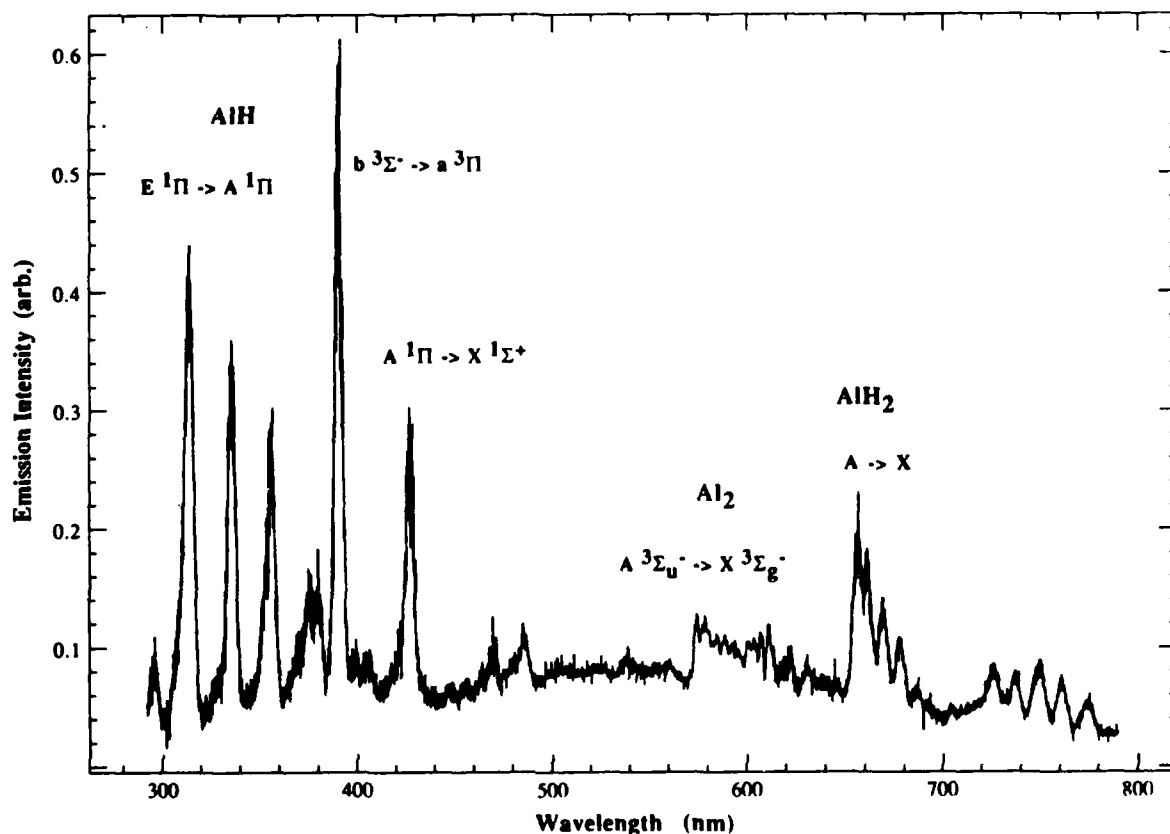


Figure 7. Spectrum of the aluminum hydride emission produced by the pulsed discharge nozzle using aluminum electrodes with H_2 carrier.

AlH and BH have $^2\Pi$ ion ground states, subject to spin-orbit splitting as in HCl . We are planning similar double-resonance experiments to explore these and related fragmentation dynamics. Also of interest, are the triatomics, BH_2 and AlH_2 . These are extra-electron molecules with closed-shell ion cores. On this basis, we might expect the higher-energy electronic structure of the neutral molecules to simplify along the lines suggested above by Figure 1. Such simplicity tends to isolate the dynamics of the coupling between electronic and vibrational degrees of freedom, which in a polyatomic molecule presents an opportunity to explore topologically different directions in the course of high-energy intramolecular relaxation. The class of possible experiments and their potential information content is well illustrated by work completed in our laboratory over the past year on NO_2 .

Normal-mode selectivity at 10 eV in the competition between vibrational autoionization and predissociation in NO₂ prepared by triple-resonant photoexcitation

Using stepwise resonant excitation methods, we have established a dramatic pattern of core-vibrational mode selectivity in the high-energy radiationless decay of NO₂ via competing paths of predissociation versus vibrational autoionization. We characterize these dynamics by analyzing patterns of intensity and lineshape in ionization-detected absorption spectra of vibrationally autoionizing states, reached in transitions from selected rotational states of a number of vibrational levels within the double-resonantly prepared gateway $3p\sigma$ $^2\Sigma_g^+$ Rydberg state. Photoselection, associated with three-color triple-resonant absorption, resolves single rotational lines in discrete electronic states that lie above the adiabatic ionization threshold at total energies as high as 85,000 cm⁻¹. Most features observed can be assigned to vibrationally-labeled $s\sigma$, $d\sigma$, and $d\pi$ series converging to associated vertical thresholds. Identified transitions typically extend over intervals of principal quantum number ranging from $n=6$ to more than 40. Observed spectra are modulated in intensity by sequences of perturbations that can be recognized as interloping series of complementary vibrational character, in which the balance of factors regulating the competition between available decay channels differs strongly.

Figure 8 below compares spectra of vertical transitions from symmetric stretch, (100), and bending, (010), excited levels of the $3p\sigma$ state. The spectrum from (100) shows a series of autoionizing resonances converging to the threshold for forming the (100) state of the cation. The intensities of these ionization-detected transitions are modulated by broad dips that form a series converging to the (110) threshold. Discrete states in these pure stretching series autoionize efficiently, as evidenced by the continuity of ionization-detected oscillator strength across the vertical threshold. The periodic mixing of bending character apparently interferes with ionization, presumably by diverting radiationless decay through neutral fragmentation channels. The behavior evidenced in the spectrum of autoionizing states reached in vertical transitions from the $3p\sigma$ (010) state confirms this hypothesis. Here we see a diminished yield from autoionization, accompanied by a definite step of increased ion yield at the vertical threshold. Thus, we can conclude that, in states with total energies near 80,000 cm⁻¹, the presence of one quantum of excitation in symmetric stretch is sufficient to direct radiationless decay strongly toward electron ejection, while a similarly small increment of the total energy deposited in bending excitation channels relaxation much more efficiently toward neutral fragmentation.

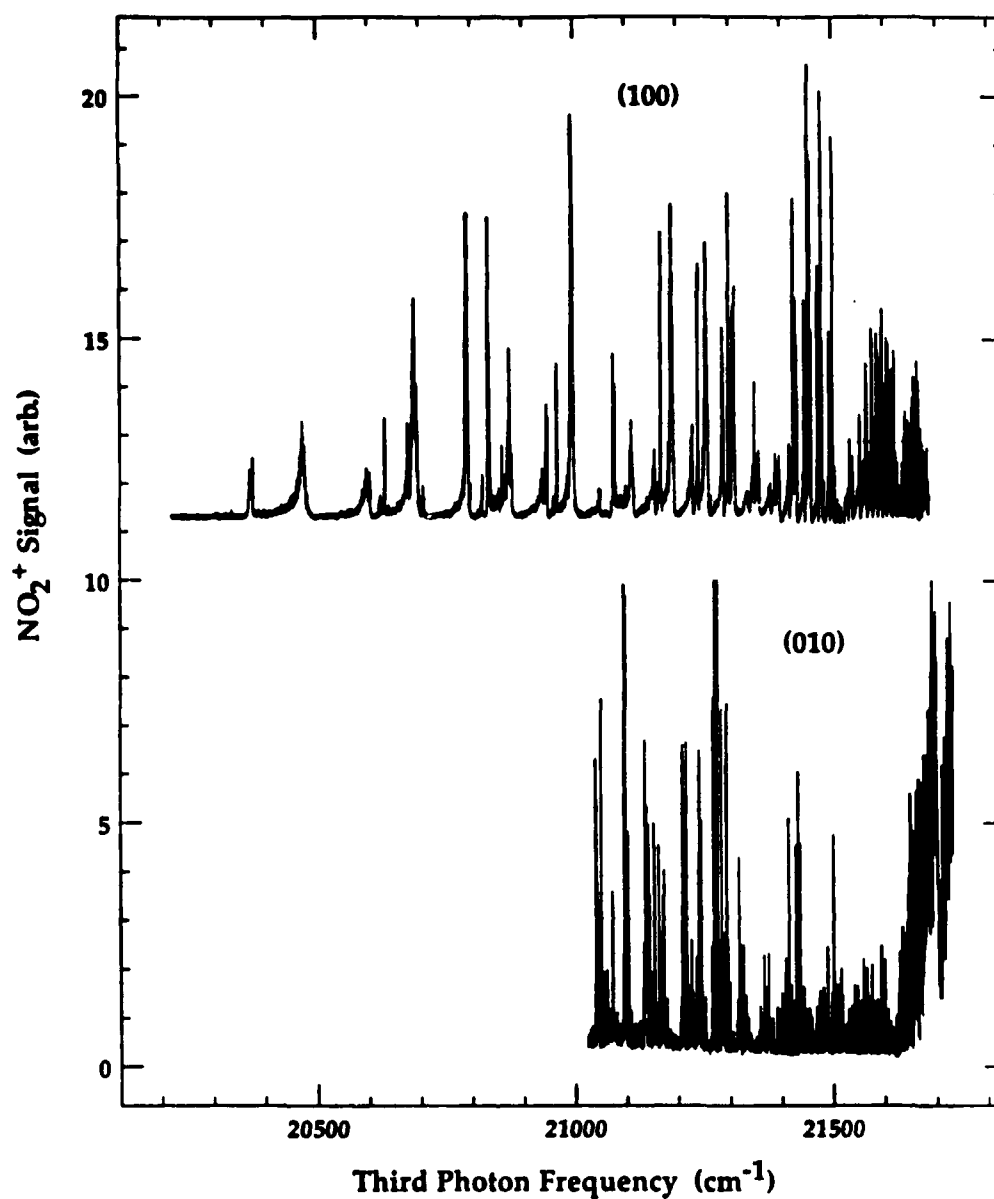


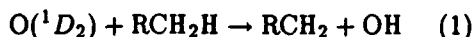
Figure 3. Ionization-detected absorption spectra of NO₂ (100) (upper) and (010) vibrationally autoionizing manifolds accessed by one-photon absorption from N'=1 levels of 3pσ ²Σ_g⁺ (100) and (010) states, optically selected by double-resonant excitation

Dynamic Constraints on Stochastic Behavior in the Chemistry of Highly Excited Molecules

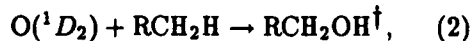
Barry K. Carpenter and John R. Wiesenfeld
Department of Chemistry, Cornell University
Baker Laboratory, Ithaca, NY 14853

February 11, 1990

Atomic oxygen in its lowest lying electronically excited state, $O(^1D_2)$, is known to react efficiently with hydrocarbons. Previous studies of its dynamics have suggested that the reaction proceeds both *via* direct abstraction



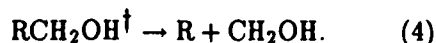
and insertion



followed by dissociation either to yield OH



or, in the case where R is other than H, the hydroxymethyl radical



The exothermicity of the reaction that yields OH ranges between 180 and 220 kJ/mol for $R = H$ and $(CH_3)_4C$, respectively. In the present experiments, complete determination of the OH product distributions arising from the $O(^1D_2)/RCH_2H$ reaction yielded detailed mechanistic information and led to the identification of cases in which RCH_2OH^\dagger dissociates prior to equilibration of reaction energy among the available modes of the complex.

Hydroxyl radical product distributions were characterized in a pump-probe experiment in which $O(^1D_2)$ was produced in the 248 nm photodissociation of O_3 , and the product OH was detected by laser induced fluorescence in both the diagonal and sequence bands of the $A^2\Sigma^+ \leftarrow X^2\Pi$ transition. By minimizing both the delay time between the photolysis and LIF probe pulses ($\Delta t = 200$ ns) as well as the ambient gas pressure ($P_{RCH_2H} = 50$ mtorr, $P_{O_3} = 10$ mtorr, $P_{He} = 90$ mtorr), the mean number of gas kinetic collisions of OH is limited to 0.5. The LIF technique permits full resolution of v'' , N'' , F'' , and λ to the limit of available energy with only minimal relaxation of the nascent energetics.

Observed signal intensities were corrected for detector sensitivity as well as variations in pump and probe laser powers and converted to populations using calculated line strengths. No correction was made for the electronic deactivation of $OH(A^2\Sigma^+)$, as the known rates are so small as to affect the observed emission of the lowest rotational levels by less than 20%. Corrections were made for predissociation of the higher rotational levels of the $A^2\Sigma^+$ state.

The OH population distributions resulting from the reaction of $O(^1D_2)$ with CH_4 and nC_3H_8 are displayed in Figs. 1 and 2, re-

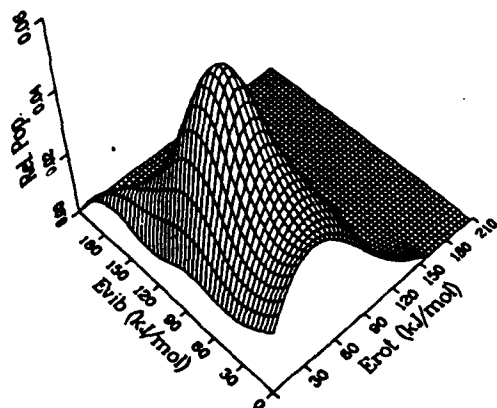


Figure 1: A 3-D view of the OH population distribution observed following the reaction of $O(^1D_2)$ with CH_4 . The relative populations are normalized so that $\sum_{v,N} P(v,N) = 1$ where v is the most highly populated vibrational level.

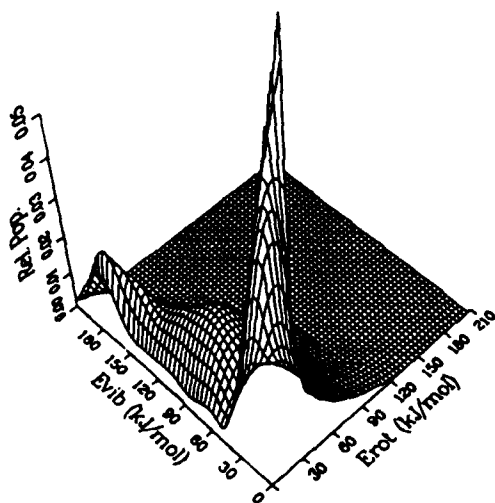


Figure 2: The OH population distribution observed following reaction of $O(^1D_2)$ with nC_3H_8 . Normalization is as in Figure 1.

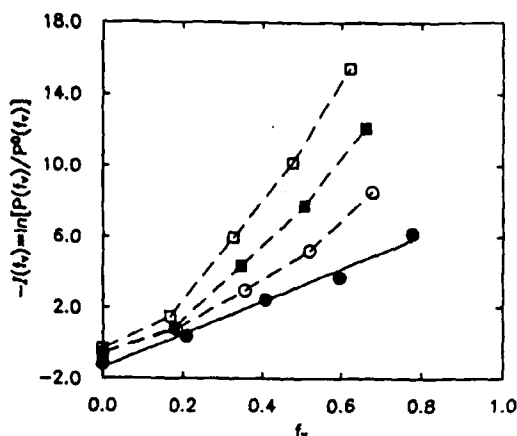


Figure 3: Surprisals for OH vibration. Results correspond to: CH_4 , C_2H_6 , nC_3H_8 , and $(CH_3)_4C$ from bottom to top.

spectively. That of $O(^1D_2)/CH_4$ is clearly unimodal; its shape is characteristic of other $O(^1D_2)$ reactions like that with H_2 , which result in the production of relatively flat vibrational and rotational distributions to the limit of reaction exothermicity. In the case of the $O(^1D_2)/nC_3H_8$ reaction, the dominant feature corresponds to rotationally and vibrationally cold OH with a "tail" of warmer products in higher-lying vibrational states. In earlier work, the dominant cold feature was associated with direct abstraction, that at higher energy with insertion followed by elimination.

Information theoretic analysis of the vibrational population distributions (Fig. 3) reveals highly nonlinear plots, especially for the heavier hydrocarbons. This suggests that the higher lying vibrational levels are more highly populated than would be expected on a statistical basis. Inspection of the rotational surprisals (Fig. 4) reveals that these too can be nonlinear, especially in the lowest OH vibrational levels arising from reaction of $O(^1D_2)$ with the heavier hydrocarbons.

Deconvolution of the nonlinear rotational

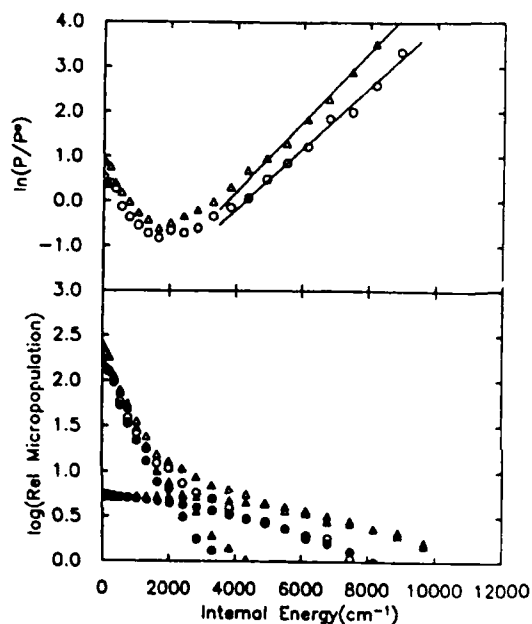


Figure 4: Example deconvolution of a bimodal rotational distribution into low- J and high- J components by constructing a linear surprisal fit to the high J component (top). Shown below are the resulting micropopulation distributions. Open symbols correspond to experimental observation. Triangles correspond to the $\Pi(A')$ sublevel, circles to $\Pi(A'')$.

Table 1: Accounting for the low- J component of OH following the reaction of $O(^1D_2)$ with RCH_2H . The values in brackets were derived from RRKM calculations.

Substrate	Overall	$P(1)/P(0)$
CH_4	0.06	0.33 [0.24]
C_2H_6	0.24	0.09
nC_3H_8	0.41	0.04 [0.05]
$(CH_3)_4C$	0.67	0.02

surprisals into low- and high- J components permits calculation of separate vibrational distributions that correspond to the two components. The vibrational surprisal corresponding to those OH product molecules that belong to the high- J component is linear (Fig. 5).

In examining the low- J component states, we note that the fraction of the OH product corresponding to that component increases monotonically as the size of the substrate increases (Table 1). In addition, the vibrational population ratio $P(1)/P(0)$ decreases in the heavier hydrocarbons. Comparison of $P(1)/P(0)$ with RRKM calculations strongly suggests that the low- J OH component arises as the result of (3), the dissociation of a relatively long-lived collision complex following statistical distribution of energy in its internal modes. That is further supported by an earlier observation that approximately 70% of the RCH_2OH^\dagger can be collisionally quenched in the $O(^1D_2)/(CH_3)_4C$ reaction. Clearly, the low- J component dominates the "cold" OH product observed in the reaction of $O(^1D_2)$ with the heavier hydrocarbons. It does *not* arise as the result of direct abstraction in (1) as has previously been suggested.

That part of the OH product that corresponds to the high- J component cannot arise from abstraction. Neither high rotational exci-

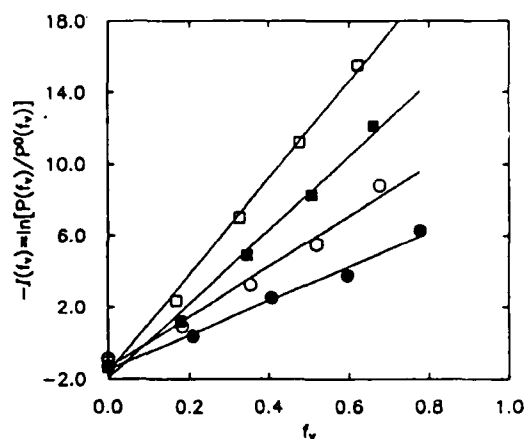


Figure 5: Surprisals for vibration of high- J OH population. See Fig. 3 for symbols.

tation nor an observed propensity for preferential production of OH with an in-plane orientation of the half-filled π orbital in the rotation plane correspond with known characteristics of direct abstraction processes. By elimination, we conclude that the high- J component of the OH produced in the $O(^1D_2)/RCH_2H$ reaction arises from the dissociation of the RCH_2OH^\ddagger complex prior to randomization of reaction exoergicity in its internal modes. This agrees well with the earlier observation that 30% of the products of the $O(^1D_2)/(CH_3)_4C$ reaction could not be collisionally quenched in classical photochemical experiments.

This work was supported by AFOSR and was carried out by Dr. Chan Ryang Park.

THEORETICAL STUDIES OF HIGHLY ENERGETIC CBES MATERIALS*

N.E. Brener, N.R. Kestner, J. Callaway, and H. Chen
Louisiana State University
Baton Rouge, Louisiana 70803

I. Identification of Candidates for Advanced Propellants

A procedure has been developed and refined for identifying new materials that have the capability to store large amounts of energy. The standard of comparison used in these studies is the current state of the art propellant, the $\text{H}_2\text{-O}_2$ system, with a specific enthalpy of 12.56 MJ/kg and a specific impulse (I_{sp}) in the neighborhood of 457 sec. In the first stage of this procedure, new molecules are investigated at the SCF 6-31G* level in order to determine their energy content, vibrational stability, and relative position on the potential energy hypersurface. Promising candidates selected from these initial screening calculations are then further studied at the SCF 6-31G* level in order to determine their activation barrier and hence stability. If a significant barrier is found, the above calculations are repeated at the CISD level, using the MESA program, in order to include correlation effects in the calculations. Molecules that are found to be stable and highly energetic at the CISD level are then studied by simulated annealing cluster programs to determine their stability and energy content in the condensed phase. The above procedure has already led to the identification of two candidates for advanced propellants, trans N_6 and the N_4 tetrahedron, both of which are described below.

II. Trans N_6

We have reported previously that at the SCF 6-31G* level, an azide-like structure, called trans N_6 , shown in Fig. 1, is found to be highly energetic, vibrationally stable, and the global minimum on the N_6 potential energy hypersurface.¹ In the geometry optimizations on trans N_6 , all possible configurations, including nonplanar and nonsymmetric structures, were allowed, but the geometry still converged to the planar symmetric (C_{2h}) configuration given in Fig. 1. Another N_6 structure, the N_6 ring, given in Fig. 2, was also found to be vibrationally stable at the SCF 6-31G* level but was significantly higher in energy than trans N_6 , indicating that trans N_6 is the global minimum of the N_6 system.¹

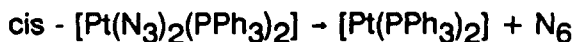
Using the energy content given in Fig. 1, which is defined as the total energy of trans N_6 minus the total energy of three N_2 molecules, we computed a specific enthalpy for trans N_6 of 11.13 MJ/kg and a corresponding I_{sp} of 430 sec. A larger I_{sp} value of 480 sec. was computed by the Astronautics Laboratory for the case of a trans N_6 monopropellant. Taking the average of these values, one obtains an I_{sp} of 455 sec., which is at the level of the current state of the art propellant system.

During the past year, substantial progress has been made in the trans N_6 studies, as described below:

- 1) Two larger basis sets, 6-311G* and 6-311G(2DF), have been used to perform geometry optimization and vibrational frequency calculations on both trans N_6 and the N_6 ring at the SCF level. The results of these geometry optimizations are given in Tables I and II. In the case of trans N_6 , all of the vibrational frequencies remain positive at both of these higher basis set levels. However, the N_6 ring exhibits one negative frequency when the largest basis set, 6-311G(2DF), is used, indicating that the N_6 ring is vibrationally unstable. This result provides further indications that trans N_6 is the global minimum or ground state of the N_6 system.
- 2) Two earlier papers^{2,3} have been found which consider several "open chain" structures of N_6 , including trans N_6 which is referred to in ref. 2 as a C_{2h} structure. Using the 6-31G basis set, the authors of both of these papers found a nonplanar C_2 structure, rather than trans N_6 , to

be the global minimum on the N_6 potential energy hypersurface. However, using the Gaussian 86 program and three larger basis sets with polarization functions, 6-31G*, 6-311G*, and 6-311G(2DF), we find in all three cases that, contrary to refs. 2 and 3, the planar trans N_6 structure (C_{2h}) is indeed the ground state of the N_6 system and that the C_2 structures given in refs. 2 and 3 as the ground state are not stationary points, but rather converge to the trans N_6 structure when the geometry is optimized.

- 3) The transition state of trans N_6 at the SCF 6-31G* level has been found and is given in Fig. 3. This structure, which is similar to the N_6 transition state reported in ref. 3, is a nonplanar C_2 configuration and leads to dissociation into three N_2 molecules, as expected. The Fig. 3 transition state yields an activation barrier of .54 eV compared with the corresponding FN_3 barrier of .47 eV. Thus at the SCF 6-31G* level, the trans N_6 barrier is approximately the same as the FN_3 barrier, indicating that the stability of trans N_6 is comparable to that of FN_3 .
- 4) Extensive CISD calculations on trans N_6 have been carried out with the MESA program using the 6-31G* basis set and the geometries that were optimized at the SCF 6-31G* level. The resulting CISD energies for the trans N_6 ground and transition states, which are given in Table III, yield an activation barrier of .80 eV compared with the FN_3 barrier of .80 eV at this same level of calculation. Thus the CISD results again indicate that the stability of trans N_6 is approximately the same as that of FN_3 and suggest that since FN_3 has been synthesized by several research groups, the synthesis of trans N_6 should also be possible. In these trans N_6 CISD calculations, the coefficient of the reference state, $c(0)$, is .91, which indicates that multi-reference CI (MRCI) calculations are not likely to produce significant changes in the above results.
- 5) A paper⁴ has been found in which the authors report the possible synthesis of the N_6 molecule in a low temperature matrix, according to the reaction



- 6) Simulated annealing cluster calculations are currently in progress to determine the stability and specific enthalpy of trans N_6 in the condensed phase.

III. N_4 Tetrahedron

Another new molecule, the N_4 tetrahedron, shown in Fig. 4 and henceforth referred to as N_4 , has also been found to be highly energetic, vibrationally stable, and a global minimum at the SCF 6-31G* level. Using the energy content given in Fig. 4, which is defined as the total energy of N_4 minus the total energy of two N_2 molecules, we computed a specific enthalpy for N_4 of 16.57 MJ/kg and a corresponding I_{sp} of 525 sec. By comparison with the case of trans N_6 , it is estimated that an I_{sp} of 586 sec. would be obtained if N_4 is treated as a monopropellant. Taking the average of these two values, one obtains an I_{sp} of 556 sec., which is approximately 100 sec. larger than the I_{sp} of the current state of the art propellant system.

N_4 geometry optimization and vibrational frequency calculations have also been done at the SCF 6-311G* level. The resulting geometry is given in Table IV. All of the vibrational frequencies remain positive and large at this higher basis set level, with the smallest frequency increasing slightly from its 6-31G* value, indicating clearly that N_4 is stable with respect to vibration.

The N_4 transition state at the SCF level has been computed with both the 6-31G* and 6-311G* basis sets and is given in Fig. 5. This transition state, which occurs at the intersection of rising and falling potential curves, leads to dissociation into two N_2 molecules, as expected. As shown in Table VI, the Fig. 5 transition state yields 6-31G* and 6-311G* activation barriers of 1.77 eV and 1.81 eV respectively, which are more than three times larger than the corresponding values of the FN_3 barrier.

CISD calculations on the N_4 ground and transition states have been carried out with the MESA program using both the 6-31G* and 6-311G* basis sets and the geometries that were optimized at the SCF 6-31G* and SCF 6-311G* levels, respectively. The resulting CISD energies are given in Table V and the corresponding activation barriers, given in Table VI, are 1.69 eV and 1.72 eV for the 6-31G* and 6-311G* basis sets, respectively. As shown by Table VI, the N_4 barrier decreases slightly at the CISD level, compared to the SCF level, but the values of the N_4 CISD barrier are still more than twice as large as the corresponding values of the FN_3 barrier, indicating that N_4 is highly stable compared to FN_3 .

IV. Simulated Annealing Cluster Calculations

We have previously reported simulated annealing calculations on clusters of FN_3 molecules that yielded a density of 1.3 g/cm^3 and an energy density of $9 \text{ kcal/(mole} \cdot \text{Å}^3)$ for the FN_3 molecular solid. In addition to the above-mentioned trans N_6 cluster calculations that are currently in progress, the simulated annealing program is also presently being used to investigate the possible stabilization of energetic molecules by adsorption on surfaces. In particular, calculations on HN_3 and FN_3 molecules adsorbed on KF surfaces have yielded stable configurations and binding energies of the order of half an electron volt in both cases, with the HN_3 binding energy being slightly larger. In the optimized geometry for the HN_3 molecule, the H atom was found to be closest to the surface and directly above an F^- ion, while in the case of FN_3 , the F atom was found to be nearest the surface and directly above a K^+ ion. In both cases the plane of the three nitrogen atoms was nearly parallel to the surface. Calculations are currently in progress to study the interaction of FN_3 and HN_3 with other alkali halide surfaces, such as NaF and RbCl, in order to more fully understand the mechanism of azide molecule surface adsorption. Preliminary results indicate that this mechanism depends at least in part on the size of the surface lattice constant.

Calculations are also underway to investigate the possible adsorption of FN_3 and HN_3 molecules on ammonium perchlorate (AP) surfaces. This type of adsorption would be of particular interest as it would lead to energetically enhanced AP and hence larger I_{sp} values for solid propellants.

* Supported by the Astronautics Laboratory (AL) under Contract F04611-87-K-0026.

1. N.E. Brener, J. Callaway, N.R. Kestner, and H. Chen, Proceedings of the High Energy Density Materials Conference, New Orleans, LA, March 12-15, 1989, edited by T.G. Wiley and R.A. Opijnen (Astronautics Laboratory, Edwards AFB, CA, 1989), pg. 211.
2. H. Huber, T.K. Ha, and M.T. Nguyen, J. Mol. Struct. (Theochem) **105**, 351 (1983).
3. M. Ramek, J. Mol. Struct. (Theochem) **109**, 391 (1984).
4. A. Vogler, R.E. Wright, and H. Kunkely, Angew. Chem. Int. Ed. Engl. **19**, 717 (1980).

NOTE: In the following tables and figures, distances are in Angstroms, angles are in degrees, and energies are in Hartrees unless otherwise labeled. The distances and angles in Tables I, II, and IV are defined in Figures 1, 2, and 4, respectively.

Table I. Trans N₆ Optimized Geometry and Total Energy

	<u>SCF 6-31G*</u>	<u>SCF 6-311G*</u>	<u>SCF 6-311G(2DF)</u>
R1	1.4298	1.4285	1.4287
R2	1.2357	1.2324	1.2288
R3	1.1011	1.0945	1.0898
A1	107.38	107.48	107.51
A2	174.81	175.02	175.19
Total Energy	-326.47505	-326.55419	-326.58743

Table II. N₆ Ring Optimized Geometry and Total Energy

	<u>SCF 6-31G*</u>	<u>SCF 6-311G*</u>	<u>SCF 6-311G(2DF)</u>
R1	1.2854	1.2836	1.2807
Total Energy	-326.44896	-326.52109	-326.55336

Table III. Trans N₆ CISD Calculations

	<u>CISD Energy</u>
6-31G* Ground State, 447,931 Configurations	-327.24143
6-31G* Transition State, 447,931 Configurations	-327.21208

Table IV. N₄ Tetrahedron Optimized Geometry and Total Energy

	<u>SCF 6-31G*</u>	<u>SCF 6-311G*</u>
d _{NN}	1.3949	1.3919
Total Energy	-217.53384	-217.58697

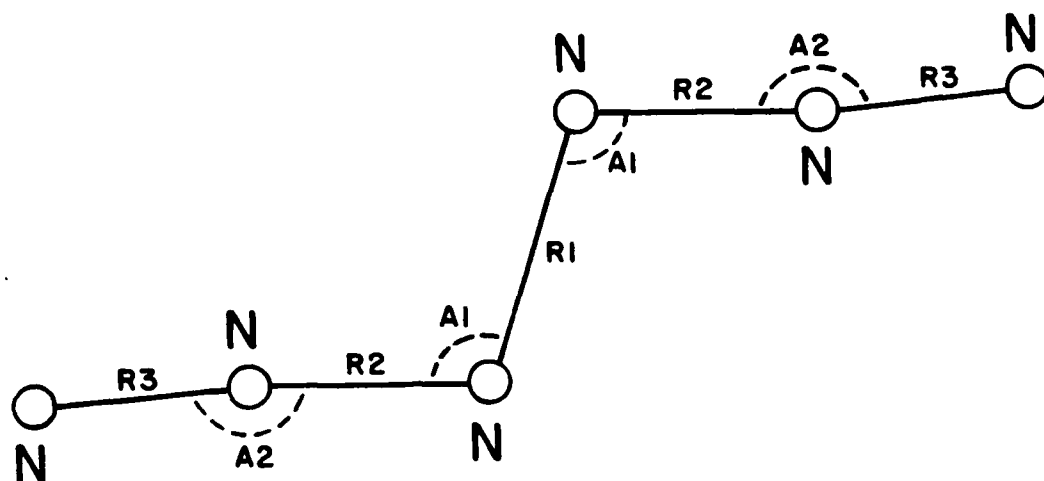
Table V. N₄ Tetrahedron CISD Calculations

	<u>CISD Energy</u>
6-31G* Ground State, 88,831 Configurations	-218.09197
6-31G* Transition State, 88,831 Configurations	-218.02970
6-311G* Ground State, 169,071 Configurations	-218.21971
6-311G* Transition State, 169,071 Configurations	-218.15646

Table VI. N₄ Tetrahedron Activation Barrier

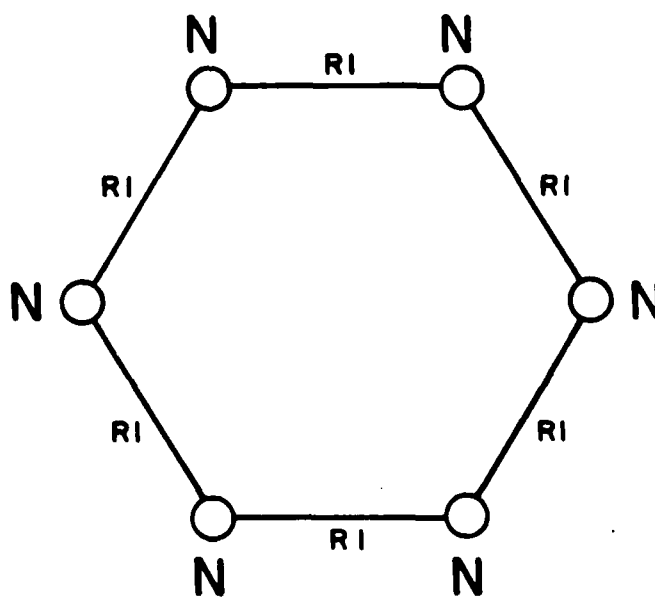
	<u>Barrier</u>
SCF 6-31G*	1.77 eV
SCF 6-311G*	1.81 eV
CISD 6-31G*	1.69 eV
CISD 6-311G*	1.72 eV

Figure 1. Trans N₆



R1 = 1.429808
 R2 = 1.235724
 R3 = 1.101074
 A1 = 107.378173°
 A2 = 174.807741°
 Total Energy = -326.4750476
ENERGY CONTENT = 9.705 eV

Figure 2. N₆ Ring



R1 = 1.285389
 Total Energy = -326.4489642
ENERGY CONTENT = 10.4145 eV

Figure 3. Trans N₆ Transition State

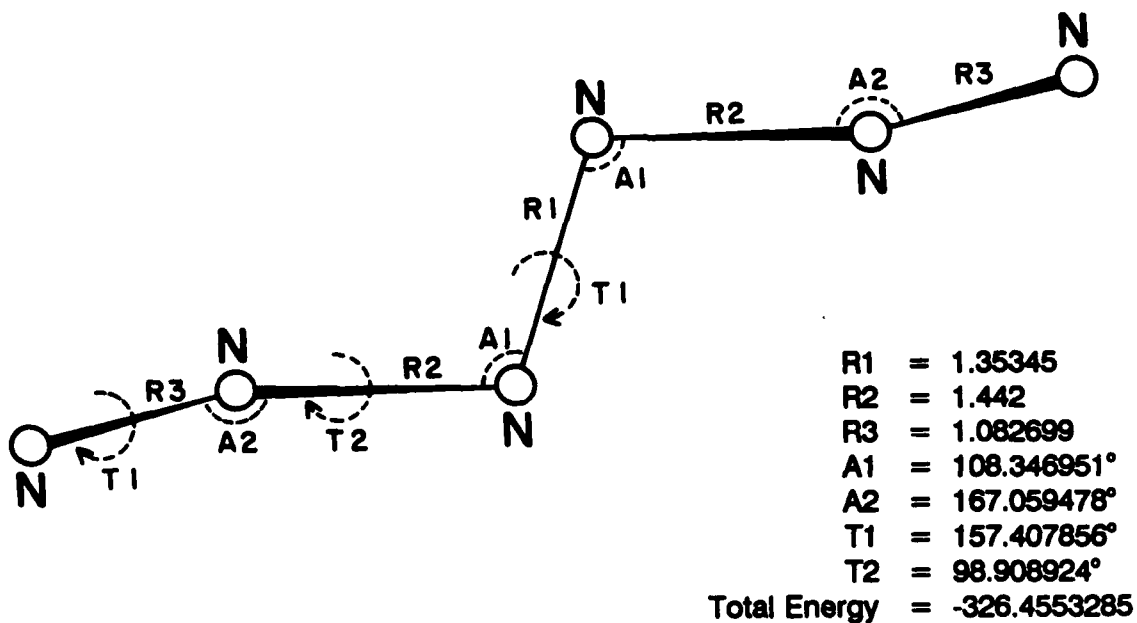
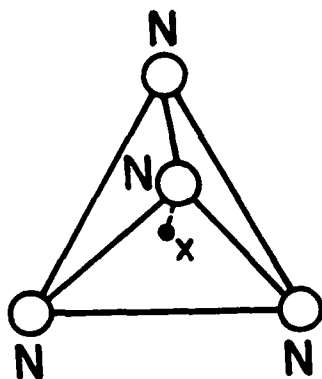
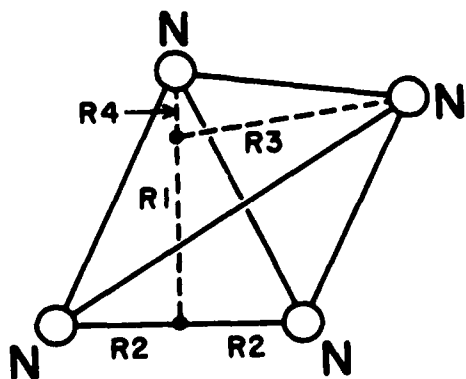


Figure 4. N₄ Tetrahedron



$d_{NN} = 1.3949$
 Total Energy = -217.5338449
 ENERGY CONTENT = 9.6303 eV

Figure 5. N₄ Tetrahedron Transition State



	SCF 6-31G*	SCF 6-311G*
R1	0.973	0.972
R2	0.644698	0.643003
R3	1.220061	1.211357
R4	0.349214	0.351998
Total Energy	-217.4688693	-217.5204419

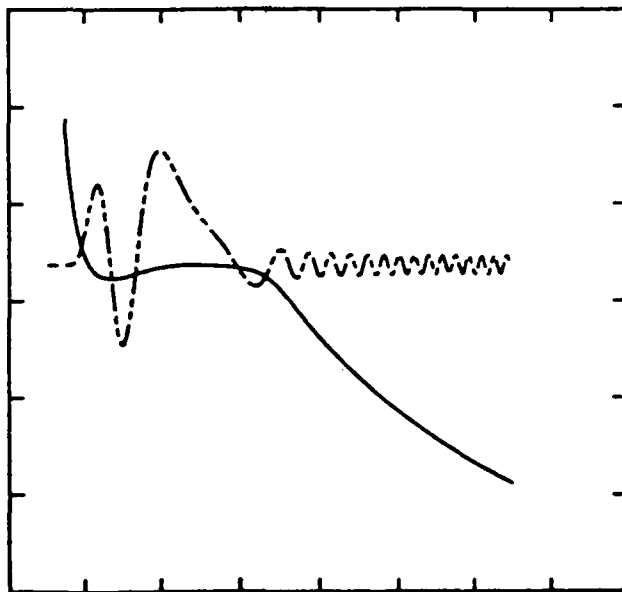
**Extended Abstract:
The Search For Tetrahedral N_4^\dagger**

**Walter J. Lauderdale, Murray J. Myers, David E.
Bernholdt, John F. Stanton, and Rodney J. Bartlett
Quantum Theory Project
University of Florida
Gainesville, FL 32611-2085**

**† Support provided by the Air Force Office of
Scientific Research under contract AFOSR-89-0207.**

Introduction

The overall objective of this work is to determine potential energy curves for molecules of the following form:

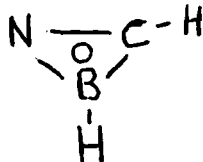


A reasonable barrier is essential if a molecule of sufficient lifetime is to be found. The semi-dashed line shows a typical metastable vibrational level with a large amplitude around the local minimum and a finite, but non-zero, amplitude outside the barrier.

In addition to identifying a molecule with such a potential, it is requisite to know where other closely lying states occur. Different electronic states can couple via non-adiabatic effects or via spin-orbit interactions, which might lead to additional dissociation pathways.

A strategy for suggesting potential geometrically metastable molecules is to exploit various kinds of isoelectronic analogies. For example propene, cyclopropene, and ozone suggest the molecule N_3H_3 , which is experimentally unknown. Because of the strength of the N_2 bond, any N_3H_3 structure will be metastable compared to N_2 and H_2 or N_2 and NH_3 . Similarly, there can be structures isovalent with those well known for heavier atoms. P_4 and As_4 are the normal forms for phosphorous and arsenic, but since N_2 is the normal form for nitrogen, tetrahedral N_4 would at best be metastable. Similarly, cubic N_8 could be considered reasonable based solely on electronic bonding patterns.

A third way to exploit isoelectronic analogies would be to form quasi-aromatic analogs by replacing CH by N or CH^+ by BH, for example, giving the analog of cyclopropenyl cation, $C_3H_3^+$ by



Obviously, many other such quasi-aromatic structures would be possible by further substitutions. However, before considering any such species, a reasonable expectation of a barrier to dissociation is essential. In many cases, symmetry arguments can be used to imply such a barrier.

In such a search for metastability, *ab initio* quantum chemistry plays a critical rôle. At sufficient levels of accuracy to be "predictive", quantum chemistry provides the following:

- Determination of critical points on a potential energy surface (PES) and their characterization
- Prediction of molecular structures
- Relative energies of metastable forms and decomposition products
- Prediction of vibrational spectra for experimental identification and interpretation
- Predictions of electronic excitation energies, excited state surfaces, and lifetimes
- Coupling between electronic states

The determination of molecular structures, transition states, and barrier height depends critically on having analytical gradient (i.e. $\partial E/\partial X_\alpha$, where X_α is some Cartesian coordinate of an atom) and $\partial^2 E/\partial X_\alpha \partial X_\beta$ available. The latter can sometimes be evaluated analytically (SCF, MBPT(2)), but more often is obtained by finite differences of analytically computed first derivatives. When all the first derivatives vanish and the matrix of second derivatives (i.e. the Hessian) has only positive eigenvalues, the point represents a minimum on the surface. When one negative eigenvalue (or one imaginary frequency) is obtained, a transition state (TS) is found. However, it is important to follow vibrational modes through the transition state to see where the barrier leads. Otherwise the TS may not correspond to the barrier of interest.

New Methodology

In our work on metastability for AFOSR, method development is a big part. Three recent developments are particularly pertinent:

- Open and closed shell analytical gradients (Watts, Salter, Trucks)
 - MBPT(2), MBPT(3), MBPT(4)

- CCD and unitary coupled-cluster variants, JCCSD(4), UCCSDT(4)
- Efficient search routines based upon Morse adjusted Newton-Raphson (MANR) method, for minima and the Cerjan and Miller transition state search procedure. (Stanton, Bernholdt)
- Optimum algorithm to exploit redundancy in force constant and dipole derivative evaluation from analytical gradients (e.g. for Methane, need 2 gradient calculations instead 13) (Stanton)

So far, these are the only open-shell many-body analytical gradient methods available. To illustrate how these methods work a few examples in Table I compare frequencies computed at different levels.

Table I. Mean absolute differences (expressed as percentage) between theoretically calculated harmonic vibrational frequencies and those inferred from experimentally determined quadratic potential constants. All calculations were performed with a DZP basis.

	Singly-bonded systems				Multiply-bonded systems		
Level of Theory	CH ₄	NH ₃	H ₂ O	HCN	C ₂ H ₂	CO ₂	H ₂ CO
SCF ^a	5.3	7.5	7.9	12.2	11.9	11.3	8.6
CISD ^a	2.4	4.8	3.3	4.2	2.4	5.3	4.1
MBPT(2) ^b	2.1	3.8	1.9	3.3	4.1	2.3	2.1
SDQ-MBPT(4) ^b	1.6	4.1	2.3	0.8	2.7	0.9	2.1
MBPT(4) ^b	1.4	3.8	1.9	3.6	5.3	4.6	1.2
CCSD ^a	1.5	3.9	2.4	1.4	2.9	1.8	2.0
UCCSDT(4)	—	3.2	1.5				

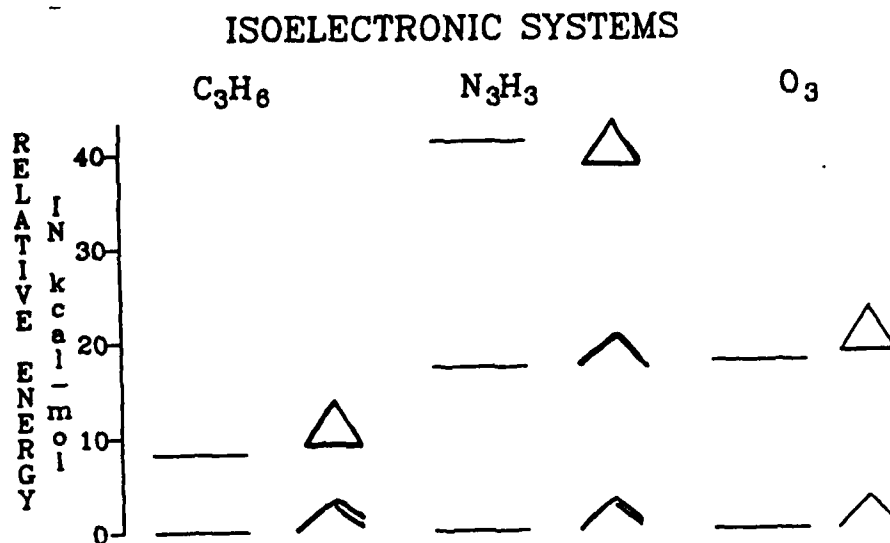
^aBesler, Scuseria, Scheiner, Schaefer, J Chem Phys, 89, 360(1988).

^bStanton, Watts, Bartlett, J Chem Phys, to be published.

Getting the analytical gradient is only part of the problem, since the surface has to be searched efficiently to locate critical points. In line with this, the MANR method has been demonstrated to be superior to most other search procedures for locating minima. Further, the eigenvalue following Cerjan-Miller technique has been implemented to facilitate locating transition states. Finally, recognizing the difficulty in evaluating analytical second derivatives, a new method making full use of symmetry in an automatic way has been developed and implemented to facilitate the evaluation of second derivatives for critical point characterization. This software also computes vibrational intensities which together with the second derivatives (force constants) provide IR spectra prediction.

N₃H₃

As a first example, consider N₃H₃. From the isoelectronic analogies shown below, one would expect these isomers for this unknown molecule. These isomers are shown in Fig. 2, with the relative energies in Table II.



D.H. Magers, E.A. Salter, R.J. Bartlett, C. Salter, B.A. Hess and L.J. Schaad, *J. Am. Chem. Soc.* **110**, 3435 (1988).

Table II. Relative Energies of N₃H₃ Isomers at MBPT(2) Optimum Energies

Isomer	Relative Energy in kcal				
	MBPT(2)	SDQ - MBPT(4)	SDTQ - MBPT(4)	CCSD	CCSD + T(CCSD)
Triaziridine	40.96	41.21	41.43	40.84	41.24*
Triimide	13.48	20.01	15.64	20.58	17.30
Triazene	0.00	0.00	0.00	0.00	0.00

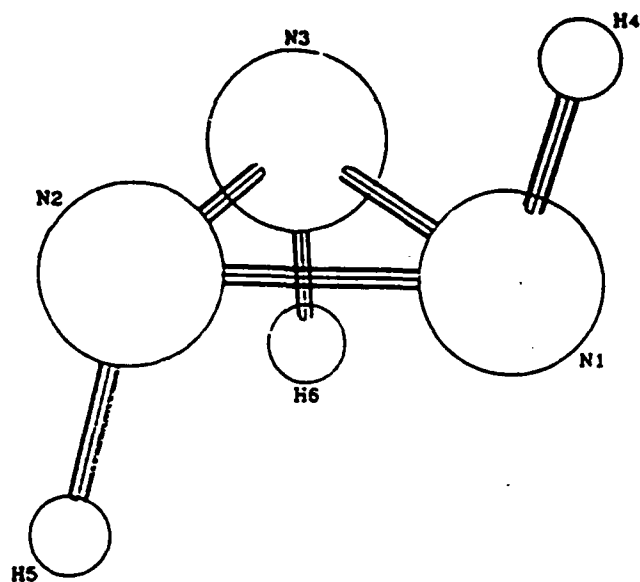
All above calculations used a DZP basis set.

* $\Delta H = 87$ kcal/mol to N₂ + H₂.

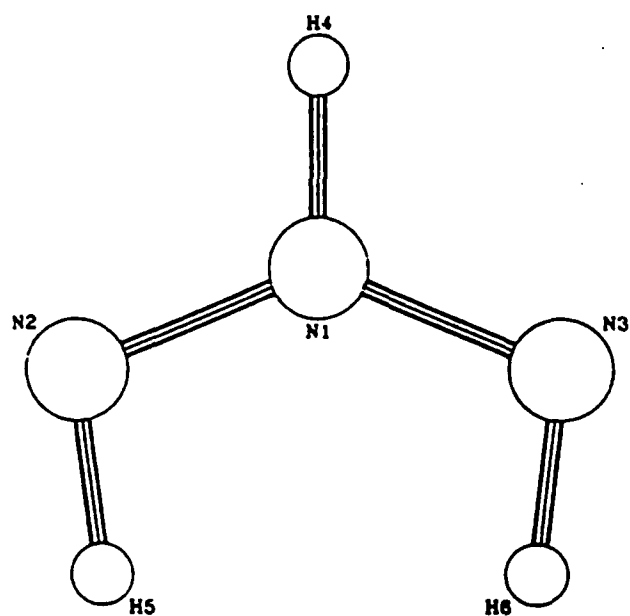
* $\Delta H = 104$ kcal/mol to N₂ + NH₃.

For identification purposes we also predict their spectra with and without correlation. As an example, consider triimide (Fig. 3). Notice the important changes from SCF to the correlated E(2) = MBPT(2) results.

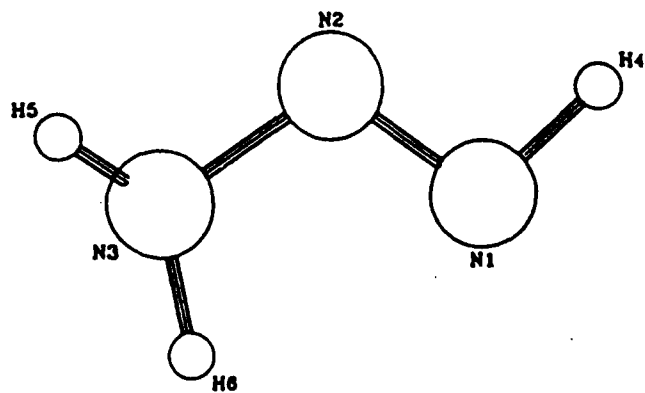
Triaziridine



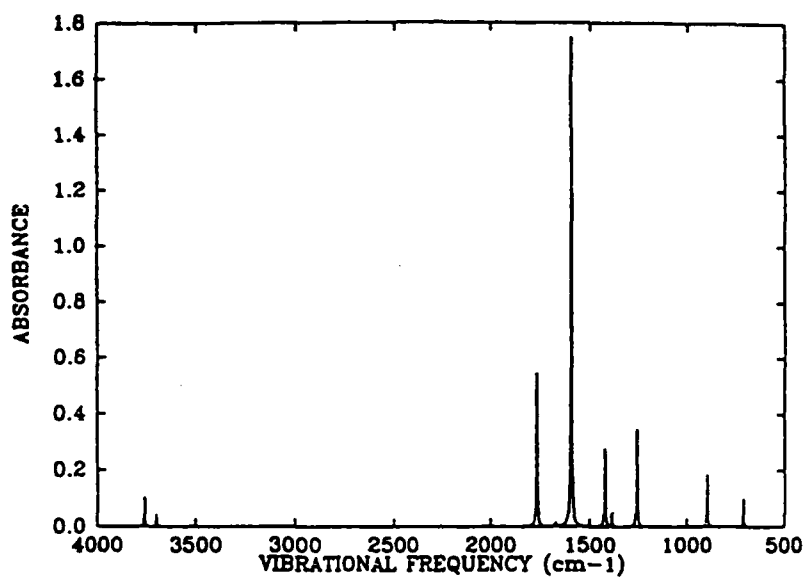
Trimide



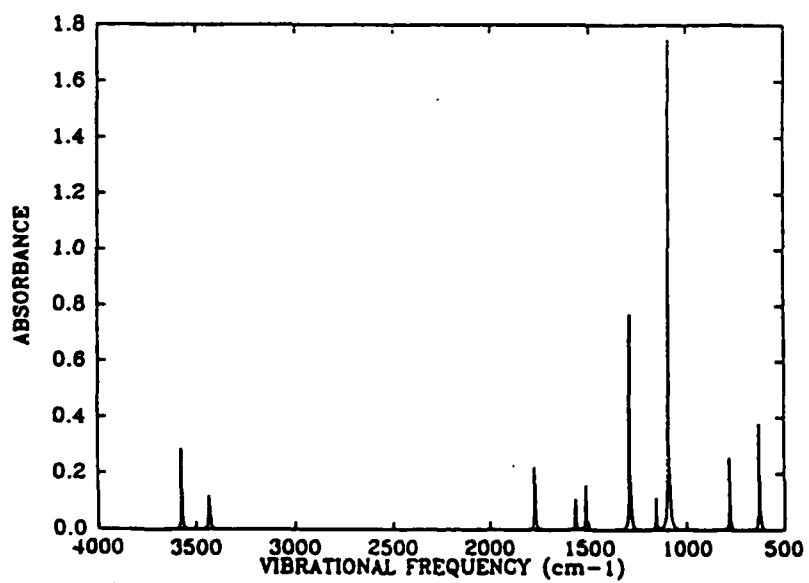
Triazene



Triimide SCF IR Spectrum

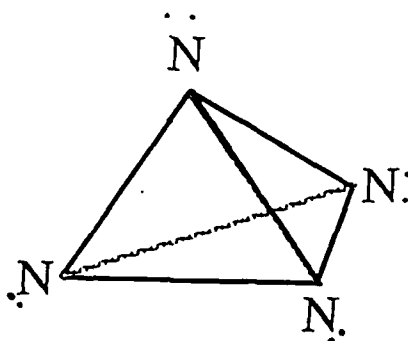


Triimide E(2) Spectrum



N₄

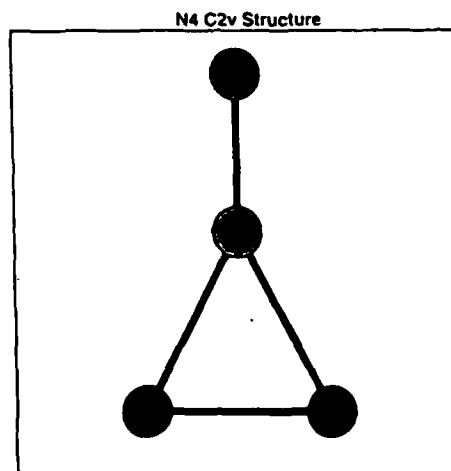
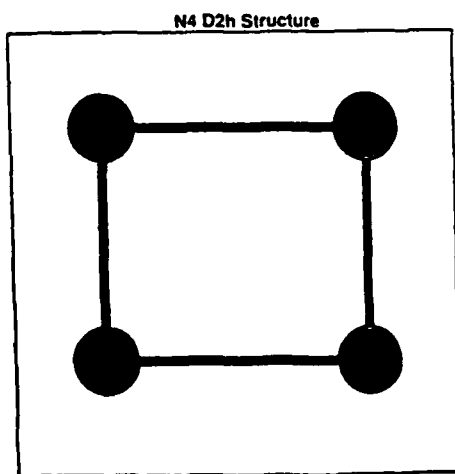
The second topic I want to discuss is tetrahedral N₄



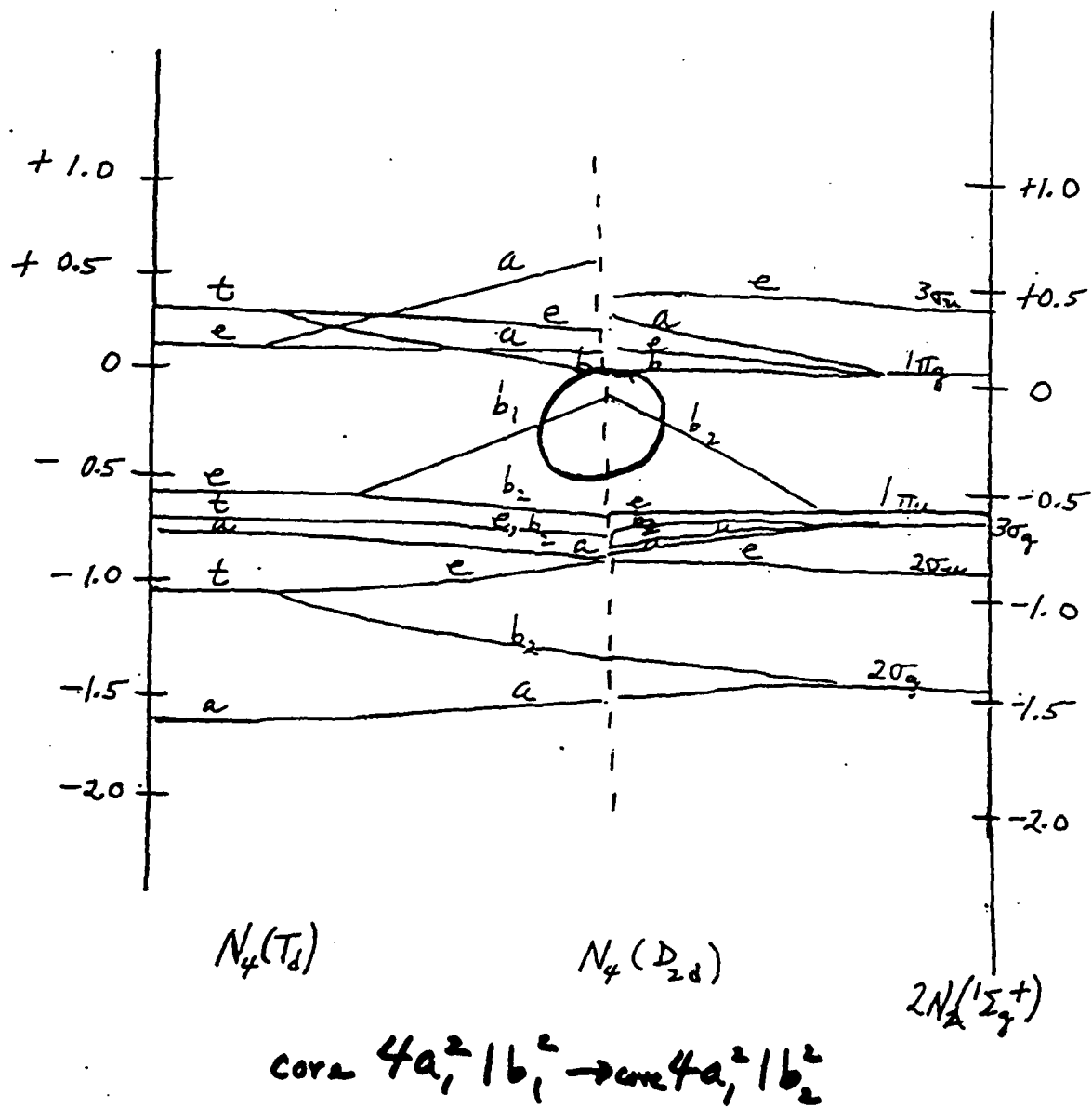
Some of its characteristics are:

- Isovalent with P₄
- Could be formed by 3 tetrahedrally directed covalent bonds (as in NH₃ and NH₄⁺)
- Lone pairs occupy fourth site
- Nitrogen sigma bonds (as in nitramines)

As can be seen from the orbital correlation diagram, the avoided crossing shown for a possible D_{2d} TS corresponds to a double excitation from the orbital $b_1^2 \rightarrow b_2^2$. This corresponds to a Woodward-Hoffman forbidden process. Hence a barrier to decomposition would be anticipated for tetrahedral N₄. A search of the energy surface at the SCF and MBPT(2) level leads to a minimum for the T_d form at a bond length of 1.393 Å and 1.476 Å, respectively. In addition, we find minima for two other structures of N₄, a D_{2h} and a C_{2v} form.



ORBITAL CORRELATION DIAGRAM



Relevant numerical results are shown in Tables III and IV.

Table III. Harmonic frequencies (in cm^{-1}) and geometry for the N_4 T_d structure, optimized with each basis set and at MBPT(2) level.

	SCF			E(2)
	MINI1	DZ	DZP	DZP (intensity; km/mol)
a	1565	1392	1684	1237(0.00)
e	728	660	896	893 (0.00)
t_2	1055	961	1203	698 (1.99)
R	1.5336 Å	1.4713 Å	1.3926 Å	1.4760 Å

Table IV. Harmonic frequencies (in cm^{-1}) and geometry for the N_4 D_{2h} structure, optimized with each basis set and at E(2) level.

	SCF			E(2)
	MINI1	DZ	DZP	DZP
a_g	1782	1802	1975	1465
a_g	1186	1064	1203	963
a_u	602	666	677	442
b_{1g}	1155	1197	1234	1038
b_{2u}	875	629	850	478
b_{3u}	1581	1585	1800	1188
R1	1.3028 Å	1.2543 Å	1.2210 Å	1.2900 Å
R2	1.5810 Å	1.5396 Å	1.4762 Å	1.5358 Å

For the C_{2v} form, the SCF structure is a minimum while the MBPT(2) C_{2v} structure corresponds to a TS. In Table V we compare the relative energies of T_d N_4 to D_{2h} N_4 with the corresponding tetrahedron to cyclobutadiene change. Unlike the carbon analogy, T_d N_4 is more stable than the D_{2h} form. A summary of the critical points on the N_4 PES at the SCF and correlated levels is shown below.

Relative Energetics of Several N₄ Stationary Points

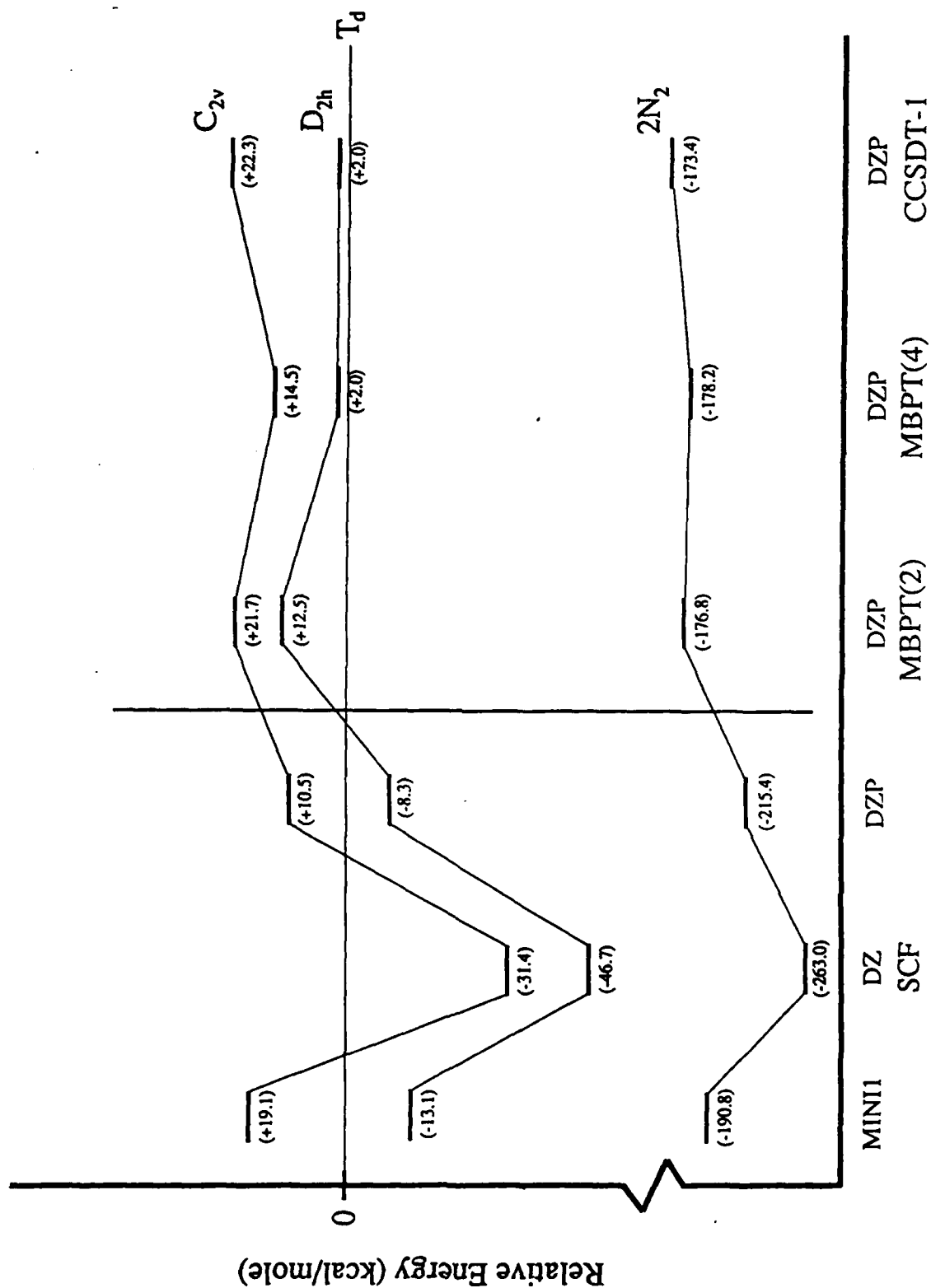


Table V. Relative energies of tetrahedrane to cyclobutadiene^a and its tetrahedral N₄ analog^b (in kcal/mole).

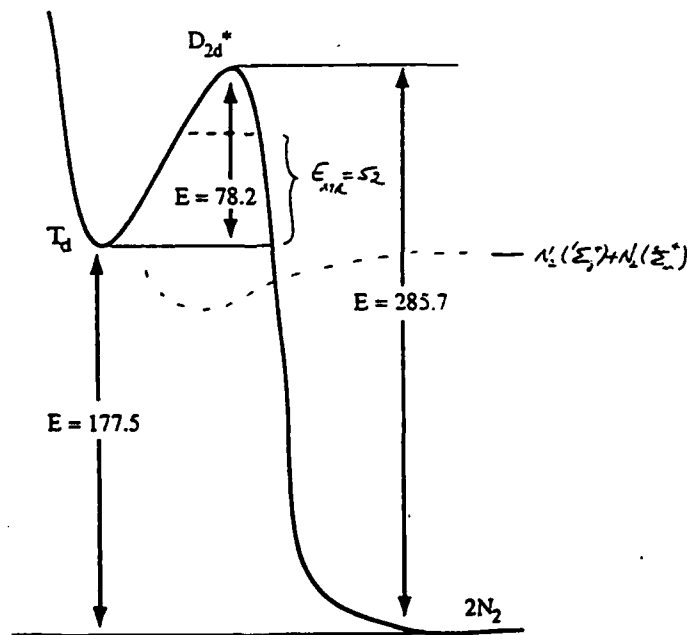
C ₄ H ₄		N ₄	
SCF	E(2)	SCF	E(2)
27	23	8.3	-12.5

^aHess, B.A. Jr.; Schaad, L. J. *J. Am. Chem. Soc.* 1985, 107, 865-866.

^bThis work.

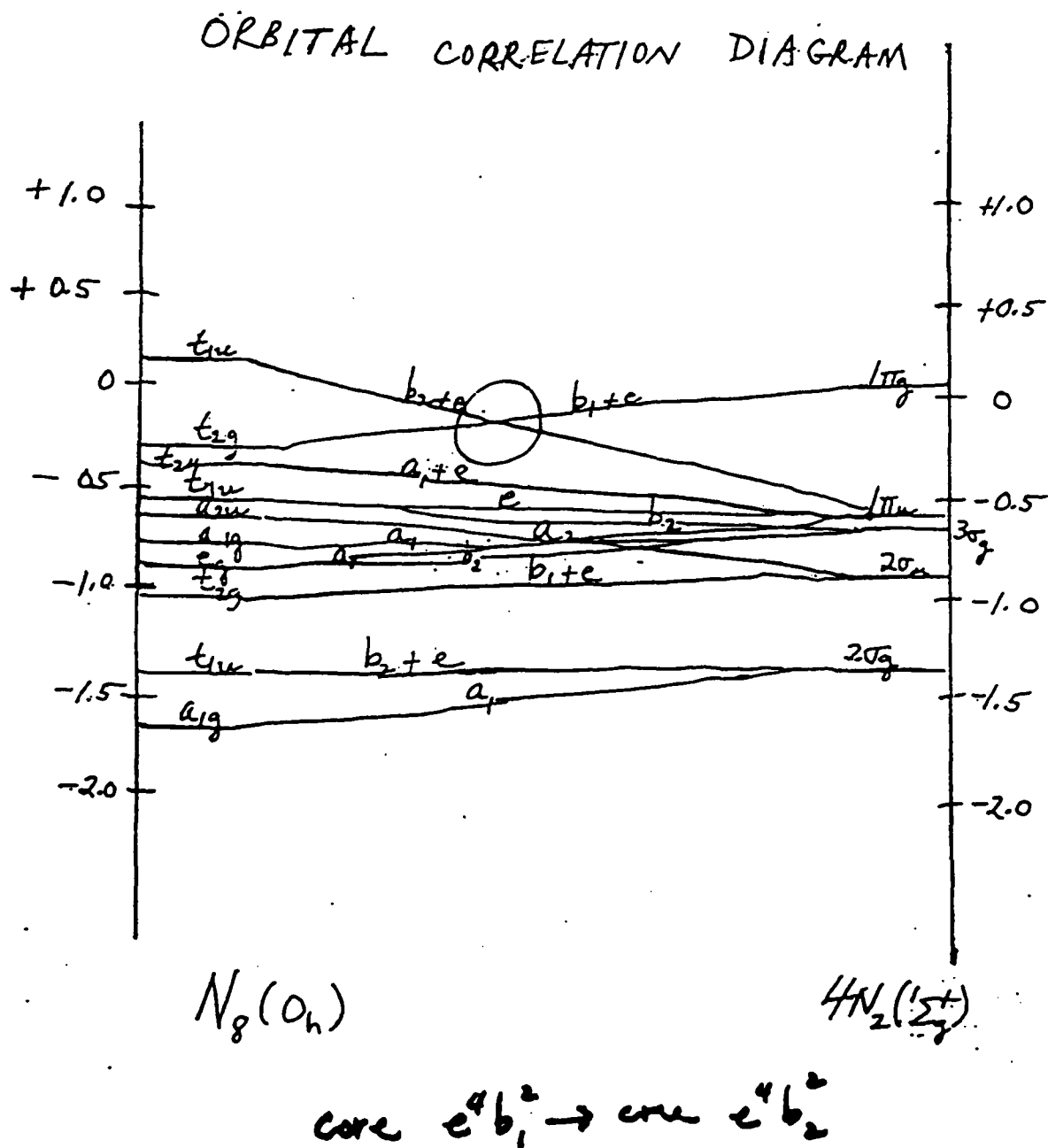
Since the correct TS for N₄ dissociating to 2N₂ requires a multi-reference method for its proper description, here we only estimate it to occur at the crossing point of the two electronic states to obtain some measure of it. The resulting numerical values at the high-level coupled-cluster CCSD + T(CCSD) level are shown on Fig. 4. When an approximate multi-reference generalization of the coupled-cluster method is applied at the TS, the barrier is reduced by 26 kcal/mol as shown. However, we would expect a fairly high barrier for the D_{2h} decomposition path. If a low symmetry path can be found, the barrier may be substantially lower. One must also consider lower lying triplet surfaces, as indicated schematically, that occur below the singlet surface for N₄. Spin-orbit coupling might play a rôle in providing an alternate pathway to decomposition.

Reaction Path for N₄
CCSD + T(CCSD)
(Energies in kcal/mole)



*Structure from Franci and Chesick, *J Phys Chem*, 94 526 (1990)
See also Venanzi and Schulman, *Mol Phys*, 30 281 (1975)

Analogous to $T_d N_4$, an $O_h N_8$ species might be considered. As shown in the following orbital correlation diagram, here, too, we have an orbital crossing that in a D_{2d} transition corresponds to $b_1^2 \rightarrow b_2^2$, suggesting a barrier to dissociation. Any higher TS symmetry like D_{2h} would introduce even more crossings.

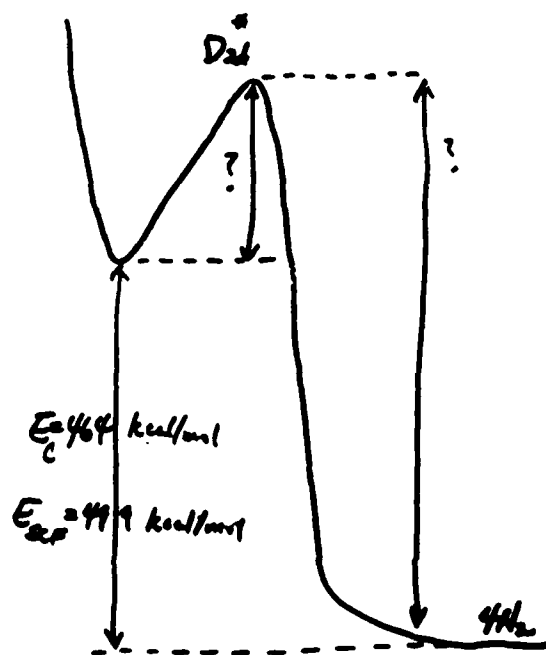


The SCF bond length frequencies are shown in Table VI and the corresponding approximate reaction path in Fig. 5.

Table VI. Harmonic frequencies (intensities) and geometry for N_8 O_h (cubane) structure, optimized using a DZP basis set at SCF and E(2) levels (in cm^{-1} and km/mol).

	SCF	MBPT(2)
e_u	741 (0.00)	
t_{2g}	988 (0.00)	
t_{1u}	1097 (8.73)	
t_{2g}	1117 (0.00)	
a_{1g}	1176 (0.00)	
t_{2u}	1191 (0.00)	
e_g	1273 (0.00)	
a_{2u}	1360 (0.00)	
R	1.459 Å	1.525 Å (1.47 Å for T_d)

REACTION PATH FOR N_8



The larger MBPT(2) bond length for O_h N_8 compared to T_d N_4 indicates less strain. The MBPT(2) energy difference of 464 compared to 4 N_2 is greater than the 177 in the N_4 case.

An estimate of the specific impulse for all systems considered is shown in Table VII.

Table VII. Specific Impulse of Several Molecular Systems (in seconds)

$\text{H}_2 + \text{O}_2$	456 (467)*	
$\text{N}_2\text{H}_4 + \text{N}_2\text{O}_4$	324	
$\text{N}_3\text{H}_3 + \text{O}_2$		
	SCF	CCSD + T(CCSD)
triazine	351	347
triimide	382	365
triaziridine	399	390
$\text{N}_4(\text{T}_d)$	520*	472*
$\text{N}_8(\text{O}_h)$	559*	539 * (MBPT(2))

*The formula $265\sqrt{\Delta H/M}$ was used.

Clearly, prospects for specific impulses that might exceed the 500 second reference are feasible for such molecules.

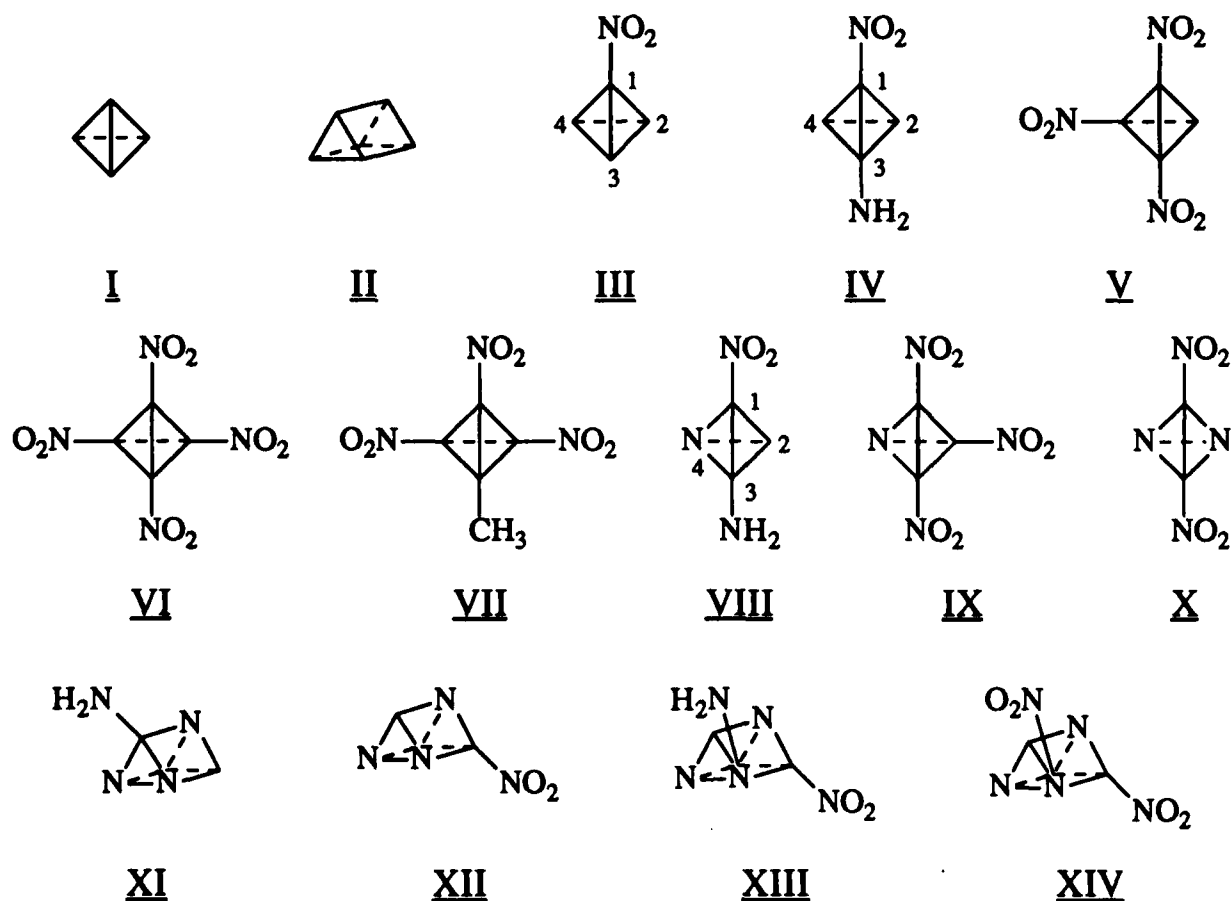
COMPUTATIONAL ANALYSES OF SOME NITROTETRAHEDRANES, NITROTRIPRISMANES AND THEIR AZA ANALOGUES.

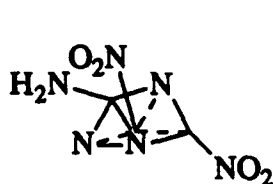
Peter Politzer, Jorge M. Seminario, Jane S. Murray and Michael Grodzicki

Department of Chemistry
University of New Orleans
New Orleans, LA 70148

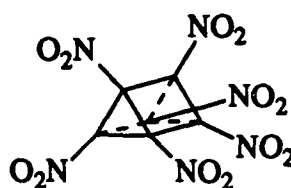
Introduction

We have carried out computational analyses and evaluations of certain strained polyhedrane molecules that are of potential importance as high energy density systems. The molecules studied (shown below) are all nitro, amino, nitro/amino and nitro/methyl derivatives of tetrahedrane (I), triprismane (II) and their aza analogues, in which one or more C-H units have been replaced by nitrogens. Our objective is to identify and/or design systems that are particularly promising as high energy density materials.





XV



XVI



XVII

Methods

Our computational analyses have been carried out primarily with the ab initio SCF-MO GAUSSIAN 86 and 88 programs [1,2]. The initial step for each molecule has been to compute an optimized structure at the 3-21G level. These geometries have subsequently been used to calculate key molecular properties and reaction energetics, as described below.

1. Isodesmic Reaction Energies:

The isodesmic reaction procedure [3,4] is a means of determining anomalous energy effects in molecules. An isodesmic reaction is a hypothetical chemical process in which the number of bonds of each formal type remains the same on each side of the equation, but their mutual relationships are changed. Representative isodesmic reactions are given in Figure 1. The ΔE values for such reactions reveal any deviations from bond energy additivity, and are therefore interpreted as being due to special features associated with the molecule being investigated, e.g. strain, resonance stabilization, etc. $\Delta E > 0$ implies destabilization, while $\Delta E < 0$ indicates the presence of stabilizing factors.

2. Bond Order:

We have used eq. (1) to compute bond orders (as measures of relative bond strengths):

$$\text{Bond Order} = 0.5574 \sqrt{\frac{k}{R_e}} \quad (1)$$

k is the force constant in $\text{mdyn}/\text{\AA}$, which we obtain from vibrational frequency calculations, and R_e is the equilibrium bond length in \AA . We have shown that bond orders calculated with eq. (1) correlate well with experimentally determined dissociation energies [5,6] and therefore provide a realistic indication of relative bond strengths, especially when comparing bonds between the same atoms in different chemical environments.

3. Isomerization Reaction Energetics:

We have computed the activation energies and total energy changes for certain isomeric rearrangements. All geometries were optimized at the SCF 3-21G level, and then were used to compute the energies with a first principles local density functional method that includes correlation energy (DMol) [7,8].

4. Electrostatic Potential:

The electrostatic potential $V(\mathbf{r})$ that is created in the space around a molecule by its nuclei and electrons is given rigorously by eq. (2):

$$V(\mathbf{r}) = \sum_A \frac{Z_A}{|\mathbf{R}_A - \mathbf{r}|} - \int \frac{\rho(\mathbf{r}') d\mathbf{r}'}{|\mathbf{r}' - \mathbf{r}|} \quad (2)$$

Z_A is the charge on nucleus A, located at \mathbf{R}_A ; $\rho(\mathbf{r})$ is the molecular electronic density function, which we compute.

The electrostatic potential is well-established as a guide for interpreting and predicting molecular reactive behavior [9-11]. For example, an approaching electrophile will initially be attracted to those regions in which $V(\mathbf{r})$ is negative, where the effects of the electrons are dominant, and in particular to those points at which $V(\mathbf{r})$ reaches its most negative values (the local minima). An important feature of the electrostatic potential is that it is a real physical property, that can be determined experimentally by diffraction methods as well as computationally [11].

5. Average Local Ionization Energy:

We define the average local ionization energy $\bar{I}(\mathbf{r})$, within the framework of self-consistent-field molecular orbital theory, by equation (3) [12]:

$$\bar{I}(\mathbf{r}) = \sum_i \frac{\rho_i(\mathbf{r}) \epsilon_i}{\rho(\mathbf{r})} \quad (3)$$

$\rho(\mathbf{r})$ is the electronic density of the i^{th} molecular orbital at the point \mathbf{r} , ϵ_i is the orbital energy, and $\rho(\mathbf{r})$ is the total electronic density. $\bar{I}(\mathbf{r})$ can be interpreted as the average energy needed to ionize an electron at any particular point in the space of the molecule. Thus, the positions where $\bar{I}(\mathbf{r})$ has its lowest values are the points at which are found, on the average, the highest energy electrons.

6. Properties on Molecular Surfaces:

We have recently developed the approach of taking the 0.002 electrons/bohr³ contour of constant electronic density to define a molecular surface upon which to compute properties such as the electrostatic potential, $V(r)$ [13,14], and the average local ionization energy, $\bar{I}(r)$ [12]. It has been shown, for a group of diatomic molecules and for methane, that this contour gives physically reasonable molecular dimensions, and encompasses at least 95% of the electronic density [15-17]. This surface is defined in terms of a molecular property, $\rho(r)$, and therefore reflects features such as bond formation, lone pairs, etc. that are unique to a molecule. In addition to providing a new format for presenting properties such as $V(r)$, which has previously been represented primarily on two-dimensional planes through a molecule, this surface also permits an understanding of the actual three-dimensional shape of the molecule.

Results and Discussion

1. Specific Impulse Calculations:

An important measure of propellant performance is the specific impulse. A propellant develops thrust (recoil force) due to the discharge of gaseous products when it undergoes combustion. The specific impulse, I_S , is the integral of the thrust, per unit weight of propellant, over the time of combustion. Among the factors that determine I_S are the number of moles (N) of gaseous products formed per unit weight of propellant and the combustion temperature ($T^\circ K$):

$$I_S \sim N^{\frac{1}{2}} T^{\frac{1}{2}} \quad (4)$$

We have calculated I_S for more than 70 molecules of a wide variety of types, using both a program that we have written and also one obtained from the Naval Weapons Center (China Lake, CA); the results obtained by these two approaches give relative values that are in good agreement.

Among the factors favoring a high specific impulse are:

- (1) The formation of light gaseous molecules, since then the number produced per unit weight of propellant is greater. Thus, CO is more desirable than CO₂ as a product gas, and it is advantageous to have hydrogen present in the molecule, so as to form gaseous H₂O, which is one of the lightest likely products.
- (2) A high positive heat of formation, since this leads to a greater release of energy upon combustion and a higher combustion temperature. Strain energy can be an important

contribution to the heat of formation, and is accordingly a very attractive feature of the tetrahedrane and triprismane systems.

Figures 2 and 3 show our calculated I_S values for various nitro derivatives of tetrahedrane, triprismane and their aza analogues. These results are given relative to the calculated I_S of HMX, since our objective is to achieve significant improvement over HMX. It can be seen that many of these derivatives do meet this goal. Certain observations can be made:

- (1) Increasing the number of NO_2 groups does not necessarily increase I_S . These groups add considerable mass to the molecule, and in some instances also lead to CO_2 being formed instead of CO , due to the extra oxygens.
- (2) The presence of aza nitrogens tends to be beneficial, probably because they replace a carbon and thus lower the oxygen (and hence NO_2) requirement.
- (3) Replacing NO_2 by NH_2 can increase I_S , because it means that some oxygen will be used to form H_2O , which is lighter than either CO or CO_2 .
- (4) NH_2 is preferred over CH_3 as a source of hydrogen, because introducing CH_3 means that some additional oxygen will be required.

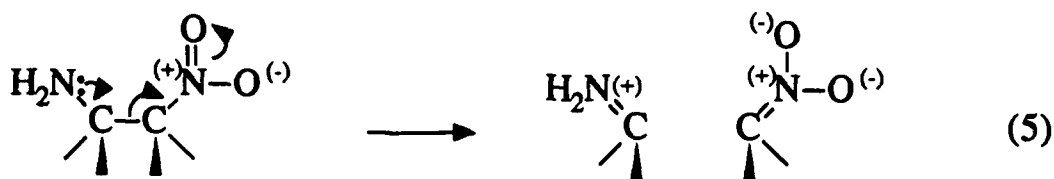
2. Stabilizing Effects of Aza Nitrogens:

While strain energy can improve I_S , the consequent instability can lead to significant problems in synthesizing the molecules. It is accordingly of considerable importance that one of the key conclusions to have emerged from this project concerns the stabilizing effect of aza nitrogens in the tetrahedrane and triprismane systems [18-20]. This is shown in the strain energies presented in Figures 4 and 5, which have been calculated by the isodesmic reaction procedure. This increased stability that is conferred by aza nitrogens, which could be an important factor in facilitating the synthesis of such highly-strained molecules, is attributed to σ -conjugation of the nitrogen lone pairs, whereby these are delocalized to some degree throughout the σ -bond framework [21].

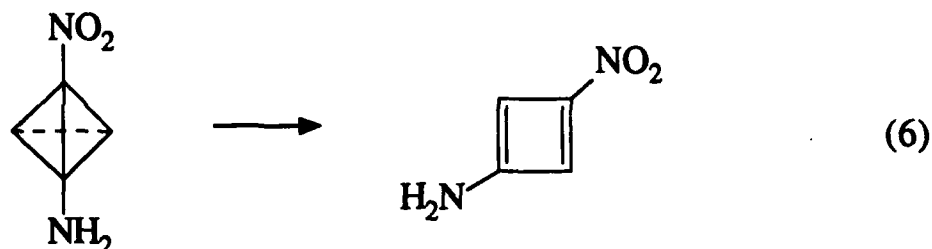
Figures 4 and 5 show that the stabilizing influence of the aza nitrogens increases with their number. The effects of NO_2 and NH_2 are opposite; the former destabilizes the molecule, increasing the strain energy, whereas NH_2 lowers it. However the latter effect, which probably again involves delocalization of the amine lone pair, is the stronger one; thus combined NO_2/NH_2 systems can show a net decrease in strain energy.

The simultaneous presence of NO_2 and NH_2 on adjacent strained tertiary carbons can introduce a significant problem, due to the mechanism that is shown in eq. (5) for the extreme case

of bond rupture:



We have shown for various strained systems that this mechanism can produce a marked weakening of the C-C bond [22,23]; indeed in the case of aminonitrotetrahedrane, it actually caused a rearrangement to the corresponding cyclobutadiene [24]:



We have found however that this bond weakening does not occur in aminonitrotetrahedranes and triprismanes that contain a suitably located aza nitrogen [24,25]; this is certainly an important consequence of aza stabilization.

3. Energetics of Isomerization Reactions:

It is known that certain benzene and monoazabenzene (pyridine) derivatives can be converted photolytically to the corresponding isomeric triprismane and azatriprismane systems (Figure 6). Analogous processes could conceivably be the basis for preparing polynitro derivatives of triprismanes and tetrahedranes. It is anticipated that such reactions would be endothermic, and therefore the transition states are expected to resemble the products (Hammond's Postulate [26]). In view of our finding that the presence of aza nitrogens stabilizes strained molecules, we have investigated the possibility that this may extend to some of the transition states as well, and would facilitate the isomerizations. We have accordingly computed the activation energies, E_{act} , and the total energy changes, ΔE , for several conceivable processes.

The results are in Figure 7. These can be put in better perspective by noting that the irradiating wavelength used to achieve the first reaction in Figure 6, 2537Å, corresponds to an energy of approximately 100 kcal/mole. It is seen that in two of the three cases, the presence of the aza nitrogen does lower the activation barrier.

4. Properties on Molecular Surfaces:

Considerable insight into molecular reactive behavior can be obtained by examining certain key properties on the surfaces of molecules, since these are what other chemical species actually "see". Figure 8 shows graphically the molecular surface of tetrahedrane. We use the 0.002 electrons/bohr³ contour of the electronic density to define the surface, as discussed earlier.

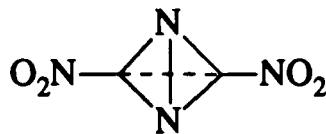
Figures 9 and 10 show the electrostatic potential plotted on the surfaces of tetrahedrane, nitrotetrahedrane and the corresponding aza systems. In the upper portion of Figure 9 can be seen the typical negative potentials associated with the bonds in strained hydrocarbons. These are seen to be eliminated by the introduction of either an aza nitrogen or a nitro substituent.

Figure 11 shows that there is an excellent correlation between the minimum values of $\bar{I}(r)$ and the Hammett constants, confirming the physical significance of the former. Figure 12 brings out the intriguing point that for strained three-membered rings, as in cyclopropane, tetrahedrane and the two ends of triprismane, the lowest values of $\bar{I}(r)$ are over the midpoints of the C-C bonds. This does not occur, however, for four-membered rings, such as cyclobutane and the sides of triprismane.

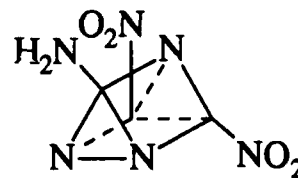
Conclusion

Our computational analyses demonstrate that a high level of propellant performance can be anticipated from relatively small highly strained polyhedrane molecules containing aza nitrogens and NO₂ or NO₂/NH₂ substituents.

Examples:



I_S: 31% better than HMX



I_S: 34% better than HMX

References

1. GAUSSIAN 86: M. J. Frisch, J. S. Binkley, H. B. Schlegel, K. Raghavachari, C. F. Melius, R. L. Martin, J. J. P. Stewart, F. W. Bobrowicz, C. M. Rohlfing, L. R. Kahn, D. J. DeFrees, R. Seeger, R. A. Whiteside, D. J. Fox, E. M. Fleuder, and J. A. Pople, Carnegie-Mellon Quantum Chemistry Publishing Unit, Pittsburgh, PA, 1984.
2. GAUSSIAN 88: M. J. Frisch, M. Head-Gordon, H. B. Schlegel, K. Raghavachari, J. S. Binkley, C. Gonzalez, D. J. DeFrees, D. J. Fox, R. A. Whiteside, R. Seeger, C. F. Melius, J. Baker, R. Martin, L. R. Kahn, J. J. P. Stewart, E. M. Fluder, S. Topiol and J. A. Pople, GAUSSIAN 88, Gaussian Inc., Pittsburgh, PA, 1988.
3. W. J. Hehre, R. Ditchfield, L. Radom, J. A. Pople, J. Amer. Chem. Soc. **92**, 4796 (1970).
4. W. J. Hehre, L. Radom, P. v. R. Schleyer and J. A. Pople, Ab Initio Molecular Orbital Theory, John Wiley and Sons, New York, 1986.
5. Politzer, P. J. Chem. Phys., **50**, 2780 (1969); **51**, 459 (1969).
6. P. Politzer and S. Ranganathan, Chem. Phys. Lett. **124**, 527 (1986).
7. E. Wimmer, A. J. Freeman, C.-L. Fu, P.-L. Cao, S.-H. Chou and B. Delley, in Supercomputing Research in Chemistry and Chemical Engineering, K. F. Jensen and D. H. Truhlar, eds., ACS Symposium Series 353, American Chemical Society, Washington, DC, 1987, p. 49.
8. B. Delley, J. Chem. Phys. **92**, 508 (1990).
9. E. Scrocco and J. Tomasi, Adv. Quantum Chem., **11**, 115 (1978).
10. P. Politzer and K. C. Daiker in The Force Concept in Chemistry, B. M. Deb, ed., Van Nostrand Reinhold, New York, 1981, p. 294.
11. P. Politzer and D. G. Truhlar, Eds., Chemical Applications of Atomic and Molecular Electrostatic Potentials, Plenum Press, New York, 1981.
12. P. Sjöberg, J. S. Murray, T. Brinck and P. Politzer, Can. J. of Chemistry, submitted.
13. P. Sjöberg and P. Politzer, J. Phys. Chem., in press.
14. P. Sjöberg, J. S. Murray, T. Brinck, P. Evans, and P. Politzer, J. Mol. Graphics, in press.
15. R. F. W. Bader, W. H. Henneker and P. E. Cade, J. Chem. Phys. **46**, 3341 (1967).
16. R. F. W. Bader and H. J. T. Preston, Theor. Chim. Acta **17**, 384 (1970).
17. S. D. Kahn, C. F. Parr and W. J. Hehre, Int. J. Quantum Chem., Quantum Chem., Symp. **22**, 575 (1988).
18. P. Politzer and J. M. Seminario, J. Phys. Chem. **93**, 588 (1989).
19. P. Politzer and J. M. Seminario, Struct. Chem. **1**, 29 (1989).
20. J. S. Murray, J. M. Seminario, P. Lane and P. Politzer, J. Mol. Struct. (THEOCHEM), in press.
21. M. J. S. Dewar, J. Amer. Chem. Soc. **106**, 669 (1984).
22. P. Politzer, G. P. Kirschenheuter and J. Alster, J. Amer. Chem. Soc. **109**, 1033 (1987).
23. J. S. Murray, J. M. Seminario and P. Politzer, Struct. Chem., submitted.
24. M. Grodzicki, J. M. Seminario and P. Politzer, J. Phys. Chem., in press.
25. J. S. Murray, M. Concha, J. M. Seminario and P. Politzer, in preparation.
26. G. S. Hammond, J. Amer. Chem. Soc. **77k**, 334 (1955).

CALCULATION OF ANOMALOUS ENERGETIC EFFECTS BY MEANS OF ISODESMIC REACTIONS

ISODESMIC REACTION: A HYPOTHETICAL
CHEMICAL REACTION IN WHICH THE
NUMBER OF BONDS OF EACH FORMAL
TYPE REMAINS THE SAME, BUT THEIR
MUTUAL RELATIONSHIPS CHANGE.

EXAMPLES:



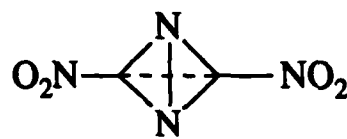
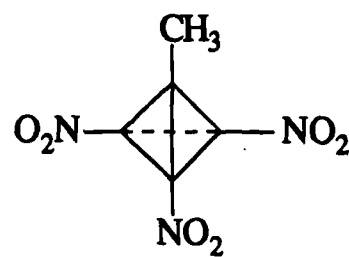
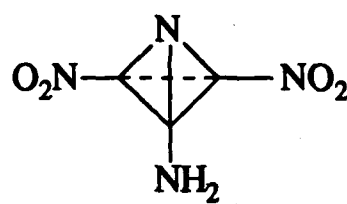
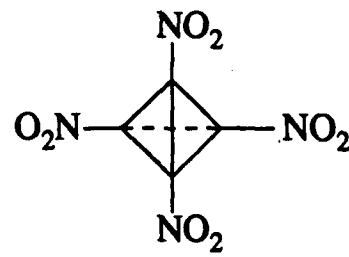
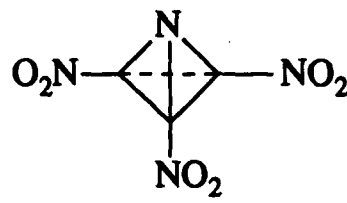
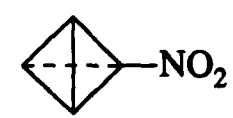
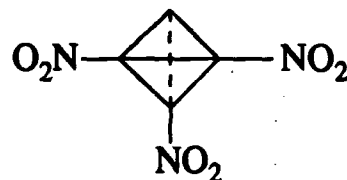
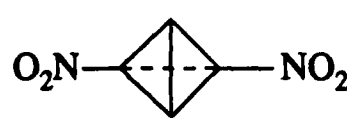
	(C ₃ H ₆)	CYCLOPROPANE
$3\text{C}_2\text{H}_6 \rightarrow \text{C}_3\text{H}_6 + 3\text{CH}_4$		
$\Delta E = E_{\text{products}} - E_{\text{reactants}} = +31 \text{ kcal/mole (3-21G)}$		
POSITIVE ΔE : DESTABILIZATION, e. g. STRAIN		
	(C ₃ N ₂ H ₈)	IMIDAZOLIDINE
$\text{C}_2\text{H}_6 + 4\text{CH}_3\text{NH}_2 \rightarrow \text{C}_3\text{N}_2\text{H}_8 + 2\text{NH}_3 + 3\text{CH}_4$		
$\Delta E = -11 \text{ kcal/mole (3-21G)}$		
NEGATIVE ΔE : STABILIZATION		

Figure 1.

RELATIVE SPECIFIC IMPULSE VALUES: TETRAHEDRANE SYSTEMS

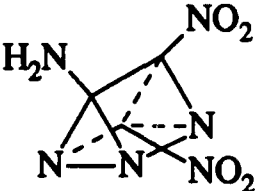
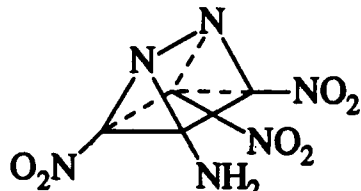
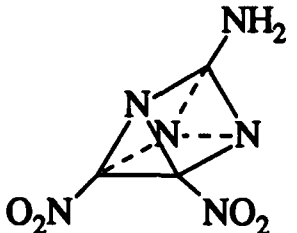
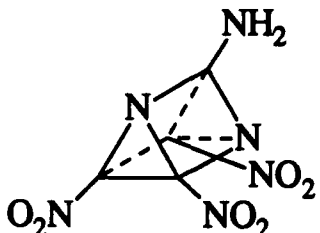
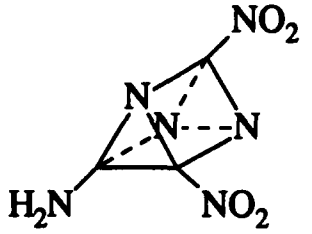
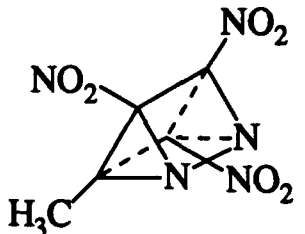
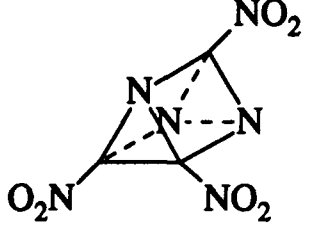
	1.31		1.19
	1.25		1.19
	1.24		1.09
	1.24	HMX	1.00
	1.24		

OBSERVATIONS

- 1) Increasing number of nitro groups does not necessarily increase I_s .
- 2) Presence of aza nitrogens tends to be beneficial.

Figure 2.

RELATIVE SPECIFIC IMPULSE VALUES: TRIPRISMANE SYSTEMS

	1.35		1.24
	1.34		1.23
	1.33		1.14
	1.30	HMX	1.00

OBSERVATIONS

- 1) Presence of aza nitrogens tends to be beneficial.
- 2) Replacement of NO₂ by NH₂ can increase I_s.
- 3) Replacement of CH₃ by NH₂ increases I_s.

Figure 3.

CALCULATED 3-21G STRAIN ENERGIES





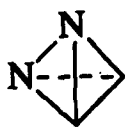




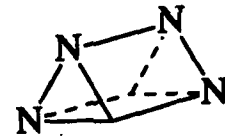
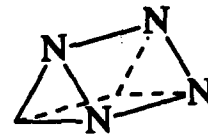

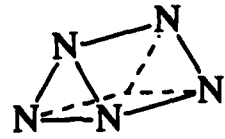

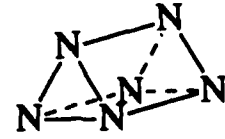
MOLECULE	$\Delta E_{\text{Isodesmic}}$ (kcal/mole)	MOLECULE	$\Delta E_{\text{Isodesmic}}$ (kcal/mole)
	151		131
	139		130
	124		125
	104		124
	82		118
-----	-----		118
	190		112
	136		108

Figure 4.

CHANGES IN STRAIN ENERGY DUE TO SUBSTITUENTS

This table gives changes in $\Delta E_{\text{isodesmic}}$ (in kcal/mole) relative to the corresponding unsubstituted molecules.

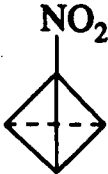
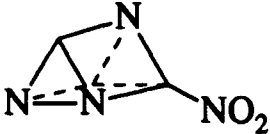
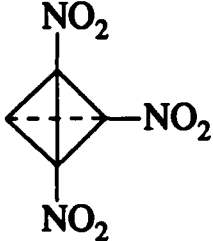
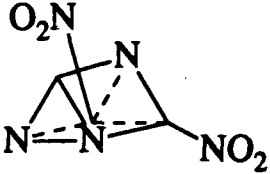
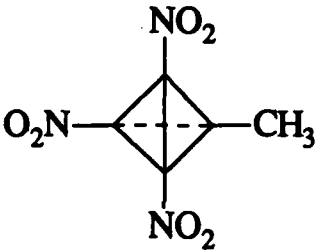
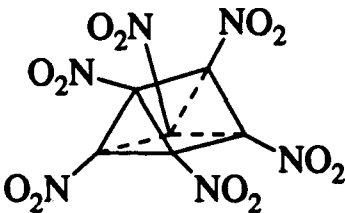
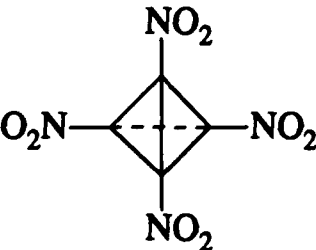
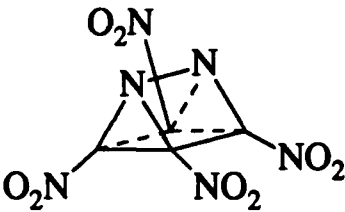
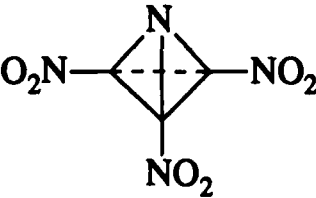
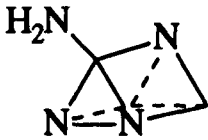
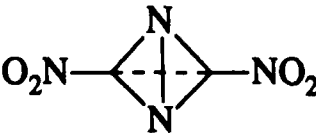
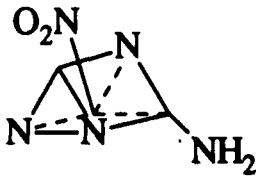
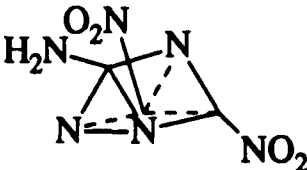
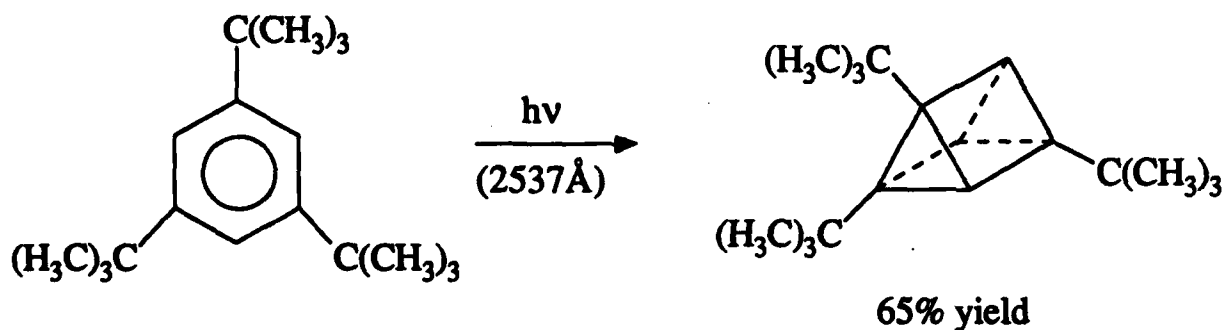
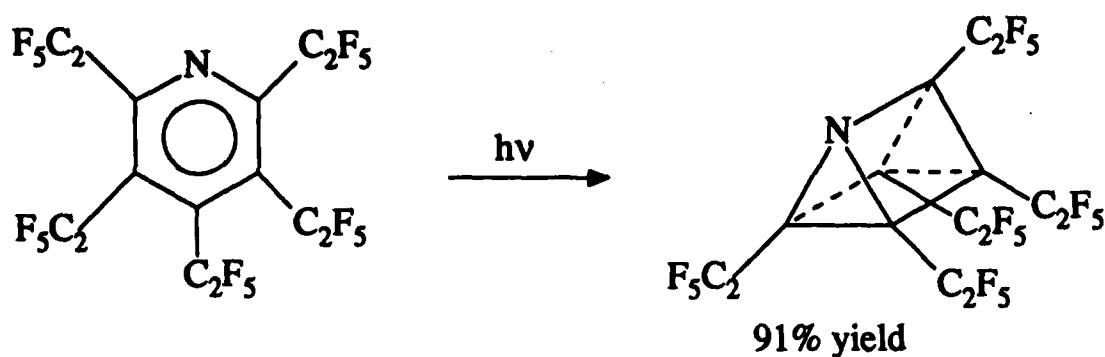
	+2		+6
	+30		+11
	+18		+24
	+52		+45
	+41		-26
	+29		-20
			-9

Figure 5.

EXAMPLES OF KNOWN PHOTOLYTICALLY-INDUCED ISOMERIZATION PROCESSES



K. E. Wilzbach and L. Kaplan, J. Amer. Chem. Soc. 87, 4004 (1965).

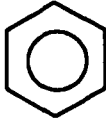



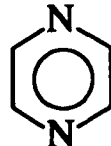


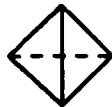


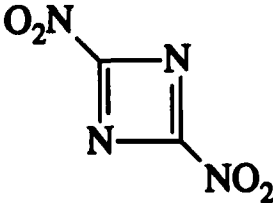
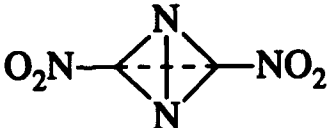


A. R. Katritzky, Handbook of Heterocyclic Chemistry,
Pergamon Press, New York, 1985, p. 149.

Figure 6.

CALCULATED ENERGIES OF ISOMERIZATION PROCESSES

Energies computed with local density functional procedure, DMol,^{1,2} using structures optimized at SCF 3-21G level. All energies are in kcal/mole.

Process		ΔE	E_{act}
	\longrightarrow 	104	182
	\longrightarrow 	103	283
	\longrightarrow 	121	159
<hr/>			
	\longrightarrow 	11	79
	\longrightarrow 	17	58
	\longrightarrow 	32	86

- ¹ E. Wimmer, A. J. Freeman, C.-L. Fu, P.-L. Cao, S.-H. Chou and B. Delley, in Supercomputing Research in Chemistry and Chemical Engineering, K. F. Jensen and D. H. Truhlar, eds., ACS Symposium Series 353, American Chemical Society, Washington, DC, 1987, p. 49.
- ² B. Delley, J. Chem. Phys. **92**, 508 (1990).

Figure 7.

MOLECULAR SURFACES

DEFINED BY 0.002 CONTOUR OF
MOLECULAR ELECTRONIC DENSITY.

(Units: electrons/bohr³)

EXAMPLE: TETRAHEDRANE

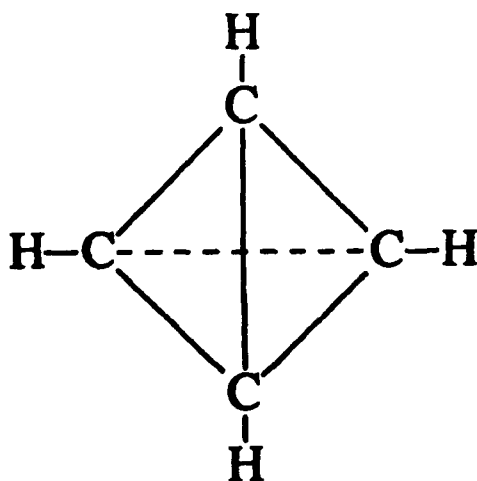
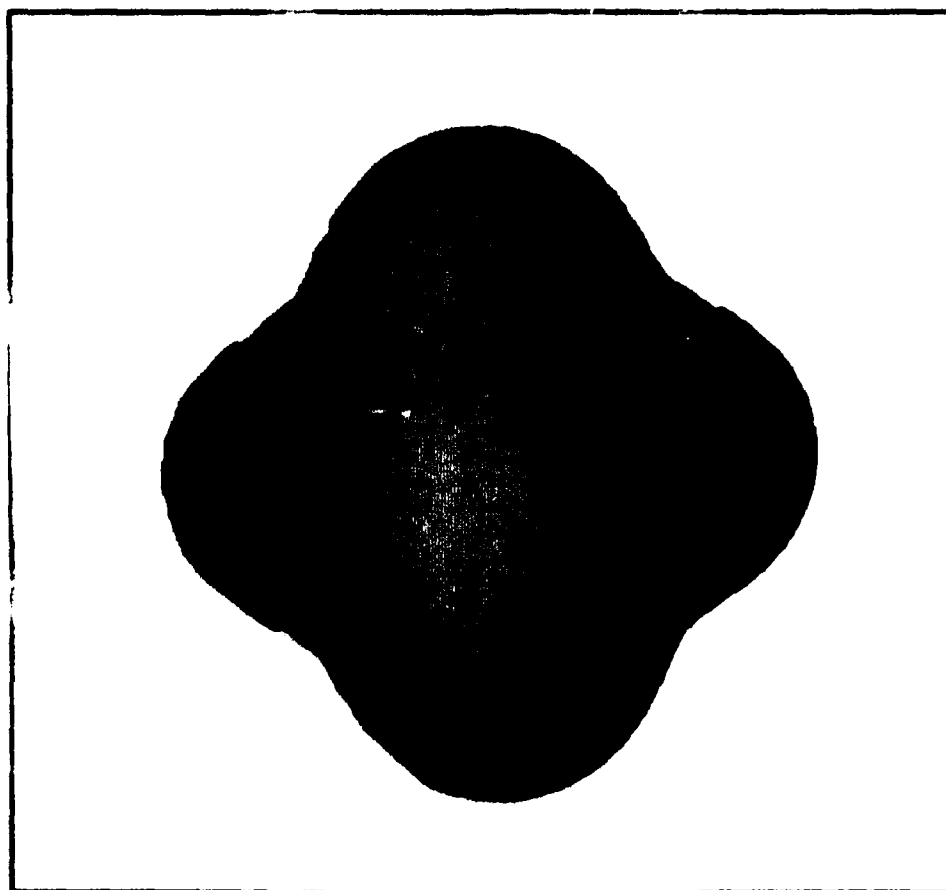
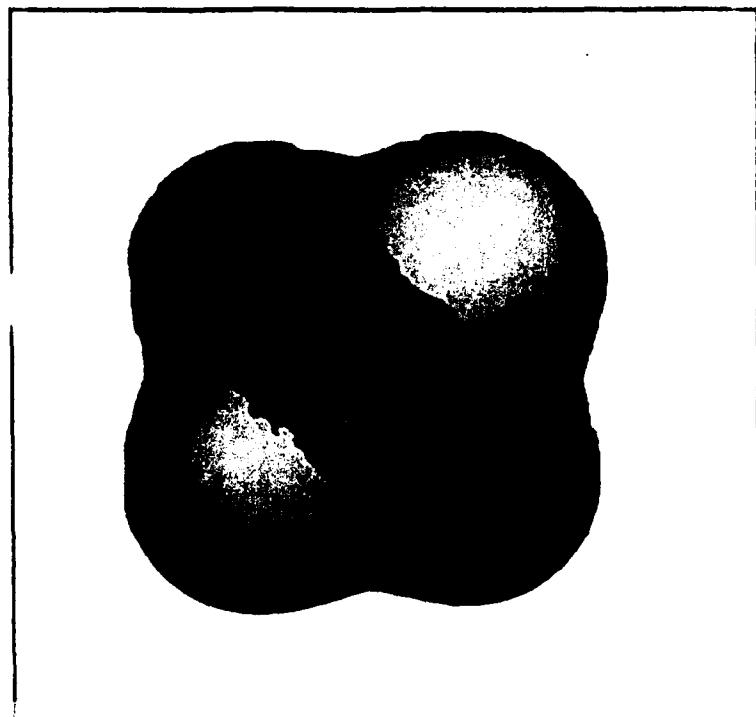
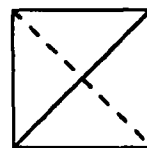


Figure 8.

EXAMPLES OF SURFACE $V(\mathbf{r})$ PLOTS:



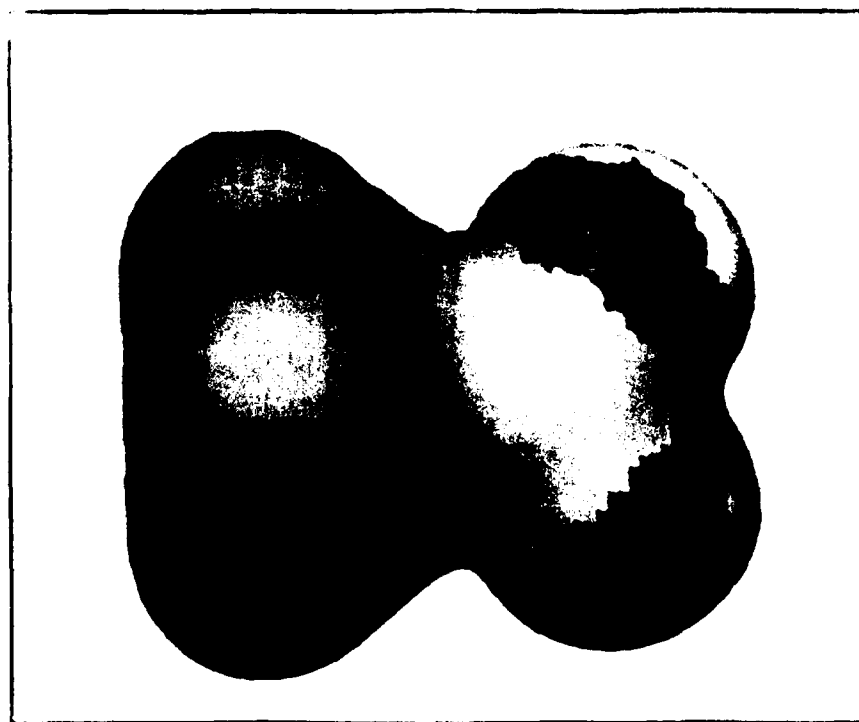
TETRAHEDRANE



YELLOW: Positive.

PURPLE: Between 0 and
-30 kcal/mole.

GRAY: Less than
-30 kcal/mole.



**NITRO-
TETRAHEDRANE**

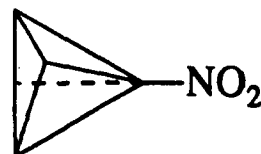
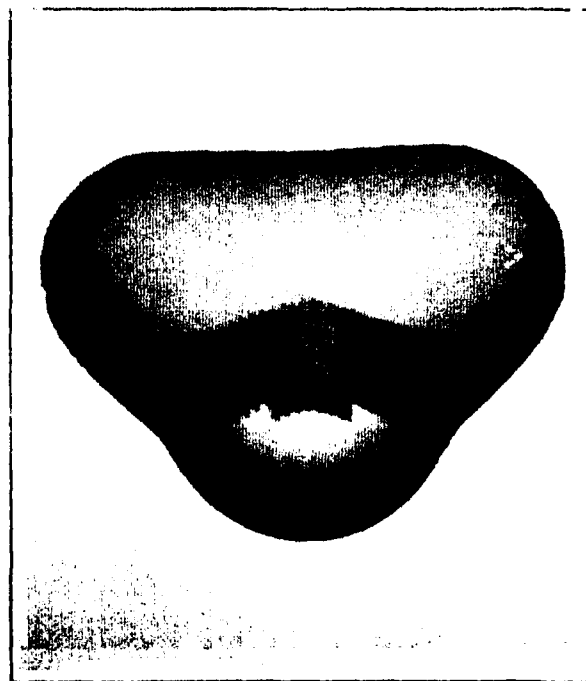
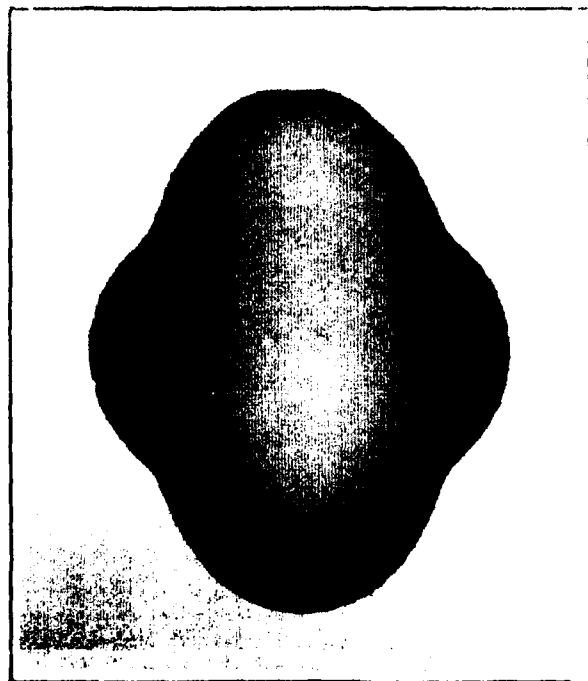
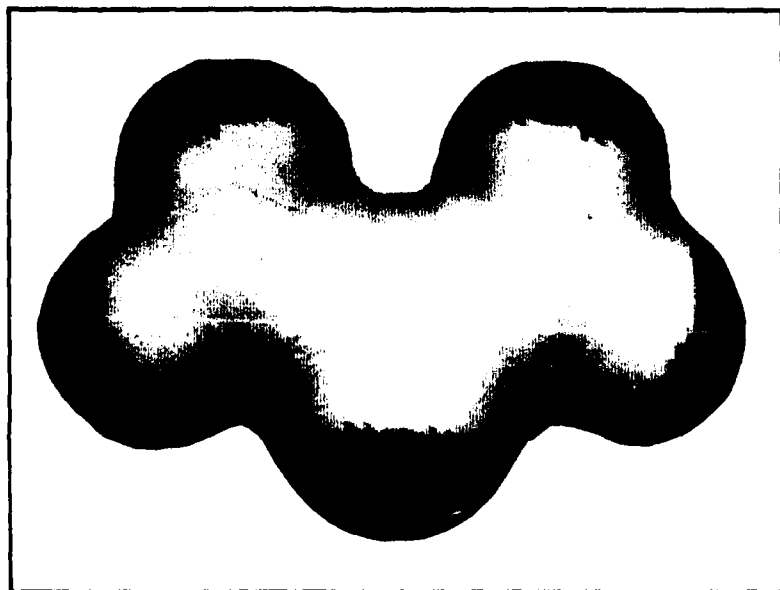


Figure 9.

EXAMPLES OF SURFACE $V(\mathbf{r})$ PLOTS:



DIAZATETRAHEDRANE



YELLOW: Positive.
PURPLE: Between 0 and
-30 kcal/mole.
GRAY: Less than
-30 kcal/mole.

DINITRODIAZA-
TETRAHEDRANE

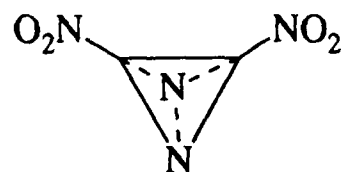
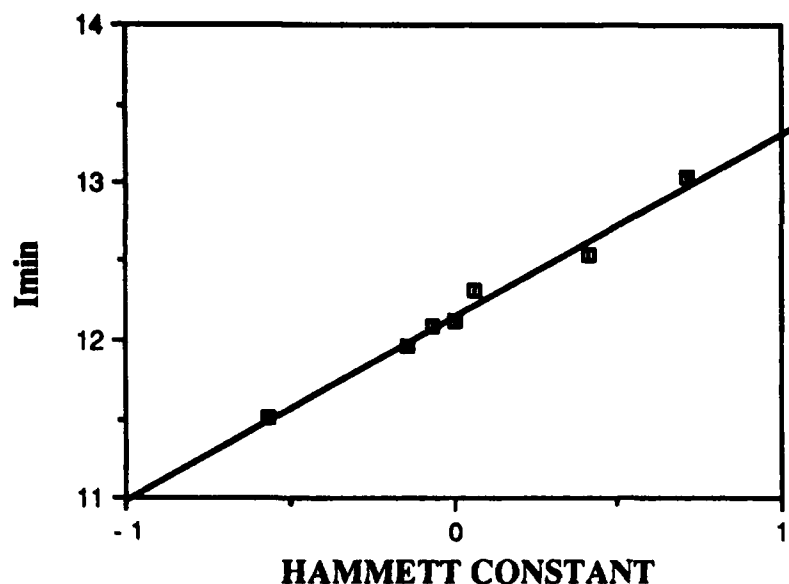
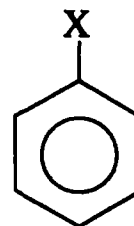


Figure 10.

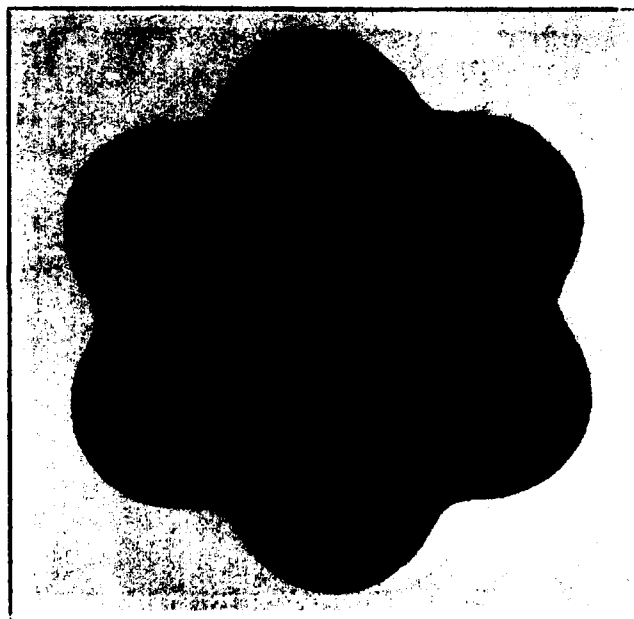
USE OF SURFACE $I(r)$:



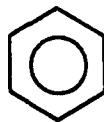
Correlation
Coefficient
= 0.99



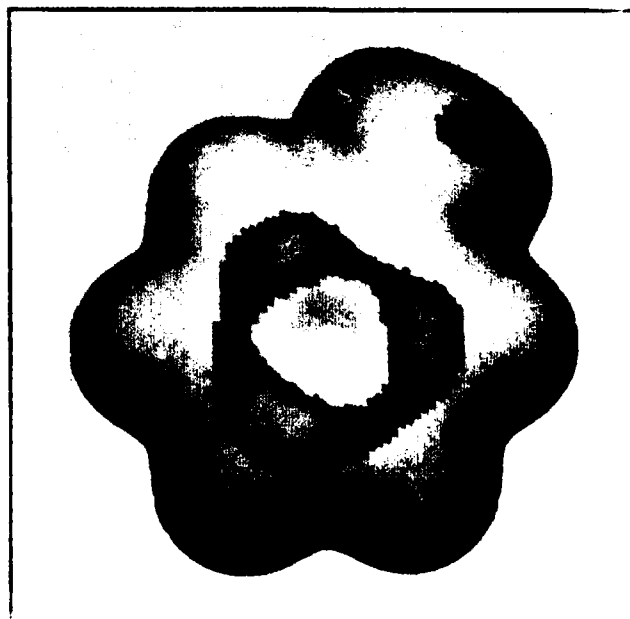
X = NH₂, CH₃, H,
F, CHO, NO₂



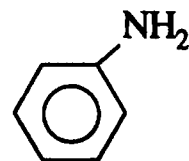
BENZENE



Yellow: less than 12.2 eV.
Purple: greater than 12.2 eV.
Minima: 12.1 eV.



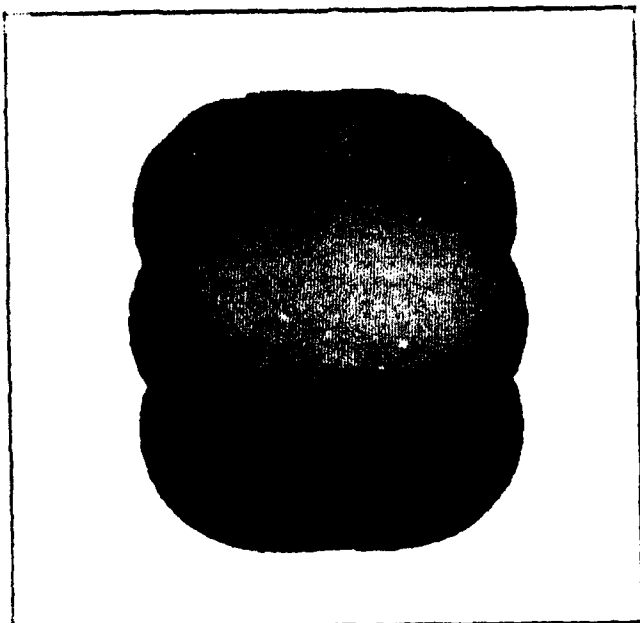
ANILINE



Yellow: less than 11.8 eV.
Purple: between 11.8 and 12.1 eV.
Gray: greater than 12.1 eV.
Minima: 11.5, 11.7, 12.1 eV.

Figure 11.

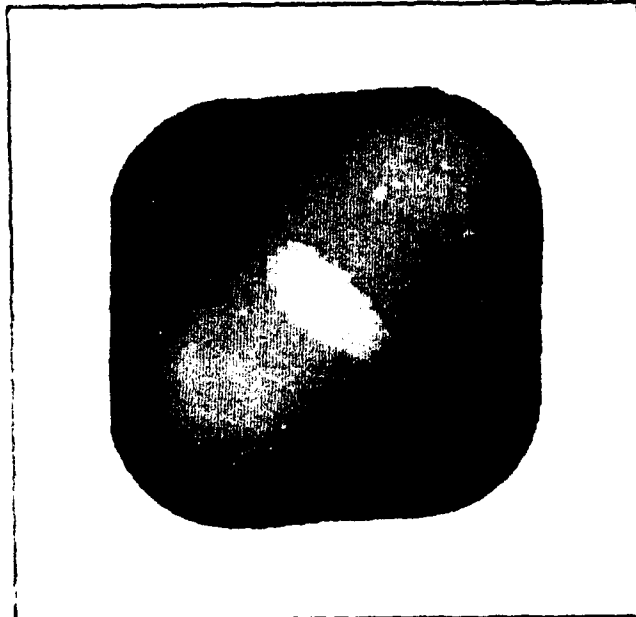
EXAMPLES OF SURFACE I(r) PLOTS:



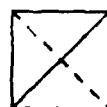
CYCLOPROPANE



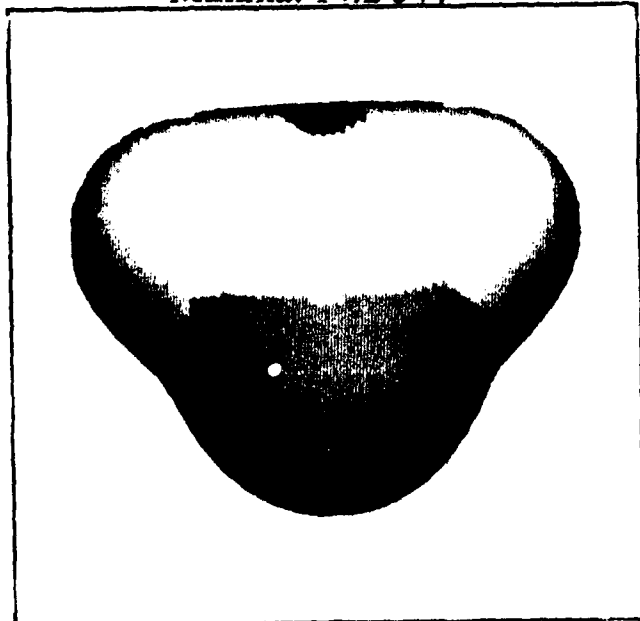
Yellow: less than 14.7 eV.
Purple: greater than 14.7 eV.
Minima: 14.2 eV.



TETRAHEDRANE



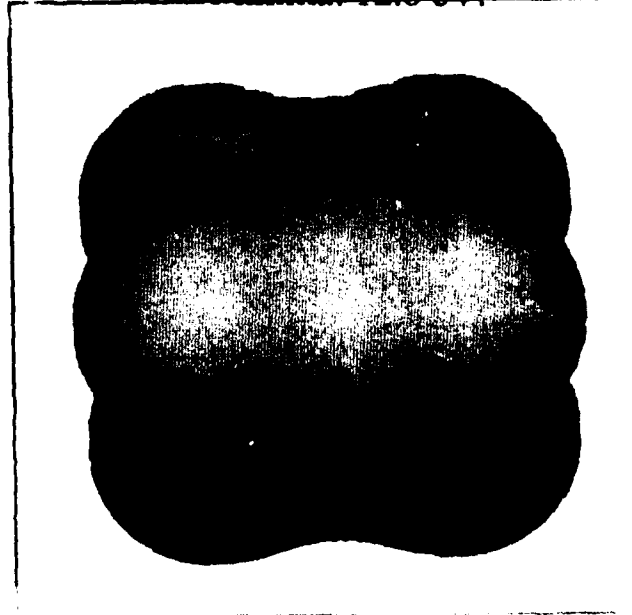
Yellow: less than 13.2 eV.
Purple: greater than 13.2 eV.
Minima: 12.6 eV.



DIAZATETRAHEDRANE



Yellow: less than 14.7 eV.
Purple: between 14.8
and 16.1 eV.
Gray: greater than 16.1 eV.
Minima: 14.6, 15.1 eV.



TRIPRISMANE



Yellow: less than 14.4 eV.
Purple: greater than 14.4 eV.
Minima: 13.4 eV.

Figure 12.

Theoretical and Experimental Investigations of Dications

W. C. Lineberger, S. R. Leone and S. V. O'Neil

Joint Institute for Laboratory Astrophysics

University of Colorado

National Institute for Standards and Technology

Boulder, Colorado 80309

As of the last annual report on the dication project, Senekowitsch and O'Neil had completed a CAS-SCF study of the first and second row hydrides and on the first row oxides. That qualitative survey identified several interesting candidates for further, more detailed, study. In the past year, most of the theoretical effort has been devoted to such quantitative calculations, in which CAS-SCF provides not the final wavefunction but an excellent zeroth order reference function for a substantially more accurate single-and-double-replacement CI (CASSCF-CI) wavefunction. Results at this level became feasible with access to the Cray-2 at Kirtland and installation of the MOLPRO computational suite.^{1,2}

The first system studied at the quantitative level was HS^{++} , interesting in part because of the parallel experimental mass-spectrometric investigation by Leone, Miller, and Rogers. The flexible basis was similar to that employed in our earlier work³ on hydrogen sulfide, and comprises a [10s,9p,4d,1f] contracted set on sulfur and a [6s,3p,1d] contracted set on hydrogen. The CAS-SCF results of last year had pointed out the chemical importance of the lowest four doublet states (Π , Σ^- , Δ , Σ^+) and lowest quartet state (Σ^-), and these potential curves were selected for characterization with CASSCF-CI. In contrast to CAS-SCF results, which suggested that the $^2\Pi$ and the $^{2,4}\Sigma^-$ states might be metastable, the more reliable CASSCF-CI finds only $^2\Pi$ quasi-bound. This may be a general result due to the inability of CAS-SCF to account adequately for the interaction of the several dominant configurations present in the region of the barrier, where the electronic structure undergoes a substantial shift.

Inserting the accurate $^2\Pi$ potential into a numerical integration of the single channel scattering equation provided phase shifts and level widths, from which we derived the tunneling lifetimes shown in Table I. Although technically metastable, the lowest vibrational levels do not tunnel easily through a barrier made very broad by the slow $1/R$ fall-off.

This work has provided significant theoretical guidance for the experimental dication work, and a joint paper³ on SH^{++} has been submitted for publication. Of special future interest will be the characterization of related species SH_2^{++} and SH_3^{++} . Emphasis will be placed on the relative thermodynamic stabilities of the three species and kinetics of interconversion in the presence of H or H_2 . Work on these species will be a point of emphasis in all three efforts.

As an excellent candidate for the collaborative spectroscopic study of Mullin, Szaflarski and Lineberger, the second system selected for detailed CASSCF-CI investigation was CF^{++} . Although this species is isoelectronic to well-known NO^{++} and so should have a similar electronic structure, discovery of the details necessary for a fruitful contact with experiment required an accurate independent calculation.

Table I. Calculated vibrational levels and tunneling lifetimes of $^2\Pi$ HS $^{++}$.

v	E (cm $^{-1}$)	t (sec)	t (sec) ^a
0	998.8	∞	∞
1	2905.7	∞	∞
2	4693.9	∞	∞
3	6363.1	(b)	11.1×10^6
4	7909.9	(b)	11.8
5	9328.0	96.0×10^{-6}	98.0×10^{-6}
6	10604.5	5.1×10^{-9}	5.2×10^{-9}
7	11701.0	2.0×10^{-12}	2.0×10^{-12}
<p>a) Calculated using the program LEVEL by R.J. Le Roy⁶.</p> <p>b) The widths of these levels are too small to be calculated by our phase shift method.</p>			

The general computational procedure was similar to that described for SH $^{++}$, and employed CASSCF-CI wavefunction in a flexible primitive basis generally contracted to [5s,4p,3d,2f] functions on each center (92 general contractions in all). Potentials for the lowest $^2\Sigma$ (ground state) and $^2\Pi$ (first excited) states were calculated, while other states from the same asymptotes were known from our CAS-SCF results to lie well above these two.

The dynamics of this system are much richer than those of SH $^{++}$ because in CF $^{++}$ there are metastable manifolds belonging to two radiatively-coupled electronic states. Thus the decay rate is the sum of individual rates for intra-state vibrational relaxation, inter-state radiative decay, and tunneling, although all three channels are not open for every vibrational level. The calculated term values and lifetimes for the various processes are presented in Tables II and III, and show that this system will indeed be approachable by the spectroscopic techniques now becoming available in the Lineberger laboratory. A full description of this work on CF $^{++}$ has been submitted⁵ for publication.

In the experimental work of Leone, an ion source has been devised to optimize the production of doubly charged molecular cations. This source consists of an electron impact ionizer which is crossed with a pulsed jet of neutral precursor molecules in a differentially pumped chamber. The ions are immediately extracted and passed through a quadrupole mass spectrometer and then detected with an electron multiplier in a large analysis chamber. The flight time in the mass selector for a typical doubly charged ion is about 10 μ s, thus molecular dication species with lifetimes longer than 10 μ s are readily observed. With this source, a wide array of well-known and new doubly charged molecular ions have been formed.

Table II. Term values, diagonal dipole matrix elements, and relaxation, electronic, tunneling, and total lifetimes of the vibrational levels of the $\text{CF}^{++} \text{X}^2\Sigma^+$ state.

v	$E_v(\text{cm}^{-1})$	$m_v(\text{au})$	$t_v(\text{s})$	$t_e(\text{s})$	$t_t(\text{s})$	$t_{\text{tot}}(\text{s})$
0	975.96	2.4181				
1	2883.45	2.4384	1.04×10^{-2}			1.04×10^{-2}
2	4737.08	2.4571	5.47×10^{-3}			5.47×10^{-3}
3	6549.88	2.4776	3.80×10^{-3}			3.80×10^{-3}
4	8329.35	2.4998	2.95×10^{-3}			2.95×10^{-3}
5	10077.33	2.5234	2.42×10^{-3}			2.42×10^{-3}
6	11793.02	2.5477	2.08×10^{-3}			2.08×10^{-3}
7	13475.01	2.5725	1.83×10^{-3}			1.83×10^{-3}
8	15122.62	2.5979	1.65×10^{-3}			1.65×10^{-3}
9	16734.80	2.6241	1.51×10^{-3}			1.51×10^{-3}
10	18310.01	2.6515	1.41×10^{-3}			1.41×10^{-3}
11	19846.26	2.6802	1.33×10^{-3}			1.33×10^{-3}
12	21340.84	2.7105	1.27×10^{-3}			1.27×10^{-3}
13	22791.11	2.7427	1.22×10^{-3}			1.22×10^{-3}
14	24195.04	2.7768	1.19×10^{-3}	5.79×10^{-1}		1.19×10^{-3}
15	25551.33	2.8128	1.16×10^{-3}	2.46×10^{-3}		1.11×10^{-3}
16	26858.49	2.8514	1.15×10^{-3}	5.23×10^{-3}		9.42×10^{-4}
17	28114.80	2.8927	1.14×10^{-3}	1.95×10^{-3}		7.20×10^{-4}
18	29318.96	2.9370	1.14×10^{-3}	9.69×10^{-4}		5.25×10^{-4}
19	30470.16	2.9843	1.15×10^{-3}	5.77×10^{-4}		3.84×10^{-4}
20	31568.04	3.0349	1.17×10^{-3}	3.90×10^{-4}		2.92×10^{-4}
21	32612.25	3.0889	1.19×10^{-3}	2.89×10^{-4}		2.33×10^{-4}
22	33602.85	3.1464	1.22×10^{-3}	2.31×10^{-4}		1.94×10^{-4}
23	34540.19	3.2074	1.25×10^{-3}	1.97×10^{-4}		1.70×10^{-4}
24	35425.24	3.2714	1.29×10^{-3}	1.77×10^{-4}		1.56×10^{-4}
25	36259.38	3.3381	1.34×10^{-3}	1.66×10^{-4}		1.48×10^{-4}
26	37043.87	3.4077	1.40×10^{-3}	1.62×10^{-4}		1.46×10^{-4}
27	37778.50	3.4807	1.47×10^{-3}	1.64×10^{-4}		1.48×10^{-4}
28	38461.32	3.5494	1.57×10^{-3}	1.72×10^{-4}	1.18×10^{-4}	6.70×10^{-5}
29	39088.95	3.6318	1.69×10^{-3}	1.86×10^{-4}	6.11×10^{-8}	6.11×10^{-8}
30	39654.38	3.6999	1.88×10^{-3}	2.12×10^{-4}	8.26×10^{-11}	8.26×10^{-11}
31	40135.27	4.0345	2.32×10^{-3}	2.62×10^{-4}	4.32×10^{-13}	4.32×10^{-13}

Using the NF_3 precursor, the species NF_2^{++} and NF^{++} are observed; the latter species is the subject of a recent theoretical investigation by the group of Radom, and our observation is the first reported confirmation of the stability of this dication. The appearance potential of NF^{++} from NF_3 is measured to be 43.8 eV. This work has recently been published in *Chemical Physics Letters*.

With HCl and DCl precursors, both HCl^{++} and DCl^{++} species are observed. Using CCl_4 , a wide variety of species are formed, including CCL^{++} , HCCl^{++} , and $\text{H}_2\text{CCl}^{++}$, several of which may be previously unreported. With CF_4 , we observe CF^{++} , CF_2^{++} and CF_3^{++} . O'Neil has completed detailed calculations on CF^{++} and shown that there are two bound states. We observe a break in the appearance potential of this species, indicative of the onset for the electronically excited state.

Table III. Term values, diagonal dipole matrix elements, and relaxation, electronic, tunneling, and total lifetimes of the vibrational levels of the $\text{CF}^{++} \text{A}^2\Pi$ state.

v	$E_v(\text{cm}^{-1})$	$m_v(\text{au})$	$t_v(\text{s})$	$t_e(\text{s})$	$t_t(\text{s})$	$t_{\text{tot}}(\text{s})$
0	309.22	3.0642		2.52×10^{-1}		2.52×10^{-1}
1	915.16	3.0960	6.14×10^{-2}	2.44×10^{-2}		1.74×10^{-2}
2	1506.00	3.1342	3.23×10^{-2}	5.35×10^{-3}		4.59×10^{-3}
3	2085.91	3.1762	2.23×10^{-2}	1.90×10^{-3}		1.75×10^{-3}
4	2653.52	3.2176	1.73×10^{-2}	9.16×10^{-4}		8.70×10^{-4}
5	3209.74	3.2587	1.44×10^{-2}	5.40×10^{-4}		5.20×10^{-4}
6	3755.06	3.2990	1.24×10^{-2}	3.61×10^{-4}		3.51×10^{-4}
7	4288.88	3.3381	1.10×10^{-2}	2.62×10^{-4}		2.56×10^{-4}
8	4810.69	3.3761	9.96×10^{-3}	2.03×10^{-4}		1.99×10^{-4}
9	5319.62	3.4129	9.20×10^{-3}	1.64×10^{-4}		1.61×10^{-4}
10	5814.55	3.4485	8.62×10^{-3}	1.38×10^{-4}		1.36×10^{-4}
11	6293.98	3.4833	8.19×10^{-3}	1.20×10^{-4}		1.18×10^{-4}
12	6755.87	3.5176	7.90×10^{-3}	1.07×10^{-4}		1.06×10^{-4}
13	7197.06	3.3933	8.10×10^{-3}	1.03×10^{-4}	1.31×10^{-5}	1.16×10^{-5}
14	7612.33	3.5638	7.93×10^{-3}	9.54×10^{-5}	1.30×10^{-8}	1.30×10^{-8}
15	7991.73	3.6220	8.53×10^{-3}	9.70×10^{-5}	3.03×10^{-11}	3.03×10^{-11}
16	8310.99	4.1488	1.02×10^{-2}	1.13×10^{-4}	3.00×10^{-13}	3.00×10^{-13}

In a recent experimental verification of O'Neil's calculations on HS^{++} , this dication has been observed to be created by electron impact on H_2S . There is no evidence for a break in the appearance potential, consistent with the finding of theory that there is only one bound state of this dication. During the course of these experiments, stable ions are also observed which are attributed to H_3S^{++} . The observation of this hydrogen rich dication is of special interest for structural reasons, since it may consist of a hydrogen molecule bound to an HS^{++} dication. This work has been submitted for publication in the Volume 100 special issue of *International Journal of Mass Spectrometry and Ion Processes*.

Two supersonic beam-electron impact dication sources have been constructed and evaluated in Lineberger's laboratory. Preliminary experiments have demonstrated collisional stability of NO^{++} , and other experiments have shown that both NO^{++} and CF^{++} have rather small photodestruction cross sections in the visible spectrum. Wavelengths investigated to date include $1.06 \mu\text{m}$, 630 nm, 532 nm, 355 nm and 256 nm. These experiments are designed to test some aspects of dication stability, while construction and testing are completed on a high resolution photodissociation apparatus. This apparatus will provide both lifetime information via linewidths of bound predissociative levels and energy release information via coincidence detection of both ionic photofragments. Construction and assembly of the detection region has been completed, and preliminary testing on NO^{++} is underway.

Work is completed on the construction of a collision cell in Leone's laboratory, so that reactions studies can begin shortly on some of these doubly charged ions. We will be measuring product branching fractions, the rates of reactions, and the stability of the dication species to perturbing gas collisions. Work is also in progress to utilize laser multiphoton ionization methods for forming doubly charged molecular ions with greater energy specificity.

References

1. H.-J. Werner and P. J. Knowles, *J. Chem. Phys.* **82**, 5053 (1985); P. J. Knowles and H.-J. Werner, *Chem. Phys. Lett.* **115**, 259 (1985).
2. H.-J. Werner and P. J. Knowles, *J. Chem. Phys.* **89**, 5803 (1988); P. J. Knowles and H.-J. Werner, *Chem. Phys. Lett.* **145**, 514 (1988).
3. J. Senekowitsch, H.-J. Werner, P. Rosmus, E. A. Reinsch, and S. V. O'Neil, *J. Chem. Phys.* **83**, 4661 (1985); a misprint in this reference shows a sulfur s function with an exponent of 0.491: the correct value, and the one actually used, is 0.0491.
4. P. J. Miller, S. A. Rogers, J. Senekowitsch, S. V. O'Neil, and S. R. Leone, H.-J. Werner, and P. J. Knowles, submitted to the centennial edition of *International Journal of Mass Spectrometry and Ion Processes*.
5. J. Senekowitsch, S. V. O'Neil, H.-J. Werner, and P. J. Knowles, submitted to *J. Chem. Phys.*
6. R. J. Le Roy, University of Waterloo Chemical Physics Research Report CP-230R, University of Waterloo, Waterloo, Ontario, Canada (1986).

CHEMICALLY BOUND EXCITED CLUSTERS III *

C.A.Nicolaides

Theoretical and Physical Chemistry Institute

National Hellenic Research Foundation

48, Vas.Constantinou Ave., 116 35 Athens

Greece

The present brief report contains two theory-guided and computationally-supported predictions concerning the formation of new types of molecular states due to intramolecular charge transfer at nonstandard geometries between the ground and first excited singlet states. This intramolecular charge transfer manifests itself as an avoided intersection between the two surfaces. In turn, the avoided intersection gives rise to absolute or local, real or virtual minima on both surfaces which cannot decay radiatively, with important consequences as regards energy trapping and transfer and the possibility of highly exothermic physicochemical reactions /1-5/.

II. The $(\text{H}_2\text{O})_2^*$ cluster at a MIES geometry.

We /6/ have computed the potential energy surfaces (PES) of a chemically bound excited state of the $(\text{H}_2\text{O})_2^*$ cluster (10.0 eV above the energy of two H_2O molecules) and of the corresponding dissociative ground state at a geometry which was predicted by applying the maximum ionicity of excited state (MIES) theory of bonding /1,2,4/. These PES confirm the existence of an avoided region

* Outline of a lecture presented at the 4th HEDM contractors conference, Febr. 26-28, 1990, Long Beach, Calif.

which is caused by intramolecular charge transfer and is characteristic of the MIES structures. Three dimensional PES plots show the excited state minimum and the overall repulsive nature of the lower state, which breaks into $(\text{H}_2\text{O}) + (\text{H}_2\text{O})$ (Fig.1). Also, by taking a slice of the two surfaces along the fragmentation coordinate for $[\text{H} \cdots^{\text{R}} \cdots \text{H}_3\text{O}_2]$, the two dimensional MIES feature of an avoided crossing is brought out (see fig.2) and connection is made with structure and PES characteristics of certain diatomic molecules where bonding due to charge transfer is recognized from the charged atomic dissociation products. The present results, together with our earlier ones [1,2] on clusters such as $(\text{H}_2)_n$ and XH_2 ($\text{X}=\text{He}, \text{Ne}, \text{Ar}$), suggest that the features associated with MIES structures should form part of our description of electronic structure and of intramolecular dynamics of a number of nonreactive closed shell species.

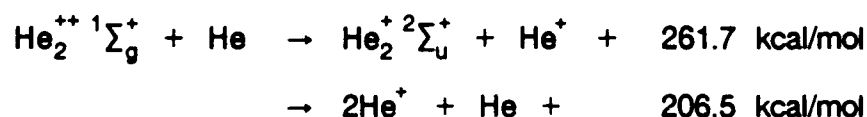
II. The "volcanic" form of ground state potentials

The ground state tunneling characteristics of fig.2 which are caused by intramolecular charge transfer in neutral, dissociating clusters, can also be identified in positively or negatively charged species from their dissociation products which involve ionic fragments. For example, the lowest state of $^2\Sigma_g^+$ symmetry in He_2^+ , which is a result of valence-Rydberg mixing ($1\sigma_g 1\sigma_u^2 \leftrightarrow 1\sigma_g^2 n\sigma_g$), has the form of curve 1 of fig.2 [7]. However, it is radiatively unstable due to the $^2\Sigma_g^+ \rightarrow ^2\Sigma_u^+ (1\sigma_g^2 1\sigma_u)$ transition. On the other hand, as we reach the ionization threshold of the $\text{He}_2^+ ^2\Sigma_g^+$ Rydberg series, the bound, lowest $\text{He}_2^{++} ^1\Sigma_g^+$ state is obtained, whose potential energy keeps a similar form (See fig.4 and Table 5 of ref.7), while its wave-function is a geometry-dependent mixture of $1\sigma_g^2$, and $1\sigma_u^2$ (with

some $1\sigma_g n\sigma_g$ character) configurations. The diabatic crossing of the $1\sigma_g^2$ and the $1\sigma_u^2$ configurations is such that, in the adiabatic situation, the volcano form is created /5/. The location of such diabatic crossings /2/ is a crucial criterion for the possibility of having a volcanic ground state. For example, in the ionic diatomic molecules the lowest curve goes asymptotically to neutral atoms while the diabatic crossing occurs at large distances (e.g. in LiF it occurs at 13.3 a.u. /8/) and therefore the eventual minimum is below the energy of the dissociation channel and no volcanic ground state is formed.

III. Generalization of the Pauling model to polyatomics: Expectation of He_3^{++} formation

The existence of metastable $\text{He}_2^{++} \ ^1\Sigma_g^+$ implies the possibility of extraordinarily exothermic reactions with hydrogenic species with specific impulses of the order of 2000s/5/. Reactions with helium are also highly exothermic/9/



How do they take place? A full answer to this question can be given from future research on the related dynamics. Nevertheless, a useful first-order concept is the possible formation of He_3^{++} , as a stable or metastable intermediate.

What are the properties of He_3^{++} ?

A reasonable expectation is that it will have a multidimensional volcanic ground state surface. This is based on arguments similar to that of Pauling for

the diatomic molecules. In particular, a volcanic He_3^{++} could be thought-of as a possible product of the interaction of the repulsive surfaces of $(\text{He}_2^+ {}^2\Sigma_u^+ + \text{He}^+)$ or of $(2\text{He}^+ + \text{He})$ which is 2.4 eV above, with the surface corresponding to the attraction of $\text{He}_2^{++} {}^1\Sigma_g^+ + \text{He}$ which, asymptotically, lies about 11 eV higher.

Such a mechanism is expected to work for other clusters of similar characteristics, such as that of Be_3^{++} . For us, a practical advantage of He_3^{++} is the fact that this molecule is sufficiently small to be amenable in our institute to a large number of configuration-interaction and MCSCF geometry optimization calculations/10,11/.

The results of our calculations show that, as long as C_s (or C_{2v}) symmetry is imposed on the He_3^{++} cluster, it is metastable with a multidimensional volcanic potential energy hypersurface for the ${}^1A'$ ground state /fig.3/. Furthermore, He_3^{++} is found to play the role of an intermediate for the reaction $\text{He}_2^{++} {}^1\Sigma_g^+ + \text{He} \rightarrow 2\text{He}^+ + \text{He}$, and this is possible because of the asymmetric stretch which breaks the C_s symmetry and leads He_3^{++} to fragmentation.

Acknowledgment

This work was partially supported by the AFOSR research grant 87-0342.

References

1. C.A.Nicolaides, I.Petsalakis and G.Theodorakopoulos, J.Chem.Phys. 81 748 (1984); A.Metropoulos and C.A.Nicolaides, J.Phys.B21, L77(1988)
2. C.A.Nicolaides and A.Zdetsis, J.Chem.Phys. 80, 1900 (1984); S.C.Farantos, G.Theodorakopoulos and C.A.Nicolaides, Chem.Phys.Lett. 100, 263 (1983)
3. C.A.Nicolaides, Proceedings of the 3rd HEDM contractors' conference, New Orleans 1989, eds.T.G.Wiley and R.A.Opijnen, AFSC, Edwards AFB, California.
4. C.A.Nicolaides, J.Mol.Str. (Theo Chem.) 202, 285 (1989)
5. C.A.Nicolaides, Chem.Phys.Lett. 161, 547 (1989); C.A.Nicolaides, M.Chrysos and P.Valtazanos, J.Phys. B23, 791 (1990)
6. C.A.Nicolaides and P.Valtazanos, Chem. Phys. to be published (1990)
7. A.Metropoulos, C.A.Nicolaides and R.J.Buenker, Chem.Phys. 114, 1 (1987)
8. H.-J.Werner and W.Meyer, J.Chem.Phys. 74, 5802 (1981)
9. P.Valtazanos and C.A.Nicolaides, Chem.Phys.Lett. in press (1990)
10. MELDF series of electronic structure programs, developed by L. E. McMurchie, S. T. Elbert, S. R. Langhoff, and E. R. Davidson and extensively modified by D. F. Feller and D. C. Rawlings.
11. M. W. Schmidt, J. A. Boatz, K. K. Baldridge, S. Koseki, M. S. Gordon, S. T. Elbert and B. Lam, QCPE Bulletin 7 (1987) 115.

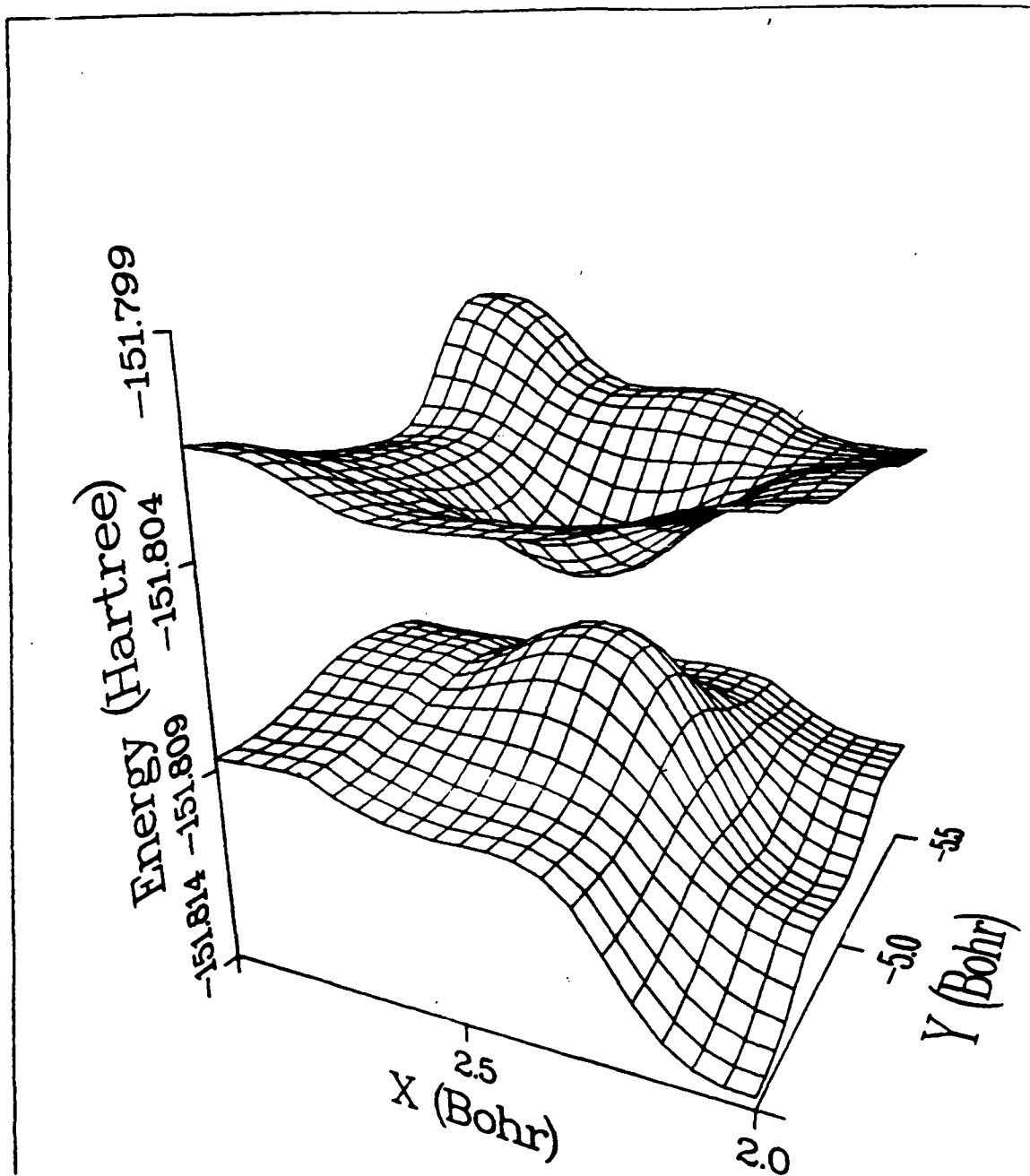


Figure 1

Ground and excited $^1A'$ surfaces of $(\text{H}_2\text{O})_2$ obtained by the multi-reference-single-and-double-excitation CI method. The energies are plotted as a function of the position of the "H"-like atom on the XY plane, the geometry of $(\text{H}_3\text{O}_2)^+$ being kept constant. The minimum of the excited surface is real and lies 10.0 eV above the energy of two H_2O molecules.

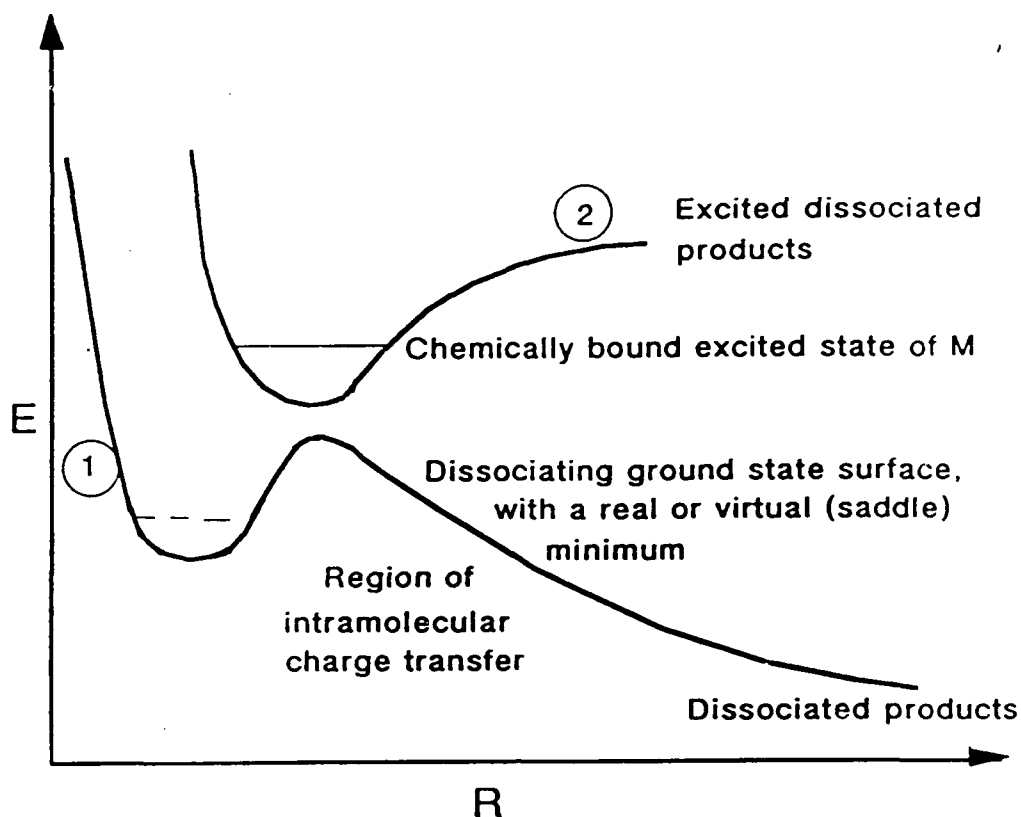


Figure 2

Potential energy surface characteristics along a fragmentation coordinate R as revealed from the calculations of refs. **1, 2** and of the present work. The ground state surface, (1), has a volcano form [7] and leads to molecular dissociation. The excited state, (2), is chemically bound. It decays via nonadiabatic coupling to the repulsive ground state. From the known results on ground state bonding as well as from our findings and interpretation of the CBECs, the following unified picture emerges. The molecule M may be neutral or charged. If the dissociated products for upper and lower curves are charged differently, the charge transfer involves large energy differences while it is physically identifiable from the charged channels ($A^q + B^q \leftrightarrow A^{q+1} + B^{q-1}$). If the two curves dissociate into neutral states (ground and excited) the charge transfer must be understood from electronic structure properties of M at the crossing region (e.g. cases of the H_4 and $(H_2O)_2$ clusters).

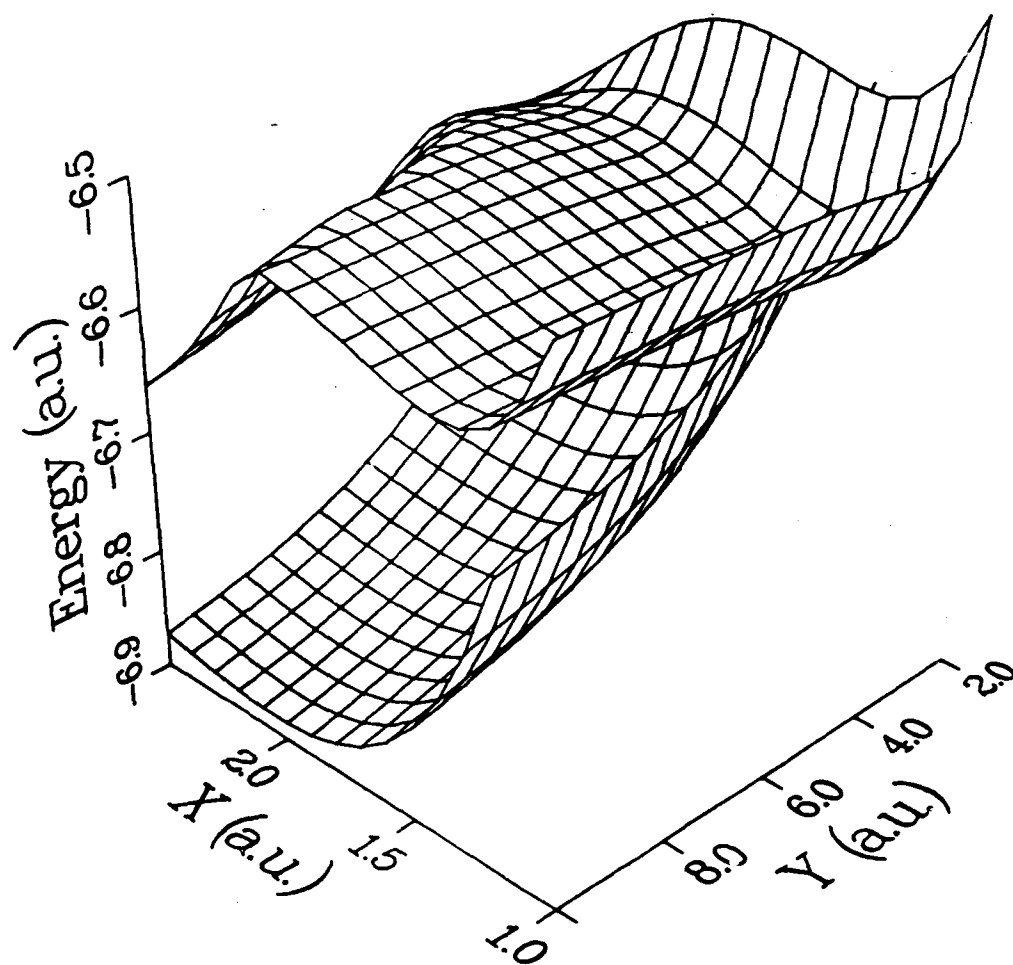


Figure 3

Three-dimensional representation of the C_s Potential Energy Surfaces of He_3^{++} . The one above is the A' surface while the one below is the A'' . Only a portion of the A'' surface lying below the A' is shown, to avoid confusion by intersecting lines. Note that the local minimum on the A' surface lies before the intersection of the two surfaces, making this minimum (which in C_1 symmetry is a saddle point) the ground state at this point.

**Potential New High Energy Density Materials: Cyclooctaoxygen
O₈, Including Comparisons with the Well-Known
Cyclo-S₈ Molecule.**

Henry F. Schaefer III

Center for Computational Quantum Chemistry
University of Georgia
Athens, Georgia 30622
U.S.A.

One of the most fundamental principles in chemistry is to analogize from known compounds to presumably related compounds by incorporating elements directly above or below in the periodic table. In this context it may be viewed as interesting that the valence isoelectronic cyclo- O_8 compound has never been observed. Cyclooctaoxygen would be particularly significant because it would presumably be a very high energy density molecule.

As discussed elsewhere for O_4 , O_6 , and O_{12} , these cyclic oxygen compounds are expected (in analogy with hydrogen peroxide and organic peroxides) to have weak oxygen-oxygen bonds. Back-of-the-envelope calculations suggest that unstrained ($n \geq 6$) O_n rings might lie about 24 kcal/mole per oxygen atom above the $n/2$ isolated diatomic oxygen molecules. If these O_n rings lie in relative minima on their potential energy hypersurfaces, they could store large amounts of energy. This energy might then be used (for example, via reaction with molecular hydrogen) to design improved conventional fuels.

In this research we have completed a detailed theoretical examination and comparison of the cyclo- O_8 and cyclo- S_8 molecules. These species are sufficiently small that good basis sets may be used in conjunction with methods that explicitly consider the effects of electron correlation. Therefore the theoretical predictions should be sufficiently reliable to encourage or discourage future laboratory investigations.

Reported in Table I are the energies of O_8 and S_8 relative to the dissociation limits $4O_2$ and $4S_2$. Since experimental data is available for S_8 these results will be discussed first. At the DZ SCF and DZ+P SCF levels of theory, S_8 lies 13.0 and 33.9 kcal/mole, respectively, below four separated S_2 molecules. The latter (DZ+P SCF)

result may readily be translated into the prediction that S_8 lies $33.9/8 = 4.2$ kcal/mole below separated S_2 molecules on a *per atom basis*. The analogous experimental value for gaseous S_8 is 12.2 kcal/mole per S atom.

Assuming the DZ+P SCF equilibrium geometry for S_8 , its dissociation energy has been predicted using second-order perturbation theory (MP2). However, the GAUSSIAN 86 codes, for an open-shell system like the S_2 molecule $^3\Sigma_g^-$ ground state, mandate the use of unrestricted Møller-Plesset second-order perturbation theory. At the S_2 RHF equilibrium geometry (DZ+P basis set, $r_e = 1.881$ Å) the UMP2 total energy is -795.25545 hartrees. The comparable MP2 energy for closed shell S_8 is -3181.11839 hartrees. Thus S_8 is predicted to lie 60.6 kcal/mole below 4 S_2 at this level of theory. On a *per atom basis*, S_8 lies 7.6 kcal/mole below 4 S_2 , in reasonable agreement with the experimental value 12.2 kcal/mole.

At the DZ SCF level O_8 lies 21.3 kcal/mole above four O_2 molecules on a per atom basis. With the DZP SCF method O_8 lies 21.6 kcal/mole/atom above four separated diatomic oxygen molecules. Thus the addition of polarization functions (d functions on each oxygen atom) lowers the energy of 4 O_2 slightly more than that of O_8 .

Assuming DZ+P SCF geometries, the DZ+P MP2 energies for O_2 and O_8 are -149.97388 and -599.68739 hartrees, respectively. Thus O_8 lies 130.6 kcal/mole above 4 O_2 or 16.3 kcal/mole higher on a per atom basis. Thus the effect of electron correlation is to significantly lower O_8 relative to the separated oxygen molecules.

More reliable yet should be the comparison of the energy of DZ+P MP2 geometry optimized O_8 with that of four comparable O_2 molecules. The O_2 geometry

optimization must be carried out at the DZ+P UMP2 level and this yields a bond distance $r_e = 1.253 \text{ \AA}$ and total energy $E = -149.97905$ hartrees. Combined with the O_8 total energy reported in Table I, one predicts that cyclooctaoxygen lies 123.5 kcal/mole above four infinitely separated O_2 molecules. Thus geometry optimization is energetically much more important for O_8 with correlated methods than is the case for O_2 . On a per atom basis the DZ+P MP2 dissociation energy for O_8 is 15.4 kcal/mole.

A number of significant relationships between the present O_8 energetic predictions and those reported earlier for O_{12} may be noted. First, the higher level theoretical methods used in the present work are broadly in agreement with the simpler methods used for O_{12} . For O_{12} the only correlated method used was DZ MP2 (using DZ SCF geometries) and those results were presented with great caution. However, the analogous DZ MP2 and DZ+P MP2 dissociation energies for O_8 are 15.7 and 16.3 kcal/mole/atom, respectively. The close agreement between the two methods suggests that our final O_{12} energetic predictions may be much more reliable than could reasonably have been anticipated.

Secondly the dissociation energies of O_8 and O_{12} appear to be very similar on a per atom basis. This may be seen from the following array of dissociation energies:

	O_8	O_{12}
DZ SCF	21.3	20.9
DZ+P SCF	21.6	21.6
DZ MP2	15.7	16.1

Both O_8 and O_{12} should be relatively free of bond angle and dihedral angle strain and their comparable energetics mirror that presumed for S_8 and S_{12} based on the latter's

stability (the precise thermochemistry of gaseous S_{12} does not appear to be established). Thus one expects O_8 and O_{12} to be perhaps the most readily synthesizable of the oxygen rings.

Probably the best opportunity for observing O_8 lies with matrix isolation infrared spectroscopy. From Table III it is evident that the prediction of theory is that the strongest IR fundamental for O_8 should be the highest frequency vibration following the O-O stretches. Thus the intensity of the harmonic vibrational frequency predicted at $\omega(b_2) = 806\text{ cm}^{-1}$ is 20.1 km/mole. Although the comparable S_8 vibration also carries the largest IR intensity (both theoretically and experimentally), for O_8 this b_2 intensity is more than three times greater than for S_8 . Thus it seems clear that the observation of $\nu(b_2)$ around 700 cm^{-1} provides a prime opportunity for the laboratory identification of O_8 .

The Raman intensities of O_8 are related to those of S_8 . The symmetric breathing mode again has the highest intensity but it is a bit lower (44 Å/amu for O_8 vs. 60 Å/amu for S_8) than for the analogous sulfur ring. Since the Raman experiment is inherently more difficult than the infrared, we would suspect that observation of O_8 in this way will be initially difficult.

Can one make a final estimate of the dissociation energy of O_8 ? Assuming a similar relationship $O_8(\text{theory})/O_8(\text{truth})$ as exists for $S_8(\text{theory})/S_8(\text{experiment})$ such an estimate may be attempted. For S_8 the DZ+P MP2 method (using DZ+P SCF geometries) yields a dissociation energy of 7.6 kcal/mole on a per atom basis, or 4.6 kcal/mole less than experiment. The same theoretical method predicts O_8 to lie 16.3 kcal/mole/atom above four O_2 . If the S_8 error of 4.6 kcal is subtracted, the final

estimate is that O_8 lies 11.7 kcal/mole/atom above four O_2 molecules.

This final prediction that O_8 lies 12 kcal/mole/atom above 4 O_2 is much lower than our original back-of-the-envelope calculation of 24 kcal/mole/atom for unstrained oxygen rings. What this means is that the oxygen-oxygen bonds in O_8 are much stronger than in hydrogen peroxide, H_2O_2 . The consequences of this changed perspective are

- (a) O_8 is probably more stable than we anticipated;
- (b) O_8 is not as high-energy-density a species as anticipated.

These conclusions mean that O_8 will probably be easier to make than initially expected but ultimately less useful as a conventional fuel. Of course the smaller rings O_4 and O_6 lie significantly higher than separated O_2 molecules on a per atom basis and thus are capable of storing more energy than O_8 . The single most critical remaining mystery concerning the oxygen rings concerns their activation energies with respect to dissociation.

Table VI. Total energies for the higher level calculations on the H₂CO system^a.

level of theory	H ₂ CO (\tilde{X}^1A_1)	H ₂ CO (\tilde{a}^3A'')	TS	HCO·	supermolecule (H·····HCO·)
MR-CISD/TZ2P ^b					
0.070 ^c	-114.256 837 (-114.285 437)	-114.141 392 (-114.169 939)	-114.095 019 (-114.130 967)	-113.617 635 (-113.644 559)	-114.115 334 (-114.142 258)
0.060 ^c	<i>d</i> <i>d</i>	-114.141 829 (-114.170 653)	<i>d</i> <i>d</i>	<i>d</i> <i>d</i>	<i>d</i> <i>d</i>
CISD/TZ(2df,2pd) ^e	-114.282 894	-114.170 861	-114.120 120	-113.635 474	-114.133 248
CISD(Q)/TZ(2df,2pd)	-114.316 818	-114.201 002	-114.154 840	-113.666 711	-114.164 485

^aTotal energies in hartree. All results in this table were obtained with the CISD/TZ2P optimized geometries.

^bMulti-reference CISD calculations using CASSCF (12e⁻/10mo CAS) molecular orbitals. The numbers in parentheses are MR-CISD(Q)/TZ2P results obtained with the use of the multi-reference Davidson correction.

^cAll configurations in the CASSCF whose coefficients were greater than or equal to this value were included in the multi-reference CI.

^dSame value as the previous entry in the table (i.e. no new references were included in the multi-reference CI).

^eThe SCF/TZ(2df,2pd) total energy for H· is -0.497 774 hartree.

Table IV. Theoretical prediction of the structures and physical properties^a for the transition structure ($\text{H}_2\text{CO } ^3\text{A}'' \rightarrow \text{HCO} \cdot ^2\text{A}' + \text{H} \cdot$) (C_1 symmetry, ^3A).

level of theory	energy	r_e (C-O)	r_e (C-H ₂)	r_e (C-H ₃)	θ_e (H ₂ CO)	θ_e (H ₃ CO)	τ_e (H ₂ COH ₂)	μ	ω_1	ω_2	ω_3	ω_4	ω_5	ω_6
SCF/DZP	-113.739 394	1.1877	1.1055	1.5110	125.61	104.86	98.08	2.398	2986	1912	1157	1047	652	2490 _i
SCF/TZ2P	-113.750 129	1.1772	1.1040	1.4955	125.64	104.82	97.89	2.299	2924	1899	1151	1060	662	2466 _i
SCF/QZ3P	-113.763 818	1.1779	1.1038	1.4949	125.88	104.70	98.49	2.223	2925	1892	1144	1046	654	2461 _i
CASSCF/DZP I ^b	-113.860 468	1.2280	1.0996	1.5578	124.47	104.68	99.45	1.778						
CASSCF/TZ2P I ^b	-113.871 870	1.2171	1.0972	1.5364	124.43	104.64	99.34	1.718						
CASSCF/DZP II ^c	-113.869 670	1.2224	1.1212	1.5594	123.83	106.71	97.00	1.637						
CASSCF/TZ2P II ^c	-113.880 326	1.2132	1.1124	1.5407	123.87	106.39	97.10	1.620						
CISD/DZP	-114.033 284 ^d	1.2015	1.1167	1.6306	123.77	106.27	93.77	1.942	2843	1848	1094	923	544	1443 _i
CISD/TZ2P	-114.087 205 ^d	1.1849	1.1141	1.6191	123.84	106.53	92.73	1.879	2759	1853	1093	950	557	1381 _i
CISD/QZ3P	-114.110 206 ^d	1.1857	1.1139	1.6179	124.08	106.49	93.52	1.790						

^aSee footnote a of Table I.

^b8e⁻/8mo CAS.

^c12e⁻/10mo CAS.

^dWith inclusion of the Davidson correction, the CISD(O) energies are -114.061 175, -114.119 264 and -114.143409 hartrees for the DZP and TZ2P basis sets, respectively.

Table III. Theoretical prediction of the structures and physical properties^a for HCO cdot (²A').

level of theory	energy	r _e (C-O)	r _e (C-H)	θ _e (HCO)	μ	ω ₁ a'	ω ₂ a'	ω ₃ a'
SCF/DZP	-113.269 795	1.1621	1.1042	127.51	2.193	3022	2135	1259
SCF/TZ2P	-113.281 027	1.1494	1.1026	127.42	2.091	2954	2125	1256
SCF/QZ3P	-113.293 534	1.1501	1.1026	127.60	2.108	2953	2118	1247
CASSCF/DZP I ^b	-113.386 221	1.1971	1.1027	126.36	1.729			
CASSCF/TZ2P I ^b	-113.398 385	1.1838	1.1005	126.26	1.673			
CASSCF/DZP II ^c	-113.393 956	1.1955	1.1165	126.08	1.582			
CASSCF/TZ2P II ^c	-113.405 336	1.1833	1.1101	126.01	1.561			
CISD/DZP	-113.551 018 ^d	1.1847	1.1145	125.28	1.797	2879	1992	1167
CISD/TZ2P	-113.603 244 ^d	1.1673	1.1113	125.24	1.725	2797	1998	1168
CISD/QZ3P	-113.624 517 ^d	1.1681	1.1105	125.47	1.742	2810	1991	1157
expt. ^e		1.175	1.119	124.4	1.3626	2790	1920	1126

^aSee footnote a of Table I.

^b7e⁻/7mo CAS.

^c11e⁻/9mo CAS.

^dWith inclusion of the Davidson correction, the CISD(Q) energies are -113.576 061, -113.631 950 and -113.654 118 hartree for the DZP, TZ2P and QZ3P basis sets, respectively.

^eThe structural parameters are r_e and θ_e values from ref. 43, the dipole moment is from ref. 44, and the frequencies are empirical harmonic frequencies from ref. 45.

Table I. Total energies (in hartrees) for the cyclo-O₈ and cyclo-S₈ molecules at their fully optimized equilibrium geometries. Relative energies (ΔE) are given in kcal/mole.

	O ₈	ΔE (O ₈ -4O ₂)	S ₈	ΔE (S ₈ -4S ₂)
DZ SCF	-598.01365	+170.4	-3179.74094	-13.0
DZ+P SCF	-598.26838	+173.1	-3180.06123	-33.9
DZ+P MP2	-599.71940	+123.5	a	a

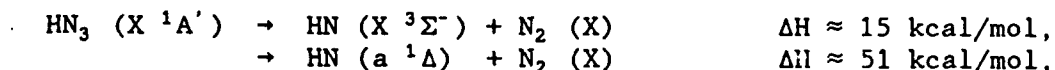
^aDZ+P MP2 energies have been evaluated assuming DZ+P SCF equilibrium geometries and are discussed in the text.

DECOMPOSITION OF ENERGETIC MOLECULES FROM METASTABLE VIBRATIONAL STATES

M.P. Casassa, B.R. Foy, J.C. Stephenson, and D.S. King
National Institute of Standards and Technology
Molecular Physics Division
Gaithersburg, Md 20899

Vibrational overtone excitation enables highly state-specific studies of the unimolecular decomposition of energetic molecules from their ground electronic states. Measurements of overtone photodissociation spectra, product state distributions, and lifetimes provide information on the energies and topologies of potential energy surfaces which are key to bonding and stability in energetic molecules.

We have studied the decomposition reactions



by direct pumping of the NH stretching overtones, $5\nu_{\text{NH}}$ (15121cm^{-1}) and $6\nu_{\text{NH}}$ (17671cm^{-1}), and four intermediate combination levels.¹⁻³ The $7\nu_{\text{NH}}$ state (20070cm^{-1}) and five additional combination levels between $6\nu_{\text{NH}}$ and $7\nu_{\text{NH}}$ were excited by IR-visible double resonance through the ν_{NH} 0 \rightarrow 1 transition. The nascent $\text{NH(X}^3\Sigma^-)$ and $\text{NH(a}^1\Delta)$ fragments were detected by laser-induced fluorescence (LIF). Most experiments were performed with HN_3 cooled to a rotational temperature of $\approx 8\text{K}$ in the free-jet expansion. This eliminates the rotational congestion which dominates 300K spectra of the overtone bands, and precludes intermolecular interactions which may perturb nascent product state distributions. Picosecond and nanosecond laser systems were used to measure product appearance rates, detailed product state distributions, and the photodissociation spectra.

OVERTONE PHOTODISSOCIATION SPECTRA

Overtone photodissociation spectra reveal extensive vibrational state mixing at high vibrational energies in ground electronic state HN_3 . We previously reported spectra of the $5\nu_{\text{NH}}$ and $6\nu_{\text{NH}}$ bands obtained by scanning a 0.03 cm^{-1} bandwidth overtone-pump laser and monitoring LIF of the $\text{NH(X}^3\Sigma^-)$ fragment. We have improved these measurements with Doppler limited (0.007cm^{-1}) resolution, and have recorded spectra of the $7\nu_{\text{NH}}$ state.

Two aspects of vibrational coupling characterize these spectra. First, extensive anharmonic mixing of the N-H stretch with other vibrational motions gives a complex spectrum of vibrational eigenstates. Comparison of vibrational state densities and the observed line densities in the $5\nu_{\text{NH}}$ and $6\nu_{\text{NH}}$ bands suggests that the zero-order NH stretching motion couples to most neighboring states. Second, coupling of these mixed states to the dissociative continuum results in measurable homogeneous broadening of individual lines. A factor of two variation in widths of individual anharmonic resonance components in the $6\nu_{\text{NH}}$ band resembles a similar variation in lifetimes (measured in real time)

for the $5\nu_{\text{NH}}$ band. These mode-specific effects are a consequence of differences in the vibrational trajectories initially excited. At the $7\nu_{\text{NH}}$ level, both the mixing and dissociation effects combine to produce an unresolved spectrum, even at 8K.

VIBRATIONAL PREDISSOCIATION LIFETIMES

We previously reported the vibrational predissociation lifetime of the $5\nu_{\text{NH}}$ and $6\nu_{\text{NH}}$ levels. Figure 1 shows these data and additional measurements on combination bands lying between $5\nu_{\text{NH}}$ and $6\nu_{\text{NH}}$. Lifetimes were measured by varying pump-probe time delay while monitoring LIF of the $\text{NH}(\text{X}^3\Sigma^-)$ fragment. The pump pulse bandwidth subtends several anharmonic resonance states so the data shown represent "band-average" dissociation rates.

Dissociation lifetimes range from 210ns for $5\nu_{\text{NH}}$ to 0.95ns for $6\nu_{\text{NH}}$. All of the rates are much faster than an RRKM calculation which does not include the spin-forbidden nature of these processes. The statistical theory also predicts a less dramatic increase in the rate with energy than is observed. Ab initio calculations by M. Alexander⁴ indicate that the steep slope in rates arises because the lowest levels shown in Fig. 1 dissociate by tunneling

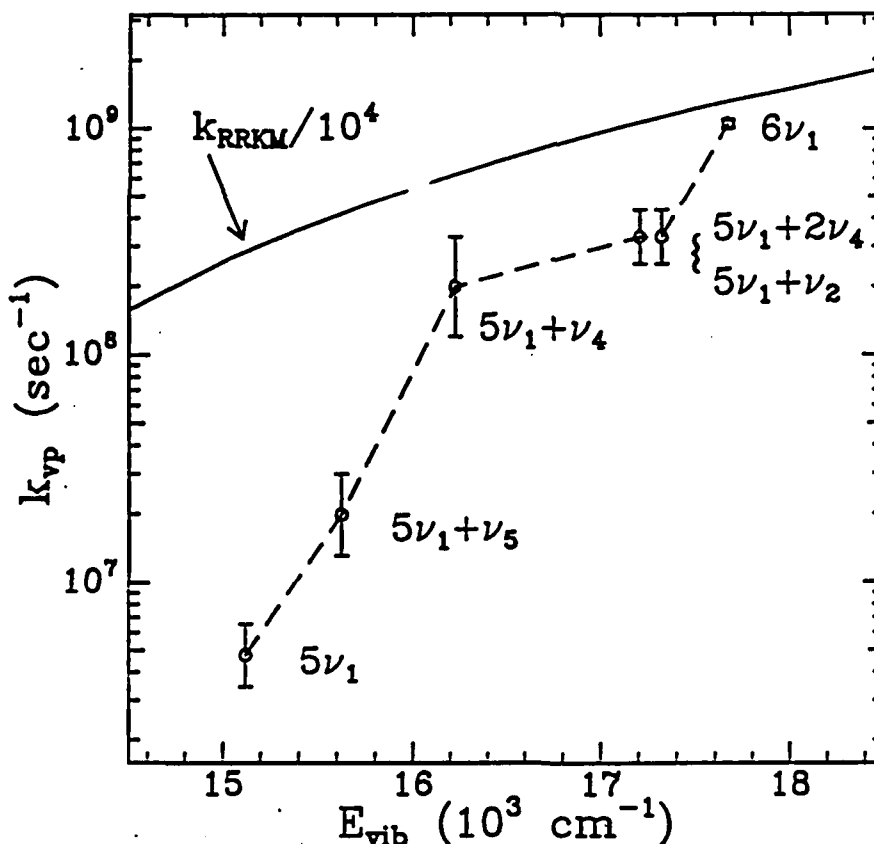


Figure 1. Unimolecular decomposition rates for HN_3 . Dissociation rate to produce $\text{NH}(\text{X}^3\Sigma^-)$ is plotted vs. total vibrational energy. The solid curve is the result of an RRKM calculation with $E_a = 12700 \text{ cm}^{-1}$. Vibrational assignments are zero-order descriptions.

through the potential energy barrier to singlet-triplet decomposition. Figure 1 shows states of comparable energy dissociate at comparable rates, even though the zero-order labels⁵ suggest significant differences in the initial vibrational motion. This may be understood in terms of the highly mixed character of the vibrational eigenstates discussed above.

PRODUCT STATE DISTRIBUTIONS

Product state distributions were determined by LIF probing of rotational, vibrational, spin-rotation and Λ -doublet states of the NH fragment. Translational state distributions were measured by recording Doppler profiles. Previously reported results for $5\nu_{\text{NH}}$ and $6\nu_{\text{NH}}$ showed that only the $\text{NH}(X^3\Sigma^-)$ channel is open, with most of the available energy converted into fragment translational energy ($\langle E_T \rangle \approx 10000$ and 12500 cm^{-1} , respectively). There is no measurable product vibrational excitation. The relatively low fraction of energy appearing in NH rotation is distributed in essentially Boltzmann fashion ($\langle E_R(\text{NH}) \rangle \approx 200$ and 400 cm^{-1} respectively), with a strong propensity to form the symmetric spin-rotation levels. All these results are in accord with predictions based on the potential energy surface of Alexander *et al.*⁶ In particular, the spin-rotation distribution is a consequence of symmetry-constrained dissociation from a planar transition state. Results presented here for higher vibrational levels were obtained using an IR-visible double resonance pumping scheme, which overcomes prohibitively small absorption cross sections for direct one-photon excitation.

Excitation to $7\nu_{\text{NH}}$ produces $\text{NH}(a^1\Delta)$. The rotational state distribution for $\text{NH}(a^1\Delta)$ is similar to that of $\text{NH}(X^3\Sigma^-)$ observed at lower vibrational energies with $\langle E_R(\text{NH}) \rangle \approx 220 \text{ cm}^{-1}$. There is a propensity to form the symmetric Λ -doublet state ($\Delta(A')$) which increases with increasing J . Figure 2 shows Doppler profiles (resolution $\approx .2 \text{ GHz}$) for $\text{NH}(a^1\Delta, v=0, J=5)$ produced by excitation to $7\nu_{\text{NH}}$. The Λ -doublet propensity is evident, as is the different appearance of profiles obtained in two pump-probe geometries. The observation of the antisymmetric $\Delta(A'')$ component suggests that this decomposition process proceeds in part through non-planar configurations.

By fitting the Doppler profiles shown in Fig. 2, and others observed for P branch lines and in different geometries, we determined that the recoil anisotropy parameter is $\beta = 0.61 \pm 0.07$. This significant anisotropy implies a lifetime short compared to parent rotational periods. Using a classical model for the recoil anisotropy, and referring to the widths observed in the overtone spectra, the dissociation lifetime of the $7\nu_{\text{NH}}$ level must lie between 2 and 10 ps. Analysis of the Doppler profiles further shows that the NH speed distribution is adequately fit by a Gaussian peaked at a speed of 1.1 km/s , giving for the total kinetic energy release $\langle E_T \rangle \approx 1150 \text{ cm}^{-1}$ with a $1/e$ half width of 530 cm^{-1} . This must be correlated with an N_2 rotational distribution peaking at $J(\text{N}_2) \geq 20$, or $\langle E_R(\text{N}_2) \rangle \geq 850 \text{ cm}^{-1}$. The disparity in rotational state distributions for the two fragments may seem surprising, but these distributions are consistent with reasonable values of impact parameters in the range 1 to 2 \AA . In fact, Alexander has predicted that just such disparate correlated distributions should occur based on the *ab initio* surfaces.⁴

Table I gives propensities (i.e. branching ratios), or limits based on signal-to-noise ratios, for the spin-forbidden and spin-allowed channels

following excitation to states in the $6\nu_{\text{NH}}$ to $7\nu_{\text{NH}}$ range. These data show that the threshold for the allowed channel lies between 18190 and 18755cm^{-1} . This threshold and the energy release measured for $7\nu_{\text{NH}}$ excitation show that there is a barrier in the singlet channel of at least 680cm^{-1} , measured from the lowest quantum states $[\text{NH}(a^1\Delta, v=0, J=2)]$ of the fragments.

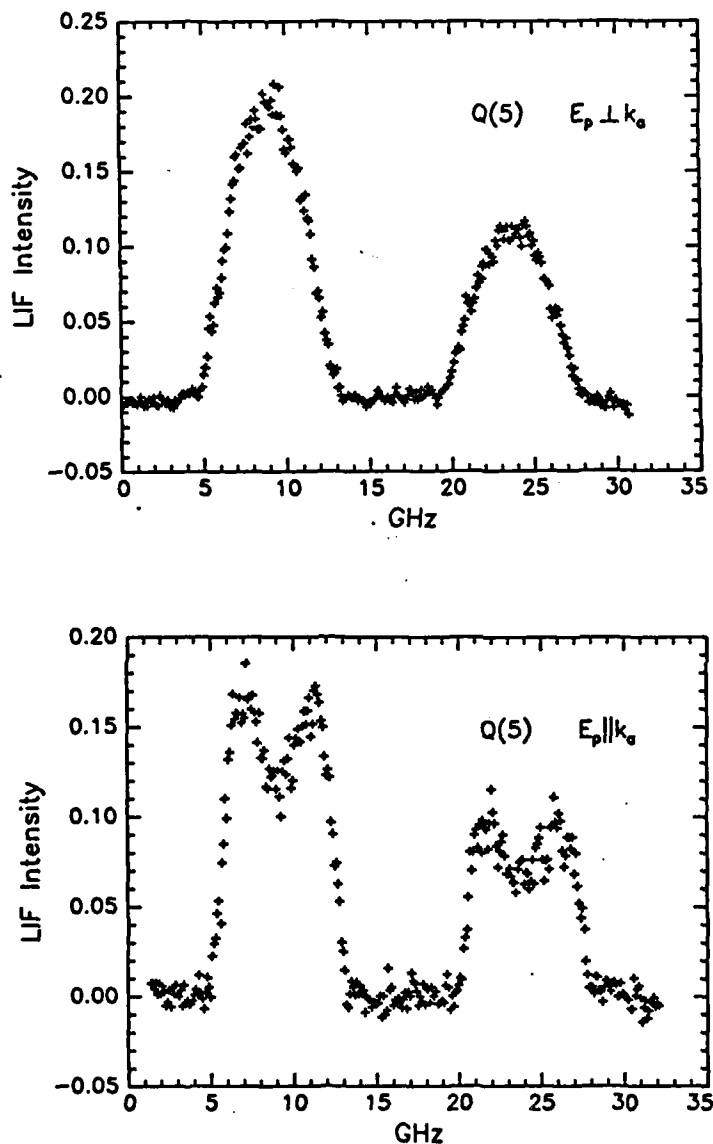


Figure 2. $\text{NH}(a^1\Delta)$ Doppler profiles following $7\nu_{\text{NH}}$ excitation. E_p is the pump polarization vector and k_p represents the probe Poynting vector. The two Λ -doublet components of the $Q(5)$ $\text{NH}(c^1\pi \leftarrow a^1\Delta)$ transition are shown.

BAND	E_{vIB}/cm^{-1}	$a^1\Delta$	$X^3\Sigma^-$
$7\nu_1$	20070	>97%	-
$6\nu_1+2\nu_4$	19740	>80%	-
$6\nu_1+\nu_2$			
$6\nu_1+\nu_4$			
$6\nu_1+\nu_5$	18190	-	>70%
$6\nu_1$	17670	-	>99%

Table I. $\text{HN}_3(X^1A') \rightarrow \text{NH } a^1\Delta/X^3\Sigma^-$ propensities.

REFERENCES

1. B.R. Foy, M.P. Casassa, J.C. Stephenson, and D.S. King, J. Chem. Phys. 89, 608 (1988).
2. B.R. Foy, M.P. Casassa, J.C. Stephenson, and D.S. King, J. Chem. Phys. 90, 7073 (1989).
3. B.R. Foy, M.P. Casassa, J.C. Stephenson, and D.S. King, J. Chem. Phys. 92, 0000 (1990).
4. M.H. Alexander, T. Hemmer, H.J. Werner and P.J. Knowles, to be published. See also the adjoining article by M.H. Alexander.
5. C.B. Moore and K. Rosengren, J. Chem. Phys. 44, 4108 (1966); D.T. Halligan, Ph.D. Thesis, Rice University (1988).
6. M.H. Alexander, H.J. Werner, and P.J. Dagdigian, J. Chem. Phys. 89, 1388 (1988).

Potential Surface Control of the Dynamics of HN₃ Decomposition and Reaction

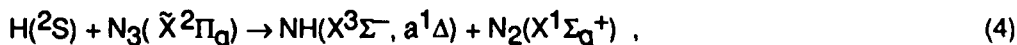
Millard H. Alexander, Department of Chemistry
University of Maryland, College Park, Maryland 20742

We have completed our *ab initio* study of the characterization of the barriers which control the lowest energy spin-allowed and spin-forbidden decomposition pathways of the HN₃ molecule, namely



Decomposition according to Eq. (1) occurs by a spin-orbit induced crossing between the singlet surface, which correlates asymptotically to N₂(X¹Σ_g⁺) + NH(a¹Δ), and the lowest triplet surface. The triplet asymptote lies below the singlet asymptote by 12,664 cm⁻¹, which is the splitting between the X³Σ⁻ and a¹Δ states of NH. In the molecular region the triplet surface correlates with an electronically excited triplet state of HN₃. The height of the barrier to spin-forbidden decomposition of HN₃ and the topology of the singlet and triplet potential energy surfaces in the neighborhood of this barrier will influence the rate at which products are formed and the degree of rotational and vibrational excitation of these products.

The relative enthalpies for dissociation of HN₃ to NH+N₂ [Eqs. (1) and (2)] or to the other spin-allowed product channel [Eq. (3)], as well as the presence of barriers in the four electronic potential surfaces which correlate with the H+N₃ asymptote, will play an important role in determining the relative branching ratios in both the UV dissociation of HN₃ and in the abstraction reaction



now under study in Dagdigan's laboratory.¹

To characterize quantitatively the behavior of the HN₃ potential surfaces in regions relevant to dissociation processes (1)-(3), it is necessary to use an *ab initio* technique which allows for the orbital distortion and changes in electron occupancies which accompany the breaking of the N-N bonds. This can be best done using multiconfiguration self-consistent-field (MCSCF)²⁻⁶ and multireference configuration-interaction (MCSCF-CI)⁷⁻⁹ techniques. We have carried MCSCF and complete active space self-consistent field (CASSCF)⁶ calculations for the HN₃ molecule at a number of geometries. The dominant configurations from the CASSCF calculations were then selected as input into subsequent MCSCF-CI calculations. The calculations we have performed within the past year are considerably more sophisticated than those described previously.¹⁰

Calculations were carried out with two different basis sets: The first consisted of, for N, six contracted *s* functions, four contracted *p* functions and two *d* functions; and, for H, six contracted *s* functions and two *p* functions — a total of 94 contracted orbitals. In the second basis set an additional *f* function was added on each N atom and an additional *d* function on the H, leading to a total of 129 contracted functions.

The valence space of the HN_3 molecule includes 13 orbitals and 16 electrons. To keep the calculations within manageable size, in the complete active space (CASSCF) calculations for HN_3 we eliminated from the active space the highest sigma antibonding orbital — a CAS(16,12) calculation, where we have introduced the notation CAS(*n,m*) with *n* and *m* denoting, respectively, the number of valence electrons and the number of orbitals in the active space. In many of the calculations we also eliminated the next highest sigma antibonding orbital, leading to CAS(16,11) calculations. Typically these CASSCF calculations involved between several thousand and several tens of thousand configuration state functions (CSF's).

Subsequently, CI calculations were carried out, using the "internally contracted" technique of Werner and Knowles,^{11, 12} and including all single and double excitations out of a reference space, built from the CAS reference by including all CSF's with coefficient greater than δ in the CAS wavefunction. We shall designate this threshold by the notation CI(δ). In most cases this threshold was taken to be 0.04, which gave rise typically to a reference space of 10–30 CSF's. These CI(0.04) calculations involved up to a total of $\approx 750,000$ contracted (12,000,000 uncontracted) configurations for the *spdf-sp* basis set (13/8/2/1 – 8/2/1).

To minimize differential correlation effects, in determining the HN–NN bond dissociation energies we have calculated the energy difference for dissociation to the lowest *spin-allowed* channel, namely $\text{N}_2 + \text{NH}(a^1\Delta)$ [Eq. (2)]. To determine the bond dissociation energies, which refer to dissociation to the ground, *spin-forbidden* channel [$\text{N}_2 + \text{NH}(X^3\Sigma^-)$], we then subtract the $\text{NH } a \leftarrow X$ excitation energy, namely $T_e = 12,664 \text{ cm}^{-1}$. Subsequent to the variational MCSCF-CI calculations, the contribution of quadruple excitations to the total CI wavefunctions of the separated and combined fragments was estimated using the approach proposed by Langhoff and Davidson.¹³

To characterize further both the singlet and triplet surfaces in the region of the lowest singlet-triplet crossing, we carried out a series of CAS(16,11)+CI(0.1) calculations with the *spd-sp* basis. While the NN and NH bond distances were held to the values in the isolated molecules, a full variation was made in the two polar angles and the NN–NH distance. Although only planar geometries were considered, a crude estimate of the dependence of the energy on the NN–NH dihedral angle was obtained by calculations for *cis* and *trans* geometries with the same NNN and NNH polar angles.

In the region of the lowest singlet and triplet crossing the singlet and triplet surfaces

were fit to a multidimensional polynomial expansion. With this fit the minimum crossing point was found to occur at a NN–NH distance of 3.354 bohr, an NNH angle of 88.7° and a *trans* NNN angle of 161°. The N–NNH and NNN–H bond lengths were equal to those corresponding to the isolated N₂ and NH molecules, namely 2.074 bohr and 1.954 bohr, respectively. In the region of the crossing between the singlet and triplet surfaces the two diabatic wavefunctions will be mixed by the small spin-orbit term in the Hamiltonian. In his recent *ab initio* calculation Yarkony¹⁴ has reported a value of 39 cm⁻¹ for this matrix element, in good agreement with our previous estimate¹⁰ of ~ 45 cm⁻¹.

The saddle point on the adiabatic surface, with respect to the energy of the HN₃ X ¹A' ground state, will define the height of the barrier for formation of N₂ (X¹Σ_g⁺) + NH (X³Σ⁻) by spin-forbidden decomposition. Our fit to the CAS(16,11)+CI(0.1) calculations with the *spd-sp* basis yields a barrier height of 13,830 cm⁻¹ above the calculated energy of HN₃ (X¹A') at the experimental equilibrium geometry. This energy difference refers to the bottom of the HN₃ well.

To obtain a more accurate value of the barrier to spin-forbidden decomposition, we have carried out a more restricted series of CAS(16,11)+CI(0.04) calculations with the both the *spd-sp* and larger *spdf-sp* bases. In these calculations the NNH and NNN angles were restricted to 90° and 165°, respectively, values close to those predicted for the minimum singlet-triplet crossing with the smaller calculation. Again, a planar geometry was assumed and the terminal NN and NH bond lengths were kept fixed at the equilibrium internuclear separations in the ground electronic states of N₂ and NH. Because these calculations allow a successively improved description of the electron correlation in the HN₃ molecule at equilibrium, relative to the more separated transition state with a correspondingly more diffuse electron distribution, the predicted barrier increases, to 14,840 cm⁻¹ for the calculations with the *spd-sp* basis and to 16,230 cm⁻¹ with the *spdf-sp* basis. In these larger calculations the point of crossing is now found to occur at an NN–NH distance of 3.520 bohr, only slightly larger than the value found with the smaller calculations. In order to investigate the effect of quadruple excitations, neglected in the present calculations, we have added the Davidson¹³ correction to the calculated energies of both the singlet and triplet states, still with the larger *spdf-sp* basis. The crossings are shifted only slightly to an NN–NH distance of 3.552 bohr and the barrier height is predicted to be 16,890 cm⁻¹, an increase of about 500 cm⁻¹ over the MCSCF-CI calculations.

To determine the thermochemical activation energy for decomposition of HN₃, it is necessary to correct the calculated barrier heights for the difference in zero-point energy of the HN₃ molecule at equilibrium and at the barrier. This correction reduces the calculated barrier heights reported above by ~ 1000 cm⁻¹. The theoretical activation energies are still notably higher than prior thermochemical estimates¹⁵⁻¹⁷

The product internal energy distributions of the nascent N_2 and NH molecules produced by the singlet-triplet crossing during the $HN_3 \rightarrow N_2 (X^1\Sigma_g^+) + NH (X^3\Sigma^-)$ decomposition will be sensitive to the forces exerted on the nascent products as the system crosses over from the $^1A'$ to the $^3A''$ surface. We predict that product recoil will be virtually uncoupled from the NNH angle, so that the large energy release which occurs as the N_2 - NH system falls down the triplet surfaces will not be transferred into rotational excitation of the NH fragment. By contrast, we predict that product recoil will be coupled with the NNN angle, so that considerable rotational excitation of the N_2 products might be expected.

We turn now to a discussion of the barrier in the spin-allowed (singlet) channel in the decomposition of HN_3 . By an extensive series of CAS(16,12) calculations with the *spd-sp* basis we were able to locate the saddle point in the singlet surface at an NN - NH distance of 4.45 bohr, an NNH angle of 85.0° and a *trans* NNN angle of 163° . As in our investigation of the barrier to spin-forbidden decomposition, we restricted our search to planar geometries and assumed that the NH and terminal NN distances were equal to the equilibrium values in the isolated molecules. Except for the larger value of the NN - NH distance, the geometry of the barrier is remarkably similar to that of the point of lowest singlet-triplet crossing. As the NN - NH distance decreases, the energy of the $10a'$ orbital, which asymptotically correlates with one of the π orbitals on NH , increases due to Pauli repulsion with the lone pair N_2 σ orbitals. Consequently, the total energy goes up slightly as the $10a'$ orbital is progressively removed from the occupied space. A more accurate value of the barrier was obtained from a restricted series of calculations with the larger *spdf-sp* basis. MCSCF-CI calculations predict the barrier height to be $1,330\text{ cm}^{-1}$, relative to the $NH(a^1\Delta)$ asymptote. With addition of the Davidson correction,¹³ the height of the saddle point is reduced slightly to $\sim 950\text{ cm}^{-1}$. Inclusion of zero-point corrections raises these estimates to $1,950$ and $1,530\text{ cm}^{-1}$, respectively. This is in good agreement with the most recent estimates from the vibrational overtone pumping experiments at NIST,¹⁸ but considerably higher than the barrier height ($450 \pm 50\text{ cm}^{-1}$) estimated from quenching experiments.¹⁹

Estimates in the literature for the dissociation energy of the HN - NN bond range from 46 kJ/mol ²⁰ to 73 kJ/mol .¹⁶ For fission of the H - N_3 single bond, our calculated dissociation energies [350 kJ/mol (MCSCF+CI), 367 kJ/mol (MCSCF+CI+Q)] are in excellent agreement with the experimental estimate of $384 \pm 21\text{ kJ/mol}$. For the multiple NN - NH bond the calculated dissociation energy [27.8 kJ/mol (MCSCF+CI with *spdf-sp* basis), 50.7 kJ/mol (MCSCF+CI+Q with *spdf-sp* basis)] agree quite well with the lower ($46 \pm 5\text{ kJ/mol}$ ²⁰) of the experimental estimates for this dissociation energy, but are somewhat lower than the semi-empirical prediction of Melius and Binkley (56.5 kJ/mol).²²⁻²⁴

In preliminary work, we have carried out extensive CASSCF calculations with the

spd-sp basis to explore the entrance channel of the $\text{H}+\text{N}_3$ reaction [Eq. (4)]. Both planar and non-planar geometries were explored. Our goal was the search for a possible geometry for a barrierless approach on the lowest triplet ($^3\text{A}''$) surface. So far such a pathway has not been found.

1. J. Chen, E. Quiñones, and P. J. Dagdigian, *J. Chem. Phys.* **XX**, xxxx (1990).
2. H.-J. Werner and W. Meyer, *J. Chem. Phys.* **73**, 2342 (1980), and references contained therein.
3. H.-J. Werner, *Adv. Chem. Phys.* **49**, 1 (1987), and references contained therein.
4. H.-J. Werner and W. Meyer, *J. Chem. Phys.* **74**, 5794 (1981).
5. H.-J. Werner and P. J. Knowles, *J. Chem. Phys.* **82**, 5053 (1985).
6. P. J. Knowles and H.-J. Werner, *Chem. Phys. Lett.* **115**, 259 (1985).
7. H.-J. Werner and E. A. Reinsch, *J. Chem. Phys.* **76**, 3144 (1982).
8. H.-J. Werner and E. A. Reinsch in *Advanced Theories and Computational Approaches to the Electronic Structure of Molecules*, edited by C. E. Dykstra (D. Reidel, 1984) p. 79.
9. H.-J. Werner and P. J. Knowles, *J. Chem. Phys.* **89**, 5803 (1988).
10. M. H. Alexander, H.-J. Werner, and P. J. Dagdigian, *J. Chem. Phys.* **89**, 1388 (1988).
11. P. K. Knowles and H.-J. Werner, *Chem. Phys. Lett.* **145**, 514 (1988).
12. H.-J. Werner and P. J. Knowles, *J. Chem. Phys.* **89**, 5803 (1988).
13. S. R. Langhoff and E. R. Davidson, *Int. J. Quant. Chem.* **8**, 61 (1974).
14. D. R. Yarkony, *J. Chem. Phys.* **92**, 320 (1990).
15. O. Kajimoto, T. Yamamoto, and T. Fueno, *J. Phys. Chem.* **83**, 429 (1979).
16. C. Paillard, G. Dupré, and J. Combourieu, *J. Chim. Phys.* **82**, 489 (1985).
17. A. I. Demin, I. S. Zaslanko, S. M. Kogarko, and E. V. Mossuhkin, *Kinet. Katal.* **14**, 283 (1973), (in Russian, as cited in Ref. 16).
18. D. S. King, private communication, 1990.
19. H. Nelson, J. R. McDonald, and M. H. Alexander, *J. Phys. Chem.* **XX**, xxxx (1990).
20. H. Okabe, *Photochemistry of Small Molecules* (Wiley, New York, 1978).
21. M. J. Pellerite, R. L. Jackson, and J. I. Brauman, *J. Phys. Chem.* **85**, 1624 (1981).
22. C. F. Melius and S. Binkley in *21st Symposium (Intl) on Combustion* (The Combustion Institute, Pittsburgh, 1986) p. 1953.
23. P. Ho, M. E. Coltrin, J. S. Binkley, and C. F. Melius, *J. Am. Chem. Soc.* **89**, 4647 (1985).
24. C. F. Melius and S. Binkley in *20th Symposium (Intl) on Combustion* (The Combustion Institute, Pittsburgh, 1984) p. 575.

DYNAMICS ON HN₃ POTENTIAL ENERGY SURFACES

The H + N₃ Reaction and the Photodissociation of HN₃

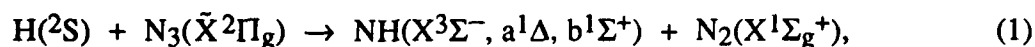
Paul J. Dagdigan

Department of Chemistry

The Johns Hopkins University

Baltimore, MD 21218.

We have nearly completed our study of the NH product state distribution from the H + N₃ reaction:¹



This reaction has been studied in a molecular beam scattering gas arrangement, and the product NH populations in specific rovibronic/fine-structure states were determined by laser fluorescence excitation. A beam of hydrogen atoms, prepared in a microwave discharge source, impinged on a flow of azide radicals, which were produced by means of the F + HN₃ prereaction in a discharge flow system mated to the scattering chamber.

We have observed NH(X³Σ⁻) products in the v=0 and 1 vibrational levels and NH(a¹Δ) in v=0 to 2. The relative cross sections for formation of the various a¹Δ vibrational levels were found to equal 1 : 1.07±0.12 : 1.8±0.8 : ≤1.7 for v=0 through 3, inclusive, while the X³Σ⁻ v=0 to v=1 population ratio was determined to be 1 : 0.012±0.003. Our detection sensitivity for the higher vibrational levels is poor because of predissociation in the excited NH electronic states. The NH product in either electronic state has relatively little rotational excitation. By summing the populations in all rovibrational levels, the NH product a¹Δ to X³Σ⁻ electronic state branching ratio was determined to be 4.6±1.4. An upper limit of ≤0.02 was also derived for the ratio of the b¹Σ⁺ v=0 to a¹Δ v=0 populations. This branching ratio could be affected by collisional relaxation of the NH product, even though the experiments were conducted at scattering chamber pressures of 0.2 mTorr. To check this point, we are carrying out further experiments in which the pumping speed on the scattering chamber has been increased in order to reduce the residence time in the chamber by a factor of 2. Preliminary results

suggests that relaxation is not strongly perturbing the nascent electronic state branching ratio.

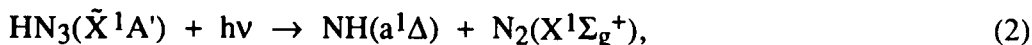
There are 4 potential energy surfaces correlating with the reactants of reaction (1). If reaction proceeds through the strongly attractive lowest surface, which includes the $\text{HN}_3(\tilde{\text{X}}^1\text{A}')$ minimum, then we expect preferential formation of $\text{NH}(\text{a}^1\Delta)$. Singlet-triplet mixing in the exit channel would provide a mechanism for production of $\text{NH}(\text{X}^3\Sigma^-)$, as in the decomposition studies of vibrationally excited HN_3 being carried out at NIST.² An alternative direct pathway for formation of $\text{NH}(\text{X}^3\Sigma^-)$ would be reaction along the $\text{HN}_3^3\text{A}''$ surface, which correlates directly with $\text{NH}(\text{X}^3\Sigma^-) + \text{N}_2(\text{X}^1\Sigma_g^+)$. Our large observed $\text{X}^3\Sigma^-$ yield suggests that this product is formed directly on the $^3\text{A}''$ surface, rather than by spin-orbit mixing in the exit channel. This would imply the absence of a substantial barrier in the entrance channel of the $^3\text{A}''$ surface. In an collaborative theoretical investigation, Alexander³ is presently carrying out a fairly exhaustive calculation of $\text{H}-\text{N}_3$ potential energy surfaces, involving both planar and nonplanar geometries, to search for barriers. The negligible yield of $\text{NH}(\text{b}^1\Sigma^+)$ can be explained by the fact that the $^1\text{A}'$ surface leading to $\text{NH}(\text{b}^1\Sigma^+) + \text{N}_2(\text{X}^1\Sigma_g^+)$ products does not cross any of the potential energy surfaces arising from the $\text{H} + \text{N}_3$ reactants.

It is interesting to note that the $\text{NH}(\text{a}^1\Delta)$ product of reaction (1) is found to be substantially vibrationally excited, with *ca.* 31% of the available energy in this channel appearing as vibrational excitation. The $\text{H} + \text{N}_3$ reaction is an example of a **L + HH** mass combination, whose product energy disposal is believed to be particularly sensitive to the degree of attractive energy release.⁴ Because of the strongly attractive nature of the $\text{HN}_3 \tilde{\text{X}}^1\text{A}'$ surface, we expect considerable vibration excitation in $\text{NH}(\text{a}^1\Delta)$, as observed. In contrast to the large degree of vibrational excitation found in $\text{NH}(\text{a}^1\Delta)$, the ground state $\text{NH}(\text{X}^3\Sigma^-)$ product was found to possess little vibrational excitation. This result can be rationalized if the reaction were to proceed on the $^3\text{A}''$ surface since this surface, as least in the $\text{NN}-\text{NH}$ exit channel, is expected to be repulsive in character.⁵

As an extension of our studies on $\text{H} + \text{N}_3$, we are now studying the analogous $\text{H} + \text{NCO}$ reaction, which is substantially less exothermic than reaction (1). We have observed

both $\text{NH}(\text{X}^3\Sigma^-)$ and $\text{NH}(\text{a}^1\Delta)$ products and have obtained a preliminary value of the $\text{X}^3\Sigma^-$ to $\text{a}^1\Delta$ branching ratio of $(2-4) \times 10^{-4}$. The formation of $\text{NH}(\text{a}^1\Delta)$ is significantly endothermic, and the small branching ratio reflects this.

We have also measured the rotational state distributions of the fragments from the photodissociation of HN_3 near 283 nm in a one-color photolysis/ionization study:⁶



At this photolysis wavelength, we are most likely accessing the first excited $^1\text{A}''$ electronic state of HN_3 . The internal state distribution of the products of process (2) has been determined by resonant-enhanced multiphoton ionization (REMPI) detection using a time-of-flight mass spectrometer. Nitrogen molecules were studied by 2+2 REMPI through the $\text{a}^1\Pi_g$ electronic state, while $\text{NH}(\text{a}^1\Delta)$ was detected through a newly discovered⁷ $^1\Delta$ Rydberg state. The N_2 fragments were observed in the $v=0$ vibrational manifold and were found to be highly rotationally excited, with a most probable J of 56 and an average rotational excitation of 0.79 eV. This large degree of rotational excitation is consistent with a linear-to-bent transition for the NNN framework of this 16-valence electron molecule. The μ - J correlation for N_2 was found to be positive, indicating that J tends to be parallel to the transition dipole. Such a positive correlation is consistent with a perpendicular transition in which the plane of rotation of the N_2 molecule lies in the plane of the NNN framework of the dissociating molecule. A search was carried out to observe vibrationally excited N_2 products; some weaker REMPI lines were observed which could be due to $\text{N}_2(v=1)$, but the low signal-to-noise ratio prevented a positive assignment.

Relatively little rotational energy was found in the NH product, as has been observed at shorter photolysis wavelengths by laser fluorescence detection.^{8,9} It is interesting to note that, in contrast with the N_2 fragment, the μ - J correlation for NH is found to be relatively small.⁹ This suggests that nonplanar geometries must be important in the dissociation process since otherwise the planes of rotation of N_2 and NH should be the same. From the observed polarization dependence of the NH REMPI mass peak profiles, the recoil anisotropy parameter β (μ - v correlation) was found to be *ca.* -0.5 at low J , consistent with a perpendicular electronic transition. For higher J_{NH} , β was seen to

increase and become positive by $J=10$. One rationalization for the change in the sign of β could be the participation of two overlapping electronic transitions. However, the lowest excited singlet state of HN_3 is well separated from the higher states. Perhaps the variation of β with J_{NH} is a further manifestation of the role of nonplanar geometries, although this needs to be worked out in detail. From the width of the NH REMPI mass peaks, we estimate the relative translational energy to be *ca.* 1.4 ± 0.4 eV. Thus, the bulk of the available energy in this photodissociation process appears as product recoil and N_2 rotational excitation.

Very recently, we have begun to investigate the analogous photodissociation process in methyl azide, CH_3N_3 . A strong mass 28 (N_2^+) is observed, as well as several masses. However, no structure as a function of wavelength, as would be expected for N_2 REMPI lines, has been thus far observed. Our other interest in studying this molecule lies in the possibility of detecting the singlet form of CH_3N , which is expected¹⁰ to isomerize to CH_2NH . Triplet bands of CH_3N , analogous to the well known A-X bands of NH, have been discovered by Carrick and Engelking.¹¹

-
1. J. Chen, E. Quiñones, and P. J. Dagdigian, *J. Chem. Phys.* **90**, 7603 (1989); (submitted).
 2. B. R. Foy, M. P. Casassa, J. C. Stephenson, and D. S. King, *J. Chem. Phys.* **89**, 608 (1988); B. R. Foy, M. P. Casassa, J. C. Stephenson, and D. S. King, *ibid.* **90**, 7037 (1989); B. R. Foy, M. P. Casassa, J. C. Stephenson, and D. S. King, *ibid.* **XX**, XXXX (1990).
 3. M. H. Alexander (unpublished).
 4. P. J. Kuntz, E. M. Nemeth, J. C. Polanyi, S. D. Rosner, and C. E. Young, *J. Chem. Phys.* **44**, 1168 (1966).
 5. M. H. Alexander, H.-J. Werner, and P. J. Dagdigian, *J. Chem. Phys.* **89**, 1388 (1988).
 6. J.-J. Chu, P. Marcus, and P. J. Dagdigian, *J. Chem. Phys.* (submitted).
 7. R. D. Johnson III and J. W. Hudgens, *J. Chem. Phys.* (submitted).
 8. F. Rohrer and F. Stuhl, *J. Chem. Phys.* **88**, 4788 (1988).

9. K.-H. Gericke, R. Theinl, and F. J. Comes, Chem. Phys. Lett. (submitted).
10. J. Demuynck, D. J. Fox, Y. Yamaguchi, and H. F. Schaefer, J. Am. Chem. Soc. **102**, 6204 (1980).
11. P. G. Carrick and P. C. Engelking, J. Chem. Phys. **81**, 1661 (1984); see also P. G. Carrick, C. R. Brazier, P. F. Bernath, and P. C. Engelking, J. Am. Chem. Soc. **109**, 5100 (1987).

Theoretical Investigation of Energy Storage
in Atomic and Molecular Systems*

H. H. Michels and J. A. Montgomery, Jr.
United Technologies Research Center
East Hartford, CT 06108

ABSTRACT

Theoretical electronic structure calculations are being carried out for several high energy species that are attractive candidates for advanced chemical propulsion systems. Using deliverable specific impulse and storability as the major criteria for the evaluation of new oxidizers or fuels, primary consideration is being given to ground state molecular structures, of low molecular weight, which exhibit a high positive heat of formation. Calculations to date have been carried out on: 1) light element C_{3v} and C_{2v} structures (H_4 , Li_3H , LiH_3 , Li_4); 2) azide-like structures (FN_3 , α - N_2O_2 , $FNCO$, CO_3 , HN_3 , $FNBF$, ClN_3); 3) cyclic boron structures (B_3H_3 , B_2H_2NH); and 4) hypervalent structures (NF_5 , PF_5 , OF_4). During the past year we have focussed attention on systems with potential as advanced oxidizers.

An *ab initio* study of the electronic structure of NF_5 and PF_5 has been carried out using Møller-Plesset perturbation theory. Optimized geometries were calculated at the SCF and MP2 levels of theory using several basis sets, ranging from 6-31G to 6-311+G*. A vibrational analysis indicates that NF_5 , in D_{3h} symmetry, has all real frequencies, even if d orbital contributions are set to zero. Dissimilar N-F bond lengths ($r_{eq} = 1.38 \text{ \AA}$, $r_{ax} = 1.58 \text{ \AA}$) are found, in contrast to PF_5 which exhibits nearly equal equatorial and axial bond lengths. A topological analysis of the calculated charge distribution in NF_5 indicates true pentavalent coordination, suggesting that synthesis of hypervalent compounds of first row-atoms may be possible. Our best estimate of the heat of formation of $NF_5(g)$ is $\Delta H_f^\circ(0 \text{ K}) = +25.1 \text{ kJ/mol}$.

The heats of formation of NF , N_3 , FN_3 , NCO and $FNCO$ have been calculated using Pople's G1 method. We find $\Delta H_f^\circ(0 \text{ K}) = +231.4$, $+450.3$, $+319.3$, $+127.4$ and -27.6 kJ/mol , respectively. These values are compared with data from several experimental studies.

Performance calculations have been carried out for the following propellant systems:

1) $Li_3H/H_2/O_2(F_2)$; 2) $H_2/F_2/NF_5$; 3) N_2H_4/NF_5 ; 4) B_5H_9/NF_5 . Most of these systems offer significant I_{sp} improvement over baseline comparisons.

*Supported in part under AFAL Contract F04611-86-C-0071.

DISCUSSION

Hypervalent Compounds

In order to assess the stability of NF_5 , parallel *ab initio* calculations of NF_5 and PF_5 were carried out at both the SCF and MP2 levels of theory, using several different basis sets. All calculations were performed using CADPAC,¹ which can perform geometric first and second derivative calculations analytically at both the SCF and MP2 levels for closed shell structures. Optimized NF_5 and, for comparison, PF_5 geometries were calculated at both the SCF and MP2 levels of theory. Harmonic vibrational frequencies were subsequently computed at the SCF and MP2 stationary points.

The results of our extensive geometry optimization calculations are given in Table 1. At the SCF level, we find that the optimum geometry is sensitive to the treatment of polarization effects on both the central coordinating atom and the fluorine ligands. Slightly extended axial and equatorial bond lengths are predicted for NF_5 if d functions are omitted entirely. This effect is somewhat larger (~ 0.1 Å) in the case of PF_5 . Introduction of d functions on the ligands alone, which mainly causes polarization of the fluorine charge, is the dominant feature in shortening the bond lengths in both NF_5 and PF_5 .

As indicated in Table 1, the optimum SCF geometry is not overly sensitive to either the magnitude of the d exponent or to the addition of diffuse orbitals, which permit a more flexible description of ligand charge transfer. However as shown in Table 2, the calculated harmonic frequencies for NF_5 are sensitive to the chosen basis set at the SCF level of theory. In particular, the asymmetric axial stretch $\omega_3(a_2'')$ is very sensitive to the basis set. The addition of diffuse functions results in the prediction of a very low or even imaginary frequency for the $\omega_3(a_2'')$ mode. At the MP2 level of theory, more consistent results are obtained for this mode.

In an attempt to understand the dependence of the $\omega_3(a_2'')$ mode of NF_5 on the diffuseness of the basis, several calculations of NF_5 were carried out in C_{3v} symmetry, corresponding to displacement along the s_3 coordinate. We find a C_{3v} stationary point at the SCF/6-31G* level of theory which is only 0.1 eV higher than the corresponding D_{3h} structure. A harmonic vibrational analysis shows that the C_{3v} structure has all real frequencies with the a_1 axial stretch mode corresponding to the weakest displacement. This observation suggests that NF_5 , at this level of theory, has a small barrier along the s_3 coordinate displacement between the nearly isoenergetic and stationary D_{3h} and C_{3v} structures. At the SCF/6-311+G* level of theory, the C_{3v} structure actually lies lower in energy than the D_{3h} structure and exhibits all real frequencies. With this basis the D_{3h} structure is a saddle point with an imaginary frequency corresponding to the asymmetric axial stretch. This is the normal coordinate displacement toward the C_{3v} structure indicating that with the 6-311+G* basis, no barrier exists between the D_{3h} and C_{3v} structures.

To test the stability of the C_{3v} structure at a higher level of theory, MP2 calculations were carried out with the 6-31G* and 6-311+G* basis sets. The starting geometry corresponded to the

optimized C_{3v} structure found at the SCF level of theory. In both cases, the optimization proceeded uniformly to the D_{3h} structure. A comparative examination of the SCF/6-31G* charge distributions in the C_{3v} and D_{3h} structures, as calculated from a Mulliken analysis, indicates that the C_{3v} structure is very ionic $[(NF_4)^{+.9}F_{ax}^{-.9}]$ relative to the more covalently bonded D_{3h} structure. At the MP2 level of theory, the ionic C_{3v} structure does not represent a stationary point, and lies higher in energy than the D_{3h} structure. Systematic geometry optimization at the MP2 level always yields the lower energy, and more covalent, D_{3h} structure.

A topological analysis of the calculated charge distribution clearly indicates that NF_5 is a vibrationally stable molecule which exhibits true pentavalent bond coordination. The calculated vibrational spectrum of NF_5 is similar to that found for PF_5 . The most significant difference lies in the a_2'' modes, where the short NF_5 equatorial bond length reverses the strengths of the asymmetric axial stretch (ω_3) and symmetric out-of-plane bend (ω_4) relative to that found in PF_5 , where the axial and equatorial bond lengths are nearly equivalent. As discussed above, the weaker $\omega_3(a_2'')$ asymmetric stretch is poorly represented at the SCF level of theory where there exists a stability competition between the D_{3h} and C_{3v} structures. The longer axial bond in NF_5 , relative to the shorter (1.38 Å) equatorial bond, is also reflected in a comparison of the a_1' symmetric stretch modes. In both NF_5 and PF_5 the symmetric equatorial stretch (ω_1) is stronger than the symmetric axial stretch (ω_2), but their frequencies are more nearly equal in PF_5 .

Azide Thermochemistry

The thermochemistry of azide-like molecules has been examined using the Pople G1 method. In this method, separate contributions to the QCISD(T)/6-311G**//MP2(FU)/6-31G* energy are evaluated to account for: basis set diffuseness (+), extended polarization (2df) and an empirical correction for basis set incompleteness (HLC). In Table 3, we list the calculated heats of formation for several azides and constituent components. Good agreement with experiment is found except for NCO. The thermochemistry of this radical has been indirectly determined by several experiments, which seem to bracket the heat of formation as $+172 \pm 17$ kJ/mol. Further comparative studies of NCO/HNCO and N_3 /HN $_3$ are in progress. All of our calculations predict a repulsive barrier for azide decomposition to singlet products. The calculated long range barriers from products: $NF[a^1\Delta] + N_2[X^1\Sigma_g^+]$ and $NF[a^1\Delta] + CO[X^1\Sigma^+]$, to the transition state geometry of these azides are similar (~ 1500 cm $^{-1}$), in agreement with the qualitative explanation of M. Alexander.²

Performance Calculations

The following propellant systems have been optimized and compared with baseline systems, wherever possible:

1. $Li_3H/H_2/O_2(F_2)$ as a hybrid. The baseline is $LiH/H_2/O_2(F_2)$.

2. $\text{H}_2/\text{F}_2/\text{NF}_5$ as a possible hybrid. The baseline is H_2/F_2 .
3. $\text{N}_2\text{H}_4/\text{NF}_5$ as an earth storable system. The baseline is $\text{N}_2\text{H}_4/\text{N}_2\text{F}_4$.
4. $\text{B}_5\text{H}_9/\text{NF}_5$ as a space storable system. The baseline is $\text{B}_5\text{H}_9/\text{N}_2\text{F}_4$.

With the exception of the $\text{H}_2/\text{F}_2/\text{NF}_5$ system, significant I_{sp} improvements were found over the baseline comparisons. The optimum I_{sp} values are compared in Table 4. These calculations indicate that the hybrid $\text{Li}_3\text{H}/\text{H}_2/\text{O}_2$ (cryogenic) and $\text{N}_2\text{H}_4/\text{NF}_5$ (earth storable) systems look promising.

-
- 1 R. D. Amos and J. E. Rice, CADPAC: The Cambridge Analytic Derivatives Package, Issue 4.0 (Cambridge 1987).
 - 2 M. H. Alexander, *Ab Initio* Study of the Energetics of the Decomposition of HN_3 and N_3 , Proc. Informal Conf. on Chem. of Energetic Azides, Univ. of Denver (1989).
 - 3 H. Kurimura, S. Yamamoto, T. Egawa and K. Kuchitsu, J. Mol. Struct. **140**, 79 (1986).
 - 4 A. D. McLean and G. S. Chandler, J. Chem. Phys. **72**, 5639 (1980).
 - 5 C. J. Marsden, J. Chem. Phys. **87**, 6626 (1987).
 - 6 T. Shimanouchi, J. Phys. Chem. Ref. Data **6**, 993 (1977).
 - 7 K. Du and D. W. Setser, Chem Phys. Lett. **153**, 393 (1988).
 - 8 JANAF Thermochemical Tables, 3rd Ed., J. Phys. Chem. Ref. Data, **14**, Supp.1 (1985).
 - 9 M. J. Pellerite, R. L. Jackson and J. I. Brauman, J. Phys. Chem. **85**, 1624 (1981).
 - 10 D. W. Setser, J. Phys. Chem. **91**, 451 (1987).
 - 11 J. I. Brauman, R. L. Jackson and M. J. Pellerite, J. Amer. Chem. Soc. **103**, 1802 (1981).
 - 12 B. L. Evans and A. D. Yoffe, Chem. Rev. **59**, 515 (1959).
 - 13 D. Patel, A. T. Pritt and D. J. Benard, J. Phys. Chem. **90**, 1981 (1986).
 - 14 H. Okabe, J. Chem Phys. **53**, 3507 (1970).
 - 15 X. Liu and R. D. Coombe, J. Chem. Phys. **91**, 7543 (1989).
 - 16 B. J. Sullivan, G. P. Smith and R.D. Crosley, Chem. Phys. Lett. **96**, 307 (1983).
 - 17 G. S. Chandler, J. Phys. Chem. **90**, 6184 (1986).

Table 1. Gradient Optimized D_{3h} Structures and Energies for NF_5 and PF_5 .

Theory	d-exponent		r _{eq}	r _{ax}	Energy
	N, P	F			
NF ₅					
SCF/6-31G	—	—	1.3860	1.5926	-550.9366 0111
SCF/6-31G(d on F)	—	0.80	1.3470	1.5447	-551.0573 9175
SCF/6-31G*	0.80	0.80	1.3267	1.5312	-551.1038 5648
SCF/6-31G(d) (opt d)	0.94	0.76	1.3260	1.5310	-551.1048 2296
SCF/6-31+G*	0.80	0.80	1.3223	1.5473	-551.1267 9968
SCF/6-31+G(d) (opt d)	0.94	0.76	1.3214	1.5479	-551.1267 0497
SCF/6-311G	—	—	1.3765	1.5979	-551.1161 2362
SCF/6-311G*	0.913	1.75	1.3151	1.5413	-551.2540 3395
SCF/DZP	0.80	1.20	1.3195	1.5458	-551.2624 0983
SCF/6-311+G*	0.913	1.75	1.3121	1.5538	-551.2688 4626
SCF/DZP (opt d)	0.76	1.13 (ax)	1.3178	1.5509	-551.2712 4802
		0.66 (eq)			
SCF/DZP+ (opt d)	0.76	1.13 (ax)	1.3156	1.5563	-551.2761 3725
		0.66 (eq)			
SCF/6-311G(2d)	1.63	1.32	1.3148	1.5428	-551.2927 9207
	0.54	0.44			
MP2/6-31G	—	—	1.5069	1.6240	-551.7849 5983
MP2/6-31G*	0.80	0.80	1.4098	1.5472	-552.2287 8033
MP2/6-31+G*	0.80	0.80	1.4073	1.5718	-552.2831 5495
MP2/6-31G(d) (opt d)	0.93	1.47	1.3962	1.5538	-552.3024 0540
MP2/DZP	0.80	1.20	1.4034	1.5652	-552.4876 5451
MP2/DZP+	0.80	1.20	1.3967	1.5768	-552.5178 3126
MP2/6-311G*	0.913	1.75	1.3908	1.5552	-552.6887 3276
MP2/6-311+G*	0.913	1.75	1.3831	1.5816	-552.7179 8409
PF ₅					
SCF/6-31G	—	—	1.6330	1.6547	-837.7343 7618
SCF/6-31G(d on F)	—	0.80	1.5591	1.5863	-837.9178 1375
SCF/6-31G*	0.55	0.80	1.5350	1.5679	-838.0507 2370
SCF/6-311G*	0.55	1.75	1.5296	1.5636	-838.1865 0668
MP2/6-31G*	0.55	0.80	1.5660	1.5950	-839.0575 0339
MP2/6-311G*	0.55	1.75	1.5587	1.5892	-839.5910 4039
Experiment [3]			1.529	1.576	

Energies (hartrees), distances (Å). r_{eq} = N-F equatorial bond length, r_{ax} = N-F axial bond length.

Note that for P, the 6-311G* basis is the McLean-Chandler⁴ (12s9p/6s5p) contraction with coefficients optimized for P^- .

Table 2. Calculated Harmonic Frequencies for NF_5 and PF_5 in D_{3h} Symmetry.

Species:	Frequencies, ω_i (cm^{-1})							
	a_1' s_1 -sym. eq. stretch	a_1' s_2 -sym. axial stretch	a_2'' s_3 -asym. axial stretch	a_2'' s_4 -sym. out-of-plane bend	e' s_5 -asym. eq. stretch	e' s_6 -axial bend	e' s_7 -eq. bend	e'' s_8 -asym. bend
Theory								
<u>NF_5</u>								
SCF/6-31G	744	480	574	743	1184	560	235	568
SCF/6-31G(d on F)	837	495	391	787	1345	627	261	632
SCF/6-31G*	857	509	459	828	1352	656	276	663
SCF/6-31G(d) (opt d)	858	509	452	828	1351	656	277	664
SCF/6-31+G*	855	489	155	802	1353	649	284	652
SCF/6-31+G(d) (opt d)	855	488	103	801	1351	647	284	657
SCF/6-311G	762	442	472	718	1230	566	243	574
SCF/6-311G*	867	481	48	829	1373	659	288	669
SCF/DZP	862	491	179	816	1360	654	287	660
SCF/6-311+G*	863	469	345i	811	1368	651	291	659
SCF/DZP (opt d)	866	500	234	809	1367	653	289	656
SCF/DZP+ (opt d)	868	494	101i	803	1375	652	291	651
SCF/6-311G(2d)	863	499	233	821	1354	656	286	664
MP2/6-31G	565	394	498	826	786	447	112	469
MP2/6-31G*	690	426	614	936	969	551	173	578
MP2/6-31+G*	672	383	584	890	941	534	177	560
MP2/6-31G(d) (opt d)	692	394	603	922	975	552	187	587
MP2/DZP	676	389	593	918	943	541	182	574
MP2/DZP+	678	369	581	886	948	537	188	566
MP2/6-311G*	691	385	593	912	980	553	188	589
MP2/6-311+G*	681	346	561	872	970	538	194	569
MP2/6-311G* (scaled)	637	355	547	893	934	527	184	577
<u>PF_5</u>								
SCF/6-31G	760	702	1049	492	1039	458	164	427
SCF/6-31G(d on F)	823	715	1058	577	1082	532	186	532
SCF/6-31G*	874	725	1081	598	1122	558	194	530
MP2/6-31G*	808	688	1024	556	1054	517	180	491
Experiment : ω_i [5]	825	657	956	578	1039	536	178	523
ν_i [6]	816	648	946	575	1026	533	174	520

^a The symmetry coordinates, s_i , describe the largest contribution to a given normal mode. All frequencies were calculated at the corresponding optimized geometries of Table 1.

Table 3. Calculated Azide Thermochemistry - G1 Theory

$\Delta H_f^0(0 \text{ K}), \text{ kJ/mol}$			
<u>Molecule</u>	<u>Theory</u>	<u>Experiment</u>	
NF	+231.4	>208	Setser ⁷
	+229.6 (QCI-CBS)	+249	JANAF ⁸
N ₃	+450.3	+469±20	Brauman ⁹
		>475	Setser ¹⁰
N ₃ ⁻	+192.5	+201±8	Brauman ¹¹
HN ₃	+300.4	+300	Evans ¹²
FN ₃	319.4	+544±20	Benard ¹³
NCO	+127.4	+151	Setser ⁷
		+154	Okabe ¹⁴
		+155	Coombe ¹⁵
		+201	Sullivan ¹⁶
HNCO	-110.5	+3	Chandler ¹⁷
		-104.2 -12	
FNCO	-27.6	+11	Setser (est.) ⁷

Table 4. Comparison of Optimum I_{sp} .

Species	I_{sp} (sec)	Conditions
$Li_3H/H_2/O_2$	455.9	@ $P_c = 800$ psia, $A/A^* = 20:1$
$LiH/H_2/O_2$	441.2	@ $P_c = 800$ psia, $A/A^* = 20:1$
$Li_3H/H_2/F_2$	492.6	@ $P_c = 800$ psia, $A/A^* = 20:1$
$LiH/H_2/F_2$	464.0	@ $P_c = 800$ psia, $A/A^* = 20:1$
H_2/NF_5	426.0	@ $P_c = 1000$ psia, $P_{ex} = 14.7$ psia
H_2/F_2	411.8	@ $P_c = 1000$ psia, $P_{ex} = 14.7$ psia
$H_2/NF_5/F_2$ (50% NF_5)	463.7	@ $P_c = 800$ psia, $A/A^* = 20:1$
H_2/F_2	465.6	@ $P_c = 800$ psia, $A/A^* = 20:1$
N_2H_4/NF_5	351.6	@ $P_c = 1000$ psia, $P_{ex} = 14.7$ psia
N_2H_4/N_2F_4	334.3	@ $P_c = 1000$ psia, $P_{ex} = 14.7$ psia
B_5H_9/NF_5	350.5	@ $P_c = 1000$ psia, $P_{ex} = 14.7$ psia
B_5H_9/N_2F_4	332.3	@ $P_c = 1000$ psia, $P_{ex} = 14.7$ psia

HEDM90.2/90

PROPERTIES OF SMALL ENERGETIC CLUSTERS *

Koop Lammertsma

Department of Chemistry
University of Alabama at Birmingham
Birmingham, Alabama 35294

Abstract

Theoretical ab initio calculations have been carried out on tetraatomic systems in the search for advanced chemical propellants. In our approach to identify systems that have revolutionary specific impulses ($I_{sp} > 500$ sec) we concentrated on systems that contain light elements with high combustion energies, that are hydrogen deficient, that have inverted geometries of tricoordinated elements, and that can display bond stretch isomerism. It is well established that ring strain in a system can increase significantly its heat of formation. Inverting the geometry of a trivalent carbon can be accomplished by adequate electron deficient bridging ligands. A case in point is the the rhombic $C_4H_2^{2+}$ dication. We have revisited this system and the parent rhombic C_4 to describe these molecules more accurately at higher levels of theory. Recently we have determined that in rhombic structures of mixed elements (i.e. C_2Si_2 and B_2Be_2) bond stretch isomerism may occur to render kinetically stable species of high energy. Several new systems are now reported. These are C_3Si , C_3BH , and C_3Be , which display bonding patterns that are different from each other. Finally, three-dimensional bond stretch isomerism in $B_2Al_2H_2$ is presented in this summary.

Methods

The calculations have been carried out with Pople's GAUSSIAN 88 program and GAMESS. All structures reported here were optimized at the MP2/6-31G* level of theory and found to be vibrationally stable with only positive eigenvalues of the Hessian matrix at that level. Relative energies of isomeric molecules were determined by single point

* Supported under AFAL Contract FO4611-86-K-0073

calculations at MP4, which include single, double, triple, and quadruple substitutions. GVB-PP calculations did not give any indication for biradical character of the bond stretch isomers.

The electronic properties and bonding patterns were investigated by analysis of the electron density (ρ) properties of the molecules. This was done with the aid of Bader's PROAIM and EXTREME programs. In short the properties of molecular charge distributions, based on Bader's topological analysis of density of atoms in molecules, are summarized in terms of its critical points. These are points where the charge density is a maximum, a minimum, or a saddle of the gradient path of the gradient vector field, i.e. $\nabla\rho = 0$. A critical point is characterized by the signs of its three principle curvatures of ρ i.e. $\lambda_1, \lambda_2, \lambda_3$. A bond critical point (3,-1) has a minimum (positive curvature) in ρ on the bond path connecting two nuclei and two negative curvatures in orthogaonal planes; the charge density has the appearance of a saddle. Ring critical points (3,+1) have one negative and two positive curvatures. Three positive curvatures (3,+3) define a minimum (cage critical point). The (3,-3) critical point represents atoms or nuclear attractors where all curvatures are positive. In the figures presented, the connectivity of atoms via bond critical points are given in plots of the gradient vector field, (which give the separation of atoms in molecules by "zero flux" lines) and the Laplacian field of the charge density $\nabla^2\rho$ (the sign of which characterizes the polarity of a bond; i.e. dashed lines indicate relative accumulation of charges and solid contours represent areas of relative charge depletion.

Discussion

The C_4 species has been generated by a variety of methods. Based on ir vibrations a linear structure was assigned. Slanina and Zahradnik were the first to suggest that the singlet rhombic form instead of the linear triplet is the ground state structure for C_4 . Vibrational calculations at MP2/6-31G* suggest that the observed absorption at 1544 cm^{-1} , previously assigned to the linear C_5 molecule, results from rhombic C_4 . The possible coexistence of linear and rhombic C_4 emphasizes the special stabilization of the cyclic form and highlights our concept of inverted tricoordinate carbons. A variety of theoretical calculations have been reported on C_4 . We have calculated this molecule at various levels of theory and find transannular CC separations of 1.457 (HF/6-31G*), 1.523 (MP2(Full)/6-31G*), and 1.546 Å (MP4SDTQ/6-311G*). Clearly, this rhombic structure is very sensitive to the theoretical method employed. Previously, we have noted that the transannular interaction in this molecule has a negative Mulliken overlap population

at HF/6-31G*. However, the electron density analysis indicates the presence of a bond critical at the center of the structure, but its high ellipticity of 296 and its 0.06 Å separation with the two ring critical points illustrate that the center of C₄ is near a catastrophe in the HF/6-31G* charge distribution. Indeed at the correlated level a ring critical point is found in the center of the molecule. It is interesting to note that a bond critical point is found between the inverted tetracoordinate carbons of [1.1.1]propellane which are separation of 1.592 Å (MP2/6-31G*). However, analysis of C₄ at the higher MP4/6-311G* level gives again a bond critical point, although its ellipticity has a high value of 60, which is indicative of a near catastrophe point. The presence of the bond critical point and the two nearby located ring critical points can be inferred from the displayed Laplacian. Apparently, the electron density analysis gives a consistent picture rather independent of the theoretical level. It is then concluded that rhombic C₄ contains a short transannular CC separation, which is at the length of making (or breaking) a CC bond. Small perturbations are expected to have a significant influence on the character of this rhombic structure. This is evident from the mono- and diprotonations to C₄H⁺ and C₄H₂²⁺, respectively. The MP2/6-11G* transannular CC separation in the monocation is 1.641 Å and that in the dication amounts to 1.789 Å, neither of which contains a bond critical point. It is relevant to note that the coexistence of rhombic and triplet linear C₄H₂²⁺ can be inferred from the mass spectroscopic charge separation reaction.

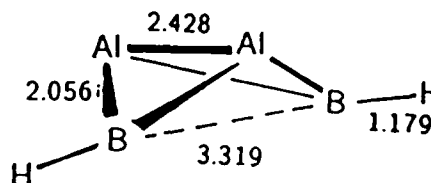
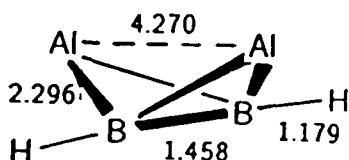
The Mulliken overlap population between rhombic bridgehead carbons varies significantly with the nature of the bridging ligands even though the CC separations remain rather constant. We have investigated whether this phenomenon can be used to increase the energy content of tetraatomics. This led us to bond stretch isomerism. In the case of C₂Si₂ two rhombic forms exist that are minima on the potential energy surface. The global minimum has a transannular CC bond of 1.453 Å (MP2/6-31G*) and peripheral C-Si bonds of 1.836 Å. The 78.2 kcal/mol (MP4) higher energy isomer has transannular CC and Si-Si separations of 3.003 and 2.279 Å, respectively, neither of which represents a bond. In fact this latter structure has only electron density at the periphery of the molecule with a "basin" in the middle, while the global minimum contains a strong CC bond. The high energy isomer is expected to lie in a deep well, because its conversion into the global minimum is a symmetry forbidden process.

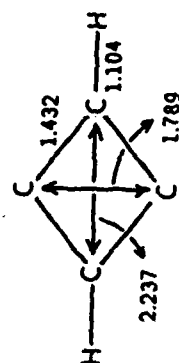
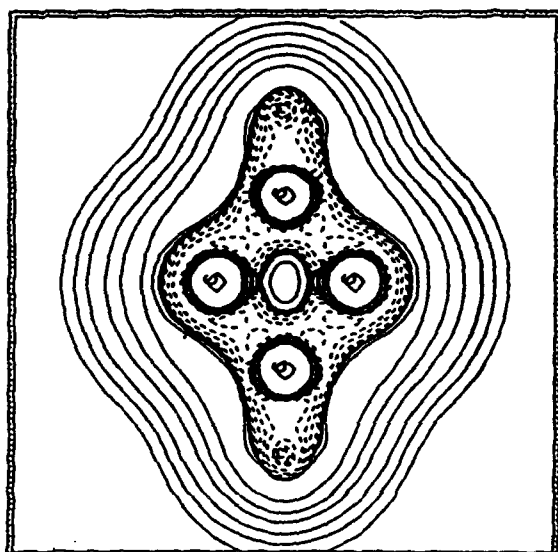
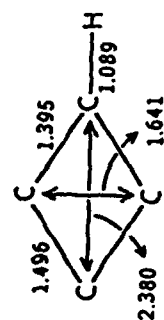
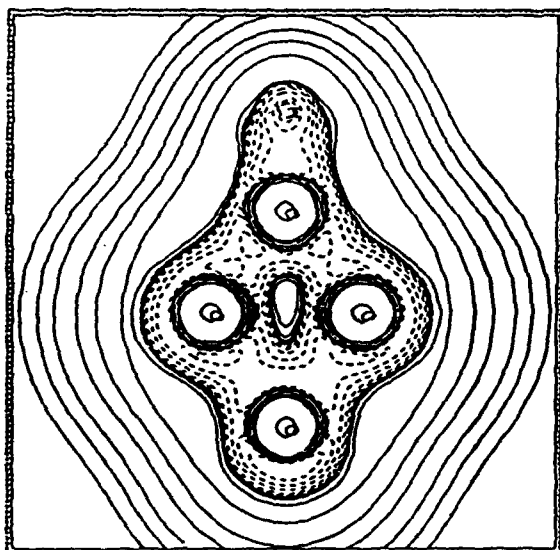
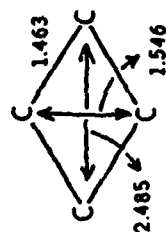
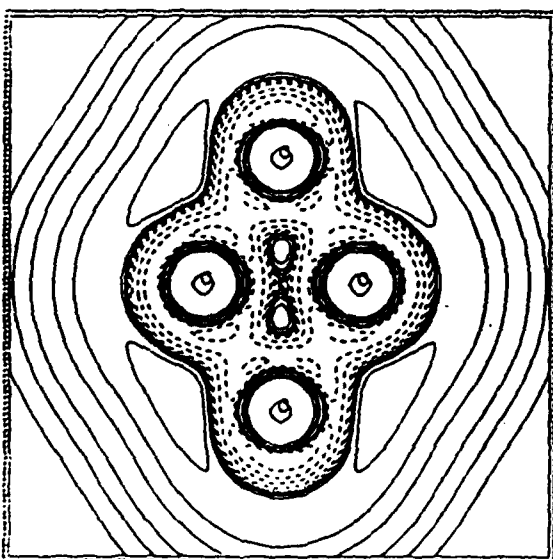
To explore the effect of different ligands on the effect of bond stretch isomerism we studied C₃Si, C₃BH, and C₃Be at the MP2/6-31G* level of theory. For each system

rhombic bond stretch isomers were found that showed much smaller energy differences than in C_2Si_2 . In the case of C_3Si , isovalent with C_4 and C_2Si_2 , the global minimum has a MP2/6-31G* 1.500 Å CC bond, which lengthens to 2.619 Å in the only 8.4 kcal/mol (MP4) higher energy rhombic form. Despite a 1.884 Å short CSi distance there is no transannular bonding between these elements in the latter isomer. The two structures, displayed in the figure with relief maps of the electron density and the Laplacians of ρ , seem to display the covalent interaction of Si with a triangular C_3 and a near linear C_3 .

The rhombic forms of C_3BH , isoelectronic with C_4 , and C_3Be display similar characteristics as C_3Si although subtle differences in bonding properties exist. For example, the lower energy isomer of C_3BH has a transannular CC distance of 1.538 Å (MP2/6-31G*) and does not show a bond critical point. The 18.5 kcal/mol (MP4) higher energy form can be represented as a covalent interaction of BH with the terminal carbons of the near linear C_3 unit. Similarly, the energy separation between the two rhombic forms of C_3Be is small and amounts to only 8.5 kcal/mol (MP4). Interestingly, the lower energy form has its Be covalently complexed to the center of the 1.464 Å CC bond of the triangular C_3 unit. The higher energy bond stretch isomer has its Be covalently complexed to the terminal carbons of the near linear C_3 form.

The characteristics of C_3Be seem to resemble those of the B_2Be_2 bond stretch isomers on which we reported earlier. In this system ($I_{sp} = 646$ sec from MP4/6-31G*) we noted that the two Be atoms are covalently complexed to the center of a strong BB bond. In the higher energy rhombic form the BB bond is broken and this bond stretch isomer is characterized by covalent BBe bonds only. We have explored other ligands bridging the B_2 unit. In relation to the extensive theoretical studies on B_2H_2 , B_2H_4 , B_2Li_2 , B_2Li_4 , and B_4H_2 , we investigated the properties of bridging diborane(2) with two aluminium atoms. The two bond stretch isomers that are shown have a large energy difference of 40.6 kcal/mol (MP4/6-31G*).

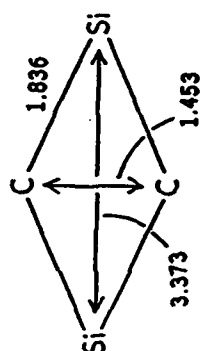




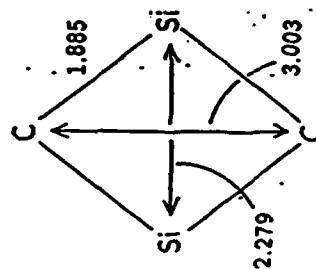
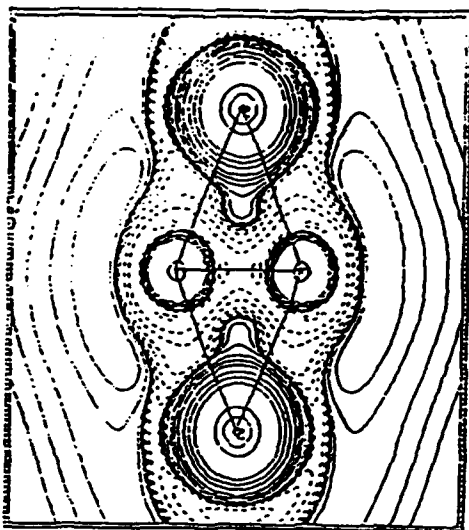
MP2/6-311G**

Bond Stretch Isomerism in Rhombic C_2Si_2

MP2/6-31G*

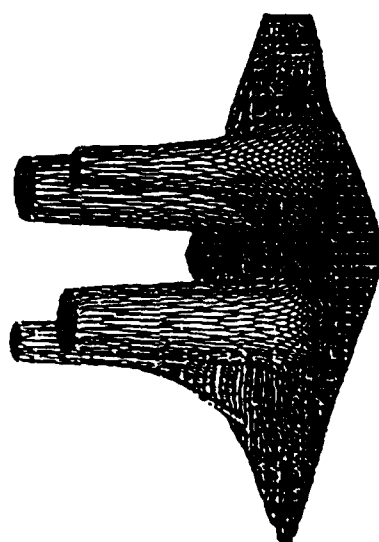
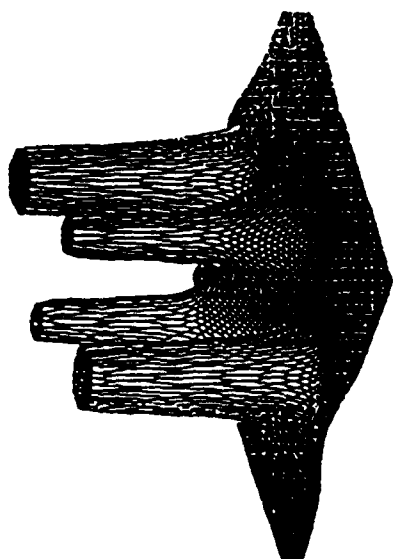
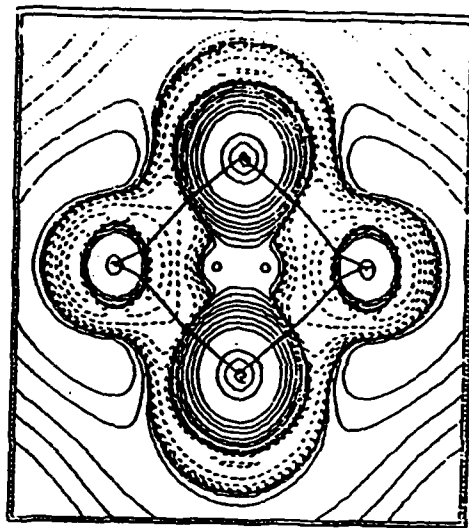


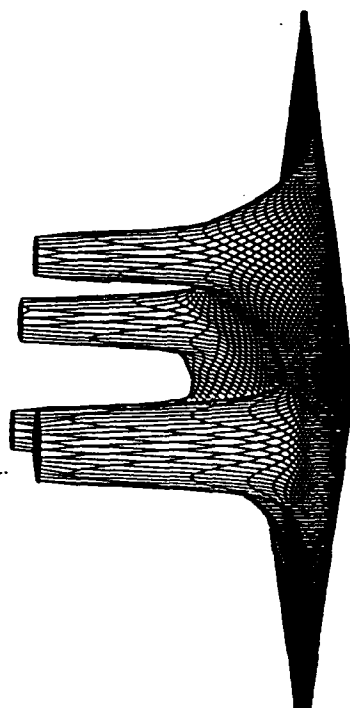
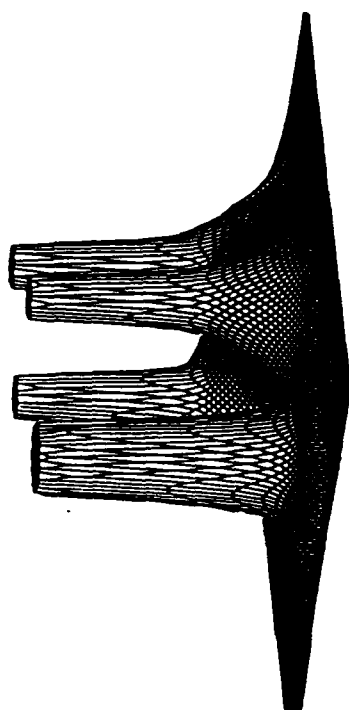
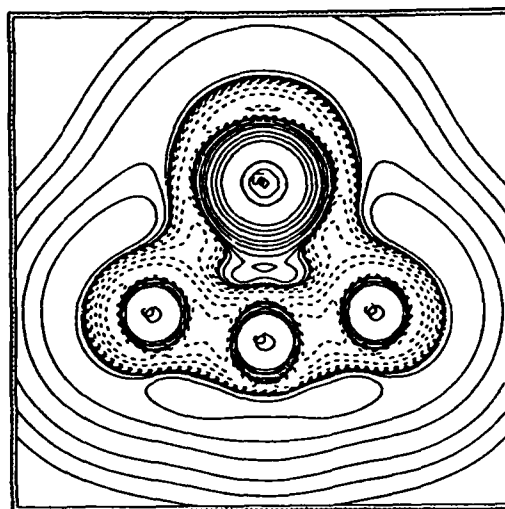
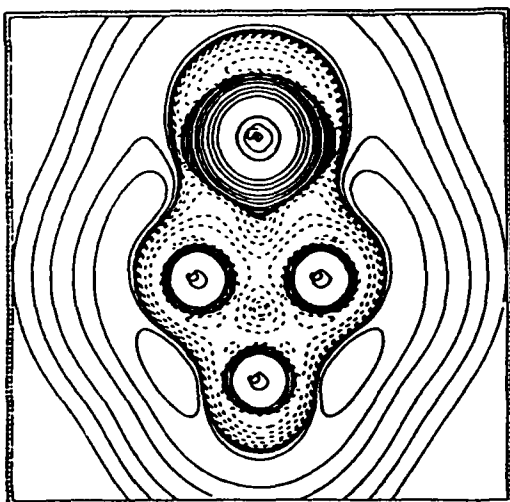
0.0



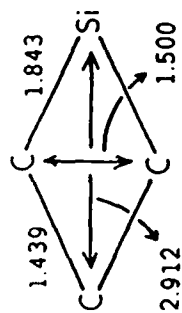
78.2

(MP4)

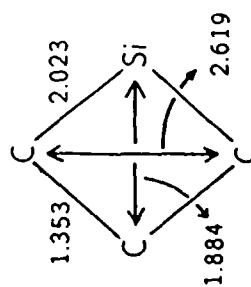




MP2/6-31G*



0.0



8.4

(MP4)

Electronic Structure Calculations on AlLi

by

Marcy E. Rosenkrantz

University of Dayton Research Institute

at the

Air Force Astronautics Laboratory

In this long abstract I will discuss the background of the use of metal additives to liquid oxygen/hydrogen propellents, explain the results of our I_{sp} calculations on the tripropellant, liquid oxygen/hydrogen/AlLi and our goals for this study. The preliminary results of our AlLi calculations will be discussed, and finally, plans for extensions of this study will be presented.

The history of the use of tripropellents goes back over twenty years. The primary candidates for metal additives to liquid oxygen/hydrogen ($l\text{ O}_2/l\text{ H}_2$) propellents were beryllium, lithium and aluminum. Each of these has advantages and disadvantages. The best choice for an increase in I_{sp} over that of neat $l\text{ O}_2/l\text{ H}_2$ is Be (69 sec). It has relatively high density, but it is toxic. As a result, testing of Be/ $l\text{ O}_2/l\text{ H}_2$ propellents was ended in the 1970's. Lithium, with its light weight is the next logical choice. But it has relatively low density, is incompatible with gaskets and corrosive to metals. Aluminum gives an increase in I_{sp} significantly less than either Be or Li but has a very high density. It is used as an additive to solid propellents but was found difficult to incorporate in the $l\text{ O}_2/l\text{ H}_2$ motors. It has a tendency to melt but not burn when incorporated in rocket test motors as a metal slug. Attempts to use Al powders and slurries were unsuccessful. As recently as 1987, NASA reopened the use of metal additives in a technical memorandum and in a technical report¹. The present work is an attempt to follow up on Dan Konowalow's suggestion that mixtures of the metal dimers with liquid or solid H_2 might also be useful additives.

For the I_{sp} calculations which Steve Rodgers performed for us we estimated the binding energy of AlLi and BLi from the separated *atoms* to be 1 eV. The heat of formation of these molecules from their solid states are 92.5 kcal/mole and 148.2 kcal/mole, respectively. These numbers are then used as inputs to the I_{sp} code which optimizes the I_{sp} as a function of stoichiometry. The I_{sp} obtained for AlLi is 508 sec, while that for BLi is 559 sec. Either of these is a revolutionary increase in the I_{sp} of the neat propellant.

We present here results of our preliminary ab initio calculations of the potential energy surfaces of AlLi which derive from the separated ground state atoms, $^2S\text{ Li} + ^2P\text{ Al}$. These calculations were begun as a means to characterize the low-lying electronic states of AlLi as an aid to experiments planned in this laboratory and to compare our results for AlLi with those for BLi obtained by Knowles and Murrell² (KM).

We began these calculations by optimizing polarization functions for use in the McLean and Chandler³ [12s9p]/6s5p aluminum basis. Two d functions ($\zeta=2.56, 0.25$) were added to the basis. For lithium I used Dan Konowalow's modified 6-31G basis augmented by two d functions ($\zeta=0.03053, 0.01009$). With the state averaged MCSCF code of B. H. Lengsfeld which he incorporated into the MESA codes⁴, I performed 2-in-7 CASSCF calculations of the potential curves of AlLi in its $^3\Pi$ and $^1\Pi$ states. The latter of these is entirely repulsive. The potential curve of the former is shown in figure 1 along with those of the $^1\Sigma^+$ and $^3\Sigma^+$ states. The ground state of AlLi is the $^1\Sigma^+$ state. The two triplet states are nearly degenerate, with the Σ slightly deeper than the Π state. The characteristic constants for these three states are presented in table 1. Obviously, we did well to estimate the binding energy of AlLi to be 1 eV. These results are in contrast to those obtained by KM for BLi. They determined the ground state of BLi to be the $^3\Pi$ state, with the $^3\Sigma^+$ state the completely repulsive state. The singlet states of BLi are considerably more weakly bound than the $^3\Pi$ state, as can be seen in table 2. Kaufman³ has reported an SCF calculation on the ground $^1\Sigma^+$ state of AlLi and finds its R_e to be $5.66a_0$. The dipole moment function for the ground $^1\Sigma^+$ and $^3\Sigma^+$ states of AlLi is presented in figure 2. We intend to

determine the vibrational lifetimes of these states using these functions and those obtained from CI wavefunctions.

We plan to extend these calculations and determine the energy of these states at the multi-reference CI level. If necessary, we will improve the Li basis and then recalculate the CASSCF and CI results. We will also examine the wavefunctions in an attempt to account for the differences between AlLi and BLi.

Acknowledgements

I wish to thank Byron Lengsfeld for providing me with a version of his State Averaged MCSCF program for use with MESA⁴. Thanks also to D. Konowalow for many helpful discussions.

References

1. R. L. Zurawski, NASA Technical Paper 2602, June 1986; R.L. Zurawski and J.M. Green, NASA Technical Memorandum 100104, 1987.
2. D.B. Knowles and J.N. Murrell, J. Mol. Struct. (Theochem), 135, 169 (1986).
3. A.D. McLean and G.S. Chandler, J. Chem. Phys. 72, 5639 (1980).
4. MESA, Molecular Electronic Structure Applications, , Paul Saxe, Richard Martin, Michael Page, and Byron H. Lengsfeld III.
5. J.J. Kaufman, J. Chem. Phys. 58, 1680 (1973).

Figure. 1

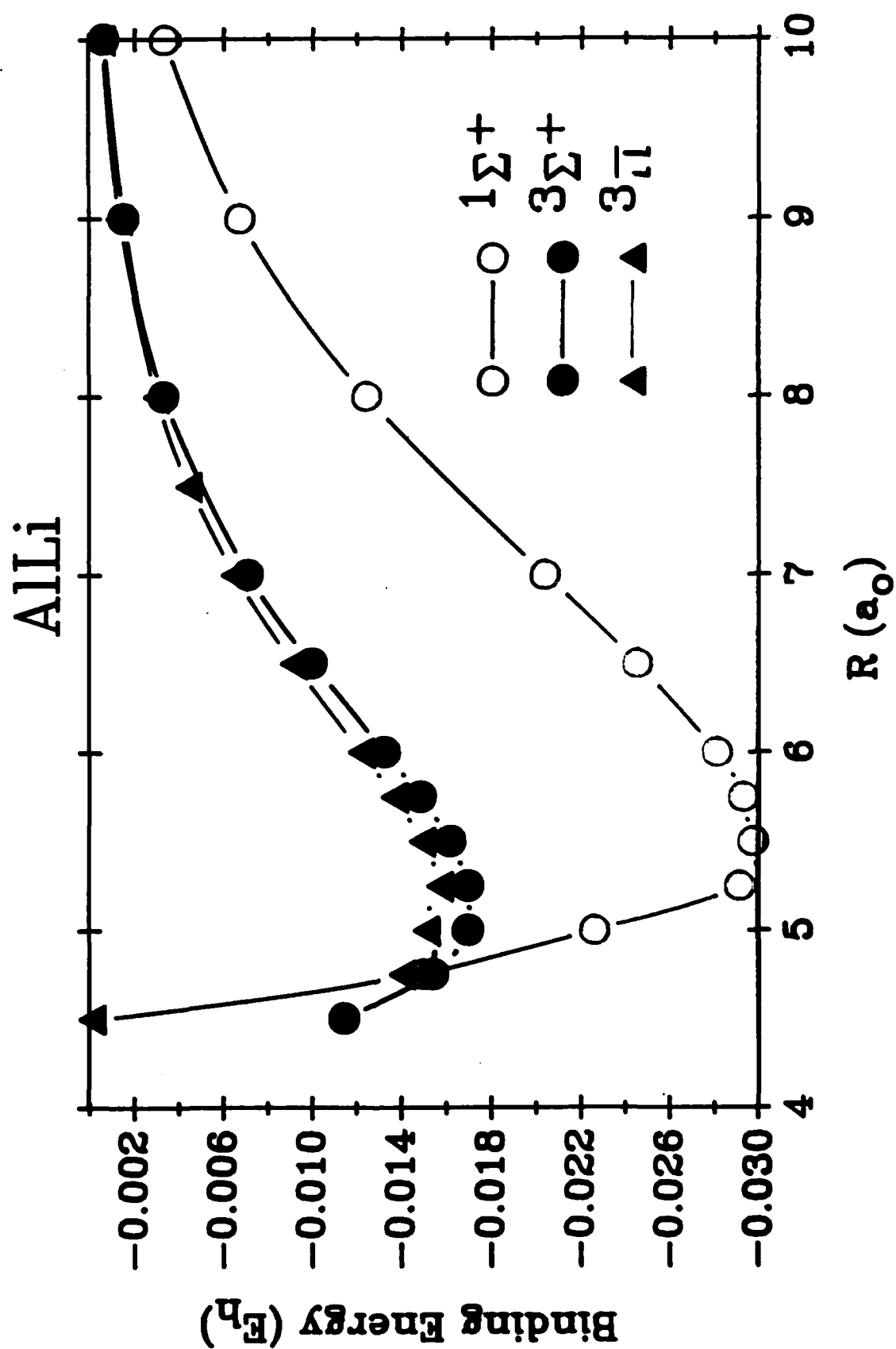
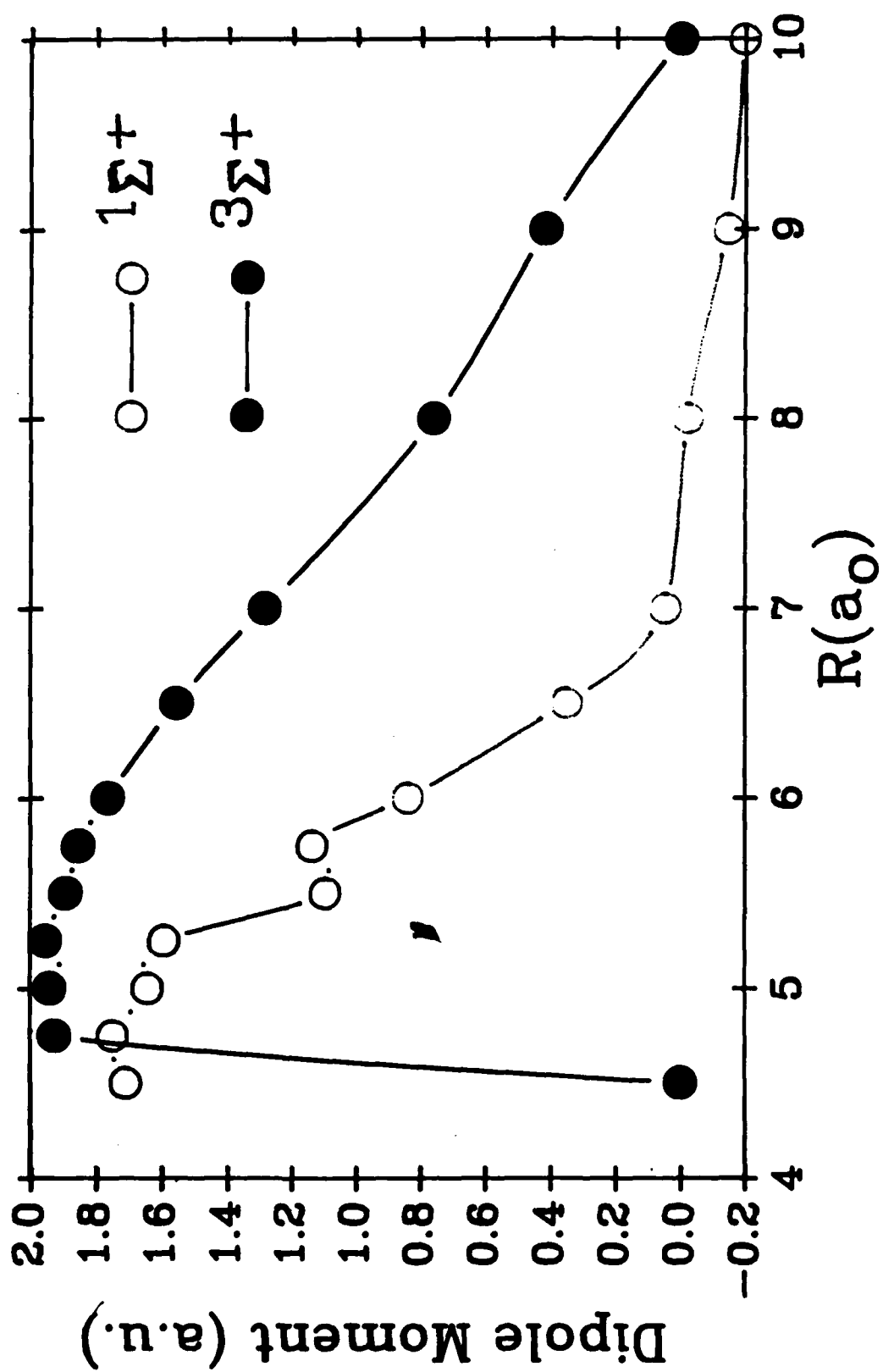


Figure 2



Alli

Characteristic Constants

State	$R_e(a_0)$	$D_e(\text{eV})$	$\omega_e(\text{cm}^{-1})$	$\omega_e X_e(\text{cm}^{-1})$
$1\Sigma^+$	5.61	0.813	331.47	4.19
$3\Sigma^+$	5.11	0.469	310.19	6.36
3Π	5.22	0.451	376.87	9.76

Table 1. Characteristic Constants for Alli.

BLi

Characteristic Constants

State	$R_e(a_0)$	$D_e(\text{eV})$	$\omega_e(\text{cm}^{-1})$
$1\Sigma^+$	4.58	0.834	398
3Π	4.05	1.106	498
1Π	4.19	0.223	500

Table 2. Characteristic Constants for BLi.

LEWIS ACID BEHAVIOR OF NOBLE-GAS CATIONS AND THE SYNTHESSES OF NOVEL
Ng-O and Xe-N BONDS (Ng = Kr, Xe)

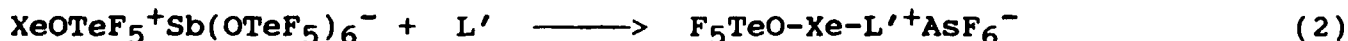
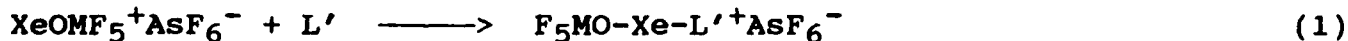
Neil T. Arner, Alison Paprica, Jeremy C.P. Sanders
and Gary J. Schrobilgen

Department of Chemistry, McMaster University, Hamilton, Ontario
L8S 4M1, Canada

INTRODUCTION

In the course of the present contract we have made a significant extension of the chemistry of xenon and krypton by taking advantage of the Lewis acid properties of the XeF^+ and KrF^+ cations. Based on considerations of the high electron affinities of the cations ($\text{KrF}^+ \approx 13.2$ eV, $\text{XeF}^+ \approx 10.9$ eV) and first adiabatic ionization potentials of selected bases, where the IP is equal to or greater than the estimated EA of NgF^+ , it has been possible to prepare a diverse range of noble-gas adduct cations; F-Xe-L^+ , $\text{F-Kr-N}\equiv\text{CH}^+$ and $\text{F-Kr-N}\equiv\text{CR}_\text{F}^+$ ($\text{L} = \text{HC}\equiv\text{N}$, $\text{RC}\equiv\text{N}$, $\text{R}_\text{F}\text{C}\equiv\text{N}$, $\text{C}_5\text{F}_5\text{N}$, $\text{s-C}_3\text{F}_3\text{N}_3$). The adduct salts; whose stabilities range from explosive at -60°C for $\text{F-Kr-N}\equiv\text{CH}^+\text{AsF}_6^-$, the first example of a Kr-N bond, to stable at room temperature for $\text{s-C}_3\text{F}_3\text{N}_2\text{N-Xe-F}^+\text{AsF}_6^-$; have been characterized by multi-NMR spectroscopy and Raman spectroscopy.

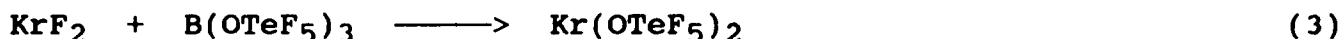
We have now extended this work to the related noble-gas cations XeOTeF_5^+ and XeOSeF_5^+ and to the inorganic base $\text{F}_3\text{S}\equiv\text{N}:$. The XeOSeF_5^+ cation was previously unknown and has been characterized in the course of this work. While the XeOMF_5^+ cations ($\text{M} = \text{Se}, \text{Te}$) are expected to be weaker Lewis acids, they are expected to be less strongly oxidizing than NgF^+ cations, and may be expected to form stable adducts at low temperature with more strongly reducing bases. The syntheses have been carried out in BrF_5 or SO_2ClF solvent at -50°C and have led to the first examples of O-Xe-N linkages (equations (1) and (2)).



where $\text{L}' = \text{F}_3\text{S}\equiv\text{N}:$, $\text{CH}_3\text{C}\equiv\text{N}:$, $\text{C}_5\text{F}_5\text{N}:$, $\text{s-C}_3\text{F}_3\text{N}_3$.

The gap resulting from our syntheses of the first examples of Kr-N bonds and the previous existence several examples of Kr-F bonds (KrF_2 , KrF^+ and $\text{F}(\text{KrF})_2^+$) has prompted us to investigate the possibility of forming the first Kr-O bonded species. Using ^{19}F and ^{17}O NMR

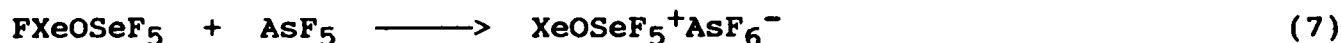
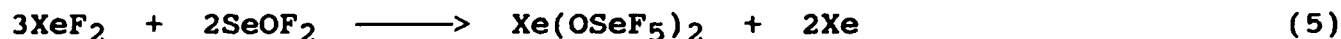
spectroscopy of ^{17}O enriched samples, we have been able to document the formation of the first Kr-O bonds by the synthesis and decomposition of thermally unstable $\text{Kr}(\text{OTeF}_5)_2$ (equations (3) and (4)).



Attempts to synthesize Kr-O compounds by the reaction of KrF_2 with IO_2F_3 in SO_2ClF were not successful, although the reactions did give rise to some interesting chemistry.

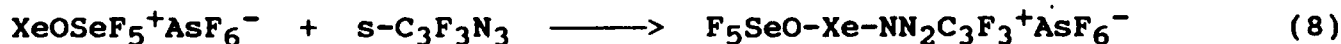
SYNTHESIS AND CHARACTERIZATION OF $\text{XeOSeF}_5^+\text{AsF}_6^-$

The XeOSeF_5^+ cation has been prepared for the first time according to equations (5) - (7).



The $\text{XeOSeF}_5^+\text{AsF}_6^-$ salt has been characterized in the solid state by Raman spectroscopy and in SbF_5 and BrF_5 solutions by ^{19}F , ^{77}Se and ^{129}Xe NMR spectroscopy. Unlike the Te analog, the XeOSeF_5^+ cation does not undergo solvolysis in BrF_5 . Based on our NMR findings, the OSeF_5 group is shown to be more electronegative than the OTeF_5 group and possesses oxidant properties which are greater than those of either OSF_5 or OTeF_5 .

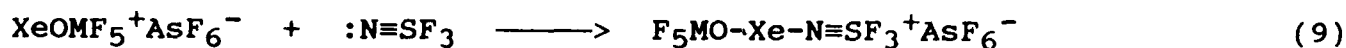
The XeOSeF_5^+ cation also reacts with s-trifluorotriazine to give a novel nitrogen-bonded Lewis acid-base adduct cation according to equation (8).



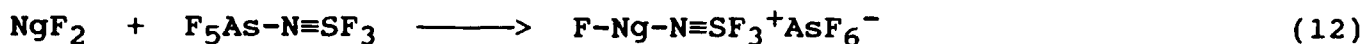
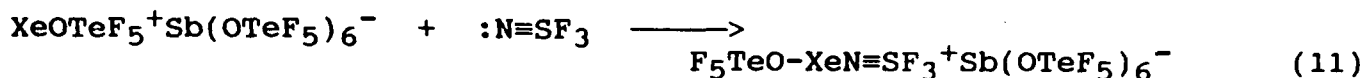
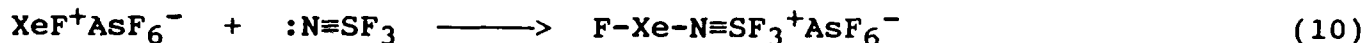
The compound is stable at room temperature and has thus far been characterized by ^{19}F and ^{129}Xe NMR spectroscopy.

REACTIONS OF NOBLE-GAS CATIONS WITH THE LEWIS BASE $:\text{N}=\text{SF}_3$

We have begun to investigate the synthesis of $:\text{N}=\text{SF}_3$ Lewis acid-base adducts with the noble-gas cations XeF^+ , XeOSeF_5^+ , XeOTeF_5^+ and KrF^+ . While the XeOMF_5^+ cations ($\text{M} = \text{Se}, \text{Te}$) are expected to be weaker Lewis acids, they are expected to be less strongly oxidizing than NgF^+ cations, and generally may be expected to form stable adducts at low temperature with more strongly reducing bases. Several synthetic approaches are being used (equations (9) - (12)).



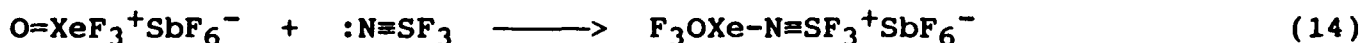
where M = Se or Te



Two of the proposed syntheses have already been successfully carried out in BrF_5 solvent at -50°C and have led to additional examples of novel O-Xe-N linkages (equation (9), where M = Se, and equation (10)).

Structures are being characterized using primarily ^{19}F and ^{129}Xe NMR spectroscopy in solution and by low-temperature Raman spectroscopy in the solid state. It appears that $\text{F-Xe-N}\equiv\text{SF}_3^+\text{AsF}_6^-$ is stable at room temperature and that it may prove possible to isolate suitable single crystals allowing the X-ray crystal structure to be determined for this interesting new class of compound.

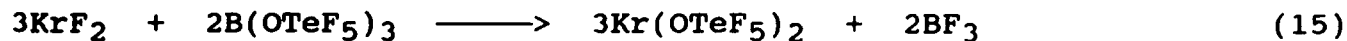
In the course of these preliminary investigations we have been able to show that $:\text{N}\equiv\text{SF}_3$ and its adduct $\text{F}_5\text{As-N}\equiv\text{SF}_3$ are both highly resistant to oxidation by the strongly oxidizing solvent, BrF_5 , suggesting that it may be possible to synthesize the first example of a Kr-N bonded species involving an inorganic base. As BrF_5 is the only practical solvent available we have been able to find in which to carry out syntheses involving the strong oxidant, KrF_2 , we will concentrate some of our efforts on reaction (12) where Ng = Kr using this solvent. Again, because of the established resistance of $:\text{N}\equiv\text{SF}_3$ to oxidation by BrF_5 , we will also attempt to form the first examples of a noble gas, xenon, in higher oxidation states (+4 and +6) bonded to nitrogen. This will involve the interaction of stoichiometric amounts of the strong oxidant salts $\text{XeF}_3^+\text{SbF}_6^-$ or $\text{O=XeF}_3^+\text{SbF}_6^-$ and $:\text{N}\equiv\text{SF}_3$ in BrF_5 solvent at -50 to -60°C according to equations (13) and (14).



THE KRYPTON-OXYGEN BOND₁

A previous published attempt to form Kr-O bonds reports the reaction of KrF_2 with $\text{B}(\text{OTeF}_5)_3$ in ClO_3F at -100°C for 16 hours followed by a further 3 hours at -78°C . The ^{19}F NMR spectrum of the sample only revealed resonances attributable to $\text{F}_5\text{TeOOTeF}_5$ and the solvent. Similar results have been obtained in this laboratory for the reaction of KrF_2 with $\text{B}(\text{OTeF}_5)_3$ in SO_2ClF at -78°C for several minutes. In contrast, the reaction of XeF_2 with $\text{B}(\text{OTeF}_5)_3$ yields the

thermally stable $\text{Xe}(\text{OTeF}_5)_2$. It was proposed that the $\text{F}_5\text{TeOOTeF}_5$ resulted from the decomposition of the intermediate, $\text{Kr}(\text{OTeF}_5)_2$, according to equations (15) and (16).



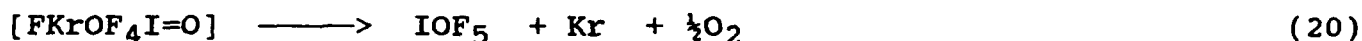
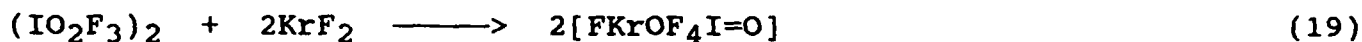
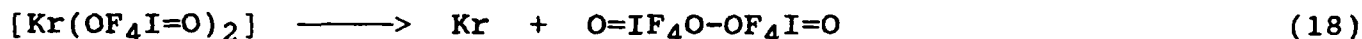
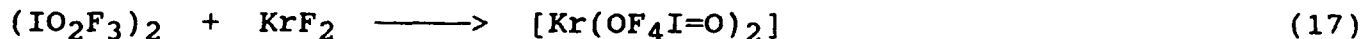
The thermolyses of $\text{Xe}(\text{OTeF}_5)_2$ and FXeOTeF_5 have been re-investigated in glass at 160 °C in the present study and shown to yield almost quantitatively $\text{F}_5\text{TeOOTeF}_5$ and Xe, and $\text{F}_5\text{TeOOTeF}_5$, XeF_2 and Xe, respectively. Contrary to previous reports in which the thermolyses of the two xenon compounds had been carried out in a Monel vessel at 130 °C, only traces of $\text{F}_5\text{TeOTeF}_5$ (< 2 %) and other members of the series $\text{TeF}_n(\text{OTeF}_5)_{6-n}$ were observed for the thermolyses in glass tubes. These findings suggested that analogous decompositions of FKrOTeF_5 and/or $\text{Kr}(\text{OTeF}_5)_2$, but at much lower temperatures, may be responsible for the formation of $\text{F}_5\text{TeOOTeF}_5$ resulting from the reaction of KrF_2 and $\text{B}(\text{OTeF}_5)_3$. These findings prompted the reinvestigation of reactions (15) and (16) at lower temperatures with the view to providing definitive evidence for FKrOTeF_5 and/or $\text{Kr}(\text{OTeF}_5)_2$.

The reaction of $\text{B}(\text{OTeF}_5)_3$ and 21% ^{17}O enriched $\text{B}(\text{OTeF}_5)_3$ with KrF_2 at -110 °C was monitored in SO_2ClF by both high-field ^{19}F (470.599 MHz) and ^{17}O (67.801 MHz) NMR spectroscopy. Owing to the increased dispersion afforded in the ^{19}F spectra at 11.744 T, it was possible to observe a new AB_4 pattern to high frequency of the AB_4 pattern attributable to $\text{Kr}(\text{OTeF}_5)_2$ alongside the intense resonance of $\text{F}_5\text{TeOOTeF}_5$. The AB_4 pattern of this species resembles the AB_4 spectra of $\text{Xe}(\text{OTeF}_5)_2$ and FXeOTeF_5 in that the A part occurs to high frequency of the B_4 part and are well separated from each other at an external field strength of 11.744 T. Furthermore, the new AB_4 pattern cannot be attributed to any of the species in the $\text{BF}_n(\text{OTeF}_5)_{3-n}$ series, since the A parts of the AB_4 spectra are almost coincident with the B_4 parts. The signals ascribed to $\text{Kr}(\text{OTeF}_5)_2$ slowly diminished at -90 °C and rapidly decreased upon warming to -78 °C for 3 minutes, yielding Kr and additional $\text{F}_5\text{TeOOTeF}_5$. However, a new F-on-Kr signal was not observed in these spectra, ruling out the formation of FKrOTeF_5 . The formation of small amounts of the $\text{TeF}_n(\text{OTeF}_5)_{6-n}$ species was also observed and is analogous to the results obtained for the high-temperature decompositions of FXeOTeF_5 and $\text{Xe}(\text{OTeF}_5)_2$. The ^{17}O NMR spectrum of the $\text{KrF}_2/\text{B}(\text{OTeF}_5)_3$ reaction mixture also yielded a new ^{17}O resonance to low frequency of the $\text{F}_5\text{TeOOTeF}_5$ resonance. The new resonance displayed analogous behavior to the new ^{19}F resonance when the sample was warmed and is assigned to $\text{Kr}(\text{OTeF}_5)_2$. The new ^{19}F and ^{17}O chemical shifts are consistent with the OTeF_5 ligands possessing more ionic character than in their FXeOTeF_5 and $\text{Xe}(\text{OTeF}_5)_2$ analogs, whose ^{17}O chemical shifts have now been determined for the first time.

We had discovered, prior to the outset of the present contract that the interaction of KrF_2 and $(\text{IO}_2\text{F}_3)_2$ in SO_2ClF solvent presumably leads to peroxide formation at ca. -10 - 0 °C by the route proposed in equations (2) and (3). Our preliminary findings suggest that it may

not be possible to isolate $\text{Kr}(\text{OF}_4\text{I}=\text{O})_2$ or $\text{FKrOF}_4\text{I}=\text{O}$ by this route owing to the higher temperatures required to dissociate the IO_2F_3 dimer. As a result, any Kr-O bonded derivative that might form would decompose at these higher temperatures (approaching -45°C). We have already shown from our work on $\text{Kr}(\text{OTeF}_5)_2$ that this species can only be observed in appreciable amounts in solution at or around -100°C .

We have now carried out detailed high-field ^{19}F NMR studies on the $\text{KrF}_2/\text{IO}_2\text{F}_3$ systems in both SO_2ClF and BrF_5 solvents. Although there is no direct evidence for a Kr-O bonded species, our detailed findings are consistent with the formation of unstable Kr-O bonded intermediates. The following sequence of equations summarizes our findings regarding the reactions of IO_2F_3 and KrF_2 ; compounds in brackets have not been observed in these systems but are proposed as reasonable intermediates:



The observation of IOF_5 in these systems has not been reported previously and lends strong evidence to our argument that Kr-O species are formed as unstable intermediates. Moreover, the proportion of IOF_5 in these reactions increases dramatically when KrF_2 is in stoichiometric excess and supports reactions (19) and (20).

In addition we have observed that $\text{O}=\text{IF}_4\text{O}-\text{OF}_4\text{I}=\text{O}$ is initially formed as the colorless trans, trans isomer, which upon warming to room temperature isomerizes to the yellow cis, cis isomer.

REFERENCE:

1. J.C.P. Sanders and G.J. Schrobilgen, J.C.S. Chem. Commun., 1989, 1576.

Experimental Studies on the Synthesis of
New High Oxidation State Energetic Fluorine Compounds

W.W. Wilson and K.O. Christe
Rocketdyne Division of Rockwell International Corporation
Canoga Park, California 91303

The primary objective of this program is the synthesis of new "super oxidizers" based on hypervalent or high oxidation state fluorides of nitrogen, oxygen, chlorine, and the noble gases. The target compounds include NF_5 , ClF_5O , ClF_6^- , NF_2^- , catenated nitrogen fluorides, and ArF^+ which are among the most challenging synthetic problems encountered in high energy chemistry.

After showing that NF_5 cannot exist for steric reasons and numerous unsuccessful attempts at the syntheses of ClF_5O and NF_2^- , we have focused our efforts on ClF_6^- . Taking advantage of a technique, recently developed under this contract for the syntheses of $\text{N}(\text{CH}_3)_4\text{ClF}_4$ and $\text{N}(\text{CH}_3)_4\text{BrF}_6$, we have succeeded with the first synthesis of a ClF_6^- salt. The ClF_6^- anion was prepared as either the $\text{N}(\text{CH}_3)_4^+$ or Cs^+ salt from CH_3CN solutions at low temperature.

Both salts are thermally unstable and were very difficult to characterize. The $\text{N}(\text{CH}_3)_4^+$ salt is more stable than the Cs^+ salt, thus permitting the removal of the CH_3CN solvent and excess ClF_5 at -30°C .

The composition of the white solid residue was shown by a material balance to be in agreement with $\text{N}(\text{CH}_3)_4\text{ClF}_6$. However, all attempts to further characterize this solid by spectroscopic methods were terminated by consistent explosions.

The CsClF_6 salt is thermally unstable at -30°C , and attempts to remove the CH_3CN solvent at this temperature resulted also in the removal of all the ClF_5 . However, slow cooling of the $\text{CsF}-\text{ClF}_5-\text{CH}_3\text{CN}$ system to -110°C allowed the recording of the Raman spectra of CsClF_6 in frozen CH_3CN . The Raman frequencies and relative intensities observed for ClF_6^- are in excellent agreement with the values predicted for ClF_6^- from the known BrF_4^- , BrF_6^- , BrF_5 , BrF_6^+ and ClF_4^- , ClF_5 , ClF_6^+ spectra. Furthermore, the similarity between the BrF_6^- and ClF_6^- spectra strongly suggests that by analogy with BrF_6^- the ClF_6^- anion is also octahedral and that the free valence electron pair on the chlorine central atom must be sterically inactive.

Additional evidence for the existence of the ClF_6^- anion was obtained by ^{18}F radiotracer and ^{19}F NMR studies carried out in collaboration with Prof. Schrobilgen of McMaster University. The ^{18}F radiotracer study showed that within several minutes at room temperature complete randomization of ^{18}F in an $^{18}\text{FNO} + \text{ClF}_5$ mixture had occurred. The ^{19}F NMR study of neat ClF_5 and ClF_5 in anhydrous HF solution in the presence and absence of excess CsF demonstrated that ClF_5 undergoes chemical exchange also with CsF .

For the syntheses of the $\text{N}(\text{CH}_3)_4^+$ salts of the halogen fluorides, anhydrous and HF_2^- free $\text{N}(\text{CH}_3)_4\text{F}$ was needed as a starting material. According to the most recent literature, truly anhydrous $\text{N}(\text{CH}_3)_4\text{F}$ had never previously been prepared. A simple method for the synthesis of anhydrous $\text{N}(\text{CH}_3)_4\text{F}$ was developed, and the material was characterized by x-ray diffraction, NMR, infrared and Raman spectroscopy. It crystallizes in the hexagonal system with a hexagonal closest packing of the $\text{N}(\text{CH}_3)_4^+$ cations. It is thermally stable up to about 160°C and above that temperature decomposes to $\text{N}(\text{CH}_3)_3 + \text{CH}_3\text{F}$. Furthermore, some of the properties, previously ascribed to the free fluoride anion, were shown to be due to HF_2^- or other secondary reaction products and were corrected.

EXTENDED ABSTRACTS

POSTER PRESENTATIONS

Extremely Large Atom Densities in Tritiated Solid Hydrogen

G. W. Collins, P. C. Souers, E. R. Mapoles, F. Magnotta
J. R. Gaines, and P. A. Fedders

The nuclear decay of the triton in solid hydrogen initiates the conversion of nuclear energy into stored chemical energy by producing unpaired hydrogen atoms inside the molecular hydrogen lattice. Utilizing electron spin resonance (ESR) at 9.4 GHz, thermal measurements, and optical techniques, we have studied the buildup and transient decay of large atom densities in tritiated solid hydrogen down to temperatures of 1.2 K. Our main goal is to see how much energy can be stored in this solid, self energized, H₂ battery and understand the fundamental principles limiting this quantity.

Since each unpaired atom is in a metastable state lying above the ground molecular state by 4.5/2 eV, the stored energy goes approximately as $4.5 \text{ eV} \cdot n/2$ where n is the number of unpaired atoms. We routinely store over 1000 ppm or about 40 Joules /gram in solid T₂ below 3 Kelvin. We have seen energies up to 10,000 ppm or 372 Joules/gram stored in T₂. ESR is a very natural tool to study the unpaired hydrogen atoms since each isotope has a unique signature given by its hyperfine splitting. In figure 1 we plot the buildup of unpaired atoms, and thus stored energy, as a function of time in solid T₂.

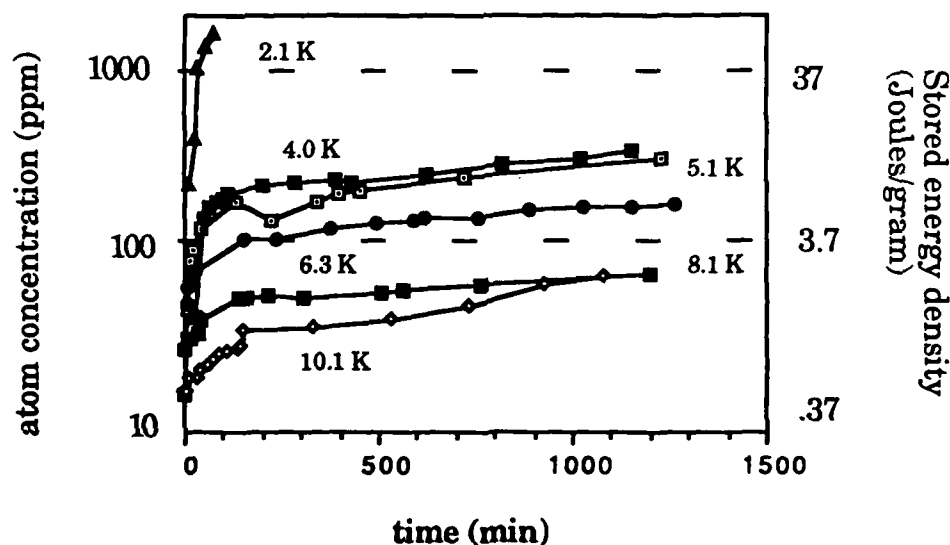


Figure 1: Atom concentration vs time in T₂

We have also started characterizing unpaired atoms in tritiated H₂. Over 3 J/cc have been observed in H₂+2%T₂ with minimal effort.

Most of atomic growth curves in the tritiated hydrogens can be modeled by a simple bimolecular rate equation with a constant production term, and a term that grows linearly with time that takes into account the

growth of radiation induced trapping sites for the atoms. The result is summarized by

$$n = \sqrt{\frac{K}{\alpha}} \tanh(\sqrt{K\alpha} t) + mt \quad \text{Eq(1)}$$

where n is the atomic concentration, K is the atomic production term, α is the recombination coefficient, and m is the rate of production of radiation induced trapping sites. The recombination coefficient α can be written in terms of a diffusion coefficient that characterizes the process that limits recombination of atoms.

$$\alpha = 4\pi R_0 D(\text{recombination}) \quad \text{Eq(2)}$$

To build up larger concentrations of atoms in H_2 we need to decrease the recombination rate. One important point is that $D(\text{recombination})$ is not necessarily the diffusion coefficient for the hydrogen atoms moving about the lattice, but a bottleneck process that characterizes the tunneling of an atom through a strain field imposed by another atom, and the final step in the recombination process. In other words we can write

$$\frac{1}{D(\text{recombination})} = \frac{1}{D(\text{polaron tunneling} + \text{spin flip})} + \frac{1}{D(\text{percolation thru lattice})} \quad \text{Eq(3)}$$

where the first term on the right hand side limits the recombination process. Cooling the lattice increases the atomic concentration and thus decreases $D(\text{recombination})$ for all the samples studied. We intend to further characterize ways to limit this process (ie magnetic fields, lower temperatures etc).

By experimentally determining the ESR relaxation times of the hydrogen atoms we can determine how fast the atoms move around the lattice before they recombine. Figure 2 shows the diffusion coefficient from the relaxation times and the recombination coefficient. This shows explicitly that there is a bottleneck in the recombination rate that allows large amounts of energy to be stored in the hydrogen lattice.

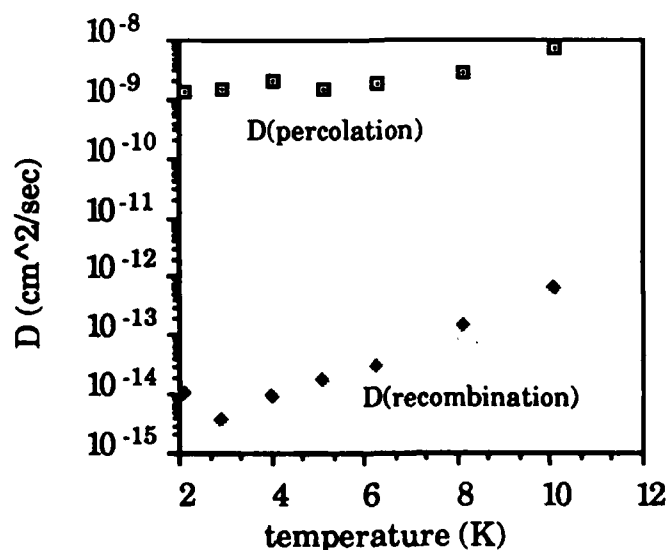


Figure 2: Diffusion of atoms percolating through the lattice and recombination diffusion in solid T_2 .

At low temperatures the atomic concentration gets very large and becomes unstable to small thermal fluctuations. When a small positive thermal fluctuation perturbs the lattice, the lattice quickly distributes the energy through the sample. The atomic concentration is now too large for the lattice temperature owing to the steep dependence of the atomic concentration on the temperature. Thus, atoms recombine to come into equilibrium with the lattice releasing the recombination energy, and further heating the lattice. This process sets off a deflagration wave of recombining hydrogen atoms, releasing all the stored energy in milliseconds! We have studied this phenomenon with ESR, NMR, thermal conductivity, thermal emission, and optical emission. The most convincing and illuminating experimental result is that each time a thermal spike occurs, the atoms disappear in the ESR spectrum!

Our latest results come from optical emission data. As solid tritiated hydrogen is cooled below 10 K, it begins to emit light that increases in intensity as the temperature decreases, similar to the temperature dependence of the atomic concentration. Figure 3 shows the relative intensity vs temperature within the bandwidth of 450 nm to 900 nm.

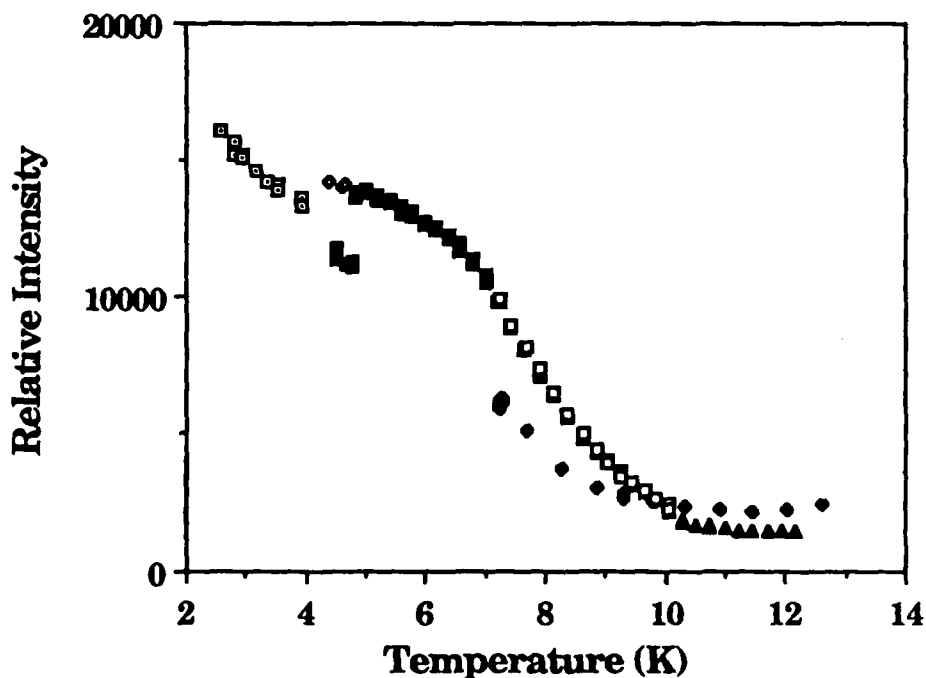


Figure 3: Optical emission from solid DT vs temperature

Under very similar conditions used to generate heat spikes from other experiments where the sample could be considered in bulk form, here where the sample forms a thin layer of solid hydrogen we found a pulse of light was emitted from the tritiated hydrogen. Moreover, just after the flash, the steady state light emitted from the sample vanished and slowly increased over the next ten minutes! Before the first flash the sample

formed a thin layer of ice at the bottom of the sample cell. During the flash the sample exploded and redistributed over the sample cell! After several flashes the sample formed a relatively uniform layer around the sample cell. When the flash of light is resolved in time within the bandwidth of 400 nm to 1100 nm, we find the peak intensity increases with decreasing temperature and the duration decreases with decreasing temperature, such that the area of the integrated emission remains relatively constant. Figure 4 shows the response of a photodiode with a bandwidth of 400nm to 1100nm during a stimulated flash at 2.4 K. Figure 5 shows the peak intensity and full width at half maximum of the optical pulse as a function of temperature.

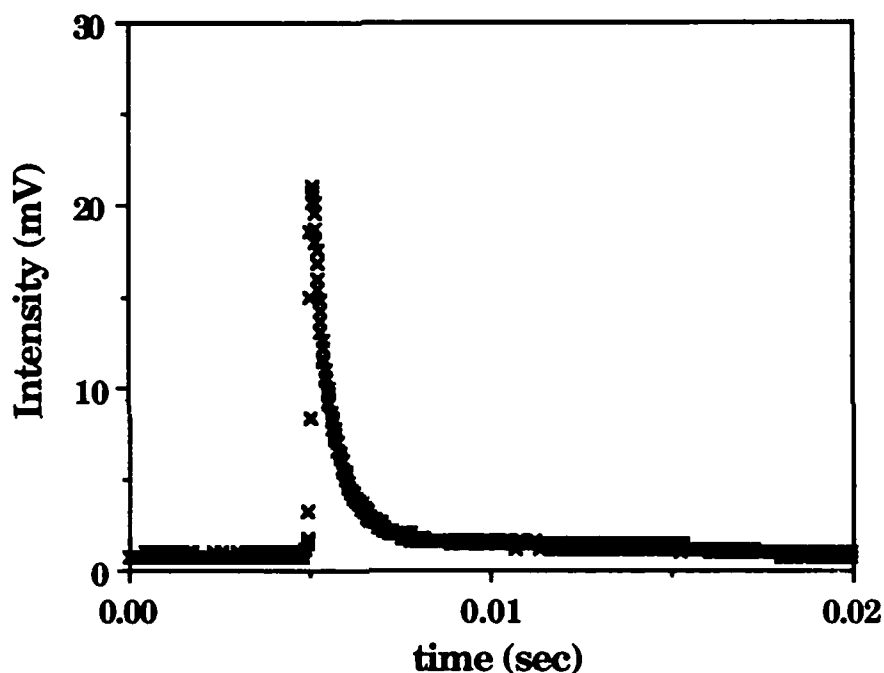


Figure 4: Stimulated optical pulse from DT at 2.4 K

After a flash is stimulated the sample cell temperature drops by 20 millikelvin. It then increases exponentially to the equilibrium temperature with a time constant of about 560 seconds, similar to the recovery of the steady state light emission. We believe during this period of time the energy from the triton decay is stored by the unpaired atoms and then the sample warms up as the the atoms start recombining in steady state. Figure 6 shows the thermal response of the sample cell after a flash.

A crude calculation of the energy stored from this thermal response curve gives 12.5 Joules/gm. By calculating the amount of energy released from the flash, within the bandwidth of the photodiode, we obtain about 26.8 mJoules/gm, much less than found from the thermal response. We used a series of filters to crudely characterize the spectral distribution. A long pass filter at 780 nm cuts off about half the light. Since the sensitivity of the detector is falling off very rapidly there, we cannot distinctly identify the spectral response, but we can state that over half of the light is past 780 nm. By resolving the spectral information from the light emission we hope to be

able to know what states are important in the recombination process and break the matrix elements leading to recombination!!

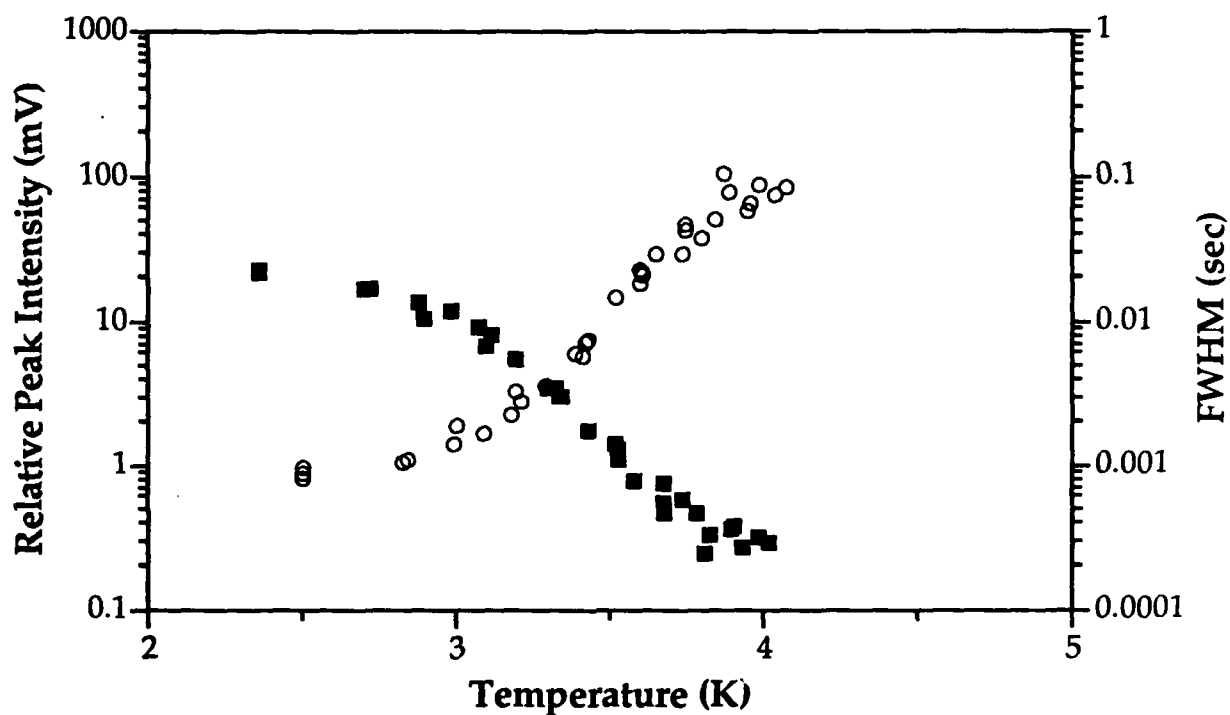


Figure 5: peak intensity and full width at half max from optical pulses versus temperature

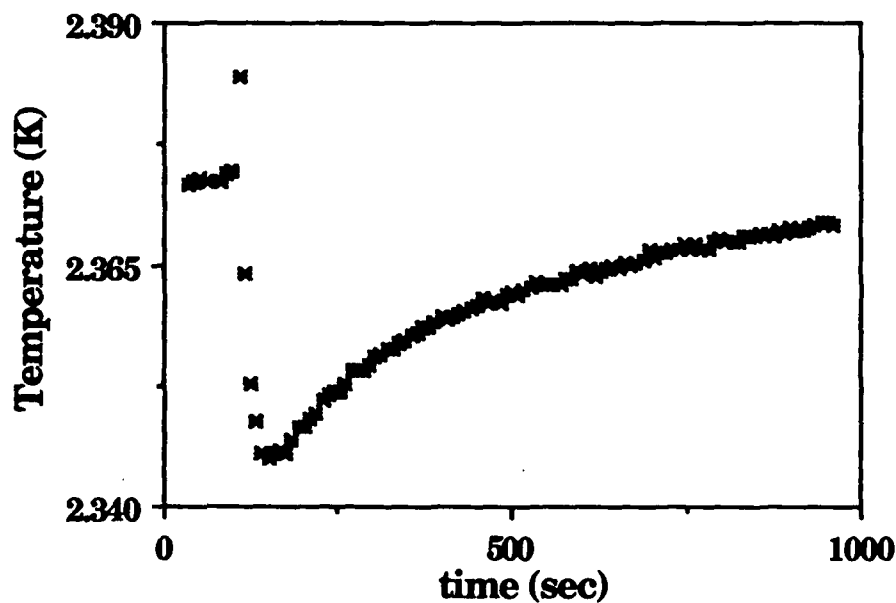


Figure 6: Thermal response of the sample cell temperature after a flash

Work performed under the auspices of the U. S. Department of Energy by Lawrence Livermore National Laboratory under contract No. W-7405-ENG-48.

POTENTIAL ENERGY SURFACES AND DYNAMICS FOR UNUSUAL HYDRIDES AND FLUORIDES

AFOSR/HEDM CONTRACTORS' MEETING
FEBRUARY, 1990

MARK S. GORDON, THERESA L. WINDUS, AND NIKITA MATSUNAGA
DEPARTMENT OF CHEMISTRY
NORTH DAKOTA STATE UNIVERSITY
FARGO, ND

LARRY P. DAVIS AND LARRY W. BURGGRAF
AIR FORCE OFFICE OF SCIENTIFIC RESEARCH
BOLLING AFB, DC

DONALD L. THOMPSON
DEPARTMENT OF CHEMISTRY
OKLOHOMA STATE UNIVERSITY
STILLWATER, OK

The general goal of this research (initiated in November, 1989) is to combine state-of-the-art electronic structure theory with modern methods for predicting dynamics and kinetics of chemical reactions to elucidate the structure, bonding, and reaction energetics for a variety of metastable species.

The species investigated to date include (1) SiH_5^- , (2) hexacoordinated sila-dianions; (3) silabicyclobutanes; and (4) NH_4^- and PH_4^- .

SiH_5^- is the simplest pentacoordinated silicon dianion, and as such, it is the prototype for this general class of compounds. Unlike most of its carbon analogs, pentacoordinated silicon anions tend to be stable structures and therefore potentially isolable experimentally. Typically, these species form by a nucleophilic attack of a small anion at a tetracoordinated silane center. Since this process is energetically downhill, the available energy could be used either to dissociate to reactants or to some other tetravalent silane or in some internal vibrational motion of the pentacoordinated compound. The most logical of the latter is the Berry pseudorotational motion of the ligands about the silicon center. This is important for two reasons. First, dissipation of the energy in this way can stabilize the pentacoordinated structure. Second, the

pseudorotational motion will have an impact on the final products. A key question in the overall process, then, is the efficiency with which energy is transferred from the initial reaction path into the pseudorotational motion. The first step we have taken to explore the answer to this question is to determine the reaction path hamiltonian (RPH) for the pseudorotational motion. This is carried out by first calculating the structures, energies, and harmonic vibrational frequencies of the minimum energy (trigonal bipyramidal) and transition state (tetragonal) structures at the MP2/6-31++G(d,p) and MP2/6-31G(d,p) levels of theory. Since the two sets of calculations are virtually identical, the minimum energy path (MEP) leading from transition state to minimum has been determined with the smaller basis set. After the complete MEP was mapped out using our fourth order Runge-Kutta (RK4) algorithm, the full hessian was determined at every 10th point along the MEP, giving rise to approximately 30 sets of force constants and projected harmonic frequencies. These results have been used to generate the adiabatic ground state curve, in which the zero point vibrational energies are added to the MEP, as well as the free energy curves at various temperatures. The next steps are to determine the rate coefficients for this reaction with variational transition state theory (VTST: currently underway at NDSU) and to explore the classical trajectories (currently underway at OSU).

Hexacoordinated sila-dianions are also generally stable compounds, such that the reaction



is very exothermic. For X=H, MP2/6-31++G(d,p) calculations suggest that the barrier to reaction (1) is only 2 kcal/mol and might disappear altogether at higher levels of theory. In addition, SiH_6^{2-} is found to be unstable to loss of an electron (negative vertical ionization potential). On the other hand, for X=F the barrier for reaction (1) is more than 20 kcal/mol and the hexacoordinated species has a positive ionization potential. AM1 calculations

find that the hexacoordinated species with $X=Cl$ and OH are also stable to both dissociation and autoionization. In addition, we have now investigate the compounds with the general formula SiF_nH_{6-n} . All of these compounds are minima on their respective potential energy surfaces, but only when $n>3$ are the hexacoordinated species stable to autoionization. The transition state for the $n=4$ compound has been found at the RHF/6-31+G(d) level of theory, and the MEP for reaction (1) is being calculated. This will be followed by the prediction of the RPH and an investigation of the reaction dynamics.

Tetrasilabicyclobutane displays an unusual structural isomerism. This and related compounds can undergo bond stretch isomerization, such that two stable isomers exist which differ only in the length of the Si-Si bridge bond. The isomer with the unusually long bond is the more stable structure, but when non hydrogen substituents are placed on the bridgehead atoms, the relative energies are reversed. For the parent compound, the relative energies of the two isomers and the transition state have been determined at the GVB/6-31G(d) level of theory. Then, using the hessian matrices at several points along the MEP, a RPH and free energy paths at several temperatures have been determined. The dynamics of this process will now be investigated.

The structures of all stationary points on the NH_4^+ and PH_4^+ potential energy surfaces have been determined at the MP2/6-311++G(2d,2p) level of theory, with relative energies being obtained with MP4. For both species, two stable structures are found, one with C_s symmetry and a much higher isomer with T_d symmetry. The MEP's are now being followed from the transition states to the appropriate minima.

Synthesis of high density BeH₂: A potential high hydrogen fuel.

J. Akella, G. S. Smith, N. Winter and Q. Johnson

Lawrence Livermore National Laboratory

P.O. Box 808, Livermore, CA 94550

RATIONALE:

Among materials containing high levels of available hydrogen per unit weight (mol H/cc), BeH₂ is quite unique. At room temperature BeH₂ has a crystalline density of 0.78 g/cc and a hydrogen density of 0.127 mol H/cc. As a missile propellant BeH₂'s major asset is the net amount of it needed, and according to one estimate is ~30% by weight less than other potential fuels. Indeed, if a higher density form of BeH₂ could be made stable at ambient conditions, then the further reduction in weight and volume of propellant (needed) could be significant.

BeH₂ has a loosely packed crystal structure: application of pressure is expected to create a more densely packed structure. In the case of SiO₂ which has a somewhat similar framework structure, the high pressure forms are retained indefinitely at ambient conditions when the pressure is released (Fig. 1). Thus, a metastably retained form the BeH₂ having a density increase of 10% or even greater is not unrealistic. To establish this we propose a study of BeH₂ under pressure and also temperature.

EXPERIMENTAL PROCEDURE:

Crystal structure changes and pressure-volume relationship in BeH₂ will be investigated in a diamond-anvil cell and multi-anvil device (MAX80 type) by X-ray diffraction techniques. Because of its low atomic number, it will be difficult to conduct high pressure structural studies on BeH₂ using conventional X-ray generators. We plan to use synchrotron X-ray source, which is orders of magnitude more intense than the conventional units, to obtain diffraction data. We intend further, through experimental and theoretical studies on BeH₂ to locate exactly at what pressure new phase(s) appear and their stability range. We also seek to establish unequivocally retention of the high pressure phase metastably under ambient conditions (eg. as in graphite-diamond).

PRELIMINARY RESULTS:

The crystal and molecular structure of BeH₂ at ambient-conditions has been determined from high-resolution powder diffraction data obtained by members of our group at the National Synchrotron Light Source (Smith et al., 1988). Computer indexing methods resulted in a determination of the unit cell as body-centered orthorhombic with $a = 9.082(4)$, $b = 4.160(2)$, $c = 7.707(3)$ Å; $V = 291.2(2)$ Å³, with systematic absences corresponding to space groups, Ibam or Iba2. The structure solved by quasi-three dimensional techniques is based on a corner-sharing BeH₄ tetrahedra rather than flat infinite chains containing hydrogen bridges previously assumed. There are 12 BeH₂ molecules in the unit cell.

In an exploratory experiment with BeH₂ under pressure using diamond-anvil cell apparatus at Stanford Synchrotron Radiation Laboratory (SSRL), there were indications that room pressure BeH₂ phase undergoes a structural change which is retained metastably after release of pressure. Unfortunately the present data are too sparse to be conclusive and for any further interpretation.

FUTURE DIRECTIONS:

First, we want to reestablish the quenchability of the high pressure phase to room pressure and temperature. Second, we will explore the synthesis of high density BeH₂ using mineralizers or dopants to discover feasible fabrication methods for industrial production. Third, we can extend similar studies to other materials that may hold promise as high energetic materials in the future.

REFERENCE:

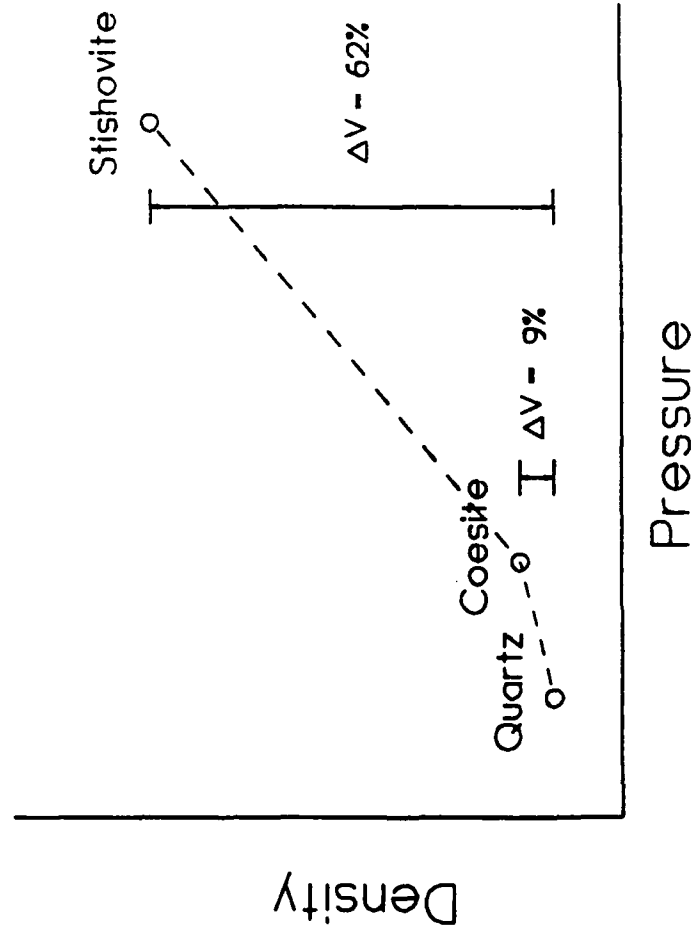
G. S. Smith, Q. C. Johnson, D. K. Smith, D. E. Cox, R. L. Snyder, R.-S. Zhou, and A. Zalkin, The crystal and molecular structure of beryllium hydride, Solid State Comm, 67, pp. 491-494, 1988.

FIGURE CAPTION:

Fig. 1 Schematic representation of the density changes in SiO₂ phases.

Pressure Causes Large Density Changes

Example: SiO_2



- Quartz: Open framework of SiO_4 tetrahedra
- Coesite: More compact packing of SiO_4 tetrahedra
- Stishovite: TiO_2 - like packing of SiO_6 octahedra

AIR FORCE OFFICE OF SCIENTIFIC RESEARCH: ANNUAL CONTRACTORS MEETING, 1990

Synthesis of New High Energy Density Materials. Synthesis and Reactions

of meso- and d,l-D₃-Trishomocubylidene-D₃-trishomocubane

Principal Investigator: Dr. Alan P. Marchand

Department of Chemistry, University of North Texas
NT Station, Box 5068, Denton, TX 76203-5068

Grant Number AFOSR-88-0132

INTRODUCTION

A significant portion of our current research program is concerned with the synthesis and chemistry of novel, strained polycyclic "cage" molecules. As part of this program, we have developed syntheses of new polycyclic C₁₁-C₂₂ cage systems. Cage molecules possess rigid, highly compact structures. An important feature of such systems is that they generally exhibit unusually high densities, and they often contain considerable strain energy. Hydrocarbon systems of this type are expected to possess unusually high net volumetric heats of combustion. Such compounds are of intense current interest to U. S. military agencies as a potential new class of energetic solid and liquid fuels for airbreathing missiles. In addition, polynitro-functionalized cage systems are of interest as a potential new class of high energy/high density explosives.

Progress that has accrued on grant AFOSR-88-0132 is summarized below.

**I. NOVEL C₂₂H₂₄ ALKENE DIMERS FORMED VIA REDUCTIVE DIMERIZATION OF
POLYCYCLIC CAGE KETONES. POTENTIAL NEW FUELS FOR AIRBREATHING MISSILES**

1. We have synthesized a new class of relatively nonvolatile energetic materials via titanium-promoted reductive dimerization of pentacyclo[5.4.0.0^{2,6}.0^{3,10}.0^{5,9}]undecan-8-one (PCU-8-one).
2. This reaction affords all four possible C₂₂H₂₄ PCU alkene dimers. One isomer has been isolated by column chromatography; its structure has been determined by single crystal

X-ray structural analysis. The calculated crystal density of this material is 1.284 g-cm⁻³.

3. Treatment of a chloroform solution of a mixture of the four PCU alkene dimers with trifluoroacetic acid at room temperature affords a mixture of two adducts along with two unreacted alkene dimers. The mixture of the two adducts was isolated and then was subjected to hydrolysis with aqueous base. Oxidation of the mixture of alcohols thereby obtained afforded a mixture of two isomeric C₂₂H₂₄O ketones (5a and 5b).

4. The structures of 5a and 5b have been elucidated via X-ray crystallographic techniques.

5. Titanium-promoted reductive dimerization of D₃-trishomocubanone affords two diastereoisomeric C₂₂H₂₄ alkene dimers, meso (7a) and d,l (7b). The X-ray structure of 7a is shown; the calculated crystal density of this material is 1.302 g-cm⁻³.

6. The X-ray structure of 7b is shown. The calculated crystal density of this compound is 1.269 g-cm⁻³. Note the dramatic difference in calculated crystal densities between 7a and

7b. The origin of this effect is of considerable theoretical interest and merits further scrutiny.

7. Electrophilic additions of trifluoroacetic acid and of bromine to the C=C double bonds in meso- and in d,l-D₃-trishomocubylidene-D₃-trishomocubane have been studied. These isomeric compounds display remarkably different behavior toward electrophiles. Based upon the results of MM2 and AM1 computations, the observed reactivity differences can be rationalized in terms of a secondary steric effect that is a consequence of the molecular symmetries of the meso- and d,l-alkene dimers.

8. The synthesis of homocubylidenehomocubane and the X-ray structure of this highly strained alkene are shown. Note the unusually high calculated crystal density of this compound, i.e., 1.38 g-cm⁻³. The results of molecular mechanics calculations (MM2) indicate that the standard heat of formation of homocubylidenehomocubane is +228.7 kcal/mol, and its strain energy content is 243.33 kcal/mol. This is an outstanding

candidate fuel system!

9. When reacted with silver nitrate impregnated silica gel, trishomocubylidenetrishomocubane undergoes valence tautomerism to afford the corresponding "norsnoutane alkene dimer". The X-ray structure of this material is shown (calculated crystal density: 1.349 g-cm^{-3}).

10. Reaction of D_3 -trishomocubyl bromide with magnesium results in reductive coupling with concomitant formation of a mixture of meso- and d,l- D_3 -trishomocubane dimers. The pure d,l isomer, mp $185.5\text{--}186.5^\circ\text{C}$, has been isolated via fractional recrystallization of this mixture from benzene.

11. The structure of the d,l isomer thereby obtained has been elucidated via X-ray crystallographic techniques. The calculated crystal density of this compound is 1.290 g-cm^{-3} .

12. Two unusual spirocyclic cage hydrocarbons, **11a** and **11b**, have been synthesized.

13. WORK IN PROGRESS: (a) Titanium-promoted dimerization of a novel heptacyclic diketone mono(ethylene ketal). (b) Polymerization of the parent D_{2d} heptacyclic diketone.

II. SYNTHESIS OF NEW, SUBSTITUTED HOMOPENTAPRISMANES

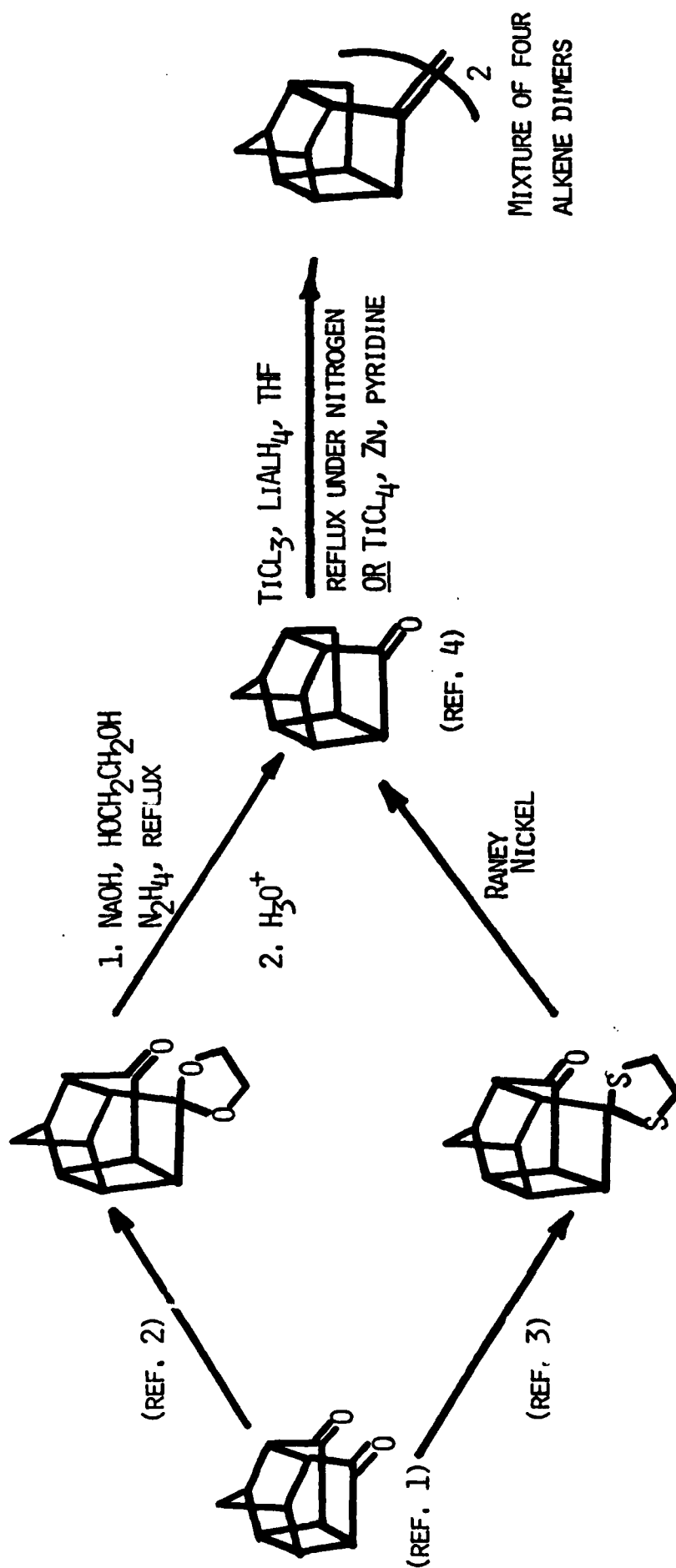
14. Our synthesis of homopentaprismane-8-carboxylic acid is shown. This illustrates a new and potentially general method for introducing a functionalized methylene bridge across the 8,11-positions of PCU. We plan to utilize this methodology for synthesizing other new polycyclic systems.

III. SYNTHESIS OF POLYNITROPOLYCYCLIC CAGE COMPOUNDS. A NEW CLASS OF HIGH DENSITY/HIGH ENERGY EXPLOSIVES

15. Our synthesis of 4,4,8,8,11,11-hexanitro-PCU is shown. The results of flyer plate tests on small quantities of this material (ca. 40-50 mg) provide preliminary evidence that it is both a more powerful and less sensitive explosive than TNT.

ACKNOWLEDGMENTS

We thank the Air Force Office of Scientific Research (Grant AFOSR-88-0132) for financial support of the studies reported herein. Our synthesis of 4,4,8,8,11,11-hexanitro-PCU received additional support from the U. S. Army Armament Research, Development & Engineering Center, Picatinny Arsenal, NJ under contract number DAA21-86-C-0091. The contributions of the many students and colleagues who have been associated with this study and whose names appear in the Figures are gratefully acknowledged.



REFERENCES:

1. A. P. MARCHAND AND R. W. ALLEN, J. ORG. CHEM. **39**, 1536 (1974).
2. P. E. EATON, ET AL., J. ORG. CHEM. **41**, 1445 (1976).
3. B. M. LEMAN, ET AL., J. ORG. CHEM. USSR **14**, 2336 (1978).
4. A. P. MARCHAND AND R. KAYA, J. ORG. CHEM. **48**, 5392 (1983).

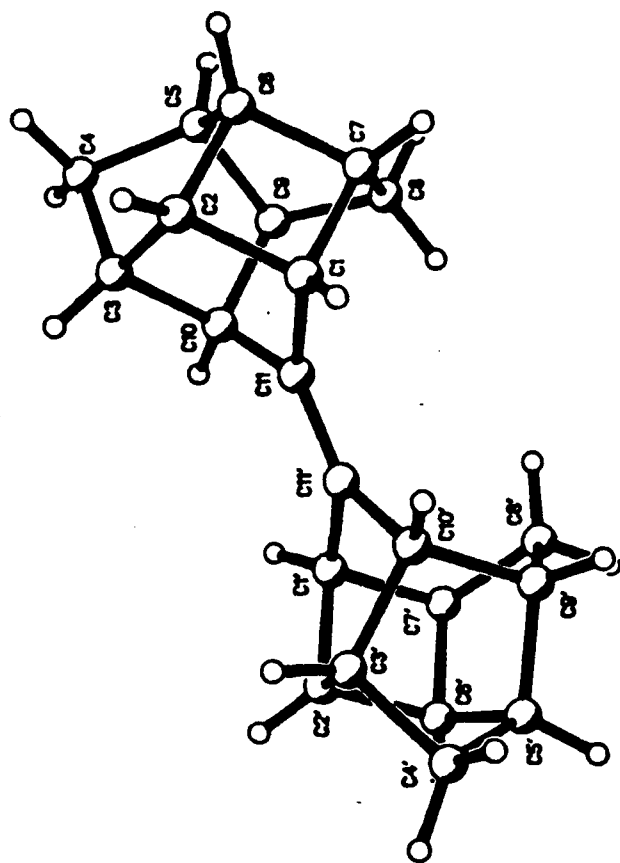
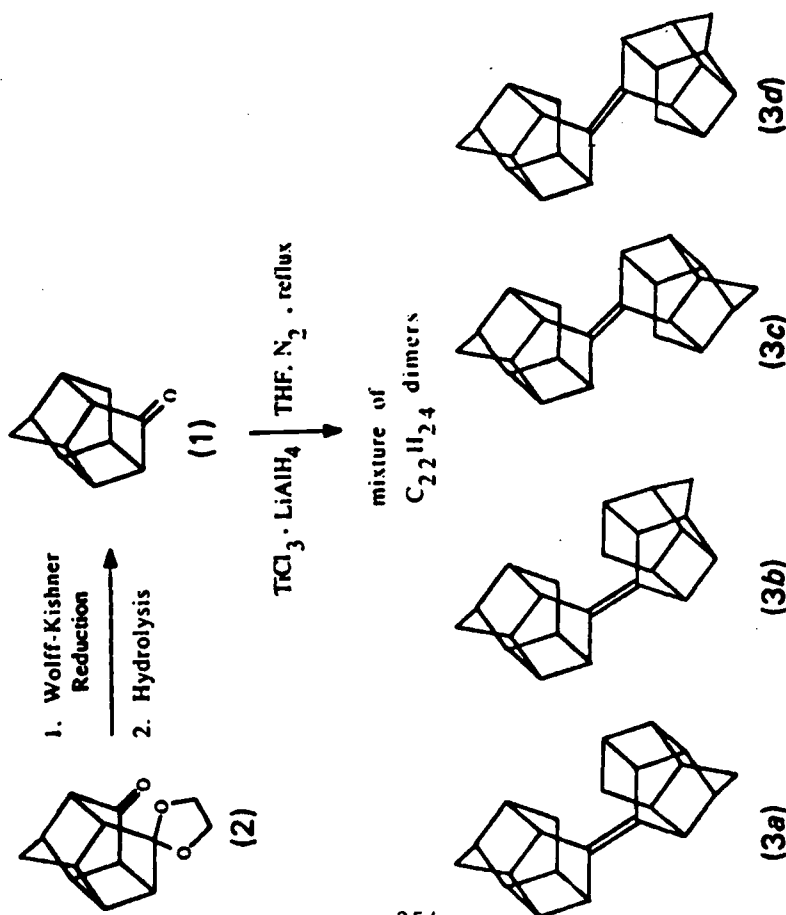


Fig. 1. Results of the X-ray study on (3a).

Results of Single Crystal X-ray Structural Analysis

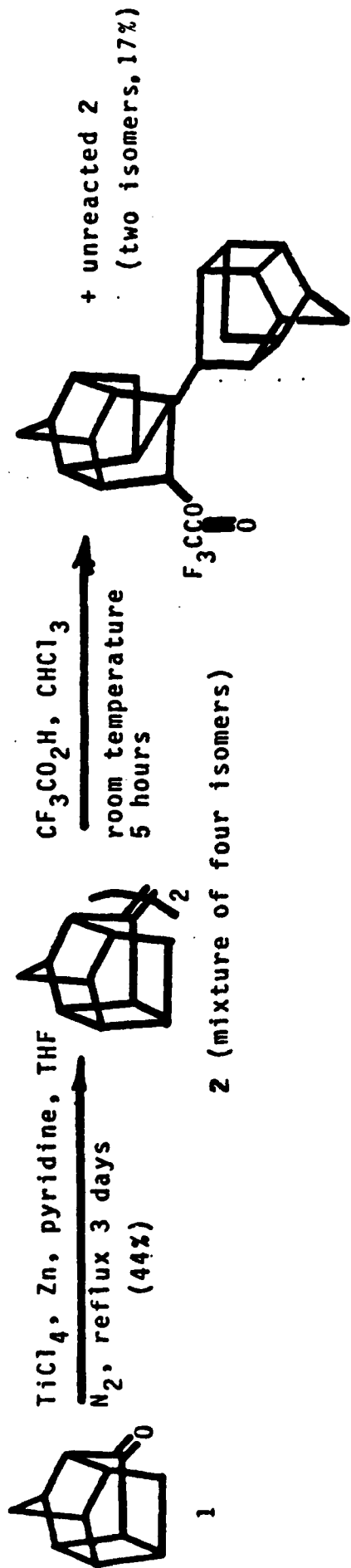
a =	6.613 (1) Å
b =	10.809 (2) Å
c =	10.993 (2) Å
α =	97.5 (2)°
β =	9.8 (1)°
γ =	99.3 (2)°

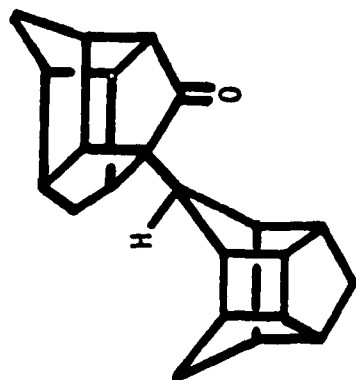
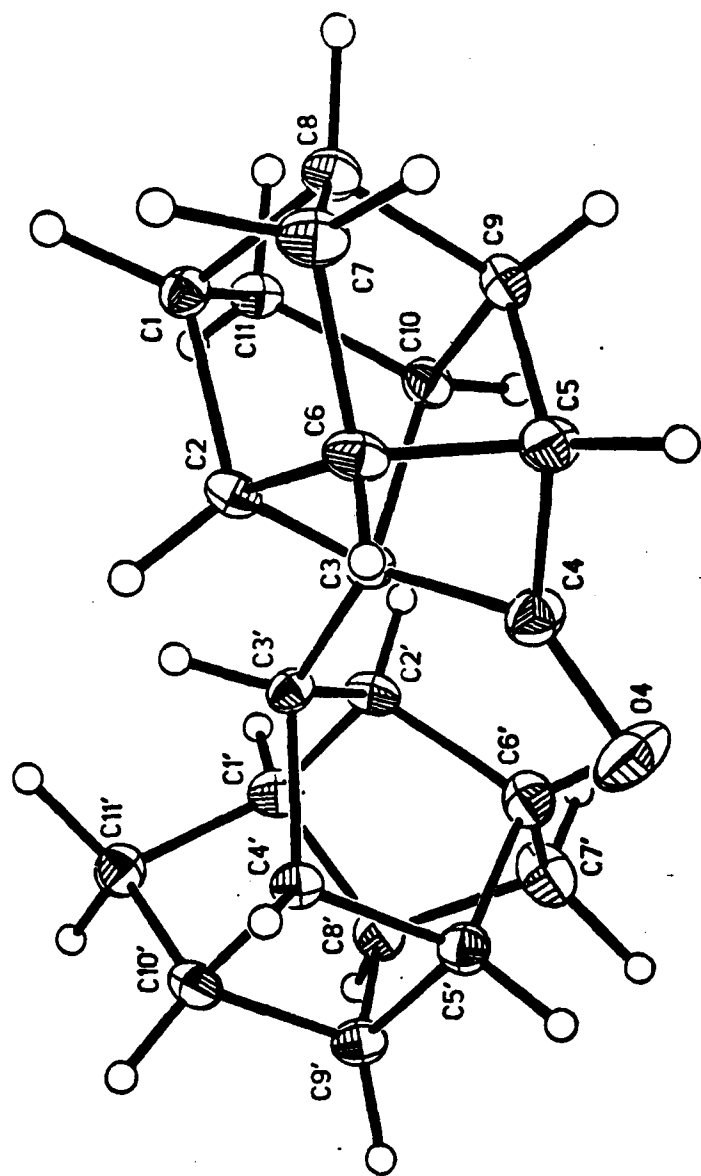
Space Group $P\bar{1}$

Triclinic

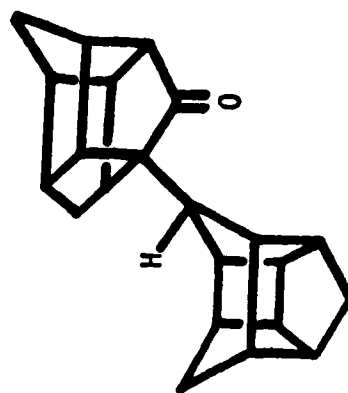
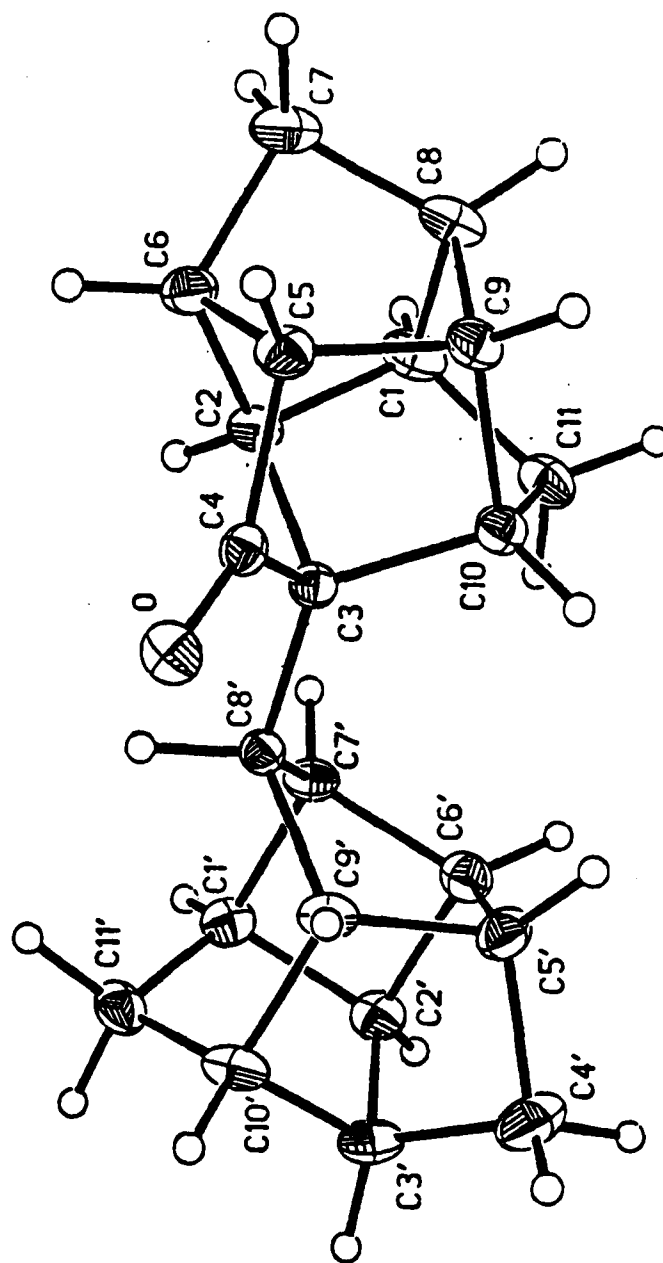
$\rho_{\text{calcd}} = 1.284 \text{ g-cm}^{-3}$

J. L. Flippen-Anderson, R. Gilardi, C. George,
 A. P. Marchand, P.-w. Jin, and M. N. Deshpande,
 Acta Cryst. 1988, C44, 1617-1619.

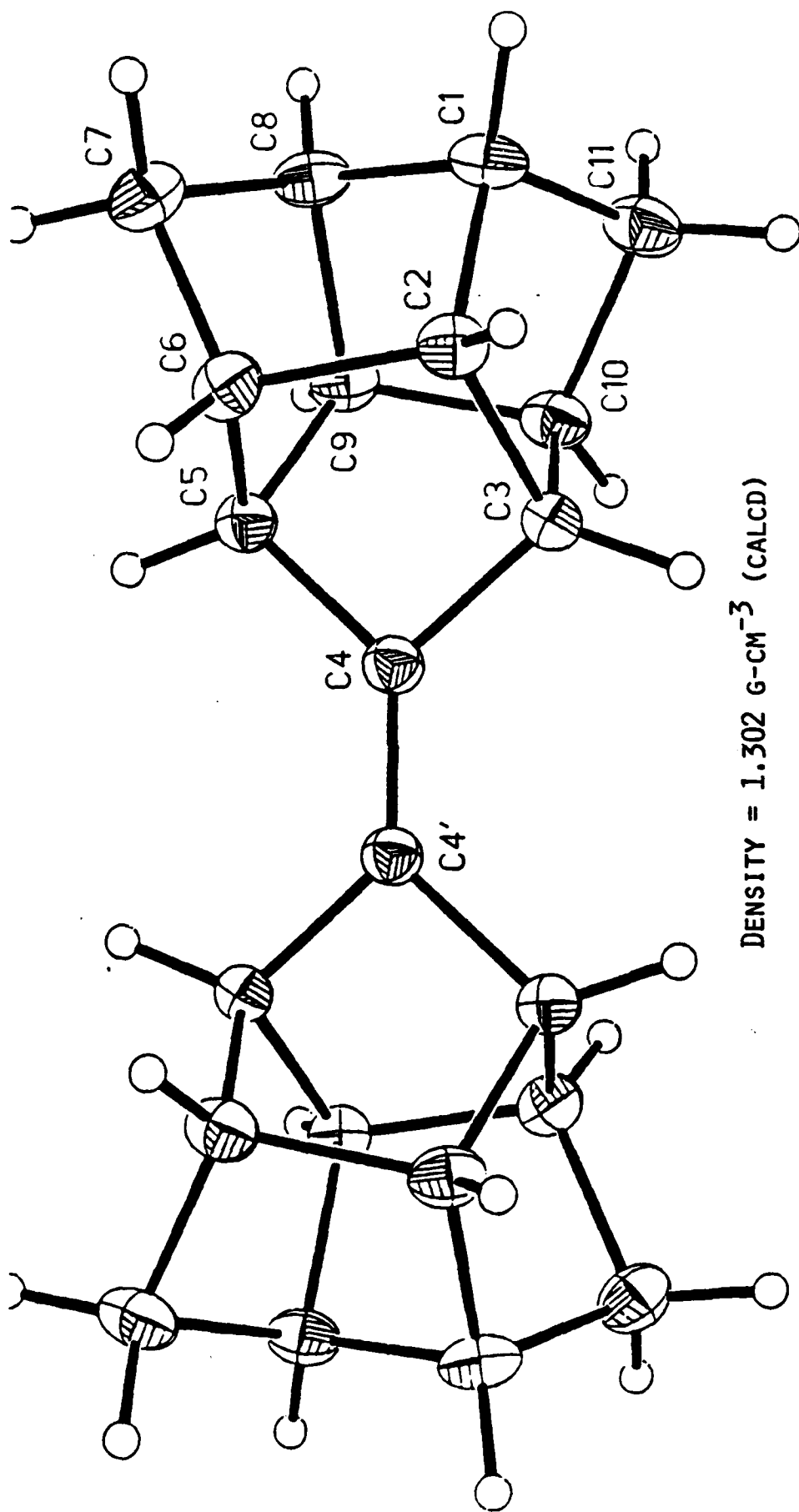




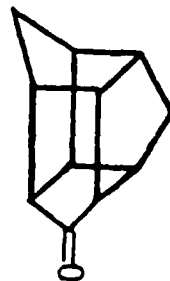
Density = 1.358 g-cm⁻³



Density = 1.340 g-cm⁻³

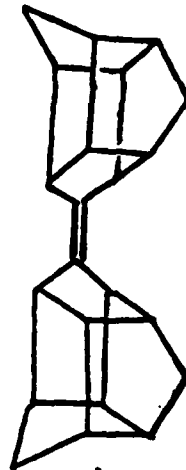


DENSITY = 1.302 G-CM⁻³ (CALCD)



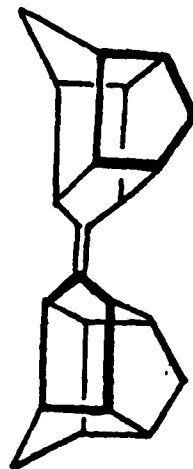
6

TiCl₄-Zn, THF
PYRIDINE, N₂
REFLUX 24 H (65%)



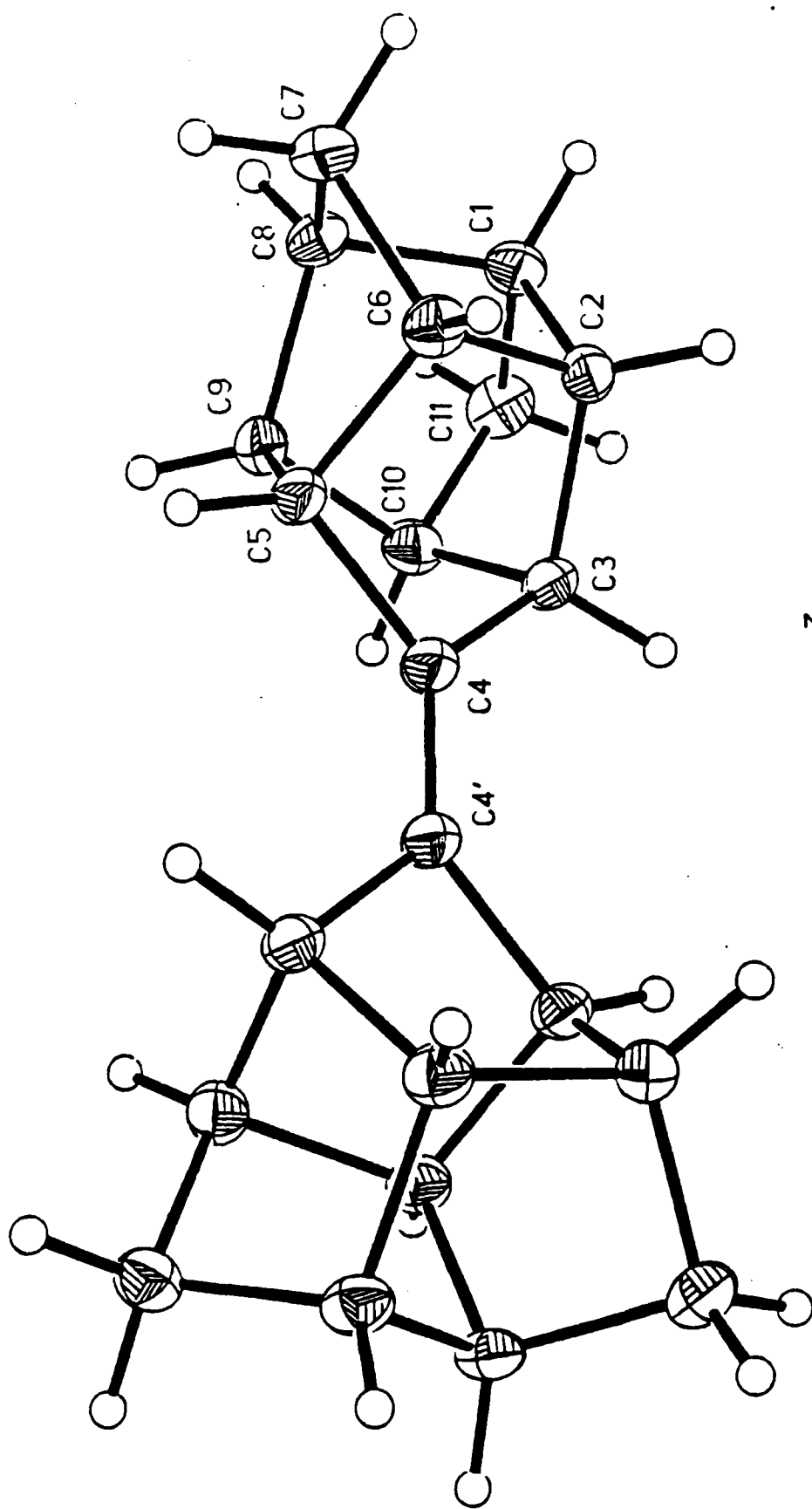
7A (MESO)

+



7B (D,L)

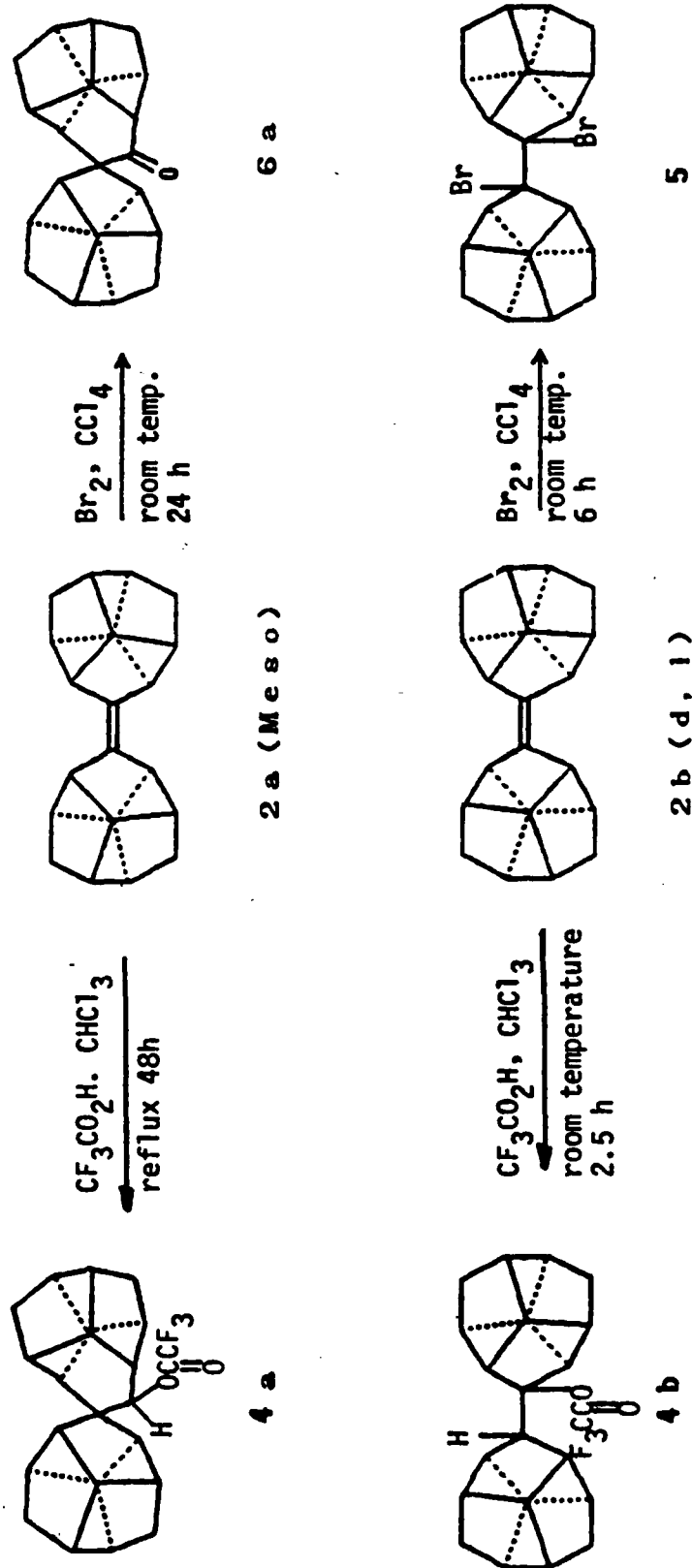
THE MESO ISOMER (7A) WAS ISOLATED VIA CAREFUL FRACTIONAL RECRYSTALLIZATION OF THE PRODUCT MIXTURE FROM LIGROIN. THE MATERIAL THEREBY OBTAINED DISPLAYED MP 246 °C.
SYNTHESIS: A. P. MARCHAND, M. N. DESHPANDE, AND G. MADHUSUDHAN REDDY, UNIVERSITY OF NORTH TEXAS
X-RAY CRYSTALLOGRAPHY: WILLIAM H. WATSON AND ANTE NAGL, DEPARTMENT OF CHEMISTRY,
TEXAS CHRISTIAN UNIVERSITY, FORT WORTH, TEXAS 76129

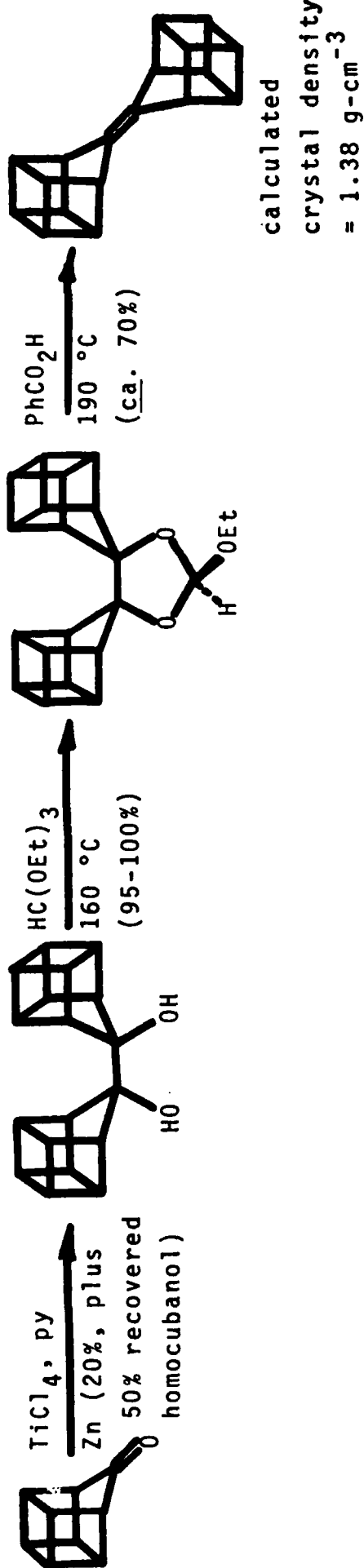


DENSITY = 1.269 G-CM⁻³ (CALCD)

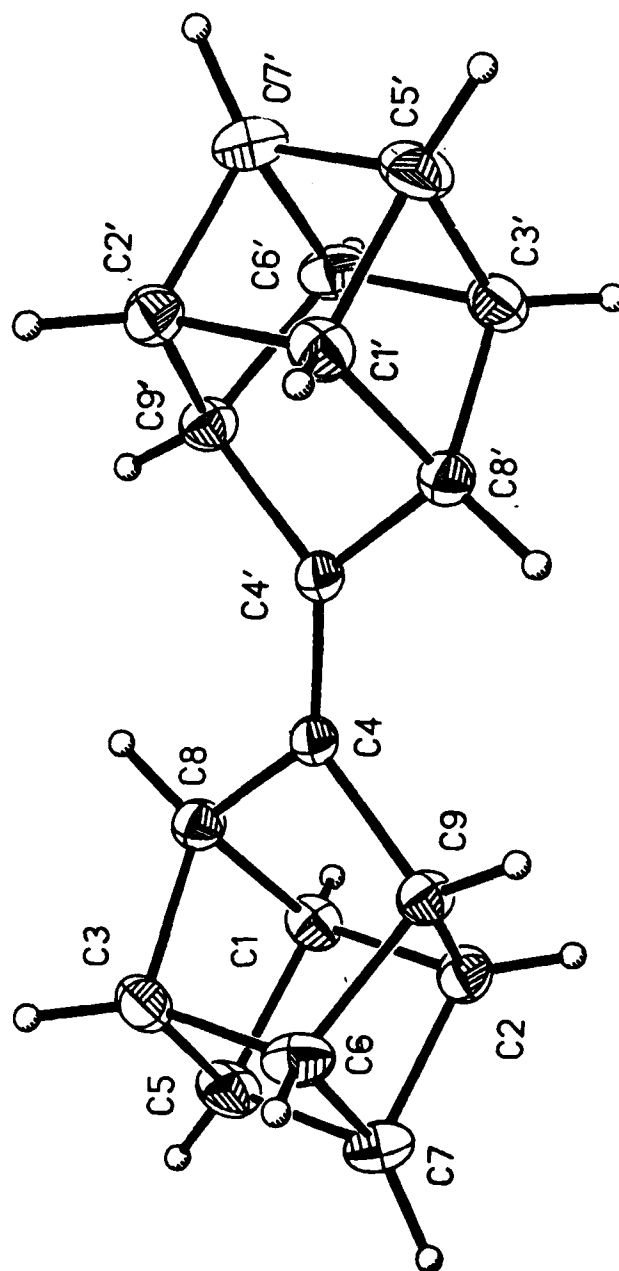
WE HAVE ALSO ISOLATED THE D,L DIMER, 7B, MP 186 °C (RECRYSTALLIZED FROM HEXANE-ETHER). THE D,L ISOMER CRYSTALLIZES IN SPACE GROUP P1 (TRICLINIC); IT IS SIGNIFICANTLY LESS DENSE THAN THE CORRESPONDING MESO ISOMER (SPACE GROUP C2/C, MONOCLINIC, DENSITY = 1.302 G-CM⁻³).
SYNTHESIS: A. P. MARCHAND, M. N. DESHPANDE, AND G. MADHUSUDHAN REDDY, UNIVERSITY OF NORTH TEXAS
X-RAY CRYSTALLOGRAPHY: WILLIAM H. WATSON AND ANTE NAGL, DEPARTMENT OF CHEMISTRY
 TEXAS CHRISTIAN UNIVERSITY, FORT WORTH, TEXAS 76129

ELECTROPHILIC ADDITION OF BROMINE TO THE C=C DOUBLE BOND IN MESO-D₃-TRISHOMOCUBYLIDENE-D₃-TRISHOMOCUBANE ALSO WAS STUDIED. THE PRODUCT OBTAINED FROM THIS REACTION, AFTER CHROMATOGRAPHIC WORKUP, WAS FOUND TO BE REARRANGED SPIROKETONE **6a**.



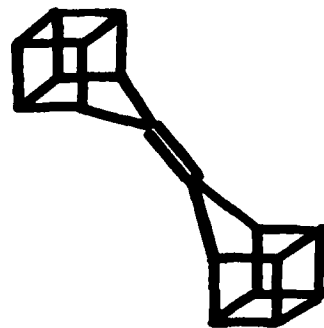


X-ray Crystal Structure of Homocubylidenehomocubane

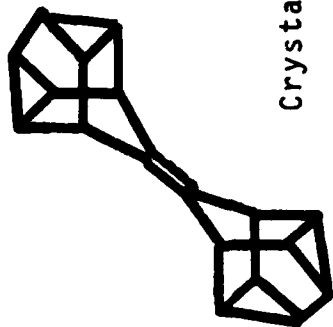


SYNTHESIS:

DR. V. VIDYASAGAR
 DEPARTMENT OF CHEMISTRY
 UNIVERSITY OF NORTH TEXAS
 X-RAY CRYSTALLOGRAPHY:
 PROFESSOR WILLIAM H. WATSON
 DEPARTMENT OF CHEMISTRY
 TEXAS CHRISTIAN UNIVERSITY



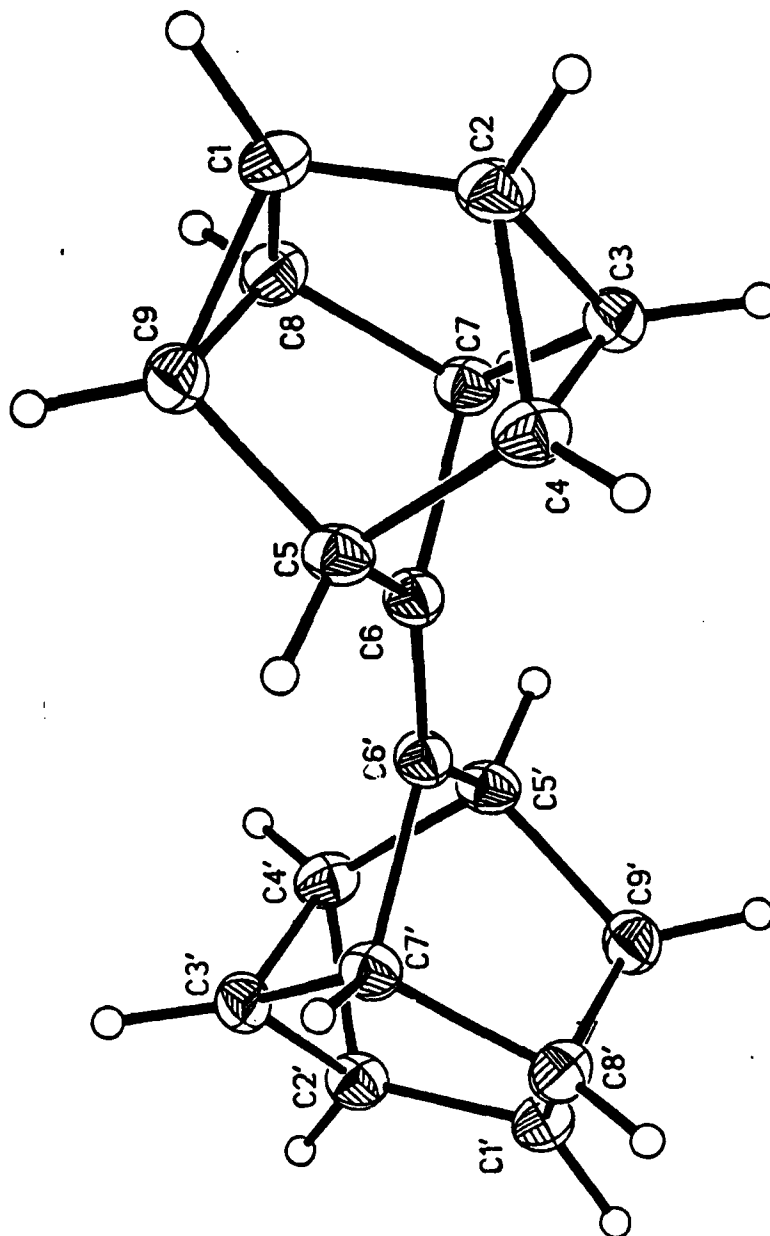
10% AgNO₃ on silica gel
 Benzene, 25 °C, 6 days



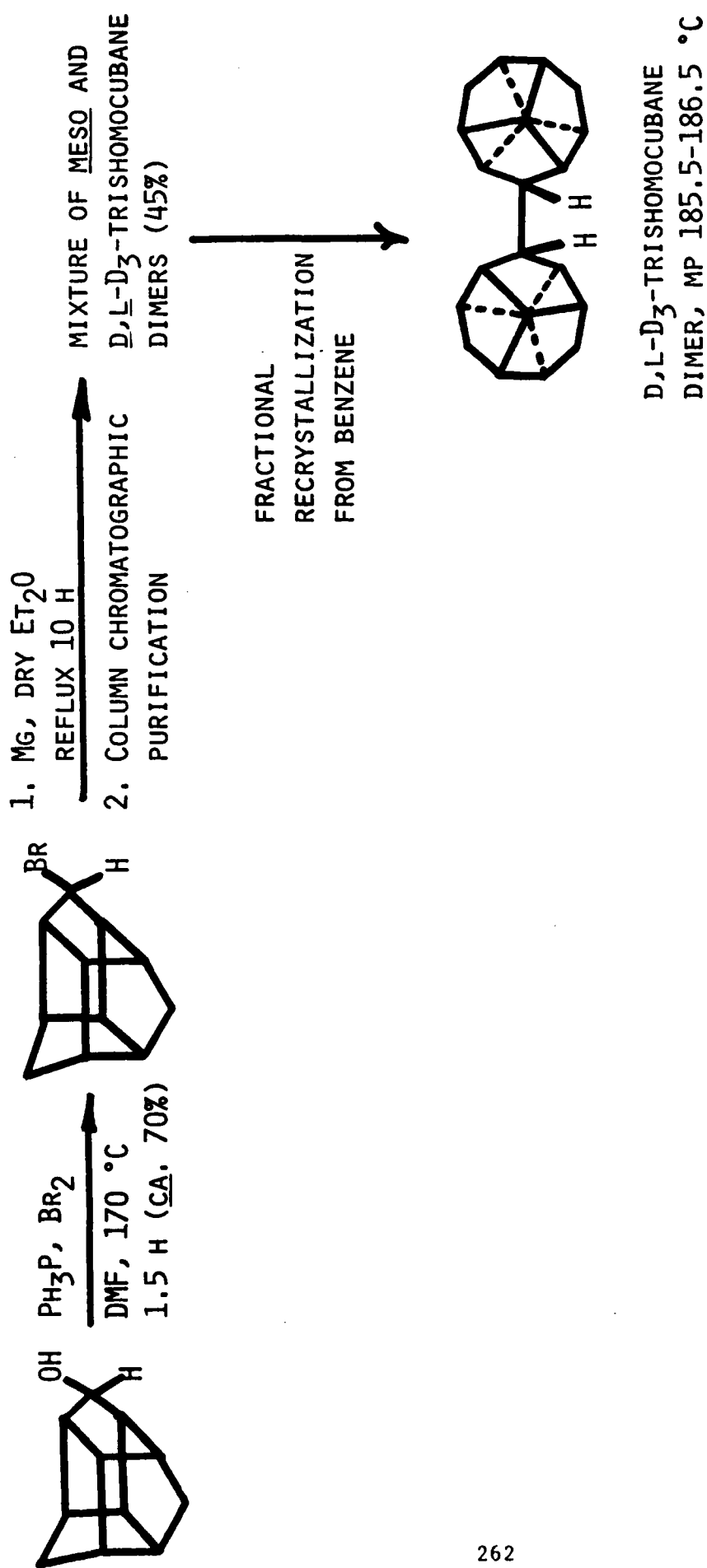
Crystal Density = 1.349
 g-cm⁻³

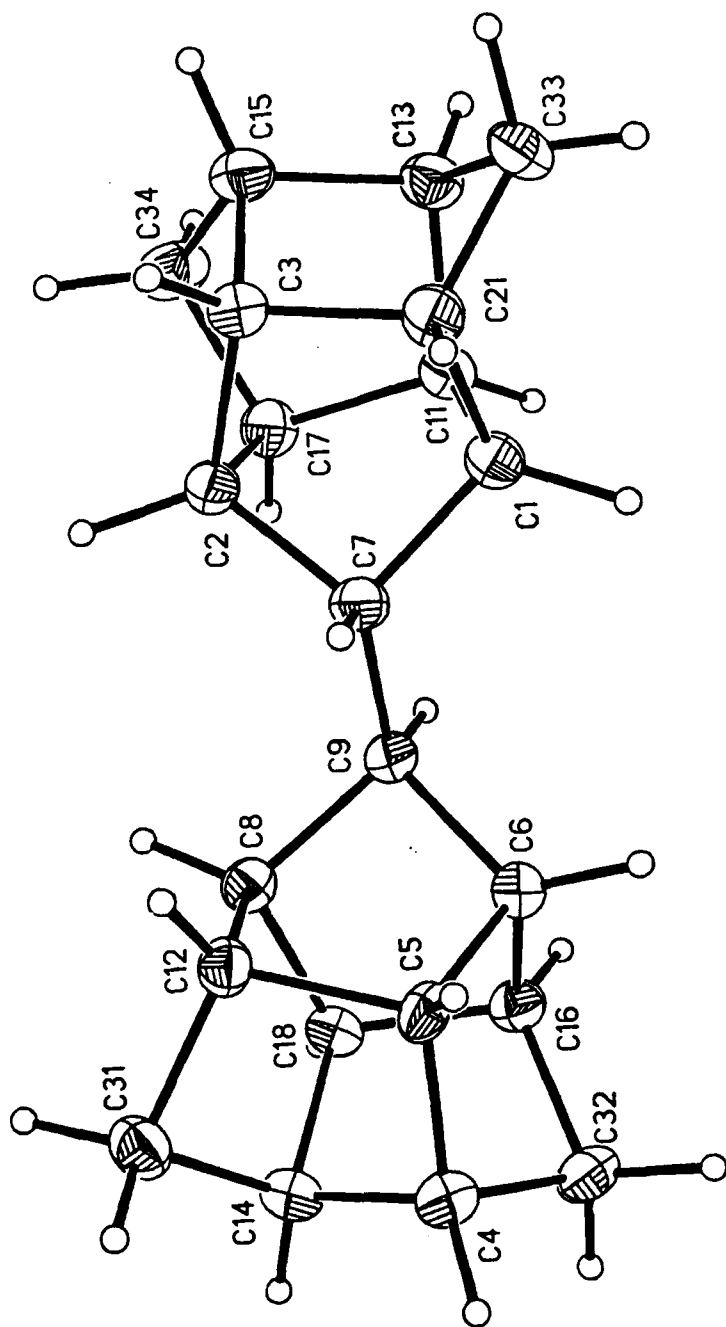
(Dr. V. Vidyasagar)

X-ray crystal structure of "norsnoutane alkene dimer":



(Professor W. H. Watson,
 Dr. Ram Kashyap)





D,L-D₃-TRISHOMOCUBANE DIMER, C₂₂H₂₆

CALCULATED CRYSTAL DENSITY = 1.290 G-CM⁻³

CRYSTAL SYSTEM: TRICLINIC
SPACE GROUP P1

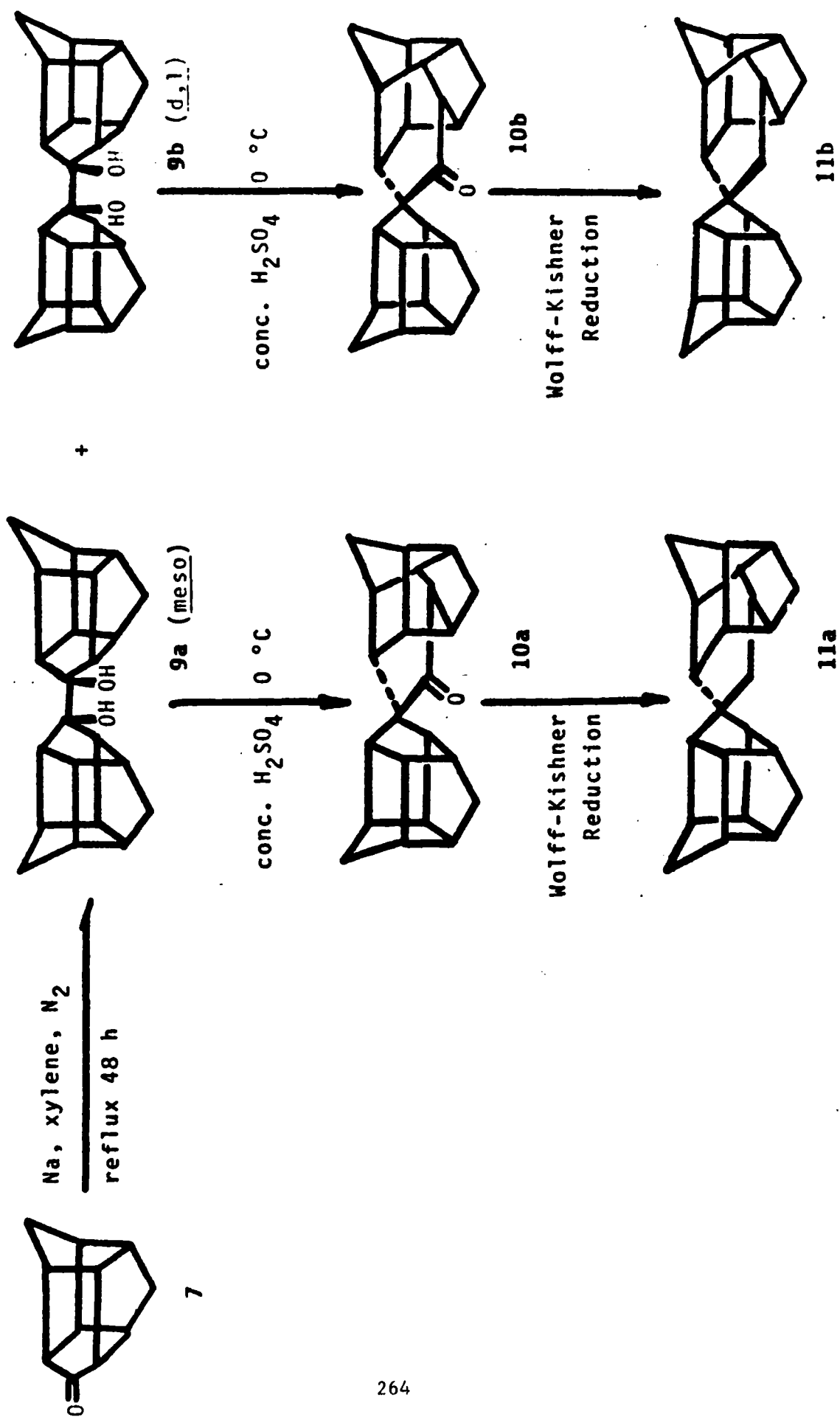
SYNTHESIS: ALAN P. MARCHAND AND G. MADHUSUDHAN REDDY

DEPARTMENT OF CHEMISTRY, UNIVERSITY OF NORTH TEXAS

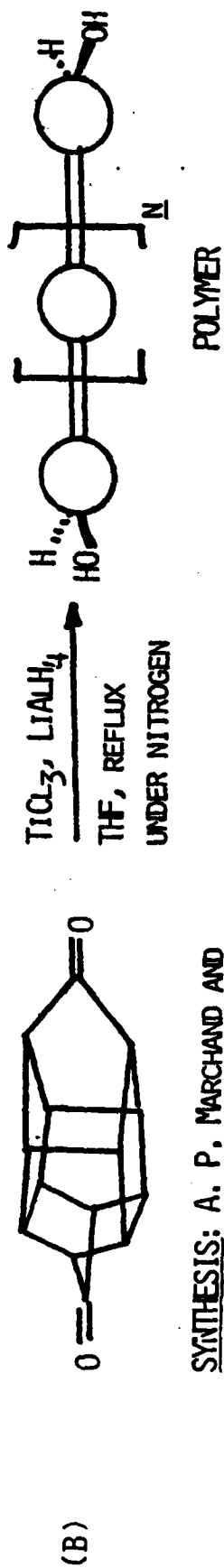
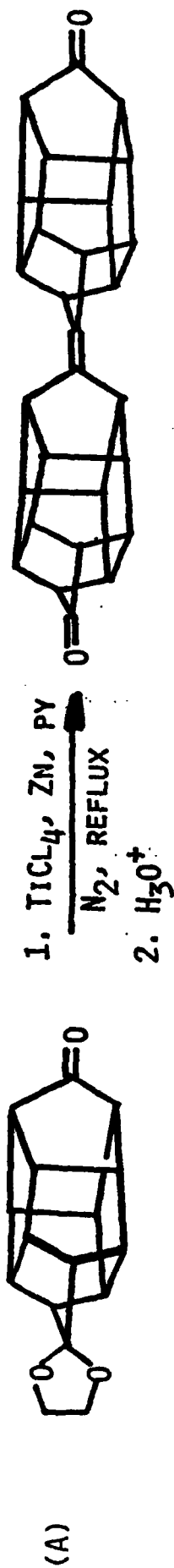
X-RAY STRUCTURE:

WILLIAM H. WATSON AND RAM P. KASHYAP

DEPARTMENT OF CHEMISTRY, TEXAS CHRISTIAN UNIVERSITY



WORK IN PROGRESS



SYNTHESIS: A. P. MARCHAND AND
A. D. EARLYWINE, J. ORG. CHEM.,
49, 1660 (1984).

SYNTHESIS OF FUNCTIONALIZED HOMOPENTAPRISMANES

Synthesis of Hexacyclo[5.4.0.0^{2,6}.0^{3,10}.0^{5,9}.0^{8,11}]undecane-8- carboxylic Acid (Homopentaprismane-8-carboxylic Acid)

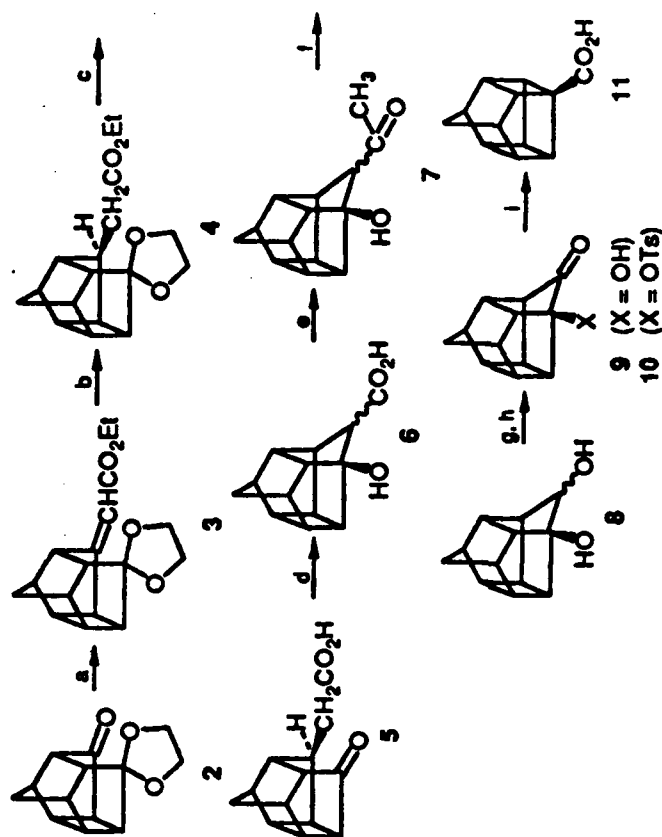
Alan P. Marchand* and Mahendra N. Deshpande

Department of Chemistry, University of North Texas,
Denton, Texas 76203-5068

Received November 28, 1988

As part of a continuing program concerned with the synthesis and chemistry of novel polycyclic systems,¹ we are seeking new synthetic entries into highly strained cage molecules. In a previous study,² a synthesis of 1,3-bishomopentaprismane was developed that involved introduction of a methylene bridge across the 8,11-positions of a readily available³ cage dione, pentacyclo[5.4.0.0^{2,6}.0^{3,10}.0^{5,9}]undecane-8,11-dione (1, Scheme I). More recently, another, potentially generalized method has been developed to introduce a *functionalized* methylene bridge across the 8,11-positions of 1. We now report the successful application of this strategy for the synthesis of the title compound (11). The parent hydrocarbon, homopentaprismane,^{3,4} and several substituted homopentaprismanes have been synthesized previously in our laboratory⁴ and by other investigators.⁵⁻⁷

Scheme II^a



^a (a) (EtO)₂P(O)CH₂CO₂Et, NaH, THF, reflux 36 h (93%); (b) H₂ (1 atm), Pd-C, EtOAc, room temperature, 2 days (100%); (c) 10% aqueous H₂SO₄, dioxane, reflux 2 days (90%); (d) NaH, DMF-THF, 20 h (91%); (e) MeLi, THF (80%); (f) (CF₃CO)₂O, 90% aqueous H₂O₂, 1 day, followed by 5% aqueous NaOH, MeOH, 50 °C, 17 h (60%); (g) NCS, Me₂S, Et₃N, -25 °C (77%) or (COCl)₂-DMSO, -60 °C → -40 °C (42%); (h) TsCl, py (88%); (i) 20% aqueous KOH, reflux 7 h (94%).

Synthesis of 4,4,8,8,11,11-Hexanitropentacyclo[5.4.0.0^{2,5}.0^{3,10}.0^{4,9}]- undecane

Alan P. Marchand,* Paritosh R. Dave, D. Rajapaksa, and
 Benny E. Arney, Jr.

*Department of Chemistry, University of North Texas,
 Denton, Texas 76203-5068*

Judith L. Flippen-Anderson,* Richard Gilardi, and
 Clifford George

*Laboratory for the Structure of Matter, Naval Research
 Laboratory, Washington, D.C. 20375-5000*

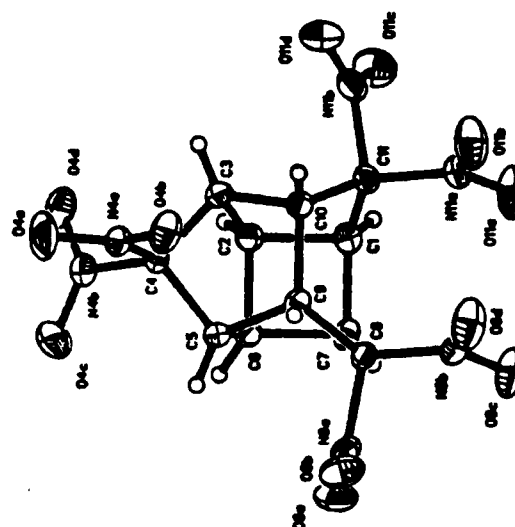
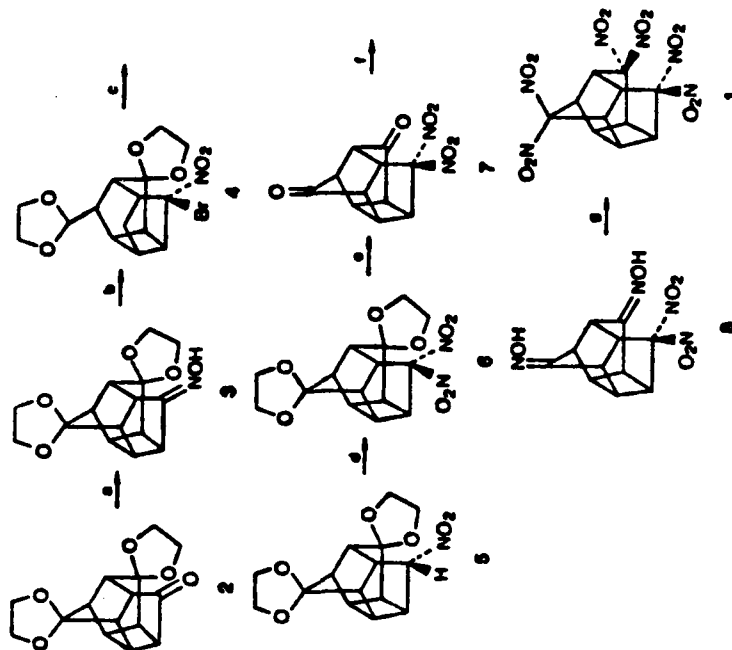


Figure 1. X-ray structure drawing of 1.

Scheme 1^a



^a(a) $\text{NH}_2\text{OH}\cdot\text{HCl}$, K_2CO_3 , EtOH , reflux 24 h (79%); (b) NBS, dioxane, room temperature, overnight (62%); (c) NaBH_4 , 60% aqueous EtOH , $0^\circ\text{C} \rightarrow \text{room temperature}$, 1 h (84%); (d) $\text{K}_3\text{Fe}(\text{CN})_6$, NaNO_2 , aqueous MeOH , room temperature, 2 h (83%); (e) concentrated H_2SO_4 , CH_2Cl_2 , room temperature, 24 h (80%); (f) $\text{NH}_2\text{OH}\cdot\text{HCl}$, NaOAc , MeOH , reflux 2 h (75%); (g) 98% red nitric acid, NH_4NO_3 , urea, dry CH_2Cl_2 , reflux 0.5 h, then 30% aqueous H_2O_2 , reflux 15 min (19%).

THEORETICAL STUDY OF NOVEL BONDING IN MOLECULES*

Roberta P. Saxon
Molecular Physics Laboratory, SRI International
Menlo Park, California 94025

Species which show promise as high energy density materials must exhibit novel bonding mechanisms which distinguish them from conventional stable molecules. One class of species that has been suggested previously is ion-pair states. Our extensive theoretical study¹ of the H_3O system has been reported at previous HEDM meetings.² Because of the open shell nature of the O^- ($2p^5\ 2P$) anion, more than one electronic state can result from the interaction of H_3^+ and O^- . While there exists a region of the lowest potential energy surface that may be described as an ion-pair, our results have shown that the ion-pair is not even a local minimum on that surface. The ion-pair minimum identified on the excited 1^2E surface in C_{3v} geometry is only a local minimum which is not stable in lower symmetry.

Our study¹ of H_3O , along with the work of Montgomery and Michels^{3,4} on H_4 and H_3Li and of Huang and Lester⁵ on H_4 have led to the generalization that ion-pair states based on the H_3^+ cation will not be stable. The reasoning underlying this prediction is based on the fact that ground state neutral H_3 is not a stable species. Therefore, any back-charge transfer to H_3^+ will lead to the neutral H_3 , which is unstable with respect to $\text{H}_2 + \text{H}$. However, the greater the detachment energy of the negative ion, the greater the possibility of stability. The fluorine atom with an electron affinity of 3.4 eV,⁶ the largest of the first-row elements, would be expected to be the most favorable choice for the anion. Calculations on H_3F reported here, however, support the prediction that there are no stable ion-pair states based on the H_3^+ cation.

H_3F

There is one electronic state arising from the interaction of $\text{H}_3^+(1\text{A}_1')$ and $\text{F}^-(1\text{S})$. Geometry optimizations were performed with a C_{3v} symmetry constraint, as anticipated for the ion-pair state, and without symmetry constraint to search for the global minimum on the ground state potential surface. Calculations were carried out at the SCF level with standard basis sets and at the MCSCF level with the F atom ($4s3p2d$) basis set of Bauschlicher and Taylor⁷ used in work on the electron affinity of the fluorine atom.

Optimized geometries, energies, and frequencies are presented in Table 1. The conclusions are independent of the basis set and type of calculation. The C_{3v} symmetry pyramidal minimum of the ion-pair state, which is found for an H-H separation very close to that of H_3^+ , has a doubly degenerate E-symmetry imaginary frequency. In lower

symmetry, distortion of this geometry according to the normal modes corresponding to these imaginary frequencies leads to optimization of the global minimum, which is a very slightly bound van der Waals complex of H₂ and HF. The optimization is not very sensitive to the relative orientation nor the internuclear separation of the H₂ and HF moieties. The binding energy of the van der Waals complex, although not well determined in any of these calculations, is negligible. There is no predicted stable ion-pair state and no energy content in the H₃F system.

FUTURE WORK

Four novel bonding situations that may be expected to give rise to anomalously energetic molecules have been identified: (1) hypervalent compounds, molecules with "too many" ligands, (2) electron-deficient compounds, e.g., compounds of B and Be with insufficient numbers of valence electrons, (3) "superalkali" compounds, based on combinations of alkalis and halogens with exceptionally low ionization potentials, and (4) cyclic strained structures.

Examples of several of these categories are already being explored under the HEDM program. The "superalkali" category requires further explanation. On the basis of molecular symmetry, Gutsev and Boldyrev⁹ have recently suggested combinations of alkalis and halogens or chalcogens, e.g., Li₂F or Li₃O, which they termed "superalkalis" because of their anomalously low ionization potentials, lower than that of the isolated alkali. Similarly, they have identified¹⁰ "superhalogens", e.g., BO₂⁻, BeF₃⁻ and BF₄⁻ based on the large electron affinity of the corresponding neutrals. They suggest combinations of these species will have little charge transfer and should lead to stable ionic species. However, their calculated energies were based on a variation of the X_α computational method. It should be valuable to explore this contention by more accurate theoretical techniques.

* Supported by AFAL contract F04611-86-C-0070, 8/86 - 8/89.

1. D. Talbi and R. P. Saxon, *J. Chem. Phys.*, **91**, 2376 (1989).
2. R. P. Saxon and D. Talbi in, "Proceedings of the HEDM Conference," p.55 (1989).
3. J. A. Montgomery and H. H. Michels, *J. Chem. Phys.*, **86**, 5802 (1987).
4. H. H. Michels and J. A. Montgomery in "Proceedings of the Air Force HEDM Contractors Conference," p. 93 (1988).
5. S. -Y. Huang and W. A. Lester in, "Proceedings of the Air Force HEDM Contractors Conference," p. 213 (1988).
6. H. Hotop and W. C. Lineberger, *J. Phys. Chem. Ref. Data*, **4**, 539 (1975).
7. C. W. Bauschlicher and P. R. Taylor, *J. Chem. Phys.*, **85**, 2779 (1986).
8. A. -M. Sapse, *J. Chem. Phys.*, **78**, 5733 (1983).
9. G. L. Gutsev and A. I. Boldyrev, *Chem. Phys. Lett.*, **92**, 262 (1982).
10. G. L. Gutsev and A. I. Boldyrev, *Chem. Phys.*, **56**, 277 (1981).

Table 1.

H₃F GEOMETRIES, FREQUENCIES, AND ENERGIES^a

Ion-Pair State (C _{3v})			
	6-31G [*] /SCF	6-311G ^{**} /SCF	DZP+ ^b /MC
Geometry			
H-H	0.851	0.857	0.862
F-H	1.633	1.665	1.696
h	1.557	1.590	1.620
Frequencies			
E	2052i	1786i	1750i
A ₁	1194	1135	1059
E	2810	2914	2780
A ₁	3598	3604	3593
Total energy ^d	-100.916774	-100.986778	-101.051231
Relative energy ^e	133.66 ^f	120.91	115.79
Global Minimum (van der Waals Complex)			
	6-31G [*] /SCF	6-311G ^{**} /SCF	DZP+ ^b /MC
Geometry ^g			
H-F		0.8963	0.9229
H-H		0.7356	0.7367
d		2.9979	3.3834
Torsion		4.8	0.0
Frequencies			
HF			4127
H ₂			4608
Total energy ^d		-101.180541	-101.235704
Relative energy ^e		-0.72	-0.17

Table 1.

H₃F GEOMETRIES, FREQUENCIES, AND ENERGIES^a
(Continued)

	H ₂ + HF Asymptote ^h		
	6-31G [*] /SCF	6-311G ^{**} /SCF	DZP+ ^b /MC
Geometry			
H - F		0.8960	0.9226
H - H		0.7355	0.7348
Frequencies			
HF			4133
H ₂			4637
Total energy ^d		-101.179395	-101.235430

- a. Distances in Å; frequencies in cm⁻¹.
 b. F basis set of Bauschlicher and Taylor, Reference 7.
 c. h = vertical distance from F to H₃ plane.
 d. Total energies in hartrees.
 e. Relative energies in kcal/mol with respect to HF + H₂.
 f. Using HF + H₂ energy of Sapse, Reference 8.
 g. d = distance between HF and H₂ centers of mass; torsion angle in degrees.
 h. Spectroscopic values: $R_e(\text{H}_2) = 0.74144\text{Å}$, $\omega_e(\text{H}_2) = 4401.21\text{cm}^{-1}$
 $R_e(\text{HF}) = 0.91680\text{Å}$, $\omega_e(\text{HF}) = 4138.32\text{cm}^{-1}$

Theoretical Studies of Spin-Forbidden and Electronically Nonadiabatic Processes: Avoided and Allowed Surface Crossings

David R. Yarkony
Department of Chemistry
Johns Hopkins University
Baltimore, MD 21218

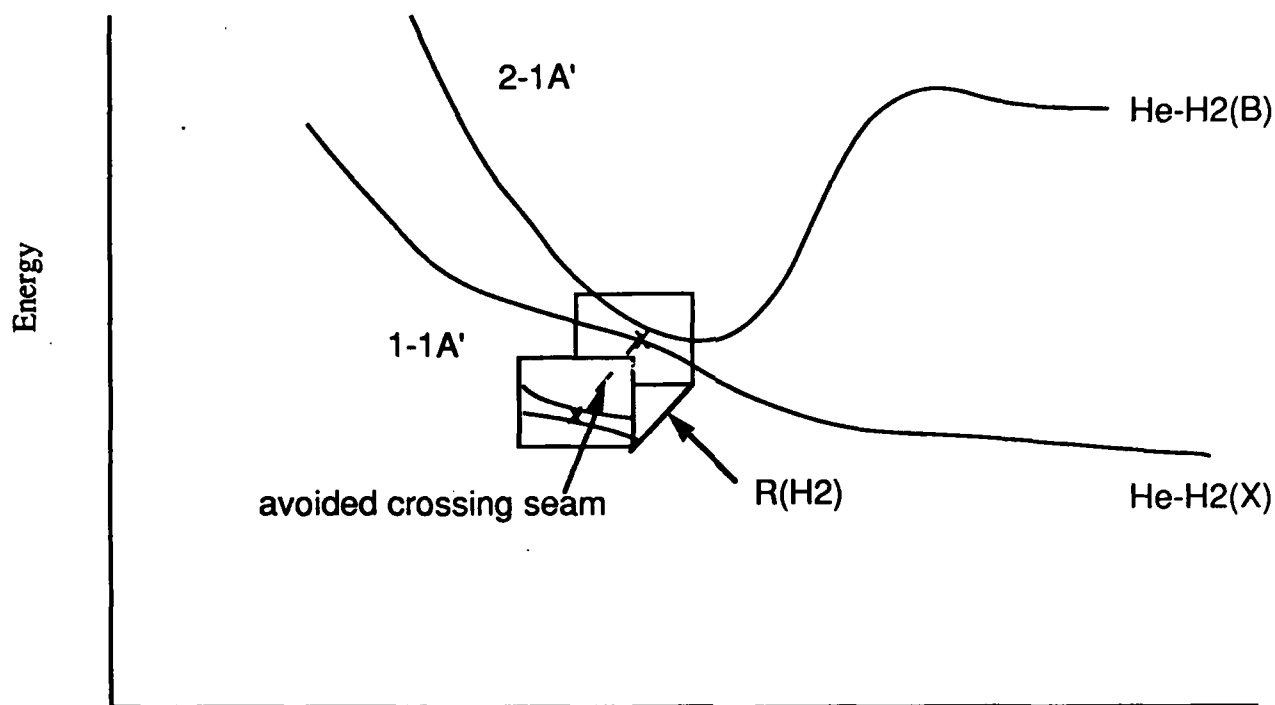
Our work in the HEDM program has considered the electronic structure aspects of the stability of potential high energy density materials. In particular we have been concerned with electronically nonadiabatic *radiationless decay pathways*. Electronically nonadiabatic processes involve motion on more than one electronic potential energy surface or avoided crossings on a single potential energy surface. Previously we have developed a system of computer codes known as BROOKLYN designed to treat the electronic structure aspects of these processes using large scale correlated wavefunctions. Specifically we have developed advanced methods for determining the various types of INTERSURFACE couplings which can lead to the breakdown of the single surface Born-Oppenheimer approximation. The coupling between the potential energy surfaces may be either of the derivative form $f_{\alpha}^U(\mathbf{R}) \equiv \langle \Psi_I(\mathbf{r}; \mathbf{R}) | \partial / \partial R_{\alpha} \Psi_J(\mathbf{r}; \mathbf{R}) \rangle_r$ or in the case of spin-nonconserving reactions result from the spin-orbit interaction which is given by $H_{IJ}^{SO}(\mathbf{R}) \equiv \langle \Psi_I(\mathbf{r}; \mathbf{R}) | H^{so} \Psi_J(\mathbf{r}; \mathbf{R}) \rangle_r$.

These algorithms focus on WHAT needs to be determined to characterize an electronically nonadiabatic process. As part of our current HEDM research we are considering the efficient determination of WHERE these interactions need to be calculated. In particular we are interested in methods which permit identification of the regions of nuclear coordinate space for which the intersurface couplings should be determined WITHOUT detailed determination of the individual potential energy surfaces in question.

Two problems we have studied in our previous HEDM research serve to motivate the algorithm development we have begun. The problems in question are (1) the mechanism of the spin-forbidden radiationless decay of hydrazoic acid $\text{N}_3\text{H}(\text{X}^1\text{A}') \rightarrow \text{N}_2 + \text{NH}(\text{X}^3\Sigma^-)$ [D. R. Yarkony, J. Chem. Phys. 92, 320(1990)] and (2) the mechanism of the quenching reaction $\text{H}_2(\text{B}^1\Sigma_u^+) + \text{He} \rightarrow \text{H}_2(\text{X}^1\Sigma_g^+) + \text{He}$. [J. K. Perry and D. R. Yarkony, J. Chem. Phys., 89, 4945 (1988).]

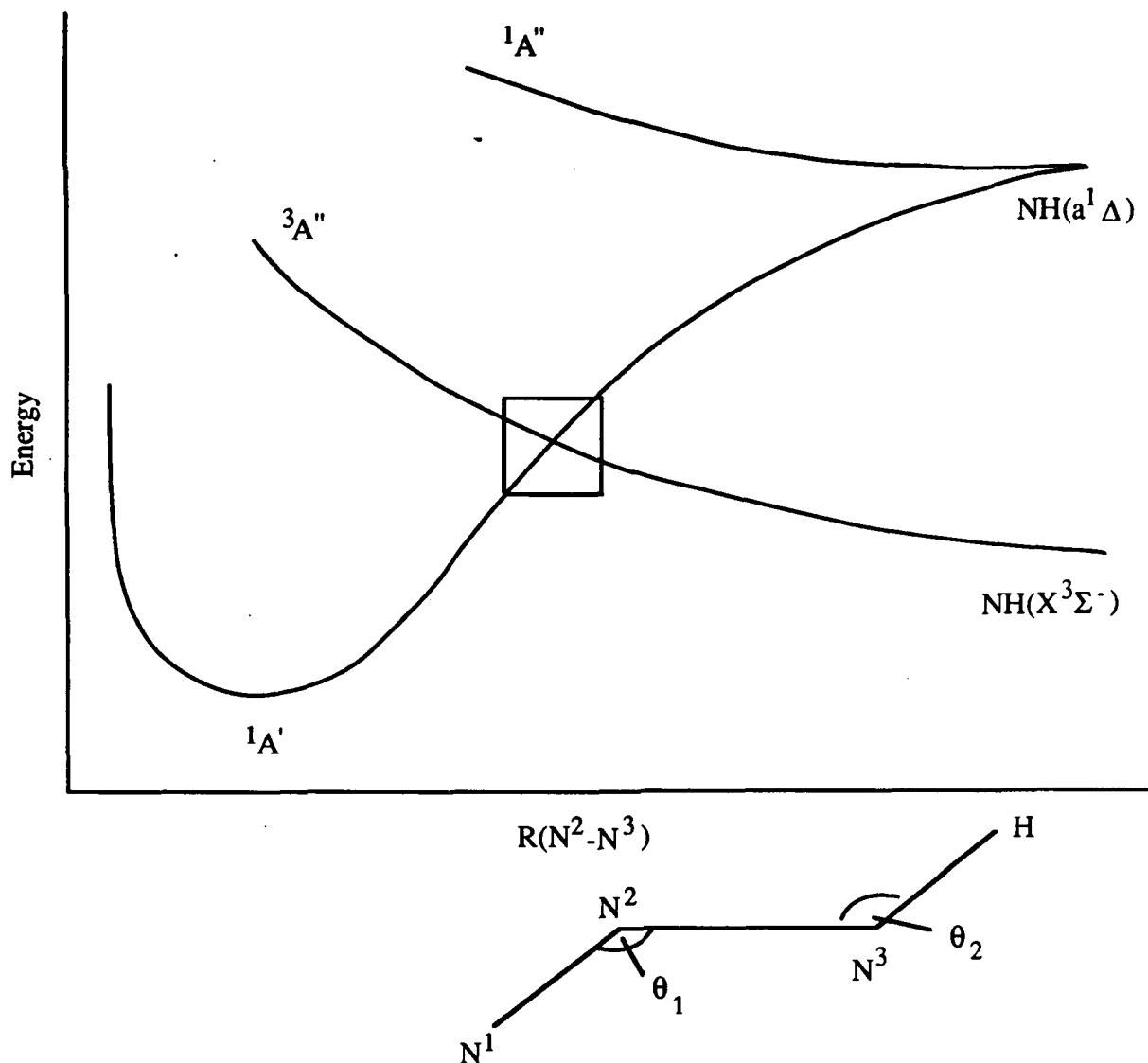
The elucidation of the mechanism of the electronic quenching reaction $\text{H}_2(\text{B}^1\Sigma_u^+) + \text{He} \rightarrow \text{H}_2(\text{X}^1\Sigma_g^+) + \text{He}$ required the determination of the nonadiabatic coupling matrix elements between the $1^1\text{A}'$ and $2^1\text{A}'$ potential energy surfaces $f_{\alpha}(1^1\text{A}', 2^1\text{A}')$. These matrix elements are required where the surfaces in question are closely spaced. It was found that the potential energy surfaces are closely spaced *NOT* in the vicinity of a *single point* in nuclear coordinate space but rather in the vicinity of a *seam of (avoided) crossings* pictured below. For each value of the PARAMETER r , the H_2 distance, the avoided crossing is given by the ordered pair $[\text{R}(r), \gamma(r)]$ with R , the He-H_2 , and γ the

He-H₂ angle, chosen to minimize the separation between the potential energy surfaces. The situation is depicted below.



In the original study of the He-H₂ system the avoided crossing seam was determined (somewhat tediously) by considering the energies of the individual potential energy surfaces. This motivated us to consider the possibility of developing a generally applicable procedure for determining avoided crossing seams. An initial implementation of an analytic gradient driven procedure for determining avoided crossing seams has been developed [D. R. Yarkony, J. Chem. Phys. in press] and interfaced into the BROOKLYN codes.

Before outlining the nature of these algorithms we consider the algorithmic requirements for the second problem noted above the mechanism of the spin-forbidden radiationless decay of hydrazoic acid $\text{N}_3\text{H}(\text{X}^1\text{A}') \rightarrow \text{N}_2 + \text{NH}(\text{X}^3\Sigma^-)$. Quantitative determination of the rate of this reaction requires evaluation of the spin-orbit coupling matrix elements, $h_z^{\text{SO}} \equiv \langle \Psi_{1\text{a}'}(1\text{A}') | H^{\text{SO}} | \Psi_{1\text{a}'}(3\text{A}'') \rangle$ and $h_y^{\text{SO}} \equiv \langle \Psi_{1\text{a}'}(1\text{A}') | H^{\text{SO}} | \Psi_{2\text{a}'}(3\text{A}'') \rangle$. Here $\Psi_{1\text{a}'}(1\text{A}') \equiv \Psi[1^1\text{A}'(0)]$ and the components of the lowest triplet state are given by $\Psi_{1\text{a}'}(3\text{A}'') \equiv i\Psi[1^3\text{A}''(0)]$, $\Psi_{2\text{a}'}(3\text{A}'') \equiv \frac{1}{\sqrt{2}}\{\Psi[1^3\text{A}''(1)] - \Psi[1^3\text{A}''(-1)]\}$. It is most important to evaluate these matrix elements at the reaction bottleneck which in this case corresponds to the *minimum energy crossing point* of the $1^1\text{A}'$ and $1^3\text{A}''$ potential energy surfaces. The situation is pictured below, using the NH- N₂ distance as an approximate reaction coordinate.



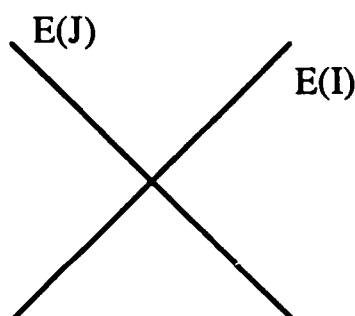
In the N_3H system the minimum energy crossing point is a point on a 5 dimensional hypersurface corresponding to the intersection of the lowest singlet and triplet potential energy surfaces. In our original study an approximate minimum energy crossing point was taken from the work of Alexander, Werner and Dagdigian [M.H. Alexander, H. -J. Werner and P. J. Dagdigian, J. Chem. Phys **89**, 1388 (1988),] who determined this point by considering sections of the crossing hypersurface. Again this procedure can be quite cumbersome. However it is possible to avoid characterization of the actual crossing hypersurface and determine the minimum energy crossing point directly using an approach first proposed by Koga and Morokuma[Chem. Phys. Lett. **119**, 371 (1985)]. Our initial implementation of this approach is also discussed below.

In order to characterize avoided, allowed and minimum energy, crossings [and determine the requisite nonadiabatic couplings] we have developed a unified density matrix driven computational

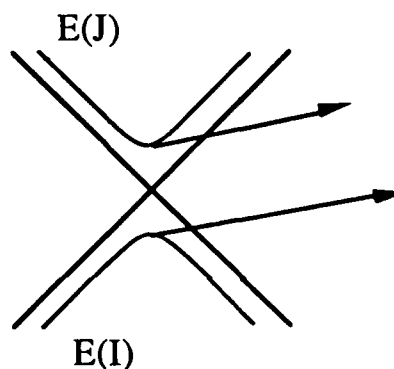
procedure which enables determination of three classes of derivatives: (A) energy difference gradients (using difference density matrices), (B) energy gradients (using standard density matrices), and (C) (the CI contribution to) first derivative nonadiabatic coupling matrix elements (using transition density matrices). As discussed below the direct evaluation of the energy difference gradient provides considerable computational advantage for the characterisation of avoided surface crossings and can offer numerical advantages for the evaluation of minimum energy crossings.

AVOIDED SURFACE CROSSINGS

An (avoided) crossing represents the solution of the equations which minimize the square of the separation of the potential energy surfaces $[\Delta E(J,I)]^2$ in question, that is $\partial/\partial R_\alpha [\Delta E(J,I)]^2 = 0$ where $\Delta E(J,I) \equiv E(J) - E(I)$ so that $G_\alpha^{IJ} \equiv \partial \Delta E(J,I) / \partial R_\alpha \equiv \Delta E(J,I) g_\alpha^{IJ} = 0$. Thus two situations obtain (a) $\Delta E(J,I)=0$, the allowed crossing case and (b) $g_\alpha^{IJ} = 0$, the avoided crossing case. These situations are pictured below.



(a) actual crossing



(b) avoided crossing

$$\Delta E(J, I) \frac{\partial}{\partial R_\alpha} \Delta E(J, I) = 0$$

These extrema on the $\Delta E(J,I)^2$ surface can be located using a Newton-Raphson procedure

$$\mathbf{F}^{IJ}(\mathbf{R}_0) \delta = -\mathbf{G}^{IJ}(\mathbf{R}_0) \quad 1$$

where $\mathbf{F}^{IJ}(\mathbf{R}_0)$ is the second derivative or hessian matrix given by:

$$F_{\alpha,\beta}^{IJ}(\mathbf{R}_0) = \partial / \partial R_\alpha G_\beta^{IJ}(\mathbf{R}_0) \quad 2$$

and is approximated by forward or centered divided difference of the gradient $G_\alpha^{IJ}(\mathbf{R}_0)$.

SEAMS OF (AVOIDED) CROSSINGS

Instead of requiring $G_\alpha^{IJ}(\mathbf{R})=0$ with respect to *all* coordinates, that is all R_α , a seam of (avoided) crossings is obtained by solving for $G_\alpha^{IJ}(\mathbf{R})=0$ in a space of *reduced dimensionality*. In this case $G_\alpha^{IJ}(\mathbf{R})=0$ for all R_α *except* those coordinates which parametrize the seam for which

$G_{\alpha}^{IJ}(\mathbf{R}) \neq 0$. A particularly appealing implementation uses ξ , an approximate reaction coordinate, to parametrize the seam.

MINIMUM ENERGY CROSSING

The minimum energy crossing point can be determined directly by minimizing the function $K^{IJ}(\mathbf{R}, \lambda) = E^I(\mathbf{R}) + \lambda [E^I(\mathbf{R}) - E^J(\mathbf{R})]$. At second order the minimum in this function is obtained from the following Newton-Raphson equations:

$$\begin{pmatrix} W(\mathbf{R}_0, \lambda) & \mathbf{g}^U(\mathbf{R}_0) \\ \mathbf{g}^U(\mathbf{R}_0)^T & 0 \end{pmatrix} \begin{pmatrix} \delta \\ \partial \lambda \end{pmatrix} = - \begin{pmatrix} E^I(\mathbf{R}_0) + \lambda \mathbf{g}^U(\mathbf{R}_0) \\ \Delta E(\mathbf{R}_0) \end{pmatrix} \quad 3$$

as originally discussed by Koga and Morokuma.

In eqs. 1,3 the principal computational effort is expended in the evaluation of the energy difference gradient $\mathbf{g}_{\alpha}^{IJ}(\mathbf{R})$. For the minimum energy crossing evaluation of the energy gradient is also required. As $\mathbf{g}_{\alpha}^{IJ}(\mathbf{R})$ represents the difference between the slopes of the potential energy surfaces it can be determined from two independent evaluations of the energy gradient. However the requisite computational effort will be reduced considerably if $\mathbf{g}_{\alpha}^{IJ}(\mathbf{R})$ can be evaluated directly. $\mathbf{g}_{\alpha}^{IJ}(\mathbf{R})$ can in fact be evaluated directly using the one-, and two-, particle *difference density matrices* $\Delta\gamma^{IJ}$ and $\Delta\Gamma^{IJ}$ defined in terms of the standard one-, and two-, particle density matrices γ^I and Γ^I by $\Delta\gamma^{IJ} = \gamma^I - \gamma^J$ and $\Delta\Gamma^{IJ} = \Gamma^I - \Gamma^J$. Key is the observation that evaluation of $\mathbf{g}_{\alpha}^{IJ}(\mathbf{R})$ is formally identical to the evaluation of the energy gradient $E_1^{\alpha}(\mathbf{R})$ provided the difference density matrices replace density matrices in standard expression for the energy gradient at the CI level. We have the following

EXPRESSION FOR ENERGY DIFFERENCE GRADIENT: DIFFERENCE DENSITY MATRICES

$$\mathbf{g}_{\alpha}^{IJ}(\mathbf{R}) = \Delta E_{IJ}^{\alpha}(\mathbf{R}) + \Delta E_{IJ}^{U\alpha}(\mathbf{R}) \quad 4$$

where

$$\Delta E_{IJ}^{\alpha} = \sum_{i,j} \Delta\gamma_{ij}^{IJ} h_{ij}^{\alpha} + \sum_{i,j,k,l} \Delta\Gamma_{ijkl}^{IJ} (ij||kl)^{\alpha} \quad 5$$

and

$$\Delta E_{IJ}^{U\alpha} = \sum_{i,j} \Delta L_{ij}^{IJ} U_{ij}^{\alpha} \quad 6$$

Here the difference Lagrangian ΔL_{im}^{IJ} is given by

$$\Delta L_{im}^{IJ} = 2 \left[\sum_j \Delta \gamma_{ij}^{IJ} h_{mj} + 2 \sum_{j,k,l} \Delta \Gamma_{ijkl}^{IJ} (mj||kl) \right]$$

7

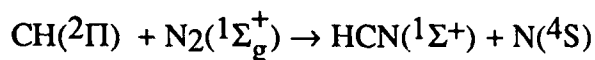
ENERGY GRADIENT- STANDARD DENSITY MATRICES

If the standard one- and two- particle density matrices γ^I and Γ^I replace the difference density matrices in the equations for the energy difference gradient (eqs. 4-7) then these equations yield the energy gradient $E_{\alpha}^I(\mathbf{R})$.

DERIVATIVE COUPLING MATRIX ELEMENTS-TRANSITION DENSITY MATRICES

The principal computational steps in the evaluation of the derivative coupling matrix elements also use eqs. 4-7. In the case of the derivative couplings the *difference* density matrices are replaced by *transition* density matrices γ^{IJ} and Γ^{IJ} and eq. 4, when divided by $\Delta E_{IJ}(\mathbf{R})$, yields the CI contribution to the total first derivative nonadiabatic coupling matrix element $f_{\alpha}^{IJ}(\mathbf{R})$.

At the HEDM meeting the methodology presented here was illustrated by considering the chain initiating step in the Fenimore mechanism for prompt NO formation.

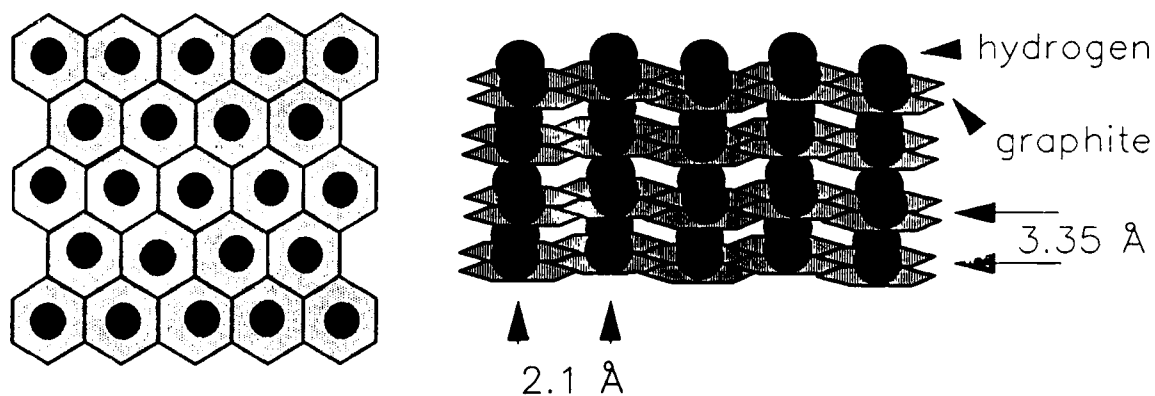


This reaction, which is spin-forbidden and hence electronically nonadiabatic provides a low energy pathway for the breaking of the $\text{N}\equiv\text{N}$ bond by carbon containing radicals.

Preliminary Studies of Energetic Room Temperature Carbon/Hydrogen Solids

Dr. Patrick Carrick
ARIES Office
Astronautics Laboratory
Edwards Air Force Base, CA 93523

A corona excited supersonic expansion source was used to make carbon-based room temperature matrices by discharging mixtures of various hydrocarbons in helium or hydrogen and directing the discharge onto selected substrates. Such matrices may contain trapped atomic hydrogen, which would provide considerable energy when released (Ref. 1). Figure 1 shows a proposed structure for atomic hydrogen stabilized by graphite layers. The possible energy content given in this figure was determined by calculating the density of the atomic hydrogen using known graphite distances (Ref. 2).



Energy from $H + H \rightarrow H_2$	2.08 Kcal./g.(H/C)
-------------------------------------	--------------------

Energy from $C + O_2 \rightarrow CO_2$	2.14 Kcal./g.(C/O ₂)
----------------------------------------	----------------------------------

Energy from $H_2 + \frac{1}{2}O_2 \rightarrow H_2O$	3.21 Kcal./g.(H ₂ /O ₂)
-----------------------------------------------------	------------------------------------------------

Figure 1

Both infrared spectroscopy (IR) and differential scanning calorimetry (DSC) were used to study such films deposited on a variety of substrates. Some of the substrates were chosen to directly obtain IR absorption of the matrix, so that the chemical composition of the matrix might be determined. One such IR absorption spectrum, shown in Fig. 2, compares the C-C stretch and C-H stretch regions of four different matrix samples, one set with helium as carrier gas and the other with hydrogen as carrier gas, on two different substrates. The preliminary IR data shows variations in the chemical structure of the matrix when deposited on different substances.

The energy content of these samples was determined with the DSC to range from 173 to 1010 cal/gram. One such DSC run is shown in Figure 3. The bottom line is the first DSC run that shows the energy content of the 0.50 mg sample. The top broken line shows the DSC scan that was run immediately after the first run and indicates the baseline from which the total energy content can be determined. These results indicate that the carbon/hydrogen matrices made in this manner contain some source of energetic molecules, but it is unclear if this source of energy is due to trapped atomic hydrogen.

References

1. K. Ashida, K. Ichimura, M. Matsuyama, and K. Watanabe, J. Nuc. Mat, 128, 792 (1984).
2. C. Mantell, "Carbon and Graphite Handbook", Interscience (1968).

CH4_J2001
105.088 XT
43.248 XT

CH4_J2002
98.972 XT
48.823 XT

CH4_He001
97.322 XT
36.045 XT

CH4_He004
95.742 XT
28.534 XT

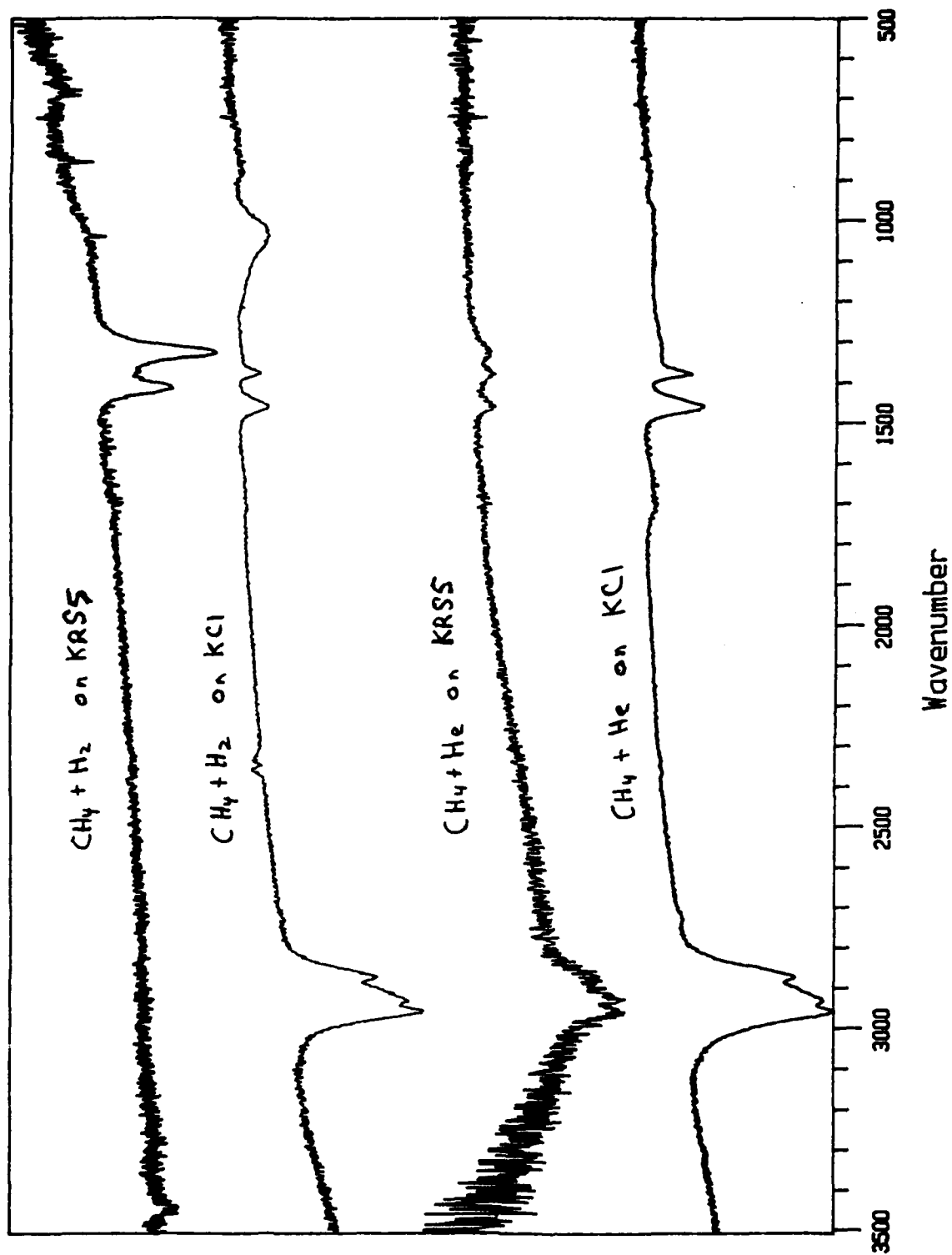


Figure 2

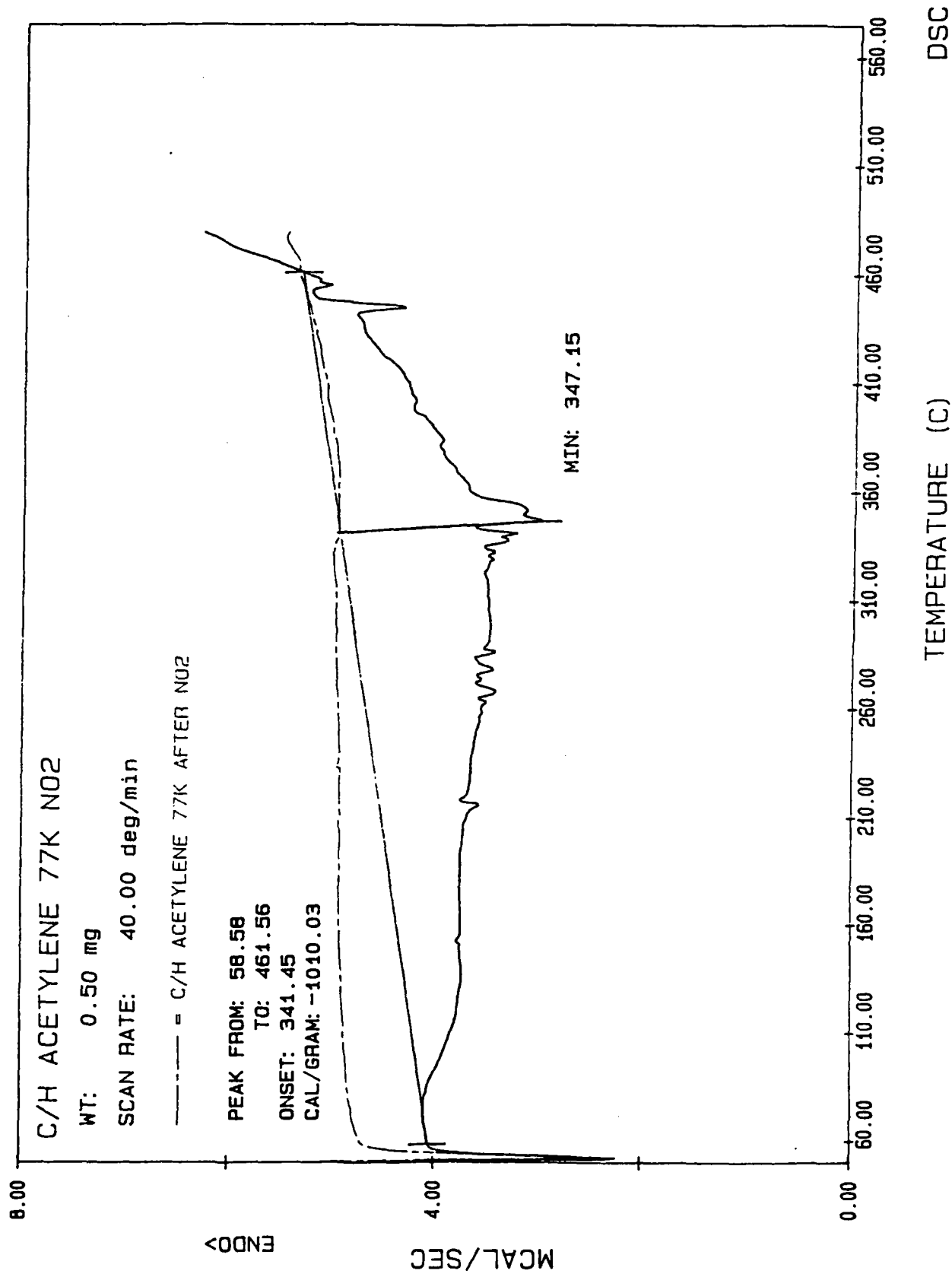


Figure 3

Stabilization of HEDM Materials

S.D. Thompson, R.A. van Opijnen, M.I. Kenney¹, S.L. Rodgers
Applied Research in Energy Storage Office,
Astronautics Laboratory (AFSC)
Edwards AFB, CA 93523

Introduction

High energy density matter (HEDM) development for practical purposes is dependent on the ability to store in some stable fashion the energetic materials for use upon demand. Many HEDM species are very reactive or unstable. Their usefulness is dependent on how well they can be "packaged". This work examines one such "packaging" concept.

The concept involves stabilizing the HEDM material by interaction with a solid substrate. Stabilization might be obtained through absorption, adsorption or complex formation with the solid. If the solid substrate is a solid rocket propellant, and sufficient concentrations and stabilization levels can be attained, then the HEDM compound can boost the performance of that solid propellant ingredient.

A 1942 Ph.D. dissertation by J.F. Haller from Cornell University suggested that fluorine azide was stabilized appreciably by interaction with potassium fluoride. Preliminary experiments to examine this concept were done in collaboration with Dave Bernard and Tom Seder at the Rockwell Science Center. Fluorine azide was passed over potassium chloride and examined using DSC and mass spectroscopy. Indications were that indeed the fluorine azide was being trapped on the solid. Experiments were then begun at the Astronautics Laboratory to determine the nature of the interaction as well as applicability to other HEDM species and other likely propellant substrates.

Description

Experiments to date have been done using hydrogen azide and various salts in an attempt to understand the interaction of the azide on the solid. Hydrogen azide was produced by the reaction of stearic acid and sodium azide. The gas was passed through the solid as it sat in a fritted glass funnel. The solid material was then examined by DSC, IR and mass spectroscopy. Figure 1

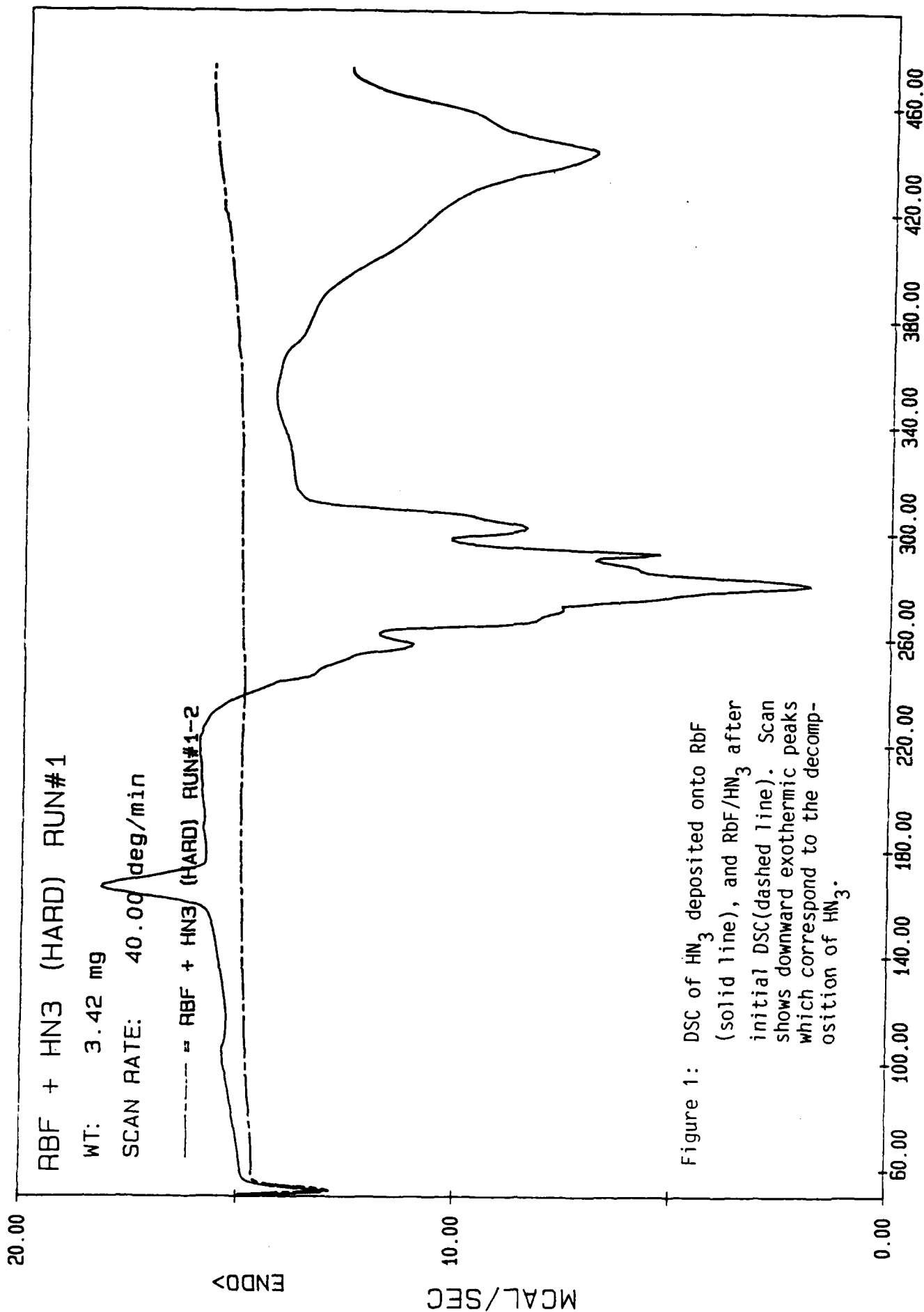
¹ Current address: University of Eastern New Mexico, Portales, New Mexico

shows the DSC scan of RbF before (the dashed line) and after (the solid line) deposition of the hydrogen azide. The hydrogen azide decomposition curve, with the initial endothermic event followed by a multistep exothermic process, is characteristic of the DSC scans on which the azide was stabilized. Figure 3 shows the IR spectra of hydrogen azide treated potassium fluoride before and after DSC runs. The characteristic peaks (*J. Chem. Phys.* 23, 1258(1955)) of the azide are readily seen before heating and have essentially disappeared after heating. We have found that using the gas deposition method, hydrogen azide gas will bind to KF, RbF, and CsF. It did not bind to NaF, NH_4ClO_4 , NH_4NO_3 , LiNO_3 , and RbCl. The hydrogen azide coated materials have been checked periodically for a period in excess of six months and no apparent decrease in hydrogen azide concentration has been noted. Under these conditions concentrations of at least 15% by weight of the hydrogen azide were seen on those substrates that had interactions. These hydrogen azide - fluoride salts are quite stable to shock and provide a safe effective method for storing and using hydrogen azide. The gas can be released simply by heating the salt.

An alternate deposition process on the ammonium perchlorate was also tried. The hydrogen azide gas was bubbled through an ammonium perchlorate saturated acetone solution. The acetone was evaporated and the remaining solid analyzed by DSC and mass spectroscopy. Figure 2 shows the DSC of the ammonium perchlorate before and after exposure to the hydrogen azide. Mass spectral analysis was done by heating the exposed ammonium perchlorate and examining the effluent, which showed hydrogen azide present. Experiments are currently being conducted to maximize the deposition process.

FUTURE

Small rocket motor tests will be conducted with the coated ammonium perchlorate to determine the propellant properties. Additional solid propellant ingredients will be examined to determine their effectiveness as a stabilization medium. Other work in this project will include deposition attempts of fluorine and methyl azides, as well as other energetic, unstable species. Increased spectroscopy will be incorporated to attempt to elucidate the structure and mechanisms of these complexes. Additionally, theoretical calculations will be conducted to support and confirm mechanisms as well as attempt to ascertain which species would benefit from the substrate stabilization process.



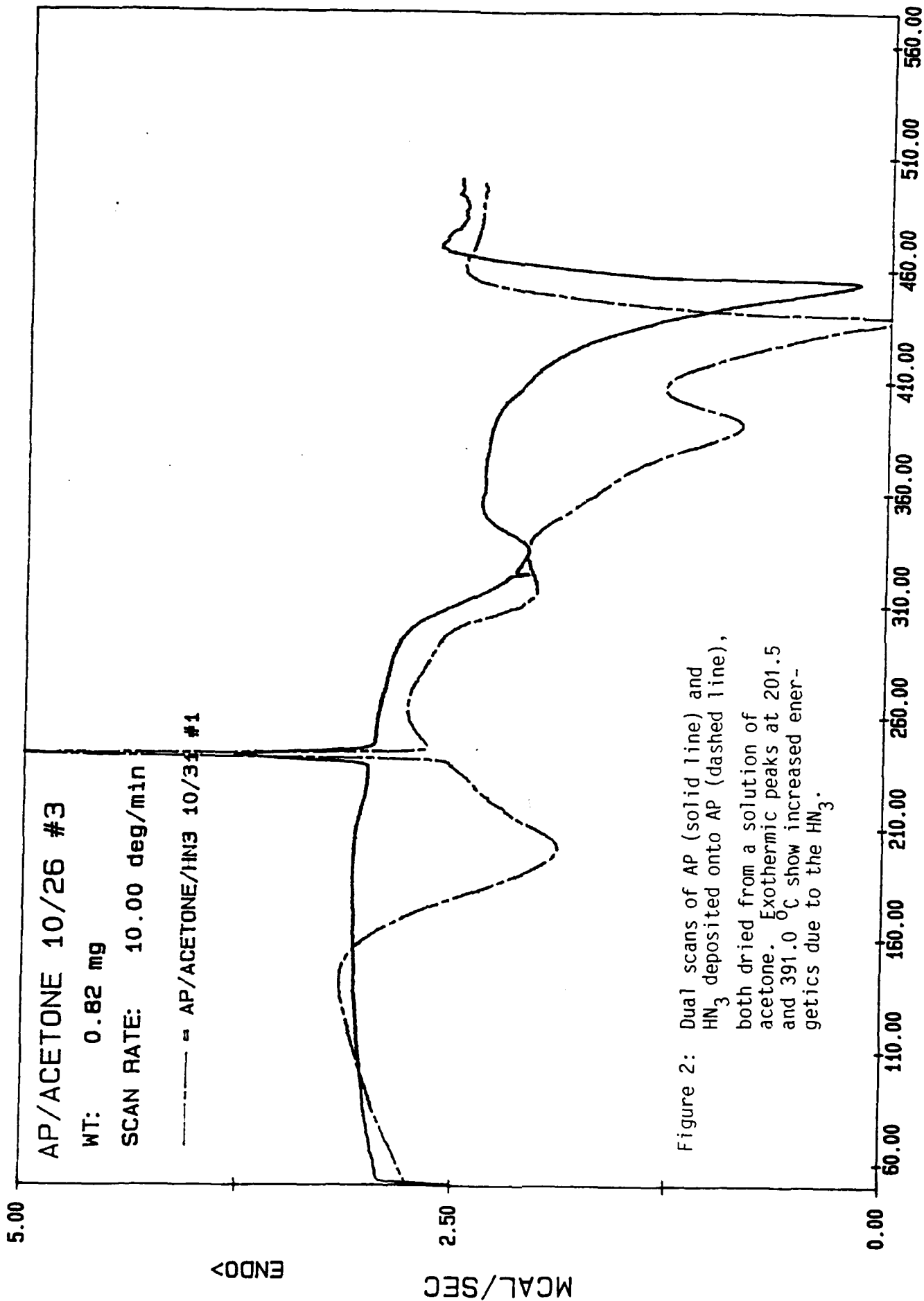


Figure 2: Dual scans of AP (solid line) and HN₃ deposited onto AP (dashed line), both dried from a solution of acetone. Exothermic peaks at 201.5 and 391.0 °C show increased energetics due to the HN₃.

ROELAND FILE: S263.D4

DATE: 89/10/26 TIME: 11:08

HN3KF02-02
53.958 XT
-0.257 XT

HN3KF02-04
58.938 XT
3.437 XT

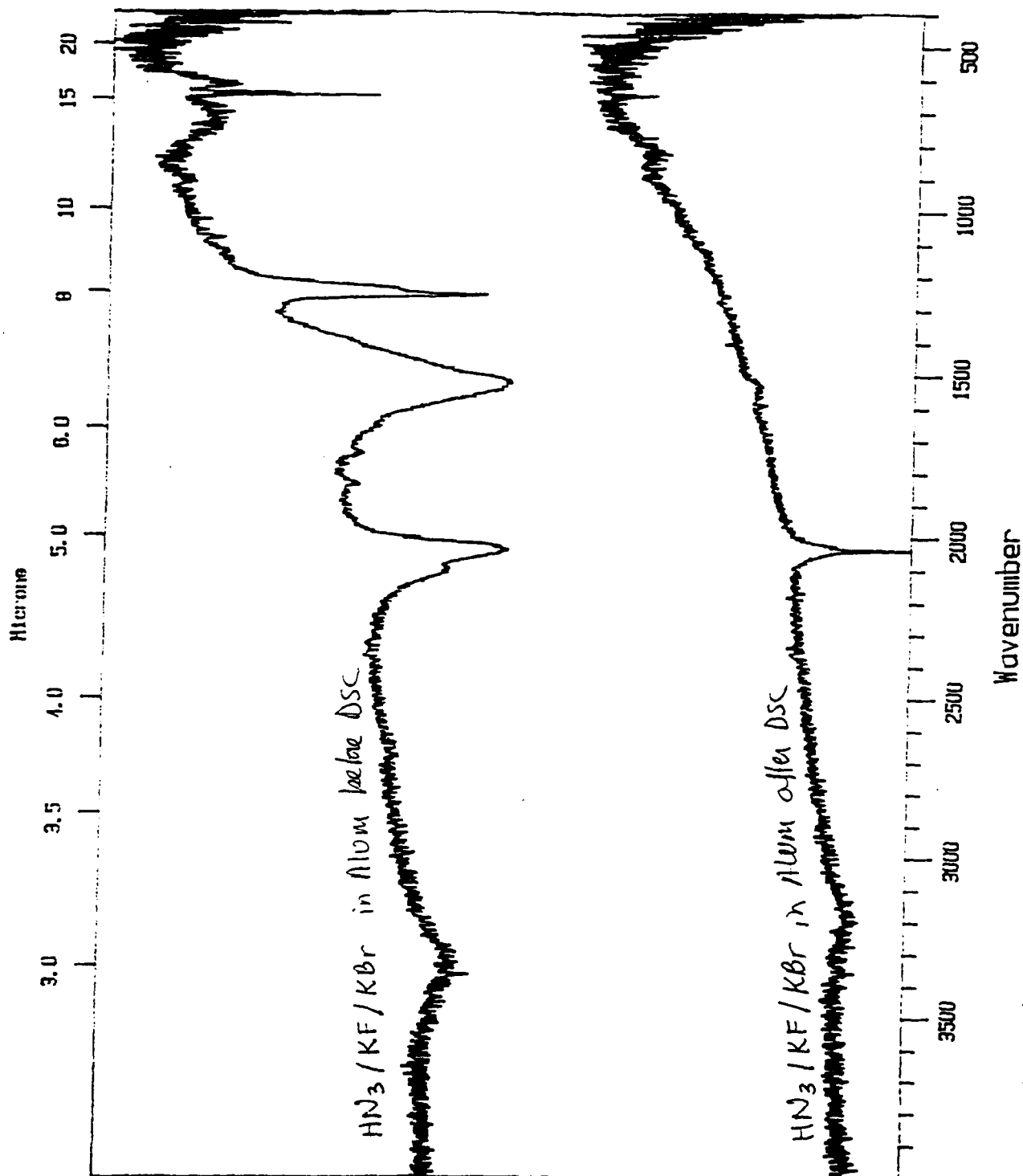


Figure 3: FT-IR scans of HN₃ deposited onto KF (top) and after (bottom) DSC analysis. Scans show the disappearance of HN₃ peaks.

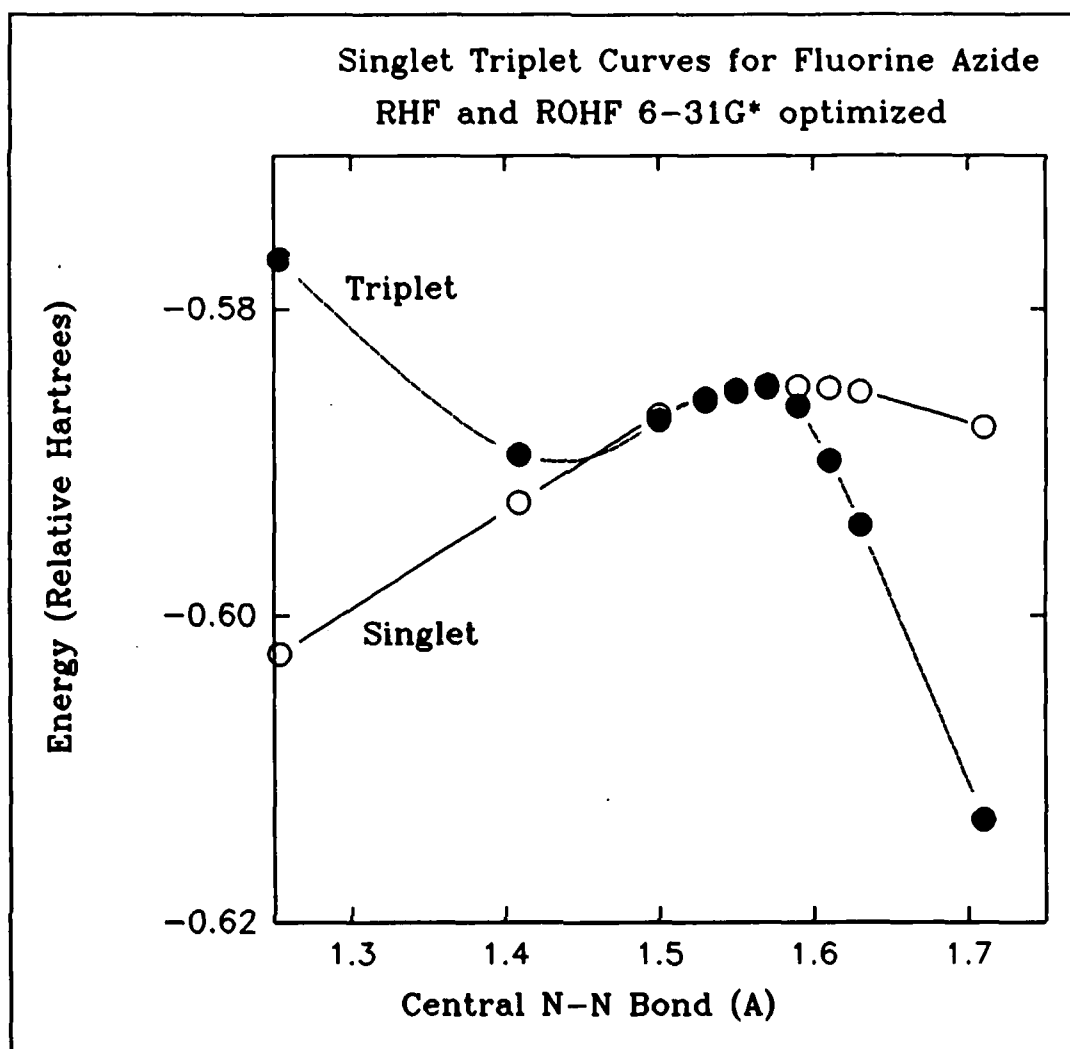
Theoretical Gas Phase Dissociation and Surface Adsorption Studies of Fluorine Azide

by
Neil R. Kestner
Chemistry Department
Nathan E. Brener, and Joseph Callaway
Physics Department
Louisiana State University
Baton Rouge, LA 70803

Fluorine Azide Dissociation-

We have made detailed theoretical studies of fluorine azide at the gas phase dissociation geometry in order to obtain the dissociation energy and mechanism to guide us in studies of energy release in the solid state. We have paid particular attention to stability of the lowest energy state, particularly to its spin configuration in order to insure that it properly dissociates to the correct products, using both the Gaussian 86 and the MESA programs (thanks to Byron Lengsfeld) and basis sets of 6-31G* and larger to do restricted and unrestricted Hartree Fock calculations, open shell singlet calculations and configurational interaction(CI) studies based on the various reference states. Both the singlet and triplet states have been optimized in terms of all relevant geometrical parameters at the appropriate Hartree Fock level and then configuration interaction was performed to include correlation effects. At large separations the open shell singlet is the most important configuration as this allows proper dissociation of the molecule to the singlet products. There are also large correlation effects in the triplet state which had to be properly included. The open shell singlet is found to lie above both the triplet and closed shell singlet in the neighborhood of the barrier but crosses the closed shell singlet curve between 2.0 and 2.5 Å (center bond distance). This suggests that the single reference SCF is valid even in the neighborhood of the barrier.

The next figure summarizes singlet-triplet results using completely optimized RHF and ROHF calculations at the 6-31G* level.



We
hav
e
als

o done some larger basis calculations at the crossing point of 1.60 Å to indicate the effect of higher levels of calculation, specifically using a 6-311G(2d) basis with the geometry optimized at the closed shell singlet RHF or the triplet ROHF..

	SINGLET	TRIPLET
Hartree Fock	-262.6642895	-262.6950675
mp2	-263.4052972	-263.3790496
mp3	-263.396783	-263.3852959
mp4d	-263.4183001	-263.4020111
mp4dq	-263.4019964	-263.3886113
mp4sdq	-263.4150461	-263.4053265
mp4sdtq	-263.4531782	
CISD	-263.3092018	-263.3107401
cisd w/scc	-263.41401639	-263.40679594
uhf		-262.6950675
rohlf		-262.66610797

The conclusion is that the singlet and triplet cross in the area of 1.60 Å for the central N-N bond. There are major effects of correlation and also basis sets, but the Hartree Fock does seem to predict the correct ordering of states if Restricted Open Shell theory is used (ROHF). The use of the Davidson (css) correction can be misleading in these cases.

Below we list some of the values determined for the barrier at various levels of calculation. There is concern that the MP2 geometry might be somewhat unstable with respect to the Hartree Fock and thus these values should only be compared to each other.

For reference we list some barrier values at both the optimized RHF and MP2 levels using several levels of calculation.

BARRIER CALCULATIONS AT SCF GEOMETRY

Hartree Fock (SCF)	.47 eV(1.59 Å)
Configuration Interaction	.88 (1.7 Å)
	.78 (1.59 Å)
CISD	
with Davidson Correction	.95 (1.7 Å)

BARRIER CALCULATIONS USING MP2 GEOMETRY

Barrier Values in eV for 6-31G** Basis Set

scf	.31397 eV
mp2	1.3126
mp3	1.0794
mp4d	1.0544
mp4dq	.9092
mp4sdq	.9456
mp4sdtq	1.1258
ccd	0.9073
st4ccd	1.0163

Barrier values in eV for 6-311G(2d) Basis Set

scf	0.3082
mp2	1.2728
mp3	1.0216
mp4d	0.9924
mp4dq	0.8393
mp4sdq	0.8832
mp4sdtq	1.0849

At the CI level the barrier is of the order of 0.8 eV but when one corrects for zero point energies, the value is near the 0.6 eV value predicted by Benard from gas phase thermal and collisional dissociation studies. The barrier is also characterized by only one negative eigenvalue in the vibrational Hamiltonian.

Fluorine and Hydrogen Azide Adsorption-

We have begun a major study of adsorption of the azides on various surfaces. Initial work has been on the potassium fluoride crystal surface where it has been known to adsorb. To undertake this study we had to estimate the interaction potentials of the major components. To do that very accurately is a major undertaking involving enormous computer times and so we tried to get a good estimate of those potentials in a more constrained way. The potential used was obtained by fitting results from smaller molecules. If the smaller molecule is picked in a reasonable way, its interactions should reproduce those in a larger system. This should especially be true for the repulsive part of the interaction, the part most important for our work since the electrostatic terms tend to dominate dispersion effects and the repulsive terms then provide the major counter interactions. We performed Gaussian 86 calculations at the MP2 level for the two ions involved interaction with H₂ and N₂ in the perpendicular orientation to the ions. The molecules themselves were then approximated by atom-atom potentials and charges determined by a Lowdin population analysis at the CISD level. These potentials were then used in a simulated annealing program developed by Dr. Han Chen at LSU.

Typical patterns of adsorption are shown below for both hydrogen and fluorine azide.

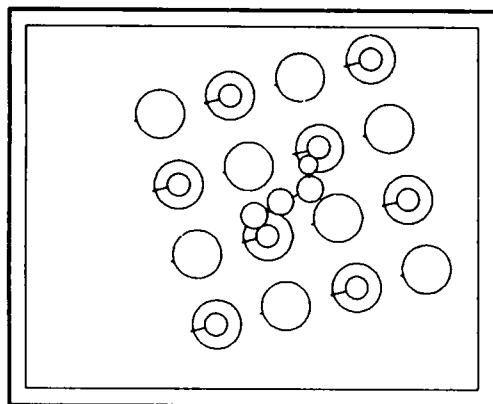


Figure 2 Hydrogen Azide on Potassium Fluoride Surface

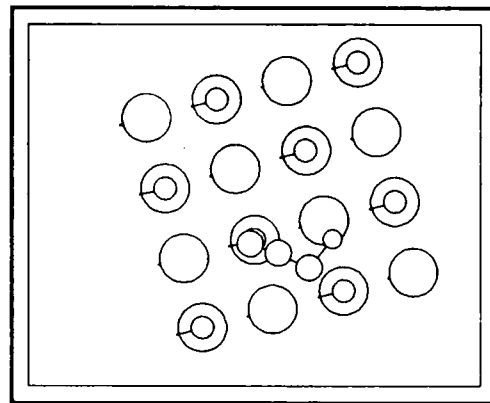


Figure 3 Fluorine Azide on Potassium Fluoride Surface

In these pictures the potassium ion has been arbitrarily been made larger than the Chloride ion for presentation purposes. Also the fluorine in fluorine azide is smaller than it should be to make the analogy to the hydrogen azide pictures.

Hydrogen azide as a more ionic species obviously binds more strongly; nevertheless, fluorine azide is bound almost as strongly to potassium fluoride, specifically for these parameters which are appropriate to an orientation parallel to the surface, 10.8 vs. 10.4 kcal/mol to all of the lattices. To obtain correct results these calculations required major corrections for Basis Set Superposition errors. The calculations suggest that it is not obvious that potassium fluoride or any one ionic crystal should be a much superior binding agent for fluorine azide. Our studies are now being extended to more relevant systems like Ammonium Perchlorate as well as other alkali halide surfaces and to improvements in the intermolecular potentials to include all effects.

ADVANCED LAUNCH VEHICLE PROPULSION
AT THE
NASA-LEWIS RESEARCH CENTER

Bryan Palaszewski
National Aeronautics and Space Administration
Lewis Research Center
Cleveland, OH

ABSTRACT

At the NASA Lewis Research Center, several programs are investigating the benefits of advanced propellant and propulsion systems for future launch vehicles and upper stages. The two major research areas are the Metallized Propellants Program and the Advanced Concepts Program. Both of these programs have theoretical and experimental studies underway to determine the system-level performance effects of these propellants on future NASA vehicles.

METALLIZED PROPELLANTS

The Metallized Propellants Program is determining the performance and the system benefits of propellant combinations such as oxygen/kerosene/aluminum and oxygen/hydrogen/aluminum. In these combinations, the aluminum is gelled with the kerosene or the hydrogen. Adding the aluminum to the propellant increases its overall density and/or the specific impulse. The density increases reduce the volume of the vehicle, the tank mass and the total launch mass. All of these factors also contribute to reducing the drag of the launch vehicle during ascent. The specific impulse increases further reduce the vehicle size and mass. These mass reductions can significantly reduce the launch mass to orbit and potentially reduce the overall cost of space transportation.

Vehicle and System Performance Studies

A set of systems studies to determine the benefits for metallized propellant are underway. Using detailed upper stage and launch vehicle mission analysis and design codes, the payload performance for various propellant combinations can be determined. These studies include earth orbital, planetary and lunar missions. The initial mass in Low Earth Orbit (LEO) reductions over existing and planned propulsion systems are estimated. These LEO mass savings can also be translated into payload mass increases.

For launch vehicles, metallized propellants can provide increased propellant density. A higher density propellant can reduce the size of the launch vehicle stages and its dry mass. The reduced size reduces the drag losses on the vehicle. Also, the higher density propellant provides the ability to improve the Space Transportation Systems (STS). Liquid Rocket Boosters with the same physical dimensions as the current Solid Rocket Boosters have been studied

by NASA and its contractors. Used in the Liquid Rocket Boosters, metallized propellants can deliver the same payload to LEO as the current Solid Rocket Boosters within their volume constraints. Other liquid propellant combinations cannot deliver the same payload within these volume restrictions. Metallized propellants can also be employed in improved versions of the current Atlas, Delta and Titan systems.

Experimental Program

In the experimental program, both in-house and contracted experimental work are continuing. Subscale test hardware using oxygen/hydrocarbon/aluminum propellants has been fired at NASA-Lewis (Ref. 1). This test apparatus has produced preliminary data on the aluminum combustion, specific impulse efficiency and the erosion of the injector elements and the nozzle. Additional experiments are being conducted using this and other subscale hardware. Higher thrust levels will be tested in future contracted work. Propellant rheology is also being studied both with computer models and test facilities. Propellant batches are being formulated to determine their flow properties and their long-term storage properties. Other contracted research into novel propellants and gellants is also funded under the NASA Research Announcement (NRA) Program.

University Research Program

Penn State University is conducting a series of experimental and theoretical investigations of the formation of aluminum oxide and its effect on metallized propellant performance. This work has led to additional understanding of the mechanisms for agglomeration and breakup of aluminum oxide particles in the rocket exhaust.

ADVANCED CONCEPTS FOR CHEMICAL PROPULSION

In the Advanced Concepts Program, very-high energy propellants, such as atomic hydrogen and other High Energy Density Matter (HEDM) propellant candidates, are being studied. This program has received much valuable information from the research underway at the Air Force Astronautics Laboratory and the Air Force Office of Scientific Research.

Many of the high energy propellants provide large increases in specific impulse. But along with the great potential of high-energy propellants are the attendant problems of free-radicals: production, storage and transportation. All of these factors are being investigated to determine the critical research directions for applying this material to propulsion. Only if these technical barriers are overcome will we gain the benefits of these propellants and propulsion systems.

Vehicle and System Performance Studies

Currently, atomic hydrogen is being analyzed for launch vehicles and upper stages. Using atomic hydrogen, the launch mass of future launch vehicles can be reduced by a factor of 3 to 10 over currently planned Space Transportation System-Cargo (STS-C) and Advanced Launch System (ALS) vehicles (Ref. 2). The specific impulse range to deliver this reduced mass is 750 to 1500 $\text{lb}_f\text{-s}/\text{lb}_m$. Advanced upper stages using this propellant can also provide a benefit to the planetary program. Placing a spacecraft on a very high energy trajectory is possible if the specific impulse of atomic hydrogen can exceed 750 $\text{lb}_f\text{-s}/\text{lb}_m$.

In addition to the vehicle studies, the facilities for producing, transporting and storing atomic hydrogen are being analyzed. Large cryogenic storage facilities and magnetic field coils or generators are required for atomic hydrogen propellants. These facilities are being studied to determine the what size facility is best suited to each launch vehicle configuration.

University Research Program

A set of experimental and theoretical studies are underway at the University of Hawaii at Manoa and the University of Iowa (Iowa City). Atomic hydrogen research is being conducted at the University of Hawaii. The storage density and the methods which may enable increases in that density are under investigation. Experiments are being conducted to understand the energy release phenomena during recombination. The atomic hydrogen is stored in solid cryogenic hydrogen. Tritium decay is used to form the atomic hydrogen in the solid hydrogen.

At the University of Iowa, a survey of advanced propellants is being conducted. From this survey, the potential specific impulse of the very advanced propellants will be estimated. This study will allow a preliminary screening of the high energy density propellants and identify which propellant may be applicable to future NASA missions.

CONCLUSIONS

Advanced propulsion technology can provide several benefits to high-energy space missions. Some of these benefits are significantly reduced launch mass, increased payload delivery and potentially lower transportation system costs. Several current research programs in both metallized propellants and advanced concepts are identifying the research directions to gain significant benefits for future NASA missions. With a combination of in-house studies and experiments, contracted research and university grants, a wide range of propulsion system technologies with potentially significant benefits are under investigation.

REFERENCES

Galecki, D., "Ignition and Combustion of Metallized Propellants," NASA Lewis Research Center, AIAA Paper 89-2883, presented at the 25th AIAA/ASME/SAE/ASEE Joint Propulsion Conference, Monterey, CA July 10-12, 1989.

Palaszewski, B., "Atomic Hydrogen As A Launch Vehicle Propellant, NASA Lewis Research Center, NASA Technical Memorandum 102459, AIAA Paper 90-0715, presented at the 28th AIAA Aerospace Science Meeting, Reno, NV, January 8-11, 1990.

SPECTROSCOPY AND DYNAMICS OF ENERGETIC HALOGEN AMINES

R. A. Conklin, J. Pestovich, R. F. Hanson, and J. V. Gilbert
Chemistry Department, University of Denver
Denver, Colorado

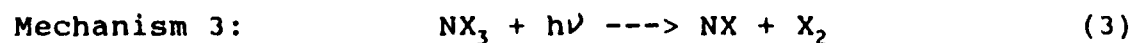
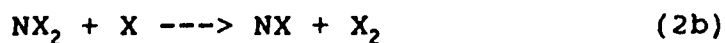
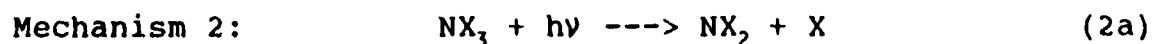
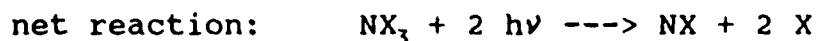
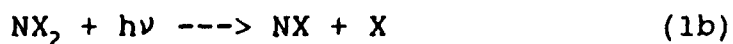
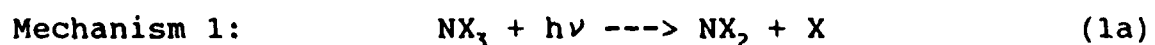
The halogen amines are in general very energetic and have a tendency to explosively decompose, liberating large amounts of energy. The channels through which this energy is released are not known and this effort was undertaken to probe these processes. An understanding of the decomposition mechanisms is of general importance since studies of this type add to the body of knowledge concerning the dynamics of high energy systems. In addition, the halogen amines serve as precursors to a variety of excited and ground state fragments, many of which are difficult or impossible to produce under controlled conditions from other precursors. The production of excited fragments, including nitrenes in excited singlet states, halogens in excited triplet states, and various NX_2 compounds, via reactions or photolysis of the halogen amines is possible because of their high energy content.

All three amines are synthesized in the laboratory and the experimental details are discussed in references 1, 2, 3, and 4.

Presented here are the results from the photolysis of low temperature matrix isolated NCl_3 , $NFCl_2$, and NF_2Cl , with Ar as the matrix gas. The photolysis wavelengths were chosen on the basis of the gas phase UV absorption spectra, which for all three amines consist of broad structureless features indicative of unbound excited states. The NCl_3 UV spectrum shows a strong band at 220 nm ($\epsilon \approx 20001/(\text{mole cm})$)⁵, a much weaker band at 250 nm, and a band at 330 nm due to Cl_2 . Cl_2 is present due to the decomposition of the

NCl_3 in the gas phase. No changes were observed following photolysis of the NCl_3 matrix at 220 nm, but upon photolysis at 280 nm (the low energy end of the 250 nm feature) NCl was produced in the matrix. Photolysis at 330 nm produced NCl_2 only in matrices in which NCl_3/Cl_2 aggregates were present. Broad band photolysis of a matrix that contained NCl_3 and NCl_3/Cl_2 aggregates produced both NCl and NCl_2 . The NFCl_2 UV spectrum consists of a band at 270 nm. Photolysis of the NFCl_2 matrix at this wavelength produced NF . Since Cl_2 , a by-product of the synthesis, is virtually impossible to remove from the NFCl_2 samples, photolysis at 330 nm was also performed, but no changes were observed indicating that the Cl_2 photolysis had no effect on the NFCl_2 in the matrix. NF_2Cl has a single absorption feature at 230 nm in the UV. Photolysis in this band and at several other wavelengths produced no changes in the IR spectrum of the matrix.

Three mechanisms are proposed for the production of NF from NFCl_2 and of NCl from NCl_3 .



The fact that no photolysis products are observed in the photolysis of NCl_3 at 220 nm and in the NF_2Cl experiments, (even though the states accessed are clearly unbound) suggests that these wavelengths break an N-Cl bond leaving NCl_2 or NF_2 and Cl fragments which recombine to form the parent molecule and do not react to form NCl and Cl_2 or NF and ClF . This implies that movement is greatly restricted within the matrix cage. Because the absorption spectra of NX_2 radicals are not in general known, it is not possible to distinguish between mechanisms 1 and 3 from these results. Mechanism 2, however, appears to be the most unlikely of the three since it would require some motion within the matrix cage for the newly formed X atom to pull off a second X atom.

The production of NCl_2 appears only to be an important process in high concentration matrices in which NCl_3/Cl_2 aggregates exist. Photolysis at 330 nm photolyzes the Cl_2 bond and the Cl atom produced can then act to break one N-Cl bond in NCl_3 leaving NCl_2 , Cl_2 and the remaining Cl atom in the matrix cage. No reaction of the NCl_2 and the Cl atom is apparent in these matrices, indicating again that motion in the cage is restricted.

References

1. J. V. Gilbert, X.L. Wu, D. H. Stedman, R. D. Coombe, J. Phys. Chem., 89, 4082 (1988).
2. J. V. Gilbert, R. A. Conklin, R. D. Wilson, K. O. Christe, to be published, J. Fluorine Chem. (1990).
3. R. A. Conklin, J. V. Gilbert, to be published, J. Phys. Chem. (1990).
4. R. F. Hanson, J. Pestovich, J. V. Gilbert, unpublished results.
5. T. C. Clark, M. A. A. Clyne, Trans. Faraday Soc., 65, 2994 (1969).

THEORETICAL STUDIES OF METASTABLE MOLECULAR SYSTEMS

K. Kirby

Harvard-Smithsonian Center for Astrophysics

The adjective "metastable" is not quantitative, and can be applied to many different excited states which will eventually decay to some lower-lying state. An excited state may be considered "metastable" if its lifetime before decay is on the order of microseconds, a thousand times longer than the lifetime of an upper state involved in a strongly-allowed dipole transition. However, microsecond lifetimes are much too short for the rocket engineer to consider as useful for energy storage in single-stage propellants. The practical application of metastable molecular systems for energy storage is critically dependent on "how metastable" a system is—that is, the length of time the state exists before decaying. Over the past two years we have identified and characterized the binding in three very different types of metastable molecular systems: (1) a doubly charged molecular ion CH^{+2} in which we have found a metastable excited state; (2) the $v=0$ vibrational levels of the $I^1\Sigma^-$ and $D^1\Delta$ states of CO which lie ~ 8 eV above the ground state; and (3) the high-spin states of $^6\Sigma^+$ symmetry in CN and NO which arise from ground state separated atom limits. We are now working to determine the lifetimes for each of these metastable species.

A doubly charged cation is itself a metastable species due to its vulnerability with respect to electron capture and charge transfer with neutrals. Most of the potential energy curves of a molecule such as CH^{+2} are unbound because of the coulomb repulsion dominating the interaction of the two nuclei C^+ and H^+ . There has been considerable debate in the literature as to the existence of the CH^{+2} ion¹⁻⁵, and the most accurate theoretical calculation⁴ has shown that there is no binding in the ground state which has $^2\Sigma^+$ symmetry. Recently, Hamdan et al.⁶ have reported the observation of a metastable excited state of CH^{+2} with lifetime $\tau > 3 \mu s$ lying at $35 \pm .5$ eV above the $v=0$ level of the $X^1\Sigma^+$ state of CH^{+2} .

Bound states of CH^{+2} can arise from asymptotes $C^{+2} + H$ due to charge-induced dipole polarization. The lowest such asymptote, $C^{+2}(2s^2, ^1S) + H(^2S)$ gives rise to the $3^2\Sigma^+$ state

which does exhibit some binding, but 10 eV higher than the $1^2\Sigma^+$. The second such asymptote, $C^{+2}(2s2p, ^3P) + H(^2S)$ gives rise to doublet and quartet states of Σ^+ and Π symmetry. The $^4\Sigma^+$, as the lowest state of its symmetry, is the focus of our investigation. The doublet states were thought to decay very rapidly by radiation to 12 lower-lying doublet states.

Using a full five-electron single- and double-excitation configuration interaction wavefunction I have computed the potential energy curves of the $1^4\Sigma^+$ and $2^4\Pi$ states of CH^{+2} . Those are shown in Figure 1. The binding energies were found to be 1522 cm^{-1} and 1252 cm^{-1} , with R_e 's of 5.44 and $5.90\ a_0$ for the $1^4\Sigma^+$ and $2^4\Pi$, respectively. The $1^4\Sigma^+$ state supports five vibrational levels and the $2^4\Pi$ state supports four. Wavefunctions for the $1^4\Pi$ were also computed. In order to obtain the radiative lifetimes of both the $1^4\Sigma^+$ and the $2^4\Pi$ states, transition moments to the $1^4\Pi$ were computed. The energy separation between these energetic states and the $1^4\Pi$ is $\sim 7\text{ eV}$ and the computed radiative lifetimes of the $2^4\Pi$ and $1^4\Sigma^+$ are $2.1 \times 10^{-8}\text{ s}$ and $3.7 \times 10^{-6}\text{ s}$, respectively. The lifetimes of the $1^4\Sigma^+$ state and the energy of its calculated minimum (34.5 eV above $v=0$ of CH^+) are in good agreement with the experimental observations of Hamdan et al.⁶

Two metastable electronic states of CO, $D^1\Delta$ and $I^1\Sigma^-$, lie more than 8 eV above the ground state of CO. They are almost energy degenerate with the $A^1\Pi$ state, the only electronic state to which they can radiatively decay via an electric dipole transition. The $v=0$ level of the $I^1\Sigma^-$ state lies below the $v=0$ level of the $A^1\Pi$ state and thus this vibrational level has $\tau_{\text{rad}} = \infty$ for electric dipole radiation. The $v=0$ level of $D^1\Delta$ lies just above the lowest vibrational level of the $A^1\Pi$ and $\tau_{\text{rad}} = 1.6\text{ s}$.⁷

We (Rosenkrantz and Kirby) have considered various ways to populate these $v'=0$ levels. Two-photon absorption or electron-impact excitation from the $v=0$ level of the ground state will not populate these $v'=0$ levels because the Franck-Condon overlap is vanishingly small. In order to get Franck-Condon factors of .1 or more, the excitation needs to originate from $v''=8$ to $v''=12$ of the $X^1\Sigma^+$ state. Pumping of the $W^1\Pi$ Rydberg state of CO^8 and

subsequent decay to the $I^1\Sigma^-$ and $D^1\Delta$ would also be a viable mechanism, especially if stimulated emission were used to aid in populating the $v'=0$ levels specifically. The $W-X$ oscillator strength is very large, but the wavelength necessary ($\sim 965\text{\AA}$) is not very convenient experimentally. As in the production of the metastable $c^3\Pi_u^-$ state of H_2 , charge transfer could be used to populate these states of CO : $CO^+ + X(\text{gas}) \longrightarrow CO(I^1\Sigma^-, D^1\Delta; v'=0?) + X^+$.

Once these $v'=0$ levels are populated, the question remains as to their true lifetime. According to the selection rules, these states cannot decay by magnetic dipole transitions to the $X^1\Sigma^+$ state. Electric quadrupole transitions however appear to be allowed. An estimate of the lifetime for electric quadrupole decay can be given, assuming the quadrupole transition moment squared is of order 1 to 10, and $\Delta E \sim 6\text{ eV}$ (for decay to $v''=8$ to 12 of the X -state which have the largest Franck-Condon factors with $v''=0$ of $I^1\Sigma^-$ and $D^1\Delta$). The lifetime for electric quadrupole decay is approximately 0.13 to 0.01s. Observation of this transition in the laboratory would be the first measurement of an electric quadrupole transition in a heteronuclear molecule.

Another possible decay path is through spin orbit coupling of the $I^1\Sigma^-$ and $D^1\Delta$ to the triplet manifold of states and then radiation to low-lying triplets such as $a^3\Pi$ and $a'^3\Sigma^+$. The calculation of this coupling and the resultant radiative lifetimes is a very large problem involving many channels and states that need to be considered. We are working toward solving this problem. However the $a^3\Pi$ state is itself metastable and is the upper state of the well-known Cameron-band system at $\sim 48,473\text{ cm}^{-1}$. The lifetime of vibrational levels in the $a^3\Pi$ state is $\sim 10\text{ ms}$, but no definitive calculations of this transition have been performed, a situation we intend to remedy in the next several months.

References

1. T. Ast, C.J. Porter, C.J. Proctor, and J.H. Beynon, *Chem. Phys. Lett.* **78**, 439 (1981).
2. D. Mathur, *Chem. Phys. Lett.* **150**, 547 (1988).
3. R.W. Wetmore, R.K. Boyd and R.J. LeRoy, *Chem. Phys.* **89**, 329 (1984).
4. W. Koch, B. Liu, T. Weiske, C.B. Lebrilla, T. Drewello and H. Schwarz, *Chem. Phys. Lett.* **142**, 147 (1987).
5. D. Mathur and C. Badrinathan, *J. Phys. B: At. Mol. Phys.* **20**, 1517 (1987).
6. M. Hamdan, A.G. Brenton, and D. Mathur, *Chem. Phys. Lett.* **144**, 387 (1988).
7. M.E. Rosenkrantz and K. Kirby, *J. Chem. Phys.* **90**, 6528 (1989).
8. D.L. Cooper and K. Kirby, *Chem. Phys. Lett.* **152**, 393 (1988).

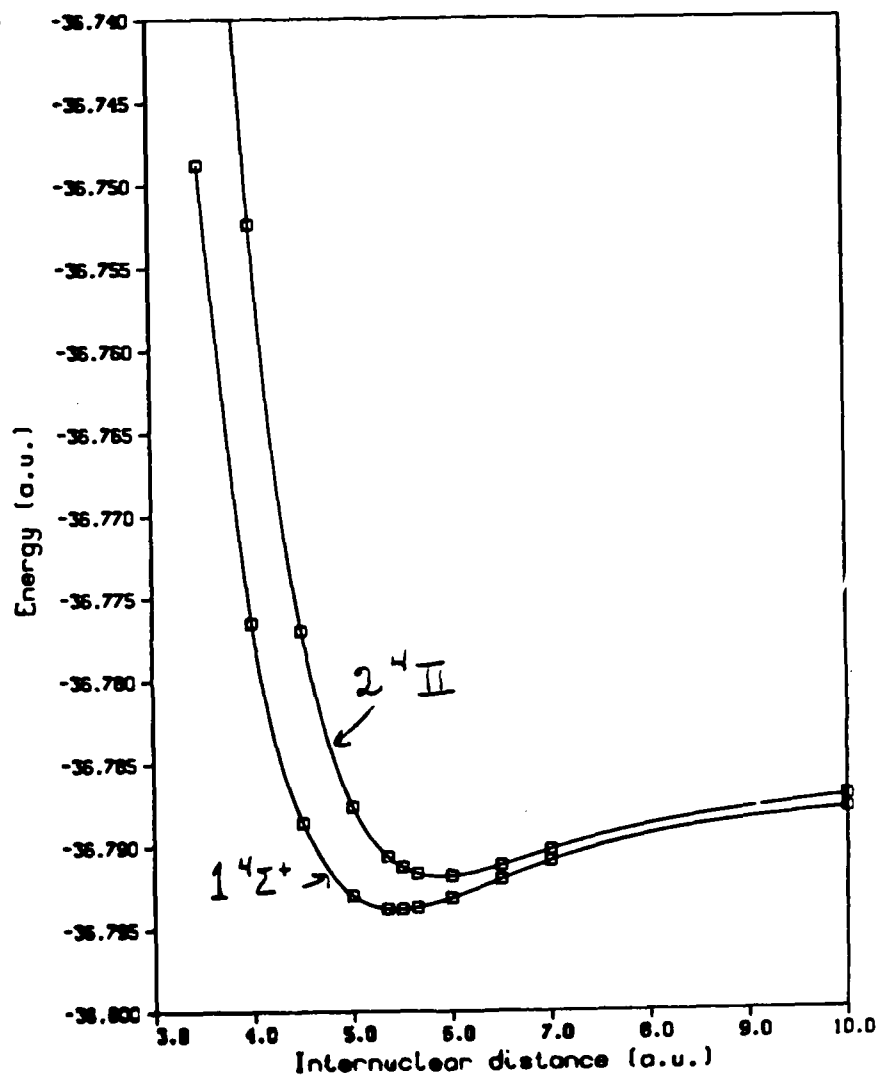


Figure 1: Potential energy curves of two excited states of CH^{+2} arising from the separated atom limit: $\text{C}^{+2}({}^3\text{P}) + \text{H}$

Extended Abstract

Theoretical Studies of HEDM Molecules

Byron H. Lengsfeld III

Theoretical Atomic and Molecular Physics Group, L-446

Lawrence Livermore National Laboratory

P.O. Box 808, 7000 East Ave

Livermore, CA 94550

This work was supported by the Air Force Astronautics Laboratory under LLNL Contract Number 6761-01 and was performed under the auspices of the U.S. Department of Energy at Lawrence Livermore National Laboratory under contract W-7405-Eng-48.

Two tasks were undertaken during the past year. The first task was to improve and document the **MES_A¹** series of electronic structure codes. The second task was to carry out theoretical studies of B_2H_2 and Be_2H_2 in order to assess their potential as high energy density materials.

The **MES_A** electronic structure package is designed to characterize both ground state and excited state molecular potential energy surfaces. It is based on multiconfiguration self-consistent-field, MCSCF, and multireference configuration interaction, MRCI, methods and, the code has the ability to employ analytic gradient techniques to locate stable points on a multidimensional potential energy surface. Thus, the code is capable of providing both the thermodynamic quantities (heats of reaction) and the kinetic quantities (reaction rates and excited state lifetimes) needed to ascertain if a molecule is stable and if it is energetic enough to be of interest to the Air Force's High Energy Density Matter program.

The two molecules that were studied during the past year, B_2H_2 and Be_2H_2 , were chosen because high performance propellants are well-known which employ similar boron and beryllium hydrides and, the linear forms of B_2H_2 and Be_2H_2 are more energetic than their well-known counterparts. It was postulated that the bridged isomers of these molecules would be stable and more energetic than the linear isomers.

SUMMARY OF B_2H_2 AND Be_2H_2 CALCULATIONS:

High performance propellants which consist of boron and beryllium hydrides have been known and studied for some time.²

<i>Propellants</i>	<i>I_s (Specific Impulse)</i>
BeH ₂ -F ₂	395
H ₂ -O ₂	391
B ₅ H ₉ -OF ₂	367

The lowest energy isomers of these molecules are known to be linear but these systems have exhibited a propensity to form stable bridged structures, so it was postulated³ that a stable high energy bridged isomer of these molecules could be found. The linear $^3\Sigma^-$ state of B_2H_2 has a heat of formation of 106 kcal/mole^{3,4} but is not suitable as a propellant as it polymerizes⁵ The bridged singlet structure of B_2H_2 offers the possibility of storing additional energy in the bridged bonds. In addition, one might expect the singlet state of the bridged isomer to be lower in energy than the triplet state as bridged B_2H_2 is isoelectronic with C_2 , which has a singlet ground state. The closed shell singlet state would be expected to be less reactive than the triplet so the bridged structure not only provides a means for storing additional energy in an energetic molecule but also serves to reduce its reactivity. Since boron hydrides are known to form stable bridged structures,⁶ the isomerization barrier may well be high enough to produce a new, long-lived energetic material.

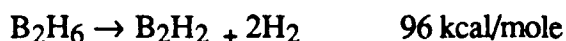
Beryllium hydrides, like boron hydrides, also have a propensity to form stable, bridged isomers.⁷ However, the lowest energy isomer of Be_2H_2 is a singlet and thus less reactive than B_2H_2 .

The issues that were addressed in this study were:

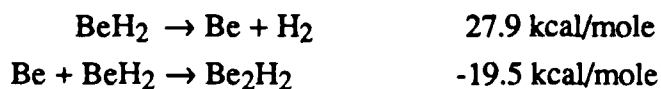
- 1) Do bridged isomers of B_2H_2 and Be_2H_2 exist
- 2) If the bridged isomers exist, how much energy is stored in the bridged structures and what is the heat of formation of these isomers.
- 3) Are the bridged isomers long-lived if they do indeed exist.

These questions were answered by a series of calculations that are described in a subsequent section of this report. I only note here that a variety of basis sets and computational methods were employed in these studies to insure that the calculations had indeed converged.

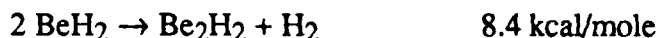
Preliminary multiconfiguration self-consistent-field calculations indicated that the bridged isomers of both Be_2H_2 and B_2H_2 were stable. The energy stored in the bridged structures was found to be 39 kcal/mole for B_2H_2 and 30 kcal/mole for Be_2H_2 in these early calculations. In light of these results, emphasis was given to B_2H_2 calculations as the following reactions indicated that B_2H_2 is much more energetic than B_2H_6 ⁸.



while the advantages of Be_2H_2 over BeH_2 are much smaller as ^{7,9}



or



Multireference configuration interaction, CI, calculations were then undertaken to determine the isomerization barrier and to obtain a more accurate value for the relative stability of the linear and bridged isomers. The height of the isomerization barrier was found to be 3.4 kcal/mole when corrected for zero point vibrational motion. The classical barrier height was 4.6 kcal/mole. In the largest CI calculations, the bridged isomer was found to be 45 kcal/mole above the linear triplet. These calculations are described in greater detail in a FY89 final report that was submitted to the Air Force Astronautics Laboratory.

These results support the arguments which originally motivated this research. The bridged isomers of B_2H_2 and Be_2H_2 are indeed stable and are significantly more energetic than their linear counterparts. The isomerization barrier in B_2H_2 is small enough so that this molecule would not be long-lived at room temperature but it is large enough that it may well be long-lived at liquid H_2 temperatures. There are three issues which still need to be addressed;

- 1) The lifetime of bridged B_2H_2 needs to be determined as a function of temperature.

- 2) The stability of bridged B_2H_2 to dimerization and to reactions with H_2 needs to be determined.

and

- 3) If the molecules is long-lived and stable to the reactions cited above, then a way to synthesize this isomer must be devised.

CODE DEVELOPMENT:

In order to theoretically assess the performance of a novel propellant one needs to determine the energy released during the course of the combustion reaction and the molecular weight of the gases produced. When studying new materials, one may also need to determine the lifetime of the reactants. The energy released during a reaction is obtained by determining the relative energy of the reactant and product molecules at their equilibrium geometries and their zero point vibrational energies. The lifetime of a molecule is more difficult to ascertain theoretically as it requires the ability to determine the activation barriers in the energetically accessible decay channels. In order to characterize these activation barriers, or transition state regions of the potential energy surface, one needs to have the capability of describing the change in a molecule's electronic structure that occurs when a bond is being broken or formed. If one of the reactants is in an excited state then radiative and nonradiative decay channels to lower state surfaces must also be considered. Standard electronic structure packages, such as Gaussian86, are well suited to determine thermodynamic quantities as the theoretical models employed in these codes use a single determinantal (Hartree-Fock) starting point in their calculations. Accurate heats of reaction are obtained with codes by using Moller-Plesset perturbation theory or variations of coupled-cluster theory to account for the changes in electron correlation energy between the reactants and products of the reaction. These methods are limited by the use of a single determinantal reference configuration and can not, in general, treat the changes in electronic structure which occur during bond formation. Therefore, these methods are not suited for study of transition state regions of a potential energy surface. The **MESA** series of codes addresses these problems by employing a general multiconfiguration self-consistent-field, MCSCF, wavefunction as a starting point in the treatment of the electron correlation problem. These MCSCF wavefunctions contain the terms needed to describe bond formation where single determinantal wavefunctions do not. This allows the code to be

used in studies of excited states as well as studies of transition state regions of ground state potential energy surfaces.

In order to rapidly locate a molecule's equilibrium structure or a transition state on a multidimensional potential energy surface one must have the ability to analytically differentiate the quantum mechanical energy expression with respect to the position of the atoms. **MES**A has the capability of analytically determining first derivatives of SCF, MCSCF and multireference configuration interaction, MRCI, wavefunctions. Analytic second derivatives, and thus harmonic vibrational frequencies, are available for SCF and MCSCF wavefunctions. Geometry optimization and finite-difference second derivatives for SCF, MCSCF and MRCI wavefunctions are also standard options in the code and don't require user intervention at intermediate points in the calculations. The input was designed to be as "user friendly" as possible and includes a standard library of basis sets which can be easily expanded. The capabilities of the **MES**A codes and a detailed description of the input options are contained in the documentation that was prepared as part of this contract. A copy of the **MES**A documentation is included in my FY89 final report to the Air Force Astronautics Laboratory.

CONCLUSIONS:

The bridged isomers of B_2H_2 and Be_2H_2 were found to be stable and the heat of formation of these molecules were large enough for them to be of interest to the Air Force's High Energy Density Materials Program. The B_2H_2 molecule was deemed to hold the most promise as a new rocket propellant and a series of calculations were undertaken to determine the isomerization energy and isomerization activation energy of this molecule. The isomerization energy was found to be 45 kcal/mole which results in a heat of formation of 151 kcal/mole. The isomerization barrier was found to be 3.4 kcal/mole, which is too small for the molecule to be long-lived at room temperature. While the molecule might live long enough to be useful at liquid H_2 temperatures, tunneling calculations and a determination the rate of reaction with H_2 molecules would need to be determined before its lifetime in this environment could be ascertained. The propensity of the bridged isomer to dimerize would also have to be determined.

REFERENCES:

- 1) **MES~~A~~** is a general electronic structure code package written by Paul Saxe (LANL), Richard Martin (LANL), Michael Page (NRL) and Byron Lengsfeld (LLNL)
- 2) R. Holzmann, **Chemical Rockets**, Marcel Dekker, New York, 1969, pg 286.
- 3) B. Lengsfeld, in **Proceedings of the High Energy Density Matter (HEDM) Conference**, New Orleans, March 1989, released by the Air Force Astronautics Laboratory, pg 147.
- 4) G. Adams and M. Page, "Structures and Energies For Small Boron Compounds. One and Two Boron Compounds", U.S. Army Ballistic Research Laboratory Technical Report, in press.
- 5) D. Armstrong, Theor. Chim. Acta 60,159(1981)
- 6) W. Lipscomb, **Boron Hydrides**, W. A. Benjamin, New York, 1963.
- 7) R. Cimiraglia, M. Persico, J. Tomasi and O. Charkin, J. Comp. Chem. 5,263(1984)
- 8) L. Curtiss and J. Pople, J. Chem. Phys. 91,4809(1989)
- 9) P. Jasien and C. Dykstra, J. Am. Chem. Soc. 107,1891(1985)

Metastable Metals in Matrix Materials

N. Presser, R. Poole and A. T. Pritt, Jr.

Chemistry and Physics Laboratory

The Aerospace Corporation

INTRODUCTION

We have previously proposed a fuel for improving Isp for launch vehicles.¹ This fuel consists of dissolving light mass metal atoms and dimers in a weakly binding cryogenic matrices. In this environment the enthalpies of the free metal atoms and dimers are essentially those of the gas phase species. The stabilization of these atoms and dimers in such matrices eliminates the need to overcome the enthalpies of liquifaction and vaporization, thus storing more potential energy than the best practical fuel/oxidizer combination available, liquid H₂ / liquid O₂.

This concept was tested by calculating the Isp for various metal/matrix fuels reacting with liquid O₂, using the AFAL developed code, EDCONVU. In all these calculations the matrix was assumed to be H₂, and to predict the distribution of monomers, dimers, and higher order oligomers that might arise in the matrix at higher metal mole fractions, a statistical model developed previously was used.² This model assumes that the population of any species is statistically determined with no barrier to bond formation between nearest neighbor metal species. In addition, it is assumed that deposition dynamics do not play a role in determining the metal species' distribution. The results, in some cases, were quite dramatic and indicated that for a number of metal atom systems such fuels could significantly increase Isp's. For example, the calculated Isp for the B/H₂/O₂ system is 17 percent greater than that for the baseline H₂ + O₂ system, and this improvement occurs over a narrow range of boron atom mole fractions from 0.1 to 0.2. These results emphasize the need for *quantitative* measurements of free metal atom concentrations in matrices rather than order of magnitude estimates. During this year a number of diagnostic techniques have been developed to accurately determine the free metal atom concentration in cryogenic matrices produced by vapor phase deposition on substrates at 4.5 K.

RESULTS

Free metal atom concentrations in cryogenic matrices produced by vapor deposition on a cold substrate are determined by integrating the absorption of a known electronic transition of the metal atom in a sample matrix having a thickness which is determined from laser interferometric techniques. Implicit in this approach is that the mass density (and therefore its index of refraction) of the deposited cryogenic material is equal to its bulk density and that the oscillator strength of the metal atom is unchanged in the matrix. The matrix oscillator strength for the atomic transition can be determined independently if one assumes: (a) that the deposition flux of the metal atoms is known; (b) that the atoms stick with unit efficiency; and (c) that at low concentrations all the metal atoms in the gas flow remain as metal atoms in the matrix. This past year several techniques have been developed to test the validity of these assumptions.

A dual beam interferometric apparatus shown in Figure 1 was assembled to measure the refractive indices of matrices *in situ*. A beam splitter splits the HeNe laser beam. Each beam is passed through the substrate and deposited matrix at two separate angles, θ_1 and θ_2 . Each of the reflected beams is modulated at a characteristic rate corresponding to the individual optical paths. At constant deposition rates the refractive index of the matrix is related to the characteristic modulation times τ_1, τ_2 and angles θ_1, θ_2 through the following expression,

$$n = (\Delta^2 \sin^2 \theta_1 - \sin^2 \theta_2)^{1/2} / (\Delta^2 - 1)^{1/2} \quad (2)$$

where Δ equals τ_1/τ_2 . The measured index values may be related to the matrix mass density by the Lorentz-Lorenz relation,

$$(n^2 - 1) / (n^2 + 2) = (4\pi/3)(L \alpha / M) \rho, \quad (3)$$

where L is the Loschmidt number, α is the gas phase polarizability, M is the molecular weight of the material being deposited, and ρ is the mass density. Our results presented in Table 1 indicate that rare gas and hydrogen matrices deposited at 4.5 K are porous and their densities are significantly less than those reported for the bulk phase. The results are independent of deposition flux in the range studied, $5 - 100 \times 10^{15} / \text{cm}^2/\text{s}$ and agree reasonably well with those obtained by Schulze and Kolb³ who used a different detection scheme. The presence of significant levels of impurity species, metal atoms, might effect the density of deposited matrices. For the sodium in xenon (Na/Xe) system, we find that the added presence of the sodium does effect the measured densities. In the range up to 5 mole percent Na, the observed matrix density increases monotonically. Densification occurs, but at the highest doping levels the measured density is still 15 percent below that reported for bulk Xenon.

Table 1. Refractive Indices and Densities of Pure Matrix Materials (4.5 K)

Property	Xe	Kr	Ar	Ne	H ₂
n_{bulk}	1.49	1.38	1.29	1.11	0.1097
n_{matrix}	1.332	1.313	1.25	1.079	0.1086
ρ_m/ρ_b (This work)	0.71	0.83	0.87	0.64	0.85
ρ_m/ρ_b (Reference 3)	0.65	0.68	0.80	0.95	---

As we noted earlier, several terms contribute to the uncertainty in the determination of free metal atom levels. Quantities affecting this determination include, the flux of free metal atoms, their sticking coefficient under experimental conditions, and the assumption that at sufficiently low metal atom mole fractions all the metal atoms from the vapor appear as monomers in the matrix. In our experiments care has been taken to establish effusive metal atom flow from an oven cell; however, the sticking coefficient for the alkali atoms at 4.5 K has not been measured.

Using a home built quartz microbalance the rate of mass deposition has been measured as a function of oscillator temperature and source oven temperature. Any mass deposited, m_d , on the crystal oscillator produces a change in the resonant frequency of the system. The mass deposited can be related to this frequency change, Δf , through the Saubry equation,

$$m_d = (D/f_0^2) \Delta f$$

where f_0 is the intrinsic oscillator frequency and D is a material constant. This measurement yields the net deposited flux. The deposition rate of Na on the quartz oscillator surface increases gradually as the surface temperature is decreased over the range 298 - 111 K. Figure 2 shows this gradual increase in the deposition rate as the temperature of the quartz oscillator is lowered. At the lowest temperatures the rate of mass deposited reaches a constant. This leveling off in the rate

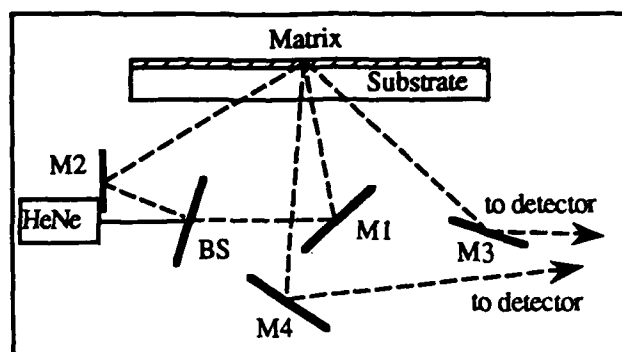


Figure 1. Experimental configuration of the dual beam interferometric measurement of the refractive index for the deposited matrix. BS refers to the beam splitter and M to the mirrors.

of mass deposition for a fixed flow is interpreted as a condition in which the sticking coefficient approaches unity. At 300 K therefore, the sticking coefficient of Na on quartz is ~ 0.73 . The measured mass deposition at the lower temperatures confirms our earlier assumption that the Na oven source is effusive over the temperature range from 488 - 583 K. With this mass flow determination capability we no longer require that the oven source be effusive.

The results from the microbalance measurements suggests that the sodium sticking coefficient at temperatures below 111 K is unity for a quartz crystal. In our experiments our substrate is sapphire not quartz. If we assume that the sticking coefficient is unity, the concentration of free metal atoms in a matrix for low molar concentrations can be determined. Measurement of the integrated absorption strength under these conditions yields the oscillator strength for the free atom in the matrix. Under appropriate conditions it can be related to its gas phase value through a lifetime measurement. These measurements are currently underway. However, because the system we are dealing with, Na, has a very large gas phase oscillator strength (0.65) it is possible to set a bound to the magnitude of the error that might be produced in our measurements. This turns out to be 50%.

DISCUSSION

Our motivation in studying the model systems Na/Xe and Li/Xe is twofold. The first is to establish procedures necessary to quantify free metal atom concentrations in matrices. The second is to determine if the distribution of free metal atoms in matrices could be described by the statistical model. Welker and Martin⁴ studied xenon matrices doped with varying amounts of Li, Na, and Ag. Their interest was determining the mole fraction of atoms necessary for the onset of bulklike optical properties and plasmon absorption associated with small metal clusters. Their data show that the free atom distribution reported for Li/Xe can be described by our statistical model.² Figure 3 shows the comparison of their data with the statistical model. By contrast their Na/Xe data show significant deviations from such predictions as graphically presented in Figure 4. To determine whether their Na/Xe results were indicative of some inherent limitation on the concentrations achievable in this system or whether the distribution was being dominated by the mechanics of the deposition process, we re-examined the Na/Xe system. Our results⁵ reported last year indicated that the non-statistical distributions observed in their study could be ascribed to artifacts associated with their deposition rates. The results we obtained agreed well with the statistical predictions at the extremes, high and low concentration, but deviated in the intermediate regime. In our earlier analysis bulk densities for the matrix was assumed. Correcting our data for the measured Xe matrix densities bring our measured free atom sodium concentration into close agreement with the statistical model as shown by the closed circle symbols and solid curve in figure 4.

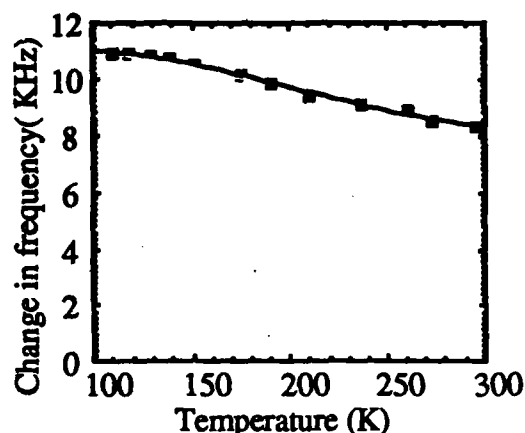


Figure 2. Variation of the change in the quartz oscillator frequency with deposited sodium as a function of the temperature of the quartz.

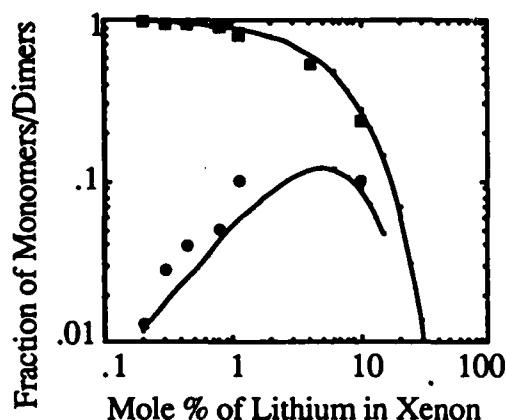


Figure 3. Fraction of monomers and dimers as a function of total mole percent of lithium deposited in a xenon matrix. The solid lines is that predicted from the statistical model. The squares are the monomer fraction and the circles, the dimer fraction as reported in ref. 4.

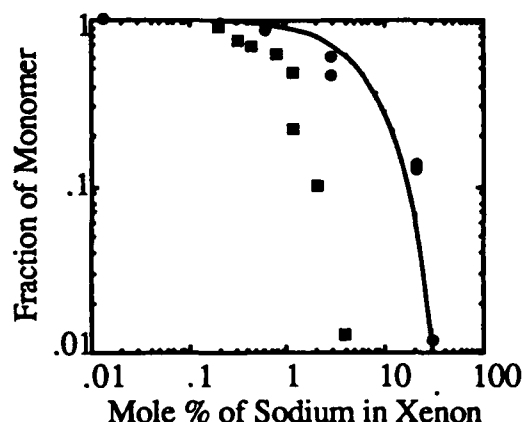


Figure 4. Fraction of monomers as a function of the total mole percent of deposited sodium in a xenon matrix. The solid line is that predicted from the statistical model. The square symbols are the data reported in ref. 4; the circles represent this work which includes corrections to the matrix density.

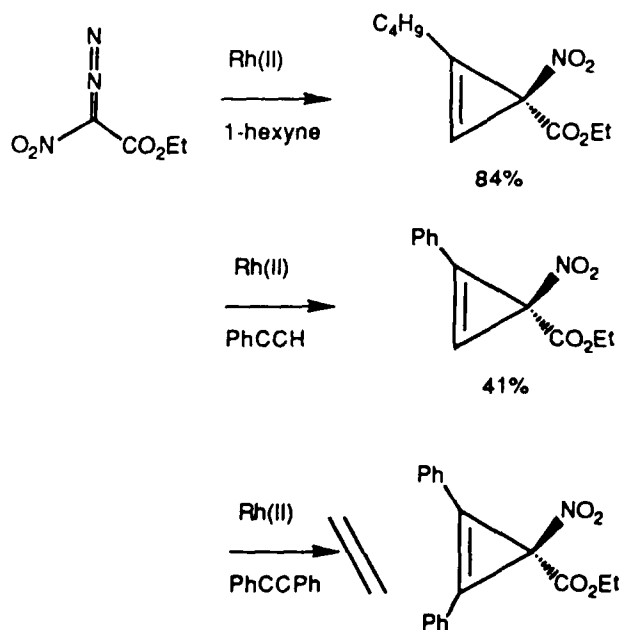
REFERENCES

1. N. Presser and A.T.Pritt, Jr., "High Energy Density Materials in Cryogenic Matrices," Proceedings of the High Energy Density Matter (HEDM) Conference, W. J. Lauderdale and W. A. Sowell (eds.), Rosslyn, VA, 12-13 May, 1987.
2. A. T. Pritt, Jr., N. Presser, and R. R. Herm, "Limitations on Atom Densities in Cryogenic Matrices," Proceedings of the High Energy Density Matter (HEDM) Conference, T. G. Wiley and R. A. van Opijnen (eds.), New Orleans, LA, 12-15 March, 1989.
3. W. Schulze, and D. M. Kolb, *J. Chem. Soc. Faraday Trans II* **70**, 1098 (1974).
4. T. Welker and T. P. Martin, *J. Chem. Phys.* **70**, 5683 (1979)
5. N. Presser, A.T.Pritt, and R. R. Herm, "Metastable Metals in Matrix Materials," Proceedings of the High Energy Density Matter (HEDM) Conference, T. G. Wiley and R. A. van Opijnen (eds.), New Orleans, LA, 12-15 March, 1989.

Synthesis and Properties of Novel Nitrocyclopropenes: Potential High Energy Density Materials.

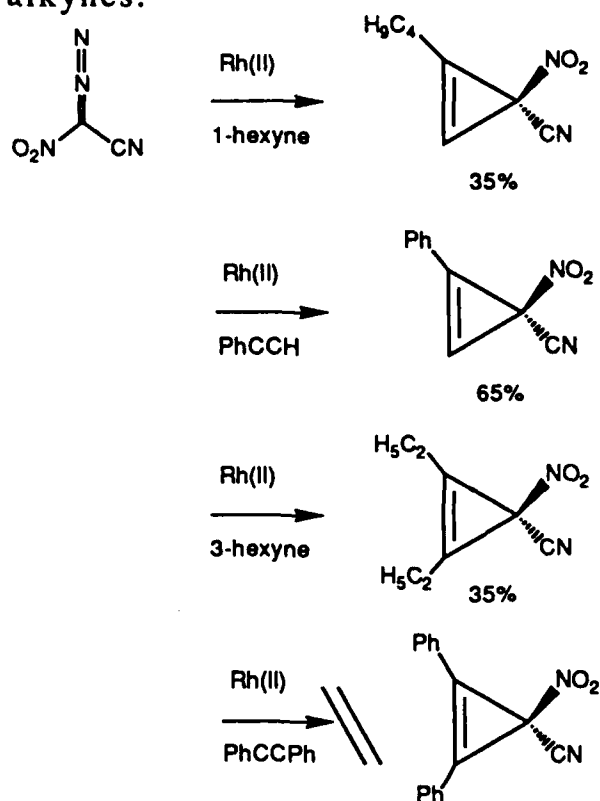
William P. Dailey
Department of Chemistry
University of Pennsylvania
Philadelphia, Pennsylvania 19104-6323

Cyclopropenes are highly energetic hydrocarbons. The parent cyclopropene has a ΔH_f of 66 kcal/mol and a strain energy of 55 kcal/mol. Addition of energetic groups such as nitro onto the nitrocyclopropene skeleton provides an opportunity to prepare even more energetic materials. To date, there is only one reported example of a nitrocyclopropene. 3-Nitro-1,2-diphenylcyclopropene was prepared by reaction of diphenylcyclopropenium ion with nitrate anion.¹ Over the past several years we have developed methodology to prepare nitrocyclopropanes using the transition metal mediated cyclopropanation of alkenes with nitrodiazomethanes.² Recently we have found that this cyclopropanation reaction may be extended to include alkynes. For instance, we have found that ethyl nitrodiazoacetate will cyclopropanate terminal alkynes in reasonable yields.

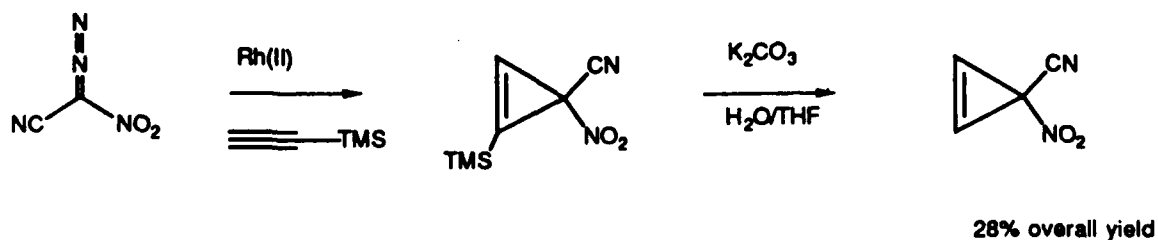
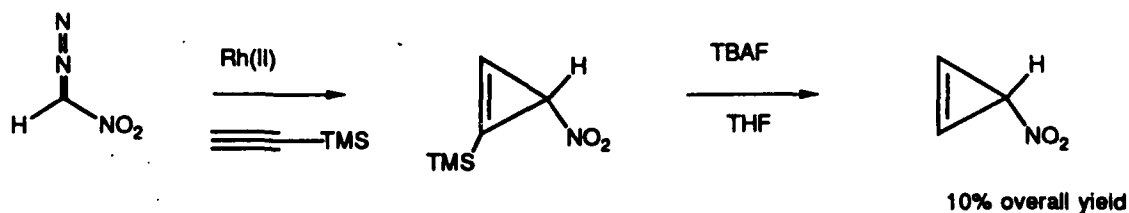


The reactions with both nitrodiazomethane and cyanonitrodiazomethane and terminal alkynes yield similar results.

In addition, both diazo compounds will cyclopropanate some internal alkynes.



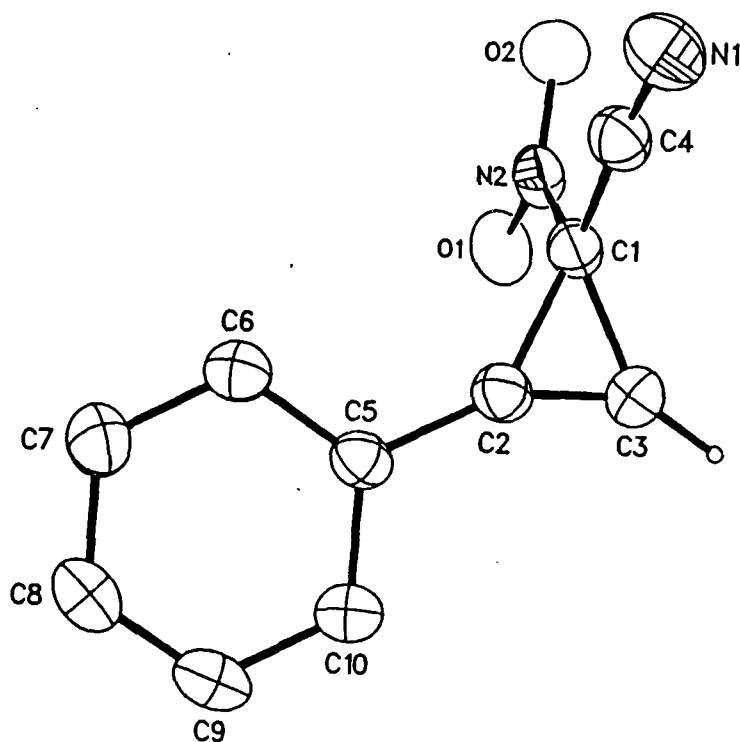
The synthesis of the parent 3-nitrocyclopropene and 3-cyano-3-nitrocyclopropene were accomplished by starting with trimethylsilylacetylene. After cyclopropanation using the appropriate diazo compound, the trimethylsilyl groups were removed to give the parent hydrocarbons.



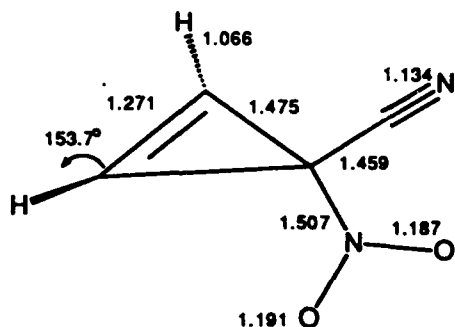
3-Cyano-3-nitrocyclopropene is a colorless oil which is stable at room temperature for extended periods of time. Ab initio calculations (see below) predict that it will have $\Delta H_f = 90$ kcal/mol. This compound may be a useful high energy fuel.

We have succeeded in obtaining a crystal structure for one on these nitrocyclopropenes. An ORTEP diagram for 3-cyano-3-nitro-1-phenylcyclopropene is shown below.

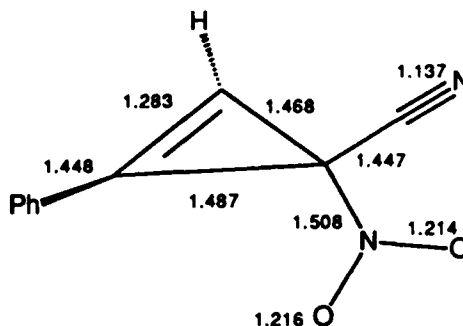
ORTEP diagram of 3-Cyano-3-nitro-1-phenylcyclopropene



We have carried out ab initio calculations at the HF/6-31G* level on the parent 3-cyano-3-nitrocyclopropene and compare the optimized geometry with the X-ray data for the phenyl derivative.



HF/6-31G*



X-ray

References

- 1 Cheer, C. J.; Bernstein, D.; Greenberg, A. Lyu, P. *J. Am. Chem. Soc.* **1988**, *110*, 226-230.
- 2 See, *Tetrahedron Letters* **1988**, 987-990; 5719-5722; 6031-6032; **1989**, 4197-4200. *J. Organic Chemistry* **1989**, 3096-3101; **1990**, 353-355. *J. American Chemical Society* **1989**, 9244-9245.

PRODUCTION AND PROPERTIES OF CLUSTER IONS

Y. K. Bae

Molecular Physics Laboratory

SRI International

Menlo Park, CA 94025

Studies of cluster ions can provide important information on the behavior of trapped ions in matrix. To provide spectroscopic information we have measured photofragment spectrum of H_5^+ between $5,400\text{ cm}^{-1}$ and $10,000\text{ cm}^{-1}$ by monitoring H_3^+ photofragment and have observed four new bands.

Further application of clusters to high energy density materials has been recently discovered by Beuhler et al.¹ for dramatically enhancing nuclear fusion yield. The new fusion scheme will potentially open the feasibility of a very compact fusion rocket engine. For the cluster impact fusion, generation of high intensity cluster beams of deuterium containing materials, such as D_2O and LiD , is essential. We have developed a new type of cluster ion source for this application. We summarize here the progress in our experimental program.

1. Observation of high-lying vibrational predissociation states of H_5^+

H_5^+ cluster ion is the first member of the H_{2n+1}^+ clusters which are the simplest cluster ions. Ab initio quantum calculations^{2,3} have predicted H_{2n+1}^+ clusters are roughly described as an H_3^+ surrounded by H_2 molecules and among them the simplest H_5^+ deviates the most from the model. Okumura et al.⁴ observed their vibrational spectra and found the observed frequencies of H_7^+ and H_9^+ agreed well with ab initio values,² but those of H_5^+ did not.³ They conjectured that the discrepancy might result from its characteristics as a proton bound dimer $H_2-H^+-H_2$ which is expected to have a large anharmonicity.

To investigate this problem further, we have measured vibrational predissociation of H_5^+ between $5,400$ and $10,000\text{ cm}^{-1}$. The schematic diagram of the experimental apparatus is shown in Figure 1. The H_5^+ ions are

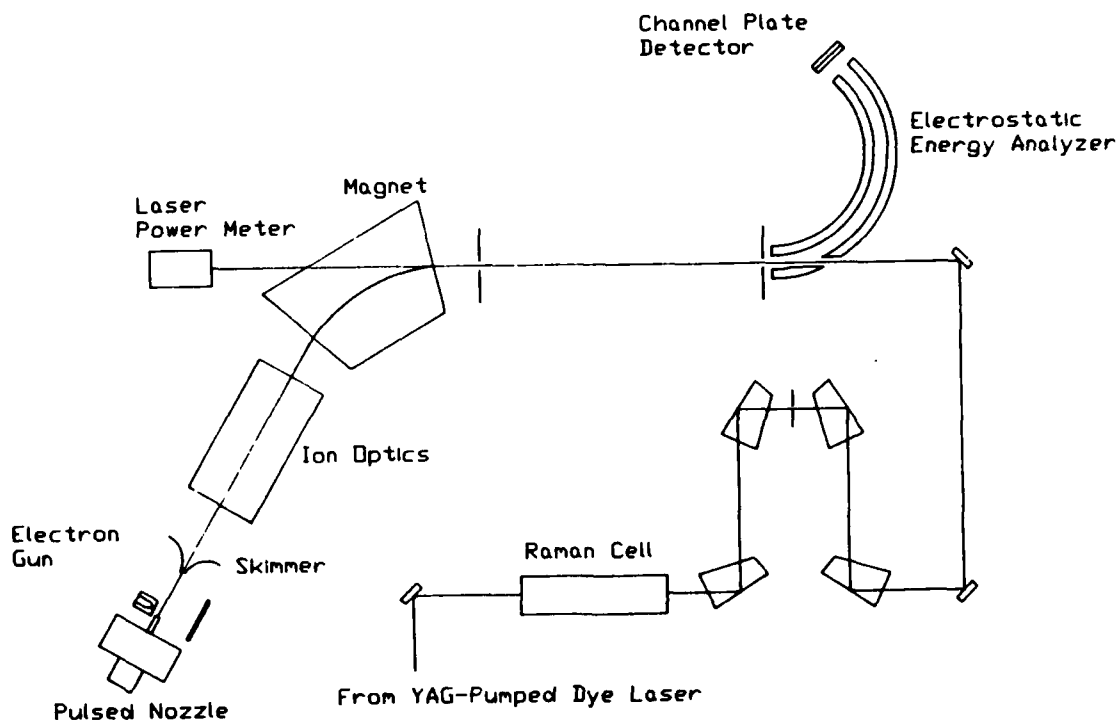


Figure 1

generated by 200 eV electron impact near the nozzle of a pulsed supersonic expansion of room temperature H_2 gas. The generated ions are extracted coaxially from the expansion through a skimmer by a weak (1 V/cm) electric field, accelerated to 2 keV, and mass selected by a 60° magnetic sector to produce an H_3^+ beam composed of 200 μs FWHM pulses with a peak current of 20 nA. The collimated H_3^+ beam is overlapped over a distance of 60 cm by a laser beam. The laser photons were generated by Raman shifting a YAG-pumped dye laser output in 30 atm H_2 gas. The laser was operated synchronously at 10 Hz with the pulsed ion beam. Only the second order Stokes lines was selected and interacted with the ion beam using a setup with four Pellin-Broca prisms. The setup practically eliminated the laser beam walk during wavelength scanning. Charged dissociation products produced in this region are selected in energy (mass) by a cylindrical electrostatic energy analyzer and detected by a microchannel plate electron multiplier.

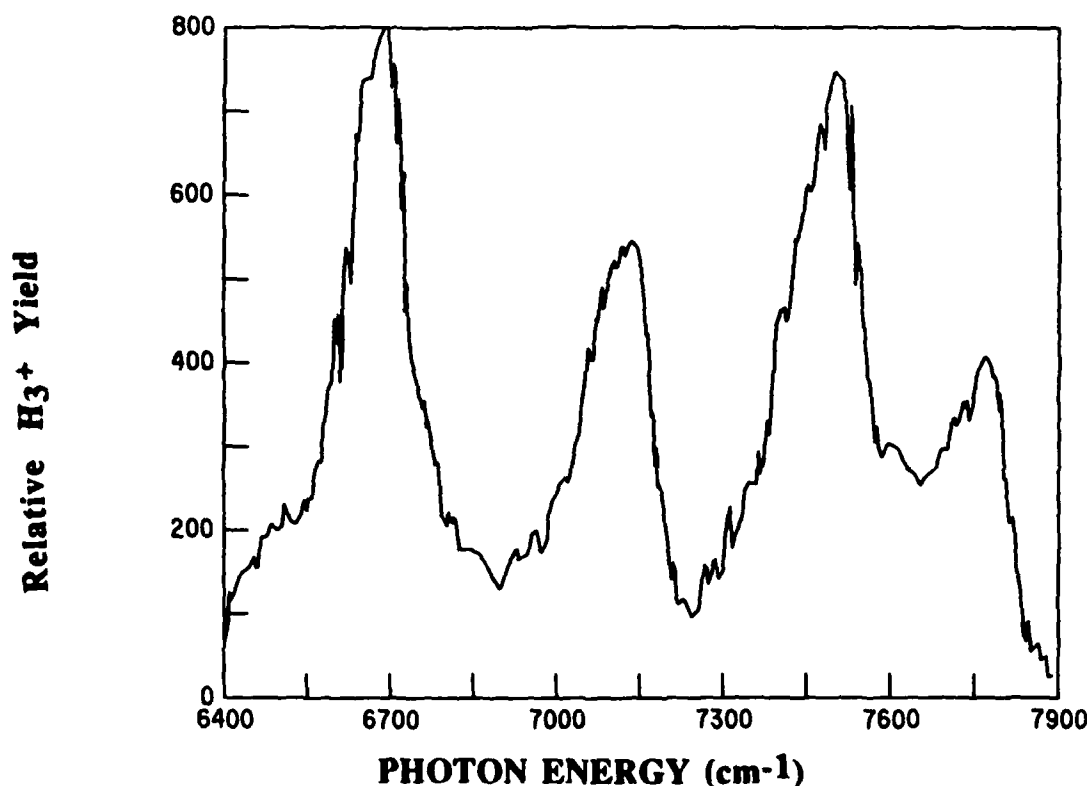
In the measured wavelength region between 5,400 and 10,000 cm^{-1} , only the $\text{H}_3^+ + \text{H}_2$ channel was observable. Four prominent broad bands are observed with energies 6690, 7130, 7490, and 7770 cm^{-1} . The spectrum between 6400 and 7900 cm^{-1} is shown in Figure 2. Rotational structure was not resolved by the 1 cm^{-1} linewidth of the laser. Okumura et al.² reported three vibrational transitions near 4000 cm^{-1} . Their assignments are summarized in the Table 1.

Table 1

Observed Bands (cm^{-1})	Tentative Assignments
3532*	ν_2
3910*	ν_1
4230*	$\nu_1 + \nu_8$ or $3\nu_4$
6690	$\nu_2 + 2\nu_4$
7130	$\nu_1 + 2\nu_4$
7490	$\nu_1 + \nu_2$
7770	$\nu_1 + \nu_2 + \nu_8$

* Measured by Okumura, Yeh, and Lee.⁴

Figure 2



Here ν_1 is the stretch mode of H_2 , ν_2 and ν_4 are symmetric and asymmetric stretch modes of H_3^+ , and ν_8 is the intramolecular stretch between H_3^+ and H_2 in H_5^+ . Based on their assignments we tentatively assign bands at 6690, 7130, and 7510 cm^{-1} to $\nu_2 + 2\nu_4$, $\nu_1 + 2\nu_4$, and $\nu_1 + \nu_4$ respectively. The band at 7770 cm^{-1} could be interpreted as either $\nu_1 + \nu_2 + \nu_8$ or as $\nu_2 + 3\nu_4$. This latter assignment, however, would imply the existence of a $\nu_1 + 3\nu_4$ band near 8100 cm^{-1} as strong as 7770 cm^{-1} band, which is clearly not present in the observed spectra. Thus, we assign the 7770 cm^{-1} to $\nu_1 + \nu_2 + \nu_8$.

2. Development of a new high intensity cluster ion source

An unexpectedly high fusion rate has been discovered by Beuhler et al.¹ when singly charged clusters of ~ 200 D_2O molecules, accelerated to 200 to 325 keV, impinge on a TiD target. The observed fusion rate is more than a factor of 10^{17} larger than that computed using the standard fusion cross sections for an isolated D-D reaction. The observed rate is strongly dependent on the projectile energy: a factor of 100 increase in the fusion rate was observed when the projectile energy increased from 200 to 300 keV. These preliminary results indicate that the fusion scheme that uses cluster impact will be a very simple and efficient path to a very compact fusion rocket engine.

The cluster impact fusion requires very high intensity ion beam of large clusters of deuterium containing materials, such as D_2O and LiD. We have developed a new ion source that can generate extremely high intensity large (size > 1000) clusters almost any type of materials including LiD. The schematic diagram of the source is shown in Figure 3. The principle of the source is based on the combination of two key techniques: (1) pulsed laser evaporation and (2) evaporation in a subsonic inert gas environment to condense large clusters. With the source we have successfully generated large carbon clusters. Carbon vapor was evaporated from a rotating graphite rod by the second harmonic of a YAG laser in room temperature Ar gas. The laser

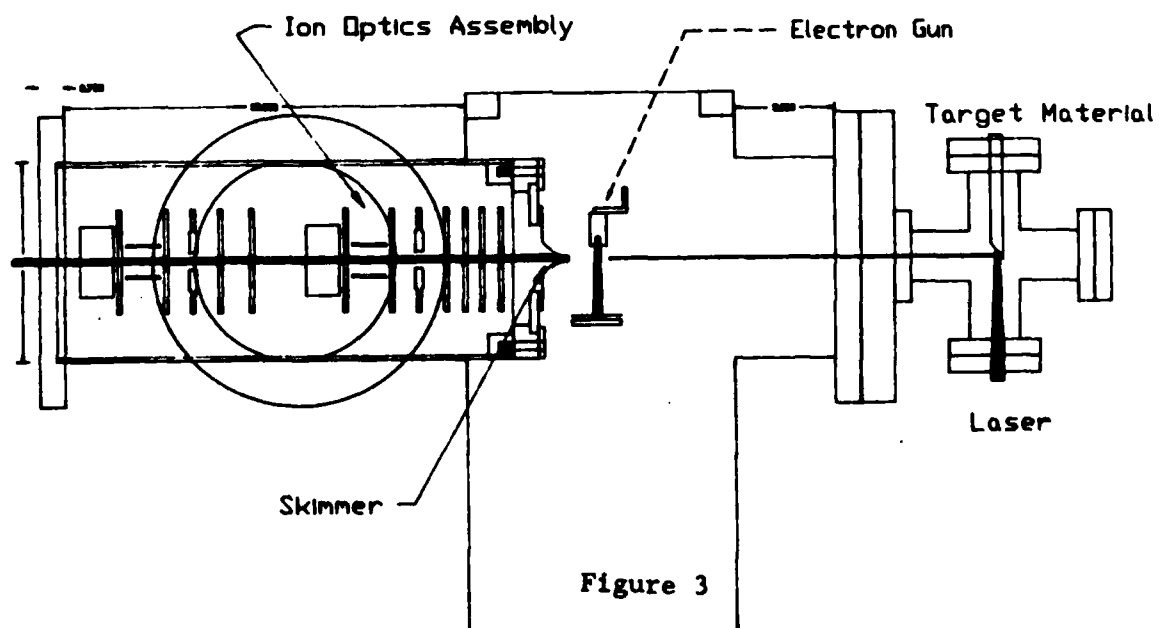
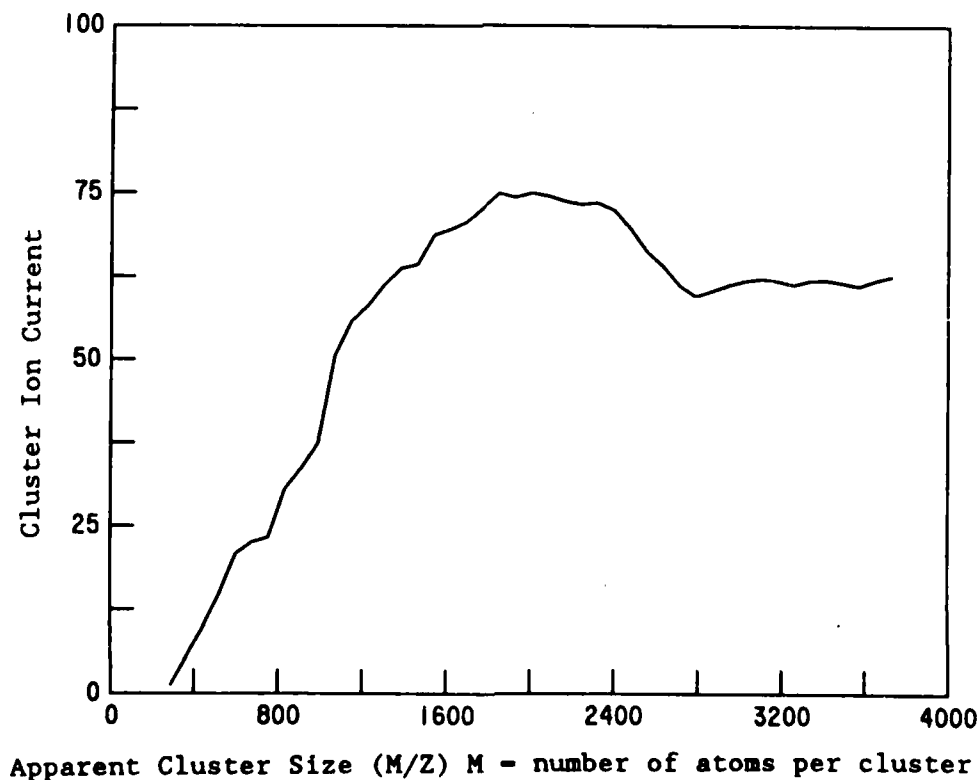


Figure 3

energy on the graphite was kept to be less than 2 J/cm^2 to prevent plasma generation. The Ar pressure was about 10 Torr. The carbon vapor condensed in Ar gas and formed large carbon clusters. The clusters were extracted through a long (30 cm) 2 mm diameter tube, ionized by electron impact, accelerated to 100 eV, mass selected by a 60° magnetic sector, and detected by a large Faraday cup. The resulting current was monitored with a current meter and recorded by a computer. With the given setup, the mass resolution $M/\Delta M$ was only 2. The observed cluster current as a function of apparant mass (number of atoms per unit charge of the clusters) is shown in Figure 4. The relative current 100 in Figure 4 corresponds to $\sim 10^8$ clusters/sec.

We noticed extremely fast carbon deposition on the skimmer which cannot be explained by the observed cluster ion current. In about 20 min the skimmer was completely clogged by the carbon deposit. To measure the actual total mass flux (numbers of atoms per second) of the generated clusters we replaced the skimmer with a blank plate, deposited clusters on a surface located for 20

Figure 4



min, and weighed the deposit. The total mass flux was about 10^{18} atoms/sec and the observed mass flux of the clusters of between 1000 to 4000 atoms/cluster was about 10^{13} atoms/sec assuming an 1 % ionization efficiency. The large difference between the mass flux might result from either the existence of much larger clusters in the beam or a very poor collimation of the cluster ion beam.

References

1. R. J. Beuhler, G. Friedlander, and L. Friedman, Phys. Rev. Lett. 63, 1292 (1989).
2. Y. Yamaguchi, J. F. Gaw, and H. F. Schaefer III, J. Chem. Phys. 78, 4074 (1984).
3. Y. Yamaguchi, J. F. Gaw, R. B. Remington, and H. F. Schaefer III, J. Chem. Phys., 86, 5072 (1987).
4. M. Okumura, L. I. Yeh, and Y. T. Lee, J. Chem. Phys. 88, 79 (1989).

INVESTIGATIONS OF METASTABLE MOLECULES CONTAINING HYDROGEN

H Helm, L J Lembo, D L Huestis, P C Cosby, and M C Bordas
Molecular Physics Laboratory
SRI International
Menlo Park, CA 94025

We report a measurement of the lifetime of metastable H_3 in a fast beam using a novel position-sensitive photoionization technique. A surprisingly short lifetime is observed, almost two orders of magnitude below that predicted previously. We have also studied the influence of external electric fields on the lifetime and energy structure of excited states of H_3 .

Our measurements illustrate that weak higher-order effects can drastically shorten lifetimes. In the search for a suitable candidate metastable fuel this issue can be critical. The exemplary measurements described below forcefully indicate the necessity for investigating the stability of candidate species at the level of higher-order internal and external perturbations, such as configuration mixing due to external electric and magnetic fields, and spin-orbit and hyperfine coupling effects.

LIFETIME MEASUREMENT

In our fast neutral beam apparatus¹ metastable molecules are formed by near resonant electron transfer from cesium vapor to mass selected ions traveling at keV energies. The charge transfer cell is 1-cm long. For a beam of H_3^+ at 1.5 keV this cell length defines the place of creation of the neutral molecule with a precision of about 30 ns. By monitoring the density of metastable molecules as a function of distance from the charge transfer cell, the lifetime of the species can be determined. To accomplish this measurement we photoionize the metastable molecules using a laser that runs coaxial with the neutral beam over a distance of 140 cm. The pulsed laser (pulse duration of 15 ns) provides a clock for the time (t') when an ion was generated by photoionization. This time is recorded by monitoring the arrival time spectrum of ions at a detector at the end of the 140 cm interaction region. Typically one to five molecules are photoexcited per laser shot and their arrival times are monitored using a multistop time-to-digital converter. The age (t) of the molecule after its formation in the charge transfer cell is related to the measured arrival time by the transformation

$$t \rightarrow L/v - t'$$

where L is the distance from the charge transfer cell to the detector and v is the velocity of the neutral beam molecules. A typical measurement of the survival time of metastable H_3 is shown in Figure 1. (In this measurement the non-vibrating metastable $2p$ level was photoexcited to the $40d$ state which in turn was detected by field ionization. Identical decay curves were obtained for direct photoionization of $2p$). The exponential decay can be fitted to a lifetime of about 1 μs . Similar measurements were carried out in other systems to investigate apparatus effects such as the divergence of the laser beam which has a direct influence on the measured decay curve.² For example, $\text{H}(2s)$ formed by charge transfer of protons in Cs showed no measurable decay with distance from the charge transfer cell, consistent with the long natural lifetime of the $\text{H}(2s)$ state.

The observed lifetime of metastable H_3 is about two orders of magnitude shorter than that predicted³ on the basis of the calculated allowed far-infrared transition $2p \rightarrow 2s$. We interpret this as indication that additional decay channels are open for the $2pA_2''$ state of H_3 .

Two candidate decay channels that had not been considered so far are:

- 1) predissociation by spin-orbit and hyperfine coupling of $2pA_2''$ into the ground $2pE'$ state, and

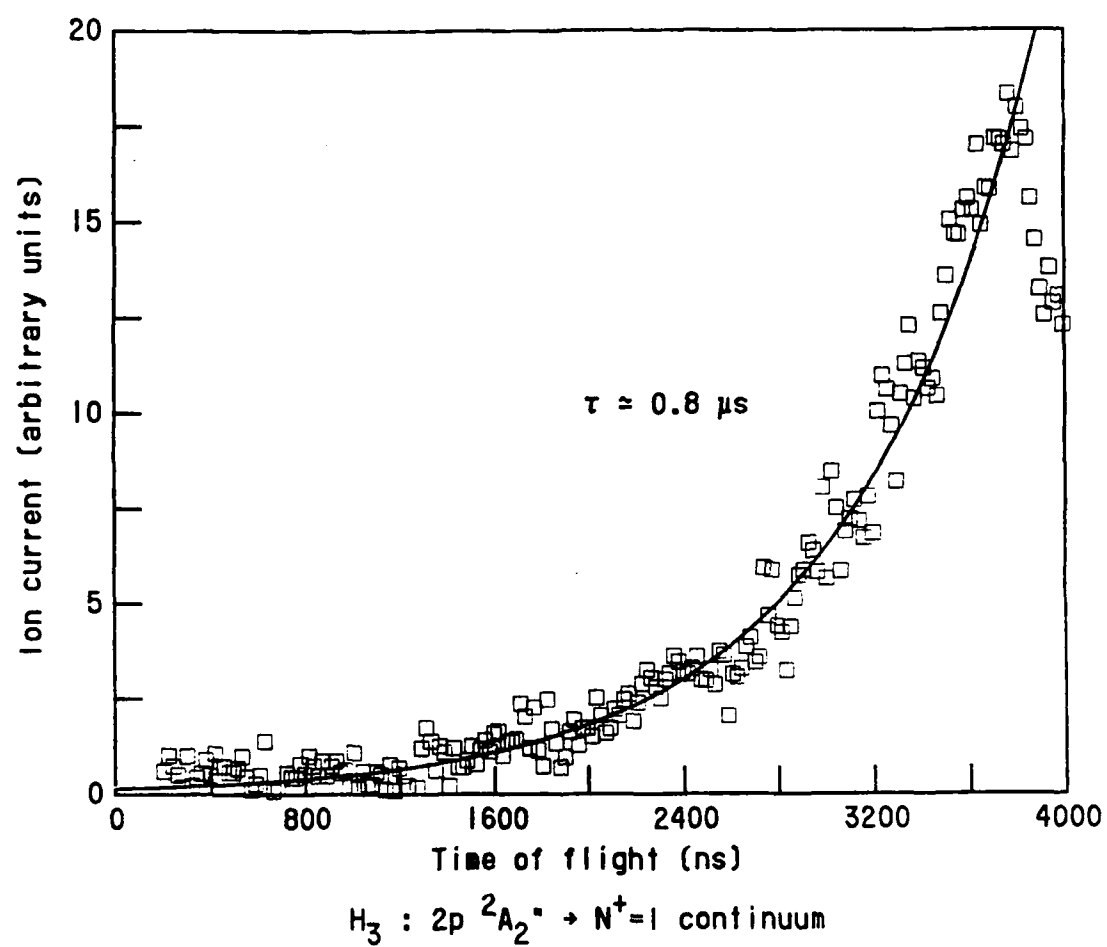


Figure 1

- 2) the weak vibrationally allowed radiative transition from the nonvibrating, nonrotating $2pA_2''$ state into the "bending-mode excited" ground $2pE'$ state.

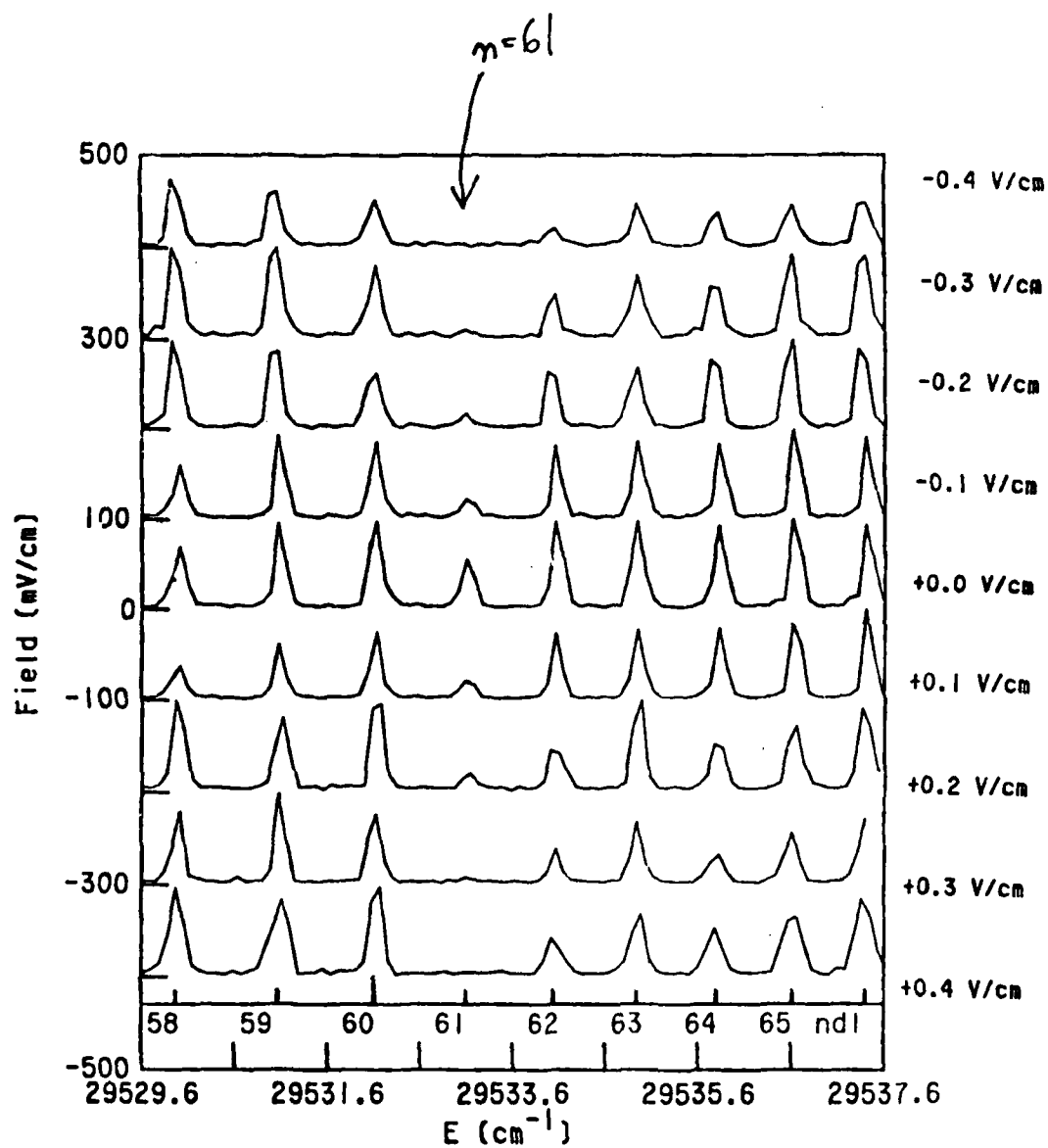
Experimental evidence for the latter has been found in the sense that the transitions from the metastable $2pA_2''$ state to the bending mode excited $3pE'$ levels can readily be driven by a laser.⁴ Experimental evidence for the former comes from our⁵ observation of unimolecular decay of metastable H_3 . In this process product $H+H_2$ fragments are formed with energies up to 5.5 eV. This energy value is consistent with our measured energy of the $2pA_2''$ state, 5.563 eV and therefore a direct indication that a weak predissociation channel is active. We note here that these measurements were carried out in the absence of external electric fields.

EFFECT OF ELECTRIC FIELDS

Using the experimental setup described above we have monitored the stability of metastable H_3 in external electric fields. We observe that at fields up to several kV/cm no significant loss of molecules in the $2pA_2''$ state occurs that can be attributed to the electric field. However, severe reductions in the lifetime occur for higher excited states of this molecule. A most dramatic example is described below: In Figure 2 we show a series of photoexcitation spectra of the nd Rydberg series of H_3 . These spectra are obtained by field ionizing the excited state approximately 1 μ s after the excitation process, that is we require that the excited state survives this time in order to be recorded. Spectra at various values of the external electric field are shown in Figure 2. We note a substantial loss of signal at $n = 61$ as the external field is raised to values as low as 100 mV/cm. In an separate, double-resonance experiment such as described in reference 6, we observed that the external electric field does not diminish the excitation probability to the $n = 61$ state, but rather limits the lifetime of $n = 61$ to values below 1 μ s. We attribute this limitation to electric field induced mixing of the ($n = 61$)d state with the bending mode excited 7p level. This level rapidly predissociates into the ground state, $2pE'$ by homogenous coupling.

Similar observations were made in other spectral regions and a more detailed account of the effects of external fields on the lifetime of triatomic hydrogen is currently being prepared.

Research supported by AFOSR under contract No. F49620-87-K-0002



H₃ nd Rydberg series - Small fields - n=58 to 66

Figure 2

REFERENCES

1. H. Helm, Phys. Rev. Lett. **56** 42 (1986), Phys. Rev. A **38** 3425 (1990).
2. M. C. Bordas, P. C. Cosby and H. Helm, in preparation.
3. G. I. Gellene and R. F. Porter, J. Chem. Phys. **79** 5975 (1983).
4. L. J. Lembo, H. Helm and D. L Huestis, J. Chem. Phys. **90** 5299 (1989).
5. P. C. Cosby and H. Helm, Phys. Rev. Lett. **61** 298 (1988).
6. L. J. Lembo and H. Helm, Chem. Phys. Lett. **163** 425 (1989).

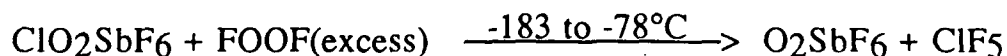
NEW HIGH ENERGY OXIDIZER SYSTEMS FOR PROPELLANT AND ENERGY STORAGE APPLICATIONS

Scott A. Kinkead, Jon B. Nielsen, P. Gary Eller
Los Alamos National Laboratory
MS-C346
Los Alamos, New Mexico 87545

The objective of this program is to provide basic research involving the syntheses, characterization, and application of inorganic compounds potentially useful for advanced rocket propellants and energy storage applications.

During the past year, our efforts have concentrated on the synthesis of inorganic peroxides of Cl, N, and xenon through reactions of FCIO_2 , ClO_2SbF_6 , N_2O , NO_2 , and xenon with FOOF or F· atoms.

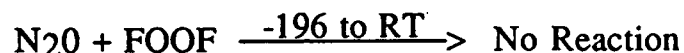
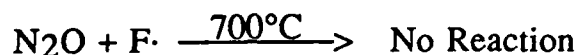
The reaction of FOOF with chlorine oxides typically gave ClF_5 as the major products. When FCIO_2 is reacted with an excess of FOOF, ClF_5 was isolated in quantitative yield with respect to FCIO_2 . Furthermore, when ClO_2SbF_6 is reacted with FOOF in CF_3Cl at -183°C and slowly warmed to -78°C , a simple metathesis reaction occurs.



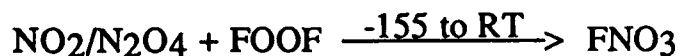
The conversion to the oxygenyl salt is quantitative and verified by Raman spectroscopy. When FCIO_2 and FOOF were reacted in our hot

wire reactor by *in situ* preparation of FOOF, very little reaction took place. Following removal of noncondensable gases, only a small amount of ClF₅ was observed by infrared spectroscopy. The bulk of the material was identified as unreacted FClO₂.

The reactions of nitrogen oxides proved to be more interesting. For example, the reaction of nitrous oxide with F· atoms or FOOF resulted in no reaction.



Whereas the reaction of FOOF with NO₂/N₂O₄ yielded FNO₃.



However, the FNO₃ decomposed over time to give NO₂/N₂O₄ as the final product.



We were not able to isolate or spectroscopically observe FNO₂ as would be expected from the thermal decomposition of FNO₃. However, it is believed that the FNO₂ participated in the passivation

(or repassivation) of the stainless steel vacuum line and traps that were used during the course of the reaction. This reaction requires further investigation since it is not apparent how the FNO_3 is formed. Several different reaction pathways can be rationalized. A low temperature matrix experiment may be useful to elucidate a reaction mechanism.

During further testing of our thermal $\text{F}\cdot$ atom generator we also attempted to prepare ClF_5 by reaction of ClF_3 and $\text{F}\cdot$ atoms at 700°C . After 2 hours of circulating fluorine through the reactor, in which 10.2 mmol of ClF_3 had been condensed, the power was turned off and the reactor allowed to cool. Fractional condensation of the resulting products gave approximately 5 mmol of ClF_5 . With further testing and optimization of conditions this could prove to be an efficient method of preparing ClF_5 .

Finally, in our continuing efforts to study the oxidizing power of FOOF, we have found that the reaction of FOOF with Xe is a highly efficient method of preparing pure XeF_4 . Also, the reaction of XeF_4 with an excess of FOOF does not yield give XeF_6 . Thus it may be concluded that hot fluorine atoms are a stronger oxidizing agent than FOOF.

Reactions of Size Selected Singly and Doubly Charged Transition Metal Ions and Cluster Ions

Michael T. Bowers
Department of Chemistry
University of California
Santa Barbara, CA 93106

A new instrument has been developed that allows for generation and reactivity of both singly and doubly charged metal cluster ions (Figure 1).¹

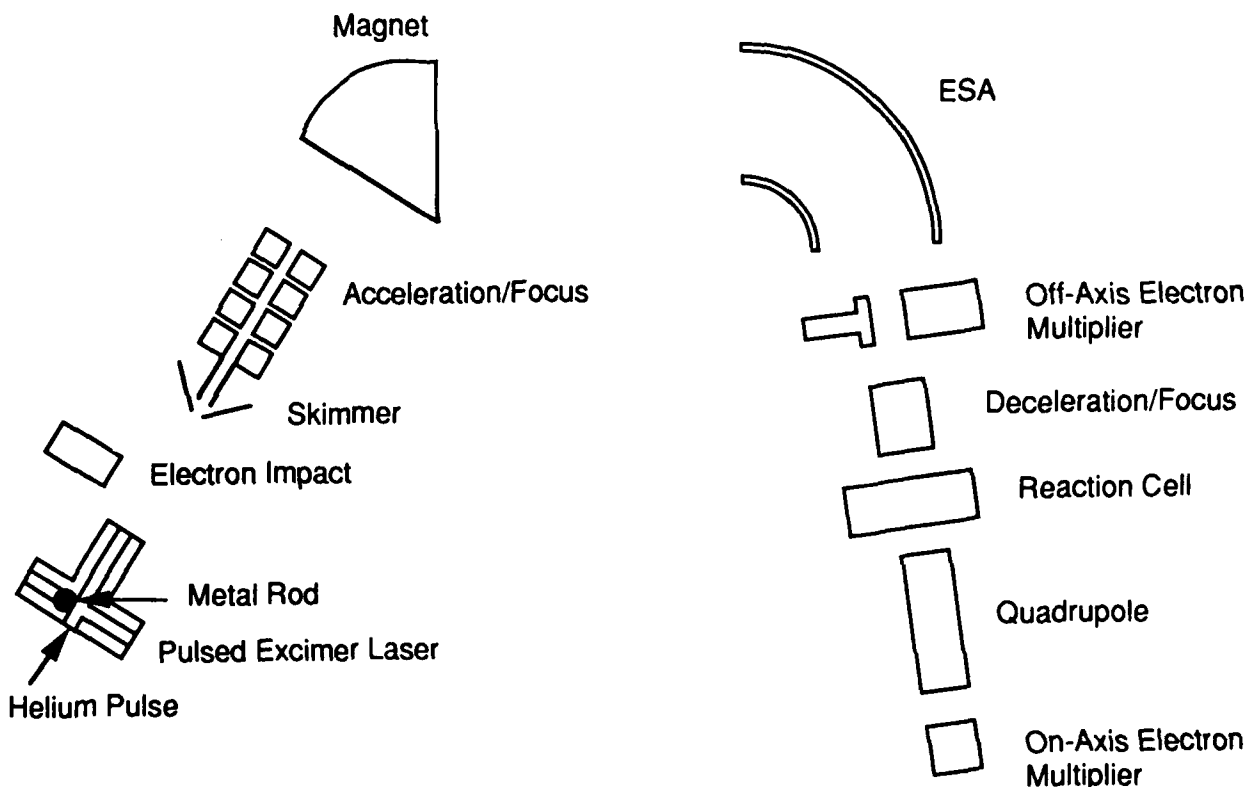


Figure 1

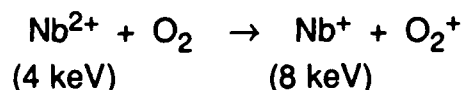
In this instrument ions can be made either by laser ablation coupled to a supersonic expansion² or by electron impact on suitable precursor molecules. After acceleration the ions are size selected and interrogated using a high resolution, reverse geometry mass spectrometer. Several kinds of experiments can be performed depending on the information desired. Three different examples will be given that are of possible interest to the HEDM program.

1. Doubly Charged Ions

A mass spectrum of the low mass niobium cluster ions directly emitted from the laser ablation source are given in Figure 2a. No doubly charged clusters are observed, presumably due to recombination reactions with electrons or chemical

reactions with neutral Nb atoms or clusters as the plasma is swept toward the nozzle by the high pressure helium pulse. However, if the material spraying from the nozzle is subjected to a high energy electron beam, the mass spectrum given in Figure 2b is observed. In this case substantial fractions of doubly charged clusters are observed, presumably from direct double ionization of neutral clusters. Under certain conditions, Nb_3^{2+} can be made 30% as intense as Nb_3^+ ! These are rather startling observations since it had been generally believed³ that doubly charged metallic clusters would be unstable until $n > 20$.

In Figure 2b only the odd doubly charged clusters are noted. The even clusters are almost certainly there, but are hidden under the singly charged cluster of half the mass. To check this, we put O_2 in a collision cell between the magnet and ESA and tuned the magnet to pass $m/z = 93$, corresponding to Nb^+ and/or Nb_2^{2+} . We then scanned the energy near 8 keV, looking for the charge transfer product.



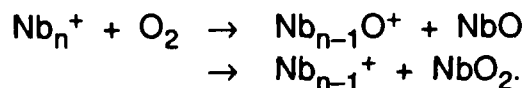
A strong signal was observed at 8 keV indicating a substantial amount of Nb^{2+} in the ion beam.

This technique is general and can be applied to lower mass metals that may lead to very large values of specific impulse for the doubly charged cluster ions.

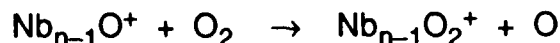
2. Reactions of Size Selected Cluster Ions

In this experiment a specific cluster is mass selected by the magnet and the ESA. The cluster is then slowed down to a few eV, focused and injected into a drift cell with a high pressure of helium bath gas (~ 2 torr). Reaction occurs with a small fraction of neutral reagent ($\sim 1 \times 10^{-4}$ torr).

Initial experiments have been done with O_2 as the reactant gas. The principle reactions observed are



The loss of NbO dominates due to the tremendous strength of the NbO bond (~ 8 eV). Of importance is the fact sequential reactions occur



and it is virtually certain that O atoms would be rapidly consumed in the reaction



which is very exoergic. All reactions occur at efficiencies greater than 30% at thermal

energies.²

While the reaction of the dimer is 5.04 eV exoergic, the substantial mass of Nb makes the specific impulse of this system too low to be competitive. Nonetheless, this method offers an opportunity for studying smaller systems (Be_n^+ , B_n^+ and possibly their doubly charged counterparts) which may well be competitive with reactions of H_2 with O_2 .

3. Electronic State Chromatography

When measuring rate constants using the drift cell filled with He buffer gas, it is necessary to measure the ion drift time through the cell. This is accomplished by pulsing the entrance plate to admit a narrow burst of ions ($\sim 1 \mu\text{sec}$) and then measuring the time it takes the ions to reach the detector. A typical result for atomic cobalt ion is given in Figure 3. The obvious bimodal distribution was at first very puzzling. Other first row transition metal ions also gave structured arrival time distributions and it soon became apparent the structure was due to dramatically different mobilities for the $3d_n$ and $3d_{n-1}4s$ electronic configurations!!⁴ This astonishing result allows us to interrogate the electronic structure of M^+ formed from a variety of sources. The variations are often very large. In the case of Ni^+ , for example, it is possible to make 90% excited state and it appears Zn^+ can be made 100% in metastable excited state with energies in excess of 2.5 eV. It is apparent this technique will have far reaching applications in the very active field of gas phase organometallic chemistry.

From an HEDM perspective this technique offers promise. For example, we have shown using translational spectroscopy⁵ that C^+ ions can be made in reasonable abundance in the $^4\text{P}_g$ metastable state. This state is very long lived and contains 5.3 eV of energy above the ground state. Preliminary experiments indicate we will be able to resolve the $^4\text{P}_g$ metastable state from the $^2\text{P}_u$ ground state using our "chromatography" method. Reactions of this highly energetic species with O_2 , NH_3 , H_2O and other light species are expected to be rapid⁶ and have specific impulse rivaling O_2 and H_2 . Details of the reaction pathways must first be sorted out, however.

1. P.R. Kemper and M.T. Bowers, *J. Am. Soc. Mass Spectrom.* **3**, xxxx (1990).
2. P. Radi, G. von Helden, P.R. Kemper, M-T. Hsu and M.T. Bowers, *J. Chem. Phys.* (to be submitted).
3. K. Sattler, J. Mühlbach, O. Echt, P. Pfau and E. Recknagel, *Phys. Rev. Lett.* **47**, 160 (1981).
4. P.R. Kemper and M.T. Bowers, *J. Am. Chem. Soc.* (in press).
5. M. Rincon, N. Kirchner and M.T. Bowers, *Int. J. Mass Spectrom. Ion Proc.* **86**, 369 (1988).
5. The ground state of carbon ion, $\text{C}^+(^2\text{P}_u)$, reacts at the collision limit with O_2 , NH_3 and H_2O . For a compilation see Y. Ikezoe, S. Matsuoka, M. Takebe and A. Viggiano, Maruzen Co. Ltd. (distributor), Tokyo (1987).

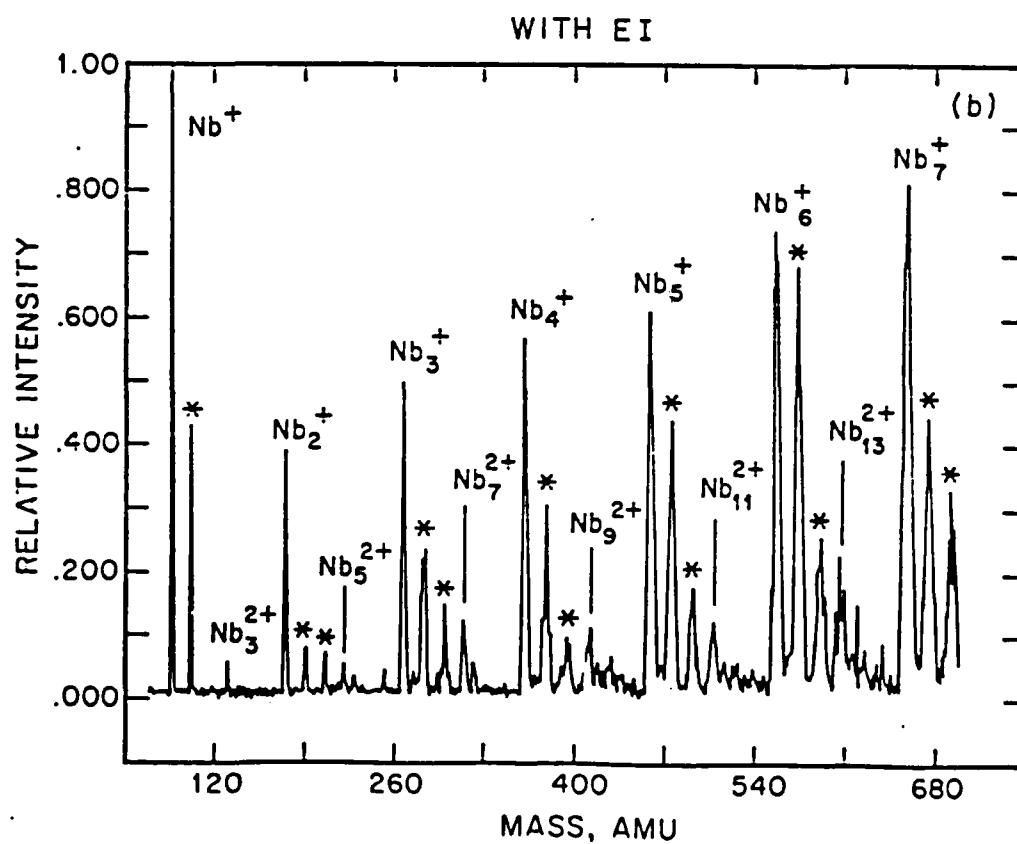
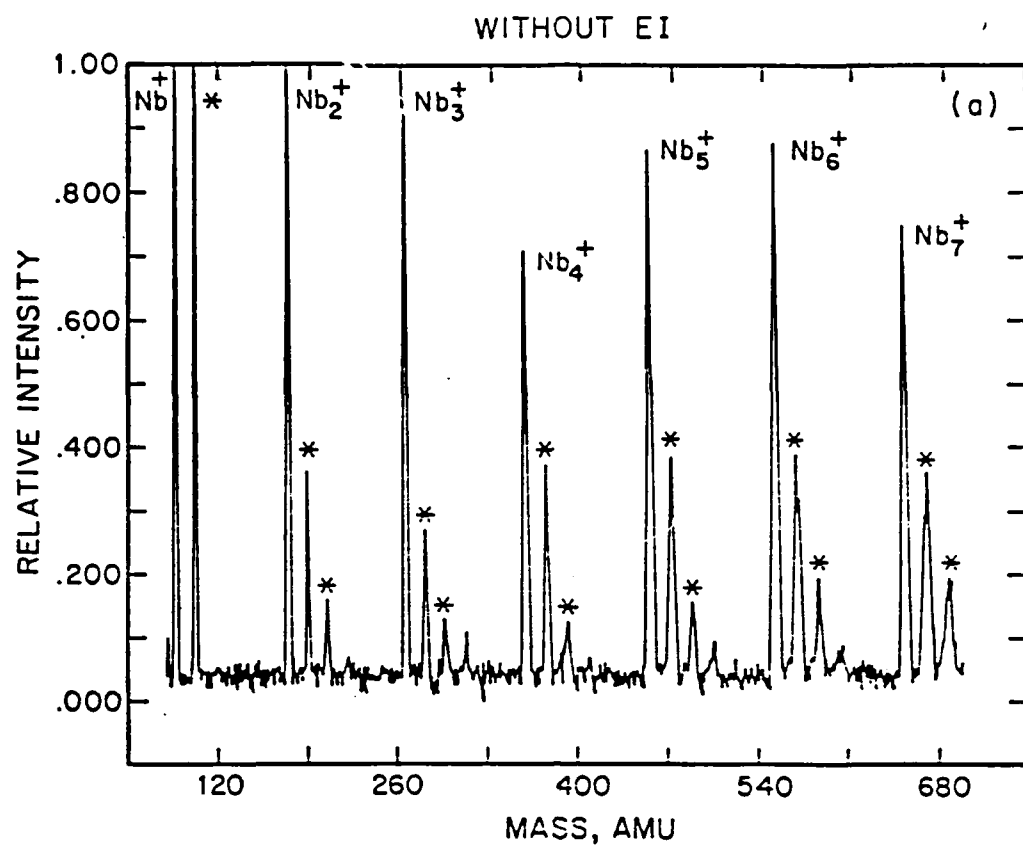


Figure 2

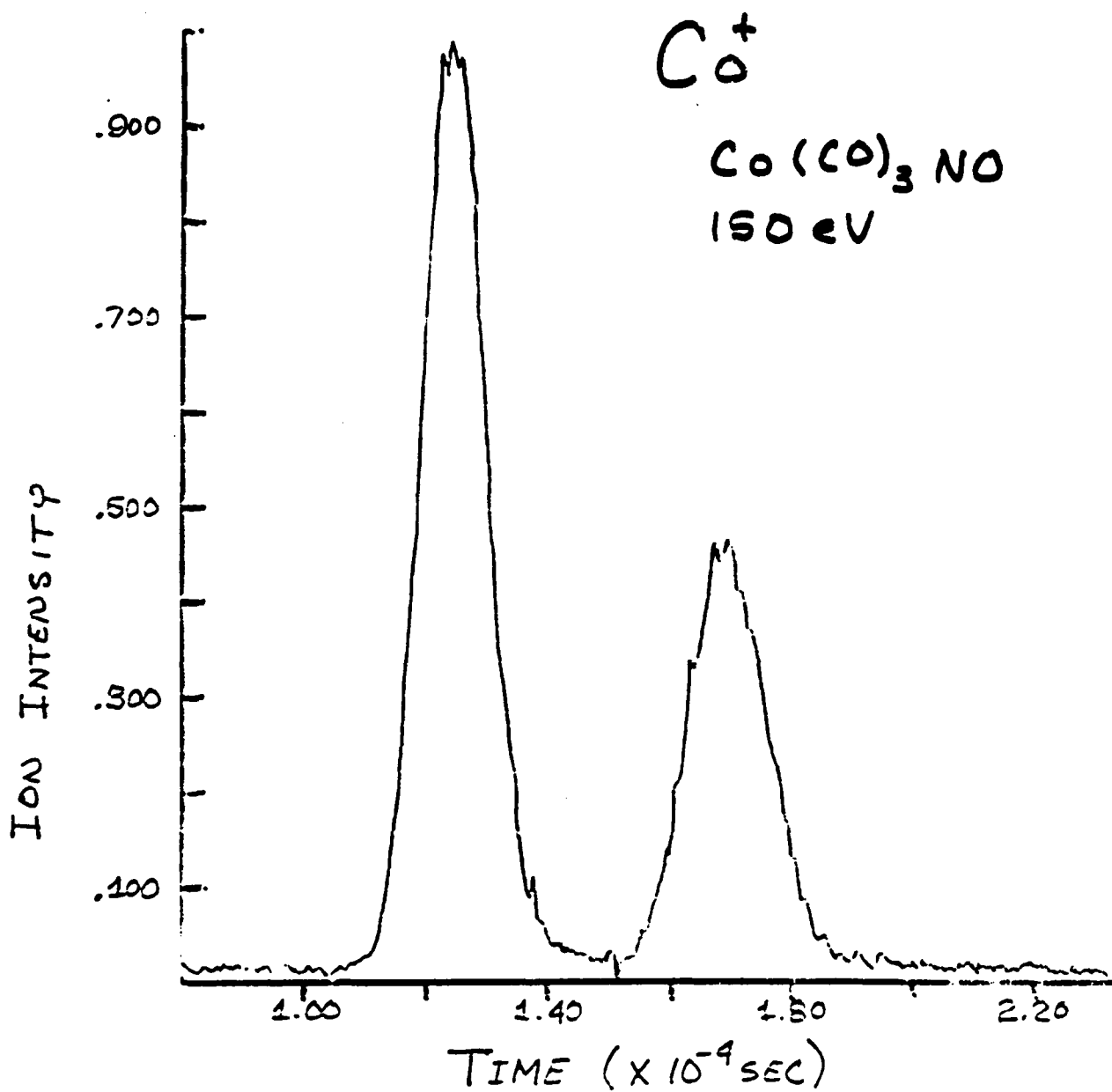


Figure 3

PRODUCTION OF NCl(a) BY THERMAL DECOMPOSITION OF ClN_3

M. A. Chowdhury, B. K. Winker, T. A. Seder and D. J. Benard

Rockwell International Science Center

1049 Camino Dos Rios

Thousand Oaks CA 91360

Telephone: (805) 373 4468

EXTENDED ABSTRACT

Generation of electronically excited species by chemical reactions is of interest because of potential applications in short wavelength chemical lasers. Recently large concentrations of metastable NF(a) radicals have been generated by thermal dissociation of FN_3 using approximately 1 J/cm^2 CO_2 laser pulses in the presence of SF_6 .¹ The efficient dissociation of FN_3 has been attributed to a low energy barrier arising from the extremely weak FN-N_2 bond and to a spin-constraint which allows only singlet dissociation products from the ground state FN_3 . Since these considerations also apply to ClN_3 its decomposition is expected to yield NCl(a) efficiently. Coproduction of NCl(a) along with NF(a) may then be used to pump lasers such as NF(b) or IF(B) by resonant energy pooling reactions. NCl(a) is also interesting because it resembles $\text{O}_2(\text{a})$ closely in stored energy and electronic symmetry.² Thus NCl(a) may be able to replace $\text{O}_2(\text{a})$ in the chemical oxygen iodine laser (COIL).³ Such replacement may be advantageous under certain circumstances. Therefore dissociation of ClN_3 has been investigated under similar conditions suitable to FN_3 dissociation.

The ClN_3 was generated by the reaction of a flowing dilute mixture of Cl_2 in Ar with moist NaN_3 contained in an ice-chilled tube.⁴ Mass spectrometry as well as FTIR and uv spectroscopy were used to identify the ClN_3 , to establish that it did not contain any significant amount of undesirable impurities and to determine its concentration in the effluent of the ClN_3 generator. The ClN_3 was mixed with SF_6 in a flowtube and was instantaneously heated to a high temperature using approximately 1 J/cm^2 CO_2 laser pulses. The products of pyrolysis were observed in emission using an optical multichannel

analyzer and the time profiles of the various species were obtained using a calibrated Si PIN photodiode with appropriate filters.

The products of thermal decomposition of ClN_3 were found to be NCl(a) and NCl(b) . Time-resolved uv absorption of ClN_3 showed that the rate coefficient of ClN_3 dissociation is approximately half of that for FN_3 implying a higher dissociation energy barrier for ClN_3 . This result is expected because of lower electronegativity of the Cl-atom and the consequently stronger ClN-N_2 bond. The NCl(a) and NCl(b) yields were determined from their emission intensities using the radiative lifetimes,⁴⁻⁷ the calculated photon collection efficiency and the gain of the calibrated detector/filter combination at the respective wavelengths.

The NCl(b) yield per ClN_3 molecule was found to be 0.5% based on the 630 μs radiative lifetime reported in the literature.⁴ The radiative lifetimes of NCl(a) that are reported in the literature⁵⁻⁷ vary widely from 2.1 ms to 3.7 s. We used a value of 1.4 s which is supported by theoretical calculations of Yarkony⁷ and also by the reported trend in the a state lifetimes and the b/a lifetime ratios in the NX (X = halogen atom) series.⁴⁻⁸ Thus the NCl(a) yield was determined to be approximately 100%.

We have also investigated energy transfer reactions of NCl(a) . Three-fold enhancement of $\text{NF(b} \rightarrow \text{X)}$ emission intensity was observed upon addition of equimolar amount of ClN_3 to FN_3 in the pyrolysis reactor indicating that NCl(a) can upconvert NF(a) to NF(b) . The upconversion efficiency was found to be greatly enhanced, however, by a small amount of added I_2 . This result was anticipated since I^* efficiently pumps⁹ NF(a) to NF(b) and since, in terms of stored energy and electronic symmetry, NCl(a) closely matches² $\text{O}_2(\text{a})$ which is capable of efficiently generating¹⁰ I^* from I_2 . This result also demonstrates that NCl(a) is capable of mimicing $\text{O}_2(\text{a})$ in the chemical oxygen-iodine laser.

Strong $\text{IF(B} \rightarrow \text{X)}$ emissions were observed at 583 nm upon addition of CF_3I to a mixture of NF(a) and NCl(a) . Addition of I_2 then decreased the $\text{IF(B} \rightarrow \text{X)}$ emission intensity. Since I_2 increases the NF(b) concentrations this result indicates that pumping of IF(B) by NF(b) which is inefficient,¹¹ can be ruled out. The $\text{IF(B} \rightarrow \text{X)}$ emission intensity

was observed to scale linearly with CF_3I pressure. Since in our experiments the F-atom concentrations were much lower than the CF_3I concentrations this result indicates that the $\text{IF}(\text{X})$ was derived from thermal dissociation of CF_3I rather than the $\text{CF}_3\text{I} + \text{F-atom}$ reaction. Thermal dissociation of CF_3I at the ambient temperatures of our experiments is likely to be inefficient in generating the $\text{IF}(\text{X})$. Therefore the strong emission from $\text{IF}(\text{B})$ points towards efficient pumping by $\text{NF}(\text{a})$ and $\text{NCl}(\text{a})$. On the basis of the above we suggest a resonant-ladder-climbing mechanism as shown in Figure 1 for the $\text{IF}(\text{B})$ production.

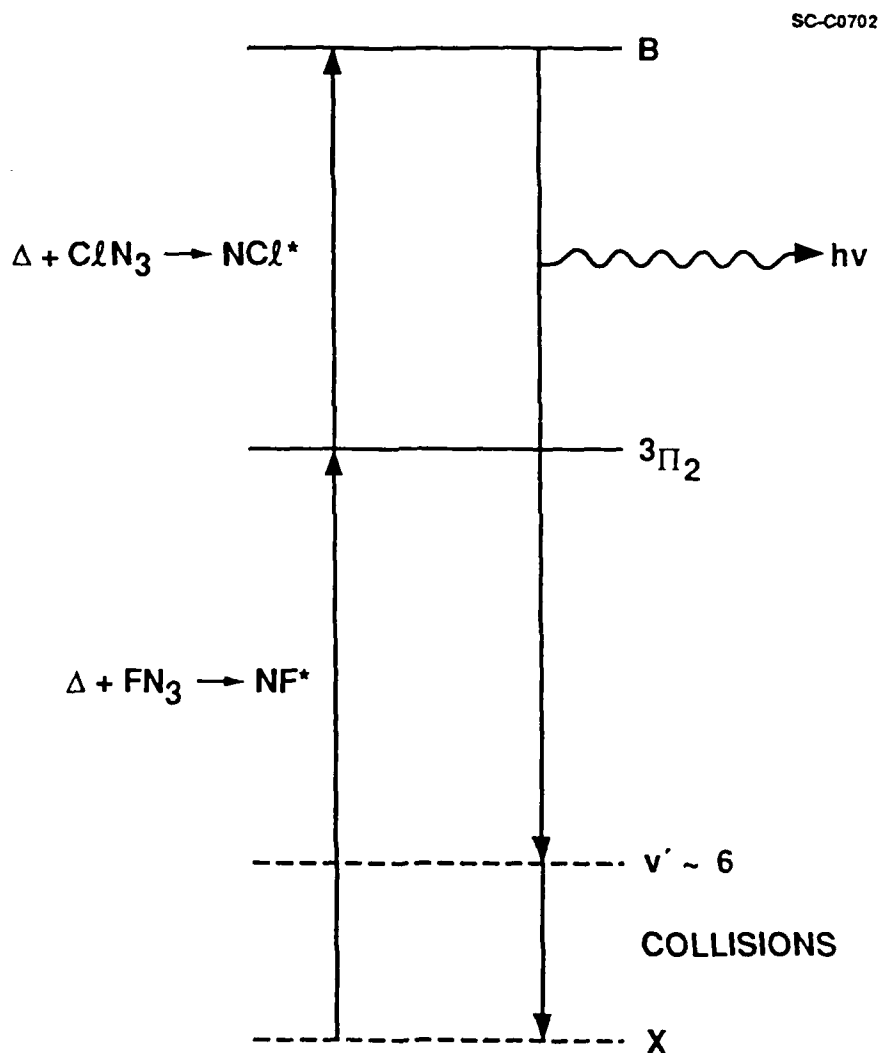


Figure 1. Energy level diagram of IF showing resonances with $\text{NF}(\text{a})$ and $\text{NCl}(\text{a})$

In conclusion, the yield of NCl(a) from thermal decomposition of ClN_3 has been found to be near unity. NCl(a) has been found to transfer energy to NF and IF efficiently. These results indicate a potential for development of chemical lasers operated on the $\text{NF(b} \rightarrow \text{X)}$ transition at 529 nm and the $\text{IF(B} \rightarrow \text{X)}$ transitions at 580-625 nm using the large NCl(a) and NF(a) concentrations that can be obtained from thermal dissociation of ClN_3 and FN_3 , respectively.

REFERENCES

1. D. J. Benard, B. K. Winker, T. A. Seder and R. H. Cohn, *J. Phys. Chem.*, **93** 4790 (1989)
2. A. T. Pritt, D. Patel and R. D. Coombe, *J. Mol. Spectroscopy*, **87** 401 (1981)
3. W. E. McDermott, N. R. Pchelkin, D. J. Benard and R. R. Bousek, *Appl. Phys. Lett.*, **32** 469 (1978)
4. R. D. Coombe, D. Patel, A. T. Pritt Jr. and F. J. Wodarczyk, *J. Chem. Phys.*, **75** 2177 (1981)
5. R. D. Coombe and M. H. Van Benthem, *J. Chem. Phys.*, **81** 2985 (1984)
6. A. C. Becker and U. Schurath, *Chem. Phys. Lett.*, **160** 586 (1989)
7. D. R. Yarkony, *J. Chem. Phys.*, **86** 1642 (1987)
8. R. J. Malins and D. W. Setser, *J. Phys. Chem.*, **85** 1342 (1981)
9. J. M. Herbelin, M. A. Kwok and D. J. Spencer, *J. Appl. Phys.*, **49** 3750 (1978)
10. R. G. Derwent and B. A. Thrush, *Farad. Disc. Chem. Soc.*, **53** 162 (1972)
11. D. J. Benard, M. A. Chowdhury and A. T. Pritt, *J. Appl. Phys.*, **60** 4051 (1986)

BERYLLIUM AND BORON-BERYLLIUM HYDRIDES: HIGH ENERGY FUELS FOR THE FUTURE

Donald F. Gaines,* Joseph R. Wermer, and Dovas A. Saulys, Dept. of Chemistry, University of Wisconsin-Madison, Madison, WI 53706

Abstract

Beryllium hydrides and their lithium salts are good candidates for both fusion and combustion fuel components, but their formation in polymeric intractable forms has largely precluded synthesis of adequately high purity and high density materials for target applications. We will describe our investigations of new and modified routes to beryllium hydrides and their lithium salts that will ultimately produce materials suitable for fuel applications.

Boron-beryllium hydrides are potentially valuable combustion fuel components. They combine the high hydrogen binding potential of beryllium with the covalent small molecule characteristics of the boron hydrides to produce high hydrogen content molecular materials whose physical properties are similar to those of hydrocarbons, but whose potential combustion energy densities are considerably higher. Representative synthetic routes and physical properties of selected boron-beryllium hydrides will be illustrated.

Introduction

A search for the ultimate in high energy density fuels leads naturally to consideration of the hydrides of lithium, beryllium, and boron. A significant portion of our research is focused on the syntheses of such compounds, and on investigations of their chemical properties.

Prior research has produced a single binary hydride of beryllium, BeH_2 , which is a polymeric, largely amorphous, and essentially intractable solid material. Until recently the only route to BeH_2 was via thermally induced β -Hydride transfer from an organoberyllium precursor. A crystalline phase of BeH_2 has been observed when amorphous BeH_2 is subjected to very high pressure. Several of our recent investigations of

new routes to BeH_2 , and its precursors and derivatives are described below.

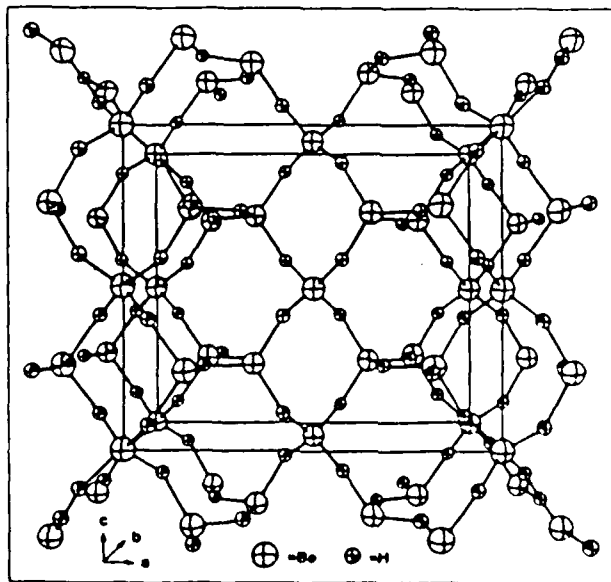
Synthetic investigations of boron hydrides and mixed boron-beryllium hydrides have been an integral part of our research program for a number of years. The primary thrust of the research has been to discover new classes of boron and beryllium-boron hydride molecules and to elucidate their chemical properties and applications. Several of the new classes of compounds that we have prepared have high hydrogen content, light weight non-hydrogen elements, and low thermodynamic stability.

Beryllium Hydrides

We have recently begun synthetic chemical and mechanistic studies of beryllium hydrides and lithium beryllium hydrides. Beryllium hydrides have not been successfully prepared from the elements, but rather by β -hydride transfer from organoberyllium compounds.¹⁻³ The most commonly used organoberyllium precursor is bis-*t*-butyl-beryllium etherate.

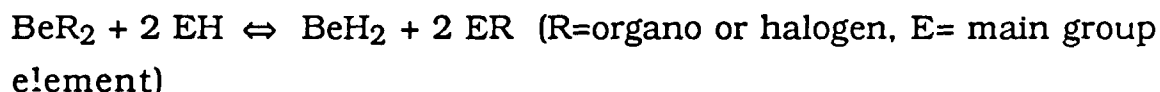


While this method is suitable for moderate purity BeH_2 , the preparation of high purity BeH_2 is complicated by significant physical and chemical problems. As typically prepared, BeH_2 is amorphous and polymeric⁴, but recent high pressure compaction of BeH_2 has produced a crystalline form whose structure is shown below.⁵



One major problem in the currently available β -hydride transfer route to BeH_2 is the formation temperature of ca 200° , which is only ca 40° below its decomposition temperature. We are exploring the syntheses of new organoberyllium reagents that should undergo the β -hydride transfer reactions at lower temperatures and thereby produce higher purity BeH_2 . An integral part of these investigations is the production of other molecular and crystalline forms of beryllium hydrides via modifications of the synthetic precursors and the β -hydride transfer process. We are also searching for synthetic routes to cluster type Be_nH_y molecules, none of which have been shown to exist.

We have recently initiated an investigation of beryllium hydride syntheses using hydrogen exchange between main group hydrides and suitable beryllium precursors via the general reaction:



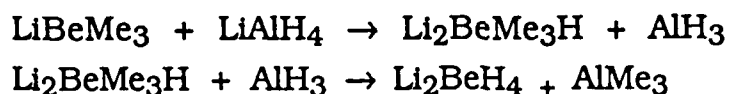
The major constraints of these investigations are as follows.

1. The availability of high purity reagents.
2. The exchange temperature, which must be substantially below 250°C .
3. EH and ER must both be volatile or soluble in inert solvents.
4. The equilibrium must be large enough so that the reaction can be driven to completion.
5. It is desirable to be able to use high and low pressures in the syntheses in order to influence potential crystallinity of the BeH_2 products.

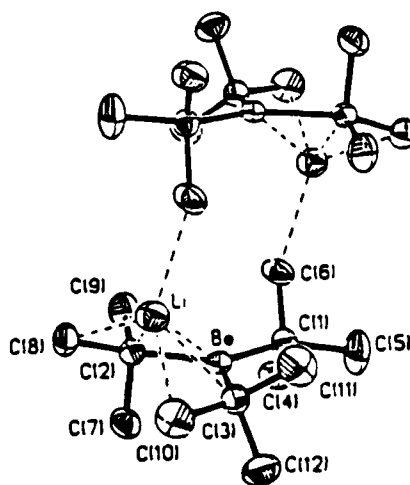
Preliminary survey experiments have utilized silane, SiH_4 as the EH source and $(\text{BeMe}_2)_n$ and $[\text{Be}(\text{i-Pr})_2]$ as the RBe sources have shown that hydrogen/alkyl exchange occurs under mild conditions to produce the expected MeSiH_3 and i-PrSiH_3 , respectively. These experiments will be extended to other Group IV hydrides, to Group III hydrides (Boron hydrides), and possibly to heavier group V hydrides.

1. Coates, C.E.; Glockling, F. *J. Chem. Soc.*, **1954**, 2526.
2. Baker, R. W.; Brendel, G. J.; Lowrance, B. R.; Mangham, J. R.; Marlett, E. M.; Shepherd, L. H., Jr. *J. Organomet. Chem.*, **1978**, 159, 123.
3. Baker, R. W.; Baker, W. C.; Brendel, G. J. *Technical Report AFML-TR-68-335*, **1968**.
4. Brendel, G.J.; Marlett, E. M.; Niebyski, L. M. *Inorg. Chem.*, **1978**, 17, 3589.
5. Smith, G. S., Johnson, Q. C., Smith, D. K., Cox, D. E., Zalkin, A. *Solid State Comm.*, **1988**, 67, 491-494.

A study of beryllium hydrides leads naturally to queries regarding hydridoberyllate anions. While lithium hydridoberyllates such as LiBeH_3 and Li_2BeH_4 have been prepared, their syntheses are not straight forward. The compounds are not fully characterized as they appear to be intensely insoluble though crystalline solid state materials. The detailed mechanism by which Li_2BeH_4 is formed is not clear, but a possible representation is shown below.¹



In the course of our preliminary investigations of improved syntheses of precursor organoberyllium compounds we have prepared the first uncomplexed tricoordinate organoberyllium compound, lithium tri-*tert*-butylberyllate, $\text{Li}[\text{Be}(\text{t-C}_4\text{H}_9)_3]$,² a potential precursor to LiBeH_3 .



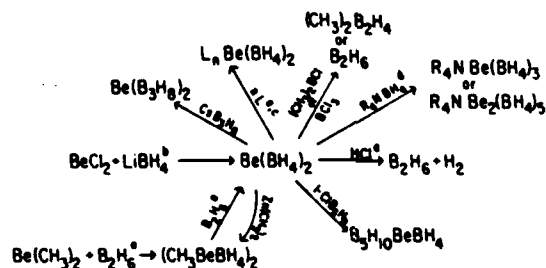
All previously reported alkylberyllate salts contain complexed Lewis bases.

We are exploring improved synthetic routes to lithium beryllium hydrides, including extensions of the $\text{Li}_n\text{BeH}_{2+n}$ ($n=1,2$, and possibly 3)⁷ formulations to larger values of n in hopes of finding larger, more tractable cluster type species.

1. Ashby, E. C., and Prasad, H. S. *Inorg. Chem.*, **1975**, *14*, 2869-74.
2. Wermer, J. R.; Gaines, D. F.; Harris, H. A. *Organometallics*, **1988**, *7*, 2421-2422.

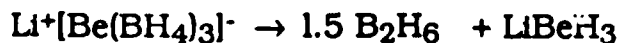
Beryllium-Boron Hydrides

Our initial investigation in this area was an nmr study of beryllium borohydride, $\text{Be}(\text{BH}_4)_2$,^{1,2} the only beryllium-boron compound known at the time. Crystalline beryllium borohydride, $\text{Be}(\text{BH}_4)_2$,³ is a very interesting material in that it is polymeric in the solid phase, monomeric in the gas phase,⁴ and appears to liquify only at elevated temperatures under pressure. Our gas phase nmr studies indicated that monomeric $\text{Be}(\text{BH}_4)_2$ undoubtedly has a linear B-Be-B framework and that rapid intramolecular exchange occurs within each borohydride group.^{1,2} A summary of most of the known chemistry of $\text{Be}(\text{BH}_4)_2$ is shown below.



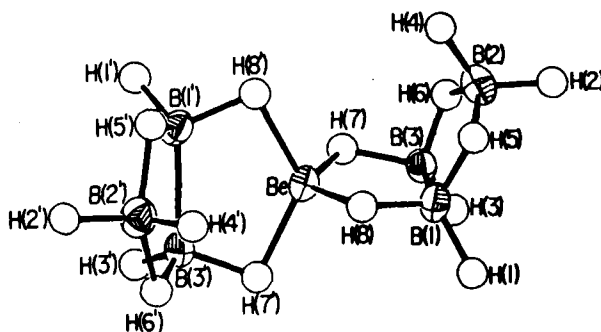
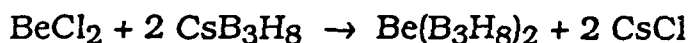
Summary of the reaction chemistry of $\text{Be}(\text{BH}_4)_2$.

We are interested in beryllium polyborohydride compounds, of general form $[\text{Be}_n(\text{BH}_4)_{2n+1}]^{-1}$. With suitable counterions they may function as solid state sources of diborane and other boranes. With lithium as the counterion these materials may also function as sources of lithium beryllium hydrides.

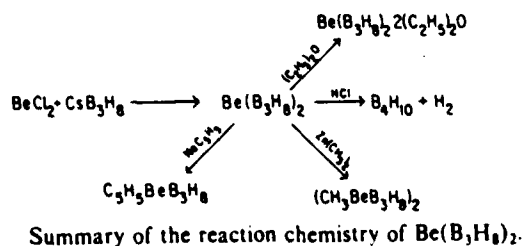


The $[\text{Be}_n(\text{BH}_4)_{2n+1}]^{-1}$ anions may be important energy storage materials themselves, and they may act as delivery systems for BH_4^- , BH_3 , BeH_2 and other hydride moieties for the synthesis of other, larger, hydride clusters. The special properties of beryllium in hydride clusters are not yet well understood, but our studies have shown that beryllium can exhibit bonding interactions with 4, 5, and 6 neighboring atoms, and it acts as a *como-* atom (i.e. functions as a vertex in two cluster fragments simultaneously) in $\text{Be}(\text{B}_3\text{H}_8)_2$ ^{6,7} and $\text{Be}(\text{B}_5\text{H}_{10})_2$ ^{8,9}. In these compounds the Be atom has four Be-H-B bridge hydrogens, while boron atoms almost never have more than two B-H-B bridge hydrogens, and rarely (if ever) act as single *como-* atoms in the way that beryllium does in the above examples. The presence of beryllium in known boron hydride clusters favors a high ratio of hydrogen to cluster atoms and a larger ratio of bridge to terminal hydrogens than in many boron hydrides.

The synthesis of beryllium bis(octahydrotriborate), $\text{Be}(\text{B}_3\text{H}_8)_2$, marked the beginning of our investigations into several areas of beryllium-boron hydride synthesis.

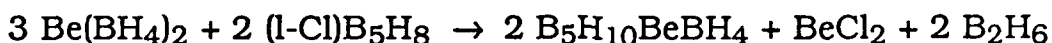


The $\text{Be}(\text{B}_3\text{H}_8)_2$ exhibits more conventional physical properties than $\text{Be}(\text{BH}_4)_2$. Its known reaction chemistry is outlined below.

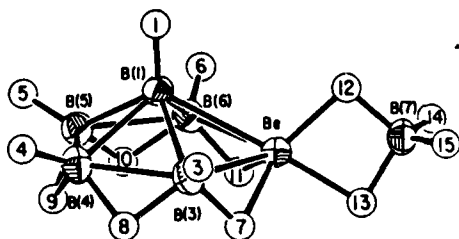


The known chemistry of $\text{Be}(\text{B}_3\text{H}_8)_2$ indicates lability of one B_3H_8 unit under appropriate conditions, this lability is moderated in the Lewis base adducts at low temperatures. Reactions of Lewis base adducts at low temperatures with other reagents will most likely follow differing pathways, dependent on the base.

One of the most interesting reactions of $\text{Be}(\text{BH}_4)_2$ is with $\text{l-ClB}_5\text{H}_8$:

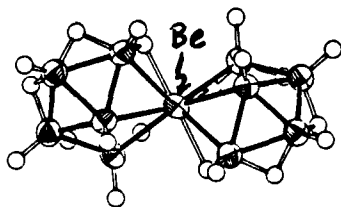


The $\text{B}_5\text{H}_{10}\text{BeBH}_4$ product is the only known beryllium-boron hydride in which the beryllium is in an asymmetric environment.



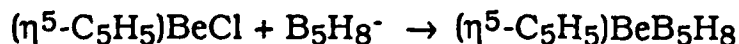
$\text{B}_5\text{H}_{10}\text{BeBH}_4$

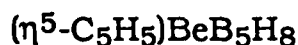
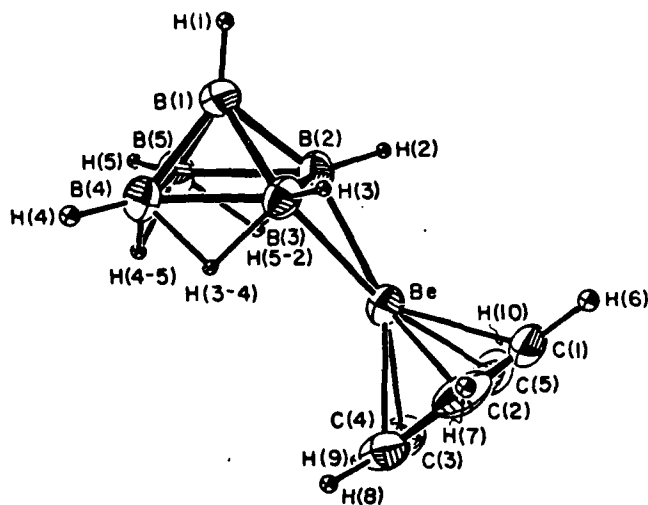
We think that this is an indication that beryllium is a unique heteroatom in boron hydride based cluster systems, giving rise to unusual chemical and physical properties. Its related 2,2'-*commo*-bis[2-berylla-*nido*-hexaborane(11)], $\text{Be}(\text{B}_5\text{H}_{10})_2$ exhibits most unusual geometry about the *commo*-beryllium atom.



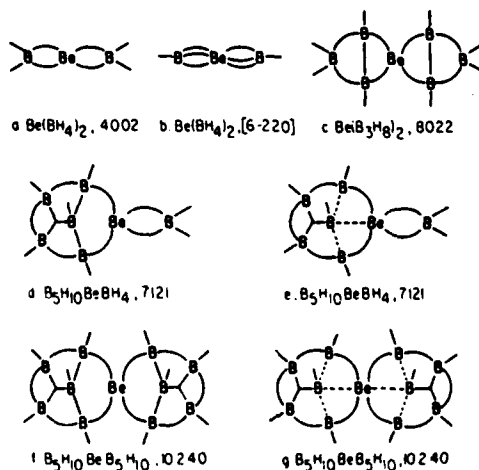
$\text{Be}(\text{B}_5\text{H}_{10})_2$

In addition we were able to partially insert organoberyllium moieties as shown below.¹⁰





Selected bonding schemes for several of the beryllaboranes are shown below. the curved lines in the sketches correspond to three-center two-electron bridge hydrogen bonds between the atoms indicated. The dotted lines indicate undefined bonding interactions that distribute 4 bonding electrons over three boron atoms and one beryllium atom.



Some examples of *styx* type structures for beryllaboranes.

References

1. Gaines, D.F.; Walsh, J.L.; Hillenbrand, D.F. *J.C.S., Chem. Commun.*, **1977**, 224-225.
2. Gaines, D.F.; Walsh, J.L.; Morris, J.; Hillenbrand, D. *Inorg. Chem.* **1978**, 17, 1516-1521.

3. Schlesinger, H. I.; Brown, H. C.; Hyde, E. K. *J. Am. Chem. Soc.* **1953**, 75, 209.
4. Marynick, D. S.; Lipscomb, W. N. *Inorg. Chem.* **1972**, 11, 820.
5. Cook, T. H.; Morgan, G. L. *J. Am. Chem. Soc.* **1969**, 91, 774.
6. Gaines, D.F.; Morris, J.H. *J.C.S., Chem. Commun.*, **1975**, 626-627.
7. Calabrese, J.C.; Gaines, D.F.; Hildebrandt, S.J.; Morris, J.H. *J. Am. Chem. Soc.* **1976**, 98, 5489-5492.
8. Gaines, D.F.; Walsh, J.L.; Calabrese, J.C. *Inorg. Chem.* **1978**, 17, 1242-1248.
9. Gaines, D.F.; Walsh, J.L. *Inorg. Chem.* **1978**, 17, 1238-1241.
10. Gaines, D.F.; Coleson, K.M.; Calabrese, J.C. *Inorg. Chem.* **1981**, 20, 2185-2188.
11. Popp, G.; Hawthorne, M. F. *Inorg. Chem.* **1971**, 10, 391

H₂/O₂ Three-Body Rates at High Temperatures

William J. Marinelli, William J. Kessler, Lawrence G. Piper, and W. Terry Rawlins

Physical Sciences Inc.
20 New England Business Center
Andover, MA 01810

Abstract

The extraction of thrust from air breathing hypersonic propulsion systems is critically dependent on the degree to which chemical equilibrium is reached in the combustion process. At hypersonic velocities the residence time for combustion within the engine is severely shortened and static pressures are reduced. These factors result in the failure of many slow reactions to come to completion, thus limiting the amount of energy extracted from the combustion process. In the combustion of H₂/Air mixtures, slow three-body chemical reactions involving H-atoms, O-atoms, and the OH radical play an important role in energy extraction.¹ The reactions:



have been identified as the most critical for the extraction of thrust from these systems. However, these three-body reaction rates are poorly determined over the range of temperatures and third bodies important for hypersonic combustion.

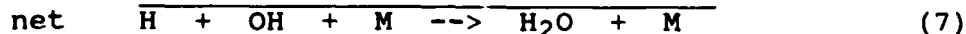
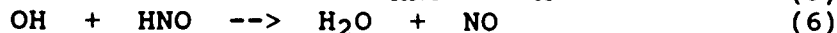
We have designed and constructed a first-generation high temperature and pressure flash-photolysis/laser-induced fluorescence (FP/LIF) reactor to measure these important three-body rates. The reactor operates at temperatures up to 1500 K and pressures up to 5 atmospheres. The system employs a high power excimer laser to produce these radicals via the photolysis of stable precursors. A novel two-photon LIF technique is employed to detect H-atoms without optical thickness or O₂ absorption problems. In this technique the H-atoms absorb two photons at 205.14 nm to produce the excited (n=3) ²D and ²P states. Fluorescence on the allowed n=3 to n=2 transitions at 656.2 nm is observed with a filtered photomultiplier. The delay between the photolysis and probe laser pulses is varied to obtain the H-atom

concentration decay rate. This apparatus is shown schematically in Figure 1.

We have used the apparatus to perform preliminary measurements on the $\text{H} + \text{O}_2 + \text{N}_2 \rightarrow \text{HO}_2 + \text{N}_2$ reaction at temperatures from 300 K to 835 K. In these experiments photolysis of H_2S at 193 nm was used to produce H-atoms in a bath gas of N_2 and O_2 . The decay of H-atom fluorescence was monitored as a function of O_2 concentration, under pseudo first-order conditions, to obtain the reaction rate coefficient. Our value of the rate coefficient, $(3.4 \pm 0.4) \times 10^{-33} \exp((733 \pm 56)/T)$, compares favorably with previous measurements of the rate coefficient^{2,3} measured for atmospheric chemistry applications but is somewhat higher than those used for combustion modeling⁴⁻⁷. These results are summarized in Figure 2. We will present calculations showing the impact this higher rate coefficient has on combustion efficiency under non-equilibrium conditions.

The reaction of H-atoms with O_2 also has a two-body channel which forms OH and O-atoms. The $\text{H} + \text{O}_2$ reaction is important because the branching of this reaction along these two channels determines whether chain propagation (two-body) or chain termination (three-body with subsequent reaction of HO_2 with OH) is dominant at any point in the combustion system. The two and three body reactions have drastically different temperature dependencies and the importance of each of the reactions is a strong function of temperature in the 1200 K - 1500 K range. This effect is further complicated by the varying third-body efficiencies of the fuel, air, and reaction products present in the combustor. In the future we hope to use a similar apparatus to refine these initial measurements and extend them to include the third-bodies H_2O , Ar, and H_2 at temperatures up to 1500 K. The reactor would also be used to measure the rate coefficient for another critical reaction, $\text{H} + \text{OH} + \text{M} \rightarrow \text{H}_2\text{O} + \text{M}$ ($\text{M} = \text{H}_2\text{O}$, N_2 , H_2 , and Ar).

We also hope to investigate ignition and catalytic recombination phenomena through measurements of the $\text{HO}_2 + \text{H}_2$ reaction (ignition) and the $\text{H} + \text{NO} + \text{M}$ reaction (NO catalysis) using similar methods. The efficiency with which the catalytic cycle



can enhance recombination efficiency is critically dependent on the rate of Reaction (5). The rate coefficient for this reaction is poorly determined, even at 300 K, and is known for only rare gas collision partners. We will present model

calculations showing the impact NO catalysis can have on combustion efficiency for a range of NO injections and realistic rate coefficients.

*Sponsored by NASA Lewis Research Center under the Small Business Innovative Research Program.

References

1. Harradine, D., Lyman, J. Oldenborg, R., Schott, G., and Watanabe, H., AIAA Paper No. AIAA-88-2713 (June 1988).
2. Kurylo, M.J., J. Phys. Chem. 76, 3518 (1972).
3. Hsu, K.J., Anderson, S.M., Durant, J.L., Kaufman, F., J. Phys. Chem. 93, 1018 (1989).
4. Baulch, D.L., Drysdale, D.D., Horne, D.G., and Lloyd, A.C., Evaluated Kinetic Data for High Temperature Reactions, Vol. 1 (CRC Press, 1972).
5. Dixon-Lewis, G. Combust. Sci. and Tech. 34, 1 (1983).
6. Slack, M.W., Combustion and Flame 28, 241 (1977).
7. Pirraglia, A.N., Michael, J.V., Sutherland, J.W., and Klemm, R.B., J. Phys. Chem. 93, 282 (1989).

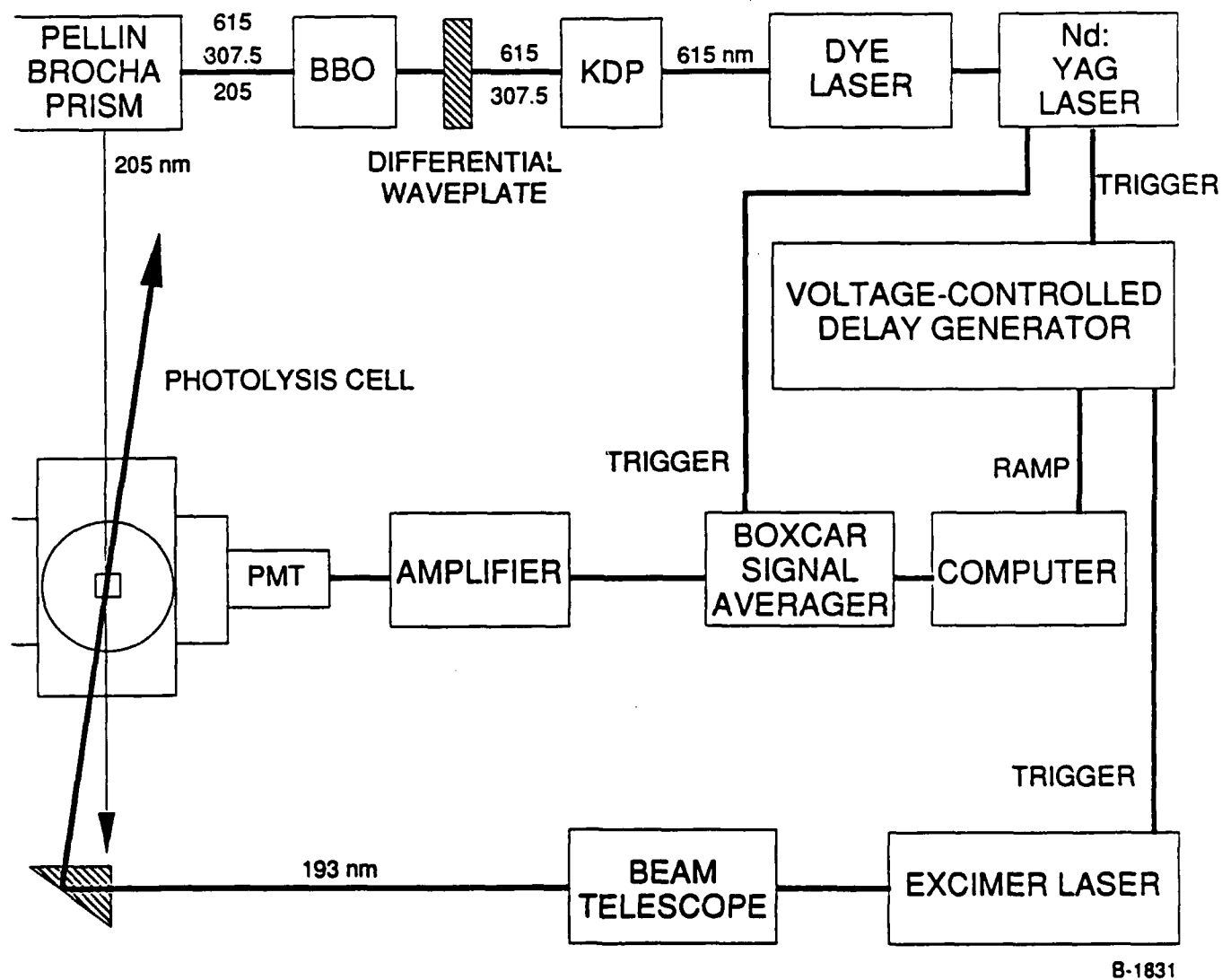
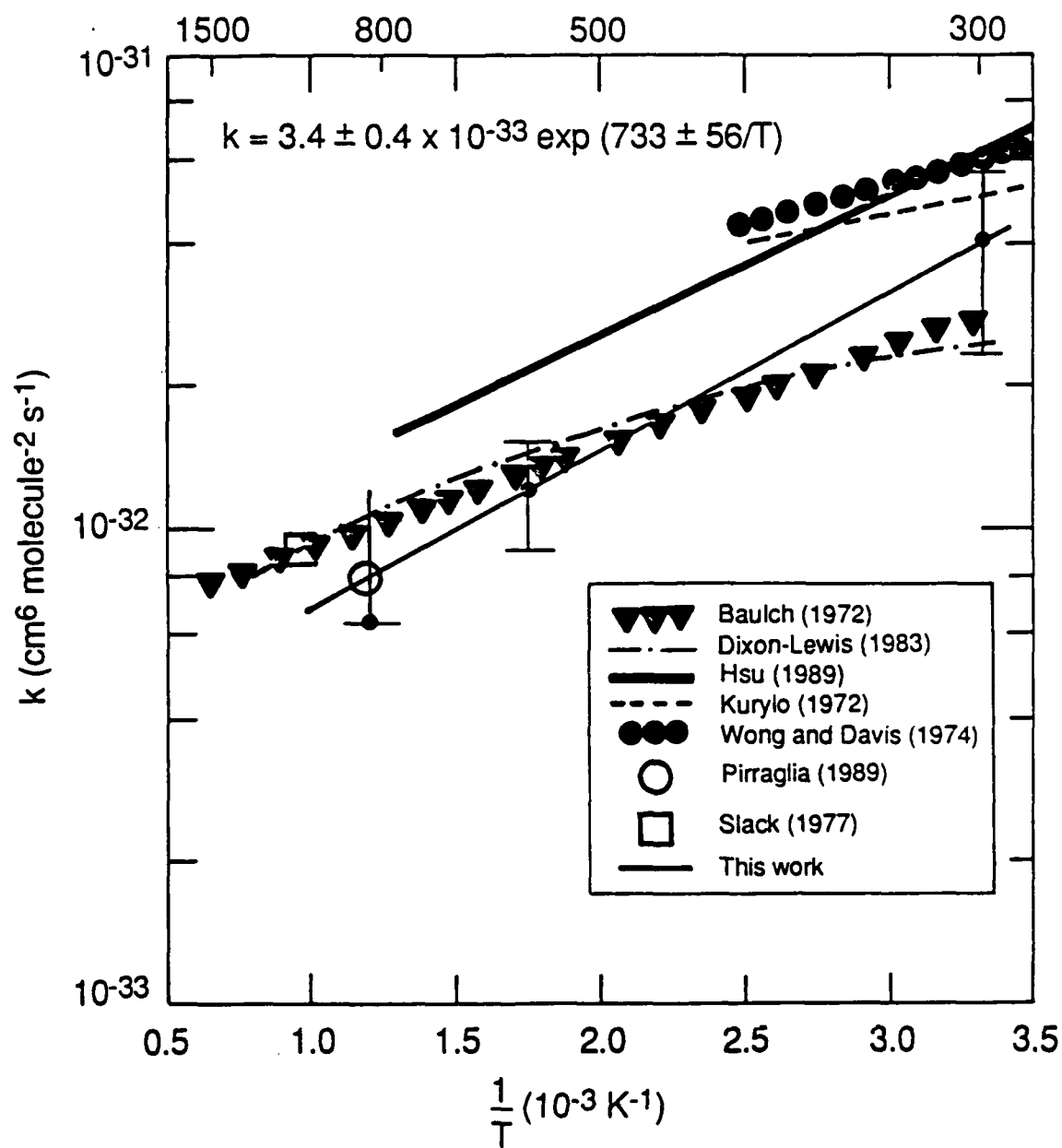


Figure 1. Schematic diagram of experimental apparatus employed in kinetic measurements.



B-1872a

Figure 2. Arrhenius plot of k_2 measured in this program and comparison with other measurements.

Laser and Fourier Transform Spectroscopy of
Novel Propellant Molecules

Grant F04611-87-R-0020

Peter F. Bernath
Department of Chemistry
University of Arizona
Tucson, Arizona 85721

In our continuing study of energetic and metastable molecules, we have recorded electronic spectra of SiC, BC, BH, BD and C₃. These molecules were all observed by Fourier transform emission spectroscopy in the visible or infrared regions of the spectrum.

A. Silicon Carbide, SiC.

SiC is a very elusive molecule. Although C₂ and Si₂ are well-known molecules, SiC escaped detection until our discovery of the infrared electronic transition¹ $d^1\Sigma^+ - b^1\Pi$ near 6100 cm⁻¹. In our experiment, SiC was sputtered from a pressed composite-wall hollow cathode made from a mixture of Cu and SiC powders.

In this work the collaboration of A. D. McLean was critical because without his *ab initio* calculations we could not assign our spectrum. In fact, with our experimental r_0 value for the $b^1\Pi$ state, he was able to calibrate his calculations and predict an r_0 value for the ground $X^3\Pi$ state. This accurate prediction helped in the detection of the microwave spectrum of SiC in space and in the laboratory by Gottlieb, Thaddeus and co-workers². Their microwave data, in turn, have now allowed us to assign another infrared electronic transition,³ $A^3\Sigma^- - X^3\Pi$, near 4600 cm⁻¹.

BC $B^4\Sigma^- - X^4\Sigma^-$

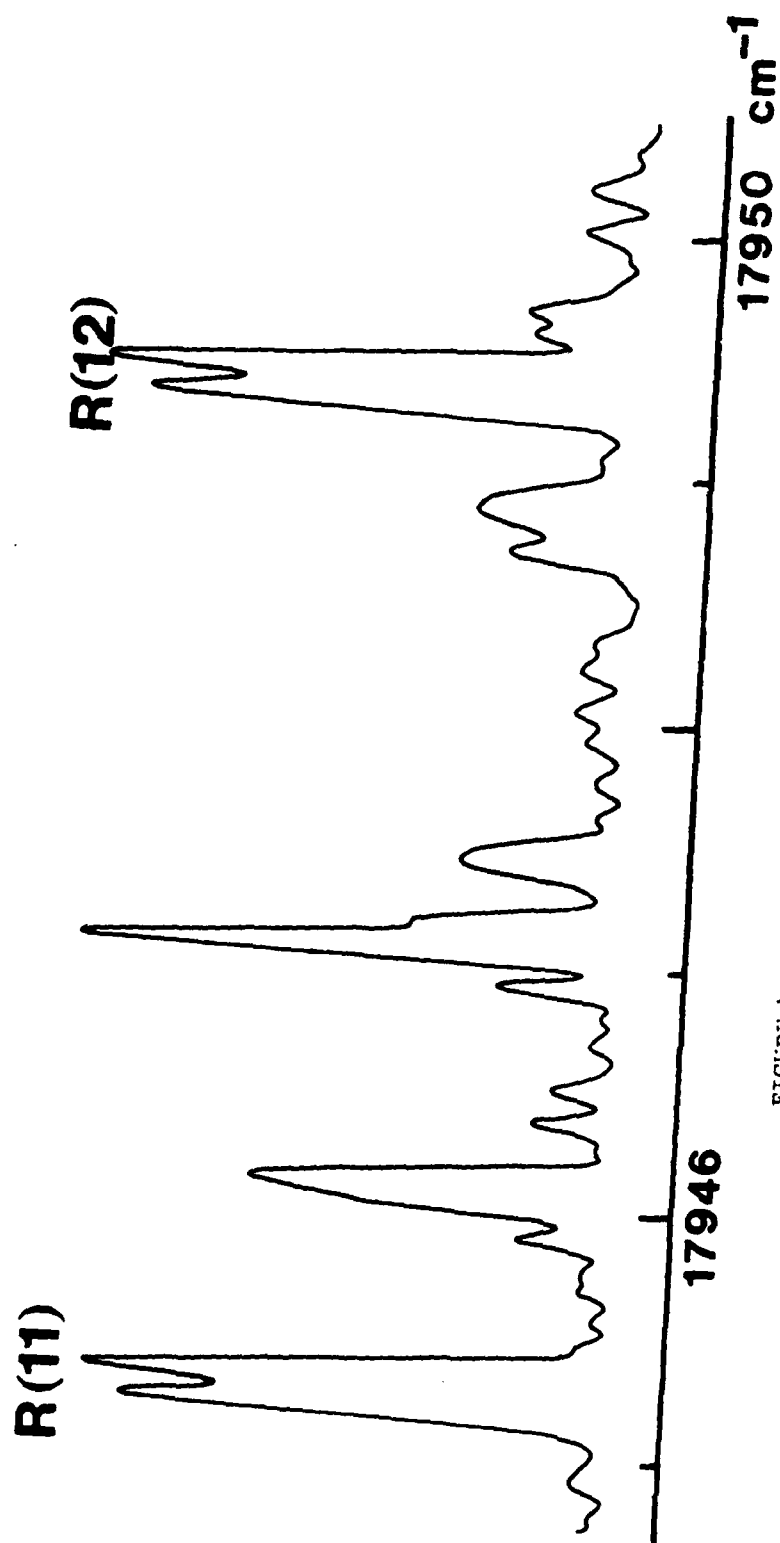


FIGURE 1

B. Boron Carbide, BC

Light elements with very stable oxides such as B and C are excellent propellants so we explored the simple binary BC system. Our production of BC was similar to our work with SiC. A composite-wall (B_4C/Cu) hollow cathode discharge served as a light source for the Kitt Peak Fourier transform spectrometer.

In the initial spectra the $B^4\Sigma^- - X^4\Sigma^-$ transition of BC was very weak and the first lines were not detected. Some evidence of spin-splitting was found in the lines. We recently recorded much improved spectra containing the 0-0, 1-1, 2-2, and 3-3 bands of the B-X transition. These spectra allow an unambiguous rotational assignment and show evidence of the spin-splitting between $^4\Sigma_{3/2}^-$ and $^4\Sigma_1^-$ components (Figure 1). The preliminary molecular constants are provided in Table I.

TABLE I

Spectroscopic Constants for the 0-0 Band of the $B^4\Sigma^- - X^4\Sigma^-$ transition of BC (in cm^{-1}).

Constant	$B^4\Sigma^-$	$X^4\Sigma^-$
T_0	17904.8567(14)	--
B_0	1.369356(51)	1.311849(52)
$D_0 \times 10^5$	7.166(46)	7.492(45)
λ_0	-0.0462(33)	0.0275(32)

C. Boron Hydride and Deuteride, BH and BD

Boron derivatives, particularly borohydrides, are often suggested as advanced propellants. In the course of our work with BC,

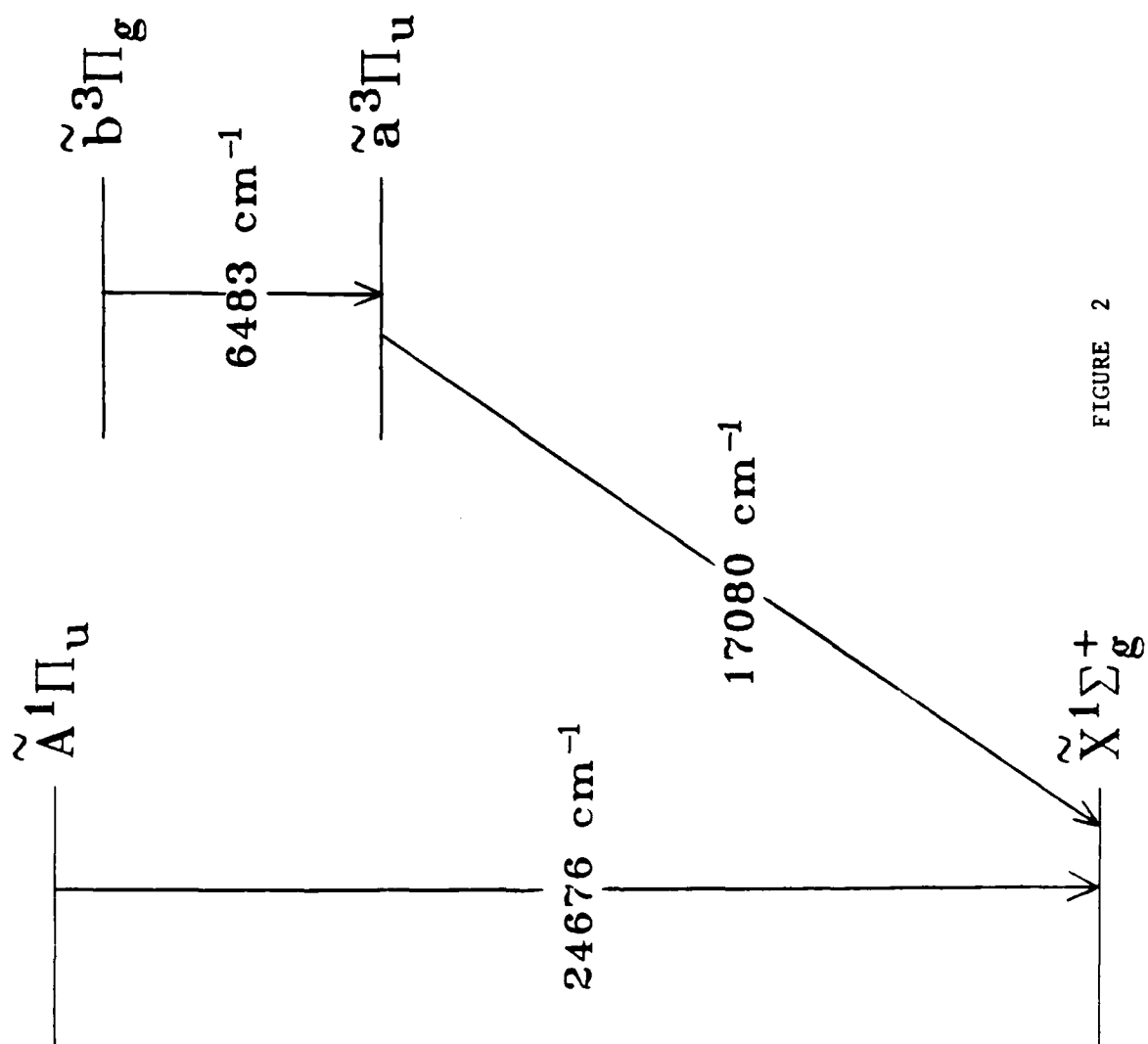


FIGURE 2

we accidentally observed the $A^1\Pi - X^1\Sigma^+$ transition of BH. Addition of a small amount of D_2 then provided the corresponding electronic transition of BD. Our re-analysis resulted in much improved spectroscopic constants for BH and BD.

D. Triplet Tricarbon, C_3

In collaboration with T. Amano and H. Sasada of the National Research Council of Canada, we have discovered the $\tilde{b}^3\Pi_g - \tilde{a}^3\Pi_u$ electronic transition of C_3 (Figure 2). This infrared electronic transition occurs near 6480 cm^{-1} . Although a long-lived, matrix-induced $\tilde{a}^3\Pi_u - \tilde{X}^1\Sigma_g^+$ emission⁴ of C_3 is known near 17000 cm^{-1} , this work is the first gas-phase characterization of triplet states of C_3 . The $\tilde{a}^3\Pi_u$ state of C_3 is a metastable energy reservoir.

Pure carbon molecules such as C_3 , C_5 (and C_{60}) are in vogue as research topics. These molecules may be involved in many astrophysical processes, as well as in soot production in flames. Pure carbon molecules are also attractive as advanced propellants, if they can be stabilized.

References

1. P.F. Bernath, S.A. Rogers, L.C. O'Brien, C.R. Brazier and A.D. McLean, *Phys. Rev. Lett.* **60**, 197 (1988).
2. J. Cernicharo, C.A. Gottlieb, M. Guelin, P. Thaddeus, and J.M. Vrtillek, *Astrophys. J.* **341**, L25 (1989)
3. C.R. Brazier, L.C. O'Brien, and P.F. Bernath, *J. Chem. Phys.* **91**, 7384 (1989).
4. W. Weltner, Jr. and D. McLeod, Jr., *J. Chem. Phys.* **40**, 1305 (1964)

ENERGY TRANSFER PROCESS IN RARE GAS SOLIDS

L. WIEDEMAN, B. WEILLER
AND H. HELVAJIAN

It is commonly true that the potential energy extracted from a charge neutralization reaction exceeds that available from ground state neutral or radical reactions for most systems. With the specific intent of developing new rocket propellants, it can be shown that the parameter to be maximized is the net energy released per unit weight of propellant (I_{sp}). In essence we are searching for high enthalpy exoergic reactions utilizing low molecular weight species. In addition, for the propellant to be useful requires that the reaction potential energy be storable with high densities.

Our criteria for new rocket propellants are to exceed current fuel potentials by at least 10%, and also to be environmentally safe. One convenient approach is to find fuel additives which enhance the I_{sp} of the current propellants. Reactive species do exist which can be added to the LOX (liquid O_2)/ H_2 dual propellant scheme used on the NASA Shuttle Spacecraft. However, calculations show that this approach provides limited I_{sp} enhancement, though it may meet the near term goals of the HEDM Program. To attain the target 10% I_{sp} enhancement will require new conceptual approaches.

Our approach has been to test the feasibility of impregnating a cryogenic solid with separated cation/anion charged pairs. The net energy released from a single charge neutralization reaction can exceed 10 eV/amu, however the storability of charged species may ultimately limit the available energy density. Using the I_{sp} program of Beckman & Acree, we have the calculated I_{sp} increase above that of the LOX/ H_2 system for several systems. The Table 1 lists the results at two trapped ion mole fraction percentages. The systems shown in Table 1 are an attempt to solvate protons in a "working" cryogenic host (solid O_2). Our experimental program involves developing condensed phase reagents (solid O_2 / H_2) which have been suitably impregnated with separated cation/anion pairs. Using this approach the incremental I_{sp} increase over that from LOX/ H_2 system will be due to: a) the % cation/anion mole fraction trapped, and b) the $H + H \rightarrow H_2$ recombination energy (4.5 eV/ H_2), in the case of solvated protons. A critical issue is the ion mole fraction which can be maintained in the condensed phase. Our experiments are designed to test various deposition schemes with the intent to maximize the ion trapped fraction. Initial experiments use the rare gases (Ar in particular) as the host material; after refinement we propose to move on to solid oxygen.

TABLE 1
% I_{sp} INCREASE RELATIVE TO LOX/ H_2 (400 sec)

SYSTEM	2% mole fraction trapped	4% mole fraction trapped
$[(HO_2^+ : HO_2^-) / O_2] : H_2$	3%	7%
$[(OH_3^+ : OH^-) / O_2] : H_2$	2%	4%
$[(OH^+ : OH^-) / O_2] : H_2$	5%	9%
$[(OH^+ : OF^-) / O_2] : H_2$	3%	7%

EXPERIMENTAL

Figure 1 schematically shows our experimental apparatus. A cryogenically cooled finger (APD Cyogenics CS202 compressor) is mounted on a rotatable flange and sits in the center of our high vacuum (HV; 10^{-8} torr) experimental chamber. The cryogenic thin film matrix is grown on a polished copper block (6.25 cm^2) mounted at the end of the cold finger. Our mounting scheme uses a sapphire window with indium gaskets to separate the copper block from the cold finger. With this configuration we maintain good thermal contact and electrically insulate the deposition surface. When desired, this configuration allows a bias voltage to be placed on the copper block during ion deposition. To date we have conducted preliminary experiments designed to test the feasibility of various ion deposition schemes. In all the experiments, the copper target faces the ion source which is in a separate chamber and has its own HV pumping station. An electrically isolated tube allows the ion beam to pass between the two chambers. In our apparatus, the Colutron ion source and ion optics power supplies have been modified to allow extraction of either cation or anion species from the source discharge region. In addition, by using an external timer, we can toggle between extracting either cation or anion species. Using this technique, we have measured mass selected ion currents exceeding several nanoamps at the copper target. We also have a provision for decelerating the ions ($<2 \text{ eV}$) just prior to deposition. The matrix host gas (e.g. Ar or $\text{D}_2\text{O}/\text{Ar}$) is released into the HV chamber either in a CW slow flow or pulsed and in synchronous with the alternating cation/anion beam current. Dual pulsed solenoid valves are used to release, near the cold surface, a precise amount of gas from a calibrated volume. By monitoring the main reservoir pressure, we can accurately measure the gas number density admitted into the chamber. Less accurate is our measure of the fraction which deposits on the cold surface. However, in the future we will employ an optical interference technique for measuring film thickness. Currently an FTIR (Mattson Galaxy 4020, 2 cm^{-1} resolution) is used for spectroscopic identification of trapped species.

RESULTS

We have conducted three preliminary experiments to help us in solving the potential problems. The three experiments are schematically shown in Figure 2. They are 1) an alternating anion/cation charged sandwich using NO_2/Ar in the ion source region with an Ar insulating layer (molecular capacitor), 2) a mass selected cation beam (Ar^+/ArH^+) co-condensed with Ar on to a negatively biased copper target (direct ion deposition), and 3) a high current flux (80 nAmps) Ar^+ cation beam with $\text{D}_2\text{O}/\text{HDO}/\text{Ar}$ neutral codeposition (in situ charge transfer chemistry). In all the above experiments the APD calibrated thermocouple (Tc_1) reading at the cryostat neck measured 16 K, while an uncalibrated thermocouple (Tc_2) at the target read 20 - 26 K. Depending on the experiment, the flow rate of the neutral species was set between 0.1 - 1 mmole/hr with the deposition times normally exceeding three hours. We gained only limited information from experiment (1) since the discharge filament used lasted only 2 hours. In all the experiments conducted, no spectroscopic identification of trapped charged species could be made. We attribute this to a) a target temperature warm enough so that the mobility of trapped radical species is increased, b) inadequate number density of trapped species given the S/N of the FTIR, and c) poor control of the charge deposition dynamics for impregnating at the cryogenic surface accretion layer, or via ion implantation. Though we could not spectroscopically identify trapped charges, we can conclude from some of the experiments that we were indeed trapping charges. In experiment (2) with cation velocities exceeding 50 eV, we could detect periodic (60 sec) bursts of light emanating from growing thin film surface. We attribute this effect to Ar^+/ArH^+ charge buildup and dielectric breakdown in the thin film. Based on our measured ion beam current (1-2 nAmps), the estimated ion beam focal area ($10^{-2} - 10^{-1} \text{ cm}^2$), and the estimated number of neutral surface layers deposited per gas valve opening (10 monolayers/shot), then the predicted maximum ion fraction at the focal zone approaches 1%. A more refined experiment (2) is being prepared.

Additional evidence for trapped charges is experiment (3) in which cation currents (80 nAmps) measured just above the target (1cm) failed to produce a measurable cation/anion current at the copper

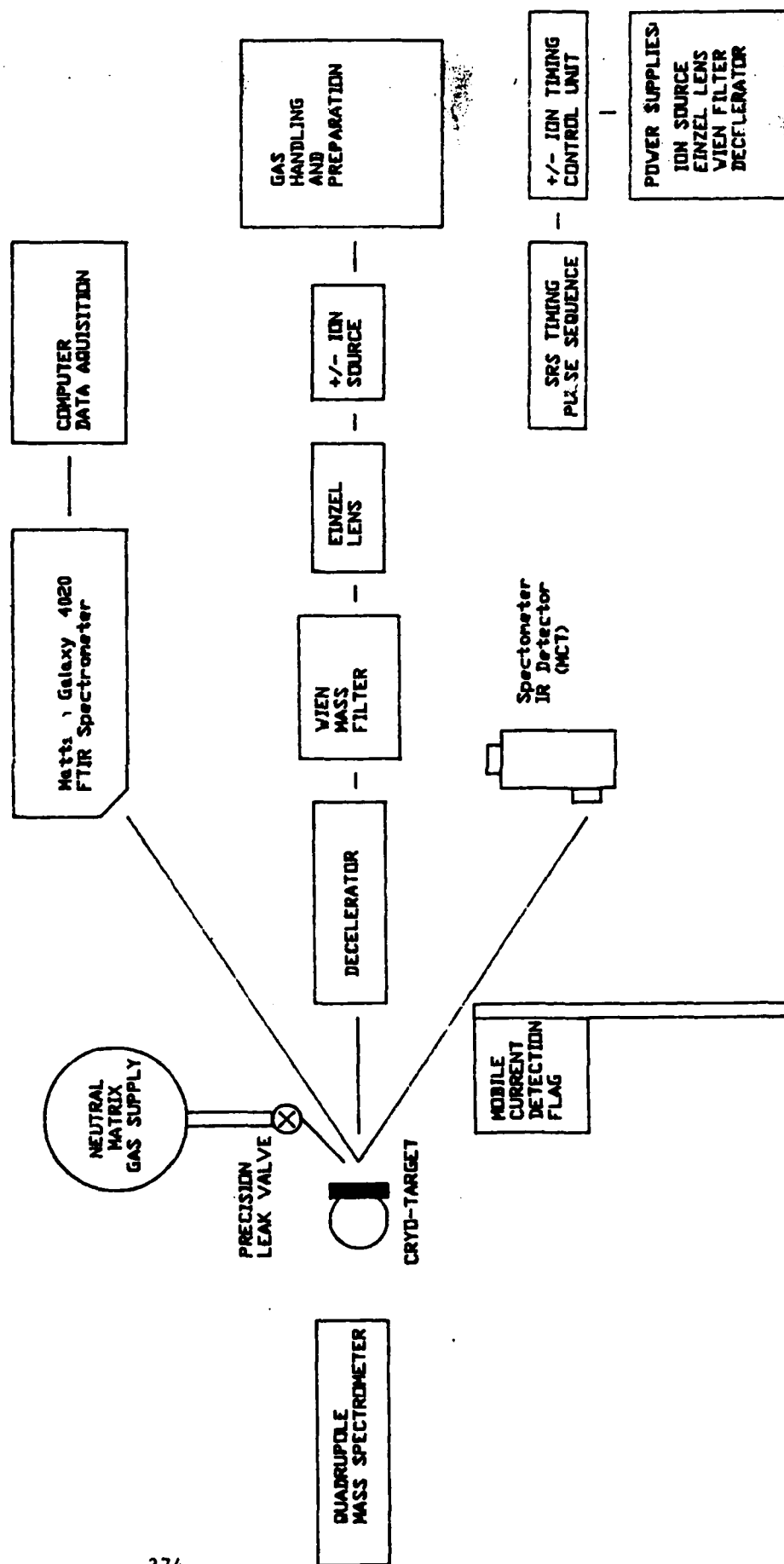
substrate. We placed our movable Faraday cup "flag" at various perimeter locations surrounding the copper substrate, to assure that the anion beam was not being deflected away. No measurable current (<1 picoAmp) could be detected at any of these locations, which indicated that the charges are in fact hitting the target. Contrary to experiment (2) where visible emission was observed, none was observed in this experiment. This difference may be explained by a smaller charge density as a result of the larger ion beam area on the target ($1-2 \text{ cm}^2$). In summary, the experimental observations are: a) we measure no free charges outside the target perimeter and nearly 10^{12} charges/sec just above the surface, b) we measure no current (+/-) at the matrix substrate, and c) no visible emission is observed. Since we do not monitor a loss process for the deposited cations, one could deduce that a large fraction are in fact being trapped. To assure ourselves that we are sensitive to measuring anion/cation currents at the substrate, near the end of this experiment the cation kinetic energy was increased from 10 to 50 and then to 100 eV. With 50 eV of kinetic energy we measure 5% of the beam current at the substrate, this value increases to nearly 40% when the ion kinetic energy is 100 eV.

At the very least these results show that several experimental refinements are necessary prior to developing cryogenic solids with large trapped charge densities. We intend to upgrade our FTIR to 0.1 cm^{-1} , modify our ion optics to allow higher current throughput, and consider using more sensitive spectroscopic techniques. It must be mentioned that other established techniques do exist for preparing and trapping of ionic species in cryogenic matrices. With these techniques it is possible to generate sufficient densities for spectroscopic study. We are trying to develop a new approach where each deposited layer is carefully controlled, and if successful, it could be used in developing a host of condensed phase cryogenic fuels.

ACKNOWLEDGMENTS

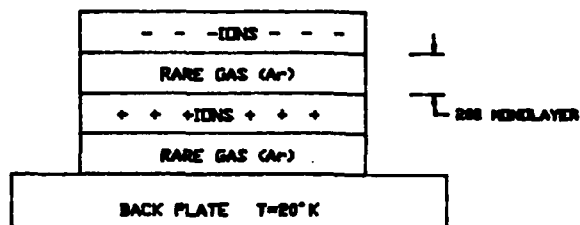
We thank Mattson instruments for temporarily providing us a demonstration instrument for these preliminary studies.

Experimental Setup



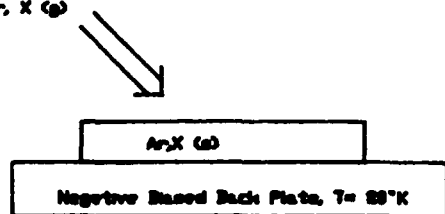
EXPERIMENTAL SCHEMES TO TRAP IONS IN SOLID ARGON

1) CHARGED LAYERS: ANION - RARE GAS - CATION "MOLECULAR CAPACITOR"



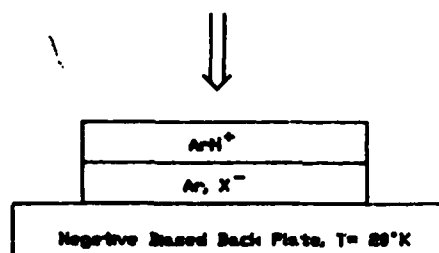
2) DIRECT ION DEPOSITION

■ CV Deposition
Ar, X (g)



Initial Layer
X= O₂, SF₆

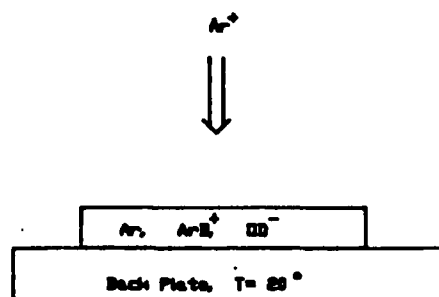
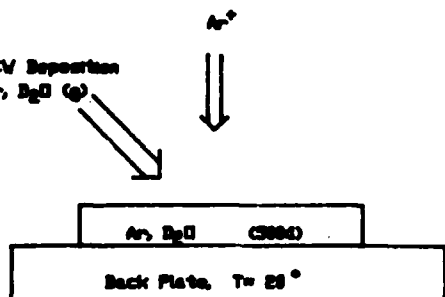
ArH⁺



Counter Ion Formed by
Electron Scavenging
X= O₂, SF₆

3) INSITU ION CHARGE TRANSFER CHEMISTRY

■ CV Deposition
Ar, BpO (g)



MAGNETO CIRCULAR DICHROISM (MCD) SPECTROSCOPY OF CRYOGENIC METAL-CONTAINING MATRICES PREPARED BY LASER ABLATION

John W. Kenney, III
Department of Physical Sciences--Chemistry
Eastern New Mexico University
Portales, New Mexico 88130

High Energy Density Metals in Rocket Propulsion:

It has been known for some time that significant increases in the specific impulses (I_{sp}) of rocket propellants may be achieved by incorporating small amounts of finely divided metal powders content into the propellant. Metal additive research has focused primarily on the energetic low mass metals Li, Be, and Al (1-6). Technical complexities associated with the practical implementation of such [liquid/solid fuel]-[metal powder]-[liquid/solid oxidizer] tripropellant systems have forestalled their adoption. Moreover, the use of metal powders as rocket fuel additives suffers from a fundamental thermodynamic constraint; crystal lattice forces must be overcome in the metal powder before it can react with the fuel and oxidizer. The large endothermic ΔH_{vap} for the metal additive (Li--146 kJ/mol, Be--292 kJ/mol, Al--293 kJ/mol) diminishes the net exothermic ΔH for the chemical reaction that produces rocket propulsion and consequently reduces the I_{sp} from the value it would have if the energetic metal additive could be introduced as a vapor rather than as a powdered solid.

One way to diminish the I_{sp} loss arising from the ΔH_{vap} penalty due to the additive is to trap the additive in dispersed form (e.g., individual metal atoms, dimers, trimers, or small clusters) in a cryogenically-cooled solid fuel matrix or to dissolve the additive in the fuel itself (6). This advantage arises because the weak attractive forces between the additive and the matrix or the fuel are much smaller than the lattice forces in the solid additive. It is also possible, in principle, to trap the metal additive in energetic metastable lattice sites in a condensed fuel and hence build in additional metastable lattice energy content. These concepts have been the subjects of a number of recent theoretical and experimental studies on the preparation, stability, and energy content of alkali metal--solid hydrogen cryogenic matrices, especially Li--H₂ (s) (5).

Laser Ablation to Produce High-Energy-Content Cryogenic Metal-Containing Matrices

Experimentalists seeking to produce cryogenic matrices containing small amounts of dispersed metal atoms for rocket propellant enhancement studies have drawn upon the rich literature of matrix isolation spectroscopy for fundamental spectroscopic and thermodynamic data and for those basic experimental techniques used to produce metal-containing cryogenic matrices (7-34). Almost all reported examples of matrix-isolated metal atoms were produced by co-depositing metal vapor from a Knudsen oven cavity together with the chosen matrix gas(es) onto a cryogenically cooled window (see for example Refs. 11-12). The kinetic energy range of the metal atoms effusing from a Knudsen oven is well approximated by a Maxwell-Boltzmann energy distribution at the oven temperature. In the case of Li, a typical kinetic energy for atoms effusing from a 750 K oven is on the order of 0.1 eV. An alternative and highly promising method for producing matrix isolated metal atoms in unusual metastable trapping sites--of potential significance in propulsion energy storage technology--utilizes a high-power laser with incident intensity near the metal's plasma production threshold to ablate the metal surface to produce a high-kinetic-energy metal vapor plume (0-20 eV range with typical energies of 1-5 eV) (37-38). Recent

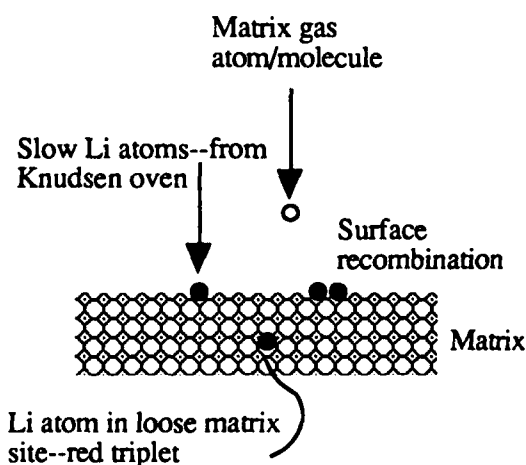


FIGURE 1A. Metal-guest matrix formation by Knudsen oven effusion.

spectroscopic studies on laser-ablated Li atoms trapped in Ar lattices show clear evidence of the elusive "blue triplet" absorption feature. The "blue triplet" is attributed to the production of unusual, higher energy trapping sites not observed in Li/Ar matrices produced with Knudsen-oven-generated Li vapor (37-38). These sites give a "red triplet" absorption feature.

To assess the significance of the laser ablation technique, it is necessary to compare the dynamics of metal-guest/matrix-host formation for metal vapor streams generated by laser ablation and by the Knudsen oven method. The key to the interpretation of the observed differences lies in the order-of-magnitude difference between the translational kinetic energy distributions of the metal vapors generated by the two methods (37). Studies of the dynamics of the matrix deposition process indicate that the thermal load associated with the collision of room temperature matrix gas molecules with the surface of the matrix effectively induces surface heating.

Consequently, all surface species (i.e., both matrix molecules and trapped metal atoms) experience increased thermally-induced mobility. During the cool-down and crystallization of the metal-containing matrix, it is expected that slow metal atoms from a Knudsen source will be stopped in the surface layer where they will have the opportunity to find stable trapping sites in the matrix host (see Figure 1A). In contrast, the fast Li atoms in the plume emanating from the laser ablated metal surface have sufficient kinetic energy to burrow deeply into the matrix and to access more energetic (i.e., tighter) trapping sites by virtue of this energy (see Figure 1B). Moreover, the deep penetration puts these metal atoms well beyond the mobile surface layers of the matrix and hence protects them from surface recombination reactions that can ultimately lead to undesired metal cluster formation. The matrix can be loaded with a significantly higher percentage of trapped atomic Li before recombination occurs (37). At this point much remains unknown about the details of these new trapping sites. Recently acquired experimental data on the laser ablation technique conclusively shows that it is possible to use the technique to trap Li in cryogenic matrices of Ne and D₂ (37).

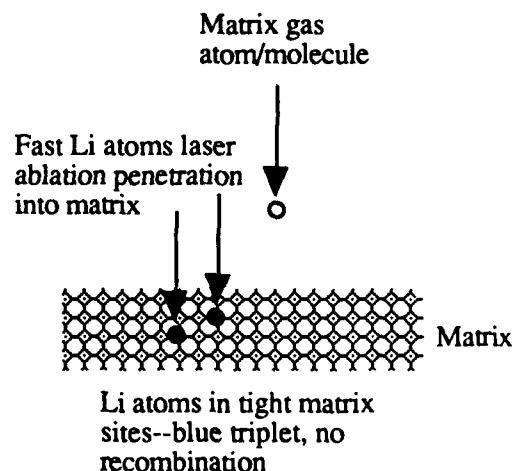


FIGURE 1B. Metal-guest matrix formation by laser ablation.

Spectroscopic Probes of Metal Containing Matrices: Magneto Circular Dichroism (MCD)

Metals isolated in cryogenic hosts by the matrix isolation technique have been studied primarily by infrared (IR) and Raman spectroscopy, electron spin resonance (ESR) spectroscopy, electronic absorption and luminescence spectroscopy, and MCD spectroscopy (7-34,39-67). Each of these spectroscopic probes yields unique insights into the nature of the interactions between the isolated metal atom and its host lattice. Of particular significance is the recent adaptation of MCD technology to matrix isolation experiments at liquid helium temperatures and above (1.8-20 K) (46-57). This has allowed the powerful theoretical formalism of MCD (39-45) to be used to extract crucially significant and hitherto inaccessible spectroscopic, structural, and dynamic observables from matrix-isolated systems. MCD experiments, coupled with the appropriate theoretical interpretations, have been utilized as evidence for--and in some cases to discriminate between-- Jahn-Teller interactions, spin-orbit coupling interactions, and single vs. multiple trapping site models of metal atom--matrix interactions (58-67). This is precisely the type of information needed to probe the details of novel matrix environments where unusual trapping sites and host--guest interactions are being produced by using laser ablation to generate high-energy metal vapors. The utility of MCD spectroscopy lies in the fact that it is a "signed" spectroscopy which measures the exceedingly small absorbance differences between left and right circularly polarized light as a function of photon energy (i.e., wavelength) (39-45). The relevant normalized MCD spectral plot is $\Delta A(\lambda)/A(\lambda)$ where $\Delta A(\lambda) = A_L(\lambda) - A_R(\lambda)$. High-resolution MCD instruments using the dynamic polarization measurement techniques based upon the photoelastic modulator (PEM) with lock-in detection routinely can

resolve $\Delta A/A$ values on the order of 10^{-6} (68-81). These small differences in a sample's capacity to absorb left and right circularly polarized light are highly sensitive to subtle details in the microscopic environment of the absorbing chromophore(s) (e.g., host-guest interactions, trapping sites, surface effects, vibronic and phonon modes, spin-orbit coupling, Jahn-Teller distortions, etc.) and to external macroscopic environmental factors such as temperature, magnetic field strength, and crystal or matrix orientation (58-67).

RESEARCH GOALS

The primary goal of this research program is to apply highly sensitive MCD spectroscopic methods to the analysis of cryogenic matrices prepared by co-depositing matrix gases with small quantities of energetic laser-ablated Li atoms. While laser ablative generation of energetic metal vapor plumes for use in matrix isolation experiments is straightforward experimentally and MCD spectroscopy on cryogenic matrix-isolated metal atoms is well established at sophisticated levels of experimental design and theoretical interpretation, the two methods have not yet been used together. An important secondary goal of this research program is, therefore, to develop the specifics of the new experimental protocols needed to combine MCD spectroscopy with laser ablative metal vapor deposition techniques. The MCD data will be used in conjunction with theoretical models of metal-matrix interactions (37) currently under development at the Astronautics laboratory to probe the details of unusual, high-energy metal trapping sites of potential importance in propulsion energy storage technology. Experiments designed to produce such trapping sites for metal-guest atoms in noble gas host matrices will be followed up with experiments at very low temperature (1.8 K) using pure hydrogen, and hydrogen-noble gas mixtures. Some MCD-ablative matrix isolation studies will be carried out with selected metals other than Li (e.g., Na, Al, Mg) and/or with selected heavier energetic matrix-host molecules (e.g., N_2H_2 , HN_3 , NH_3). Each MCD-ablative matrix isolation study involving a particular choice of metal-guest-matrix host will be checked against a control study in the same apparatus under the same conditions using Knudsen-oven-generated metal atoms. Breakthrough experiments will be designed to look in detail at new phenomena from the perspective of MCD spectroscopy: e.g., the ablative generation and observation of missing "blue triplets" associated with the trapping of energetic metal atoms in tight binding sites in the light noble gases, the trapping of Li in hydrogen and hydrogen-noble gas mixtures, the possible "deep" trapping of Li in the hydrogen layer of a stratified matrix covered over by a noble gas crust layer that acts to dissipate some of the kinetic energy of the fast ablatively-generated Li atoms (see Figure 2), the effects of thermal annealing of metal-containing matrices generated by laser ablation at very low temperatures.

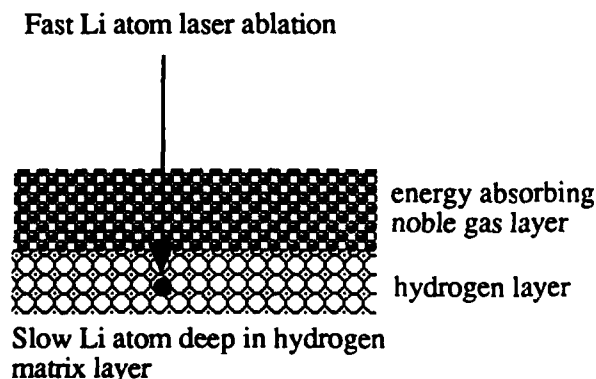


FIGURE 2. Laser ablation into a stratified matrix with a moderating outer layer

Experiments designed to produce such trapping sites for metal-guest atoms in noble gas host matrices will be followed up with experiments at very low temperature (1.8 K) using pure hydrogen, and hydrogen-noble gas mixtures. Some MCD-ablative matrix isolation studies will be carried out with selected metals other than Li (e.g., Na, Al, Mg) and/or with selected heavier energetic matrix-host molecules (e.g., N_2H_2 , HN_3 , NH_3). Each MCD-ablative matrix isolation study involving a particular choice of metal-guest-matrix host will be checked against a control study in the same apparatus under the same conditions using Knudsen-oven-generated metal atoms. Breakthrough experiments will be designed to look in detail at new phenomena from the perspective of MCD spectroscopy: e.g., the ablative generation and observation of missing "blue triplets" associated with the trapping of energetic metal atoms in tight binding sites in the light noble gases, the trapping of Li in hydrogen and hydrogen-noble gas mixtures, the possible "deep" trapping of Li in the hydrogen layer of a stratified matrix covered over by a noble gas crust layer that acts to dissipate some of the kinetic energy of the fast ablatively-generated Li atoms (see Figure 2), the effects of thermal annealing of metal-containing matrices generated by laser ablation at very low temperatures.

REFERENCES

I_{sp} Enhancement via Energetic Metal Additives to Rocket Fuels

1. Gordon, L.J.; Lee, J.B. *J. Am. Rocket Soc.* **1962**, *32*, 600.
2. Siegal, B.; Schieler, L. *Energetics of Propellant Chemistry*; Wiley: New York, 1964.
3. Herm, R.R. "Metastable Metal in Matrix Materials"; Research Proposal; The Aerospace Corporation: Los Angeles, 1986.
4. Kit, B.; Evered, D.S. *Rocket Propellant Handbook*; Macmillan: New York, 1960.
5. Konowalow, D.D. *Proceedings of the High Energy Density Matter (HEDM) Conference*; New Orleans, LA, 1989, pp 251-258.
6. Pritt, A.T., Jr.; Presser, N.; Herm, R.R. *Proceedings of the High Energy Density Matter (HEDM) Conference*; New Orleans, LA, 1989, pp 245-249.

Metal-Guest Matrix Isolation Spectroscopy

7. Jen, C.K.; Bowers, V.A.; Cochran, E.L.; Foner, S.N. *Phys. Rev.* **1962**, *126*, 1749.
8. Smith, D.Y. *Phys. Rev.* **1964**, *133*, A1087.
9. Meyer, B. *J. Chem. Phys.* **1965**, *43*, 2986.
10. Weyhmann, W.; Pipkin, F.M. *Phys. Rev.* **1965**, *137*, A490.
11. Lester, W.; Andrews, S.; Pimentel, G.C. *J. Chem. Phys.* **1966**, *44*, 2361.
12. Andrews, L.; Pimentel, G.C. *J. Chem. Phys.* **1967**, *47*, 2905.
13. Belyaeva, A.A.; Predtechenskii, Y.B.; Shcherba, L.D. *Opt. Spectrosc.* **1968**, *24*, 233.
14. Meyer, B. *Low Temperature Spectroscopy*; Elsevier: New York, 1971.
15. Belyaeva, A.A.; Predtechenskii, Y.B.; Shcherba, L.D. *Opt. Spectrosc.* **1973**, *24*, 21.
16. Pimentel, G.C. *Angew. Chem. internat. Edit.* **1975**, *14*, 199.
17. Balling, L.C.; Havey, M.D.; Dawson, J.F. *J. Chem. Phys.* **1978**, *69*, 1670.
18. Welker, T.; Martin, T.P. *J. Chem. Phys.* **1979**, *70*, 5683.
19. Hofmann, M.; Leutwyler, S. *Chem. Phys.* **1979**, *40*, 145.
20. Dawson, J.F.; Balling, L.C. *J. Chem. Phys.* **1979**, *71*, 836.
21. Balling, L.C.; Dawson, J.F.; Havey, M.D.; Wright, J.J. *Phys. Rev. Lett.* **1979**, *43*, 435.
22. Wright, J.J.; Balling, L.C. *J. Chem. Phys.* **1980**, *73*, 994.
23. Wright, J.J.; Balling, L.C. *J. Chem. Phys.* **1980**, *73*, 3103.
24. Ossicini, S.; Forstmann, F. *J. Chem. Phys.* **1981**, *75*, 2076.
25. Mehreteab, A.; Andrews, J.R.; Smith, A.B., III; Hochstrasser, R.M. *J. Phys. Chem.* **1982**, *86*, 888.
26. Ossicini, S.; Forstmann, F. *Il Nuovo Cimento* **1982**, *1D*, 688.
27. Hormes, J.; Karrasch, B. *Chem. Phys.* **1982**, *70*, 29.
28. Wright, J.J.; Balling, L.C. *J. Chem. Phys.* **1983**, *79*, 2941.
29. Schwentner, N.; Koch, E.-E.; Jortner, J. *Electronic Excitations in Condensed Rare Gases*; Springer-Verlag: New York, 1985.
30. Schwentner, N.; Chergui, M. *J. Chem. Phys.* **1986**, *85*, 3458.
31. Lindsay, D.M.; Thompson, G.A.; Wang, Y. *J. Phys. Chem.* **1987**, *91*, 2630.
32. Howard, J.A.; Mile, B. *Acc. Chem. Res.* **1987**, *20*, 173.
33. Krishnan, C.N.; Hauge, R.H.; Margrave, J.L. *J. Mol. Structure* **1987**, *157*, 187.
34. Presser, N.; Pritt, A.T., Jr.; Herm, R.R. *Proceedings of the High Energy Density Matter (HEDM) Conference*; New Orleans, LA, 1989, pp 267-270.

Metal Deposition Techniques: Laser Ablation

35. Ready, J.F. *Effects of High-Power Laser Radiation*; Academic Press: New York, 1971.
36. Freechtenicht, J.F. *Rev. Sci. Instrum.* **1974**, *45*, 51.
37. Fajardo, M.E. *Proceedings of the High Energy Density Matter (HEDM) Conference*; New Orleans, LA, 1989, pp 259-266 and *Proceedings of the High Energy Density Matter (HEDM) Conference*; Long Beach, CA, 1990.
38. Fajardo, M.E.; Carrick, P.; Kenney, J.W., III to be published.

Theory of MCD

39. Serber, R. *Phys. Rev.* **1932**, *41*, 489.
40. Buckingham, A.D.; Stephens, P.J. In *Annual Review of Physical Chemistry*; Eyring, H; Christensen, C.J.; Johnston, H.S., Eds.; Annual Reviews: Palo Alto, CA, 1966; Vol. 17, p 399.
41. Caldwell, D.; Thorne, J.M.; Eyring, H. In *Annual Review of Physical Chemistry*; Eyring, H; Christensen, C.J.; Johnston, H.S., Eds.; Annual Reviews: Palo Alto, CA, 1971; Vol. 22, p 259.
42. Stephens, P.J. In *Annual Review of Physical Chemistry*; Eyring, H; Christensen, C.J.; Johnston, H.S., Eds.; Annual Reviews: Palo Alto, CA, 1974; Vol. 25, p 201.
43. Richardson, F.; Riehl, J.P. *Chem. Rev.* **1977**, *77*, 773.
44. Piepho, S.B.; Schatz, P.N. *Group Theory in Spectroscopy with Applications to Magnetic Circular Dichroism*; Wiley: New York, 1983.
45. Riehl, J.P.; Richardson, F. *Chem. Rev.* **1986**, *86*, 1.

MCD of Matrix-Isolated Species

46. Douglas, I.N.; Grinter, R.; Thomson, A.J. *Chem. Phys. Lett.* **1974**, *28*, 192.
47. Douglas, I.N.; Grinter, R.; Thomson, A.J. *Mol. Phys.* **1974**, *28*, 1377.
48. Barton, T.J.; Douglas, I.N.; Grinter, R.; Thomson, A.J. *Mol. Phys.* **1975**, *30*, 1677.
49. Barton, T.J.; Grinter, R.; Thomson, A.J. *Chem. Phys. Lett.* **1976**, *40*, 399.
50. Barton, T.J.; Douglas, I.N.; Grinter, R.; Thomson, A.J. *Ber. Bunsenges. Phys. Chem.* **1976**, *80*, 202.
51. Goetschalckx, M.A.; Mowery, R.L.; Krausz, E.R.; Yeakel, W.C.; Schatz, P.N.; Ault, B.S.; Andrews, L. *Chem. Phys. Lett.* **1977**, *47*, 23.
52. Krausz, E.R.; Mowery, R.L.; Schatz, P.N. *Ber. Bunsenges. Phys. Chem.* **1978**, *82*, 134.
53. Brittain, R.; Powell, D.; Voigtman, E.; Vala, M. *Rev. Sci. Instrum.* **1980**, *51*, 905.
54. Schlosser, D.W.; Devlin, F.; Jalkanen, K.; Stephens, P.J. *Chem. Phys. Lett.* **1982**, *88*, 286.
55. Lund, P.A.; Hasan, Z.; Schatz, P.N.; Miller, J.H.; Andrews, L. *Chem. Phys. Lett.* **1982**, *91*, 437.
56. Nyokong, T.; Gasyna, Z.; Stillman, M.J. *Inorg. Chem.* **1987**, *26*, 548.
57. Nyokong, T.; Gasyna, Z.; Stillman, M.J. *Inorg. Chem.* **1987**, *26*, 1087.

MCD of Matrix-Isolated Alkali, Alkaline Earth, Transition, and Main Group Metals

58. Mowery, R.L.; Miller, J.C.; Krausz, E.R.; Schatz, P.N.; Jacobs, S.M.; Andrews, L. *J. Chem. Phys.* **1979**, *70*, 3920.
59. Miller, J.C.; Mowery, R.L.; Krausz, E.R.; Jacobs, S.M.; Kim, H.W.; Schatz, P.N.; Andrews, L. *J. Chem. Phys.* **1981**, *74*, 6349.
60. Grinter, R.; Stern, D.R. *J. Mol. Structure* **1982**, *80*, 147.
61. Hormes, J.; Grinter, R.; Breithaupt, B.; Kolb, D.M. *J. Chem. Phys.* **1983**, *78*, 158.
62. Vala, M.; Zeringue, K.; ShakhEmampour, J.; Rivoal, J.-C.; Pyzalski, R. *J. Chem. Phys.* **1984**, *80*, 2401.
63. Lund, P.A.; Smith, D.; Jacobs, S.M.; Schatz, P.N. *J. Phys. Chem.* **1984**, *88*, 31.
64. Rose, J.; Smith, D.; Williamson, B.E.; Schatz, P.N.; O'Brien, M.C.M. *J. Phys. Chem.* **1986**, *90*, 2608.
65. Grinter, R.; Singer, R.J. *Chem. Phys.* **1987**, *113*, 87.
66. Samet, C.; Rose, J.L.; Williamson, B.E.; Schatz, P.N. *Chem. Phys. Lett.* **1987**, *142*, 557.
67. VanCott, T.C.; Rose, J.L.; Misener, G.C.; Williamson, B.E.; Schrimpf, A.E.; Boyle, M.E.; Schatz, P.N. *J. Phys. Chem.* **1989**, *93*, 2999.

High Pressure Burn Rate Studies
in a Diamond Anvil Cell*

Steven F. Rice
and
M. Frances Foltz

Energetic Materials Section
Dept. of Chemistry
Lawrence Livermore National Laboratory
P.O.B. 808 Livermore, CA 94550

Motivation:

All high energy density systems are, of course, condensed phase materials. More importantly, many of the applications of these chemical systems involve chemical reaction not at ambient conditions, but at very high pressure and temperature. It is the reaction characteristics (pathways and rates) under unusually severe conditions that must be understood to develop a predictive model of energetic material sensitivity and performance.

Our goal is to generate a fundamental understanding of the relationship between composition, sensitivity, and performance of high explosives and propellants. As chemists, this issue motivates a coupled theoretical and experimental investigation into the nature of the chemical bond in a very hot, dense environment.

Approach:

We have developed a technique combining low energy pulsed laser ignition of an energetic sample within a diamond anvil cell and streak camera detection of the ensuing high speed propagation of the chemical reaction front. The technique is general to many energetic materials, but only nitromethane has been studied to date. We have identified three different reaction product pressure regimes from 0 - 40 GPa. An unusual variation in the condensed phase "flame" propagation rate has been observed. Efforts to computationally simulate these results have identified a number of crucial material and molecular properties which control the overall front propagation rate.

* Work performed under the auspices of the U.S. Department of Energy by the Lawrence Livermore National Laboratory under contract No. W-7405-ENG-48.

Experimental Results:

The diamond anvil cell (DAC) affords a unique environment for the study of high density chemical systems. The design used in our laboratory is capable of 40 GPa at room temperature, and greater than 20 GPa when heated in a furnace to as high as 900 K. Small samples of nitromethane and other energetic materials (0.2 mm diameter, 0.05 mm thick) are easily raised to these high pressures and then ignited with a 10 microjoule 532-nm pulse from a Q-switched Nd:YAG laser. Once ignited, the sample deflagrates (time scale of about 20 microseconds) in a well defined way, characterized by the propagation of the burn front outward from the 0.006 mm diameter ignition point.

The sample is illuminated with light from an argon ion laser and the optical transmission properties are recorded by a streak camera. The propagation of the reaction front has an easily discerned disturbance on the transmission of the speckle pattern of the focused ion laser. This disturbance is seen to propagate at a constant velocity for a given pressure. This "flame" front propagation rate varies from a few meters per second at 0.5 GPa to near 100 m/s at 30 GPa. At pressures above 30 GPa the propagation rate begins to slow down to as low as 40 m/s at 40.8 GPa, the current experimental limit of our apparatus.

The detailed characteristics of the overall transmission properties of the reaction intermediates and products are also recorded. There are three distinct reaction product regimes. In the pressure range of 0 to 5 GPa, the products are gases that vent from within the cell and a white oily solid. From about 5 GPa to 20 GPa the products are gases that vent, but the solid residue is a very dark sooty material. As pressure is increased from 3 to 7 GPa the residue becomes darker. Above 20 GPa there is a abrupt change in the product composition. The laser initiated micro-explosion results in no apparent product gases. The product is a clear compressed fluid which transforms to a white crystalline solid when the pressure on the sample is released. We are beginning efforts to better identify the composition of these residues. This has been difficult so far due to the very small amount of sample (about 1×10^{-6} g).

Discussion:

This large variation in the burn velocity as a function of pressure and the dramatic changes in the reaction products for nitromethane deflagration illustrate an important point. Not only may the reaction characteristics of an energetic molecule change a great deal from the gas phase to the condensed phase, but also increases in density beyond ambient conditions can have a profound effect on a variety of properties. These include reaction rates and the overall amount of energy released.

We have begun an effort to theoretically model, or simulate, this reaction front propagation phenomenon. We use a finite element heat transport code, TOPAZCHEM, that has the added versatility of including heat releasing chemical reactions and a temperature dependence of material properties such as heat capacity and thermal conductivity. With simple single step Arrhenius reaction kinetics and material property values obtained from available sources, these calculations have been successful in reproducing condensed phase "flame" rates in the velocity range we have observed. This modeling, although still at a very early stage, shows great promise in illuminating the relationship between condensed phase molecular reactivity and bulk properties of energetic materials such as detonation velocity and initiation sensitivity.

Although the pressures present in these experiments are very high, the densities obtained with the diamond anvil cell are precisely in the range found during shock initiation and detonation of a high explosive. Issues involving these processes are not only limited to concerns regarding the performance of an explosive, but also are central to the need for an improved understanding of hazards related to detonation sensitivity in high performance propellants.

